WOODHEAD PUBLISHING SERIES IN ELECTRONIC AND OPTICAL MATERIALS

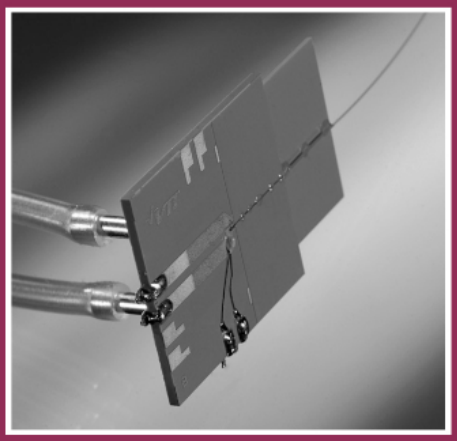

Printed films

Material science and applications in sensors, electronics and photonics

Edited by Maria Prudenziati and Jacob Hormadaly

WP
WOODHEAD PUBLISHING

Printed films

© Woodhead Publishing Limited, 2012

Related titles:

Electromigration in thin films and electronic devices: Materials and reliability
(ISBN 978-1-84569-937-6)
Electromigration is a significant problem affecting the reliability of microelectronic devices such as integrated circuits. Recent research has focused on how electromigration affects the increasing use by the microelectronics industry of lead-free solders and copper interconnects. Part I reviews ways of modelling and testing electromigration, Part II discusses electromigration in copper interconnects and Part III covers solder and wirebonds.

In situ *characterization of thin film growth*
(ISBN 978-1-84569-934-5)
Recent advances in techniques to characterize thin films *in situ* during deposition could lead to an improved understanding of deposition processes and to better, faster diagnosis of issues with the deposition process. In situ *characterization of thin film growth* provides a comprehensive review of this increasingly important topic. Part I reviews electron diffraction techniques, including the methodology for taking observations and measurements. Part II covers photoemission techniques; the principles and instrumentation. Part III contains alternative *in situ* characterization techniques and the trend for combining different techniques. It covers real-time characterization of the nucleation, growth, structural and electronic properties of thin films.

Thin film growth: Physics, materials science and applications
(ISBN 978-1-84569-736-5)
Thin film technology is used in the application of microelectronics, optics, magnetics, hard and corrosion resistant coatings and micromechanics, among others. This book provides a review of the theory and techniques for the deposition of thin films. *Thin film growth* will help the reader understand the variables affecting growth kinetics and microstructural evolution during deposition. Part I covers the theory and modelling of thin film growth whilst Part II describes the techniques and mechanisms of film growth. This section covers examples such as silicon nanostructured thin films, colloidal crystal thin films and graphene thin films. It also contains discussion of pliable substrates and thin films for particular functions.

Details of these and other Woodhead Publishing books can be obtained by:

- visiting our web site at www.woodheadpublishing.com
- contacting Customer Services (e-mail: sales@woodheadpublishing.com; fax: +44 (0) 1223 832819; tel.: +44 (0) 1223 499140 ext. 130; address: Woodhead Publishing Limited, 80 High Street, Sawston, Cambridge CB22 3HJ, UK)
- contacting our US office (e-mail: usmarketing@woodheadpublishing.com; tel. +1 (215) 928 9112; address: Woodhead Publishing, 1518 Walnut Street, Suite 1100, Philadelphia, PA 19102-3406, USA)

If you would like e-versions of our content, please visit our online platform: www.woodheadpublishingonline.com. Please recommend it to your librarian so that everyone in your institution can benefit from the wealth of content on the site.

© Woodhead Publishing Limited, 2012

Woodhead Publishing Series in Electronic and Optical Materials:
Number 26

Printed films

Materials science and applications in sensors, electronics and photonics

Edited by
Maria Prudenziati and Jacob Hormadaly

Oxford Cambridge Philadelphia New Delhi

© Woodhead Publishing Limited, 2012

Published by Woodhead Publishing Limited,
80 High Street, Sawston, Cambridge CB22 3HJ, UK
www.woodheadpublishing.com
www.woodheadpublishingonline.com

Woodhead Publishing, 1518 Walnut Street, Suite 1100, Philadelphia,
PA 19102-3406, USA

Woodhead Publishing India Private Limited, G-2, Vardaan House,
7/28 Ansari Road, Daryaganj, New Delhi – 110002, India
www.woodheadpublishingindia.com

First published 2012, Woodhead Publishing Limited
© Woodhead Publishing Limited, 2012
The authors have asserted their moral rights.

This book contains information obtained from authentic and highly regarded sources. Reprinted material is quoted with permission, and sources are indicated. Reasonable efforts have been made to publish reliable data and information, but the authors and the publishers cannot assume responsibility for the validity of all materials. Neither the authors nor the publishers, nor anyone else associated with this publication, shall be liable for any loss, damage or liability directly or indirectly caused or alleged to be caused by this book.

Neither this book nor any part may be reproduced or transmitted in any form or by any means, electronic or mechanical, including photocopying, microfilming and recording, or by any information storage or retrieval system, without permission in writing from Woodhead Publishing Limited.

The consent of Woodhead Publishing Limited does not extend to copying for general distribution, for promotion, for creating new works, or for resale. Specific permission must be obtained in writing from Woodhead Publishing Limited for such copying.

Trademark notice: Product or corporate names may be trademarks or registered trademarks, and are used only for identification and explanation, without intent to infringe.

British Library Cataloguing in Publication Data
A catalogue record for this book is available from the British Library.

Library of Congress Control Number: 2012938839

ISBN 978-1-84569-988-8 (print)
ISBN 978-0-85709-621-0 (online)
ISSN 2050-1501 Woodhead Publishing Series in Electronic and Optical Materials (print)
ISSN 2050-151X Woodhead Publishing Series in Electronic and Optical Materials (online)

The publisher's policy is to use permanent paper from mills that operate a sustainable forestry policy, and which has been manufactured from pulp which is processed using acid-free and elemental chlorine-free practices. Furthermore, the publisher ensures that the text paper and cover board used have met acceptable environmental accreditation standards.

Typeset by RefineCatch Limited, Bungay, Suffolk
Printed by TJ International Ltd, Padstow, Cornwall, UK

© Woodhead Publishing Limited, 2012

Contents

Contributor contact details *xi*
Woodhead Publishing Series in Electronic and Optical Materials *xv*
Preface *xxi*

Part I Materials and properties of printed films 1

1 Technologies for printed films 3
M. Prudenziati, University of Modena and Reggio Emilia, Italy and J. Hormadaly, Ben-Gurion University, Israel

1.1 Introduction: printed films in microelectronics 3
1.2 From thick-films and hybrids to printed electronics 7
1.3 Other systems 24
1.4 Conclusion 26
1.5 References 26

2 Materials for printed films 30
J. Hormadaly, Ben-Gurion University, Israel and M. Prudenziati, University of Modena and Reggio Emilia, Italy

2.1 Introduction 30
2.2 Active phases 31
2.3 Deposition medium – vehicle 46
2.4 Glasses and glass ceramics 48
2.5 Substrates 50
2.6 Conclusion 51
2.7 References 51

3 Materials Science concepts for printed films 63
J. Hormadaly, Ben-Gurion University, Israel and M. Prudenziati, University of Modena and Reggio Emilia, Italy

3.1 Introduction 63

© Woodhead Publishing Limited, 2012

3.2 Interactions of conducting materials with the organic vehicle at room temperature 65
3.3 Redox reactions 65
3.4 Chemical diffusion-related interactions during the firing cycle 70
3.5 Sintering, grain growth and Ostwald ripening 80
3.6 Reactivity interactions in other systems 82
3.7 The Kirkendall effect 83
3.8 Conclusions and future trends 83
3.9 Sources of further information 84
3.10 References 84

4 Properties of printed films as electrical components and metallization of solar cells 90
J. HORMADALY, Ben-Gurion University, Israel and M. PRUDENZIATI, University of Modena and Reggio Emilia, Italy

4.1 Introduction 90
4.2 Thick-film resistors 91
4.3 Conductors 99
4.4 Dielectrics 106
4.5 References 108

5 Conduction mechanisms in printed thick-film resistors 112
C. GRIMALDI, École Polytechnique Fédérale de Lausanne, Switzerland

5.1 Introduction 112
5.2 Current understanding of the conduction mechanisms in thick-film resistors 114
5.3 Conclusion and future trends 130
5.4 References 130

6 Multilayer low-temperature co-fired ceramic systems incorporating a thick-film printing process 134
M. SOBOCINSKI, J. PUTAALA, and H. JANTUNEN, University of Oulu, Finland

6.1 Introduction 134
6.2 Low-temperature co-fired ceramic (LTCC) compositions 136
6.3 LTCC manufacturing methods 141
6.4 An overview of LTCC applications 150
6.5 Future trends 157
6.6 Sources of further information 157
6.7 References 158

© Woodhead Publishing Limited, 2012

Part II Applications of printed films in devices 165

7 Printed resistive sensors for physical quantities 167
M. Prudenziati, University of Modena and Reggio Emilia, Italy

7.1 Introduction 167
7.2 Temperature sensors 168
7.3 Piezoresistive properties and related sensors 174
7.4 Magnetoresistive effects and sensors 180
7.5 Radiant sensors 184
7.6 Potentiometric sensors 185
7.7 Conclusion and future trends 187
7.8 References 187

8 Printed thick-film capacitive sensors 193
V. Ferrari, University of Brescia, Italy and M. Prudenziati, University of Modena and Reggio Emilia, Italy

8.1 Introduction 193
8.2 General concepts 194
8.3 Configurations and technologies 195
8.4 Capacitive sensing based on geometrical variations 198
8.5 Capacitive sensing based on permittivity variations 203
8.6 Examples of devices and their applications 205
8.7 Conclusion and future trends 216
8.8 Sources of further information 217
8.9 References 218

9 Printed thick-film piezoelectric and pyroelectric sensors 221
V. Ferrari, University of Brescia, Italy

9.1 Introduction 221
9.2 Piezoelectricity, pyroelectricity and ferroelectricity 222
9.3 Basic theory and relationships of the piezoelectric effect 226
9.4 Thick-films based on ferroelectric inorganic compounds 228
9.5 Piezoelectric sensors 231
9.6 Pyroelectric sensors 243
9.7 Future trends 251
9.8 Sources of further information 252
9.9 Acknowledgments 252
9.10 References 252

10 Printed thick-film mechanical microsystems (MEMS) 259
S. P. Beeby, University of Southampton, UK

© Woodhead Publishing Limited, 2012

10.1 Introduction 259
10.2 Printed films with silicon MEMS 260
10.3 Printed films with ceramic MEMS 270
10.4 Conclusion and future trends 274
10.5 References 275

11 Printed semiconducting gas sensors 278
V. Guidi, C. Malagù, M. C. Carotta and B. Vendemiati, University of Ferrara, Italy

11.1 Introduction 278
11.2 Principles of operation and modeling 283
11.3 Functional materials 289
11.4 Morphological, structural and electrical properties 302
11.5 Applications 318
11.6 Future trends 324
11.7 Acknowledgments 325
11.8 References 325

12 Printed gas sensors based on electrolytes 335
C. Lucat, F. Menil and H. Debeda, University of Bordeaux, France

12.1 Introduction 335
12.2 Solid electrolytes 336
12.3 Potentiometric sensors 338
12.4 Thermodynamically controlled sensors 338
12.5 Sensors controlled by both thermodynamics and kinetics 352
12.6 Amperometric sensors 356
12.7 NO_x sensing device, associating upstream oxygen pumping with potentiometric and amperometric operating principles 360
12.8 Conclusion and possible future trends 361
12.9 References 362

13 Printed thick-film biosensors 366
K. C. Honeychurch, University of the West of England, UK

13.1 Introduction 366
13.2 Pharmaceutical and medical applications of thick-film biosensors 376
13.3 Environmental applications of screen-printed electrodes 388
13.4 Conclusions 399
13.5 Sources of further information 399
13.6 Acknowledgements 400
13.7 References 400

© Woodhead Publishing Limited, 2012

14 Printed actuators 410
R. A. Dorey and G. J. T. Leighton, Cranfield University, UK

14.1 Introduction 410
14.2 Films as actuators 410
14.3 Actuation mechanisms 412
14.4 Piezoelectric actuators 417
14.5 Piezoelectric actuator fabrication 419
14.6 Processing–properties–microstructure interrelationship 420
14.7 Conclusion and future trends 424
14.8 Further information and advice 426
14.9 References 426

15 Printed heater elements 429
G. Radosavljevic and W. Smetana, Vienna University of Technology, Austria

15.1 Introduction 429
15.2 Materials for heater fabrication 430
15.3 Heater designs 438
15.4 Heaters for sensor and actuator applications 455
15.5 Conclusion 466
15.6 References 466

16 Screen-printing for the fabrication of solid oxide fuel cells (SOFC) 469
C. Pijolat, École Nationale Supérieure des Mines, France

16.1 Introduction 469
16.2 Fuel cells: principle, types and challenges 469
16.3 Electrolytes 472
16.4 Electrodes 476
16.5 Single-chamber SOFCs 482
16.6 Micro single-chamber SOFCs 488
16.7 Conclusion and trends 492
16.8 References 492

17 Printed varistors 496
M. A. de la Rubia, Glass and Ceramic Institute (CSIC) and ETSI Telecommunication (UPM), Spain

17.1 Introduction 496
17.2 The varistor action 497
17.3 Composition, preparation and microstructure of ceramic ZnO-based varistors 502
17.4 Printing process in varistors fabrication 503
17.5 Multilayer varistors 504

© Woodhead Publishing Limited, 2012

17.6	Screen-printed and fired thick-film varistors	506
17.7	Progress in the development of ZnO-based thick-films and tape-casted varistors	507
17.8	Microstructural and electrical characterization of ZnO-based varistors prepared by screen printing and tape casting	510
17.9	Conclusion	521
17.10	Acknowledgements	522
17.11	References	522
18	Laser-printed micro- and meso-scale power generating devices A. Piqué, Naval Research Laboratory, USA	526
18.1	Introduction	526
18.2	Background to laser-induced forward transfer (LIFT)	528
18.3	Laser transfer of complex rheological systems	531
18.4	Laser-printed micro-power sources	532
18.5	Laser-printed embedded micro-power sources	542
18.6	Challenges and opportunities	543
18.7	Conclusion and future trends	544
18.8	Acknowledgements	545
18.9	References	545
19	Printed polymer solar cells M. Helgesen, M. Jørgensen, T. D. Nielsen and F. C. Krebs, Technical University of Denmark, Denmark	550
19.1	Introduction	550
19.2	Printing and coating methods	554
19.3	Manufacturing methods for complete polymer solar cells	557
19.4	Applications and demonstrations of polymer solar cells	562
19.5	Conclusions and future trends	572
19.6	Acknowledgements	573
19.7	References	573
	Index	*575*

© Woodhead Publishing Limited, 2012

Contributor contact details

(* = main contact)

Editors and chapters 1, 2, 3 and 4

M. Prudenziati
Department of Physics
University of Modena and Reggio Emilia
Via G. Campi, 213/A
41125 Modena
Italy
E-mail: maria.prudenziati@unimore.it

J. Hormadaly
Department of Chemistry
Ben-Gurion University
Hashalom #1
PO Box 653
Beer Sheva 84105
Israel
E-mail: hormadj@bgu.ac.il

Chapter 5

C. Grimaldi
Laboratoire de Production Microtechnique (LPM)
École Polytechnique Fédérale de Lausanne (EPFL)
Station 17
CH-1015 Lausanne
Switzerland
E-mail: claudio.grimaldi@epfl.ch

Chapter 6

M. Sobocinski*, J. Putaala and H. Jantunen
University of Oulu
Department of Electrical and Information Engineering
Microelectronics and Materials Physics Laboratories
PO Box 4500
FIN-90014 University of Oulu
Finland
E-mail: maciej.sobocinski@ee.oulu.fi; jussi.putaala@ee.oulu.fi; heli.jantunen@ee.oulu.fi

Chapter 7

M. Prudenziati
E-mail: maria.prudenziati@unimore.it

Chapters 8 and 9

V. Ferrari
Department of Information Engineering
University of Brescia
Via Branze 38
25123 Brescia
Italy
E-mail: vittorio.ferrari@ing.unibs.it

© Woodhead Publishing Limited, 2012

Chapter 10

S. P. Beeby
School of Electronics and Computer Science
University of Southampton
Highfield
Southampton
SO17 1BJ
UK
E-mail: spb@ecs.soton.ac.uk

Chapter 11

V. Guidi*, C. Malagu, M. C. Carotta and B. Vendemiati
University of Ferrara
Via Paradiso 12
I-44100 Ferrara
Italy
E-mail: guidi@fe.infn.it; malagu@fe.infn.it; carotta@fe.infn.it

Chapter 12

C. Lucat*, F. Menil and H. Debeda
University of Bordeaux
Laboratoire IMS
351 cours de la Libération
33405 TALENCE
France
E-mail: claude.lucat@ims-bordeaux.fr

Chapter 13

K. C. Honeychurch
Centre for Research in Biosciences
Faculty of Health and Life Sciences
University of the West of England
Frenchay Campus
Coldharbour Lane
Bristol
BS16 1QY
UK
E-mail: kevin.honeychurch@uwe.ac.uk

Chapter 14

G. J. T. Leighton and R. A. Dorey*
Building 70
Cranfield University
Cranfield
Bedfordshire
MK43 0AL
UK
E-mail: r.a.dorey@cranfield.ac.uk

Chapter 15

G. Radosavljevic and W. Smetana*
Institute of Sensor and Actuator Systems
Vienna University of Technology
Gusshausstrasse 27–29
1040 Wien
Austria
E-mail: goran.radosavljevic@tuwien.ac.at; walter.smetana@tuwien.ac.at

Chapter 16

C. Pijolat
École Nationale Supérieure des Mines
Département MICC, LPMG (UMR CNRS 5148) 158
Cours Fauriel
42023 Saint-Étienne Cedex 02
France
E-mail: cpijolat@emse.fr

Chapter 17

M. A. de la Rubia
Electroceramic Department
Glass and Ceramic Institute (CSIC)
Kelsen 5
28049
Madrid
Spain
E-mail: miguelangel.rubia@icv.csic.es

© Woodhead Publishing Limited, 2012

and

ETSI Telecommunication (UPM)
Ciudad Universitaria s/n
28040
Madrid
Spain
E-mail: miguelangel.rubia@upm.es

Chapter 18

A. Piqué
Materials Science and Technology Division
Code 6364
Naval Research Laboratory
4555 Overlook Ave, SW
Washington, DC 20375
USA
E-mail: pique@nrl.navy.mil

Chapter 19

M. Helgesen, M. Jørgensen, T. D. Nielsen and F. C. Krebs*
Department of Energy Conversion and Storage
Technical University of Denmark
Frederiksborgvej 399
DK-4000 Roskilde
Denmark
E-mail: frkr@risoe.dtu.dk

© Woodhead Publishing Limited, 2012

Woodhead Publishing Series in Electronic and Optical Materials

1 **Circuit analysis**
J. E. Whitehouse

2 **Signal processing in electronic communications: For engineers and mathematicians**
M. J. Chapman, D. P. Goodall and N. C. Steele

3 **Pattern recognition and image processing**
D. Luo

4 **Digital filters and signal processing in electronic engineering: Theory, applications, architecture, code**
S. M. Bozic and R. J. Chance

5 **Cable engineering for local area networks**
B. J. Elliott

6 **Designing a structured cabling system to ISO 11801: Cross-referenced to European CENELEC and American Standards**
Second edition
B. J. Elliott

7 **Microscopy techniques for materials science**
A. Clarke and C. Eberhardt

8 **Materials for energy conversion devices**
Edited by C. C. Sorrell, J. Nowotny and S. Sugihara

9 **Digital image processing: Mathematical and computational methods**
Second edition
J. M. Blackledge

10 **Nanolithography and patterning techniques in microelectronics**
Edited by D. Bucknall

11 **Digital signal processing: Mathematical and computational methods, software development and applications**
Second edition
J. M. Blackledge

12 **Handbook of advanced dielectric, piezoelectric and ferroelectric materials: Synthesis, properties and applications**
Edited by Z.-G. Ye

© Woodhead Publishing Limited, 2012

13 **Materials for fuel cells**
Edited by M. Gasik

14 **Solid-state hydrogen storage: Materials and chemistry**
Edited by G. Walker

15 **Laser cooling of solids**
S. V. Petrushkin and V. V. Samartsev

16 **Polymer electrolytes: Fundamentals and applications**
Edited by C. A. C. Sequeira and D. A. F. Santos

17 **Advanced piezoelectric materials: Science and technology**
Edited by K. Uchino

18 **Optical switches: Materials and design**
Edited by S. J. Chua and B. Li

19 **Advanced adhesives in electronics: Materials, properties and applications**
Edited by M. O. Alam and C. Bailey

20 **Thin film growth: Physics, materials science and applications**
Edited by Z. Cao

21 **Electromigration in thin films and electronic devices: Materials and reliability**
Edited by C.-U. Kim

22 **In situ characterization of thin film growth**
Edited by G. Koster and G. Rijnders

23 **Silicon-germanium (SiGe) nanostructures: Production, properties and applications in electronics**
Edited by Y. Shiraki and N. Usami

24 **High-temperature superconductors**
Edited by X. G. Qiu

25 **Introduction to the physics of nanoelectronics**
S. G. Tan and M. B. A. Jalil

26 **Printed films: Materials science and applications in sensors, electronics and photonics**
Edited by M. Prudenziati and J. Hormadaly

27 **Laser growth and processing of photonic devices**
Edited by N. A. Vainos

28 **Quantum optics with semiconductor nanostructures**
Edited by F. Jahnke

29 **Ultrasonic transducers: Materials and design for sensors, actuators and medical applications**
Edited by K. Nakamura

30 **Waste electrical and electronic equipment (WEEE) handbook**
Edited by V. Goodship and A. Stevels

31 **Applications of ATILA FEM software to smart materials: Case studies in designing devices**
Edited by K. Uchino and J.-C. Debus

32 **MEMS for automotive and aerospace applications**
Edited by M. Kraft and N. M. White

© Woodhead Publishing Limited, 2012

33 **Semiconductor lasers: Fundamentals and applications**
Edited by A. Baranov and E. Tournie

34 **Handbook of terahertz technology for imaging, sensing, and communications**
Edited by D. Saeedkia

35 **Handbook of solid-state lasers: Materials, systems and applications**
Edited by B. Denker and E. Shklovsky

36 **Organic light-emitting diodes: Materials, devices and applications**
Edited by A. Buckley

37 **Lasers for medical applications: Diagnostics, therapy and surgery**
Edited by H. Jelínková

38 **Semiconductor gas sensors**
Edited by R. Jaaniso and O. K. Tan

39 **Handbook of organic materials for optical and optoelectronic devices: Properties and applications**
Edited by O. Ostroverkhova

40 **Metallic films for electronic, optical and magnetic applications: Structure, processing and properties**
Edited by K. Barmak and K. Coffey

41 **Handbook of laser welding technologies**
Edited by S. Katayama

42 **Nanolithography: The art of fabricating nanoelectronics, nanophotonics and nanobiology devices and systems**
Edited by M. Feldman

43 **Laser spectroscopy for sensing: Fundamentals, techniques and applications**
Edited by M. Baudelet

44 **Chalcogenide glasses: Preparation, properties and applications**
Edited by J.-L. Adam and X. Zhang

45 **Handbook of MEMS for wireless and mobile applications**
Edited by D. Uttamchandani

46 **Subsea optics and imaging**
Edited by J. Watson and O. Zielinski

47 **Carbon nanotubes and graphene for photonic applications**
Edited by S. Yamashita, Y. Saito and J. H. Choi

48 **Optical biomimetics**
Edited by M. Large

© Woodhead Publishing Limited, 2012

This book was conceived and edited in honor of Gianfranco C.

© Woodhead Publishing Limited, 2012

Preface

Traditionally, *printing* is a process of reproducing text and images with ink on paper. More generally, it is a process of adhering one or more material layers on a surface. In the context of electrical and electronic applications it is understood as the process of adhering electronically functional materials to various flexible or rigid substrates. A significant distinctive feature of printed films as opposed to films deposited in the usual microelectronic technologies is that printed films are obtained via a (semi) direct-write approach, i.e. by means of an additive process, which minimizes material waste: no part of the coating has to be removed after the deposition. Also, generally speaking, the printed films are deposited in air: no vacuum chamber or inert atmosphere is required and most printed films are also stabilized in their functional structure by a post-deposition process, again in standard ambient.

According to this broad definition, the subject of *printed films* spans a wide range of materials and technologies. Very popular printed films in the electronic community are 'thick-films', also known as 'screen-printed-and-fired films'. These films are prepared by means of a technology that mimics the ancient art of Greeks and Egyptians to produce scripts and drawings, for example on ceramic or glassy surfaces. The basic concept is in fact to force a paste through apertures of a stencil screen, or a mask, in order to deposit a pattern on the substrate. Although interest in this technology and its applications are far from faded away, they are currently joined by a wide arsenal of different printing techniques for functional films, either well assessed or under development. They are intended to add (or to extend) the benefits of this mature technology, in terms of its capacity for very efficient mass production of cheap functional films, environmentally compatible (and sometimes simply disposable) passive elements or even active devices. The perspective is to print not only dielectrics, conductors and resistive materials for integrated circuits, microelectro mechanical (MEMS) and labels for broad-band wireless communications but also light emitters and semiconductors for solar energy conversion, sensors, power, memory, logic, lighting and much else besides.

With these prospects, we are witnessing the birth of new companies, the substantial involvement of many large consortia, wide research programs on materials and ideas for innovative applications of printable materials and methods.

© Woodhead Publishing Limited, 2012

Some commercial products of this 'printed electronics' have already reached the market, and many new announcements appear every day.

In this framework the novice may believe himself to be working in an almost virgin background and miss precious knowledge gained in the past. We hope that this book will bridge the gap between the mature field of screen-printing technology and the most promising newer printing technologies.

Hence we start with a description of screen-printing technology, with its intrinsic capabilities, limitations and variants, and then proceed to examine alternative processes such as ink-jet printing, laser micro-fabrication, writing through dispersing tools and direct gravure offset printing. The focus is on the interrelations of materials' processing properties rather than on more technical aspects of design, manufacture and testing that have been extensively covered elsewhere.

Next, the applications of printed films in devices such as solar cells, sensors, actuators, heaters, fuel cells and microsystems are presented with a twofold view. One perspective is to look back at successful achievements, to review important learnt lessons and possibly to identify further advances in traditional fields that might increase possible future applications. The other view is to look forward, to new evolving technologies that may take advantage of recently developed or improved equipment and materials, as well as incorporate emerging methods for further future applications.

We have compelled ourselves and other contributors to present materials, processes and applications with constant care to underline the principles and methods of materials science which, according to our current level of knowledge, justify the choice of materials, procedures and systems appropriate to printed films. This has appeared a useful exercise because experience teaches that rapid development, along with an enthusiastic approach and/or prospects of new and profitable results tend to distract people from the task of taking into account the knowledge gained in the past and the responsibility of progressing rapidly and securely with a rigorous scientific understanding of the work.

We have been lucky enough to gain the cooperation of real specialists in well-assessed applications, and of scientists. Our unique regret is to have been able to cover only marginally the topics related to organic printed films, because of the late withdrawal of some of the experts in this scientific field. Our hope is, however, to have contributed an updated survey in the field of printed films, to offer food for thought to novices, and to provide suggestions to both scientists and practitioners in this fascinating area of research and development.

Maria Prudenziati
Jacob Hormadaly

© Woodhead Publishing Limited, 2012

1

Technologies for printed films

M. PRUDENZIATI, University of Modena and Reggio Emilia, Italy and J. HORMADALY, Ben-Gurion University, Israel

Abstract: The terms 'printed electronics' and 'direct-write deposition' are increasingly familiar to manufacturers and consumers of electronic products. The trend is to make use of new cost-efficient ways to mass-produce electronic devices and in prospective to open new huge product markets. There are already several apolications of functional printed films, but further improvements in performance/cost ratios are envisaged, especially in 'organic electronics' and 'flexible' products. Development in these fields is progressing rapidly on several parallel paths, each with its own strengths and limitations. In this chapter, a broad overview of technologies capable of printing functional films for the microelectronic and electrical industries is presented. First, the history of the most mature and traditional print process known as 'screen printing' is delineated and the steps that have resulted in improved, increasingly integrated systems and diversified materials are retraced. Motivations for ever-increasing resolutions are then approached and technologies on which current research is mainly focused are briefly outlined.

Key words: printed electronics, hybrid circuits, thick-film technology, dispensing systems, ink-jets, reel-to-reel printing systems, evolutionary progress.

1.1 Introduction: printed films in microelectronics

1.1.1 An historical perspective

The earliest printed films appeared as screen-printed films in microelectronics for making more efficient and cheaper printed circuit boards (PCB); soon, thick-film technology advanced in a variety of versions, all of them still applied in the manufacture of microelectronic devices, circuits or systems, for either mass or niche markets. The starting point was indeed simple: to screen-print photo-resist layers aimed at defining exposed areas (or vice versa the protected areas) during the process of etching away the copper laminate layer and so creating the pattern of conductive interconnections in the circuit. The applied ink is dried, the whole board treated with the chemical etching solution to dissolve away the unwanted metal and finally the dried ink removed with an organic solvent or alkaline solution. Next, small holes are drilled in the board at predetermined places and components placed on the insulated side of the board with their connecting leads projecting through sufficiently to contact the copper tracks on the other side of the board. Finally, the connections are made secure and permanent by soldering,

© Woodhead Publishing Limited, 2012

either manually or by treating the surface with a flux and passing briefly over a wave of molten solder. In this second event again a 'solder resist' is printed on the copper side, leaving exposed only those sites where solder is required. Similar strategies and operations are today valid and exercised for the mass production of PCBs and 'surface mount technology' (SMT).

The second step for introducing printed films in electronic applications was perhaps the most challenging and inventive: to manufacture the whole set of electric passive components, their interconnections and protective layers on a single face of a dielectric substrate, usually a ceramic substrate. This was accomplished by using the 'drawing' technology known as 'serigraphy' to lay down defined patterns of pastes or inks containing the required functional materials. The development of the proper ink composition and post-deposition processes needed to accomplish the prospected functionality of the films can be traced to the dawn of the nineteenth century, although remarkably a patent was issued in January 1899 for printed and fired meanders for resistive components prepared 'after the manner in which lustrous gold, silver and platinum decorations are applied' (Voigt and Haeffner, 1899), i.e. from a resinate-ink, in the current jargon.

The earliest use of particulate-based films (i.e. films from inks containing metal together with glass powders) reportedly concerned the preparation of capacitors (Deyrup *et al.*, 1945), which pre-dated the birth of the term 'thick-film' by at least twenty years. The term 'thick-film technology' was in fact coined only in the early 1960s to distinguish it from 'thin films', typically applied by a vapor deposition process, vacuum evaporation or sputtering (Bouchard, 1999).

But thick-printed and fired film for passive components and interconnections had already been mounted in 1947 on modules supporting subminiature radio-tubes (Hoffman, 1984); hence we might say that the 'hybrid microelectronics', i.e. the use of printed and fired interconnections to add and package active electronic devices, came before the invention of transistors (1949).

Turning back to the definition of 'thick-films' we observe that in the early days Kelemen proposed defining them as

> inorganic conductive or dielectric films, applied to a ceramic or glass substrate from a composition containing a temporary organic binder, as a coating of the order of 40 μm in thickness, and then fired in air at a temperature not exceeding 1100 °C. In most cases the fired film would be several micrometer thick, but in some instances its thickness may be in the tenth-micron range. (Kelemen, 1970)

This definition evolved substantially over the years.

The 'boundaries' implied in Kelemen's definition have been overcome, leaving only the initial link between 'thick-films' and 'printed films' unchanged. New classes of substrates have been incorporated including metals, polymers and silicon among others, the thickness of the deposited layers have varied widely, firing in many atmospheres has been used, as well as firing at peak temperatures over 1100 °C.

© Woodhead Publishing Limited, 2012

The very beginning of the thick-film hybrid circuit industry as we know it today occurred in the 1960s with the first 'fired on' resistors adopted by the military for the Minuteman missile and by IBM for its System 360 (Bouchard, 1999).

The large credit granted by IBM to thick-films technology (TFT) has contributed greatly to its adoption by the electronic community, promoting recognition that TFT allowed one to lay down passive components with easy and cost-effective techniques on relatively rough and therefore low-cost substrates, without the need for vacuum equipment and with the added advantage that resistors and circuits could be trimmed. These features entailed advantages over both thin films technology and conventional PCB, making thick-film hybrid microelectronics competitive in a wide and diversified spectrum of application areas, including telecommunication, automotive, medical equipment, radio and television, and the full range of consumer electronics.

Within a short period of time, thick-film hybrids invaded a large fraction of the industrial electronic markets, and these successes stimulated a variety of technological efforts in the development of new materials (substrates, paste compositions, circuit structures) and processes, to increase circuit density, operating frequencies, flexibility of design, etc.

Very important innovations in spreading TFT to various application areas soon followed. In the 1970s membrane touch switches (Hicks *et al.*, 1980) and thick-film defoggers for windshields (Tarnapol and Snyder, 1969) were developed, and piezoresistive effects in thick-film resistors were investigated and exploited in mechanical sensing systems (Canali *et al.*, 1980; Cattaneo *et al.*, 1980; Morten *et al.*, 1983). Pioneering studies on screen-printed metallization of silicon solar cells were published (e.g. Bube *et al.*, 1980; Frisson *et al.*, 1978, p. 590), and the first photoformable compositions were developed (Jolley *et al.*, 1974).

In the 1980s the use of TFT was extended to the manufacture of solid-state sensors for mechanical, chemical, thermal quantities and biosensors, heating resistors for kettles, and platinum electrodes for exhaust gas sensors (Prudenziati, 1994). In the meantime, studies were promoted for printed film fine lines fabrication (Shankin, 1978): innovations included improved photolithographic processes (for pattern definition on dried films) and photo-etching processes (pattern definition on fired films), MD-Films® (registered mark by Ferro Corporation, Naguib *et al.*, 1980), MicroPen writing (Drumhelelr, 1982), and Ink-jet printing (Teng and Vest, 1987). It was also in the early 1980s that low-temperature co-fired ceramics entered the market, driven mainly by the need for radio-frequency (RF)-circuits to operate above 10 GHz (Vitriol and Steinberg, 1983).

The advent of SMT, enabling a significant increase in the density of connected components, and the continuous successes in very-large-scale integration (VLSI), resulted in restricted market opportunities for thick-films in hybrid microelectronics at the beginning of the 1990s. But a renewal of interest arose from evidence of the superior benefits of low-temperature co-fired ceramics (LTCC) technology in terms of packaging reliability, performance in microwave circuits, high

© Woodhead Publishing Limited, 2012

density, fast digital applications and good thermal management; in addition, the flexibility of this technology for the realization of microsystems was recognized (see Chapter 6). In the 1990s, we witnessed innovations in the compositions of lead-free and cadmium-free dielectrics and conductive pastes, of piezoelectric and pyroelectric films, varistors (Chakrabarty *et al*., 1980), novel thick-film sensors and actuators.

As usual in the evolution of a technology, some development steps gained only partial success. An example is the development of base metal thick-film conductors and nitrogen-fireable compatible systems (e.g. Buzan *et al.*, 1977; Friedman and Bartholomew, 1969): these products find major applications where a relevant fraction of precious metals would result in expensive components such as in multilayer ceramic capacitors (Kishi *et al.*, 2003). On the contrary, and significantly when resistors are required, promises of cheaper components were often frustrated by evidence of more expensive and difficult processes, as well as inadequate properties. Likewise, new generations of inks were offered that could be printed-and-fired below 650 °C on enameled steel (e.g. Wilson and Johnston, 1977); however, the introduction of dielectric pastes for insulation of metal substrates, especially steels, made these systems obsolete.

Materials and methods were also developed for the 'sequential multilayer technology', i.e. for multilayer ceramic modules (MLCM), where on the fired ceramic substrate alternate layers of metallurgy and dielectric are deposited and fired. The layering and firing steps are repeated, thus building a 3D structure, with the number of firing cycles at least equal to the number of added layers (Young and Knickerborker, 1991). LTCC tapes available on the market made the manufacture of multilayer modules easier and faster.

On the side of materials, important achievements, not easy to locate in a precise period of time, are recognized in:

- AlN substrates, a valuable alternative to alumina, due to its higher thermal conductivity and lower dielectric constant, with a thermal expansion coefficient similar to that of silicon (Werdecker and Aldinger, 1984).
- Polymer thick-films, or PTF, a variety of composites consisting of a polymer matrix filled with conductive, resistive and dielectric powders to be screen-printed and cured at modest temperatures (<200 °C), for a myriad of applications, such as passive components in polymer hybrid circuits, potentiometers, low-cost strain gauges and membrane switches (e.g. Kirby, 1989), to name but a few.

The 1990s was also the period of increasing interest and early success in the development of new versions of printing technologies with two most declared targets: printing of fine lines and/or on large areas. The approaches comprise offset printing, gravure, pen writing, ink-jetting, thermal spraying, laser sintering, etc.

From the early years of the 2000s onwards we have seen continuing advancements and huge international projects in these technologies, either for

© Woodhead Publishing Limited, 2012

increased resolution capabilities, easier, cost-effective deposition or increased areas of application. The printing of organic materials, including intrinsically organic conductors and semiconductors for new devices and applications, is one of the actively pursued targets towards creating flexible electronics, described in chapters 18 and 19 of this book.

1.2 From thick-films and hybrids to printed electronics

The focus in this book is on films with structural or functional applications, especially in microelectronics, optical or sensing applications, with thickness ranging from a few nanometers to a millimeter, deposited with a technology capable of achieving films of the desired (or at least of suitable) composition and microstructure, with or without very fine pattern definition. Therefore, with no constraints on geometry or in composition and use, the only condition delimitating the field is the character of the deposition technology: this should be one in which the film is deposited in normal ambient conditions, i.e. without a vacuum environment during the printing operations.

This character is shared by a myriad of different technologies from the well-assessed screen-printing to the most recent direct-write techniques. A brief overview of the most promising printing technologies is given in this section. The ideal printing technology should be that which offers all these benefits, not necessarily in the following order:

- accuracy of position; e.g. reproducible (mask) aligning;
- controllable amount of deposited material, i.e. thickness and content of active material;
- easy, cost-effective process;
- fine lines and interlines, i.e. resolution;
- fast turnaround and on-demand production;
- high production speed;
- breaking limitations in materials and performances;
- environmental consciousness/economy.

The ideal is as ever a target to aim at, with clever research programs, supporting knowledge and tough development efforts. However, considerations on the state of the art should compare and contrast the various printing technologies with the listed targets.

For an easier comparison, two classes of printing technologies can be identified: the first one, which allows patterning by means of a mask, the second one being a mask-less technology and then a real direct-write technology (Piqué and Chrisey, 2002).

While the former class encompasses the most mature technologies, supporting well-established markets and applications, the latter one is very full of promise and is entering our daily life.

© Woodhead Publishing Limited, 2012

All of the printing technologies offer an additive process, with the intrinsic advantage of minimizing material waste; all of them are intended to deposit patterned functional films on adequate substrates, either for electronic circuits or for diverse entirely functional components such as sensors, heaters, actuators, or parts of devices such as solar cell metallization, interconnections for displays, etc.

Another approach to divide printing technologies is in terms of sheet-based and rotary printing processes. The first class includes screen printing, ink-jets, filament micro-dispensing systems and direct gravure offset methods, whereas the latter class encompasses a series of different processes, based on methods borrowed from graphic industry, which share the ability to transfer a pattern, image or document from an engraved plate (or cylinder) to the proper substrate. These technologies, also referred to as roll-to-roll, reel-to-reel or R2R processes, are signified by offset lithography, flexography and Rotogravure as the most important examples.

1.2.1 Screen-printing technologies

In the rich palette of technologies nowadays available to print films for microelectronics and electronic-related systems, screen printing is the most simple, flexible and cheap.

Historically, screen printing is rooted in the decoration of ceramics and glassware, which is an art traceable to prehistoric times, nurtured in China many centuries BC and traditionally called silk-printing or serigraphy (from the Greek *seri* meaning 'silk' and *grafia*, i.e. 'writing or imaging'). Serigraphy is indeed still a widely practised process used to apply dyes in embossed patterns on surfaces varied in shape and material; nowadays artisans and industries use serigraphy to make logotypes and trading signs, visiting cards and labels, envelopes and folders, forms and leaflets; it is suitable for tile coloring, artistic reproductions of masterpieces of previous centuries, the labeling of containers, decals and so on.

Screen printing is basically a slightly more elaborate version of this process when, in the electronic industry, films of functional materials are deposited on to a target (substrate) surface. Figure 1.1(a) schematically illustrates the printing process. A frame holds out a screen, which supports an ink-blocking layer to form the stencil, i.e. a negative of the image to be printed. The latter, produced with computer-aided design (CAD) software, has been transferred on a sensitized emulsion in contact with the screen, then exposed to UV radiation, developed and washed in warm water to leave open only the areas through which the printing shall occur. A viscous ink (0.1 to 10 Pa s) is then applied on top of the stencil screen, filling the open areas of the mesh and finally forced through its openings by a squeegee, which depresses the screen toward the substrate as it traverses the pattern.

When practised properly, screen printing is a non-contact printing process: the screen itself should not touch the substrate. Proper printability is given by an essential constituent of the paste: the 'organic vehicle' or 'medium', an adequate

© Woodhead Publishing Limited, 2012

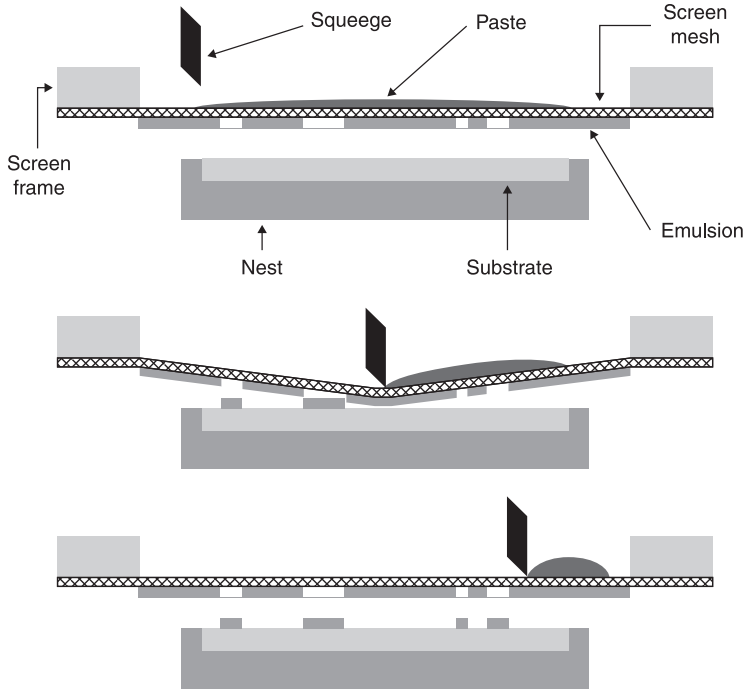

(a)

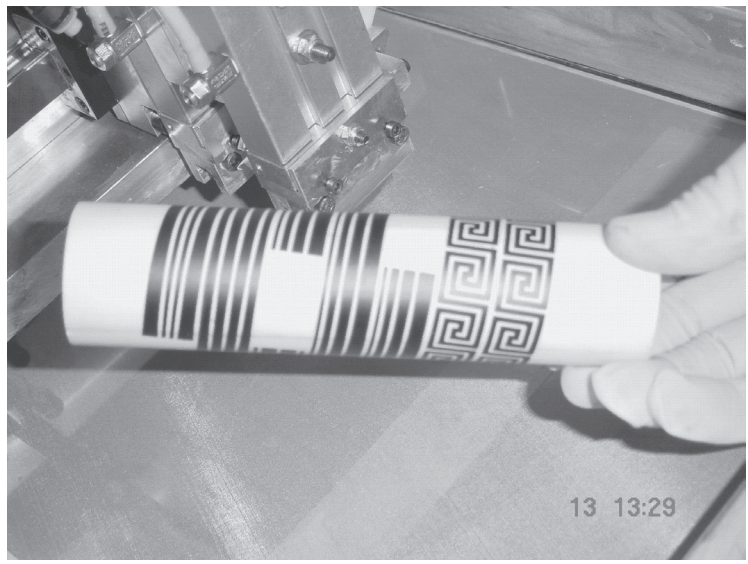

(b)

1.1 (a) The screen-printing process; (b) lines on an alumina tube screen-printed with IKO screen printer model T-620-80200 (courtesy of Institut für Sensor- und Aktuatorsysteme Technische Universität Wien).

© Woodhead Publishing Limited, 2012

resin dissolved in a solvent (see Chapter 2). This vehicle endows the paste with its special thixotropic properties, i.e. the viscosity of the ink is high when it is at rest but it drops when a shear force is applied so that the ink flows easily through the apertures in the screen (Kay *et al.*, 2003; Licari and Enlow, 1998). After the film has been deposited on the substrate, there is no shear force acting on the ink, and the viscosity of the ink increases to reduce further flow. The same basic equipment and procedures allow the manufacture of quite different films, either organic or inorganic films (e.g. metal, glass, dielectrics, etc.).

The density of the wet printed film varies as a result of the number of meshes per unit length, mesh aperture, emulsion thickness, snap-off distance (i.e. the initial distance between screen and substrate) and the properties of the paste (e.g. its thixotropy, the homogeneity of solid components). This technique produces wet patterns with thicknesses greater than 2.5 μm (usually 20–30 μm thick from standard pastes used for electronic components) with line width and pitch down to 80–100 μm (Licari and Enlow, 1998). The printed film is normally dried and 'fired' in a belt furnace. Different types of films undergo different post-deposition events in order to develop the final microstructure and functionality. Temperature ranges for sintering inorganic films are usually between 600 and 1200 °C (most frequently from 850 to 900 °C) according to the system's structure and application (and limitations imposed by the substrate properties, if any), whereas polymers are cured usually in the range 100 to 200 °C, with bio-materials cured at even lower temperatures. Also, other curing process can be applied such as UV-curing, or with infrared radiation or electron beam radiation.

Although actual screen-printing processes in microelectronics (for hybrid circuits, resistive chips, sensors, actuators, etc.) are mainly performed with flat masks on plane surfaces, the use of cylindrical or rotary mesh shapes is possible, either for increasing the throughput with a continuous operation or for deposits on non-planar surfaces (Fig. 1.1(b)).

Multiple layer devices can be built using co-fired ceramic tapes. This process differs from the conventional thick-film process in that the base substrate and all the dielectric layers are initially used in the unfired conditions. The unfired tape, called 'green ceramic' or 'green tape', is soft and somewhat rubbery. It is punched to form vertical (through thickness) vias and cut to size, or vice versa cut and then punched. In the high-temperature co-fired ceramic (HTCC) process the green tapes essentially consist of alumina grains mixed with organics and binders; conductor thick-film pastes consisting of refractory metals are screen-printed to form the conductor lines and fill the vias. Each layer of the module is processed separately, then all the layers are aligned ('registered') and the stack laminated in a press. The stack is therefore sintered as a single unit in the furnace at very high temperatures (e.g. 1600 °C) in a hydrogen atmosphere. Typically, tungsten, molybdenum or other refractory materials are used in this process, however for special applications platinum, palladium or other high-temperature precious metal alloys may be used and the sintering can be done in air atmosphere.

© Woodhead Publishing Limited, 2012

In the LTCC process a lower sintering temperature (typically 850–950 °C) is allowed by the composition of the green tape (glassy phases are added to alumina mixed with organics and binders: see Chapter 6); moreover, each layer can support not only conductive thick-film lines and vias, but also other passive components printed from 'standard' thick-film pastes. This approach allows the design of high-density devices, and is particularly appreciated in applications where compact hermetic packages for high or medium operating temperatures are required (e.g. Opto-electronic and wireless packages, Chapter 6), or for complex structures (e.g. ceramic microelectr (MEMS), Chapter 10; Gongora-Rubio *et al.*, 2001), and very high frequency operations (Chapter 6). New compositions for tapes now promise to offer technological opportunities for novel devices and systems that would have been inconceivable previously.

The benefits of conventional screen-printing technology for electronic components and devices include the ability to produce thick layers from paste-like materials, simplicity of the process, good throughputs (e.g. 50 m^2/h), a very high level of automation (substrate loading and unloading), versatility in compositions of the printable functional materials, including metal-organic-based inks, semiconductors, resistors, dielectrics, etc. The maximum resolution remains usually under 50 lines per centimeter. For better resolutions (e.g. 100 lines/cm), etched metal masks, or electroformed masks, are an alternative solution but these are expensive and fragile and preferably used with (commercially available) highly thixotropic inks (Dziedzic *et al.*, 1993).

The smearing of line edges and surface roughness, responsible for high attenuation and losses of microwave microstructures at frequencies above 1 GHz, are largely mitigated by the use of photoimageable inks with a positive mask (Minalgiene *et al.*, 1994; Sue and Naguib, 1984) and photoformable systems, e.g. the Fodel® pastes (Fig. 1.2) which, in addition, result in better resolutions. Both conductors and dielectrics can be fabricated using this method and feature sizes down to 25 µm with 50 µm pitches and 75 µm vias are obtainable (Licari and Enlow, 1998). The success of photo-lithographic processes is tightly linked to success in developing new application-driven inks. One interesting example is DuPont's Fodel™ systems used to fabricate the bus lines in a plasma display panel (PDP); the material must be conductive, black in color (to minimize reflections that degrade contrast) and capable of being applied in fine lines. The eighth generation of Fodel™ system meets these requirements, and thanks to a reduction of noble metal contents, with a relatively inexpensive paste.

As already stressed, what makes the standard screen-printing technology attractive is not the pattern resolution, as one struggles to produce feature sizes below 100 µm (Carr, 1994). The most valuable advantages of screen printing are the low cost of investment in equipment and maintenance, flexibility in choice of materials, including substrates and pastes, easy automation, fast production rate, and the ability to trim components with a laser.

© Woodhead Publishing Limited, 2012

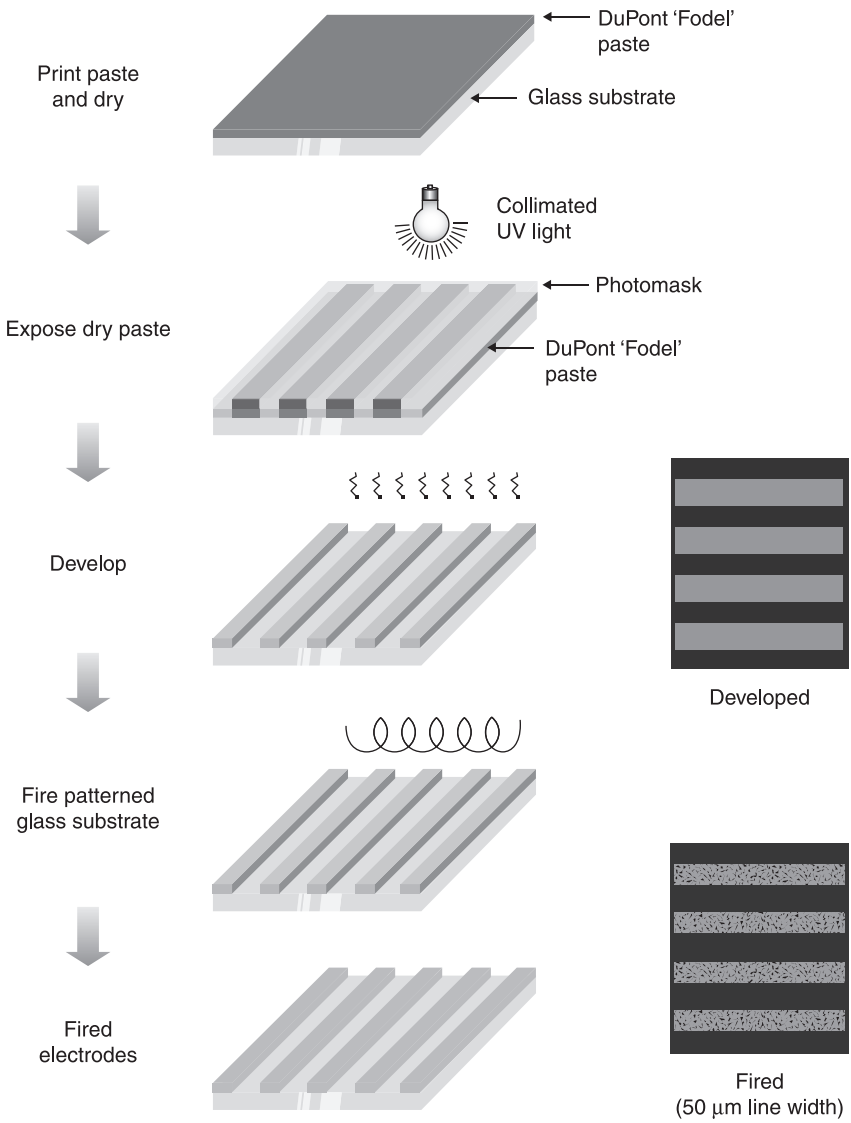

1.2 Fodel® process illustration.

Most of today's uses of screen printing in electronics are well represented by the production of resistor chips, circuits and packaging for microelectronics (Chapter 6), resistive sensors (Chapter 7), heaters (Chapter 15), electrodes and parts for biosensors (Chapter 13). Screen printing provides conductive patterns where high-speed printing technology has not been able to cope with the inks, or if it was not possible to produce layers sufficiently thick for the requisite conductance at one pass. Therefore this is the technology of choice for production

© Woodhead Publishing Limited, 2012

of membrane keyboards and RFID (radio frequency identification) antennas. Also it is used for dielectric, phosphor and passivation layers in a.c. electroluminescent printed wide area displays. The application of rotary screen printing will probably increase in future to get over the relatively modest throughput of conventional screen printing.

1.2.2 Filament micro-dispensing systems – MicroPen® and nScrypt® systems

Direct-write deposition of precise 3D patterns can be accomplished with tools referred to as 'filament dispensing' or 'liquid dispensing' systems. As in ink-jet systems, the printing pattern or paths are created by common compact disk (CD) software, but the ink is printed via capillary action from a stylus in a continuous stream, in close analogy with a digital plotter. The ink is commonly loaded in a syringe, compressed and squeezed out into the writing head by controlled pressure. One such system is the MicroPen® (Fig. 1.3), which was developed by OhmCraft, Inc. (Honeoye Falls, NY) to meet the requirements of fast prototyping of multilayers for multifunctional circuits in the 1980s; it can lay down potentially

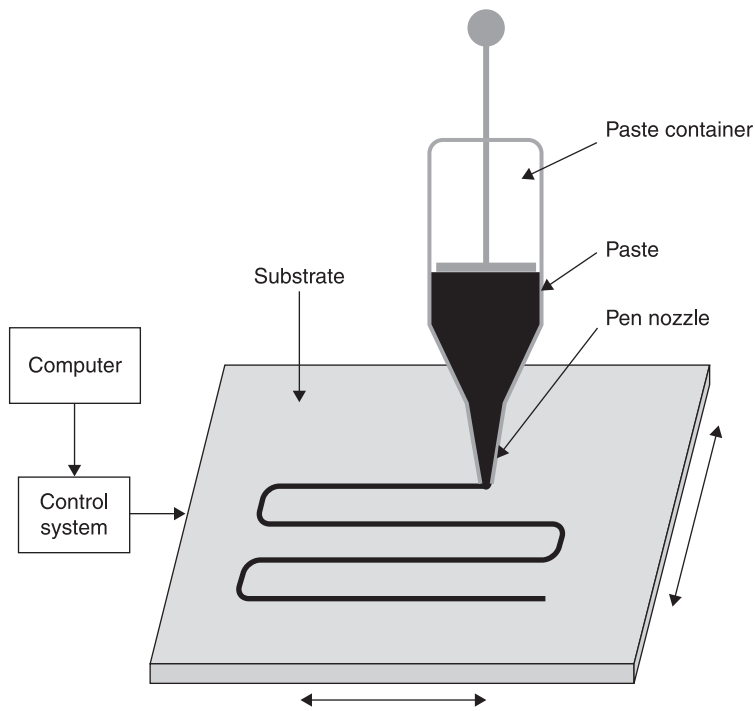

1.3 The MicroPen system.

© Woodhead Publishing Limited, 2012

any material ranging in viscosity from 0.005 to 500 Pa·s, including particle suspensions, polymer inks and biological materials, onto a range of substrates including flexible and non planar substrates, at an overall speed up to about 75 mm/s. Lines, from 50 μm to 2.5 mm wide, are printed; the line thickness is kept uniform and lines over-printed safely on previous films or fragile materials. Also, precise patterns can be drawn uniformly on irregular and contoured surfaces of any type of substrate.

A more recent filament direct writing tool is the nScrypt system (Li *et al.*, 2007) where a direct-print dispensing tool is integrated with nScrypt's novel pump called Smart Pump™. This pump is able to dispense materials with viscosity of up to 1000 Pa·s with accurately controlled air pressure, valve opening times and dispensing height. When dispensing is initiated, a valve opens so as to allow the material to be dispensed to flow through the tip onto the substrate. Once dispensing stops, the valve closes to block material from leaking. One advantage of the Smart Pump is that it includes a sucking-back movement of materials into the nozzle when deposition is terminated. A negative pressure is maintained in the dispensing tip chamber to induce material sucking back when deposition is ceased. This feature allows the orifice to be left clean and clear without any agglomeration of material or the possibility of nozzle clogging. Consequently, line printing can be precisely controlled and the width of the deposited material can be maintained consistently without bulges at the ends. Writing on complex 3D architectures comprising cavities, vias, raised lands, concave surfaces and tubes is made feasible with such techniques. Demonstrations of this include direct-write fabrication of integrated passive devices over surfaces of about 20 to 80 mm^2, printing of silver collectors on fragile and rough polymer silicon solar cells, devices for medical applications and high precision thick-film micro-resistors (King *et al.*, 1999; Li *et al.*, 2007; Yang *et al.*, 1999, http://www.ohmcraft.com).

1.2.3 Ink-jet technology

Ink-jet technology is a class of direct-write processes, which share the appealing characteristic of unparalleled versatility: printing is possible onto virtually any substrate, of any size, with a resolution exceeding 200 lines/cm. As in home/small office desktop ink-jet printers, tiny ink droplets of functional materials are reproducibly dispensed from inks of adequate viscosity, typically below 20 mPa.s. Therefore the inks may be liquid solutions, dispersion of small (preferably nano) particles, melts or blends.

Droplets with diameters of 15–200 μm and volumes down to a few pico-liters, are deposited at a few KHz up to 1 MHz rates according to the equipment and inception of the deposition methods.

Two different ink-jet techniques have become mature and well understood in the printing industry for decades: drop-on-demand (DOD) and continuous ink-jet (CIJ).

© Woodhead Publishing Limited, 2012

Continuous ink-jet systems (CIJ) utilize a pressurized fluid in the reservoir under vibration (at 20 to 80 kHz). The latter increases the pressure inside the reservoir and capillary waves are generated within the fluid domain to break up the fluid stream (Fig. 1.4a). Then a continuous and consistent stream of uniformly spaced and sized droplets can be generated. With conductive material in the fluid, an electric charge can be impressed on selected drops as they break-off from the fluid jet. These charged droplets can then be steered by means of high voltage deflector plates to form various patterns onto the substrate. The uncharged droplets are captured by a gutter mechanism and can be re-circulated through the system. This process allows very high deposition rates but the resolution is limited to 60 lines per centimeter (Blayo and Pineaux, 2005).

Drop on demand (DOD) ink-jet uses print head nozzles placed vertically above, and very close to, a substrate (within 10 mm) to eject a single drop of ink when activated (Fig. 1.4b). This happens when the pressure within the reservoir increases either due to the action of a piezoelectric element or to a bubble resulting from the rapid evaporation of the heated ink. Numerous companies produce ink-jet devices for everyday printing purposes. This equipment can in principle be adapted for printing functional materials, but specialized devices are also on the market.

With both ink-jet printing systems (DOD and CIJ), multiple small volumes of metallic, semiconducting, or insulating material can be deposited at computer-defined positions. The advantages of ink-jet printing as compared to silk screen printing are: direct patterning including 3D coatings, non-contact processing with some chance to write on complex silhouettes of substrates, real time production by digital design, lower waste of precious materials, deposition at the exact location where needed of a precisely controlled amount of ink.

However, advancement in production of electronic materials and devices still requires extensive research and a significant amount of work. The greatest challenge consists in the set of specific constraints for the ink formulation, mainly in terms of rheological properties but also for surface energy, environmental stability, compatibility of materials and post-deposition process for curing/sintering.

Ideally the fluid should be a Newtonian fluid with a viscosity less than 0.02 N·s/m. Very low viscosities can lead to problems such as satellite formation and lack of acoustic damping. The surface tension should be greater than 35 mN/m and the size of any particles suspended in the liquid should be less than 5 percent of the orifice diameter (Calvert, 2001). Any viscoelastic behavior will also cause problems with the jet detaching from the orifice. Problems with the ink arise when it interacts with the substrate, including a tradeoff between a viscosity low enough not to clog the orifice but high enough that it does not spread on the substrate. The preferred inks for write metal traces are particle-free inks, derived for instance by MOD (metal organic decomposition) (Teng and Vest, 1987; Vest *et al.*, 1983) or suitable salt solutions (Mei *et al.*, 2005). Dispersions of nano-particles or organic polymer, perhaps with a nano-sized filler, have also been found to be suitable for ink-jet printing.

© Woodhead Publishing Limited, 2012

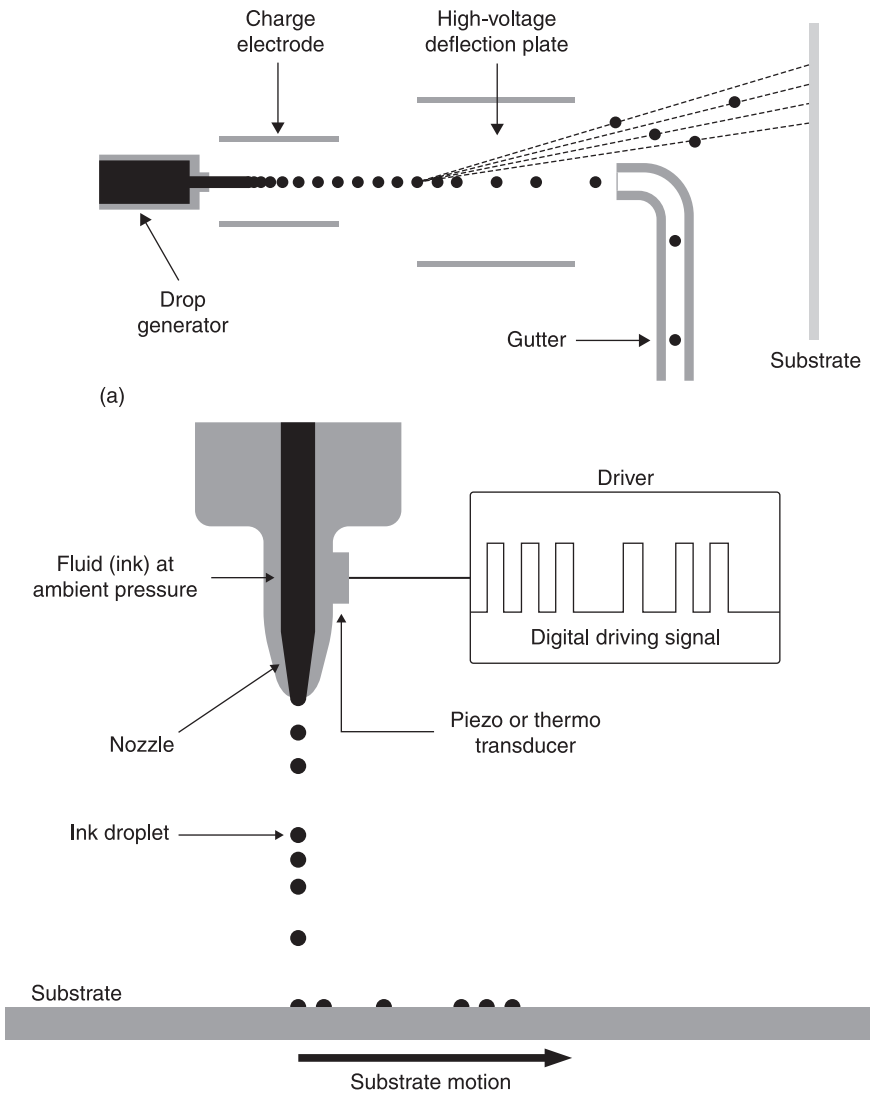

1.4 Ink-jet printing; (a) continuous ink-jet (CIJ) printing: multiple-deflection system; (b) drop on demand (DOD) system: single droplets ejected through an orifice at a specific point of time.

Issues under continuous scrutiny involve consideration of the morphology and surface energy distribution (hence wettability) of the substrate, which affect the pattern resolution; also the substrate porosity might contribute to the small concentration of functional material, imposed by rheological requirements, to give a layer that is not thick enough, after solvent evaporation, for a dense continuous

© Woodhead Publishing Limited, 2012

film. Decomposition of metallo-organic or salt solutions can lead to deposits that are too thin, lack wear resistance, and/or are poor in electrical conductivity. Adhesion of the printed materials is not obvious. Progress in understanding features like drop formation, landing and interactions with the substrate is noticeable. Recent achievements and remaining problems are discussed by Singh *et al.* (2010). Besides organic films for organic light-emitting diodes (OLEDs) or metal electrodes for thin film transistors, particle suspensions and complex oxide compounds have been successfully deposited (de Gans *et al.*, 2004). Ink-jet printing is used by Xerox, Plastic Logic and others for thin film transistor circuits and by CDT and others for OLEDs. Other pursued industrial applications are in photovoltaics (van Hest *et al*., 2010) and RFID tags (Redinger *et al.*, 2004; Rida *et al.*, 2007). Applications for large-batch production are probably limited because ink-jet is fundamentally a serial process; however, special systems with multi-nozzles containing several hundreds of individual nozzles have been reported for the manufacturing of polymer LED displays (Halls, 2005).

1.2.4 Direct gravure offset

The principle of gravure-offset-printing is illustrated in Fig. 1.5. The pattern to be printed is engraved on the plate, and the printing process involves first filling the engraving with ink by doctor-blading. Then the paste is picked up, for example, by a pad rolled over the filled plate, and finally the pattern is transferred to the substrate by a similar rolling action. Several printing plate materials have been used in direct gravure-offset-printing, such as steel, aluminum, copper, zinc, polymer, glass and ceramics. The manufacturing processes depend

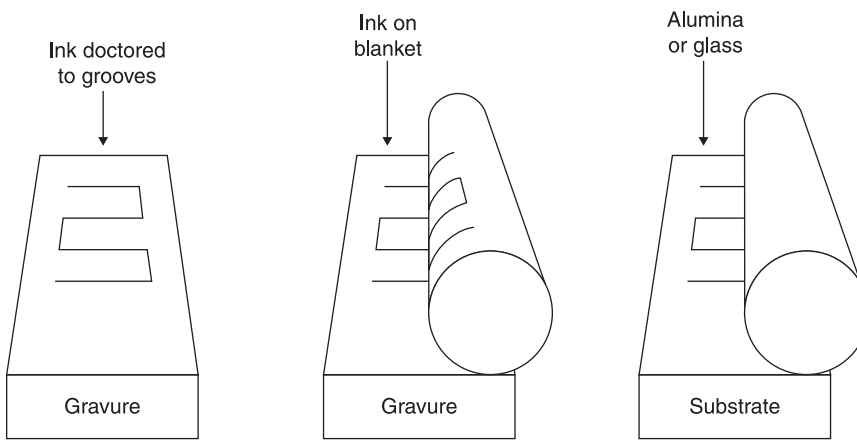

1.5 Gravure printing process, after 'Gravure-offset-printing in the manufacture of ultra-fine line thick-films for electronics', Pudas, M., academic dissertation, University of Oulu, 2004.

© Woodhead Publishing Limited, 2012

on the plate material. The most common methods are chemical etching (e.g. by ferric chloride), mechanical engraving (e.g. by diamond stylus) and laser engraving.

The length of time that elapses between the various process steps may be a critical parameter; for example, in the case of conventional thick-film paste, during transfer of the inked pad to the substrate, evaporation of the 'thinner' occurs so that the paste has the optimum properties for its transference and adherence to the substrate. After printing, the pattern is dried in order to evaporate the solvents. The final structure is obtained by firing with heat or UV light, depending on the ink. The main disadvantage of metal gravure printing is that a 100% pick up of paste from the grooves is not obtained and, thus, the printed line heights are inadequate. Also, with the hard metallic gravure, it is not possible to print directly onto a hard substrate such as alumina. The main advantage in using a hard metallic gravure is that there are no paste-doctoring problems because the grooves cannot be forced down by the doctor blade.

Direct offset printing consists in a modification of this technique, in which a silicone polymer is engraved first and the substrate pressed on it to capture the printed pattern. Therefore, the process follows the sequence of steps: (1) a patterned photoresist is created on a glass or steel plate, to create a mould; (2) a silicone polymer is poured onto the mould, left here to harden and then removed; (3) the gravure is fastened to a smooth metal plate to kept it rigid; (4) a doctor blade is passed over the gravure to fill the grooves in the silicone with microelectronic ink, as shown in Fig. 1.6. Figure 1.6(b) shows the substrate as it is pressed against the gravure to transfer the ink from the grooves.

The main benefit of this method compared with the earlier presented metal gravure printing is reportedly (Kittilä *et al.*, 2004) that a 100% release of paste can

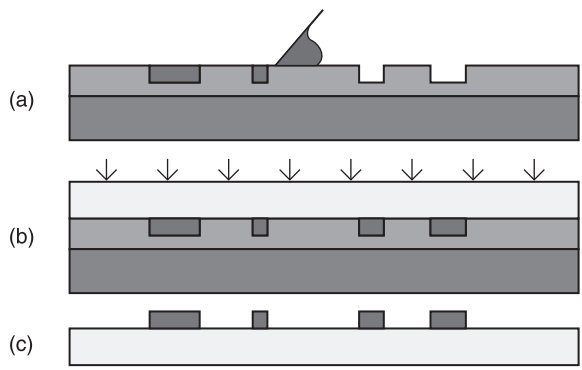

1.6 Direct gravure-offset-printing process from Kittilä *et al.* (2004): (a) doctor-blading the gravure to apply ink; (b) pressing the substrate against gravure to transfer ink; and (c) final printed pattern on substrate.

© Woodhead Publishing Limited, 2012

be obtained with commercial thick-film pastes, when an adequate polymer (in terms of stiffness, thickness, surface energy) is carefully selected. With groves 35 μm deep and an Ag-based commercial paste, conductive (resistivity of about 2.4 μΩ cm) continuous lines (10 cm long) with feature sizes below 20 μm and 8–17 μm thick on LTCC substrates have been demonstrated.

The feasibility of using the offset printing method to generate fine-line thick-films was described about 20 years ago. Among other applications, the printing of transistors (Mikami *et al.*, 1994), solar cell top layers (Hahne *et al.*, 1998), and ceramic thick-films (Leppävuori *et al.*, 1994) have been reported. Both conventional and fine-line thick-film pastes have been tested, by adjusting the type and amount of solvents and binders to finely tailor the viscosity and evaporation rate of the ink.

Gravure-offset-printing was performed for printing on unfired LTCC tapes, in addition to normal alumina substrates (Lahti, 2008). Yet, efforts to optimize the technology are in continuous progress, to adapt materials and processes to the new requirements, especially in terms of the composition and properties of inks and pastes. In fact, it is easy realized that different and optimized properties of the inks (e.g. viscosity, surface energy, content of volatile components, amount of functional material) are demanded in electronic applications that are not asked for in the graphic industry; similarly more stringent requirements in terms of reliability and performances of the deposited films are intrinsically linked to the new applications.

The direct gravure-offset-printing technique has similar advantages and limitations to screen printing. It is a parallel process and has the potential for high throughputs. In addition, it is capable of much smaller feature sizes because it is not limited by a mesh. However, the fabrication of the gravure does not lend itself to rapid prototyping or low-production runs and there may also be problems with selecting arbitrary conventional thick-film materials because of adherence to the gravure.

1.2.5 Reel-to-reel systems

Rotogravure

Rotogravure offset or simply gravure is commonly used in the graphic arts industry for medium to long print runs where uniformity and versatility are required. Gravure printed products span from bank notes and high-quality publications to postage stamps. Figure 1.7 shows a schematic of a typical gravure printing process. A large steel cylinder is electroplated with copper and then polished to a predetermined diameter. Once engraved, with microscopic cells, using either electromechanical or laser engraving, the cylinder is electroplated with a thin layer of chrome to ensure a surface hardness that protects the softer copper against scratches and abrasion by the doctor blade during printing. Low viscosity, or fluid ink is held in a bath beneath the rotating gravure cylinder, filling

© Woodhead Publishing Limited, 2012

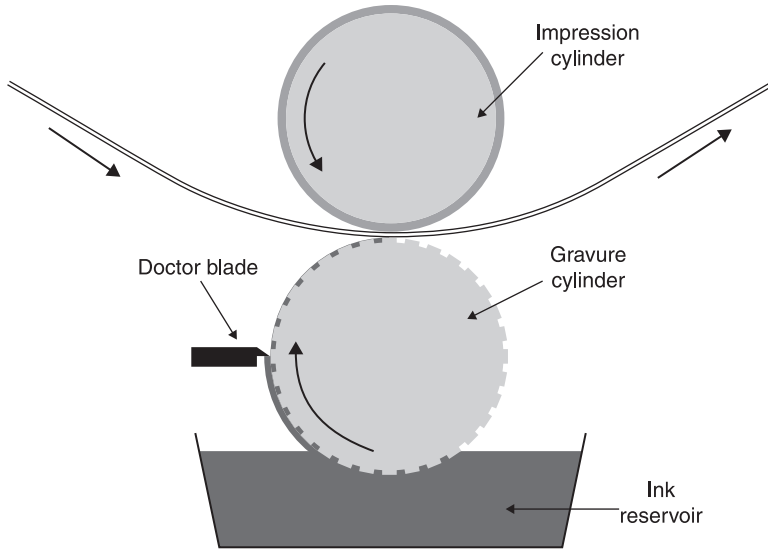

1.7 Schematic description for the ink transfer unit of the R2R gravure printing process; image elements on the gravure cylinder are typically 10–25 µm and equally spaced but variable in depth and area.

the etched cells with ink. The doctor blade scrapes off any excess ink from the cylinder as it rotates. A roll, or web, of paper travels between the etched cylinder and an impression cylinder, using capillary action to transfer the ink from the cells onto the paper, e.g. at a speed of 50 m/min.

Gravure inks may be water-based, solvent-based or even UV-curing. Their viscosities vary from 0.01 to 0.05 Pa. s. The printed ink film thickness increases from 8 to 12 µm, which is interesting for electronics applications.

The use of gravure for printed electronics has the potential to be a cost-effective way of mass-producing functional electronic devices (Hrehorova and Kattumenu, 2007; Sung, 2008). While still in its infancy, many companies are promoting research in this technology for various electronic applications. Promising future applications have been identified in the production of organic semiconductors for OLEDs, photovoltaic cells, thin film transistors (Hambsch *et al.*, 2010) and batteries.

Although the process is very well optimized for graphical purposes, the requirements for electronics printing are more demanding in terms of resolution and registration. A major limiting factor of other applications is presently due to difficulties in the production of consistent straight lines with conductive inks. In fact, lines printed from the typical row of dots are poorly delineated: jagged edges and ragged thickness are common with this type of engraving. Efforts are directed to optimize substrate wetting and ink spreading to get better patterns. The alternative strategy, i.e. printing from engraved intaglio trenches, has not yet

© Woodhead Publishing Limited, 2012

resulted in better conductive connections because of poor conformity between the specified width and height of the printed lines to those of the engraved lines; moreover, the former depends on the printing direction, a feature that might result in an unpleasant complexity in designs of electrical components.

Offset lithography

Offset lithography is one of the most common printing processes for the mass production of books, newspapers and packaging. The technique involves the use of an entirely smooth surface and relies on the dissimilar wetting properties set on different areas of the plate to produce the image. Figure 1.8 describes the process. The printing plate's surface chemistry is such that the hydrophobic image area repels water and attracts oil-based inks, whilst the hydrophilic non-image area is damped to repel the ink. The image is then transferred to the surface of the substrate via an intermediate or blanket roller. In such a way, high-resolution printing is achievable, as minimum feature sizes of 10 μm are readily achieved. The offset cylinder is typically made of a flexible material such as rubber to allow better contact with the surface of the target material. Consequently, quality is increased and the printing output is more consistent. In addition, the use of an intermediary offset cylinder prolongs the lifespan of the printing plates due to reduced wear and tear compared to directly contacting the printing plate with the target material. The quality of offset printing is high, considered only slightly inferior to the quality of the rotogravure technique. In standard processes with web-fed presses, printings up to 900 m of substrate per minute are performed.

The benefits of lithography are excellent resolution and registration of the circuit pattern, high volume/high speed production and low environmental impact. An advantage over intaglio printing is the fact that a flat plate surface allows longer and more detailed print runs. Among the limitations of this process as far as printed electronics are concerned, is that the ink film thickness remains low (1 to 2 μm) making it difficult the achieve electrical conductivity. Therefore, multiple passes may be necessary in order to print thick enough layers. Another limitation of offset lithography is the presence of water, which may affect the behavior of the functional materials including the electrical properties of the films. This drawback may be overcome by using waterless offset lithography: in this process, the dampening solution is replaced by a silicone layer covering the non-image areas of the plate. A mechanical accuracy of 2.5 μm is commonly achieved.

In printed electronics, offset lithography has been used primarily for printing conductive features, but not used extensively in organic electronics. One of the reasons may be the viscoelastic requirements necessary to formulate offset lithographic ink. The latter needs to start out very viscous (5 to 50 Pa. s) and thin out considerably when sheared. In order to achieve these viscoelastic properties,

© Woodhead Publishing Limited, 2012

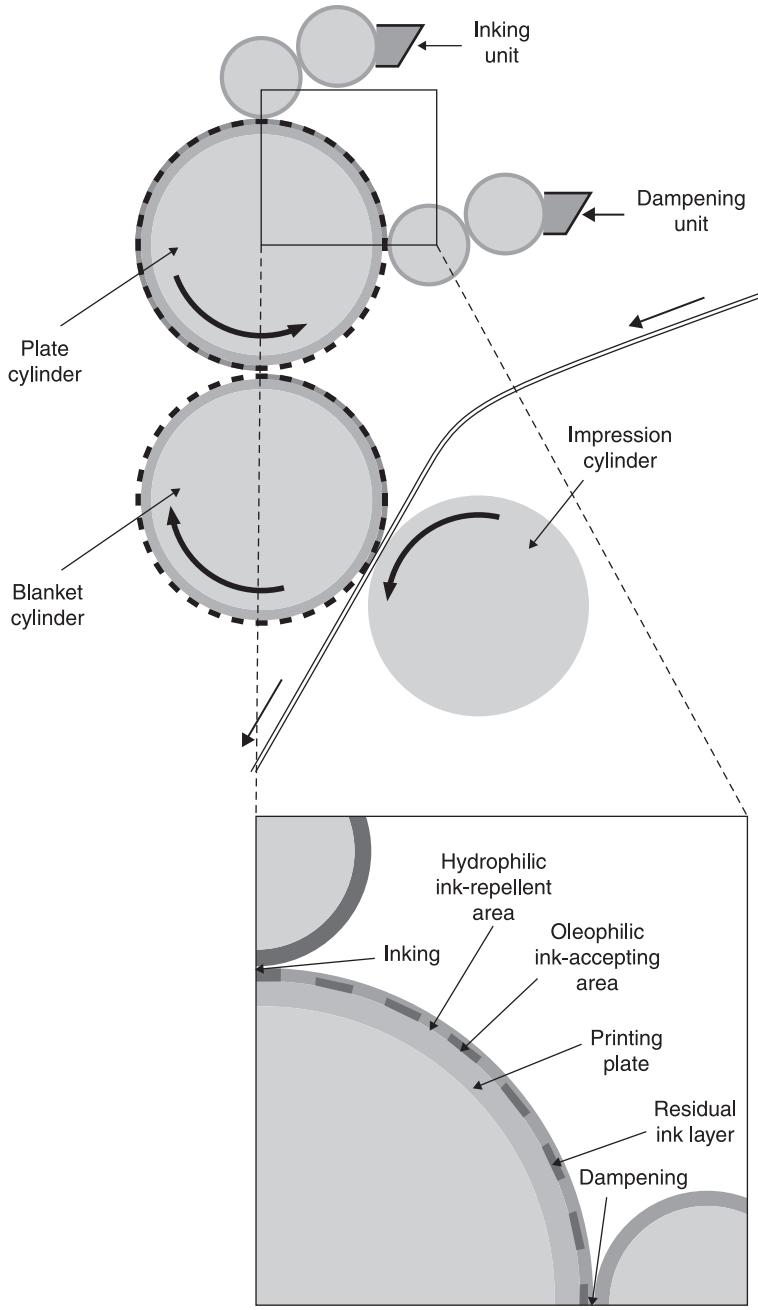

1.8 Offset lithographic printing process. In insert, the surface of the plate cylinder is shown in the region between the inking and dampening units.

© Woodhead Publishing Limited, 2012

additives are generally required that can reduce or inhibit the electrical functionality. Offset lithography has been applied in printing doped conductive polymers like PEDOT:PSS, which can be used as either conventional inks with few modifications or contained in the aqueous fountain solution.

Flexography

Flexography printing (or simply Flexo) typically utilizes a rubber or polymer cylindrical printing plate that has the desired to-be-printed pattern engraved as a positive relief in it and that applies a fluid ink to the substrate (Fig. 1.9). The ink usually comes from an ink chamber, in contact with a metering roller called 'anilox', which contains cells of regular size and shape, according to the ink film thickness and to the resolution needed on the plate. The doctor blade wipes the excess ink from the surface of the anilox, leaving only the amount needed within the cells. The printing cylinder is then allowed to roll over the surface of the target material, transferring ink onto it.

Flexography inks are relatively low in viscosity (usually from 0.01 to 0.5 Pa.s) and can be formulated from functional organic materials or particulate suspensions.

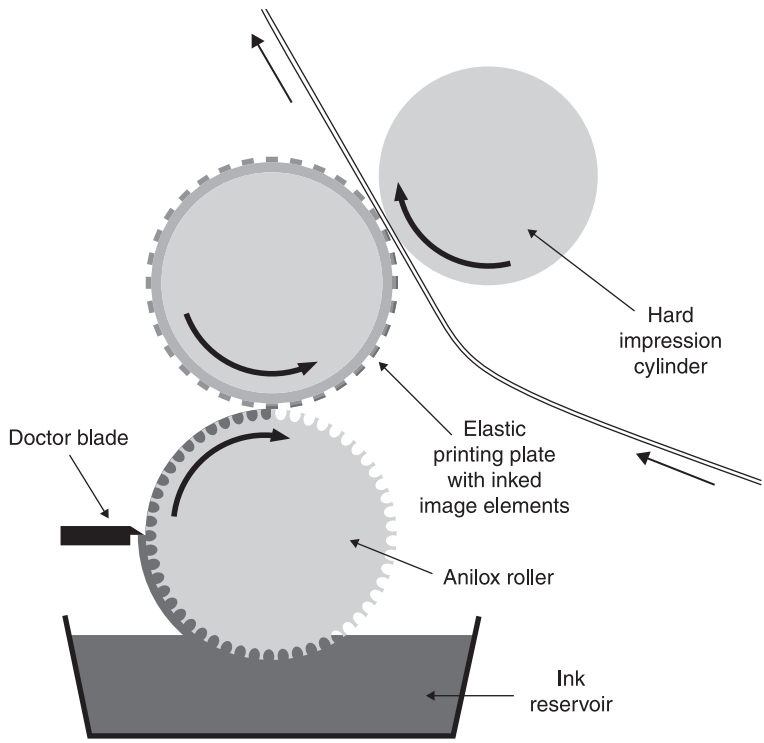

1.9 R2R flexographic printing process.

© Woodhead Publishing Limited, 2012

Substrates may be flexible or rigid, plane or corrugated, metal, glass, etc. The printed film thickness increases from 6 to 8 μm and the resolution can reach 60–75 lines per centimeter when thinner rigid plates are used. The process is conformal and quite tolerant of substrate abnormalities. Among the benefits of the flexographic process compared to lithography are the wider variety of inks that can be used, the many options for the target materials and the more suitable thickness of the printed films. Among the limitations of this printing process for functional materials is that a halo tends to form around the edges of the printed surfaces, caused by the squeezing of the ink out from under the edges of the printing plate.

Flexography is just starting to see use in printing electronics; examples are printing of conductive materials, including silver-containing inks, conductive organic polymers, and devices containing both, and to pattern the source and drain electrodes of an organic transistor.

1.3 Other systems

In addition to the previously described approaches, a wide variety of further processes have been developed, aimed at depositing and/or patterning films with potential applications in printed electronics and organic electronics. These include, among others, many laser-based processes such as laser-induced forward transfer (Bohandy *et al.*, 1986; Yamada *et al.*, 2002; Zhang *et al.*, 2009), matrix-assisted pulsed laser evaporation (Chrisey *et al.*, 2000), laser chemical vapor deposition (CVD) and pulsed laser deposition. Most of them are interesting direct-write technologies, typically for very thin films and high resolution. Further direct-write technologies involve the use of novel microdispensing tools (Zhang *et al.*, 2009; Metz *et al.*, 2009) or plasma spray (Herman *et al.*, 2000). Only selective laser sintering (SLS) and atmospheric plasma spray (APS) are briefly delineated here as non-vacuum technologies with promise for industrial applications.

Selective laser sintering (SLS) can achieve fine patterns of fully sintered screen printable inks in a single step process without the use of any high-temperature post-processing, unlike the current standard manufacturing process in which annealing of the printed layers is carried out at 850 °C. For infrared laser wavelengths (1–10 μm), the penetration depth of radiation is very dependent on laser and material properties, but for most combinations is between 1 and 10 μm. It was shown that with a proper choice of the parameters (laser-power density, rastering speed, wavelength) the laser radiation locally heats up the surface of the dried films, 3–10 μm thick, while the thermal energy diffuses laterally to the surrounding ink: the heating is enough to drive the sintering process in the material but limits the exposure of the substrate to high temperatures. Therefore, SLS has the potential to extend the range of possible substrates to thermally sensitive but technologically important substrates, such as glass and

© Woodhead Publishing Limited, 2012

polymers, while maintaining the conventional thick-film performance. Only evaporation and burn-out of the organic vehicle are performed in a conventional furnace at 120–150 °C to prevent rapid expansion of the films and pattern damaging.

The pattern is traced by computer data, and the process is performed in an ambient non-clean room environment. The resolution may be high, e.g. continuous lines less than 25 µm wide, about 1 µm thick and with a 100 µm pitch have been shown (Kinzel *et al.*, 2007). After patterning, the unsintered ink is dissolved in an organic solvent (e.g. in methanol). The SLS process has been demonstrated for metal and dielectric films in Patch Antennas on FR4 (Sigmarsson *et al.*, 2005), microwave components (Kinzel *et al.*, 2005), multilayers and other high frequency components (Sigmarsson *et al.*, 2006) on soda–lime glass, conductor carbon paste on plastic substrate (Kelkar *et al.*, 2009), Positive temperature coefficient (PTC) and thermistors (Cai *et al.*, 2009).

Traditional thermal spray technology is a large family of spray processes in which a stream of molten or softened particles (the drops) is created by injecting materials into a high-temperature combustion chamber or into a plasma and accelerating the drops to high velocities. The stream eventually impinges upon a substrate, where a dense and strongly adhered deposit is formed by rapid solidification of flattened, solidified platelets, referred to as splats (Herman *et al.*, 2000). By controlling the process parameters it is possible to deposit a wide range of materials (metals, ceramics, polymers, semiconductors and combinations thereof) onto virtually any substrate in various conformal shapes. With appropriate masks, 'mesoscopic' (i.e. millimeter wide and micrometer thick) components and devices, such as resistors, heaters, sensors, etc. are printed (Sampath, 2010). The Direct-write Thermal Spray is an extension of this technology, developed at SUNY-Stony Brook under the DARPA's Mesoscopic Integrated Conformal Electronics (MICE) Initiative. The process involves the use of adequate collimators that confine the stream of droplets and allow the spraying of precision patterns (100–500 µm wide) directly onto the substrate. When driven by CD data, direct-write spray allows for the deposition of blankets, patches and lines of a variety of sensor, electronic and coating materials on conformal substrates (Sampath, 2010). These are done at high speeds, efficiently and at low cost. Furthermore, because of the nature of the direct-write process, it is straightforward to deposit sensors on large areas, conformable surfaces, and even flexible surfaces without masks (Sampath *et al.*, 2003).

Among the virtues of thermal spray are: the limited thermal input for film consolidation, allowing for deposition on to a variety of substrates; the ability to integrate the technology with robotics; the easy prototyping of special sensor systems; moreover, it is a green technology vis-à-vis plating, lithography, etc. Limitations include possible compositional changes of sprayed materials, due for example to in-flight oxidation of molten droplets; furthermore, the process cannot be applied to materials that decompose at high temperatures.

© Woodhead Publishing Limited, 2012

1.4 Conclusion

The basic characteristics of the main printing processes for electronic components have been addressed. The long and rich historical path of thick-film technology has been surveyed and the potential capabilities of the newer processes examined with brief references to, and inevitable personal views about the relevance of, successful accomplishments and potential issues in material preparation and applications. The substantial involvement of many large consortia, big companies and institutions in search of cost-effective and technically sound printing technologies, in conjunction with the variety of technically conceivable solutions, offers promising outlooks for future applications of printed films; it is clear that all the various printing technologies will find a role to play in the incoming era of printed electronics.

1.5 References

Blayo A. and Pineaux B., 2005, Printing processes and their potential for RFID printing, *Joint sOc-EUSAI conference, Grenoble*, pp. 27–20.

Bohandy J., Kim B. F. and Adrian J., 1986, Metal deposition from a supported metal film using an excimer laser, *Journal of Applied Physics*, 60(4), 1538–1539.

Bouchard R. J., 1999, Thick-film technology: an historical perspective, *Ceramic Transactions*, *100* (Dielectric Ceramic Materials), 429–442.

Bube K. R., Kapur V. K., Gay C. F. and Lewis K. J., 1980, Thick-film metallization for solar cells, *Proceedings International Microelectronics Symposium*, pp. 265–271.

Buzan F. E., Grier J. D. Sr., Bertsch B. E. and Thoryk, H., 1977, A thick-film base metal resistor and compatible hybrid system, *European Hybrid Microelectronic Conference*, Bad Homburg, Paper XIX.

Cai Z., Li X., Hu Q. and Zeng X., 2009, Laser sintering of thick-film PTC thermistor paste deposited by micro-pen direct-write technology, *Microelectronic Engineering*, 86(1), 10–15.

Calvert P., 2001, Inkjet printing for materials and devices, *Chemistry of Materials*, 13(10), 3299–3305.

Canali C., Malavasi D., Morten B., Prudenziati M. and Taroni A., 1980, Piezoresistive effects in thick-film resistors, *Journal of Applied Physics*, 51(6), 3282–3288.

Carr B. P., 1994, Introduction to thick-film fine line printing screens, *Hybrid Circuits*, 33, 4–7.

Cattaneo A., Dell'Acqua R., Dell'Orto G., Pirozzi L. and Canali C., 1980, A practical utilization of the piezoresistive effect in thick-film resistors: a low cost pressure sensor, *Proceedings of International Microelectronics Symposium*, pp. 221–228.

Chakrabarty N., Einzinger, R. and Weitze A., 1980, *Thick-film varistor and method of producing same*, US Patent 4186367.

Chrisey D. B., Pique A., Fitz-Gerald J., Auyeung R. C. Y, McGill R. A., *et al.*, 2000, New approach to laser direct writing active and passive mesoscopic circuit elements, *Applied Surface Science*, 154–155, 593–600.

de Gans B.-J., Duineveld P. C. and Shubert U. S., 2004, Inkjet printing of polymers: State of the art and future development, *Advanced Materials*, 16(3), 203–213.

Deyrup A. J., Kermit H., Ballard K. H., and Strickarz J. J., 1945, *Preparation of electrical capacitors*, US Patent 2.389.419.

© Woodhead Publishing Limited, 2012

Drumhelelr C. H., 1982, Dynamic pen control in synchronous positive displacement CAD/CAM thick-film writing systems, *International Journal of Hybrid Microelectronics*, 5(2), 449–454

Dziedzic A., Nijs J. and Szlufcik, J., 1993, Thick-film fine-line fabrication techniques – application to front metallization of solar cells, *Hybrid Circuits*, 30, 18–22 and 26.

Friedman A. I. and Bartholomew R. L., February 1969, *Applications of conductive inks*, US Patent 3,647,532.

Frisson L., Lauwers P., Bulteel P., De Smet L., Mertens R., *et al.*, 1978, Screen-printed contacts on silicon solar cells with low series resistance, *Proceedings 13th Photovoltaic Specialists' Conference, Washington, DC, June 5–8*. IEEE, New York, pp. 590–592.

Gongora-Rubio M. R., Espinoza-Vallejos P., Sola-Laguna L. and Santiago-Aviles J. J., 2001, Overview of low temperature co-fired ceramics tape technology for meso-system technology, *Sensors and Actuators A*, 89(3), 222–241.

Hahne, P., Reis, I. E., Hirth, E., Huljic, D., Preu, R., *et al.*, 1998, Pad printing – a novel thick-film technique of fine-line printing for solar cells, *2nd World Conference and Exhibition on Photovoltaic Solar Energy Conversion, Proceedings of the International Conference*, Vol. 2. Luxembourg: Office for Official Publications of the European Communities, pp. 1646–1649.

Halls J., 2005, Ink-jet printing of PLED displays, *Information Display*, 2(5), 10–15.

Hambsch M., Reuter K., Stanel M., Schmidt G., Kempa H., *et al.*, 2010, Uniformity of fully gravure printed organic field-effect transistors, *Materials Science and Engineering B*, 170, 93–98.

Herman H., Sampath S., and McCune R., 2000, Thermal spray: Current status and future trends, *MRS Bulletin*, 25(7), 17–25.

Hicks W. T., Allington T. R. and Johnson V., 1980, Membrane touch switches: Thick-film materials systems and processing options, *IEEE Transactions on Components, Hybrids and ManufacturingTechnology*, 3(4), 518–524.

Hoffman L. C., 1984, An overview of thick-film hybrid materials, *American Ceramic Bulletin*, 63(4), 572–576.

Hrehorova E. and Kattumenu R.-C., 2007, Evaluation of gravure print forms for printed electronics, *GravurEzine*. Retrieved online February 10, 2011, http://www.gravurexchange.com/gravurezine/0702-ezine/hrehorova.htm.

Jolley J. E., Weaver R. V., Wells J. H., Felten J. J. and Roe D. W., 1974, Photoprintable materials and processing equipment for thick-film microcircuitry, *Solid State Technology*, 17(5), 33–37.

Kay R. W., Desmulliez M. P. Y., Stoyanov S., Bailey C., Durairaj R. K., *et al.*, 2003, Advanced microsystems assembly using screen printing technology, *Proceedings of MicroSystems Technologies*, Munich, Germany.

Kelemen D. G, 1970, Metallographic aspects of thick-film technology, *Metallurgical Transactions*, 1(3), 667–677.

Kelkar R., Kinzel E. C. and Xu X., 2009, Laser sintering of conductive carbon paste on plastic substrate, *Optical Engineering*, 48(7), 074301–074305.

King B. H., Dimos D., Yang, P. and Morissette S. L., 1999, Direct-write fabrication of integrated, multilayer ceramic components, *Journal of Electroceramics*, 3(2), 173–178.

Kinzel, E. C., Sigmarsson, H. H., Xu, X. and Chappell, W. J., 2005, Selective laser sintering of microwave components, *European Microwave Conference*, Paris, France.

Kinzel E. C., Sigmarsson H. H., Xu X., and Chappell W. J., 2007, Laser sintering of thick-film conductors for microelectronic applications, *Journal of Applied Physics*, 101(6), 063106-063106-9.

© Woodhead Publishing Limited, 2012

Kirby P. L., 1989, Origins and advances in polymer thick-film technology, *Proceedings of 7th European Hybrid Microelectronic Conference, Hamburg, ISMH*, Paper 4.1.

Kishi H., Mizuno Y. and Chazono H., 2003, Base-metal electrode-multilayer ceramic capacitors: Past, present and future perspectives, *Japanese Journal of Applied Physics*, 42(1), 1–15.

Kittilä M., Hagberg J., Jakku E. and Leppävuori S., 2004, Direct gravure printing (DGP) Method for printing fine-line electrical circuits on ceramics, *IEEE Transactions on Electronics Packaging Manufacturing*, 27(2), 109–114.

Lahti M., 2008, *Gravure offset printing for fabrication of electronic devices and integrated components in LTCC modules*, Academic dissertation, Faculty of Technology of the University of Oulu, October 10, 2008. Available online at http://herkules.oulu.fi/isbn9789514288944/index.html?lang=en.

Leppävuori, S., Väänänen, J., Lahti, M., Remes, J., and Uusimäki, A. 1994, A novel thick-film technique, gravure offset printing, for the realization of fine-line sensor structures, *Sensors and Actuators A*, 42(1–3), 593–596.

Li B., Clark P.A. and Church K.H., 2007, Robust direct-write dispensing tool and solutions for micro/meso-scale manufacturing and packaging, *Proceedings of the ASME International Manufacturing Science and Engineering Conference*, Atlanta, Georgia, October, pp. 1–7.

Licari, J. J. and Enlow, L. R., 1998, *Hybrid Microcircuit Technology Handbook* (2nd edn), Noyes Publications, Westwood, NJ.

Mei J., Lovell M. R. and Mickle M. H., 2005, Formulation and processing of novel conductive solution inks in continuous inkjet printing of 3-D electric circuits, *IEEE Transactions on Electronics Packaging Manufacturing*, 28(3), 265–273.

Metz T., Birkle G., Zengerle R. and Koltay P., 2009, Starjet: pneumatic dispensing of nano-to-picoliter droplets of liquid metal, *Proceedings of IEEE-MEMS 2009*, Sorrento, Italy, pp. 43– 46.

Mikami Y., Nagae Y., Mori Y., Kuwabara K., Saito T., *et al.*, 1994, A new patterning process concept for large-area transistor circuit fabrication without using an optical mask aligner, *IEEE Transactions on Electronic Devices*, 41(3), 306–312.

Minalgiene J., Baltrushaitis V. and Muckett S., 1994, Very fine line photoimageable thick-film technology developed at hibridas, *Microelectronics International*, 11(2), 25–30.

Morten B., Prudenziati M. and Taroni A., 1983, Thick-film technology and sensors, *Sensors and Actuators*, 4, 237–245.

Naguib M., Kavanagh K. L. and Hobbs L. H., 1980, A new process for printing fine conductor lines and spaces on large area substrates, *Solid State Technol*, 23, 109–114.

Piqué A. and Chrisey D. B., 2002, *Direct-Write Technologies for Rapid Prototyping Applications*, Academic Press, San Diego, CA.

Prudenziati M. (ed.), 1994, *Thick-film Sensors*, Elsevier, Amsterdam.

Redinger D., Molesa S., Yin S., Farschi R. and Subramanian, V., 2004, An ink-jet deposited passive component process for RFID, *IEEE Transactions on Electronic Devices*, 51(12), 1978–1983.

Rida A., Li Y., Vyas R., Basat S., Bhattacharya S. K. and Tentzeris M. M., 2007, Novel manufacturing processes for ultra-low-cost paper-based RFID tags with enhanced 'wireless intelligence', *IEEE: Proceedings Electronic Components and Technology Conference*, pp. 773–776.

Sampath S., 2010, Thermal spray applications in electronics and sensors: past, present, and future, *Journal of Thermal Spray Technology*, 19(5), 921–949.

© Woodhead Publishing Limited, 2012

Sampath S., Herman H. and Greenlaw R., 2003, *Method and apparatus for fine feature spray deposition*, June 10, USA Patent 6.576.861.

Shankin M., 1978, Write it, don't screen it, *Proceedings IMS (ISHM USA)*, pp. 18–25.

Sigmarsson H. H., Kinzel E. C., Chappell W. J. and Xu X., 2005, Selective laser sintering of patch antennas on FR4, *IEEE Antennas and Propagation Conference*, Washington, DC, Vol. 1A, pp. 280–283.

Sigmarsson H. H., Kinzel E. C., Chappell W. J. and Xu X., 2006, Selective laser sintering of multilayer, multimaterial circuit components, *IEEE Microwave Theory and Techniques Symposium*, San Francisco, pp. 1788–1791.

Singh M., Haverinen H. M., Dhagat P. and Jabbour G. E., 2010, Inkjet printing-process and its applications, *Advanced Materials*, 22(6), 673–685.

Sue R. and Naguib H. M., 1984, Mid-film interconnects for multilayer microcircuit packages, *ElectroComponent Science and Technology*, 11(2), 97–108.

Sung D., 2008, *Gravure as an industrially viable process for printed electronics*, May 23, University of California Berkeley, February 9, 2010. Retrieved online: http://www.eecs.berkeley.edu/Pubs/TechRpts/2008/EECS-2008-70.pdf.

Tarnopol, M. S. and Snyder, T, P., 1969, *Applying electroconductive heating circuits to glass*, US Patent 3671311.

Teng K. F. and Vest R. W., 1987, Liquid ink jet printing with MOD inks for hybrid microcircuits, *IEEE Transactions on Components, Hybrids and Manufacturing Technology*, 12(4), 545–549.

van Hest M. F. A. M., Habas S. E., Underwood J. M., Pasquarelli R. M., *et al.*, 2010, Direct write metallization for photovoltaic cells and scaling thereof, *Photovoltaic Specialists Conference (PVSC), 35th IEEE*, pp. 003626–003628.

Vest R. W., Tweedell E. P. and Buchanan R., 1983, Ink jet printing of hybrid circuits, *International Journal for Hybrid Microelectronics*, 6(1), 261–267.

Vitriol W. A. and Steinberg J. I., 1983, Development of a low temperature, cofired multilayer ceramic technology, *International Journal for Hybrid Microelectronics*, 6(1), 593–598.

Voigt J. F. H. and Haeffner J. A., 1899, *Electrical resistance*, US Patent 617,375.

Werdecker W. and Aldinger F., 1984, Aluminum nitride – an alternative ceramic substrate for high power applications in microcircuits, *IEEE Transactions on Components, Hybrids and Manufacturing Technology*, 7(4), 399–404.

Wilson D. G. and Johnson G. W., 1977, New materials for low cost thick-film circuits, *Solid State Technology*, October, pp. 49–54 and 75.

Yamada H., Sano T., Nakayama T. and Miyamoto I., 2002, Optimization of laser induced forward transfer process of metal thin films, *Applied Surface Science*, 197–198, 411–415.

Yang P., Dimos D., Rodriguez M. A, Huang R. F., Dai S. and Wilcox D., 1999, Direct-write precision resistors for ceramic packages, *Materials Research Society Symposium, Proceedings 542: Solid Freeform and Additive Fab*rication, pp. 159–164.

Young W. S. and Knickerborker S. H., 1991, Multilayer ceramic technology, in R. C. Buchanan (ed.), *Ceramic Materials for Electronics Processing Properties and Applications*, 2nd edn, Marcel Dekker Inc, New York, pp. 489–526.

Zhang Y, Liu C. and Whalley D, 2009, Direct-write techniques for maskless production of microelectronics: A review of current state-of-the-art technologies, *International Conference on Electronic Packaging Technology and High Density Packaging (ICEPT-HDP)*, pp. 497–502.

© Woodhead Publishing Limited, 2012

2

Materials for printed films

J. HORMADALY, Ben-Gurion University, Israel and
M. PRUDENZIATI, University of Modena and
Reggio Emilia, Italy

Abstract: The chapter provides a critical survey of the compositions of materials (pastes and substrates) for applications in thick-film microelectronics and sensors. The evolution of the technology is illustrated with wide references to publications and patents.

Key words: thick-film compositions, air- and nitrogen-fired resistors, conductors, dielectrics, deposition medium, glass and glass ceramics, substrates.

2.1 Introduction

Thick-film (TF) materials or TF compositions and the general term 'thick-film technology' have been the subject of reviews (Bouchard, 1999; Hoffman,1984; Larry *et al.*, 1980; Vest, 1986) and books (Borland, 1989; Holmes and Loasby, 1976, 1988; Prudenziati, 1994; Rikoski, 1973; Sergent, 2004; Vest, 1991). Traditionally, TF materials, which are also known as pastes, dispersions and inks, were classified into three material categories: conductive, resistive and dielectric. Nowadays, the term TF materials comprises a larger group of inorganic and organic materials and the previous classification needs revision to include new materials and new applications. TF materials have three major constituents:

1. the active phase, which was considered the phase that imparts the functional properties;
2. the glass/glass–ceramic binder;
3. the vehicle that controls the dispersion of the active phase, the glass/glass–ceramic binder and the viscosity of the paste.

This simple description of the paste does not include interactions of the active phase with the glassy binder, substrate, vehicle and the metallic terminations. The interactions of the paste ingredients with the substrate and the terminations are very important, and are the subject of Chapter 3.

This chapter is a critical review of the chemistry and material science of TF materials. While it is intended to be comprehensive treatment of TF materials, it makes no attempt to be historically complete, or to cover all the information available in the journals and patent literature.

© Woodhead Publishing Limited, 2012

2.2 Active phases

2.2.1 Classification of active phases

The TF literature refers to the functional, pigment or the active phase as the constituent that controls the electrical properties of fired paste composition. Thus, the metallic phase (Ag, Ag/Pd, Ag/Pt, Ag/Pt/Pd, Au, Au/Pd, Au/Pt, Au/Pd/Pt for air-fired conductors or Cu, Ni for nitrogen-fired conductors), which is the major constituent of the conductor composition, determines the electrical properties. For TF resistors the metallic oxide (RuO_2, IrO_2, Bi_2 Ru_2O_7, $Pb_2Ru_2O_{6+\delta}$, etc. for air-fired compositions) and the conducting phase (LaB_6, borides, silicides, carbides, doped tin oxide, etc. for nitrogen-fired compositions) are considered as the active or the functional phases. In fact, the combination of materials, i.e. metallic oxide, glass and additives, determines the characteristic resistor properties, rather than the metallic phase alone. The same applies to the dielectric active phase: the combination of glass, high dielectric ceramic and additives determines the electrical properties.

In this chapter a different classification of the active phases is used. Metallic oxides and other electrically conducting materials are treated as a group of conducting materials for resistors. The conductors and dielectrics are treated traditionally.

Materials for nitrogen firing are treated as a separate group because the compositions and the thermodynamic properties required are different from air-fired compositions. Materials for AlN, SiC, glass and other substrates are different from standard TF composition and are treated as a separate group. All the above-listed subgroups are the subject of section 2.2. The organic vehicle for standard air-fired compositions and specialized compositions for inert atmosphere firing, photosensitive, water-based and other applications are the subject of section 2.3.

Glasses and glass ceramics are very important constituents of TF compositions and are treated as separate group in section 2.4. Glass compositions, mainly from the patent literature, are described for air-fired resistors, lead-free air-fired resistors, nitrogen-fired resistors, conductors, dielectrics overglazes and sensors.

2.2.2 Conducting materials for resistors

Resistive materials used in TF compositions are a subgroup of resistor materials that comprises metals, alloys, other elements, metal metal-oxides mixtures, inorganic oxide compositions, other inorganic compounds and organic composition. A review of resistor materials that was based on the patent literature of the period 1960 to 1971 was written by Conrad (1971), and the trends in TF resistor technology until 1971 were reviewed by Van Loan (1971). Prior to 1960, there are some resistor materials patents that facilitate the understanding of the evolution of TF resistive compositions; these are patents to Jira (1942, 1944, 1948a, 1948b), Rosenblatt (1939, 1943) and Soby (1951). One of the patents

© Woodhead Publishing Limited, 2012

(which includes materials, processing, additives and concepts that are of importance to TF materials in general and specifically to resistor materials) is by Place and Place (1960a, 1960b). In one of the embodiments of the method of preparing the resistor material, the resistance material is prepared in large batches and stored indefinitely. The large batch is prepared by milling the glass binder, metals and metal oxides and the noble metals and oxidizable metals being present in the form of soluble metal compounds. The milled mixture is heated to about 700 °F to remove volatiles and organic materials from the mixture, to decompose the metal compounds and to oxidize the oxidizable metals. The resulting dry material is ground to fine powder and calcined at about 850 °F (454 °C). The resulting calcine is ground to fine powder and stored. The method described above may result in oxidation of Ru, Ir and Rh to the oxides RuO_2, IrO_2 and Rh_2O_3. Therefore, this patent (Place and Place, 1960a, 1960b) may be considered the first one that made use of the oxides RuO_2 and IrO_2.

Palladium – silver system

D'Andrea (1960) describes a vitreous enamel resistor composition that may be applied to and fired on a ceramic body to produce an electrical resistor. The composition consists of fine powders of Pd 4–50%; Ag 0–40% and flux (frit or frit plus Bi_2O_3 and PbO) 50–92%. The glass frits used were lead borosilicate and bismuthate glass (lead borosilicate plus Bi_2O_3). A related patent is Dumesnill (1962), which uses PdO plus RhO, metallic additives Ag, Au, Pt, enamel frit (lead borosilicate) and metal oxide taken from the group consisting of Zr, Al, Sr, Ca, Sn, Mg, Zn and the rare earth metals. Related to the Pd/Ag and PdO/Ag resistance compositions are the following variations of PdO/Rh_2O_3/Ag-based compositions: Mones and Neisser (1966) developed compositions containing PdO/Rh_2O_3/Ag and lead borosilicate glass. The semiconducting oxides PdO and Rh_2O_3 may be doped by univalent, divalent and multivalent cation selected from Sb, Cr, Mo, Cu, Li and Na. These compositions have a broader resistance range and better temperature coefficient of resistance (TCR). Mones (1967) used a resistance composition based on PdO, $PdCl_2$, Pd and halides of silver like AgCl, AgBr and AgI and glass. In addition, the composition may contain Bi_2O_3, PbO and silica. Boyd *et al.* (1968) developed a process to control the crystallite size of PdO and they developed a method to prepare resistance compositions based on specified oxides of Pd and Rh. In addition to these oxides, the resistance compositions may contain Ag, Pt or Au and fine oxides of silicon and aluminium. Miller (1968a) uses a PdO/Ag composition, the synthesis of PdO and the roll milling process are described, and the correlation of roll milling with electrical properties is also discussed. This composition contains an organic vehicle based on an aromatic solvent, polystyrene resin and a nonylphenoxy polyoxyethylene ethanol surfactant. The glass used was multicomponent lead cadmium boroaluminosilicate with TiO_2, ZrO_2 and Na_2O, a typical acid-resistant glass composition.

© Woodhead Publishing Limited, 2012

Properties of this system were reported by Coleman (1975), Melan and Mones (1967) and Okamoto and Aso (1967). The properties of this system were reviewed by Finch (1969) and discussed by Holmes and Loasby (1976).

The palladium–silver system is a reactive system: Pd can oxidize to PdO during firing, form an alloy with Ag, the alloy can oxidize too and the PdO formed can easily reduce back to the metal. These properties make the system very sensitive to firing conditions, glass composition and the surface area of the metallic ingredients. A vitreous enamel resistance material developed by Janakirama-Rao and Murphy (1964) consists of lead borosilicate glass or barium calcium borosilicate glass containing Ag, Cu and Au in the ionic state and finely divided metal selected from the group consisting of Pd, Pt and Rh.

> The introduction of Ag, Cu or Au in the ionic state into the glass frit improves the melting of the frit so as to improve its wettability. In addition, it improves the overall performance of the electrical properties of the enamel resistance material in that it permits the obtaining of the desired conductivity of the material with smaller amount of the finely divided conductor – Rao and Murphy (1964).

The rationale behind the introduction of ionic Ag, Cu or Au into the glass was to improve wettability of the conductor material (Pd, Pt, Rh and Ag) by the glass frit so as to improve the conductive properties of the resistance material. The description of this patent regarding the conduction of electrical current and the role of the ionic Ag, Cu or Au in the glass is very interesting:

> In an enamel type resistance material, the conductive metal particles exist as isolated islands in the glassy matrix. When an electrical potential difference is applied across such resistance film, conduction takes place between the conductive metal particles through the glassy matrix, which glassy matrix is normally an insulator. Also, the electronic configuration of Ag, Au, or Cu ions in the glass frit of the present invention is such that the ions are deficient in an electron so that the ions can momentarily act as electron acceptors. However, the electronic configuration of Pd, Pt, Rh metal of the conductive particles is such that they have a full quota of electrons and can act as electron donor. For this reason, it is felt that when an electrical potential difference is placed across the enamel resistance material of the present invention, the silver, gold or copper ions in the glassy matrix act as a bridge between the isolated islands of the conductive metal particles by accepting and passing on an electron, and thereby improve the conductivity of the enamel resistance material again quoting from the patent to Janakirama – Rao and Murphy (1964).

It seems that the concept of having a glassy film between the conducting particles was practised in the patent literature many years before it was republished in the open literature. The mediating role assigned to the ionic species in the glassy matrix may be applied to Ru-based materials to explain conductivity and to explain the role of TCR-drivers or modifiers.

© Woodhead Publishing Limited, 2012

The ruthenium and iridium system

Ruthenium and iridium have been used in resistors as metals, the dioxides RuO_2 and IrO_2, and as complex mixed oxides such as $Bi_2Ru_2O_7$, $Bi_2\ Ir_2O_7$ and $Pb_2\ Ru_2\ O_{6+\delta}$ where $\delta = 0 - 1$. They are discussed together because both are members of the platinum metals – Group VIII, their dioxides are metallic and have the same crystal structure – rutile – and their ternary oxides are also metallic and have similar crystal structure – pyrochlore.

Most of their binary and ternary oxides are electrically conducting; the dioxides and ternary oxides of lead and bismuth $Bi_2Ru_2O_7$, $Bi_2Ir_2O_7$, $Pb_2Ru_2O_{6+\delta}$ are metallic oxides (Tsuda *et al.*, 1991). RuO_2 is not a stoichiometric compound: 'RuO_2 is seldom, if ever, obtained entirely pure but is usually defective in oxygen with corresponding amount of Ru^{III} in place of Ru^{IV}' (Cotton and Wilkinson, 1966).

The use of Ru as a resistor material prepared in a reducing atmosphere was described by Rosenblatt (1939, 1943) and in air atmosphere can be deduced from the explanation of Place and Place (1960a, 1960b). The patent to Daily *et al.* (1967) uses a resistance element consisting of minute crystals of metal (Ru) dispersed in a thin film of glass fired onto a base or substance of high temperature-resistant insulating material, such as ceramic. The composition of the resistor paste is: ground glass frit (lead–boro silicate) 8.7 wt%: ruthenium organosol (ruthenium resinate having 4% Ru by weight) 4.35 wt%, and screening and viscosifying agent 86.95wt%. This patent explains that the composition of the glass used is not critical, nor the manner in which it is produced, and the glass becomes very corrosive at 800–850 °C firing and will attack the ceramic base. Although this patent describes minute crystals of Ru metals as the resistor material, it is more likely that the Ru resinate will decompose, as do all complexes of Ru when fired (Cotton and Wilkinson, 1966) the Ru will substantially oxidize to RuO_2. Bruhl and Counts (1967) developed a process in which a cermet mixture based on an alloy of Au and Ir provides a resistance material with high resistivity and low TCR, and a second process (Counts and Bruhl, 1969) in which a cermet mixture formed of a glass and an alloy of Ir and at least one of the other noble metals, selected from the group consisting of Pt, Ag, Ru, Rh and Pd, provides a resistance material with high resistivity. During the firing of the alloys above, it is likely that some Ir, Ru and Rh will oxidize to IrO_2, RuO_2 and Rh_2O_3: the high resistance, not typical of metals, is due to the metallic oxides, IrO_2 and RuO_2.

A patent to Faber *et al.* (1967) describes a cermet-type resistor element with low TCR of about 0.01%/C and a broad resistance range from below 100Ω/□ to about 180.000Ω/□. The resistor composition is based on RuO_2 and IrO_2; substitution of IrO_2 for RuO_2 increases the resistance. The composition can be made with powders of RuO_2 and IrO_2, glass frit and an organic vehicle, or it can be made from resinates of Ir and Ru and organic precursor derivatives of the glass. The glass used is a simple lead borosilicate, PbO-63wt%; B_2O_3-25wt%; SiO_2-12wt%. To control the

© Woodhead Publishing Limited, 2012

stability of the ceramic resistance elements, small percentages of cupric oxide and/or manganese oxide are preferably dissolved in the glass.

Herbst and Dawson (1971) reviewed some of the patent literature and explored a system based on oxides of ruthenium and iridium with metallic additives Ag, Au or Pt and oxides including ZrO_2, HfO_2, TiO_2 and La_2O_3. These resistors have excellent noise, TCR and other properties at resistances up to 10 MΩ/□ and in all formulations the frit content was less than 78%. The preferred metallic oxide is the hydrate $RuO_2{*}ZH_2O$, where Z = 0.1 to 3.5.

The conductor is a mixture of metals (M) and the ruthenium or iridium oxide (O), the mixture is defined by $M_x + O_y$ and x and y define the weight ratio between M and O, both generally falling within the range of 0.2 to 0.8. The conducting mixture comprises from 20% to 70% of the composition and the remainder of the composition is the glass frit (lead borosilicate) and oxide (ZrO_2, TiO_2, HfO_2, La_2O_3). At a given conducting mixture content the resistance increases with the increase in the silver content (M). The TCR of the resistors is a function of resistivity, and not of x and y. The resistance can be varied from □500Ω/□ to 50 KΩ/□ within a relatively narrow TCR range of 150 ppm/ºC. In a series of tests with conducting mixture $Ag_{0.5}$ $(RuO_2{*}ZH_2O)_{0.5}$ wherein the conductive fraction was 33.3% of the composition, and the value of Z varied over the 0.1 to 3.5 range, it was found that as the Ru content increases (i.e. Z decreases) the resistance decreases by about an order of magnitude and as the anhydrous state (RuO_2) is approached resistance rises quickly to the megaohm range. The degree of RuO_2 hydration affects resistivity. It is also clear that, by controlling the degree of hydration, higher resistivities can be obtained at higher metal concentrations.

Angus and Gainsbury (1972) describe resistor compositions comprising ruthenium and/or iridium dioxides with fine crystallite size that does not exceed 50 nm. The resistors made from these compositions are characterized by low noise levels and low TCR. This patent shows that the TCR of an oxide–glass resistance film of a given composition depends largely upon the crystallite size of the metallic oxide, being more negative and thus less positive for smaller crystallite sizes. At the same time, the current noise of the resistance film is significantly lower than with oxides with larger crystallites. The size of the glass (lead borosilicate; 65% PbO, 25% SiO_2, 10% B_2O_3) is not critical. The patent also describes the synthesis of $RuO_2{*}XH_2O$ and IrO_2, with small crystallite sizes, from the corresponding chlorides of Ru and Ir.

Iles and Casale (1967) reported RuO_2-based glaze resistors for firing on mica and other low-temperature substrates. To stabilize the RuO_2 the authors doped it with Nb_2O_5. The Nb_2O_5 could be introduced into the RuO_2 lattice in quantities up to 50% molecular, i.e. up to the composition $Ru_{0.5}Nb_{0.5}O_2$.

Casale *et al.* (1972) report a resistor composition in the form of an oxide containing niobium and ruthenium in which the atomic ratio of metal to oxygen is 1:2 and in which the atomic ratio of niobium to ruthenium is within the range of 1:2000 to 1:1. The resistance materials are prepared by heating RuO_2 and Nb_2O_5

© Woodhead Publishing Limited, 2012

at 1400°C for several hours in a closed ceramic container. It seems that a new compound is formed between the ingredients at 1400°C, but the patent and the article do not disclose the composition.

Asada (1973) presents resistor compositions based on RuO_2 coated by Nb_2O_5, sources of Nb_2O_5 are alkoxides such as $Nb(OR)_5$ where R = $-C_2H_5$; $-C_4H_9$; $-CH_2CH_2CH(CH_3)_2$; C_3H_9; $-C(CH_3)_3$; Sec-C_4H_9; $-CH(C_2H_5)CH_2CH_3$; $-CH(CH_3)$ C_3H_7 – iso-C_4H_9; and $NbO(OR')_3$ where R′ = $-C_4H_9$; $-C_3H_7$.

Resistors based on these compositions have low TCR, a small spread of initial resistance values and excellent noise for resistance in the range of 2.7Ω/□ to ~900Ω/□. The glass used was borosilicate and the organic vehicle was a standard composition.

Brady (1972) reports resistor compositions based on RuO_2 and IrO_2 (average particle size 0.7–1 μm), glass and a crystal growth controlling agent (submicron Al_2O_3). The composition is fired at 975–1025 °C for 45 to 60 minutes. These compositions have improved voltage stability and voltage withstanding ability characteristics. When the size of the alumina is about 20 μm the voltage characteristics are not improved, and when colloidal alumina is used the fired resistance element is nonconductive. This patent teaches that the alumina is not soluble to an appreciable extent in the glass. The glasses used are high-lead glasses: glass I PbO-65; SiO_2-34; Al_2O_3-1 wt% and glass II PbO-72.15; SiO_2-13.41; B_2O_3-9.04; ZnO-5.4 wt%. They are very corrosive and, at the firing range (975–1025 °C), they will dissolve all the added alumina to form glass with higher viscosity than the initial glass. The change in the glass viscosity with 0.3 μm alumina is gradual, while with colloidal alumina it is very likely that all the alumina dissolves in the early stages of firing. Brady (1975) reported an improved resistance composition and method of making electrical elements. The compositions were based on RuO_2, iridium resinate, glass, an organic vehicle and additives such as Pd and copper resinate. The glasses used were lead borosilicates containing Bi_2O_3 and two leadless: barium borosilicate and strontium borosilicate. Three lead-free resistor compositions with resistances in the range of 3 kΩ/□ to 250 kΩ/□ and small TCR were described.

Van Loan (1975) describes RuO_2-based TF resistors, glass composition, TCR modifiers and materials that control bubble formation and viscosity. Example 1 of this patent shows that glass composition is very important in determining the resistance, TCR and noise of a given composition, i.e. the glass is not an inert binder. The glass compositions were: PbO, 55 to 75%; ZnO_2 to 10%, MnO_2 to 10%; B_2O_3, 5 to 20%; SiO_2, 5 to 20% and ZrO_2, 0 to 5%. Sb_2O_5 and V_2O_5 were used as TCR modifiers, CaF_2 as a control material for bubble formation and CeO_2 to raise viscosity without adversely affecting the electrical properties of the fired films. The roles of glass ingredients and paste additives are discussed.

Pukaite (1977) describes a low TCR cermet resistor based on RuO_2 and/or IrO_2. The low TCR is a result of the particular glass composition and vanadium oxide. The glasses used were: 44.9 wt% PbO; 20.1 wt% B_2O_3 and 35.0 wt% SiO_2. The preferred glass compositions (in wt%) were: PbO 38–45; B_2O_3 17–21; SiO_2

© Woodhead Publishing Limited, 2012

33–37; CaO 1–2 and Al_2O_3 1–2. Ruthenium, iridium and vanadium may be used as resinates or the oxides; in both cases the result is low TCR. These compositions also contain Bi_2O_3 (0.14 – 4.58 wt%, paste basis) and in some cases Al_2O_3 (0–7 wt%).

Larry (1978) describes resistor compositions based on RuO_2, PbO containing glass, Nb_2O_5 and optimally CaF_2. The glasses used were complex lead borosilicates containing MnO_2, Al_2O_3, ZnO, ZrO_2 and CuO. Resistor compositions with small TCR and a narrow spread of fired resistances in the range of about 50Ω/□ to 100 kΩ/□, were disclosed.

In 1971, Bouchard patented oxides with cubic structures containing bismuth and at least one of ruthenium and iridium. The chemistry, the structure and the electrical properties of these new compounds were reported and reviewed (Bouchard and Gillson, 1971). $Bi_2Ru_2O_7$ and $Bi_2Ir_2O_7$ are stable in air to at least 1000°C, are metallic oxides and their TCR is very small. These pyrochlores are much more stable than PdO, have remarkable stability under reducing conditions and are compatible with glass binders. Related oxygen deficient pyrochlore-type compounds $Pb_2M_2O_{7-x}$ (M = Ru, Ir, Re) were reported by Longo *et al.* (1969). The lead ruthenate pyrochlore is also a metallic oxide and has similar properties to bismuth ruthenate.

The new metallic oxides of the pyrochlore structure opened a new era in TF resistor development. A wider range of resistances, outstanding properties and ease of formulation and preparation became possible. Soon after the invention of metallic oxides of the pyrochlore family (Bouchard, 1971), patents on resistor compositions based on the new pyrochlores were issued, some of the first ones to Bouchard (1972), Hoffman (1971), Popowich (1971, 1974) and Schubert (1971).

Van Loan (1972) patented lead ruthenate ($Pb_2Ru_2O_6$), its mixtures with RuO_2 and a group of TCR modifiers (V_2O_3, Sb_2O_5, MnO_2, Fe_3O_4) to control the TCR. The lead ruthenate pyrochlore, a metallic oxide, can be formed when RuO_2 is mixed with a glass (PbO_2) vehicle and fired. Soon after the lead ruthenate patent, Kasanami and Kano (1973) patented the use of PbO and RuO_2 in the molar ratio of 3:1 to 1:3. The patent explains that some of the PbO may be substituted by Bi_2O_3 and 50% of the RuO_2 may be replaced by IrO_2. Thus, four systems may be designed for the conductive material:

1. $PbO\text{-}RuO_2$
2. $Bi_2O_3\text{-}PbO\text{-}RuO_2$
3. $PbO\text{-}RuO_2\text{-}IrO_2$
4. $Bi_2O_3\text{-}PbO\text{-}RuO_2\text{-}IrO_2$.

To obtain high resistance, less than 50% of the RuO_2 may be replaced molecularly by Ta_2O_5. The patent includes glass compositions and oxides TeO_2, WO_3, V_2O_5, TiO_2, MnO_2, SnO_2, Sb_2O_3, Sb_2O_5, CuO, ZnO, Nd_2O_3, Nb_2O_5 and Ta_2O_5 to regulate the TCR. The next modifications of lead ruthenate-based TF resistors were: (1) Langley (1978), who teaches a method to make dispersed lead ruthenate

© Woodhead Publishing Limited, 2012

or lead iridate in a glassy matrix. The glass constituents (lead oxide, silica) are mixed with RuO_2 or IrO_2 and heated to a temperature where a glass containing dispersed ruthenate is formed. After cooling the solid is comminuted and converted to a paste. This method facilitates the production of TF resistors exhibiting a low TCR, relative freedom from noise and drift, and high moisture resistance. (2) Fujimura (1979) describes a method to manufacture high resisting, low TCR and excellent voltage handling resistors. This method is similar to that of Langley but it includes other glass ingredients such as Al_2O_3 1–15%; ZrO_2 2–10% and SnO_2 0.5–20%. Other glass ingredients MgO, CaO, BaO, SrO, CdO, SnO and Bi_2O_3 are used in small quantities up to a sum of 5%. Hoffman and Horowitz (1981) in a very detailed patent described resistor compositions based on a group of pyrochlores, including 19 different glass compositions and low-expansion fillers such as zircon. In addition, the patent elucidates a new method of making the resistor compositions by presintering the solid ingredients in a temperature range of 650–850 °C for several hours, then milling and formulating the resistor pastes. Such TF resistor pastes afford resistors that have excellent stability to mechanical or thermal stresses.

Transition metal oxides, such as WO_3, V_2O_5, TiO_2, MnO_2, Sb_2O_3, Sb_2O_5, CuO, CdO, Nb_2O_5 and TiO_2 and resinates such as copper and vanadium resinates, reduce the TCR of Thick-film Resistors (TFRs) and also have other beneficial effects such as improvement of noise levels. These oxides, also known as TCR modifiers or TCR drivers, have been used as additives to the paste or as glass constituents. The mechanism of the TCR modification is not clear, but the data suggest that the TCR control is through the dissolution of the TCR modifier in the glass. Most of these oxides have one property in common: the metal ion can exist in at least two oxidation states in the glass. Cu^{2+}– Cu^{+}; Fe^{2+}– Fe^{3+}, Mn^{2+}– Mn^{2+}– Mn^{3+}– Mn^{4+};V^{3+}– V^{4+}– V^{5+}; Mo^{5+}– Mo^{6+}; Sb^{3+}– Sb^{5+}; Nb^{4+}– Nb^{5+}; Ti^{3+}– Ti^{4+}. Divalent cadmium, Cd^{2+}, does not fit this trend; however, Cd^{+} was reported to exist in glasses.

Examples of TCR modifiers used are by: Hoffman (1971) V_2O_5, Cr_2O_3, Mn_2O_3, Fe_3O_4, Co_3O_4, NiO, CuO; Van Loan (1975, 1972) V_2O_5, V_2O_3, Sb_2O_5, MnO_2, Fe_3O_4; Asada (1973), Casale (1972), Larry (1978), Nb_2O_5; Brady (1975) copper resinate; Holmes (1967) MnO_2, CuO; Hoffman and Horowitz (1981), Popowich (1971) CdO glasses; Kuo and Angel (1973) CdO and TiO_2 glass; Kasanami and Kano (1973) provide the list of oxides TeO_2, WO_3, V_2O_5, TiO_2, MnO_2, SnO_2, Sb_2O_3, Sb_2O_5, CuO, ZnO, Nd_2O_3, Nb_2O_5 and Ta_2O_5 to regulate the TCR. Most TCR modifiers lower the TCR and raise the resistance, CuO and Cu_2O increase the TCR. Hormadaly (1982, 2000) describes TCR modifiers MnV_2O_6, $Mn_2V_2O_7$, which lower the TCR but do not raise the resistance like binary modifiers and a semiconducting inverse spinel Co_2RuO_4, which lowers the TCR, does not raise the resistance like binary modifiers and preserves laser trim stability. Yamaguchi and Kanai (1992) studied the role of Cu and Mn oxides TCR modifiers in RuO_2-based resistors with emphasis on the effect of microstructure on their electrical properties. CuO addition resulted in the formation of a cell structure of Maragoni–

© Woodhead Publishing Limited, 2012

Bernard convection, which modified the aggregation of conducting particles. The effect of Mn oxides has been explained by the large negative TCR of Mn_2O_3, which precipitates in the glass matrix. Weimann and Chong (2000) studied the effects of TiO_2, GeO_2 and TeO_2 on the electrical properties of ruthenate TFRs. They argue that the addition of the oxides to the resistor glass increases the thickness of the glass barrier and reduces the impurity states in the glass by reducing the solubility of ruthenium ions.

Electrical and optical properties of RuO_2 and IrO_2 were reported by de Almeida and Ahuja (2006) and Ryden *et al.* (1968, 1970). Electrical properties, crystal structure, bonding trends and the crystal growth of ruthenium and iridium pyrochlores were discussed by Akazawa *et al.* (2004), Bouchard and Gillson (1971), Kennedy and Vogt (1996), Longo *et al.* (1969) and Tachibana *et al.* (2006). Dziedzic produced a bibliography on electrical conduction in TF resistors (1991).

Thick-film resistor materials have evolved during the last 40 years to a class of materials with wide resistance range and outstanding performances. These properties were achieved via innovation in conducting materials, glasses, dispersion techniques and proprietary additives. However, these unique properties were achieved with conducting materials and glasses that contain lead and cadmium. Cadmium compounds are carcinogens, and lead compounds are highly toxic. In recent years, the global trend has been to restrict and eventually eliminate the use of these compounds. After the RoHS (restriction of hazardous substances) directive was introduced, new conductor and solder compositions that are cadmium- and lead-free were introduced. The introduction of new lead-free TF resistor compositions (10Ω/□ to 1 MΩ/□) has not come to fruition yet, even though researchers and TF manufactures have been engaged in the development of Cd/Pb-free TFRs since the early 1980s.

Currently, TFRs are formulated with conducting materials such as RuO_2 or ruthenates like $Pb_2Ru_2O_{6+\delta}$ and $Bi_2Ru_2O_7$, and lead-containing glasses. The glasses are usually borosilicate modified with PbO, CdO, ZnO, Bi_2O_3, CaO, BaO, MnO, CuO, Al_2O_3, ZrO_2; the most commonly used are high-lead glasses. The advantages of lead glasses and the problems of developing lead-free TF glasses have already been addressed in detail by Vest (1986).

Thick-film resistor systems for nitrogen atmosphere processing were developed in the late 1970s and early 1980s. These systems were based on cadmium-free and lead-free glasses and conducting materials such as LaB_6 and $Sn_{2-x}Ta_{2-y}Sn_yO_{7-x-y/2}/SnO_2$ (Donohue *et al.*, 1987, 1988a, 1988b). Other conducting materials such as nitrides (Mulligan, 1969), carbides (Murphy and Janakirama-Rao, 1965) and silicides (Kuo, 1987a) with lead-free glasses were also described in the patent literature as nitrogen-fireable TFRs. These nitrogen-fireable TFRs are not useful for air atmosphere processing.

A model system of lead-free TFRs was prepared (Morten *et al.*, 1991) from lead-free glass and RuO_2 or $Bi_2Ru_2O_7$ as conducting phases. It was found that in

© Woodhead Publishing Limited, 2012

the lead-free glass/RuO_2 system, electrical properties are similar to leaded glass/RuO_2, TFRs but TCR is large and positive at firing temperatures higher than 850 °C. The $Bi_2Ru_2O_7$ lead-free glass system did not form resistors, and EDS analysis has shown that Bi from the conductive grains dissolved in the glass. Some properties of conducting materials RuO_2, $(Bi, Gd)_2$ Ru_2O_7 and $Bi_2Ru_2O_7$ with lead-free glasses have been described previously in the patent literature (Hormadaly, 1996). Lead-free TF resistors were investigated by Busana *et al.* (2006), Gurunathan *et al.* (2005), Kshirsagar *et al.* (2007), Prudenziati *et al.* (2002) and Rane *et al.* (2006), and the stability of lead-free resistor compositions in RuO_2-CaO-SiO_2 and RuO_2-Bi_2O_3–SiO_2 systems were evaluated by Hrovat *et al.* (2008, 2010). Recent investigations on lead-free TF resistors are Jagtap *et al.* (2009) and Kielbasinski *et al.* (2010).

Patent activity in lead-free TFRs is based on ruthenium and iridium compounds. Fukaya *et al.* (2000, 2003) teach RuO_2-based TFRs with a combination of two glasses, one calcium aluminoborosilicate and the second glass is sodium borosilicate. In a second patent the above inventors report RuO_2-based TFRs and potassium borosilicate glass where K_2O content is 0.1 wt% K_2O 10 wt%. Hormadaly (2006) describes lead-free TFRs based on $Nd_{2-y}Cu_y$ Ru_2O_{7-y} pyrochlore. Tanaka and Igarashi (2007) describe TFRs based on RuO_2 or mixed oxide of Ru and lead-free alkaline earth borosilicates containing CuO and MnO. Tanaka and Igarashi (2009a, 2009b) describe a TFR composition based on alkaline earth borosilicate glass, which may contain ZrO_2, Ta_2O_5 and Nb_2O_5 and conducting material selected from RuO_2, $Bi_2Ru_2O_7$, $Tl_2Ru_2O_7$, $MRuO_3$ (M = Ca, Sr, Ba) and $LaRuO_3$; in the second patent, $MTiO_3$ (M = Ca, Sr, Ba) additives, CuO and Cu_2O are used with RuO_2 and a Ru-composite oxide, as conducting materials. Endo *et al.* (2009) describe ruthenium-based lead-free TFR composition with alkaline earth aluminoborosilicate glasses modified with transition metal oxides. Although this patent provides a long list of Ru compounds, including those which are semiconducting, only RuO_2 and $CaRuO_3$ are used in the examples. Makuta and Maeda (2009) describe a high-resistance lead-free TFR composition based on IrO_2 or IrO_2 and RuO_2 and borosilicate glass, 10wt%-SrO, 43wt%-SiO_2, 16wt%-B_2O_3, 4wt%-Al_2O_3, 20wt%-ZnO and 7wt%-Na_2O. VerNooy *et al.* (2009) report a lead-free TFR composition based on Li_2RuO_3 and compatible glass.

Hang *et al.* (2009) discuss surface-modified RuO_2 and alkaline earth borosilicate glasses. Surface modification is done by wetting RuO_2 by K_2CO_3 solution or other modifying materials, drying and calcining at ~900 °C. Resistor pastes formulated with surface-modified RuO_2 have a broad resistance range of 10 kΩ/□ to 10 MΩ/□ and TCR of 100 ppm/ºC.

Related to the recent patents above that are based on RuO_2 and IrO_2, are the works of Dziedzic (1989), Diezdzic and Golonka (1988) and Tankiewicz *et al.* (2002), which have important data and discussions for IrO_2, RuO_2, $CaIr_xTi_{1-x}O_3$ and $Bi_2Ru_2O_7$ conducting materials.

© Woodhead Publishing Limited, 2012

2.2.3 Conductors

Thick-film conductor compositions were reviewed by Finch (1969) and later by Holmes and Loasby (1976). These compositions are based on a metallic part, which is the major constituent, a binder and an organic vehicle. The metallic part is usually noble metal or a mixture of noble metals such as Ag, Ag/Pd, Ag/Pt, Ag/Pt/Pd, Au, Au/Pd, Au/Pt, Au/Pd/Pt for air-fired conductors, or a base metal such as Al, Cu or Ni. The binder phase may be divided into three groups: oxides, glass and oxides plus glass, also known as the mix-bonded phase. The oxides were mixtures of CdO, CuO, Cu_2O and Bi_2O_3 and the glasses were based on high levels of lead and bismuth oxides. Although TF conductor compositions may be considered as a mature field, the patent literature activity of the recent decade shows that, on the contrary, the number of patents and the variety of applications are increasing at a fast rate. One of the reasons for new patents in this field is the requirement to remove CdO, lead and NiO from the compositions for toxicity and environmental considerations. Other reasons are the availability of nanoparticles of metals and the steep increase of activity in low-temperature co-fired ceramic (LTCC), solar energy and plasma display applications.

Examples of glass-bonded conductor compositions are: Christensen *et al.* (1949), Craig and Taylor (1987), Larry (1974), Larsen and Short (1958), Martin (1966), Miller (1968a), Minneman *et al.* (1974), Okamoto *et al.* (1997) and Soby (1951). Examples of oxide-bonded TF conductors are: Eustice (1994), Felten (1994), Frazee (1977) and Rellick (1982). Examples of mixed-bonded TF conductors are: Ballard and Hoffman (1969), Carrol and Kuno (1994), Gruber and Barringer (1991), Horowitz (1978, 1982), Saeki *et al.* (1991) and Taylor (1986).

Hormadaly (1995) reports lead-free glass compositions for Au conductors, conductor compositions and explanation of the role of CuO_x, Bi_2O_3 and CdO in bonding of the metallization to the ceramic substrates. These oxides partially reduce during firing and alloy with the noble metal conductor, thus modifying its surface characteristics and mechanical properties. It is believed that these elements, which are more electropositive than gold, form the strong chemical bonds at the surface of the gold film with the ceramic dielectrics. Prunchak (2010) describes lead-free glasses that contain TeO_2, SiO_2 and Bi_2O_3 as their main constituents. Hang *et al.* (2010) teach lead-free glass compositions for TF pastes and LTCC.

The variety and types of applications of TF conductors as expressed in the patent activity of recent years are illustrated in the following examples: solar energy (Rose and Young, 2010; Young *et al.*, 2010a, 2010b, 2010c); polymer-based conductors and TF conductors for use in biosensors (Chan 2000, 2003; Dorfman, 2010; Towlson 1997); low-temperature, very fast curing conductors (Kydd *et al.*, 2002); new ink-jet printable TF conductors compositions (Yang, 2010). Previous work on ink-jet composition was Vest (1980), Vest *et al.* (1983); on processes for TF patterning, Keusseyan (2010); on conductor composition for

© Woodhead Publishing Limited, 2012

plasma display, Matsuno and Barker (2010); on high conductivity Ag conductors based on very fine particles, Totokawa *et al.* (2010); on conductors for LTCC, Ollivier and Hang (2010); on conductors for Multi Layer capacitor (MLC) electrodes, Akimoto *et al.* (2010), Pepin (1990).

2.2.4 Dielectrics

The majority of current glasses for TF applications consist of lead borosilicate with minimal or no alkali oxides, therefore they are outstanding insulators. The insulating properties and moderate dielectric constants render them as candidates for TF applications such as insulators, capacitors, crossover dielectrics, multilayer materials and LTCC. For overglaze or encapsulant applications, low softening point glasses were used. Low softening point glasses typically have a high content of lead oxide, therefore they have a high linear coefficient of expansion and low durability. These glasses, which also contain CdO, were compounded with low expansion filler such as silica to lower their expansion, enhance their chemical durability and still maintain the low temperature processing characteristics. The overglazes also have a durable pigment such as Cr_2O_3. Typical composition is DuPont 9137. About 30 years ago, new compositions, which are CdO-free, were introduced by DuPont such as QQ550, which has similar properties to 9137. Environmental concerns have led to the development of lead-free and cadmium-free overglazes. Typical compositions and properties of TF overglazes are discussed by Hormadaly (1992a, 1992b) and Donohue (1990, 1998).

Dielectric compositions for crossover, capacitors and multilayers applications are described by Amin (1974), Barker *et al.* (1992), Bethke *et al.* (1998), Borland *et al.* (2010), Donohue *et al.* (1990), Hartmann (1991), Hu *et al.* (1993), Nair (1983), Shaikh *et al.* (1995), Stein *et al.* (1999), Tsuyuki (1995), Ulrich (1972) and Usui *et al.* (2002).

Rellick (1987, 1989) reports a casting composition for making green tapes that contain noncrystallizable glasses, refractory oxide, an organic vehicle for processing in nonoxidizing atmosphere and a method for fabricating multilayer circuits on rigid ceramic substrates using conventional dielectric green tape and TF-conductive pastes. Donohue (2000) describes a glass composition, a castable dielectric composition comprising the glass and refractory oxide, organic binder and vehicle. This composition is used in a method of forming a low-loss green tape. Related compositions for integrated circuits are shown by Cho and Hang (2004), Jean (1998), Jean and Gupta (1993), Kumar *et al.* (1999), Muralidhar *et al.* (1993), Senkalski and Hasenmayer (1990). Methods to control the planar shrinkage of green tapes and LTCC are described by Khadilkar *et al.* (2009) and Wang *et al.* (2004, 2006).

A non-photographic method for making patterns in organic polymer films, diffusion patterning (DP), is described by Felten (1991) and Felten *et al.* (1997).

© Woodhead Publishing Limited, 2012

2.2.5 Materials for nitrogen firing

Materials for nitrogen or inert atmosphere firing have to be stable at low concentrations of oxygen, about 5–10 ppm, and not be reduced by the organic vehicle. Materials like precious metal oxides, PbO and other oxides that reduce easily have to be replaced by materials that survive firing in harsh conditions. The replacement is easier for conductors and dielectrics because they contain one major ingredient, but much more complicated for resistors. The conducting phases RuO_2, lead ruthenate, bismuth ruthente and the glass, which contains lead, have to be substituted with other materials. Several types of conducting materials were used with leadless glasses to make TFRs, which can be processed in an inert or reducing atmosphere. The first group is based on borides, nitrides and silicides. The second group is based on oxides such doped SnO_2, In_2O_3 and ruthenates of the perovskite family, $MRuO_3$; the third group is based on the interactions of materials during firing to form a conducting phase; an example of this group is the interaction between Mo and MoO_3 to produce MoO_2, which is metallic oxide.

Examples of conducting materials based on a mixture of refractory carbide and refractory metal are given by Murphy and Janakirama-Rao (1965), who describe W and WC with barium borosilicate glass consisting of 48% BaO, 8% CaO, 23% B_2O_3 and 21% SiO_2. Mixtures of transition element nitrides and transition metals and carbide–metal mixtures, WC-W, are described by Mulligan (1969). Mackenzie (1974) describes a resistance material based on TaC and Ti and alkaline earth borosilicate glass. A vitreous enamel resistance material comprising of a glass frit and fine metal boride of the transition elements of groups IV, V and VI of the periodic table, where the metal boride may be CrB_2, ZrB_2, MoB_2, TaB_2 or TiB_2, is discussed by Huang and Merz (1970). Merz and Shapiro (1980) describe a vitreous enamel resistance material comprising barium borosilicate glass, Ta and additives Ti, B, Ta_2O_5, TiO, BaO_2, ZrO_2, WO_3, Ta_2N, $MoSi_2$ and $MgSiO_3$. Shapiro and Merz (1980) describe a vitreous enamel resistance material comprising Ta_2N, glass and additives selected from B, Ta, Si, ZrO_2 and $MgSiO_3$. Merz and Shapiro (1977) describe a resistance composition comprising glass and tantalum nitride or glass and W and WC. Nair (1987a, 1987b, 1987c) discusses resistor compositions based on a semiconducting material consisting essentially of a refractory metal carbide, oxycarbide or mixtures thereof and a non-reducing glass; an anion-deficient semiconducting material consisting essentially of a refractory metal nitride, oxynitride or mixture thereof and a non-reducing glass; and a semiconducting material consisting essentially of a cationic excess solid solution and a non-reducing glass. Kuo (1987a) describes resistor compositions based on silicides $TiSi_2$, Ti_5Si_3, Al_2O_3 and alkaline borosilicate glasses.

Donohue (1985, 1986a, 1986b) and Donohue and Marcus (1980) describe nitrogen-fireable TFR compositions, TCR modifiers, suitable glass compositions, thermodynamic calculations regarding reducibility of glass ingredients, Ta_2O_5 containing glasses and review of the literature. Watanabe *et al.* (1991) describe

© Woodhead Publishing Limited, 2012

resistive paste that contains metal hexaboride, a vitreous binder that contains a specified amount of Nb_2O_5 and in addition the paste may contain at least one nitride selected from the group consisting of AlN and BN.

Tin dixode, SnO_2, was used to fabricate refractory material that is extremely resistant to the corrosive attack of molten glass (Hood, 1941). Later, Mochel (1949) discovered that when SnO_2 is mixed with a shrinking agent comprising compounds of one of Cu, Ag, Au, Mn, Fe, Co, and Ni, and heated to 1200 °C or above, the resulting sintered body had high electrical conductivity. Doped SnO_2 was used for high voltage resistors, conducting glazes and resistors. These uses and other properties of doped SnO_2 were the subject of: Basu *et al.* (1974), Binns (1974), Burkett (1961), Dearden (1967), Gress *et al.* (1968) and Powell (1974). Whalers and Merz (1977, 1980, 1981, 1982a, 1982b, 1983a, 1983b) describe a vitreous enamel resistor material based on SnO_2, glass, Ta_2O_5 and other additives. These patents also provide pretreatment of SnO_2 and additive at reducing and nitrogen atmospheres. Hormadaly (1985a, 1985b, 1985c, 1985d, 1986a, 1987a, 1987b) describes nitrogen-fireable TFR compositions based on $Sn(II)_{2-x}$ Ta_{2-y} $Sn(IV)_yO_{7-x-y/2}$ pyrochlores, SnO_2, lead-free glass compositions and TCR modifiers. Kuo (1987a, 1987b, 1987c, 1988) describes TFR compositions based on SnO_2, resinate solutions such as transition metal resinates and heat treatment of the resinate-coated SnO_2 in reducing atmosphere, Ta_2O_5 glass and additives. Asada (1991) describes resistor compositions based on SnO_2, heat-treated powder of SnO_2 and Ta_2O_5, glass and tantalates.

In_2O_3 is an n-type semiconductor that has found uses in electrical contacts (Richardson and Swinehart, 1951) and light transmitting electrodes (Amans, 1966). Block and Mones (1968) describe an indium oxide resistor composition, method and article. Compositions were formulated with lead-free glass: 9.5wt% Al_2O_3, 49.4 wt% SiO_2, 10.4 wt% B_2O_3, 30.3 wt% BaO and 0.4 wt% of non-alkali oxides. The pastes may be fired in the air or in inert atmosphere at 800 to 1200 °C. Firing in inert atmosphere lowers the resistance and raises the TCR. The conductivity of In_2O_3 can be modified by addition of dopants. Dopants that increase the conductivity are Sb, As, P, Nb, Ce, Si, Ta, Zr, Ti, Sn and Mo and dopants that lower the conductivity are Cu, Au, Ag, Pt, Pd and Li. The conductivity can also be increased by forming oxygen-deficient In_2O_3 and by substituting halogen for oxygen. Prabhu and Hang (1983a, 1984a) describe In_2O_3 resistor compositions. The dopants used were MgO, V_2O_3, V_2O_5, ferric oxide and the glass compositions were: (1) 20.21 wt% SiO_2, 15.62 wt% B_2O_3, 51.59 wt% BaO, 12.58 wt% CaO, (2) 16.75 wt% SiO_2, 19.42 wt% B_2O_3, 51.32 wt% BaO, 12.51 wt% CaO. Compositions were fired in nitrogen atmosphere at 850 to 950 °C.

Hankey (1985) describes substituted ruthenium perovskite $A'_{1-x}A''_xB'_{1-y}B''_yO_3$, where A′-Sr, A″-Ba, La, Y, Ca, and Na, B′-Ru and B″-Ti, Cd, Zr, V, Co and alkaline earth borosilicate glass. Steinberg (1989) describes the same perovskite with additives such as Ni, Cu and CuO.

© Woodhead Publishing Limited, 2012

Pedder (1982) explains a method to make resistors compatible with a copper conductor. The resistor composition is a mixture of Mo and MoO_3, lead zinc borosilicate glass and additives such as W and V_2O_5. During firing in nitrogen atmosphere, molybdic oxide is reduced, by Mo and the organic vehicle, to MoO_2,which has high electrical conductivity and rutile structure. Prabhu and Hang (1983b, 1984b) describe low value resistor inks for porcelain-coated metal substrates, which are based on SnO-MoO_3 or Mo-MoO_3 mixtures, alkaline earth borosicate glass, organic vehicle and TCR modifiers CdO and V_2O_5. The molybdic oxide will be reduced by SnO to a mixture of two rutile structure oxides SnO_2 and MoO_2, which can form solid solution.

Some copper conductor compositions are described by Martin (1997), Prabhu *et al.* (1988, 1989a, 1989b) and Siuta (1986, 1987).

2.2.6 Materials for AlN, SiC, glass and other substrates

AlN substrates are manufactured from AlN powder, additives such as Y_2O_3, rare earth oxides, alkaline earth compounds and other compounds. The AlN and the additives are heated in nitrogen atmosphere to sinter the powders. The starting AlN powder contains oxygen as Al_2O_3, and at high temperature in nitrogen atmosphere, the alumina, AlN and the additives react to form AlON, yttrium aluminium garnet (YAG), and compounds that are products of the reaction of alkaline earth oxides with alumina. The synthesis of aluminum nitride substrates, the additives used and the process of preparation are described by Iwase *et al.* (1987), Nakahashi *et al.* (1986), Ohkawa *et al.* (1998), Sato *et al.* (1988) and Toyoda *et al.* (1998). Even with the oxygen-containing products listed above, the wettability of sintered AlN with metal is poor and the result is low bonding strength or no bonding. In addition, because of large and negative ΔG of Al_2O_3 formation, many ingredients of TF materials react with AlN; for example, PbO, a major TF ingredient (in glasses or lead ruthenate) is expected to react with aluminum nitride as follows:

$$2PbO(s)+\frac{4}{3}ALN(s) \rightarrow \frac{2}{3}Al_2O_3(s)+2Pb+\frac{2}{3}N_2$$

The ΔG of this reaction is: $\Delta G_f(1123K) = -410\,kJ\ mole^{-1}$. Detailed information about thermodynamic considerations in the TF metallization of aluminium nitride substrates is given by Norton (1990). Similar reactions are expected with many TF materials, therefore most of the TF materials developed for alumina are not compatible with AlN. Since many TF compositions contain glass or glass ceramics, which soften or melt during the firing process, and nitrogen gas is released as discussed above, bubbles and blisters are formed when conventional TF materials are fired on AlN. One way to avoid the blister formation is to oxidize the surface of AlN substrates to form a layer of alumina, 3–5 μm thick. A second way is to use TF formulations that are not reduced by AlN and a third way is to use glasses that do not spread substantially on AlN during firing, thus they form a

© Woodhead Publishing Limited, 2012

porous fired structure. Similar thermodynamic considerations can be applied to SiC substrates: here, the Si will oxidize to SiO_2 and the carbon to CO or CO_2, thus blister formation is likely with conventional TF materials. Oxidation of the surface of SiC substrates to form a thin coating of SiO_2 will prevent blister formation and will increase the bonding strength of TF materials to the substrate.

AlN-compatible TF binder glasses and pastes were reported by Harster and Mattox (1993) and Yamaguchi and Kageyama (1989). Mattox (1997) describes AlN-compatible TF binder glasses and TF compositions. The glasses discussed are mixed alkaline earth boroaluminate glasses comprising BaO combined with at least one of CaO, SrO and MgO and up to 30 mole% SiO_2. An example of an Ag conductor according to the patent is: 85 volume% of Ag and 15 volume% of glass, glass composition 54 mole% B_2O_3, 7.2 mole% Al_2O_3, 10 mole% SiO_2, 14.4 mole% BaO and 14.4 mole% CaO. Composition was fired on AlN substrate in air; no blisters or bubbles formed.

Reactions between ruthenium dioxide and aluminium nitride in resistor pastes, the development of resistor and conductor pastes for AlN and the properties of AlN-compatible pastes were reported by Kretzschmar *et al.* (1993a, 1993b, 1997) and Otschik *et al.* (1998a, 1998b).

Frit-free conductor compositions are described by Okamoto (2000). The development of glass frit-free metallization systems for AlN was reported by Adlanig and Schuster (1998) and the bonding mechanism and stress distribution of a glass frit-free TF metallization for AlN ceramic by Reicher and Smetana (1998). Recent examples of materials for aluminium nitride are described by Bloom (2001) and Cho and Hang (2006).

2.3 Deposition medium – vehicle

The organic or the carrier vehicle for printing pastes consists of three major parts: solvents, a resin binder and additives. The solvents are selected based on their ability to dissolve the resin, dissolve or disperse the paste ingredients and on the type of application required. Typical solvents and other organic ingredients that were taught in the patent literature (Christensen *et al.*, 1949; D'Andrea, 1960; Dumesnil, 1962; Faber *et al.*, 1967; Felten, 1978; Miller, 1968a, 1968b, 1968c; Minneman *et al.*, 1974; Place and Place, 1960b) are: higher-boiling paraffins, cycloparaffins and aromatic hydrocarbons or mixtures thereof; cellosolve acetate (ethylene glycol monoethyl ether acetate), carbitol acetate (diethylene glycol monoethyl ether acetate) and higher alcohols; di-alkyl ethers of diethylene glycol or their derivatines such as C_4H_9-O-CH_2-CH_2-O-CH_2-CH_2-OOCCH_3 and C_4H_9-O-CH_2-CH_2-O-CH_2-CH_2-O-C_4H_9; terpenes; esters; ketones and alcohols. Examples of resin binders include cellulose derivatives, natural gums, polyterpenes, synthetic resins such as polymethylmethacrylate, polybutylmethacrylate, polystyrene, poly alphamethylstyrene and other polymers of alkyl esters of methacrylic acid (vinyl or substituted vinyl polymer), polyisobutylene and itaconic acid polymers.

© Woodhead Publishing Limited, 2012

The additives include a long list of materials that modify the viscosity and impart special properties to the paste. Some examples are: (1) surfactants – this group includes many materials, organic and inorganic; examples of surfactants described in the literature are (Felten, 1978; Miller, 1968c) compounds like soya lecithin, Igepal CO 430 (an alkyl phenoxypoly (ethylene-oxy) ethanol and alkyl esters of phosphoric acid were used in resistor, conductor and dielectric paste compositions; (2) vaporizable solid – the vaporizable solid in the vehicle results in essential dimensional stability of the printed line. Examples of vaporizable solids (Miller, 1968b) are terphthalic acid, furoic acid and ammonium compounds such as $(NH_4)_2CO_3$ and $(NH_4)_2SO_4$.3) antioxidants; examples of food antioxidants used in paste compositions are butylated hydroxytoluene (BHT) and butylated hydroxyanisole (BHA).

The above description relates to materials used in conventional paste compositions and some pastes with improved printing characteristics (Miller, 1968c; Minneman *et al.*, 1974). Specialized vehicle compositions were formulated for the following. (1) Nitrogen-fired compositions; here, the paste compositions are fired in nitrogen where the concentration of oxygen is very low, less than 10 ppm. Therefore, the organic vehicle consists of polymers that depolymerize and evaporate before the vitreous phase softens and seals the underlying materials. Examples of organic vehicles for nitrogen firing are given by Scheiber (1981). (2) Photosensitive vehicles were developed to facilitate the formation of fine lines and spaces by TF technology. Paste containing the photosensitive vehicle and the desired function (conductor, resistor, etc.) is deposited by screen printing on a substrate and exposed through the desired pattern to actinic radiation. The exposed parts of the print harden and the unexposed parts are washed by solvent to leave thin lines of material that are subsequently fired to form a conductor, resistor or other passive component. Photosensitive vehicles were revealed in many patents and reviewed by Felten (1975) and Scheiber and Weaver (1975). (3) Water-based printing vehicles were developed to reduce the pollution from volatile organic chemicals (VOC). Chan and Dorfman (1999) describe an improved water-based vehicle for TF paste and present a review of the prior art.

The use of organic precursors for the inorganic paste ingredients (glass, conductor and resistor materials) was suggested by Faber *et al.* (1967) for all paste ingredients and by Place and Place (1960b) for most paste ingredients. Precursor-derived printable conductor compositions are described by Vest (1980) and ink-jet printing of hybrid circuits by Vest *et al.* (1983). The recent trend is the preparation of precursor compositions for the deposition of electronic components such as resistors and dielectrics and new methods for the deposition of these compositions. These compositions have low viscosity, about 1000 centipoise, and can be deposited using a direct-write tool. In addition to the above, these materials have a low conversion temperature, enabling the formation of electronic features on a wide variety of substrates including low-temperature substrates. The above-mentioned trend is described and reviewed by Kodas *et al.* (2009).

© Woodhead Publishing Limited, 2012

2.4 Glasses and glass ceramics

Glass compositions for microelectronics and TF applications were the subject of two reports, Cox (1968) and Vest (1979), respectively. The role of the glass frit in TF composition was described by Holmes and Loasby (1976) as of holding, binding, sealing the fired composition and bonding to the ceramic substrate. To fulfill these functions the glass frit has to have a compatible linear coefficient of expansion with the substrate, its sintering temperature must be below the maximum firing temperature, the glass must form a 'chemically and physically stable interface with the substrate and the conductive following firing' (Holmes and Loasby, 1976) and the glass should be inert to the environment. Vest (1979) described and listed several properties that are important to TF glasses: viscosity, surface tension, linear coefficient of expansion. Previous authors (Cox, Vest, Holmes and Loasby) were aware of the interactions of the glass frit with the substrate and the functional phase. Vest (1979) reviewed the literature and correlated physical properties with glass composition, and concluded 'that quantitative correlations between physical properties and chemical composition of glasses are only possible over very limited composition range at constant temperature', and that 'present theoretical models which describe the temperature dependence of thermal expansion, surface tension, or viscosity of glasses are woefully inadequate'. The TF industry's approach to glass development was mostly empirical and the success of this approach is evident in the many glass compositions since developed. Nowadays, because of the availability of custom glass producers for TF applications and the new model for calculating the linear coefficient of expansion of glass from its chemical composition (Hormadaly 1985a, 1986b), which were not available at the time of the Vest report (1979), it is easier to develop TF glasses.

Because TF glass is a very reactive substance, especially when molten, it dissolves small quantities of the inert container material during the frit preparation. Therefore, all glass compositions melted in a platinum crucible may contain ionic or metallic platinum, typically less than 50 ppm. During the milling process, the milling medium and the container linings erode to some extent, and the erosion products contaminate the glass powder. These materials (Pt) and the major erosion products (Al_2O_3 or ZrO_2) can modify the glass properties.

TF glasses, especially lead-containing ones, are very corrosive when molten and they interact with the active phase, substrate, terminations and additives. After the firing process the glass composition and its properties are modified. The interactions of TF glasses with TF ingredients are dealt with in Chapter 3.

Typical glass compositions used in early development of TF resistors are collected in Table 2.1. Table 2.1 shows that most of the compositions are simple high lead borosilicate glasses, some contain other elements such as Zn, Ba, Ca, Ag, Bi, Al and Zr. The patent literature after 1972 contains a large number of glass compositions used in the development of TF resistors. For example, Hoffman and Horowitz (1981) present very detailed information on TF resistors based on

© Woodhead Publishing Limited, 2012

Table 2.1 Glass compositions used in resistors (patent literature for 1948–1972 period), compositions in wt% oxides

	I (1)	II (2)	III (3)	IV (4)	V (5)	VI (6)	VII (7)	VIII (8)	IX (8)
PbO	58.0	59.1	65.0	65.7	70.3	63.0	60.0	65.0	72.2
Bi_2O_3	–	–	–	–	–	–	–	–	–
CdO	–	–	–	–	–	–	–	–	–
ZnO	–	–	–	5.4	–	–	–	–	5.4
CaO	–	–	–	–	–	–	–	–	–
BaO	–	–	–	–	–	–	–	–	–
K_2O	3.4	–	–	–	–	–	–	–	–
CoO	2.1	–	–	–	–	–	–	–	–
Ag_2O	–	–	–	–	9.0	–	–	–	–
B_2O_3	5.0	23.6	10.0	9.0	5.4	25.0	30.0	–	9.0
SiO_2	25.0	17.3	25.0	17.5	15.3	12.0	4.0	34.0	13.4
Al_2O_3	6.6	–	–	–	–	–	6.0	1.0	–
ZrO_2	–	–	–	2.4	–	–	–	–	–

Note: Roman numerals denote glass number and number in parenthesis is the reference number.

Sources for Tables 2.1 and 2.2 (patent literature, 1948–1972): (1) Jira, 1948; (2) D'Andrea, 1960; (3) Dumesnil, 1962; (4) Place and Place, 1964; (5) Janakirama-Rao and Murphy, 1964; (6) Faber *et al.*, 1969; (7) Van Loan, 1972; (8) Brady 1972; (9) Soby, 1951; (10) Martin, 1966; (11) Ballard, 1969; (12) Miller, 1968; (13) Larry, 1974; (14) Minneman *et al.*, 1974.

pyrochlores and refractory fillers and describe 19 glass compositions that are mostly lead boroaluminosilicates modified with oxides of TiO_2, ZrO_2, CdO, Li_2O, BaO, CaO, ZnO, Na_2O and MnO_2; two of these glasses are used as TCR drivers, the glass containing CdO and the glass containing MnO_2.

Typical glass compositions used in conductors are collected in Table 2.2. Table 2.2 shows that glasses used in conductors are based on lead borosilicates, bismuth borosilicates or lead–bismuth borosilicates. In addition, Table 2.2 also shows that these glasses may contain CuO and CdO, which are easily reduced oxides.

Glasses for dielectrics (overglazes, crossover, capacitors, multilayers and LTCC) are a large group based on several glass systems: lead borosilicates, bismuth borosilicates, lead silicates, lead-germanates, lead-free glasses, which may be alkaline earth borosilicates, or silicates. Some of these glasses are crystallizable, a property that is used in crossover dielectrics: after crystallization, the composition is a glass ceramics and it does not soften on subsequent thermal process.

Many glass compositions are used in TF materials and the scope of this section does not allow detailed treatment, however the citations of this chapter were selected to include hundreds of glass compositions for TF applications.

© Woodhead Publishing Limited, 2012

Table 2.2 Typical glass compositions used in TF conductors

	I (9)	II (10)	III (10)	IV (10)	V (11)	VI (12)	VII (13)	VIII (13)	IX (13)	X (13)	XI (14)
PbO	85.2	8.0	7.3	25.0	–	66.6	45.3	40.0	35.0	–	60.0
Bi_2O_3	–	75.0	68.2	60.0	–	–	–	–	–	–	–
CaO	–	–	–	–	–	–	9.7	10.0	10.0	4.0	–
BaO	–	–	–	–	–	–	–	–	–	1.0	–
Na_2O	–	–	–	–	7.3	–	–	–	–	8.5	–
K_2O	–	–	–	2.0	–	–	–	–	–	–	–
CuO	–	–	9.1	–	–	–	–	–	–	–	–
ZnO	–	–	–	–	–	–	–	–	–	27.2	–
CdO	–	8.0	7.3	2.0	63.1	–	–	–	–	–	5.9
Al_2O3	–	1.0	0.9	–	–	2.3	4.9	5.0	5.0	6.4	0.4
B_2O3	14.8	4.0	3.6	1.0	16.9	8.75	4.0	5.0	5.0	25.4	16.0
SiO_2	–	4.0	3.6	10.0	12.7	22.35	34.4	35.0	35.0	23.5	17.6
TiO_2	–	–	–	–	–	–	1.0	2.50	5.0	–	–
ZrO_2	–	–	–	–	–	–	0.7	2.50	5.0	4.0	–

Note: Roman numerals denote glass number and number in parenthesis is the reference number.

2.5 Substrates

Substrates for TF applications provide the mechanical base on which TF materials are deposited and subsequently fired at 500–1000 °C in air or inert atmosphere.

The requirements are mechanical strength, high resistivity, chemical inertness, thermal conductivity, moderate expansion, stability at a broad temperature range and price. Alumina and alumina-based ceramics have been used because they have most of the properties listed above, therefore the majority of TF materials were developed for alumina. The materials developed have linear coefficients of expansion compatible with alumina, typically 96% alumina, and they were formulated with lead-containing glasses. For applications where high thermal conductivity was required, beryllia, BeO, was used. BeO has a higher thermal conductivity than alumina, it is more expansive, its mechanical strength is lower than that of alumina, and BeO particles and vapor are highly toxic. AlN has a high thermal conductivity, a low linear coefficient of expansion, high flexural strength, low hardness and stability at high temperatures, up to 900 °C in air and up to 1600 °C in reducing atmosphere. Typical properties of ceramics used for substrates and packages are collected in Table 2.3. The data in Table 2.3 are based on Miyashiro *et al.* (1990) and Tummala (1991).

Tummala *et al.* (1993) treat a large variety of materials for microelectronics, including substrates. A system for high temperatures of 500 °C, including SiC elements, was discussed by Chen *et al.* (2001). Specialized substrates such as enameled steel substrates for TF applications and comparison of properties with common substrates were treated by Stein *et al.* (1980). Novel substrates for TF technology, such as diamond, were discussed by Lux and Smetana (1991).

© Woodhead Publishing Limited, 2012

Table 2.3 Properties of typical substrates materials

	Alumina	AlN	BeO	SiC (2% BeO)	Mullite	Borosilicate glass
Resistivity (.cm at 25 °C)	$>10^{14}$	$>10^{14}$	$>10^{14}$	$>10^{14}$		
Dielectric constant (25 °C, 1 MHz)	9.4	8.8	6.8	42	6.5	4.0
Dielectric strength (kV/cm, at 25 °C)	100	140–170	100	0.7		
Thermal conductivity (W/m.K, at 25 °C)	25	70–230	290	270	7	2
Tanδ (at 1 MHz) (10^{-4})	3	5–10	5	500		
Strength (MPa)	280	350	250	420	200	70
Coefficient of thermal expansion (20–200 °C) (10^{-7}/°C)	65	42	68	37	40	30

2.6 Conclusion

This chapter is an attempt to review the state of the art of TF materials. Most information sources are in English and from the patent literature. TF materials are commercially important and the majority of research has been done in industry. Therefore, most of the references are from the patent literature, where a basic understanding of the material is often not addressed. Furthermore, the patent literature discloses very important information regarding the materials and their interactions. Since the early 1960s, TF materials and technology have been the subject of intensive research in academic institutions. A simple search of TF materials in the literature shows well over 1000 papers. Research in universities advanced public understanding of TF materials, which were considered in the past as proprietary and very complex.

Many facets of TF materials are still not fully understood and it is hoped that this review will enhance interest in these materials, their properties and the interpretation of the conduction mechanism of TF resistors.

2.7 References

Adlanig A. and Schuster J. C. (1998). 'Development of glass frit free metallization systems for AlN', *Journal of Material Science*, 33(20), 4887–4892.

Akazawa T., Inaguma Y., Katsumata T., Hiraki K. and Takahashi T. (2004). 'Flux growth and physical properties of pyrochlore $Pb_2Ru_2O_{6.5}$ single crystals', *Journal of Crystal Growth*, 271, 445.

© Woodhead Publishing Limited, 2012

Akimoto Y., Nagashima K., Kimura T. and Kamahori Y. 'Nickel–rhenium alloy powder and conductor paste containing the same', US Patent 7-744-779; June 29 (2010).
Amans R. L., 'Light transmitting electrode including N-type semiconductive In_2O_3', US Patent 3-295-002; December 27 (1966).
Amin R. B., '$CaTiO_3$ – Crystallizable glass dielectric compositions', US Patent 3-787-219; January 22 (1974).
Angus H. C. and Gainsbury P. E., 'Oxide resistor materials', US Patent 3-679-607; July 25 (1972).
Asada E., 'Electrical resistance composition and resistance element', US Patent 3-776-772; December 4 (1973).
Asada E., 'Resistor compositions', US Patent 4-986-933; January 22 (1991).
Ballard K. H. and Hoffman L. C., 'Noble metal metalizing compositions', US Patent 3-450-545; June 17 (1969).
Barker M. F., Craig A., Donohue P. C., Hang K. W., Haun M. J. and Pickering C. R., 'Dielectric composition containing kerf additive', US Patent 5-137-848; August 11 (1992).
Basu M. K. and Lele R. V. (1974). 'Effect of reducing atmosphere of SnO_2-Sb_2O_5-based semiconducting glaze', *American Ceramic Society Bulletin*, 53(6), 488–489.
Bethke S. J., Miesem R. A., Chiou W. W. and Pastor R. D. G., 'Ceramic composition', US Patent 5-821-181; October 13 (1998).
Binns D. B. (1974). 'Conducting glazes', *Transactions of the Journal of the British Ceramic Society*, 73, 7–17.
Block M. N. and Mones A. H., 'Indium oxide resistor composition, method, and article', US Patent 3-411-947; November 19 (1968).
Bloom T., 'Copper ink for aluminum nitride', US Patent 6-207-288; March 27 (2001).
Borland W. (1989). *Thick-film Hybrids in Electronic Materials Handbook: Packaging*, L. M. Merrill, ASM International Handbook Committee.
Borland W. J., Jones A. B., Renovales O. L. and Hang K. W., 'Thick-film dielectric and conductive compositions', US Patent 7-688-569; March 30 (2010).
Bouchard R. J., 'Compositions for making electrical elements containing pyrochlore-related oxides', US Patent 3-681-262; August 1 (1972).
Bouchard R. J., 'Oxides of cubic crystal structure containing bismuth and at least one of ruthenium and iridium', US Patent 3-583-931; June 8 (1971).
Bouchard R. J. (1999). 'Thick-film technology: An historical perspective', in *Dielectric Ceramic Materials: Ceramic Transactions 100*, 429–442.
Bouchard R. J. and Gillson J. L. (1971). 'A new family of bismuth – precious metal pyrochlores', *Material Research Bulletin*, 6, 669–679.
Boyd J. R., Mones A. H. and Schottmiller J. C., 'Electrical device, method and material', US Patent 3-372-058; March 5 (1968).
Brady L. J., 'Electrical resistance elements, their composition and method of manufacture', US Patent 3-655-440; April 11 (1972).
Brady L. J., 'Resistance composition and method of making electrical resistance element', US Patent 3-916-037; October 28 (1975).
Bruhl D. A. Jr and Counts W. E., 'Cermet resistance composition and resistor', US Patent 3-326-720; June 20 (1967).
Burkett R. H. W. (1961). 'Tin oxide resistors', *Journal of the British IRE*, 301–304.
Busana M. G., Prudenziati M. and Hormadaly J. (2006). 'Microstructure development and electrical properties of RuO_2-based lead-free thick-film resistors', *Journal of Material Science: Materials in Electronics*, 17(11), 951–962.

© Woodhead Publishing Limited, 2012

Carroll A. F. and Kuno, H. 'Automotive glass thick-film conductor paste', US Patent 5-296-413; March 22 (1994).
Casale M. E. A., Collier O. N. and Iles G. S., 'Resistor composition', US Patent 3-637-530; January 25 (1972).
Chan M. S., 'Thick-film conductor composition for use in biosensors', US Patent 6-642-751; March 28 (2000).
Chan M. S., 'Thick-film conductor composition for use in biosensors', US Patent 6-627-058; September 30 (2003).
Chan M. S. and Dorfman J. R., 'Water-based thick-film conductive compositions', US Patent 5-855-829; January 5 (1999).
Chen L-Yu, Okojie R. S., Neudeck P. G., Hunter G. W. and S-Tien T. Lin (2001). 'Material system for packaging 500 °C microsystems', *Materials Research Society Symposium Proceedings*, 682, 79–90.
Cho Y. and Hang K. W., 'High thermal expansion glass and tape composition', US Patent 6-835-682; December 28 (2004).
Cho Y. and Hang K. W., 'Thick-film dielectric compositions for use on aluminum nitride substrates', US Patent 7-087-293; August 8 (2006).
Christensen C. J., Rigterink M. D. and Treptow A. W., 'Metallizing composition', US Patent 2-461-878; February 15 (1949).
Coleman M. V. (1975). 'Evaluation methods for the examination of thick-film materials', *Radio and Electronic Engineer*, 45(3), 121.
Conrad P. (1971). 'Resistor materials', *Electronics Materials Review*, 12. Nayes Data Corp., Park Ridge, NJ, USA.
Cotton F. A. and Wilkinson G. (1966). *Advanced Inorganic Chemistry*, 2nd edn, New York: Interscience Publishers.
Counts W. E. and Bruhl D. A. Jr, 'Cermet resistance element', US Patent 3-479-216; November 18 (1969).
Cox S. M. (1968). 'Survey of glass materials in microelectronics', *Report No. AD682914*, Ministry of Technology, London, UK.
Craig W. A. and Taylor B. E., 'Thick-film conductor composition', US Patent 4-636-332; January 13 (1987).
Daily A. M., Boykin O. F. and Rartman C. W., 'Electrical resistance element and method of making the same', US Patent 3-329-526; July 4 (1967).
D'Andrea J. B., 'Ceramic composition and article', US Patent 2-924-540; February 9 (1960).
de Almeida J. S. and Ahuja R. (2006). 'Electronic and optical properties of RuO_2 and IrO_2', *Physical Review B*, 73, 165102.
Dearden J. (1967). 'High voltage resistors', *Electronic Components*, 259–262.
Donohue P. C., 'Hexaboride resistor composition', US Patent 4-512-917; April 23 (1985).
Donohue P. C., 'Thick-film copper compatible based on hexaboride conductors and nonreducible glass', US Patent 4-585-580; April 29 (1986a).
Donohue P. C., 'Hexaboride resistor composition', US Patent 4-597-897; July 1 (1986b).
Donohue P. C., 'Encapsulant composition', US Patent 4-966-926; October 30 (1990).
Donohue P. C., 'Lead and cadmium-free encapsulant composition', US Patent 5-753-571; May 19 (1998).
Donohue P. C., 'Borate glass based ceramic tape', US Patent 6-147-019; November 14 (2000).
Donohue P. C. and Marcus S. M., 'Temperature coefficient of resistance modifiers for thick-film resistors', US Patent 4-225-468; September 30 (1980).
Donohue P. C., Hang K. W. and Haun M. J., 'Crystallizable glass and thick-film compositions thereof', US Patent 4-959-330; September 25 (1990).

© Woodhead Publishing Limited, 2012

Donohue P. C., Hormadaly J., Needes C. R. S., Horowitz S. J. and Knaak J. F. (1987). 'Nitrogen fireable resistors: emerging technology for thick-film hybrids', *IEEE Transactions on Components, Hybrids and Manufacturing Technology*, 10(4), 537–544.

Donohue P. C., Hormadaly J., Needes S. C. R., Horowitz S. J. and Knaak J. F. (1988a). 'Nitrogen fireable resistors: emerging technology for thick-film hybrids – Part I', *Hybrid Circuit Technology*, 11–14, February.

Donohue P. C., Hormadaly J., Needes C. R. S., Horowitz S. J. and Knaak, J. F. (1988b). 'Nitrogen fireable resistors: emerging technology for thick-film hybrids – Part II', *Hybrid Circuit Technology*, 39–43, March.

Dorfman J. R., 'High conductivity polymer thick-film silver conductor composition for use in RFID and other applications', US Patent 7-857-998; December 28 (2010).

Dumesnil M. E., 'Resistor and resistor composition', US Patent 3-052-573; September 4 (1962).

Dziedzic A. (1989). 'Thick-film resistors with IrO_2 and $CaIr_xTi_{1-x}O_3$ – Examples of chemically reactive and unreactive systems', *Microelectronics Journal*, 19(6) 24–42.

Dziedzic A., (1991). 'Bibliography on electrical conduction in thick-film resistors', *Microelectronics Reliability*, 31, 549–558.

Dziedzic A. and Golonka L. (1988). 'Electrical properties of conductive materials used in thick-film resistors', *Journal of Materials Science*, 23(9), 3151–3155.

Endo T., Mashima, H. Kanasaku T., Tanaka T. and Yamazoe M., 'Resistor composition and thick-film resistor', US Patent 7-476-342; January 13 (2009).

Eustice A. I., 'Conductor compositions', US Patent 4-446-059; May 1 (1994).

Faber W. M. Sr, Francis G. L., Holmes C. L. and Boykin O. F., 'Electrical resistance element', US Patent 3-304-199; February 14 (1967).

Felten J. J., 'Photosensitive gold compositions', US Patent 3-877-950; April 15 (1975).

Felten J. J., 'Compositions containing diethylene glycol ether', US Patent, 4-070-200; January 24 (1978).

Felten J. J., 'Non-photographic method for patterning organic polymer films', US Patent 5-032-216; July 16 (1991).

Felten J. J., 'Palladium thick-film compositions', US Patent 5-338-708; August 16 (1994).

Felten J. J., Hertler W. R. and Ma S. H., 'Compositions for diffusion patterning', US Patent 5-654-354; August 5 (1997).

Finch R. G. (1969). 'Thick-film materials', *Thin Solid Films*, 3, 189–199.

Frazee L. E., 'Humidity sensor, material therefore and method', US Patent 4-016-308; April 5 (1977).

Fujimura K., 'Method of manufacturing resistor paste', US Patent 4-175-061; November 20 (1979).

Fukaya M., Matsuo T., Watanabe Y. and Higuchi C., 'Thick-film resistor paste', US Patent 6-123-874; September 26 (2000).

Fukaya M., Shibata K., Higuchi C. and Watanabe Y., 'Thick-film resistor and ceramic circuit board', US Patent 6-544-654; April 8 (2003).

Gress R. W., Murphy J. A. and Talwalkar A. T. (1968). 'Characterizations of antimony-doped tin (IV) oxide films', *Proceedings of Electronic Components*, 108(3), 277–283.

Gruber W. C. and Barringer E. A., 'Metallic inks for co-sintering process', US Patent 5-062-891; November 5 (1991).

Gurunathan K., Vyawahare N. and Amalnerkar D. P. (2005). 'Synthesis and characterization of $CaRuO_3$ and $SrRuO_3$ for resistor paste application', *Journal of Material Science: Materials in Electronics*, 16, 47–53.

© Woodhead Publishing Limited, 2012

Hang K. W., Labranche M. H., Taylor B. E. and Vernooy P. D., 'Surface-modified ruthenium oxide conductive material, lead-free glass(es), thick-film resistor paste(s), and devices made therefrom', US Patent Application 20009/0261941, October 22 (2009).
Hang K. W., Nair K. M. and McCombs M. F., 'Lead free glass(es), thick-film paste(s), tape composition(s) and low temperature cofired ceramic devices made therefrom', US Patent 7-687-417; March 30 (2010).
Hankey D. L., 'Electrical resistance composition and methods of making the same', US Patent 4-536-328; August 20 (1985).
Hrovat M., Meader T., Holc J., Belavic D., Cileniek J. and Bernard J. (2008). 'Subsolidus phase equilibria in RuO_2-Bi_2O_3-SiO_2 system', *Journal of European Ceramic Society*, 28(11), 2221–2224.
Harster T. E. and Mattox D. M. (1993). 'AlN – Compatible thick-film binder glasses and pastes', *Proceedings of ISHM 1993*, pp. 393–398.
Hartmann H. S., 'Crystallizable, low dielectric constant, low dielectric loss composition', US Patent 5-024-975; June 18 (1991).
Herbst D. I and Dawson W. L., 'Cermet resistor composition and method of making same', US Patent 3-573-229; March 30 (1971).
Hoffman L. C., 'Resistor composition containing pyrochlore-related oxides and noble metal', US Patent 3-553-109; January 5 (1971).
Hoffman L. C. (1984). 'An overview of thick-film hybrid materials', *American Ceramic Society Bulletin*, 63(4), 572–576.
Hoffman L. C. and Horowitz S. J., 'Stable pyrochlore resistor compositions', US Patent 4-302-362; November 24 (1981).
Holmes C. L., 'Precision resistance element and method of making the same', US Patent 3-324-049; June 6 (1967).
Holmes P. J. and Loasby R. G. (1976). *Handbook of Thick-film Technology*, Electrochemical Publications Limited, Ayr, Scotland.
Holmes P. J. and Loasby L. R. (1988). *Hybrid Microcircuit Technology Handbook: Materials Processes, Testing and Production*, Noyes, Park Ridge, NJ.
Hood H. P., 'Refractory product and method of making the same', US Patent 2-244-777; June 10 (1941).
Hormadaly J., 'Thick-film resistor compositions', US Patent 4-362-656; December 7 (1982).
Hormadaly J. (1985a). 'New model for estimating the expansion coefficient of glasses used in microelectronics', *Proceedings of International Symposium on Microelectronics*, *ISHM 85*, Anaheim, CA, 77–82.
Hormadaly J., 'Borosilicate glass compositions', US Patent 4-536-329; August 20 (1985a).
Hormadaly J., 'Borosilicate glass compositions', US Patent 4-537-703; August 27 (1985b).
Hormadaly J., 'Method of doping tin oxide', US Patent 4-548-741; October 22 (1985c).
Hormadaly J., 'Resistor compositions', US Patent 4-548-742; October 22 (1985d).
Hormadaly J., 'Method of doping tin oxide', US Patent 4-613-539; September 23 (1986a).
Hormadaly J. (1986b). 'Empirical methods for estimating the linear coefficient of expansion of oxide glasses from their composition', *Journal of Non-Crystalline Solids*, 79, 311–324.
Hormadaly J., 'Resistor compositions', US Patent 4-654-166; March 31 (1987a).
Hormadaly J., 'Method of doping tin oxide', US Patent 4-707-346; November 17 (1987b).
Hormadaly J., 'Encapsulant composition', US Patent 5-114-885; May 19 (1992a).
Hormadaly J., 'Encapsulant composition', US Patent 5-137-851, August 11 (1992b).

© Woodhead Publishing Limited, 2012

Hormadaly J., 'Cadmium-free and lead-free thick-film conductor composition', US Patent 5-439-852; August 8 (1995).
Hormadaly J., 'Cadmium-free and lead-free thick-film paste composition', US Patent 5-491-118; February 13 (1996).
Hormadaly J., 'Cobalt ruthenate thermistors', US Patent 6-066-271; May 23 (2000).
Hormadaly J., 'Thick-film compositions containing pyrochlore-related compounds', US Patent 6-989-111; January 24 (2006).
Horowitz S. J., 'Novel silver compositions', US Patent 4-090-009; May 16 (1978).
Horowitz S. J., 'Thick-film conductors having improved aged adhesion', US Patent 4-318-830; March 9 (1982).
Hrovat M., Holc J., Jakubowska M., Kielbasinski K., Makarovic K. and Belavic D. (2010). 'Subsolidus phase equilibria in the CaO-poor part of the RuO_2-CaO-SiO_2 system', *Materials Research Bulletin*, 45(12), 2040–3.
Hrovat M., Maeder T., Holc J., Belavic D., Cilensek J. and Bernard J. (2008). 'Subsolidus phase equilibria in the RuO_2-Bi203-system', *Journal of the European Ceramic Society*, 28(12), 2221–2224.
Hu Y. H., Saltzberg M. A. and M. A. Shannon, 'Metaphosphate glass composition', US Patent 5-196-381; March 23 (1993).
Huang C. Y. D. and Merz K. M., 'Vitreous enamel resistance material and resistor made therefrom', US Patent 3-503-801; March 31 (1970).
Iles G. S. and Casale M. E. A. (1967). 'Ruthenium oxide glaze resistors', *Platinum Metals Review*, 11, 126–129.
Iwase N., Anzai K., Shinozaki K., Tsuge A., Kawasaki K. S. *et al.*, 'Circuit substrate having high thermal conductivity', US Patent 4-659-611; April 21 (1987).
Jagtap S., Rane S. and Amalnerkar D. (2009). 'Environmentally sustainable composite resistors with low temperature coefficient of resistance', *Microelectronic Engineering*, 86, 2026–2029.
Janakirama-Rao B. V. and Murphy R. M., 'Resistance material and resistor made therefrom', US Patent 3-154-503; October 27 (1964).
Jean J. H., 'Low dielectric ceramic compositions for multilayer ceramic package', US Patent 5-786-288; July 28 (1998).
Jean J. H. and Gupta T. K., 'Dielectric composition containing cordierite and glass', Patent No. 5-206-190, April 27 (1993).
Jira J. W., 'Metal film resistor', US Patent 2-281-843; May 5 (1942).
Jira J. W., 'Protective coating for resistors', US Patent 2-357-473; September 5 (1944).
Jira J. W., 'Alloy metal film resistor', US Patent 2-440-691; May 4 (1948a).
Jira J. W., 'Resistor and method of making', US Patent 2-457-678; December 28 (1948b).
Kasanami T. and Kano O., 'Electro-conductive material containing PbO and RuO_2', US Patent 3-778-389; December 11 (1973).
Kennedy B. J. and Vogt T. (1996). 'Structural and bonding trends in ruthenium pyrochlores', *Journal of Solid State Chemistry*, 126, 261–270.
Keusseyan R. L. 'Process for thick-film circuit pattering', US Patent 7-741-013; June 22 (2010).
Khadilkar C. S., Sridharan S. and Shaikh. A. S., 'Method of making multilayer structures using tapes on non-densifying substrates', US Patent 7-547-369; June 16 (2009).
Kielbasinski K., Jakubowska M., Mlozniak A., Hrovat M., Holc J. and Belavic D. (2010). 'Investigation on electrical and microstructural properties of thick-film lead free resistor series under various firing conditions', *Journal of Materials Science: Materials in Electronics*, 21(10), 1099–1105.

© Woodhead Publishing Limited, 2012

Kodas T. T., Hampden-Smith M. J., Vanheusden K., Denham H., Stump A.D. *et al.* (2009). 'Precursor compositions and methods for the deposition of passive electrical components on a substrate', US Patent 7-524-528; April 28.

Kretzschmar C., Otschik P. and Eichler K. (1993a). 'Influence of the solid particle size on the properties of RuO_2-based thick-film resistors', *International Conference on Materials by Powder Technology 1993*, Dresden, pp. 713–718.

Kretzschmar C., Otschik P., Jaenicke-Röβler, K. and Schlaefer D. (1993b). 'The reaction between ruthenium dioxide and aluminum nitride in resistor pastes', *Journal of Materials Science*, 28(21), 5713–5716.

Kretzschmar C. (1997). 'Thick layer resistor coatings on AlN ceramics for high operational temperature', *Werkstoffe Fuer die Info, Symposium1, Werkstoffwoche '96*, Stuttgart, 133–138.

Kshiragar A., Rane S., Mulik U. and Amalnerkar D. (2007). 'Microstructure and electrical performance of eco-friendly thick-film resistor composition fired at different firing conditions', *Materials Chemisty and Phyics*, 101, 492–498.

Kumar A. H., Thaler B. J., Prabhu A. N. and Tormey E. S., 'Low dielectric loss glass ceramic compositions', US Patent 5-958-807; September 28 (1999).

Kuo C. Y., 'Thick-film resistive paints and resistors made therefrom', US Patent 4-639-391; January 27 (1987a).

Kuo C. Y., 'Base metal resistive paints', US Patent 4-655-965; April 7 (1987c).

Kuo C. Y., 'Base metal resistors', US Patent 4-698-265; October 6 (1987b).

Kuo C. Y., 'Megaohm resistor paint and resistor made therefrom', US Patent 4-711-803; December 8 (1987d).

Kuo C. Y., 'Pre-reacted resistor paint and resistors mode therefrom', US Patent 4-720-418; January 19 (1988).

Kuo C. Y. and Angel H. S., 'Method of preparing ruthenium- or iridium-containing components for resistors', US Patent 3-769-382; October 30 (1973).

Kydd P. H., Jablonski G. A. and Richard D. L., 'Low temperature method and compositions for producing electrical conductors', US Patent 6-379-745; April 30 (2002).

Langley R. C., 'Electrical circuit element comprising thick-film resistor bonded to conductor', US Patent 4-076-894; February 28 (1978).

Larry J. R., 'High adhesion metallizing compositions', US Patent 3-827-891; August 6 (1974).

Larry J. R., 'Resistor compositions', US Patent 4-101-708; July 18 (1978).

Larry J. R., Rosenberg R. M. and Uhler R. O. (1980). 'Thick-film technology: an introduction to the materials', *IEEE Transactions on Components, Hybrids and Manufacturing Technology*, 3(2), 211.

Larsen W. R. and Short O. A., 'Vitrifiable flux and silver compositions containing same', US Patent 2-822-279; February 4 (1958).

Longo J. M., Raccah P. M. and Goodenough J. B. (1969). '$Pb_2M_2O_{7-x}$(M = Ru, Ir, Re) – Preparation and properties of oxygen', *Materials Research Bulletin*, 4, 191–202.

Lux H. and Smetana W. (1991). 'Diamond: a novel substrate for thick-film technology', *Surface and Coating Technology*, 47, 553–558.

Mackenzie G. D., 'Resistance material and electrical resistor made therefrom', US Patent 3-788-997; January 29 (1974).

Makuta F. and Maeda T., 'Resistance paste and resistor', US Patent 7-591-965; September 22 (2009).

Martin J. H., 'Ceramic with metal film via binder of copper oxide containing glass', US Patent 3-293-501; December 20 (1966).

© Woodhead Publishing Limited, 2012

Martin T. O., 'Glass frit compositions and electrical conductor compositions made therefrom compatible with reducing materials', US Patent 5-608-373; March 4 (1997).
Matsuno H. and Barker M. F, 'Conductive composition for black bus electrode and front panel of plasma display panel', US Patent 7-781-971; August 24 (2010).
Mattox D. M., 'Aluminum nitride-compatible thick-film binder glass and thick-film paste composition', US Patent 5-637-261; June 10 (1997).
Melan E. H. and Mones A. H. (1967). 'The glaze resistor – its structure and reliability', *IEEE Transactions Components Parts CP-11*, 76–85.
Merz K. M. and Shapiro H. E., 'Electrical resistor with novel termination and method of making the same', US Patent 4-053-866; October 11 (1977).
Merz K. M. and Shapiro H. E., 'Resistor material,resistor made therefrom and method of making the same', US Patent 4-209-764; June 24 (1980).
Miller L. F., 'Method of fabricating resistor compositions', US Patent 3-414-641; December 3 (1968a).
Miller L. F., 'Method of rendering noble metal conductive composition non-wettable by solder', US Patent 3-401-126; September 10 (1968b).
Miller L. F., 'Electrical resistor compositions, elements and method of making same', US Patent 3-390-104; June 25 (1968c).
Minneman L. C., Trease R. E., Wells L. J. and Dietz R. L., 'Fine line electronic micro-circuitry printing pastes', US Patent 3-830-651; August (1974).
Miyashiro F., Iwase N., Tsuge A., Ueno F., Nakahashi M. and Takahashi, T. (1990). 'High thermal conductivity aluminum nitride ceramic substrates and packages', *IEEE Transactions on Components, Hybrids, and Manufacturing Technology*, 13(2), 313–319.
Mochel J. M., 'Electrically conducting refractory body', US Patent 2-467-144; April 12 (1949).
Mones A. H., 'Electrical resistance composition and method of using the same to form a resistor', US Patent 3-337-365; August 22 (1967).
Mones A. H. and Neisser K. E. Jr, 'Electrical resistance compositions, elements and method of making the same', US Patent 3-248-345; April 26 (1966).
Morten B., Ruffi G., Sirotti F., Tombesi A., Moro L. and Akomolafe T. (1991). 'Lead-free ruthenium-based thick-film resistors: a study of model systems', *Journal of Materials Science: Materials in Electronics*, 2(1), 46–53.
Mulligan W. A, 'Vitreous enamel resistor composition and resistor made therefrom', US Patent 3-441-516; April 29 (1969).
Muralidhar S. K., Roberts, A. G., Shaikh J. S., Leandri D. J., Hankey D. L. and Vlach T. J., 'Low dielectric, low temperature fired glass ceramics', US Patent 5-258-335; November 2 (1993).
Murphy R. M. and Janakirama-Rao B. V., 'Resistance material and resistor made therefrom', US Patent 3-180-841; April 27 (1965).
Nair, K. M. 'Screen-printable dielectric composition', US Patent 4-392-180; July 5 (1983).
Nair K. M., 'Resistor compositions', US Patent 4-645-621; February 24 (1987a).
Nair K. M., 'Resistor compositions', US Patent 4-652-397; March 24 (1987b).
Nair K. M., 'Resistor compositions' US Patent 4-657-699; April 14 (1987c).
Nakahashi M., Shirokane M., Yamazaki, T. Yoshino H., Kawasaki A. H. and Takeda H., 'Method for preparing highly heat-conductive substrate and copper wiring sheet usable in the same', US Patent 4-611-745; September 16 (1986).
Norton M. G. (1990). 'Thermodynamic considerations in the thick-film metallization of aluminium nitride substrates', *Journal of Materials Science, Letters*, 9, 91–93.

© Woodhead Publishing Limited, 2012

Ohkawa Y., Ikeda M., Miyahara K. and Itoh Y., 'Aluminum nitride substrate and process for preparation thereof', US Patent 5-830-570; November 3 (1998).
Okamoto H. O. and Aso T. (1967). 'Formation of thin films of PdO and their electrical properties', *Japanese Journal Applied Physics*, 6(6), 779.
Okamoto K., Kuno H., Yaguchi I. and Koishikawa J. and 'Thick-film conductor paste for automotive glass', US Patent 5-616-173; April 1 (1997).
Okamoto K., 'Thick-film conductor paste compositions for aluminum nitride substrates', US Patent 6-103-146; August 15 (2000).
Ollivier P. J. and Hang K. W., 'Thick-film conductor paste composition for LTCC tape in microwave applications', US Patent 7-740-725; June 22 (2010).
Otschik P., Kretzschmar C. and Lefranc G. (1998a). 'AlN properties of various products', Int Wissenschaftliches Kolloquium – Technische Unviersitaet Ilmenau, 43rd (Band 2), 88–91.
Otschik P., Kretzschmar C., Reppe G. and Scheffel A. (1998b). 'Pastes for high temperature resistors in power hybrids and microwave circuits', DVS-Berichte, 191 (EuPac 1998), 147–150.
Pedder D. T., 'Thick-film circuits', US Patent 4-311-730; January 19 (1982).
Pepin J. G., 'Thick-film conductor composition', US Patent 4-954-926; September 4 (1990).
Place T. M. Sr and Place T. M. Jr, 'Electrical resistance element', US Patent 2-950-995; August 30 (1960a).
Place T. M. Sr and Place T. M. Jr, 'Electrical resistance material and method of making same', US Patent 2-950-996; August 30 (1960b).
Place, T. M. Sr and Place T. M. Jr, 'Method of making electrical resistance element', US Patent 3-149-002; September 15 (1964).
Popowich M. J., 'Resistor compositions containing pyrochlore-related oxides and platinum', US Patent 3-630-969; December 28 (1971).
Popowich M. J., 'Compositions for stable low resistivity resistors', US Patent 3-816-348; June 11 (1974).
Powell D. G. (1974). 'Semiconducting glazes for high voltage insulators', *American Ceramics Socieety Bulleetin*, 52(8), 600–603.
Prabhu A. N. and Hang K. W., 'Indium oxide resistor inks', US Patent 4-380-750; April 19 (1983a).
Prabhu A. N. and Hang K. W., 'Indium oxide resistor inks', US Patent 4-467-009; August 21 (1984a).
Prabhu A. N. and Hang K. W., 'Low value resistor inks', US Patent 4-379-195; April 5 (1983b).
Prabhu A. N. and Hang K. W., 'Low value resistor inks', US Patent 4-452-844; June 5 (1984b).
Prabhu A. N., Hang K. W. and Conlon E. J., 'Thick-film copper conductor inks', US Patent 4-733-018; March 22 (1988).
Prabhu A. N., Hang K. W. and Conlon E. J., 'Thick-film copper conductor inks', US Patent 4-808,770; February 28 (1989a).
Prabhu A. N., Hang K. W. and Conlon E. J., 'Thick-film copper conductor inks', US Patent 4-816-615; March 28 (1989b).
Prudenziati M. (ed.) (1994). *Thick-film Sensors*, Elsevier, Amsterdam.
Prudenziati M., Zanardi F., Morten B. and Gualtieri A. F., (2002), 'Lead-free thick-film resistors: an explorative investigation', *Journal of Materials Science: Materials in Electronics*, 13(1), 31–37.
Prunchak R., 'Glass frits', US Patent 7-736-546; June 15 (2010).
Pukaite C. J., 'Low temperature coefficient of resistivity cermet resistors', US Patent 4-006-278; February 1 (1977).

© Woodhead Publishing Limited, 2012

Rane S., Prudenziati M., Morten B., Golonka L. and Dziedzic A. (2006). 'Structural and electrical properties of perovskite ruthenate-based lead-free thick-film resistors on aluminna and LTCC', *Journal of Materials Science: Materials in Electronics*, 15(10), 687–691.

Reicher R. and Smetana W. (1998). 'Bonding mechanism and stress distribution of a glass frit free thick-film metallization for AlN-Ceramic', *Journal of Materials Science: Materials in Electronics*, 9, 429–434.

Rellick J. R., 'Mixed oxide bonded copper conductor compositions', US Patent 4-323-483; April 6 (1982).

Rellick J. R., 'Dielectric compositions and method of forming a multilayer interconnection using same', US Patent 4-655-864; April 7 (1987).

Rellick J. R., 'Method for fabricating multilayer circuits', US Patent 4-799-984; January 24 (1989).

Richardson L.T. and Swinehart M. R., 'Electrical contact', US Patent 2-572-662; October 23 (1951).

Rikoski R.A. (1973). '*Hybrid microelectronic circuits: the thick-film*', Wiley & Sons, New York.

Rose M. and Young R. J. S., 'Aluminum thick-film composition(s), electrode(s), semiconductor device(s) and methods of making thereof', US Patent 7-718-092; May 18 (2010).

Rosenblatt E. F., 'Platinum metal compounds and methods of making them', US Patent, 2-166-076; July 11 (1939).

Rosenblatt E. F., 'Method of providing adherent metal coatings on surfaces', US Patent 2-328-101; August 31 (1943).

Ryden W. D., Lowson A. W. and Sartain, C. C. (1968). 'Temperature dependence of the resistivity of ruthenium dioxide and iridium dioxide', *Physics Letters A*, 26(5), 209–210.

Ryden W. D., Lowson A. W. and Sartain C. C. (1970). 'Electrical transport properties of iridium oxide and ruthenium oxide', *Physics Review B*: Solid State, [3]1(4), 1494–1500.

Saeki S., Suehiro M., Echigo M., Okada S. and Sakuraba M., 'Copper paste composition', US Patent 5-035-837; July 30 (1991).

Sato H., Mizunoya N. and Nagata M., 'Aluminum nitride substrate', US Patent 4-761-345; August 2 (1988).

Scheiber D. H., 'Vehicle for thick-film resistors fireable in nonoxidizing atmosphere', US Patent 4-251-397; February 17 (1981).

Scheiber D. H. and Weaver R. V., 'Photohardenable paste compositions having high resolution', US Patent 3-914-128; October 21 (1975).

Schubert K. E., 'Resistor compositions containing pyrochlore-related oxides and cadmium oxide', US Patent 3-560-410; February 2 (1971).

Senkalski R. E. and Hasenmayer D. L., 'Dielectric composition having controlled thermal expansion', US Patent 4-961-998; October 9 (1990).

Sergent C. J. E. (2004). 'Materials and processes for hybrid micrelectronics and multichip modules', in A. Harper (ed.) *Electronic Materials and Processes Handbook*, 3rd edn, McGraw Hill.

Shaikh A. S., Roberts G. J. and Sarkar G., 'Dielectric materials', US Patent 5-397-830; March 14 (1995).

Shapiro H. E. and Merz K. M., 'Resistor material, resistor made therefrom and method of making the same', US Patent 4-205-298; May 27 (1980).

Siuta V. P., 'Copper conductor compositions', US Patent 4-687-597; August 18 (1987).

Siuta V. P., 'Metal oxide-coated copper powder', US Patent 4-600-604; July 15 (1986).

© Woodhead Publishing Limited, 2012

Soby W., 'Process of metallizing surfaces', US Patent 2-551-712; May 8 (1951).
Stein S. J., Huang C. and Gelb S. (1980). 'Comparison of enameled steeel substrate properties for thick-film use', *Electroncomponent Science and Technology*, 7, 55–61.
Stein S. J., Wahlers R. L., Bless P. W., Barclay C. and Tait R. B., 'Dielectric pastes and tapes, and metal substrates coated therewith', US Patent 5-998-036; December 7 (1999).
Steinberg J., 'Nitrogen fireable resistor compositions', US Patent 4-814-107; March 21 (1989).
Tachibana M., Kohama, Y. Shimoyama T., Harada A., Taniyama, T. *et al.* (2006). 'Electronic properties of metallic pyrochlore ruthenates $Pb_2Ru_2O_{6.5}$ and $Bi_2Ru_2O_7$', *Physics Review B*, 73, 193107.
Tanaka H. and Igarashi K., 'Resistor paste, resistor, and electronic device', US Patent 7-282-163; October 16 (2007).
Tanaka H. and Igarashi K., 'Thick-film resistor paste and thick-film resistor', US Patent 7-481-953; January 27 (2009a).
Tanaka H. and Igarashi K., 'Glass composition for thick-film resistor paste, thick-film resistor paste, thick-film resistor, and electronic device', US Patent 7-544-314; June 9 (2009b).
Tankiewicz S., Morten B., Prudenziati M. and Golonka L. J. (2002). 'IrO_2-based thick-film resistors', *Journal of Applied Physics*, 91(7), 4261–4266.
Taylor B. E., 'Binder glass of Bi_2O_3-SiO_2-GeO_2(-PbO optional) admixed with ZnO/ZnO and Bi_2O_3', US Patent 4-567-151; January 28 (1986).
Totokawa M., Ootani Y., Imal H. and Shintai A., 'Conductor composition, a mounting substrate and a mounting structure utilizing the composition', US Patent 7-807-073; October 5 (2010).
Towlson S. M., 'Flexible thick-film conductor composition', US Patent 5-653-918; August 5 (1997).
Toyoda S., Kuromitsu Y., Sugamure, K. and Nakabayashi A., 'Aluminum nitride substrate and method of producing the same', US Patent 5-780-162; July 14 (1998).
Tsuda N., Nasu K., Yanase A. and Siratori K. (1991). *Electronic Conduction in Oxides*, Springer-Verlag, Heidelberg.
Tsuyuki H., 'Glass, dielectric composition, multilayer wiring substrate, and multilayer ceramic capacitor', US Patent 5-378-662; (1995).
Tummala R. R. (1991). 'Ceramic and glass-ceramic packaging in the 1990s', *Journal of the American Ceramic Society*, 74(5), 895–908.
Tummala R. R., Haley M. R. and Czornyj G. (1993). 'Materials in Microelectronics', *Ceramics International*, 19, 191–210.
Ulrich D. R., 'Screened circuit capacitors', US Patent 3-649-353; March 14 (1972).
Usui, H., Dotani Y., Tanabe R. and Manabe T., 'Low melting point glass and glass ceramic composition', US Patent 6-355-586; March 12 (2002).
Van Loan P. R. (1971), 'Current trends in thick-film resistor technology', *Journal Canadian Ceramic Society*, 40, 49–54.
Van Loan P. R., 'Electrical resistor containing lead ruthenate', US Patent 3-682-840; August 8 (1972).
Van Loan P. R., 'Resistive glaze and paste compositions', US Patent 3-868-334; February 25 (1975).
VerNooy P. D., Walker A. T. and Hang K. W., 'Non-lead resistor composition', US Patent 7-608-206; October 27 (2009).
Vest R. V. (1979). 'Thick-film glasses', *Final technical Report No. ADA062748*, Naval Research Laboratory, January 3.

© Woodhead Publishing Limited, 2012

Vest R. W. (1980). 'Metallo-organic materials for improved thick-film reliability', *Final report, contract #N00163-79-C-0352*, National Avionic Center, November 1.
Vest R. W. (1986). 'Materials science of thick-film technology', *American Ceramic Society Bulletin*, 65(4) 631–636.
Vest R. W. (1991). 'Materials aspect in thick-film technology', Chapter 8 in R. C. Buchanan, *Ceramic Materials for Electronics: Processing, Properties and Applications*, 2nd edn, Marcel Dekker Inc., New York.
Vest R. W., Tweedell E. P. and Buchanan B. C. (1983). 'Ink jet printing of hybrid circuits', *International Journal of Hybrid Microelectronics* 6(2),261–267.
Wang C. B., Hang K. W. and Needes C. R. S., 'Tape composition and process for internally constrained sintering of low temperature co-fired ceramic', US Patent 6-776-861; August 17 (2004).
Wang C. B., Hang K. W. and Needes C. R. S, 'Tape composition and process for internally constrained sintering of low temperature co-fired ceramic', US Patent 7-147-736; December 12 (2006).
Watanabe S., Tani H. and Kasanami T., 'Resistive paste', US Patent 4-985-176; January 15 (1991).
Weiβmann R. and Chong W. (2000). 'Glasses for high-resistivity thick-film resistors', *Advanced Eng Materials*, 2(6), 359–362.
Whalers R. L. and Merz K. M., 'Resistor material, resistor made therefrom and method of making the same', US Patent 4-065-743; December 27 (1977).
Whalers R. L. and Merz K. M., 'Resistor material, resistor made therefrom and method of making the same', US Patent 4-215-020; July 29 (1980).
Whalers R. L. and Merz K. M., 'Resistor material, resistor made therefrom and method of making the same', US Patent 4-293-838; October 6 (1981).
Whalers R. L. and Merz K. M., 'Resistor material, resistor made therefrom and method of making the same', US Patent 4-322-477; March 20 (1982a).
Whalers R. L. and Merz K. M., 'Resistor material, resistor made therefrom and method of making the same', US Patent 4-340-508; July 20 (1982b).
Whalers R. L. and Merz K. M., 'Resistor material, resistor made therefrom and method of making the same', US Patent 4-378-409; March 29 (1983a).
Whalers R. L. and Merz K. M., 'Resistor material, resistor made therefrom and method of making the same', US Patent 4-397-915; August 9 (1983b).
Yamaguchi T. and Kageyama M. (1989). 'Oxidation behavior of AlN in the presence of oxide and glass for thick-film applications', *IEEE Transactions on Components, Hybrids and Manufacturing Technology*, 12(3), 402–405.
Yamaguchi T. and Kanai K. (1992). Proceedings of the International Symposium on Microelectronics, pp. 463–467.
Yang H., 'Ink jet printable thick-film compositions and processes', US Patent 7-683-107; March 23 (2010).
Young R. J. S., Rose M., Raby J. A. and Hang K. W., 'Aluminum thick-film composition(s), electrode(s), semiconductor device(s) and methods of making thereof', US Patent 7-771-623; August 10 (2010a).
Young R. J. S., Rose M., Mikeska K. R., Carroll A. F., Hang K. W. and Prince A. G., 'Lead-free conductive compositions and processes for use in the manufacture of semiconductor devices: mg-containing additive', US Patent 7-780-878; August 24 (2010b).
Young, R. J. S., Rose M. and Raby J. A. 'Aluminum thick-film composition(s), electrode(s), semiconductor device(s) and methods of making thereof', US Patent 7-824-579; November 2 (2010c).

© Woodhead Publishing Limited, 2012

3

Materials Science concepts for printed films

J. HORMADALY, Ben-Gurion University, Israel and
M. PRUDENZIATI, University of Modena and Reggio Emilia, Italy

Abstract: The chapter examines some illustrative cases of the complex interplay between the composition process and properties relations in simple printed film structures, such as resistors and interconnections. It is remarked that thermodynamics data can help, in some cases, in interpreting film phase stability, but richer information would be required to understand the complex phenomena that may occur in thick-printed films, which are typically systems far from thermal equilibrium. Examples of interactions that impact on the films' electrical properties are reported. It is remarked that the microstructure and performance of thick-films start to evolve from temperatures as low as room temperature and continue to change during the whole course of processing or, when required, in post-process thermal annealing. It is shown that the presumed ideal picture of cermet systems consisting of single-phase conducting particles imbedded in vitreous phase is very far from the reality.

Key words: composition/process/properties relationships; interactions; solubility; thick-films; glasses; thermodynamics; reaction kinetics; phase transitions.

3.1 Introduction

The paradigm for Materials Science is the concept of close inter-relation of principles–structure–processing–properties. Written like this, it may seem to be a 'linear' link instead of the very complex one depicted in Fig. 3.1.

The difficulty in realizing these complex relationships in thick-film (TF) technology is immediately apparent when one considers the myriad of ingredients in the paste compositions and the wide range of processing conditions. The ingredients encompass conducting phases such as precious metals or/and their alloys, glass powders, other inorganic materials, together with the organic vehicle and sometimes metal–organic compounds. Most precious metals, their alloys and their compounds are catalysts; therefore they can catalyze, even at room temperature, all sorts of reactions in the organic vehicle, based on the resins and solvents that provide the printability of the paste. Also other paste ingredients can react with the organic vehicle at temperatures encountered in the burn-out zone. Next, the printed films are exposed to a thermal process that spans a wide temperature range; in these conditions, TF glasses exhibit their corrosive properties (in the molten state, typically at T > ~500–600 °C) and dissolve the substrate materials, dissolved metals like Ag, interact with other inorganic materials and some glasses can crystallize.

© Woodhead Publishing Limited, 2012

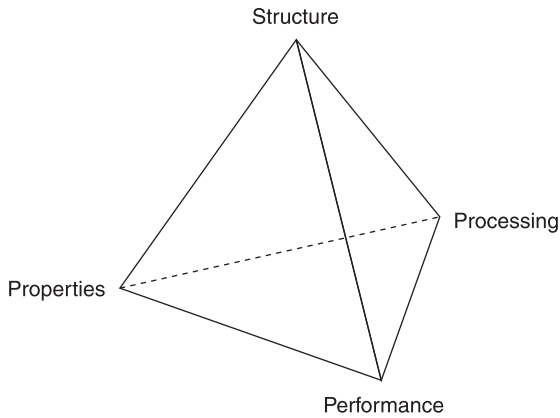

3.1 The tetrahedron often used to represent cross-relations in Materials Science.

The search for an immediate economic return and the complexity of these systems have not encouraged the systematic research of these composition–process–properties relationships.

In the first issue of *Hybrid Circuits*, the magazine of the International Society for Hybrid Microelectronics (ISHM), a contribution by P. L. Kirby (1982), then Vice President of the Society (now incorporated in IMAPS: International Microelectrics and Packaging Society), contains a heartfelt invitation to depart from the widespread attitude of beginners who design experiments 'to see what happens' without any consideration for a scientific approach or use of available knowledge.

This old attitude has been only partly overcome over the years thanks to very valuable educational efforts and research carried out in some universities in Europe (e.g. London and Southampton in the UK, the Technical University of Vienna, Wroclaw, Oulu, Italy and Switzerland) and in the USA (e.g. Purdue University). Investigations in these educational institutions, together with some multiannual research programs (e.g. in Sandia National Laboratories, Albuquerque and in Philips, Eindhoven) have greatly contributed to recall attention to Materials Science aspects for screen-printed films firstly, and more recently on films printed with the currently diversified methods to lay down functional films. However, another wide basket of knowledge in materials/process relationships have never been unfolded, because neither the scientific literature nor the patents disclose more than a small share of the results that have emerged during the development of new products by companies.

This chapter is an attempt to call the reader's attention to a few, but nonetheless important, features of TF materials, where Materials Science concepts and experimental evidence can help in realizing not only the complexity of behavior,

© Woodhead Publishing Limited, 2012

but also the fascinating and unique properties of TF technology. Of course, there is no claim of comprehensive coverage of the field, but topical examples will be presented. In addition, the order of arguments is not a systematic one but hopefully adequate to inspire further and deeper study.

3.2 Interactions of conducting materials with the organic vehicle at room temperature

Many ingredients of TF pastes are catalysts: Pd, Pt, RuO_2, IrO_2, very fine particles of Ag and Au, ruthenates and iridates. Catalytic activity increases with increases in the surface area. The RuO_2, IrO_2 and ruthenates used in TF composition have a wide range of surface areas, 10–60 m^2/g, and they may interact with the organic vehicle. Interactions of RuO_2 (similar interactions are expected for IrO_2) with the organic vehicle span a broad range: from minor chemical changes of the organic vehicle, which affect the paste viscosity and lead to viscosity drift with time, to burning of the organic vehicle. To reduce its catalytic activity, RuO_2 is usually washed by a solution of ammonium salts (Avtokratova, 1962; Gilchrist, 1929; Yi *et al.*, 1997) after precipitation. Avtokratova (p. 39) reports 'Precipitates, which have not been washed with ammonium sulfate might catch fire or even explode due to the dehydration of ruthenium hydroxide'.

RuO_2 is usually precipitated from the ruthenium chloride ($RuCl_3$) solution or by the reduction of sodium ruthenate solution (Na_2RuO_4) by alcohol (Seddon and Seddon, 1984). Both processes result in active RuO_2 powders, but the sodium ruthenate route usually yields hydrous ruthenium dioxide ($RuO_2 \cdot XH_2O$), which is contaminated with trace amounts of sodium or potassium ruthenates. These traces of Na_2RuO_4 can lead to interactions with the organic vehicle that include oxidation at room temperature and release of gas at higher temperatures. The latter, when the glass softens, may and usually does lead to the formation of blisters in resistor films (Hormadaly, unpublished).

3.3 Redox reactions

One of the most appreciated characteristics of the *traditional* TF technology (TFT) is the ability to process materials in air, most often in a belt furnace. The thermal processes are designed to allow a continuous production flow; therefore the so-called 'firing profiles' prescribe heating rate, peak temperature, T_f, and dwell time at the peak and cooling rate to ambient temperature. A typical firing profile for processing screen-printed films is shown in Fig. 3.2. Moreover, a frequent recommendation in processing schedules is to provide a controlled flow of 'clean' air in the furnace, free from humidity, dirt particles and unwanted gas.

The events allowed or prevented by these conditions include redox reactions, sometimes very far from the operator's awareness; the reactions assume a 'special'

© Woodhead Publishing Limited, 2012

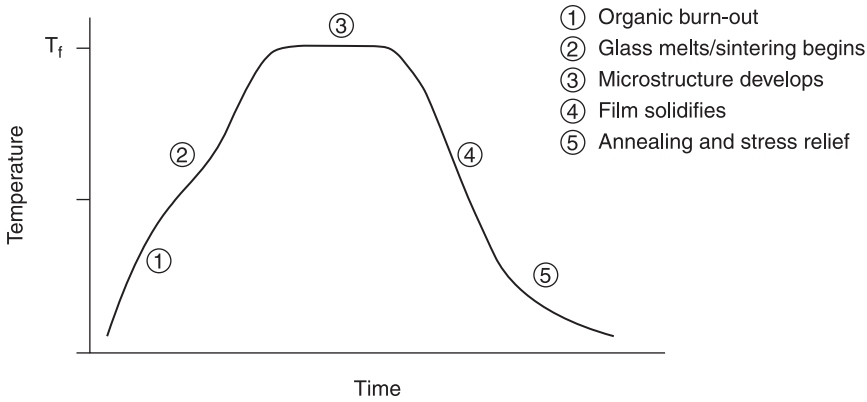

3.2 Typical firing temperature profile for thick-films.

character in the case of printed thick (and thin) films because of the large surface-to-volume ratio, which exposes a large fraction of the materials to the ambient and thus also provides easy access of oxygen or reducing gas to the material, with the consequent accelerated kinetics for oxidation and reduction.

One of the obvious and necessary reactions is the oxidation of the binder, i.e. the burn-out of the organic vehicle fraction left after the evaporation of the solvents (normally at 150–180 °C); this reaction must occur as long as the printed layer is porous enough to allow the reaction products (H_2O, CO, CO_2) to 'rapidly' leave the film, thus not charring the remains trapped inside the component. Yet, despite the excess of air in the firing furnace, in the burn-out temperature window there is a local redox disequilibrium, because the film is exposed to the reducing action of these gaseous byproducts. If and how much reduction of the material constituents in the film really takes place depends on the oxygen partial pressure (P_{O_2}) over the film, the rates of the reactions, the specific surface area of the particles and their surface preparation.

Figure 3.3 provides a phase stability diagram for metal–metal oxide systems of interest for TF compositions, i.e. the oxygen partial pressure *in equilibrium* with various metal–metal oxide couples vs. the temperature.

Each line descends from an equation of the type:

$$Pd(s) + ½\ O_2(g) = PdO(s) \quad [3.1]$$

$$4/3\ AlN(s) + O_2(g) = 2/3\ Al_2O_3(s) + 2/3\ N_2(g)$$
$$\Delta G°_f(850\,°C) = -628\ KJ\ mol^{-1} \quad [3.2]$$

$$Pb(s) + O_2(g) = 2PbO(s)$$
$$\Delta G°_f(850\,°C) = -218\ KJ\ mol^{-1} \quad [3.3]$$

$$Ru(s) + O_2(g) = RuO_2(s)$$
$$\Delta G°_f(850\,°C) = -116\ KJ\ mol^{-1} \quad [3.4]$$

© Woodhead Publishing Limited, 2012

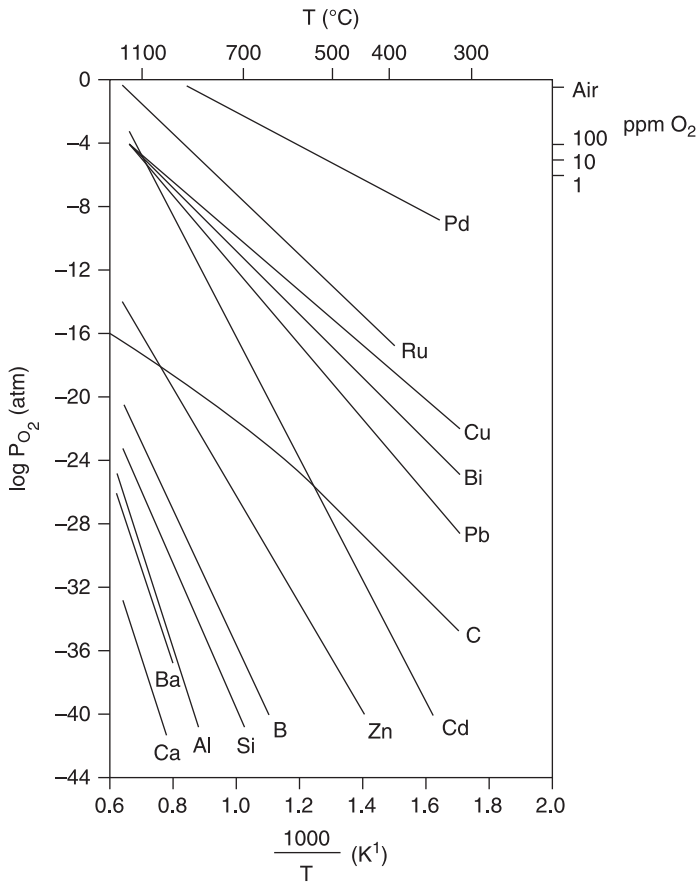

3.3 Phase stability diagram for selected elements of interest in thick-film technology.

From Eq. [3.1], the mass action law and thermodynamics dictate that:

$$\Delta G = \Delta G° + RT \ln K = \Delta G° + RT \ln(1/P_{O_2})^{1/2}, \quad [3.5]$$

where K represents the reaction equilibrium constant, R the gas constant and P_{O_2} the oxygen partial pressure where the metal and its oxide coexist at absolute temperature T. $\Delta G°$ is the standard free energy change for the formation of 1 mole of the oxide from the elements. $\Delta G°$ data are given in standard compilations of thermodynamic quantities (Turkdogan, 1980).

$$\Delta G = 0 \text{ at equilibrium. Therefore, } \ln P_{O_2} = 2\Delta G°/RT \quad [3.6]$$

For each chemical species, the element is the stable phase in the P_{O_2}-T region below its curve (reducing conditions); conversely, the oxide is stable above the curve.

© Woodhead Publishing Limited, 2012

The lines of Fig. 3.3 are strictly valid only for the equilibrium between the *pure* metal and a *pure oxide*. Otherwise, for example when the metal is a constituent of a glass, its curve is shifted downward (Wang and Huebner, 1991). Note that the log P_{O_2} in air equals −0.675 atm.

The carbon curve is introduced in order to consider the C-CO-CO_2 equilibrium for 1 total pressure of CO + CO_2 (Vest, 1986); this serves for evaluation of the P_{O_2}-T region where the vehicle burn-out affects the redox reactions of the metal/metal oxide systems.

Looking at Eqs. [3.1] to [3.4] and Fig. 3.3, a few examples of redox reactions become of obvious interest. Firstly, let us consider the stable phases of Pd, a common constituent of conductor inks also used for its catalytic property in gas sensors.

For the latter function, i.e. in enhancing the reaction rate of the specific target gas within the sensing material, PdO rather than Pd may be the more effective catalyst. This is the case for SnO_2-based methane sensors (Debéda *et al.*, 1997). Because PdO is thermodynamically stable only below ~820 °C in air, the firing process over this temperature (typically 850 °C–900 °C) to stabilize the microstructure results in a drastic decline of sensitivity in SnO_2:5% Pd methane sensors. However, a long annealing (several hours at 600 °C) restores the oxidized form of PdO as well as the desired sensing properties.

When highly conductive films are the target, Pd is not used alone (because its resistivity is not suitable) but it is added to silver-based compositions. The benefit of adding Pd is mainly the increase in solder-leaching resistance (almost absent with pure silver). On heating at the peak firing temperature, Pd would be oxidized and the PdO would contrast the solid solution formation. The lower activity of Pd in the AgPd alloys, as compared to pure Pd, results in a decrease of the temperature for dissociating the remaining PdO, but the metal would be oxidized again on cooling down at room temperature. This would be a severe drawback: PdO on the surface of the film reduces the solderability. A proper design for firing dense and highly conducting AgPd films in air may be to heat up to T_f of 850 °C (or higher) and cooling very rapidly from the peak temperature at least down to 300 °C, where the reaction rate of oxidation becomes low enough (and there is still a chance to avoid too serious thermal stress on the printed films).

Let us now look at Eqs. [3.2] and [3.3]. The equilibrium reaction equations can be added, taking account of the number of moles involved, so that we have:

$$2\ PbO(s) + 4/3\ AlN(s) \rightarrow 2/3\ Al_2O_3(s) + 2\ Pb + 2/3\ N_2(g) \qquad [3.7]$$

Based on the $\Delta G°_f$ of reactions [3.2] and [3.3], the ΔG of reaction [3.7] is: −628−(218) = −410 KJ mol^{-1} at 850°C. The negative value of ΔG shows that reaction [3.7] is favorable toward the right, leading to a reduction of lead oxide and evolution of nitrogen gas (or NOx(g)); the latter accounts for the observed blistering of high-lead glassy films or conventional resistive films on aluminum nitride substrates (Norton, 1990).

© Woodhead Publishing Limited, 2012

Similar considerations allow us to realize why conventional lead–silicate glasses are unsuitable for systems compatible with AlN substrates: new 'non-reducible' glasses were developed either for 'glass-bonded' metallization and TF resistors (Burckhardt and Vavra 1989; Kretzschmar *et al.*, 1993; Needes, 2003; Wang *et al.*, 2003). The new compositions cannot be reduced by AlN, since they are PbO-free (and Bi_2O_3-free) or contain them only in very small amounts, but take as major components oxides (such as SiO_2, B_2O_3, Li_2O, CaO, BaO) whose $\Delta G°_f$ is larger *in absolute value* than that of $\Delta G°_f$(AlN), at least for $T < T_f$.

Another effect of localized redox equilibria (Zdaniewski and Silverman, 1990) concerns gold-based metallization for dielectrics fired in nitrogen ambient conditions: the competition for oxygen (see Fig. 3.3) between the glass components of the dielectric material and decomposing organics results in a reduction of PbO to Pb metal; next, Pb and Au form an alloy, thus the wetting equilibrium between Au and ceramic is completely altered causing delamination of gold lines.

Turning back to the interactions in the burnout range (typically at $T < 450\,°C$), we note that the general expression representing the interaction of the binder with the precious metal or the glass may be described by the following:

$$MO_w + C_xH_yO_z \rightarrow CO + H_2O + M, \qquad [3.8]$$

where M = Ru, Ir, Pb, Bi, Cd, $C_xH_yO_z$ represents the general formula of the binder (either an ethyl cellulose or acrylic resin) and MO_w an oxide. For the reasons explained above, the thermodynamics shows that the enthalpy change $\Delta H_{reaction}$ of this type of reaction is negative, i.e. the reaction is likely to proceed from left to right. As far as char is present, the local atmosphere inside the film is on the carbon curve of Fig. 3.3, so that any temperature along this curve gives a sufficiently low P_{O_2} to reduce the metal listed above. The reduction rate is quite different for the different metals, however. The reduction of precious metal oxides during TF processing was reported by Pierce *et al.* (1982). More detailed study of the reduction process of RuO_2 powders and kinetics of their re-oxidation were reported by Prudenziati *et al.* (2003): the reduction is found to be an extremely fast (probably autocatalytic) phenomenon at temperatures as low as 100–150 °C, whereas on heating beyond the burnout stage – when the oxidizing conditions prevail – the reverse reaction, from Ru to RuO_2 needs much longer times. Nakano and Yamaguchi (1995) reported the effect of O_2, concentration in the firing atmosphere on the resistance of RuO_2-based TF resistors. This report clearly shows a major difference between lead-free glasses and lead-containing glasses when fired at various O_2 concentrations.

The reaction of polynary precious metal oxides with the organic binder during the burn out stage may be represented by:

$$M'_2Ru_2O_{7-\delta} + C_xH_yO_z \rightarrow CO + H_2O + M'O_v + Ru, \qquad [3.9]$$

where M' = Pb, Bi and a mixture of Pb, Bi with other metals; v is a number between 0 and 1.5.

© Woodhead Publishing Limited, 2012

Some of the pyrochlore constituents, PbO and Bi_2O_3, can also be reduced if sufficient organic binder remains. Interactions between ethylcellulose and TF resistors containing RuO_2 and polinary Ru compounds ($Bi_2Ru_2O_7$, $Pb_2Ru_2O_6$ and $Bi_{1.5}Cu_{0.5}Ru_2O_{6.5}$) were studied with a combination of techniques by Krausse *et al.* (1991).

The areas most susceptible to the reduction reactions discussed above are the surfaces of conducting grains and very small conducting particles. According to the general scheme above, the conducting particles of precious metal oxides in the burnout stage are expected to be enveloped by a diffuse zone of metallic 'shell'. Further heating in the temperature range that warrants oxidizing conditions can result in partial re-oxidation of these particles to the corresponding oxides and even to compounds' formation between the very fine oxides and other paste ingredients.

The consequences of these reactions may be quite unexpected. Horowitz (1978) reported that:

> when typical Pd/Ag conductor compositions have been used as terminations for certain ruthenium based resistors (such as low-ohm, less than 100 Ω/□/mil of thickness, resistors of pyrochlore-related oxides or RuO_2), staining of the surface of the conductive termination adjacent to the resistor often occurs during resistor firing. Such surface stains are undesirable since they prevent complete soldering of the conductor in the region of the resistor; Bi_2O_3 is present in typical conductor compositions to enhance adhesion, but it seems to be responsible for such staining.

Hormadaly (1984) studied this phenomenon and found that the addition of certain oxygen-containing materials such as Ag_2O and $CoCrO_4$, which gives off oxygen in the 200–400 °C temperature range, eliminated the staining. It seems that in the burnout zone volatile ruthenium compounds are formed, probably carbonyls of ruthenium, and they evaporate and oxidize to RuO_2, which then reacts with the Bi_2O_3 in the terminations to form black $Bi_2Ru_2O_7$. The burnout stage of TF compositions, which has not been the subject of detailed research, may reveal the formation of many volatile compounds of ruthenium and iridium.

The volatile compounds of ruthenium, RuO_3 and RuO_4, are known to coexist with RuO_2 at high temperatures (Bell and Tagami, 1963).

Among the many studies of redox interactions concerning systems of interest for TF technology, it is worth mentioning those due to Palanisamy and Sarma (1987) on processing copper TFs in nitrogen and to Hong *et al.* (2009) on front-side Ag contacts of silicon solar cells, where a singularly rich variety of redox reactions results from the competition for oxygen by the Si (the cell), PbO (in the binding glass), Si_3N_4 (in the antireflection coating) and Ag (in the metal for the burnout and fingers).

3.4 Chemical diffusion-related interactions during the firing cycle

One topical example of looking at possible interactions via dissolution, interdiffusion and chemical interactions in TF materials is represented by TF resistors

© Woodhead Publishing Limited, 2012

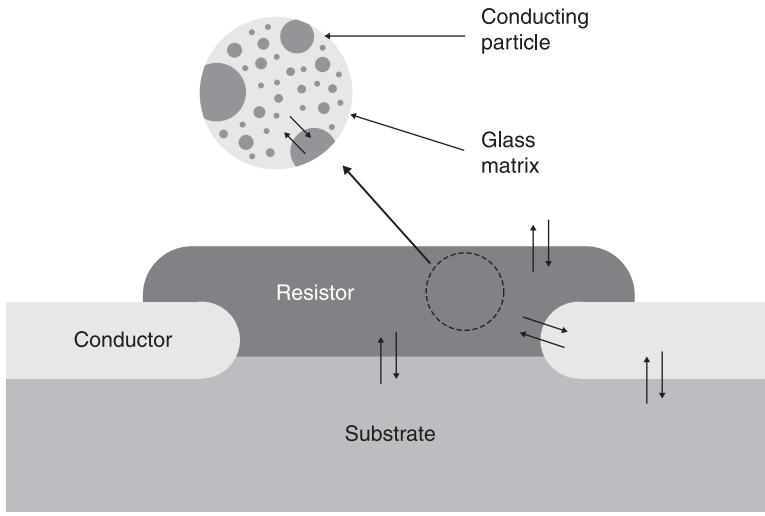

3.4 Sources of possible interactions in a printed-and-fired thick-film resistor.

(Fig. 3.4). Here these phenomena affect the couples: (1) resistive film and substrate, (2) terminations and substrate, (3) resistive film and conductive terminations, (4) resistive film and environment, (5) glassy matrix of the resistor and various phases embedded in, including the main conductive oxide, the fillers, TCR modifiers and additives such as transition metal oxides or their compounds. The following sections cover aspects of these interactions in resistors or similar systems.

3.4.1 Interactions between substrates and silicate glasses

A wide range of substrates are used in TF technology; chemistry and properties of several substrates were discussed in Chapter 2. Alumina is the main substrate used in TF technology, more specifically 96%-Al_2O_3, the remaining 4% consisting of SiO_2, CaO and MgO. The same oxides (SiO_2, CaO, MgO) are common glass ingredients. Therefore, interactions between TF glasses and alumina are not surprising and were reported in the patent literature. In fact, substantial amounts of alumina are dissolved in TF glasses even during typical TF firing profiles. This modifies the properties of the glass: its viscosity increases, the expansion coefficient decreases, the wetting characteristics are affected and the dielectric constant and the ionic conductivity are also affected. The dissolved Al does not reach equilibrium during the firing cycle, thus concentration gradients exist in the fired films where alumina concentration is high near the substrate and decreases gradually toward the film surface. Glass/alumina interactions were reported by many authors in industry and academia, e.g. by Adachi and Kuno (2000), Angus and Gainsbury (1972), Bube (1972), Hoffman (1984), Hoffman and Jones (1983),

© Woodhead Publishing Limited, 2012

Machin and Vest (1978), Moriwaki *et al.* (1993), Palanisamy *et al.* (1989) and Shah (1980).

Studies of seven compositions of high-lead glasses on 96%-Al_2O_3 (Prudenziati *et al.*, 1989) have shown that interactions occur via correlated diffusion of Al from the substrate into the glassy films and counter-diffusion of Pb and B toward the substrate. The effective inter-diffusion coefficients at 850 °C are in the range from 10^{-10} to 10^{-6} cm^2 s^{-1}, according to the glass composition. The higher the boron content, the higher the interdiffusion coefficient. In all the considered glasses, solubility of Al_2O_3 is in the range from 10 to 20% by weight, for peak temperatures of 850 °C. In some glasses this solubility is slightly dependent on T_f, whereas in other cases, and notably when high amounts of B_2O_3 are present, a relevant temperature dependence of the solubility is observed. Several consequences of alumina interaction with the glassy matrix of resistors were observed: the thickness-dependent composition of the glassy matrix results in the thickness-dependent sheet resistance of the resistor; the dissolution of Al_2O_3 affects the grain growth rate of RuO_2 particles in RuO_2-based resistors and the thermal stability of pyrochlores into ruthenate-based resistors (Prudenziati *et al.*, 1989).

Also, beryllia is not 'inert' against high-lead glasses. Interactions between BeO substrates and several high-lead glasses annealed at the thermal conditions (temperatures and times) usually employed in the preparation of TF components were studied (Moro *et al.*, 1992). Solubilities and diffusivities similar to those observed in the case of alumina were found. However, the interaction mechanisms seem quite different: no Al–Pb correlated diffusion process was observed in this case. This difference may account for the lack of relevant changes in the electrical properties of TF components prepared on beryllia, e.g. there is no evidence of thickness-dependent resistivity, or temperature-dependent phase transitions in Bi-ruthenate-based resistors.

3.4.2 Solubility of RuO_2 and ruthenium compound in silicate glasses

The solubility of the conductive oxides in the glassy phase of TF resistors during firing plays a major role in determining the sintering and ripening kinetics of the conductive particles. In addition, the concentration of metal (or ion) in solution may contribute to the electronic transport. Motivated by the need to clarify these points, many investigations have been carried out on the solubility of Ru from RuO_2 particles in lead borosilicate glass (Adachi *et al.*, 1994; Palanisamy *et al.*, 1989; Prabhu *et al.*, 1974). The experiments were generally conducted in the range from 600 to 1000 °C. The results revealed very low solubility values, generally lower than 20–30 parts per million (ppm). Prabhu *et al.* observed that the average concentration C_o of Ru in the glass (63 PbO, 25 B_2O_3, 12 SiO_2,% wt) fired at 800 °C, 15 min (hence in typical conditions of firing in a tunnel kiln furnace) is C_o= 4 ppm; even at 1000 °C, the solubility is less than 35 ppm. In addition, they

© Woodhead Publishing Limited, 2012

noted that C_o in the glass fired at 1000 °C is greater after 15 minutes (about 31 ppm) than after 13 hours (about 14 ppm). The proposed interpretation of this result was that during the initial heating, the smallest particles dissolve rapidly, creating a supersaturated solution in their vicinity. The Ru then diffuses through the glass and precipitates as RuO_2, on the surfaces of larger particles eventually decreasing the total Ru dissolved in the glass to the equilibrium value.

Palanisamy *et al.* (1989) analyzed a glass with the same composition as above, but with addition of 2 to 10% wt Al_2O_3, The measured solubility in samples annealed from 700 to 1000 °C, 12 h exhibits an exponential dependence on temperature, and the dissolved alumina decreases the solubility at any given temperature, but in the same ratio whichever is the amount of Al_2O_3 added. Concentration of dissolved Ru never exceeds 25 ppm, being in the range 5 to 25 ppm at 700 to 1000 °C.

High lead borosilicate glasses in 26 different compositions were analyzed by Adachi *et al.* (1994) for Ru solubility after thermal treatment at 900 °C for 1 hour. The values were lower than the detection limit (10 ppm) for a dozen glasses, and generally lower than 100 ppm (only one exception found). The authors concluded, 'it is evidently clear that the solubility is generally extremely low, as low as 10 ppm in weight in most glasses. When more additives are substituted for SiO_2 the solubility tends to increase slightly'. This is partly attributed to the decrease in viscosity of glasses at 900 °C at decreasing SiO_2 content. It was suggested that the additives Fe_2O_3 and TiO_2 are more effective among others in increasing the Ru solubility.

Another wide category of investigations concerns RuO_2 in lead-free glasses (Mukerji and Biswas, 1967; Pflieger *et al.*, 2009; Pinet and Mure, 2009; Schreiber *et al.*, 1986; Yamashita and Yamanaka, 2004) because of the interest in ruthenium–glass systems formed during the vetrification of nuclear wastes. In simple soda–silica glass (with 20–40 mol% Na_2O) at temperatures above 1000 °C, $C_o > 100$ ppm were measured (Mukerji and Biswas, 1967); in borosilicate and boroaluminosilicate glasses a much lower solubility was measured (or lower than the detection limit of the analytical methods used), even at the melting temperature of the glass (1200 to 1400 °C). Nevertheless, indirect evidence of dissolved Ru has been mentioned, such as modification of the glass density and diffusion-limited growth of precipitated RuO_2 grains (Pflieger *et al.*, 2009), and changes in optical absorption spectra (Herold *et al.*, 1956; Mukerji, 1972; Yamashita and Yamanaka, 2004).

It is worth noting that most of the studies on ruthenium dissolution in glasses, especially in TF glasses, were concerned with the solubility of Ru^{4+}. No report deals with the solubility of other oxidation states of ruthenium, such as Ru^{3+} and Ru^{2+}, which are likely to form during the firing of TF resistors.

The dissolution of ruthenium pyrochlores ($Bi_2Ru_2O_7$, $Pb_2Ru_2O_{6+\delta}$, $(Pb,Bi)_2Ru_2O_{6+\delta}$, $(Bi,Gd)_2Ru_2O_7$, $Bi_{1.5}Cu_{0.5}Ru_2O_{7-\delta}$, $\delta = 0–1$) in the vitreous phase during the firing cycle is very different from that of RuO_2. The majority of pyrochlores-based TF resistors make use of $Bi_2Ru_2O_7$ and $Pb_2Ru_2O_{6+\delta}$. These pyrochlores have constituents (PbO, Bi_2O_3), which are known to form

© Woodhead Publishing Limited, 2012

glasses easily with the main glass formers (SiO_2, B_2O_3) and to dissolve readily in many glasses. Glass formation ranges of PbO and Bi_2O_3 in silicate and borate glasses are very broad and can extend to 90 mole%. Janakirama-Rao (1962) reported that Bi_2O_3 can form silicate and borate glasses where the Bi_2O_3 concentration exceeds 95 wt%. Therefore, $Bi_2Ru_2O_7$ and $Pb_2Ru_2O_{6+\delta}$ are expected to interact with glasses during the firing cycle of TF resistors. The general scheme to describe these interactions may be written as:

$$M_2Ru_2O_{7-\delta} + \text{Glass} \leftrightarrow \text{M-glass} + RuO_2, \qquad [3.10]$$

where M = Pb, Bi and $\delta = 0–1$.

In fact, several investigations (Morten *et al.*, 1994; Nordstrom and Hills, 1980; Pike and Seager, 1977) have shown that in lead–silicate glasses the bismuth ruthenates dissolve Bi, while Pb from the glassy matrix replaces it in the conductive grains. Yet the newly formed $Pb_2Ru_2O_6$ pyrochlore starts another phase transformation on heating, and eventually the pyrochlore may be converted completely into the rutile phase (RuO_2). The key temperature for this final transformation decreases at increasing the Al content dissolved in the glass (Prudenziati *et al.*, 1989).

Similarly, Ru-perovskite-based resistors (Kummer and Taitl, 1977) exhibit phase transformations during the firing process.

3.4.3 Dissolution of minor constituents in a vitreous matrix

In TF resistors, together with the main phases, i.e. the vitreous matrix and the conductive oxide, other inorganic materials are typically present such as fillers, e.g. Al_2O_3, $ZrSiO_4$, SiO_2, TCR modifiers and additives such as transition metal oxides or their compounds. The dissolution of these materials in the vitreous phase is commonly triggered during the firing cycle at temperatures higher than the glass transition temperature. The total or partial dissolution of the fillers modifies the thermal and mechanical properties of the glass: the dissolution of Al_2O_3, $ZrSiO_4$ and SiO_2 increases the glass viscosity, lowers its thermal expansion coefficient and affects the melting characteristics. Conversely, the dissolution of TCR modifiers and additives, which are used in very small quantities, does not have large influence on the thermal and mechanical properties but may greatly impact the wetting characteristics of the molten vitreous phase.

3.4.4 Interactions due to diffusion at resistor/terminations and dielectric/contacts interfaces

Most of the conductor terminations used in TF technology are based on precious metals (Pt, Pd, Au), silver, alloys of precious metals and alloys of silver and copper. Because of price and properties, silver and its alloys are the choice in the majority of applications. The platinum metal group (Pt, Pd, Rh, Ru, Ir) and Au exhibit very

© Woodhead Publishing Limited, 2012

low solubility in lead-free glasses (Howes, 1957). The solubility in lead silicate glasses is slightly higher, but still in the range of several ppm and it rarely exceeds 50 ppm. Silver behaves in a different manner: its solubility in glasses and especially in lead-containing glasses is much higher than that of precious metals (Volf, 1984). Silver forms glasses with P_2O_5; in the binary Ag_2O-P_2O_5 system, Ag_2O content ranges from 34 mole% to 60 mole%, (Takahashi, 1962). Properties of silver phosphate glasses were reported by Bartholomew (1972).

Silver exists in silicate glass as neutral metal atom Ag° and as ions Ag^+. The ionic radius of Ag^+ in the glass is $r_{Ag^+}(VI) = 0.115$ nm, thus slightly larger than that of Na^+ and, like alkali ions, Ag^+ will lower the viscosity and raise the expansion coefficient of the glass. Silver and precious metals are covered by a thin layer of oxide at room temperature. This oxide dissolves into the glass during firing or by contact at temperatures above the glass transition temperature (Tg). Thus one mode of silver dissolution into TF glasses is by the reaction of Ag_2O with the glass to form Ag-containing glass. Another mode is by redox reactions. Redox reactions like the following were discussed by Nagesh *et al.* (1983):

$$2Ag(s) + PbO(gl) \leftrightarrow Ag_2O(gl) + Pb(g)$$
$$\Delta G = \Delta G° + RT\ In \frac{a_{Ag2O\,(gl)} \cdot P_{Pb(g)}}{a_{PbO(gl)}} = \Delta G° + RT\ In\ K, \quad [3.11]$$

where *a* is the activity and P is the vapor pressure. ΔG° for the above reaction is positive since the oxidation potential of Ag is lower than that of Pb. The reaction may proceed from left to right if the equilibrium constant K is very small. The dissolved silver can lower the TF glass viscosity, modify the expansion coefficient, change its wetting characteristics and increase the ionic conductivity of the glass (Nagesh *et al.*, 1983).

Table 3.1 reports the solubility and diffusivity of Ag derived by the measured concentration profiles of silver diffused in a high-lead silicate glass ($PbO/SiO_2/Al_2O_3$ = 68.2/30.5/1.3% wt, softening temperature T(s) = 606 °C) fired at various

Table 3.1 Diffusion coefficients D and solubility values C_o according to the best fits of measured diffusion profiles of silver in samples fired on alumina at various peak temperatures T_f

Glassy layer			Resistor	
T_f(°C)	Co(% wt)	D(10^{-12} m^2s^{-1})	Co(% wt)	D(10^{-12} m^2s^{-1})
700	2.0 ± 0.1	11 ± 3	2.3 ± 0.1	7.1 ± 0.1
750	2.2 ± 0.07	19 ± 3	2.3 ± 0.1	18.0 ± 0.1
800	2.0 ± 0.1	30 ± 6	3.2 ± 0.1	27.6 ± 0.3
850	2.5 ± 0.1	37 ± 8	3.7 ± 0.1	63.0 ± 0.1
900	2.9 ± 0.1	39 ± 6	3.5 ± 0.1	64.0 ± 0.8

Note: Glassy layer prepared with the frit with composition PbO: SiO_2: Al_2O_3 = 68.2: 30.5: 1.30% wt. Resistor prepared with 8%wt RuO_2 fine particles.

© Woodhead Publishing Limited, 2012

peak temperatures T_f, 8 minutes' dwell time. The solubility, C_o, remains nearly constant until the firing temperature T_f is 'close' to T(s), whereas it starts to increase at higher temperatures. Diffusivity values of the order of 10^{-11} m^2s^{-1} are observed at 850 °C (Prudenziati *et al.*, 2004).

Both solubility and diffusivity are notably affected by changes in the glass composition, e.g. seemingly irrelevant changes due to change of the glass batch (Prudenziati *et al.*, 1994) and substrate (Morten *et al.*, 1981); moreover, both quantities increase in RuO_2-based resistors, i.e. in resistors prepared with the same glass (same composition and batch) and RuO_2 powders. Figure 3.5 compares the diffusion profiles for Ag in resistor and its 'parent' glass, both fired at $T_f = 850$ °C, 10 minutes. The interest in this complex behavior stems from the relevant changes in electrical properties exhibited by resistors fired on Ag-bearing terminations. These properties are referred to as 'size effects' and will be described in Chapter 4. Another chemical element that plays a relevant role in 'size effects' is bismuth, introduced in the form of Bi_2O_3 in many conductor compositions to promote wetting and bonding the film to the substrate. The Bi-solubility in Ru-based TF resistors was evaluated at between 2 and 3%, thus not dissimilar to that of Ag, but its diffusivity is considerably lower (of the order of 1.5×10^{-12} m^2s^{-1}) in samples fired at 850 °C (Prudenziati *et al.*, 1986), as immediately apparent in Fig. 3.5.

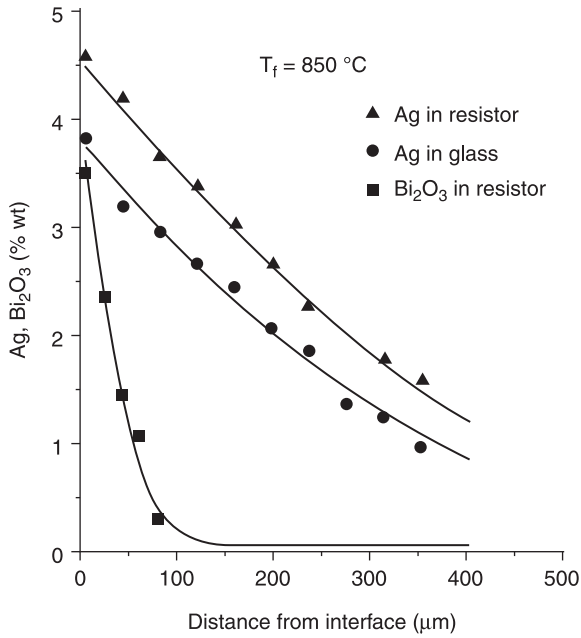

3.5 Measured concentration profiles for silver and bismuth (expressed in terms of the oxide) diffused from terminations in glassy layer and resistive layers. All samples contain the same glass and are fired using the same temperature cycle.

© Woodhead Publishing Limited, 2012

3.4.5 Reactions and exchange interactions in thick-film resistors

The reactions referred to in this section concern phase transformations such as compound formation and devitrifications. Devitrification is the term usually chosen to describe the (generally adverse) transition from the amorphous (glassy) state to the crystalline solid state; the same transition, when intentional, is more often mentioned as *crystallizatio*n. Phenomena of partial devitrification are commonly observed in glassy printed films as well as in the matrix of TF resistors (Prudenziati *et al.*, 2001, 2002); they are not a serious problem *per se* unless associated with the formation of crystalline phases which, because of their large mismatches in thermal expansion with the remaining glassy matrix, give rise to cracks in the film. The transformation may be reversible: on heating, the crystallites can be re-dissolved in the glass. However, the wetting properties, density, etc. of the system, temporarily modified, can modify the final resistor microstructure. Conversely, crystallization is intentionally designed in 'crystallizable glasses' (e.g. TF crossover and dielectrics for multilayer circuits) that are capable of flowing and that accomplish pin-hole free, dense amorphous layers in the first firing cycle but refire at the same or even higher temperatures without further softening during any subsequent firing steps. Nucleation and growth of the newly formed crystalline phase are to be completed at a temperature usually lower than 800 °C (Larry *et al.*, 1980; Vest, 1986).

Interactions with compounds of interest in TF technology encompass:

- Reactions between oxides and dielectrics; one notable example is the reaction of copper oxide, or chromium oxide (formerly also CdO was used) added in the paste for 'reaction bonded' or 'fritless' conductors for alumina substrates. The oxide reacts at high temperature (950–1000 °C) with the alumina substrate to form spinel oxides like $CuAl_2O_4$. These compounds provide the required adhesion (Licari and Enlow 1998).
- Alloy formation from the elements, e.g. AgPd alloy in conductors.
- The redox reactions already described in section 3.3.
- Crystalline phases grown in dielectric materials for capacitors and multilayers.

Interest in the above-mentioned reactions derives from the awareness that understanding their source and mechanisms, as well as knowing their evolution, may guide the operator in the choice of pastes, in planning the deposition steps, in diagnosing possible failures and in evaluating the system's thermal stability.

The most intriguing research in the field of resistors concerns the phase changes from RuO_2 to ternary compounds and *vice versa*. The effect of prolonged elevated temperatures on RuO_2-based resistors prepared by lead borosilicate glass and the $Pb_2Ru_2O_{6+\delta}$ formation was first reported by Bube (1972). He described the interaction as a partial reduction of RuO_2 at low temperature (burnout zone) and

© Woodhead Publishing Limited, 2012

a successive reaction with the lead oxide in the glass. Conversely in other systems the $Pb_2Ru_2O_{6.5}$ ruthenate is converted into the rutile phase (RuO_2) (Adachi and Kuno, 1997; Morten *et al.*, 1991; Prudenziati *et al.*, 1989). Likewise, as already noted, several investigations (Hormadaly 1990; Morten *et al.*, 1994; Nordstrom and Hills, 1980; Pike and Seager, 1977) have shown that Bi dissolves from the bismuth ruthenate grains in the glass and it is substituted for by Pb from the lead–silicate in the conductive ruthenate grains. The nucleation of the new phases and the reaction rates are apparently linked to several factors, the most important ones being: (1) the Pb activity gradient between the Pb-ruthenate and the surrounding glass (Adachi and Kuno, 1997), and (2) the glass viscosity. The latter is modified in the course of the thermal process, for instance by the interactions between glass and substrate. The key role of glass viscosity and the enhanced effect of Cu_2O in these types of interactions were evidenced by Hormadaly (1990), who studied ruthenium-based pyrochlore and short borosilicate glasses or glass mixtures. Similarly Ru-perovskite-based resistors (Kummer and Taitl, 1977) exhibit phase transformations during the firing process.

Other phase changes have been noted studying the microstructure evolution of TFRs prepared by precipitation of $RuCl_3$ on high-lead fritted-glass particles (Morten *et al.*, 1988). It was shown that RuO_2 ($RuCl_3$ converts to RuO_2 at temperatures below 400 °C; see Newkirk and McKee, 1968) reacts with lead borosilicate glass to form $Pb_2\ Ru_{2-x}\ Pb_xO_{6+\delta}$ intermediate phases in the course of firing, until $Pb_2Ru_2O_{6+\delta}$ is formed at 850 °C; the latter phase may eventually decompose to RuO_2 at higher temperatures. Synthesis and properties of $Pb_2Ru_{2-x}Pb_xO_{6+d}$ and related compounds were previously reported (Horowitz *et al.*, 1981).

No new phase has been detected in a study of IrO_2-based resistors interacting with high lead glass (Tankiewicz *et al.*, 2002). In investigations aimed at the development of new generations of lead-free TF resistors, the interactions between RuO_2 and different lead-free glasses were addressed. Bismuthate glasses do not form any bismuth ruthenate on firing; conversely, a bismuth titanate pyrochlore is the result of interactions between the glass and TiO_2, an additive in the matrix (Busana *et al.*, 2006). No phase change was noted also in RuO_2-based resistors in glass of the $CaO\text{-}BaO\text{-}B_2O_3\text{-}Al_2O_3\text{-}SiO_2$ system (Kielbasinski *et al.*, 2009; Morten *et al.*, 1991), and in $CaRuO_3$-based resistors with glass of the SiO_2-CaO-BaO-SrO-K_2O-B_2O_3 system (Rane *et al.*, 2005). On the contrary, $Bi_2Ru_2O_7$ is completely exhausted in lead-free glass-based resistors after a long firing process (Hrovat *et al.*, 2008).

The thermodynamic aspects of these phase transformations have been made clearer from the studies by Hrovat *et al.* (2006a, 2008). The subsolidus phase equilibria in the PbO-poor part of RuO_2-PbO-SiO_2 system (Hrovat *et al.*, 2006a) shows that lead ruthenate is not stable in the presence of the silica-rich glass phase. In the same conditions, RuO_2-based resistors are expected to be stable after long-term high-temperature firing, a result supported by experiments. Similarly,

© Woodhead Publishing Limited, 2012

from the phase equilibria in the RuO_2-Bi_2O_3-SiO_2 system, the instability of the bismuth ruthenate in the presence of silica-rich glass phase is apparent (Hrovat *et al.*, 2008).

Interactions between pyrochlore-based resistors and Ag-Pd alloy composite contacts were reported by Needes *et al.* (1985). These authors also reported the effects of Al_2O_3 addition to paste composition and studied the infrared firing of pyrochlore-based pastes.

Manganese in amounts larger than 1%wt added to RuO_2-based TF resistors with a lead–silicate glass reacts to form $Pb_2Si_2Mn_2O_9$ (kentrolite) (Morandi *et al.*, 1991). At lower concentrations, Mn is soluble in glass and, especially when uniformly distributed, acts as an effective additive with benefits in TCR control and noise reduction in RuO_2-based resistors.

The effect of glass composition on the electrical properties of TF resistors was reported by Adachi and Kuno (2000). A broad range of lead borosilicate glasses were studied with RuO_2 and lead ruthenium as the conducting phases. Anomalously high resistivity was found for lead-depleted compositions.

The interactions between screen-printed and fired PbO layers and alumina occur via two main processes: (1) a reaction between PbO and Al_2O_3 grains, which induces the formation of a crystalline phase, $Pb_2Al_2O_5$; and (2) an interdiffusion process involving Pb and the intergranular amorphous phase in the substrate, according to a diffusion limited process (diffusivity ranging from ~10^{-9} to 2.5×10^{-8} cm^2s^{-1} for temperatures from 700 to 1000 °C, and activation energy of ~1.20 eV) (Bersani *et al.*, 1997).

Notably different processes occur when Bi_2O_3 layers are fired on ceramic substrates (Immovilli *et al.*, 1998) in terms of reaction products: they are invariably crystalline in nature in these systems. Several transitions of Bi_2O_3 in its polymorphic phases are found to occur on BeO substrates, while newly formed compounds grow up on alumina substrates, i.e. $Al_4Bi_2O_9$ on 99.9%-Al_2O_3 and $Bi_{12}SiO_{20}$ on 96%-Al_2O_3. Bismuth deeply penetrates the ceramic interstices in all cases. Until Bi_2O_3 had not completely reacted, this penetration is a diffusion-limited process with values of the activation energy ranging from 3.7 ± 0.6 eV (on BeO) to 1.4 ± 0.06 eV (on 96%-Al_2O_3).

As a partial conclusion of this section, it is interesting to sum up the observations concerning 'simple' RuO_2-based resistors to note that the conducting material (RuO_2) undergoes a variety of changes during the processing: partial reduction to Ru in the burnout zone, reoxidation to variety of oxidation states, dissolution of Ru in several oxidation states in the vitreous phase, interaction with the PbO in the glass to form intermediate pyrochlore phase $Pb_2Ru_{2-x}Pb_xO_{6+\delta}$ and possible decomposition of the pyrochlore to RuO_2 at higher temperatures. The ideal picture of single-phase conducting particles imbedded in vitreous phase is very far from the real system, which has a variety of conducting phases (Ru, RuO_2, Pb_2, $Ru_{2-x}Pb_xO_{6+\delta}$), ($Pb_2Ru_2O_{6+\delta}$) formed during firing and the dissolution of Ru ions in various oxidation states (Ru^{2+}, Ru^{+3}, Ru^{+4}) in the vitreous phase.

© Woodhead Publishing Limited, 2012

3.5 Sintering, grain growth and Ostwald ripening

Sintering is a thermal process, below the melting temperature of the main constituent material, which transforms metallic or ceramic powders (or powder compacts) into bulk materials containing, in most cases, residual porosity. This is the final step in the mass production of complex-shaped components in both ceramic and powder metallurgy technologies (Kingery *et al.*, 1976; Ohring, 1995; Rahaman, 2008). Figure 3.6 depicts the early stages of sintering in an idealized system, consisting in two solid spheres with the same radius, in contact without a liquid phase or in the presence of the liquid. The former case describes the sintering model in 'fritless' (chemically bonded) conductors, whereas the latter case is for glass-bonded conductors. In both cases, necks develop between the two particles when the temperature is raised because of transport of materials from the solid particles to the neck area.

The driving force for sintering and densification is the drop in total surface energy, which derives from the decrease of the surface area, when particles in

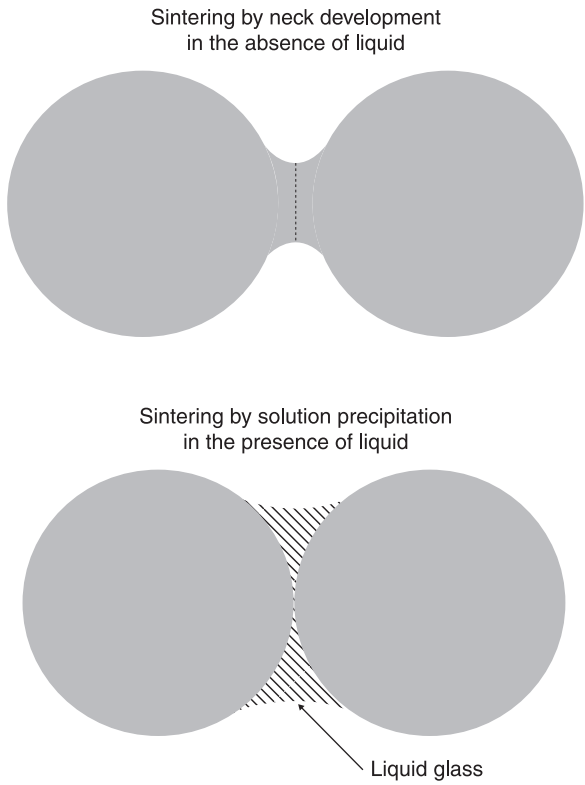

3.6 Two spherical particles at initial stages of sintering.

© Woodhead Publishing Limited, 2012

contact mutually exchange constituent material and coalesce together into large aggregates or to a continuous solid. It is found that this driving force is more effective (has higher chemical potential) the smaller the size (e.g. the diameter of spherical grains) and the higher the surface energy of interacting particles. Hence the selection of the so-called 'very active' powders made of small particles in the ceramic technology, to start the sintering shrinkage of ceramic parts. With nanoparticles, both size and an increase in surface energy in the nanometer range are effective (Nanda *et al.*, 2008), resulting in sintered films at temperatures as low as 100–200 °C (e.g. Girotto *et al.*, 2009), therefore compatible with most of the flexible substrates, and depressed even more than 450 °C relative to the use of coarse powders (Tabellion *et al.*, 2006). On the other hand, the transport of material may occur through various processes: bulk diffusion, surface and grain boundary diffusion, evaporation from the grains and condensation at negative radius surfaces (necks), and solution-precipitation in the presence of the liquid phase. The latter is the 'sintering aid', aimed at speeding up the kinetics of the transport phenomena. Hence, for example, the addition of a glassy phase in the sintering of Al_2O_3 for the production of dense alumina ceramics and in high-temperature co-fired ceramics (HTCC) technology or the various sintering aids used in low-temperature co-fired ceramics (LTCC) technology (see Chapter 6). The specific models for sintering of glass powders have been illustrated in the excellent review by Rabinovich (1985) and in Rahaman (2008). In screen-printed film technology, as in ceramic technology, the sintering process starts after the burnout of the vehicle and consists generally of two stages: 1) the neck growth between the particles and 2) the shrinking with the accompanying densification by pore annihilation and grain growth. In typical processes carried out on inks for microelectronic applications, the inks' composition is normally tailored for a complete sintering at a temperature near 850 °C and dwell times of 5–20 minutes. However, different processes are demanded for various materials and structures. Often the target is to accomplish very dense components. In fact, densification is most often associated with better performances – such as high conductivity, small contact resistance, fine esthetic appearance of electronic conductors, low moisture absorption and negligible dielectric loss degradation in dielectrics, better piezoelectric and pyroelectric responses from ferroelectric/piezoelectric films, etc. (Debéda-Hickel *et al.*, 2005).

However, there are applications such as gas sensors and fuel cells that require porous films, in spite of the processing at a temperature high enough to stabilize the structure, as well as to provide adhesion to the substrate and impart the functional desired properties. Many strategies have been envisaged for these applications. For example, in gas sensors based on nanosized semiconducting oxides, particle coarsening is prevented by adding a small amount of a further component to the main sensing oxide, namely the grain growth inhibitor (e.g. via a metal-organic, or a salt solution) aimed at retarding (shifts at higher temperatures and/or longer times) the initial stage of sintering of the original ('pure') composition (Martinelli *et al.*, 1999; Xu *et al.*, 1989). In this way, the large surface

© Woodhead Publishing Limited, 2012

of sensing oxide is available for gas interaction after the firing process, preserving the sensor sensitivity, as well as keeping thermal stability after many hours of operation at temperatures of 300–500 °C.

In Ostwald, ripening larger particles grow at the expense of smaller ones; the latter dissolve in one solid or liquid medium and the dissolved atoms/molecules redeposit onto the surface of coarser crystalline aggregates. This is the mechanism (often confused with, or hastily mentioned as, sintering) that allows for the increase in size of RuO_2 grains in RuO_2-based resistors. This process was recognized by Hoffman and Jones (1983), Prabhu and Vest (1975), Prudenziati *et al.* (1989) and carefully studied by Nakano *et al* (1994). The latter authors analyzed the shape and size of RuO_2 grains in glasses of different compositions, including high-lead and lead-free silicate glasses. It was remarked that while the particles rounded as the temperature increased – indicating that RuO_2 dissolves in glass – the absence of necks between particles denies the possibility of material transport through inter-particle contact areas. Moreover, the theory for Ostwald kinetics was found in qualitative agreement with experimental data. Therefore, even if the solubility of RuO_2 was not quantified (being lower than the detection limit of the authors' equipment), its dependence on the glass composition was indirectly inferred and suggested to increase by increasing the PbO content and by SiO_2 substitution for B_2O_3. Dissolution of Al_2O_3 in glass appeared to retard Ostwald ripening, an agreement with the results previously summarized in section 3.4.

The growth of silver grains was studied by Yata and Yamaguchi (1992a, 1992b, 1992c) in the presence of borosilicate glass with a composition common in the TF industry; they found that Ag particles grow in glass by the Ostwald ripening mechanism controlled by diffusion between 600 and 900 °C; addition of Pd retards the Ostwald ripening as a result of the decrease in solubility of Ag in glass due to the formation of Ag/Pd solid solutions.

3.6 Reactivity interactions in other systems

A lot of research has been recently focused on studies about the compatibility of films and pre-fired tapes, either buried inside, and co-fired with, laminated tapes for LTCC packages and microsystems. In terms of Materials Science, the most frequently observed interactions are due to materials transport, whose driving force is thermodynamic in nature: excess ion in a component flows to the component with deficient concentration to cancel the gradient. This is the well-known problem of TF resistors on/in LTCC tapes. To solve the problem, manufacturers of pastes for circuit components and LTCC tapes have developed systems containing the same (or very similar) glass compositions. However, this solution cannot be generalized, and many other strategies have been conceived by researchers. A possibility is to limit the interacting zone with a restriction of the glass transport, often taking glasses with relatively high transition and softening points, e.g. glasses with SiO_2 and Al_2O_3

© Woodhead Publishing Limited, 2012

content greater than in the common pastes for alumina substrates. Another possibility for contrast the interdiffusion is the use of 'diffusion barriers'. For example, Hrovat *et al.* (2006b) suggest interposing an alumina barrier layer between piezoelectric ceramic material (PZT) and LTCC substrates to avoid their mutual interactions and the consequent degradation of the PZT piezoelectric characteristics. A platinum layer between PZT and silicon for mechanical microsystems (MEMS) is taken to avoid strong interactions between the two materials (see Chapter 10).

3.7 The Kirkendall effect

A possible detrimental consequence of interdiffusion between two systems that mutually exchange elements moving through vacancies but with quite different diffusivity (at the operation temperature) is the coalescence of vacancies and thus the void formation on the side of the couple from which the most diffusing species come. This phenomenon, known as the Kirkendall effect, often occurs in microelectronics when soldering gold wires to aluminum pads (Ohring, 1995). In TF hybrid circuits, this phenomenon has been reported to affect the bond strength of aged Al wire bonds to Au conductors (Larry *et al.*, 1980); to circumvent the problem, the alloy of Au with some percentage of Pd is recommended. Likewise, metallic interdiffusion at the printed electrode/wire junction has been recognized to be an issue for reliable application of semiconductor oxide gas sensors (Ménil *et al.*, 2005); in this case, the phenomenon can appear evident after several months at the typical operating temperatures of such sensors (400–450 °C).

3.8 Conclusions and future trends

In conclusion, we have described a few examples of the wide variety of structure–properties relations experienced in TF materials. The microstructure and performance of TFs start to evolve from temperatures as low as room temperature and continue to change during the whole course of processing or, when required, in post-process thermal annealing. The flexibility of TF technology in terms of materials and processing parameters can mask the need for careful consideration and constant attention to design rules and performance evaluation guided by basic concepts typical in the approach of Materials Science to complex systems. Many other examples of interactions between the constituents of functional printed films and/or the films and other elements of the systems will be mentioned in other chapters of this book.

The lessons learned through TF materials research might form a solid basis for the development of the newer functional printed films promised by the most recently introduced printing technologies.

Some problems faced in connection with screen-printed and fired films will be exacerbated in thinner films, e.g. ink-jet printed or lithographically deposited films, or in films to be functionalized at low temperatures, due to the nature of the

© Woodhead Publishing Limited, 2012

flexible substrates. Other intrinsically new problems might arise from the diversified new functions required by films for optoelectronics applications, sensors and flexible electronics. Thus, new approaches and new solutions should be conceived but close attention to both thermodynamics and the kinetic aspects of interactions and the structure/properties relations in the framework of Materials Science will always be a powerful resource in the continuous effort to improve our knowledge in this difficult but fascinating field.

3.9 Sources of further information

For a general view of concepts and methods of Materials Science, very 'classical' texts are recommended, for example:

- Barsoum M. W., *Fundamentals of Ceramics*, 108, Bristol, 2003.
- Ohring R. A., *Engineering Materials Science*, Academic Press, San Diego, 1995.
- Swalin M., *Thermodynamics of Solids*, John Wiley and Sons, New York, 1962.

3.10 References

Adachi K. and Kuno H., 1997, 'Decomposition of ruthenium oxides in lead borosilicate glass', *Journal of the American Ceramic Society*, 80(5), 1055–1064.

Adachi K. and Kuno H., 2000, 'Effect of glass composition on the electrical properties of thick-film resistors', *Journal of the American Ceramic Society*, 83(10), 2441–2448.

Adachi K., Iida S. and Hayashi K., 1994, 'Ruthenium clusters in lead–borosilicate glass in thick-film resistors', *Journal of Materials Research*, 9(7), 1866–1878.

Angus H. C. and Gainsbury P. E., 'Oxide resistor materials', US Patent No. 3,679,607; July 25 (1972).

Avtokratova T. D., 1962 'Analytical chemistry of ruthenium', S. Monson, Jerusalem, Israel 1963 (transl. Analiticheskaya Khimya Rutheniya Isdatel' stvo Akademii Nauk SSSR, Moskva).

Barsoum M. W., 2003, *Fundamentals of Ceramics*, Institute of Physics, Bristol.

Bartholomew R. F., 1972, 'Structure and properties of silver phosphate system – infrared and visible spectra', *Journal of Non-Crystalline Solids*, 7(3), 221–235.

Bell W. E. and Tagami M., 1963, 'High-temperature chemistry of the ruthenium–oxygen system,' *Journal of Physical Chemistry*, 67(11), 2432–2436.

Bersani M., Morten B., Prudenziati M. and Gualtieri A., 1997, 'Interactions between lead oxide and ceramic substrates for thick-film technology', *Journal of Materials Research*, 12(2), 501–508.

Bube K. R., 1972, 'The effect of prolonged elevated temperature on thick-film resistors', *Proceedings of ISHM*, 2A6-1-2 A6-13, Park Ridge IL.

Burckhardt H.-G. and Vavra H., 1989, 'Reactions and thick-film metallization on aluminium-nitride substrates', in *Proceedings of the 7th European ISHM Conference*, Hamburg, May, paper 4.2.

Busana M. G., Prudenziati M. and Hormadaly J., 2006, 'Microstructure development of RuO_2-based lead-free thick-film resistors', *Journal of Material Science: Materials in Electronics*, 17(11), 951–962.

© Woodhead Publishing Limited, 2012

Debéda H., Massok P., Lucat C., Ménil F. and Aucouturier J. L., 1997, 'Methane sensing: from sensitive thick-films to a reliable selective device', *Measurement Science and Technology*, 8(1) 99–110.

Debéda-Hickel H., Lucat C. and Menil F., 2005, 'Influence of the densification parameters on screen-printed component properties', *Journal of the European Ceramic Society*, 25(12), 2115–2119.

Gilchrist R., 1929, 'Gravimetric method for the determination of ruthenium', *Bureau of Standards Journal of Research*, 3, 993–1004.

Girotto C., Rand B. P., Steudel S., Genoe J. and Heremans P., 2009, 'Nanoparticle-based, spray-coated silver top contacts for efficient polymer solar cells', *Organic Electronics*, 10(4), 735–740.

Herold P. G., Planje T. J. and Williams J. C., 'Ruthenium–containing glasses and stains', US Patent 2-739-901; March 27 (1956).

Hoffman L. C., 1984, 'An overview of thick-film hybrid materials', *Ceramics Bulletin*, 63(4), 572–576.

Hoffman L. C. and Jones A. W., 1983, 'Interaction of thick-film materials with roll compacted alumina ceramics', *International Journal of Hybrid Microelectronics*, 6(1), 603–606.

Hong K.-K., Cho S.-B., You J. S., Jeong J.-W., Bea S.-M. and Huh J-Y., 2009, 'Mechanism for formation of Ag crystallites in the Ag thick-film contacts of crystalline Si solar cells', *Solar Energy Materials and Solar Cells*, 93(6–7), 898–904.

Hormadaly J., 'Stain-resistant ruthenium oxide-based resistors', US Patent 4-476-039; October 9 (1984).

Hormadaly J., 'Thermistor composition', US Patent 4-906-406; March 6 (1990).

Horowitz H. H., Longo J. M. and Lewandowski J. T., 1981, 'New oxide pyrochlores: $A_2(B_{2-x}A_x)\,O_{7-x}$ (A = Pb,Bi: B = Ru,Ir)'. *Material Research Bulletin*, 16, 489–496.

Horowitz S. J., 'Novel silver compositions', US Patent 4-090-009; May 16 (1978).

Howes M. G., 1957, 'The platinum metals in glass', *Platinum Metals Review*, 1(2), 44–48.

Hrovat M., Holc J., Belavič D. and Bernard J., 2006a, 'Subsolidus phase equilibria in the PbO-poor part of RuO_2-PbO-SiO_2 system', *Material Letters*, 60(20), 2501–2503.

Hrovat M., Holc J., Drnovsek S., Belavic D., Cilensek J. and Kosec, M., 2006b, 'PZT thick-films on LTCC substrates with an interposed alumina barrier layer', *Journal of European Ceramic Society*, 26(6), 897–900.

Hrovat M., Meader T., Holc J., Belavič D., Cilenšek J. and Bernard J., 2008, 'Subsolidus phase equilibria in RuO_2-Bi_2O_3-SiO_2 system', *Journal of European Ceramic Society*, 28(11), 2222–2224.

Immovilli S., Morten B., Prudenziati M., Gualtieri A. and Bersani M., 1998, 'Interactions between bismuth oxide and ceramic substrates for thick-film technology', *Journal of Materials Research*, 13(7), 1865–1874.

Janakirama-Rao B. V., 1962, 'Dielectric properties of glasses in the systems Bi_2O_3-CdO-SiO_2, Bi_2O_3-CdO-B_2O_3 and Bi_2O_3-CdO-GeO_2 and their relation to the structure of glass', *Journal of the American Ceramics Society*, 45(11), 555–563.

Kingery W. D., Bowen H. K. and Uhlmann D. R., 1976, *Introduction to Ceramics*, 2nd edn, John Wiley & Sons, New York.

Kielbasinski, K., Jakubowska, M., Mlozniak, A., Hrovat, M., Holc, J. and Belavic, D., 2009, 'Electrical and microstructure evolution of thick-film lead-free resistors after various temperature treatments', *ISSE 2009, 32nd International Spring Seminar on Electronics Technology*, 1–5.

Kirby P. L., 1982, 'EmpiricISHM – A noble art', *Hybrid Circuits*, 1, 49–50.

© Woodhead Publishing Limited, 2012

Krausse R., Behr G., Schlafer D. and Krabbes G., 1991, 'Interations between ethylcellulose and thick-film resistors containing ruthenium', *Journal of Materials Science Letters*, 10(23), 1392–1393.

Kretzschmar C., Otschik P., and Jaenicke-Rößler K. and Schläfer D., 1993, 'The reaction between ruthenium dioxide and aluminium nitride in resistor pastes', *Journal of Materials Science*, 28(21), 5713–5716.

Kummer F. and Taitl I., 1977, 'Thermal expansion and laser trim stability of Ru-based thick-film resistors' in *Proceedings of the International Conference on Thin and Thick-film Technology*, Augsburg, pp. 28–33.

Larry J. R., Rosenberg R. M., and Uhler R. O., 1980, 'Thick-film technology: An introduction to the materials', *IEEE Transactions of Components and Hybrids and Manufacturing Technology*, CHMT-3(2), 211–225.

Licari, J. J. and Enlow, L. R., 1998, *Hybrid Microcircuit Technology Handbook*, 2nd edn, Noyes Publications, Westwood, New Jersey.

Machin W. S. and Vest R. W., 1978, 'Reactivity of alumina substrates with high lead glasses', *Materials Science Research*, 11, 243–251.

Martinelli G., Carotta M. C., Ghiotti G. and Traversa E., 1999, 'Thick-film gas sensors based on nanosized semiconducting oxides powder', *MRS Bulletin*, 24(6), 30–36.

Ménil F., Debéda H. and Lucat C., 2005, 'Screen-printed thick-films: From materials to functional devices', *Journal of European Ceramic Society*, 25, 2105–2113.

Morandi M., Morten B., Prudenziati M., Argentino E. and Ruffi M. G., 1991, 'Manganese in ruthenium based thick-film resistors', *Materials Engineering*, 2(3), 421–433.

Moriwaki H., Suzuki A., Watanabe Y., Ishiita M., Kamata T. and Adachi K.,'Interactions between thick-film resistors and alumina substrate', *Japan International Electronics Manufacturing Technology Symposium*, pp. 46–49,

Moro L., Lazzeri P., Prudenziati M., Morten B. and Savigni P., 1992, 'Interactions between beryllia and high-lead glasses', *Applied Physics Letters*, 61(19), 2299–2301.

Morten B., Prudenziati M., Sacchi M. and Sirotti F., 1988, 'Phase transitions in Ru based thick-film (Cermet) resistors', *Journal of Applied Physics*, 63(7), 2267–2271.

Morten B., Prudenziati M. and Taroni A., 1981, 'Metal migration from terminations in thick-film resistors: the effect of the substrate', *International Journal of Hybrid Microelectronics*, 4, 341–346.

Morten B., Ruffi G., Sirotti F., Tombesi A., Moro L. and Akomolafe T., 1991, 'Lead-free ruthenium-based thick-film resistors: a study of model systems', *Journal of Materials Science: Materials in Electronics*, 2(1), 46–53.

Morten B., Sirotti F., Prudenziati M. and Manfredini T., 1994, 'Evolution of ruthenate-based thick-film cermet resistors', *Journal of Physics D: Applied Physics*, 27(10), 2227–2235.

Mukerji J., 1972, 'Absorption spectra of ruthenium in borosilicate, phosphate and aluminoborophosphate glasses', *Glass Technology*, 13(5), 135–137.

Mukerji J. and Biswas S. R., 1967, 'Solubility of ruthenium in soda–silica glasses', *Glass and Ceramic Bulletin*, 14(2) 30–34.

Nagesh V. K., Tomasia A. P. and Pask J. A., 1983, 'Wetting and reactions in the lead borosilicate glass–precious metal systems', *Journal of Materials Science*, 18(7), 2173–2180.

Nakano T. and Yamaguchi T., 1995, 'Effect of O_2 concentration in firing atmosphere on resistance of RuO_2-glass thick-film resistors', *Journal of the American Ceramic Society*, 78(6), 1703–1704.

Nakano T., Suzuki K. and Yamaguchi T., 1994, 'Analysis of interaction between RuO_2 and glass by growth of RuO_2 particles in glasses', *Journal of Adhesion*, 46(1 and 4), 131–144.

© Woodhead Publishing Limited, 2012

Nanda K. K., Maisels A. and Kruis F. E., 2008, 'Surface tension and sintering of free gold nanoparticles', *Journal of Physical Chemistry C*, 112(35), 13488–13491.

Needes C. R. S., 2003, 'Advanced thick-film system for AlN substrates', *Microelectronics International*, 20(1), 48–51.

Needes C. R. S., Pierce J. W., Kuty D. W., Ishibashi S. and Nishii N., 1985, 'A new thick-film materials system for high volume microcircuits', *International Journal for Hybrid Microelectronics*, 8(1), 24–30.

Newkirk A. E. and McKee D. W., 1968, 'Thermal decomposition of rhodium, iridium and ruthenium chlorides', *Journal of Catalysis*, 11(4), 370–377.

Nordstrom T. V. and Hills C. R., 1980, 'Transmission electron microscopy studies of the microstructure of thick-film resistors', *International Journal of Hybrid Microelectronics*, 3(1), 14–19.

Norton M. G., 1990, 'Thermodynamic considerations in the thick-film metallization of aluminium nitride substrates', *Journal of Material Science Letters*, 9(1), 91–93.

Ohring M., 1995, *Engineering Materials Science*, Academic Press, San Diego.

Palanisamy P. and Sarma D. H. R., 1987, 'Thermodynamics of processing copper thick-film systems in a reactive atmosphere', *Microelectronic International*, 4(2), 13–20.

Palanisamy P., Sarma D. H. R. and Vest R. W., 1989, 'Solubility of ruthenium dioxide in lead borosilicate glasses', *Journal of the American Ceramic Society*, 72(9), 1755–1756.

Pflieger R., Lefebvre L., Malki M., Allix M. and Grandjean A., 2009, 'Behavior of ruthenium dioxide particles in borosilicate glasses and melts', *Journal of Nuclear Materials*, 389(3), 450–457.

Pierce J. W., Kuty D. W. and Larry J. R., 1982, 'The chemistry and stability of ruthenium based resistors', *Solid State Technology*, 25(10), 85–93.

Pike G. E. and Seager G. H., 1977, 'Electrical properties and conduction mechanisms of Ru-based thick-film (cermet) resistors', *Journal of Applied Physics*, 48(12), 5152–5169.

Pinet O. and Mure S., 2009, 'Redox behavior of platinum-group metals in nuclear glass', *Journal of Non-Crystalline Solids*, 355(3), 221–227.

Prabhu A. N. and Vest, R. W. 1975, 'Investigation of microstructure development in ruthenium dioxide–lead borosilicate glass thick-films', *Materials Science Research*, 10 (Sintering Catal), 399–408.

Prabhu A. N., Fuller G. L. and Vest R. W., 1974, Solubility of ruthenium oxide in lead borate glass, *Journal of the American Ceramic Society*, 57(9), 408–409.

Prudenziati M., Morten B., Cilloni F., Ruffi G. and Sacchi S., 1989, 'Interactions between alumina and high lead glasses for hybrid materials', *Journal of Applied Physics*, 65(1), 146–153.

Prudenziati M., Morten B., Forti B., Gualtieri A. F. and Mihai Dilliway G., 2001, 'Devitrification kinetics of high lead glass for hybrid microelectronics', *International Journal of Inorganic Materials*, 3(7), 667–674.

Prudenziati M., Morten B., Gualtieri A. F. and Leoni M., 2004, 'Dissolution kinetics and diffusivity of silver in glassy layers for hybrid microelectronics', *Journal of Materials Science: Materials in Electronics*, 15(7), 447–453.

Prudenziati M., Morten B., Moro L., Olumekor L. and Tombesi A., 1986, 'Interactions between terminations and thick-film (cermet) resistors: the role of bismuth', *Journal of Physics D: Applied Physics*, 19(2), 275–282.

Prudenziati M., Morten B., Savigni P. and Guizzetti G., 1994, 'Influence of the preparing conditions on the physico-chemical characteristics of glasses for thick-film hybrid microelectronics', *Journal Materials Research*, 9(9), 2304–2313.

© Woodhead Publishing Limited, 2012

Prudenziati M., Morten B. and Travan E., 2003, 'Reduction process of RuO_2 powders and kinetics of their re-oxidation', *Materials Science and Engineering B*, 98(2), 167–176.

Prudenziati M., Zanardi F., Morten B. and Gualtieri A. F, 2002. 'Lead-free thick-film resistors: an explorative investigation', *Journal of Materials Science: Materials in Electronics* 13(1), 31–37.

Rabinovich E. M., 1985, 'Preparation of glass by sintering', *Journal of Materials Science*, 20(12), 4259–4297.

Rahaman, M. N., 2008, *Sintering of Ceramics*, CRC, Boca Raton.

Rane S., Prudenziati M., Morten B., Golonka L. J. and Dziedzic A., 2005, 'Structural and electrical properties of perovskite ruthenate-based lead-free thick-film resistors on alumina and LTCC', *Journal of Materials Science: Materials in Electronics*, 16(10), 687–691.

Schreiber F. D., Settle F. A. Jr, Jamison P. L., Eckenrode J. P. and Headley G. W., 1986, 'Ruthenium in glass-forming borosilicate melts', *Journal of Less-Common Metals*, 115(1), 145–154.

Seddon E. A. and Seddon K. R, 1984, *The Chemistry of Ruthenium*, Amsterdam and New York: Elsevier Science.

Shah J., 1980, 'Strain sensitivity of thick-film resistors', *IEEE Transactions of Components and Hybrids and Manufacturing Technology*, CHMT-3(4), 554–564.

Swalin, R. A., 1962, *Thermodynamics of Solids*, John Wiley & Sons, New York.

Tabellion J., Zeiner J. and Clasen R., 2006, 'Manufacturing of pure and doped silica and multicomponent glasses from SiO_2 nanoparticles by reactive electrophoretic deposition', *Journal of Materials Science*, 41(24), 8173–8180.

Takahashi K., 1962, in: *Proceedings of 6th International 'Glass Congress'*, Washington, D.C., p. 366.

Tankiewicz S., Morten B., Prudenziati M. and Golonka L. J., 2002 'IrO_2-based thick-film resistors', *Journal of Applied Physics*, 91(7), 4261–4266.

Turkdogan E. T., 1980, *Physical Chemistry of High Temperature Technology*, New York: Academic Press.

Vest R. W., 1986, 'Materials science of thick-film technology', *American Ceramic Society Bulletin*, 65(4), 631–636.

Volf M. B., 1984, 'Chemical approach to glass', in *Glass Science and Technology*, Vol. 7, transl. Chemie Skla, Elsevier.

Wang S. F. and Huebner W., 1991, 'Thermodynamic modeling of equilibrium subsolidus phase relations in the Ag–Pd–O_2 system', *Journal of the American Ceramic Society*, 74(6), 1349–1353.

Wang Y. L., Carroll A. F., Smith J. D., Cho Y., Bacher R. J. *et al.*, 1991, 'Oxynitride based glass bonding to AlN for thick-films', in *Proceedings of the International Symposium on Microelectronics*, International Society for Hybrid Microelectronics, Reston, VA USA, 533–535.

Wang Y. L., Carroll A. F., Smith J. D., Cho Y., Bacher R. J. *et al.*, 2003, Advanced thick-film system for AlN substrates, *Microelectronics International*, 20(1), 48–51.

Xu C., Tamaki J., Miura N. and Yamazoe N., 1989, 'Promoting effects of additives on thermal stability of tin oxide (IV) fine particles', *Journal of Materials Science Letters*, 8(9), 1092–1094.

Yamashita M. and Yamanaka H., 2004, 'Dissolution and separation of ruthenium in borosilicate glass', *Journal of the American Ceramic Society*, 87(5), 967–969.

Yata K. and Yamaguchi T., 1992a, 'Ostwald ripening of silver in glass', *Journal of Materials Science*, 27(1), 101–106.

© Woodhead Publishing Limited, 2012

Yata K. and Yamaguchi T., 1992b, 'Effect of temperature on Ostwald ripering of silver in glass', *Journal of the American Ceramic Society*, 75(8), 2071–2075.

Yata K. and Yamaguchi T., 1992c, 'Effect of additives on Ostwald ripening of silver in glass', *Journal of the American Ceramic Society*, 75(10), 2910–2914.

Yi K. M., Lee K. W., Chung K. W., Woo W. S., Lee H. S. *et al.*, 1997, 'Conductive powder preparation and electrical properties of RuO_2 thick-film resistors', *Journal of Materials Science: Materials in Electronics*, 8(4), 247–251.

Zdaniewski W. A. and Silverman L. D., 1990, 'Effect of localized redox equilibria on adhesion between gold and thick-film dielectrics', *Journal of Materials Science*, 25(7), 3155–3158.

© Woodhead Publishing Limited, 2012

4

Properties of printed films as electrical components and metallization of solar cells

J. HORMADALY, Ben-Gurion University, Israel and
M. PRUDENZIATI, University of Modena and Reggio Emilia, Italy

Abstract: While research is in progress for the development of printed active electronic devices, including printed organic film transistors, power generator devices and memories, our age of information technology is benefitting from integrated circuit (IC) circuits with their integrated active and passive elements in a single chip and from hybrid circuits where active devices are taken from the semiconductor industry to be added to a network of passive electronic components. Thick-film passive components were developed for such hybrid circuits but their application has been spread in other areas and they continue to enter all segments of the electronics industry: military, industrial, data processing, medical, automotive, telecommunications and consumer. This chapter provides an overview of the properties of thick-films applied in this area of electronics, with sections covering resistors, conductors, dielectrics; special emphasis is on the features that make their behavior unique or at least uncommon. Where appropriate, chronological perspective is provided. In addition, the development of thick-film front metallization of silicon solar cells is illustrated.

Key words: electrical properties, thick-film resistors, thick-film dielectrics, thick-film conductors, solar cells.

4.1 Introduction

Thick-film compositions have many properties that render them technologically important, scientifically challenging and facilitate new applications. Some of these properties are unique to thick-film compositions and are not shared by other classes of materials.

The properties of thick-film compositions have been reviewed by many authors in journals and books and have been reported in the patent literature. Some selected reviews are: Altenburg *et al.* (2002), Borland (2004), Bouchard (1999), Dell'Acqua and Prudenziati (1994), Finch (1969), Kelemen (1970), Kuo (1992), Walton (1975), Larry *et al.* (1980), Prudenziati (1981), Vest (1991b), Wang *et al.* (1994), White (2006) and White and Turner (1997).

In this chapter, only some properties of thick-film compositions are reviewed. These properties were selected on the basis of their uniqueness and they are the properties that account for the broadened applications of thick-film compositions. Two unique properties are from the field of thick-film resistors, one is the sheet resistance (ρ_s) and the second one the temperature coefficient of resistance (TCR).

© Woodhead Publishing Limited, 2012

Other selected topics are the Ag-migration of silver-based conductors, Ag front metallization for solar cells and the applications of dielectrics.

4.2 Thick-film resistors

Thick-film resistors (TFRs) have several technologically important properties such as sheet resistance (ρ_s), temperature coefficient of resistance (TCR), low excess noise, low voltage coefficient of resistance (VCR), stability and trimmability.

Two of the above-listed properties, ρ_s and TCR, are unique in the sense that they are not exhibited by other classes of materials widely used in microelectronics and they are still a challenge for theoreticians.ρ_s has very broad range, 0.1 to 10 Ω/□ (see for instance Figure 4.1) and the shape of the Resistance (R) plot as a function of temperature of typical TFR is almost parabolic, as given in Figure 4.2; therefore, the TCR is negative at low temperatures $T < T_{min}$ and becomes positive over T_{min} where the resistance attains a minimum value.

4.2.1 Sheet resistance, R_s

The resistance R of a TFR is given by:

$$R = \rho \frac{l}{wt}$$

where l, w and t are the resistor length, width and thickness, respectively, and ρ is the resistivity in Ω.cm. For a TFR with $l = w$ (one square), the resistance is $R = \rho/t$; for a TFR with $l = w$ and t = 25μm the R /25μm = R_s (Ω/□). Therefore, the resistance of any TF resistor is given by:

$$R = \rho \frac{l}{wt} = \rho_s N_s \left(\frac{25}{t} \right),$$

where $N_s = \frac{l}{w}$ is the number of squares or the aspect ratio and t is the dried TFR thickness in microns. R_s defined above is a unit for describing the 'resistivity' of TFRs in Ω/□. ρ_s has very broad range 0.1 to 10^9 (Ω/□). The *low range* 0.1 to ~10Ω/□ is obtained by the combined use of metallic oxides and precious metals, usually Ag and Pd. The 10–10^6 Ω/□ range is obtained by changing the volume fraction of the metallic oxide in the glass–fillers–conducting materials composite. A typical TF resistor composition consists of glass, fillers and a conducting phase. The TF resistance is a very complex function of many variables, which include the glass, fillers, the conducting phase and TCR modifier concentrations, variables such particle size distribution of all the solid phases, glass composition, processing variable, termination type and composition and substrate type and ib composition.

Figure 4.1 (Morten *et al.* 1994) presents ρ_s as a function of the conducting phase volume fraction. This dependence is also known as 'blending curve'. Blending

© Woodhead Publishing Limited, 2012

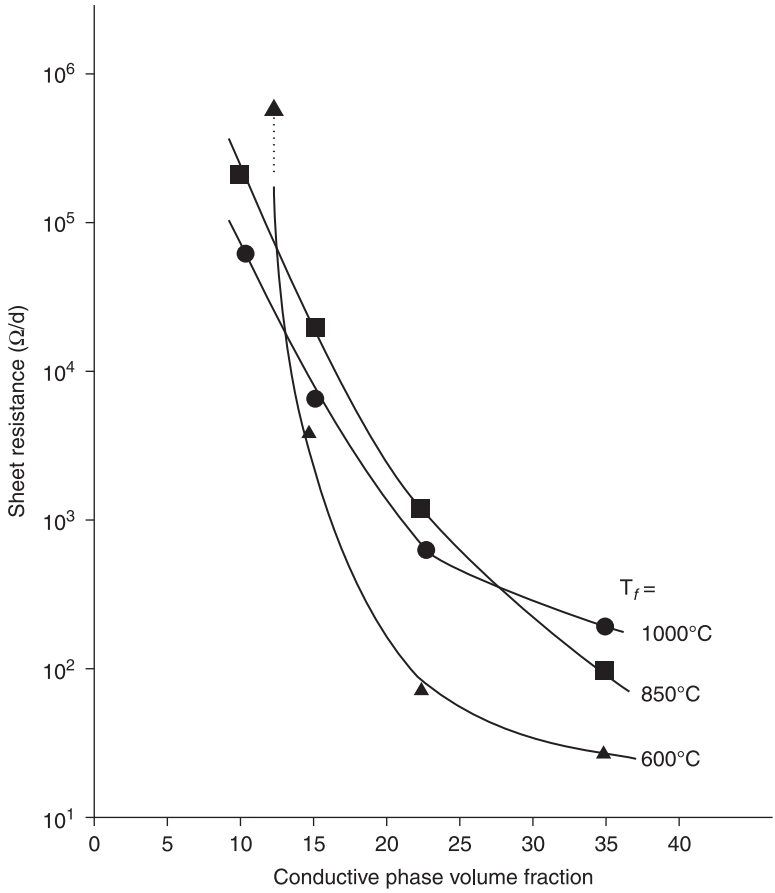

4.1 Sheet resistance as a function of conductor particle volume fraction. Different curves due to samples prepared at different peak temperature T_f (after Morten *et al.,* 1994).

curves were the subject of intensive experimental research: effects of glass composition (Vest, 1991a), nature and size of conductive particles (Abe and Taketa, 1989; Listkjewicz and Kusy, 1985; Pike and Seager, 1977; Tamborin *et al.*, 1997), firing conditions (Morten *et al.*, 1994, Vionnet-Menot *et al.*, 2005) and substrate composition (Kurihara *et al.*, 1991) were studied. The shape of these curves, because of their substantial departure from those common to other cermet resistors, were also the subject of a myriad of theoretical speculations (Monneraye, 1978; Pešić, 1988; Pike and Seager, 1977; Prudenziati, 1981; Vest, 1991a).

Nowadays there is a general consensus on a percolative approach in which a relevant role is played by the peculiar distribution of conductive particles embedded in the fired film. This distribution is characterized by large regions of

© Woodhead Publishing Limited, 2012

glass that constrain the much smaller conducting grains to be segregated in between the interstices of neighboring glass grains. This 'segregated microstructure' forces the classical percolation theories to deviate from the 'universal' values of the parameters (see Grimaldi, Chapter 5). As far as the electrical transport is concerned, inter-particle tunneling seems the prevalent mechanism. However, there are still differences in the various proposed models regarding the 'details' of the tunneling steps; these are: (1) the assistance of *resonant* centers, if any, and their possible origin, (2) the contribution of electron hopping on impurity bands or isolated states (also in the interparticle glass), and (3) the presumed contribution of the resistance of the embedded conductive grains (or their clusters) to the whole resistance.

In Chapter 5, Grimaldi explores some approaches to identify the electrical conduction mechanisms in TFRs and offers a view of the current understanding of this subject. Unfortunately, we have to admit that despite the progress in theoretical approaches and enrichment of results, regarding both the microstructure and the electrical behavior, there is little hope of arriving at a quantitative description of the blending curve: ρ_s is a function of too many variables for a comprehensive treatment with the current knowledge and computer simulations. The development of thick-film resistor pastes is still, and probably will be in the near future, based on empirical methods.

4.2.2 Temperature coefficient of resistance (TCR)

TFRs are known for their low TCR, typically lower than 100 ppm/°C in a temperature range of −55 to 125 °C. Figure 4.2 presents the typical temperature dependence of resistance *R* for TFRs. The plot shows a resistance minimum and two branches of *R* versus *T*; one 'semiconducting' (i.e. *R* declines when *T* increases) leading to a negative TCR, and one branch with *R* behaving as a 'metal' thus with a positive TCR. This is a characteristic property of TFRs and, as far as we know, it is a unique one, its appearance near room temperature making TFRs very useful passive components for microelectronic applications and sensors.

A number of models have been proposed over the years to explain both findings: the low TCR values and the minimum of resistance. The issue comes from the consideration that there is no mechanism for combining the high negative TCR (−7000 ppm/°C) of glasses with positive TCR (e.g. +7000 ppm/°C of single crystal RuO_2, +3000 ppm/°C of ruthenates), to accomplish TCR values as low as 50–100 ppm/°C. This exercise might be successful for a single relative fraction between the dielectric and conductive component and hence for a single resistivity value. But the mentioned behavior is observed in TFRs on many decades of resistance values; in addition, the cross-over temperature T_{min}, from TCR < 0 to TCR > 0 is shifted in the desired direction with small amounts of TCR modifiers. These findings are still sufficient to suggest the essential role of the glass in the TCR control. On the other hand, layers of pure (i.e. without glass) polycrystalline sintered

© Woodhead Publishing Limited, 2012

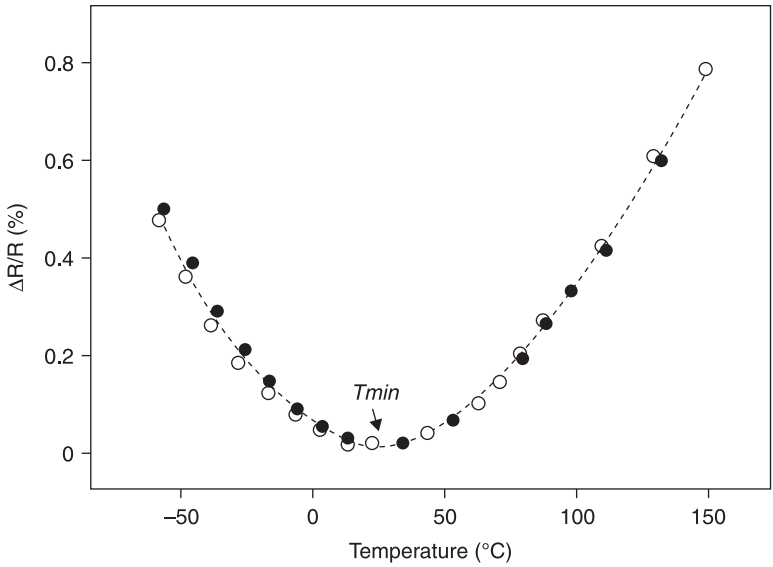

4.2 Typical temperature dependence of resistance in TFRs. $\Delta R/R \equiv \frac{R(T)-R_0}{R_0}$, with $R_0 = R(T_{min})$.

IrO_2 and RuO_2 prepared (on alumina substrates) by a thick-film technique (Dziedzic and Golonka, 1988) exhibit TCRs which, although lower than that of the single crystal counterparts, are still positive, almost linear and without any minimum in the very broad range of −200 to 800°C. Early models for electrical transport in TFRs rested on supposed (and now proved as very unrealistic) microstructures (uniform distribution of constitutive elements, or continuous channels of grains in contact, or homogeneously distributed conductive grains in glassy matrix); the models were criticized by Pike and Seager (1977). Next, the efforts were aimed at identifying a transport mechanism, compatible with the improved knowledge of the microstructure (i.e. the segregated one, mentioned above) capable of introducing a negative TCR. Currently, the most cited models consider tunneling barriers between adjacent conductive grains; the electrical transport through these barriers is thought to be assisted by resonant centers (Pike and Seager, 1977), or by hopping transport, either the nearest neighbor hopping or the variable range hopping (Flachbart *et al.*, 1998; Totokawa *et al.*, 2009), or by intrabarrier metal clusters. Also the models differ about the contribution of the grain resistivity to the total one (e.g. see Pešić, 1988; Pike and Seager, 1977; Prudenziati, 1981; Vest, 1991a).

The TCR > 0 regime has also been explained in terms of the thermal expansion affecting the inter-particle tunneling distances (Kubový, 1995), or by invoking the temperature-induced strain due to the mismatch between the thermal expansion coefficients of the resistor and the substrate (Fawcett and Hill, 2000; Sion *et al.*, 1994).

© Woodhead Publishing Limited, 2012

As the theories on transport mechanisms in insulator–conductor composites are refined these points will be clarified; however, the major step in the knowledge of TFRs will be the progress in description of source, amount, extension and behavior of 'impurities' at the interface between the conductive particle and the glass. With this knowledge the development of a new generation of competitive thick-film resistors would be anticipated.

4.2.3 Size effects

Changes of thickness and interactions between the resistive film and its terminations are responsible for the frequently observed influence of the geometry of resistors, mainly their length, on their electrical properties. 'Size effect' refers to the change of the effective sheet resistance as a function of the resistor length.

The mean thickness of a set of resistors of various lengths is a function of the resistor length: in a traditional screen-printing process the bowing of the screen can cause the center to be thinner than the edges, and the regions adjacent to the terminations to be thicker. This variation is more influential on short than on long resistors. Consequently, the actual resistance R divided by the aspect ratios of the various resistors in the set does not result in a constant *effective* sheet resistance R_s, even if the resistivity ρ_s is a constant. The apparent R_s value is usually lower in short (e.g. 0.2–0.5 mm long) resistors. This situation is largely mitigated with direct-write printing processes (Yang *et al.*, 1999).

Interactions between the resistive film and its terminations are conversely responsible for compositional changes and resistivity variations. The reduction of the effective sheet resistance near the termination is the most frequent case (denoted 'direct size effect') but also the reverse effect is possible (inverse size effect). The variety of (sometimes seemingly contradictory) experimental findings reported on the subject is currently consistent with the following picture:

1. Bi diffusion is responsible for a decrease of resistance in RuO_2 as well as in ruthenate-based resistors (Prudenziati *et al.*, 1986).
2. Ag diffusion is responsible for a decrease of resistivity in ruthenate-based resistors as well as in RuO_2-based systems, provided that the latter are free from aluminium (Prudenziati *et al.*, 1991).
3. Ag diffusion increases the resistance of RuO_2-based resistors containing aluminum, already present in the resistor composition or interdiffused from the substrate (Morandi *et al.*, 1991; Prudenziati *et al.*, 1989a).

High resistance in the resistor near the resistor/conductor interface has also been found to arise from changes in the microstructure of the resistor, where RuO_2 grains are redistributed and retreated from the region near the conductor interface (Vest, 1991b).

It is interesting to note that the diffusion of Bi partially suppresses the effect of Ag diffusion. Other elements (e.g. Mn) are even more effective in suppressing the

© Woodhead Publishing Limited, 2012

inverse effect (Morandi *et al.*, 1991). These are the same elements usually introduced in RuO_2-based resistors for the control of the TCR (see Chapter 2). This is the reason why the inverse size effect is rarely observed in films prepared with commercial pastes.

No matter what the origin of the local resistance change, the phenomenon is also associated with changes to other properties such as TCR, long-term stability and current noise. This latter quantity is especially sensitive to conductive-to-resistive layer interactions. Noise spectroscopy is quite effective in discriminating bulk noise from contact noise, if measurements are carried out with samples configured as multiterminal specimens with several side legs equally spaced along the resistor length (Masoero *et al.*, 1990; Mleczko *et al.*, 2008).

4.2.4 Trimming

The commonly observed tolerance of a population of as-fired, screen-printed resistors of the current state-of-the-art quality is between 10 and 20%. At least two factors contribute towards this large deviation from the predetermined resistance value: (1) poor control of macroscopic geometric parameters (such as resistor thickness and lateral edge smoothness, well defined interface resistor/termination) and (2) microscopic uniformity of the active materials, which impacts on the film resistivity. This latter is improved with uniform and very fine conductive particles giving at least half the dispersion of the conventional pastes (Sato *et al.*, 1993), while the former (control of geometry) may be improved through stencil printing instead of screen printing and with optimization of the whole printing process (e.g. mesh orientation of the stencil opening toward the printing direction; Cheng *et al.*, 2007). Printing with dispensing technologies (e.g. MicroPen by OhmCraft, see Chapter 1) can produce very well-defined resistor patterns and thus lower tolerances than conventionally printed resistors (Yang *et al.*, 1999).

Resistors with tolerances within typically 0.5% can be achieved by laser trimming, i.e. by burning away a part of the resistor with a laser beam (commonly a Nd-YAG laser, $V\lambda = 1.06\,\mu m$) operated in the Q-switched mode in the closed-loop control system, which shuts off the beam when the desired resistor trimming value has been achieved (Fig. 4.3). Laser trimming is applied to resistors designed to have a fired resistance value below the final target value, and may be done on glazed components. The 'green glasses' for glazing resistors are in fact optimized for optical absorption of the trimming laser radiation. In hybrid circuits, instead of trimming resistors to specific values, it is customary to trim them to produce a specific output level (e.g. voltage, frequency, current, etc.) from the circuit, a process known as 'functional trimming'. Laser beams may produce severe thermal shock in the resistors, which leads to microcracks in the neighborhood of the kerf that are a potential source of instability.

The need for alternative trimming methods emerged from the development of low-temperature co-fired ceramic (LTCC) circuits and particularly for the adjustment of

© Woodhead Publishing Limited, 2012

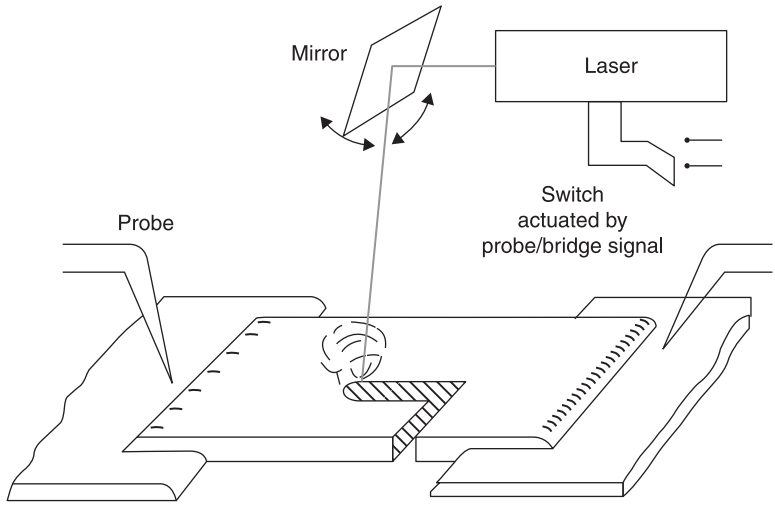

4.3 Laser trimming: a laser beam is moved on the resistor surface to 'cut' away a small portion, raising its resistance value. The operation is conducted while the circuit is tested by automatic test equipment.

resistors buried inside laminated tapes, thus not directly accessible by the laser beam. Resistors are susceptible to high voltage pulses and static electricity and so the development of pulse-trimming methods generated renewed interest in these effects, which were originally studied in the 1970s (Seager and Pike, 1976; Stevens *et al.*, 1976). Pulse trimming results in increased resistance in 'low-decade' compositions (i.e. TFRs in the range 10–100Ω/□), whereas the opposite effect is observed in high-decade resistors; the origin of these effects has yet to be fully clarified. Pulse height, pulse width, number and repetition rate are parameters of choice to reduce the tolerance at values of 0.5–1%. Reports on the (possible) change of other properties, e.g. current noise, low term stability and TCR values in trimmed resistors, do not agree with each other. For instance, noise level was reported to decrease by Tobita and Takasago (1991), to remain almost unvaried according to Dziedzic *et al.* (2005) and to increase according to Stevens *et al.* (1976) and Stanimirovi *et al.* (2006). Perhaps these discrepancies are due to the different characteristics (compositions, size, terminations) of samples investigated and underline the need for further studies on this subject.

4.2.5 Long time stability – ageing

Resistor changes as a consequence of various storage conditions that simulate processing conditions, such as solder dipping to packaging, or their operating life are common stability criteria. According to the envisaged applications, the resistance drift at temperatures as low as 40 °C with 90% relative humidity, or at exposure to 300 °C for hundreds of hours may be required. A huge amount of data

© Woodhead Publishing Limited, 2012

for TFRs aged in various conditions has been collected and cannot be briefly summarized. Here a few significant figures and common trends are reported.

Figure 4.4 shows the results of a study of ageing under an exceptionally wide temperature range (125 to 400 °C): the data suggest that the monotonous resistance drift versus time experienced at the lower temperatures is lost when the ageing temperature 'approaches' the softening point of the glassy matrix of the resistors under test (about 630 °C for the case illustrated in Fig. 4.4). Ageing tests at temperatures in the range 150 °C to 300 °C for a given time t, show that: (1) $\Delta R/R$ values obey the Arrhenius equation, i.e. $\Delta R/R(t = \text{const}) \sim \exp(-E/KT)$, where K is the Boltzmann constant and E the activation energy ($E \sim 0.46$ eV in specimens of Fig. 4.4). Also, $\Delta R/R$ after isothermal annealing is directly proportional to the square root of time, suggesting diffusion-controlled ageing mechanisms. Similar features have been experienced in other systems (e.g. Coleman, 1979; Rocak *et al.*, 2001; Wheeler, 1985) but are far from exhausting the full picture of ageing phenomena. In fact, at temperatures as low as 60–100 °C, the time dependence of the resistance drift is better approximated by $\Delta R/R \sim t^n$ with $n << 1/2$, e.g. $n \sim 1/3$ to $1/7$ was reported by Coleman (1979) and Wheeler (1985).

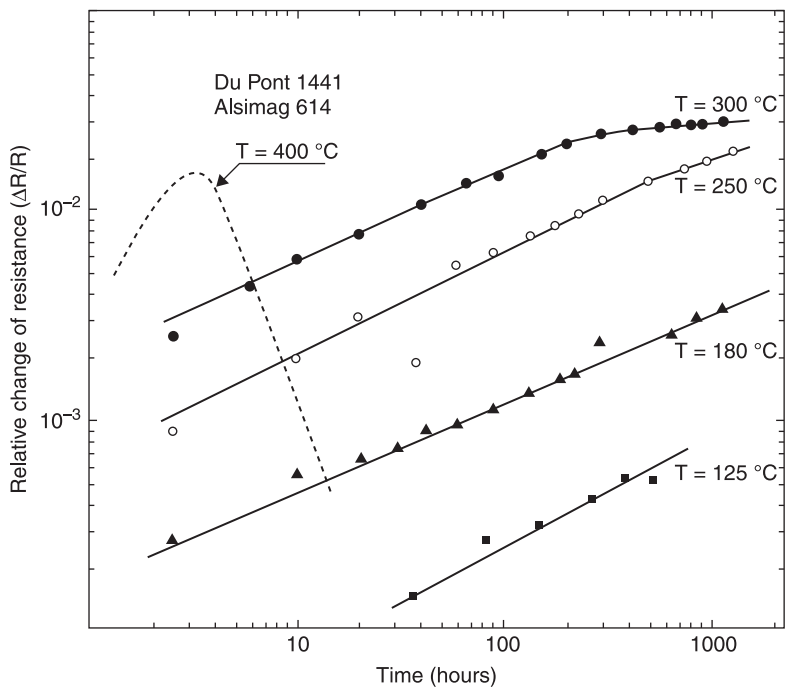

4.4 Relative change of resistance of DuPont 1441 resistor after exposure at different temperatures and times in lab air (after Prudenziati and Morten, 1983).

© Woodhead Publishing Limited, 2012

Two distinct contributing factors have been identified, i.e. (1) the resistivity change of the bulk resistor material with time and (2) the influence of the conductor materials, mainly Ag-based, particularly for the small resistor geometry. Experiments have shown that the drift of resistivity is affected by:

- *Composition and microstructure*, for instance the size of the conductive phase in the paste that is otherwise identical in composition and processing (Dietrich *et al.*, 2009), or amount of the conductive phase in otherwise identical pastes and processing conditions (Prudenziati *et al.*, 1981/82).
- The *environment*, e.g. rich or poor of oxygen, humidity (Coleman, 1979; Sinnadurai and Wilson, 1982). Out-diffusion and in-diffusion of oxygen have been postulated to interpret the effect of the atmosphere and the reduced shift of encapsulated (glazed) resistors compared to unprotected ones.
- *Stress and strain*, as shown by Dell'Acqua *et al.* (1982): the drift of resistors stored at 125 °C in stressed conditions (both tensile or compressive) is higher than that of the unstressed ones, a result that should be further systematically investigated to look for possible correlations with the composition, strain sensitivity and ageing conditions.
- *Composition of conductive terminations*: it has been found that in some resistors printed with Ag conductors, the relative change of resistance follows a linear time-dependence, suggesting a rate limited reaction, and gives *negative* resistance drift. Moreover, this contribution to the whole drift is higher for shorter resistors than in longer ones (Rocak *et al.*, 2001). The total drift for high annealing temperatures and short resistors may be negative.
- *Substrate* composition (Jakubowska and Pitt, 1995; Morten and Prudenziati, 1983; Wheeler, 1985).
- The type of laser or pulse-trimming, and the relative parameters.

The total resistance drift is dependent on the sum of all the mechanisms. There is normally a dominant mechanism over a given temperature range for a given resistor system and set of processing conditions, which enables the characteristic parameters to be identified. A comprehensive picture of all these mechanisms has never been reported, but it may be envisaged that it should include phenomena such as strain relaxation and interactions between the film constituents, with the substrate and with the environment

4.3 Conductors

4.3.1 Introduction to conductors

Applications of printed conductive films, especially thick-film conductors, are referred to in many chapters of this book. Printed conductors are in fact useful or even essential to realize inductors, heaters, resistive temperature detectors (RTDs), heat dispersing layers in high power circuits, to accomplish electrodes for display,

© Woodhead Publishing Limited, 2012

electromagnetic/radiofrequency shields, electrodes for capacitors and sensing elements, as internal electrodes in multilayer ceramic capacitors (MLCC) and multilayer varistors (MLVs), metallization for photovoltaic devices and fuel cells (SOFCs), sacrificial layers for MEMS. In hybrid circuits, thick-film conductors serve three primary tasks: (1) to terminate thick-film resistors and capacitors, (2) to interconnect discrete devices mounted on the substrate with the thick-film passives or other discrete devices, placed on the same surface or, through vias, on different levels in multilayer circuits, (3) to fulfill the needs for the circuit package, e.g. heat sink, solder pads, sealing lids. This myriad of applications calls for different compositions and processing conditions.

Table 4.1 presents a list of selected (intrinsic) properties of metals used in thick-film compositions.

The resistivity ρ(Ωcm) of the pure element, reported in the table, results in the sheet resistance R_s given by ρ/25.wμ cm hence, for example, ρ =10μ Ω.cm corresponds to $R_s = 4\,\text{m}\,/\Omega/\square$. The fired thick-film conductors exhibit resistivity that is higher by a factor of 3 to 15 than that of the parent metal, because of the inevitable porosity in the film and the presence of binder phases (oxides, glass; see Chapter 2) added in the paste to improve the adhesion to the substrate, as sintering aids, etc. Also, in most thick-film conductors the functional phase is not a pure element but a binary or ternary alloy combination, which leads to lower electrical conductivity but circumvents or mitigates some side problems (leaching in solders, migration, etc.).

In selecting a composition, considerations are due primarily to the electrical resistivity and adhesion to the substrate, but, depending on the applications, also to

Table 4.1 Some properties of precious and base metals used in thick-film conductor compositions

Metal	Density (g cm^{-3})	Melting point (K)	Electrical resistivity at 293 K ($\Omega m 10^{-8}$)	Thermal conductivity at 300 K ($Wm^{-1}K^{-1}$)	Coefficient of linear thermal expansion ($10^6 K^{-1}$)
Ruthenium	12.370	2583	7.6	117	9.1
Rhodium	12.410	2239	4.51	150	8.4
Palladium	12.020	1825	10.8	71.8	11.2
Silver	10.500	1235.08	1.59	429	19.2
Iridium	22.560	2683	5.3	147	6.4
Platinum	21.450	2045	10.6	71.6	9.0
Gold	19.320	1337.58	2.35	317	14.16
Copper	8.960	1356.6	1.673	401	16.5
Nickel	8.902	1726	6.84	90.7	13.3
Aluminum	2.698	933.52	2.65	237	23.03
Molybdenum	10.220	2890	5.2	138	5.43
Tungsten	19.300	3682.20	5.65	174	4.59

Source: Emsley (1991).

© Woodhead Publishing Limited, 2012

good line definition, wire bondability or leach resistance, compatibility with other components and substrate, migration resistance, porosity (permeability to gases) and cost. Efforts in research and development over many decades have enabled the introduction of pastes and processes to meet all these requirements adequately.

Despite their higher price, noble metals and alloys (especially Ag, Pd, Pt, Au and their binary or ternary alloys) are mostly used in conductive formulations, because they can be processed in air and offer higher corrosion resistance, wider compatibility and better electrical properties than non noble-based thick-film conductors.

For specialized applications, base metals such as Al, Ni, Cu, Mo and W are used. For example, Ni is the choice for the internal electrodes of current MLCC and magneto-resistive sensors, whereas W and Mo are used in high-temperature co-fired ceramic (HTCC) technology, Al is the major ingredient for back-contact metallization of Si solar cells and for heat dispersing layers in high power packages, etc. (Wang *et al.*, 1994).

Because of such various formulations and properties, it would be impossible to address all the thick-film conductors in full. Therefore we will confine ourselves to some considerations on silver-based conductors, i.e. on the most important class of thick-film conductors. This class includes films based on Ag and its alloys with Pd, Pt and Au. The alloys enhance the solder leach resistance (Pt) and/or increase silver migration resistance (Pd).

Also, these systems offer substantial cost benefits over the precious metals, which are more expensive and very fluctuating in price as a function of market. Although in recent years (since 2004) the cost of Ag has increased sharply following the increase in the cost of Au, Pt and Pd, it (Ag) is still below $50/troyoz, therefore at least an order of magnitude lower than the cost of Au, Pd and Pt.

Because of its unique and unsubstitutable properties, Ag is the major player in thick-film conductors and expected to maintain its position in the near future. An increase of Ag use in thick-film conductors is expected in view of the projected (BCC reports, 2010) increase in the volume of energy-related devices such as silicon photovoltaic cells. In view of this central role projected for silver, in this section only properties of silver conductor compositions are reviewed. One subject is the electrolytic migration of silver-based conductor compositions and the second subject is Ag front metallization for silicon solar cells.

4.3.2 Silver migration

Silver (Ag)-based conductors *on* dielectrics or *between* dielectrics (crossovers) in humid atmosphere and under d.c. field, migrate as ions (Ag^+) from one site (the anode) and deposit on another site (the cathode) as dendrites. The dendrites may grow on a surface or through the dielectrics and electrically connect two conductors' tracks, thus leading to shorts. This phenomenon is known *silver* (*electrolytic*) *migration* and is a major drawback of Ag conductors. Factors

© Woodhead Publishing Limited, 2012

affecting the ion migration encompass paste composition, high d.c. electric field caused by the voltage drop across closely spaced conductors, ambient temperature and relative humidity, encapsulation and finally composition, roughness and contamination of the substrate (Coleman and Winster, 1981; Lin and Chan 1996, 1997; Naguib and MacLaurin, 1979; Wang *et al.*, 1994). To compare the relative role of these factors and to evaluate different materials, information is quickly collected with the so-called water-drop (WD) tests in which a drop of deionized water is placed to bridge the gap (typically 250–1000 μm wide) between two conductor tracks, and the migration of Ag is observed upon applying a bias (a few volts) between the two tracks. The temperature humidity bias (THB) tests are more adequate to evaluate the migration resistance under (quasi) real operating conditions. In these tests, samples are studied under controlled temperature and relative humidity (RH) conditions (e.g. 85–90 °C, 85–90% RH), then somewhat more severe conditions than those projected for most circuits, which otherwize would force experiments in a time domain of days or even years. In THB, the decline in insulation resistance or the increase of leakage current across the closely spaced conductors under d.c. bias are measured as a function of time, or until the time to failure.

During WD tests, Ag migration rate under d.c. field of 0.1 V/mil (40 V/cm) with electrodes containing pure silver, either on bare alumina substrate or dielectric layers, is so fast as to cause shorts within 60–90 s. The migration is reduced by 100 times in Pd/Ag conductors with a Pd content higher than 10% (Naguib and MacLaurin, 1979). In THB tests under equivalent electrical conditions, the Ag migration rate is approximately 10^4 times lower than in WD tests. However, the glass component in the conductor paste and the method of preparing the ink may have a significant influence on its migration susceptibility, regardless of its Pd content. An additional method to minimize the migration is to encapsulate the fired film with an organic coating or a glaze layer (like DuPont 9137 used by Naguib and MacLaurin (1979), now replaced DuPont QQ550), which prevents the moisture condensation or ionic contamination on the surface.

It has been shown that migration of the Ag on the surface of – as opposed to through the thickness of – dielectric crossover was the main failure mode in these structures. Silver migration in thick-film conductors on substrates of different compositions and cleanness preparation, as well as in chip attachment resins, was reported by Coleman and Winster (1981). They stressed the importance of producing and maintaining the substrate surface free from debris and contamination. Only under very controlled conditions is the rate of Ag-migration related to the Ag content of the film. Glass as an encapsulation and as a barrier between conductors is effective in retarding migration and, to great extent, resin encapsulants have a similar effect.

The anodic formation of PdO was suggested as the effect limiting Ag dissolution and the occurrence of Ag migration with PdAg conductors, by increasing the amount of Pd from 5 to 20%, until the complete disappearance of migration at

© Woodhead Publishing Limited, 2012

30% Pd (Lin and Chan, 1996). In a second study, Lin and Chan (1997) have shown that conductors made from mixed Ag and Pd powders are more migration-resistant than those prepared from alloyed AgPd powders, having the same Ag/Pd ratio. Liu *et al.* (2011) reported on the advantages, in terms of resistance to electro-migration, offered by composite powders, such as Ag-plated Cu powders substituting silver powder in the films.

One of the challenges for the near future is to lower the cost of Ag-based conductors and maintain their properties. One obvious way is to use Ag-coated Cu powder in polymer thick-film conductors for relatively low processing and operating temperatures. For ceramic-type conductors to be processed at 850 °C, using Cu-coated Ag, new innovative approaches are required to stabilize the copper in its metallic (alloyed) state.

4.3.3 Thick-film metallization for solar cells

Several printing techniques have been used to deposit front Ag metallization on silicon solar cells. Screen printing is the leading technique nowadays. However, ink-jet printing has been modified, special compositions have been developed and sophisticated machines have also been developed to make it a strong second runner for printing front Ag metallization on silicon solar cells.

The metallization compositions for screen and ink-jet printing contain very similar materials: silver metal as a major component, glass powder(s), additions such as metal oxides or mixed oxides and an organic vehicle. The solid ingredients for ink-jet printing are typically nanometer size and for screen-printing paste they are larger and range from one submicron to several microns. The glass frits used are lead borosilicates, bismuth–lead borosilicates and lead-free glasses, which are based on bismuth–zinc borosilicates. Many publications and patents have addressed the subjects of processing, compositions and the mechanisms of forming ohmic contact between the silver and the silicon. In a recent publication, Schubert *et al.* (2006) reviewed the existing models and recent developments. Schubert *et al.* (2002) also suggested a redox reaction between silicon and metal oxides in the glass and proposed the following reaction:

$$2PbO(glass) + Si \rightarrow 2\,Pb + SiO_2\,(glass)$$

to describe the interaction of glass frit with silicon.

Sopori *et al.* (2007) reviewed the fundamental mechanisms in the fire-through contact metallization of solar cells.

A more detailed understanding of front metallization contact with silicon and current transport mechanisms were the result of the recent studies. However, many issues still remained to be unraveled.

The thermodynamics of possible reactions among paste or ink ingredients (Ag, glass, oxides additives), silicon and anti-reflective coating, SiN_X are outlined

© Woodhead Publishing Limited, 2012

below to aid the understanding of the interactions. A simple approach is to consider the standard free energies (taken from *Handbook of Chemistry and Physics*: Weast, 1987–1988) of key ingredients as separate entities and use these energies to estimate the possible direction of specified reactions. The assumptions used in these calculations are that the reactions occur between crystalline ingredients at room temperature (298 K). In reality, the reactions are between crystalline and vitreous ingredients at temperatures higher than 298 K. The differences between estimated and real values of free energies of reactions (Δ_{react}) may be large. However, for large absolute values (reactions 4.1 to 4.8, excluding 4.4), they show a clear trend.

- $Si + O_2 \longrightarrow SiO_2$(quartz) $\Delta G_f^o = -204.75$ kcal/mole
- $3Si + 2N_2 \longrightarrow Si_3N_{4(c)}$ $\Delta G_f^o = -153.3$ kcal/mole
- $Pb + \frac{1}{2}O_2 \longrightarrow PbO_{(c)}$ yellow $\Delta G_f^o = -44.91$ kcal/mole
- $Zn + \frac{1}{2}O_2 \longrightarrow ZnO_{(c)}$ $\Delta G_f^o = -76.08$ kcal/mole
- $2Bi + \frac{3}{2}O_2 \longrightarrow Bi_2O_{3(c)}$ $\Delta G_f^o = -88.0$ kcal/mole
- $2Sb + \frac{5}{2}O_2 \longrightarrow Sb_2O_{5(c)}$ $\Delta G_f^o = -198.2$ kcal/mole
- $2Ag + \frac{1}{2}O_2 \longrightarrow Ag_2O_{(c)}$ $\Delta G_f^o = -2.59$ kcal/mole

Some possible reactions among the paste ingredients, antireflection coating and silicon base are:

$$Si + 2PbOSiO_2 + 2Pb$$
$$\Delta G_{react}^o = -204.75 - 2(-44.91) = -114.9 \text{ kcal} \quad [4.1]$$

$$Si_3N_4 + 6PbO3SiO_2 + 2N_2 + 6Pb$$
$$\Delta G_{react}^o = -3(-204.75) - 6(-44.91) - (-153.3) = -191.49 \text{ kcal} \quad [4.2]$$

$$2Zno + SiSiO_2 + Zn$$
$$\Delta G_{react}^o = -204.75 - 2(-76.08) = -52.59 \text{ kcal} \quad [4.3]$$

$$Si_3N_4 + 6ZnO3SiO_2 + 2N_2 + 6Zn$$
$$\Delta G_{react}^o = 3(-204.75) - 6(-76.08) - (-153.3) = -4.47 \text{ kcal} \quad [4.4]$$

$$Bi_2O_3 + \tfrac{3}{2}Si\tfrac{3}{2}SiO_2 + 2Bi$$
$$\Delta G_{react}^o = \tfrac{3}{2}(-204.75) - (-88.0) = -219.13 \text{ kcal} \quad [4.5]$$

$$Sb_2O_5 + \tfrac{5}{2}\,Si\tfrac{5}{2}SiO_2 + 2Sb$$
$$\Delta G_{react}^o = \tfrac{5}{2}(-204.75) - (-198.2) = -313.68 \text{ kcal} \quad [4.6]$$

$$Ag_2O + PbPbO + 2Ag$$
$$\Delta G_{react}^o = -44.91 - (-2.59) = -42.32 \text{ kcal} \quad [4.7]$$

$$Si_3N_4 + 2Bi_2O_33SiO_2 + 2N_2 + 4Bi$$
$$\Delta G_{react}^o = 3(-204.75) - 2(-88.0) - (-153.3) = -284.95 \text{ kcal} \quad [4.8]$$

The estimated free energies of reactions 4.1, 4.3, 4.5 and 4.6 indicate that it is very likely that glass ingredients such as PbO, Bi_2O_3, ZnO and Sb_2O_5 (a similar

© Woodhead Publishing Limited, 2012

conclusion is expected for Sb_2O_3) will be reduced by the silicon base. The zinc oxide is a special case: although the estimated free energies of reactions may be small negative numbers, the reaction can be driven to the right by the high vapour pressure of the liquid zinc, owing to its low melting point and fairly low boiling point. Thus, zinc oxide as a glass ingredient or as an additive is expected to be reduced by the silicon base and interact via redox reaction with the antireflection coating.

All the metals that are expected to be formed by the redox reactions (Pb, Bi, Zn, Sb) will interact with the silver oxide in the glass (see, for example, reaction 4.7) and oxidize with the formation of metallic silver.

The literature describes the interactions of the Ag front metallization with the antireflection coating (Si_3N_4) as fired through, dissolution or etching. The reactions above (4.2, 4.4 and 4.8) point out that the mechanism might be a redox reaction to form silicon dioxide, which will dissolve in a glass, nitrogen gas and metal (Pb, Zn, Bi).

Besides the interactions with the silicon base and dissolution of metallic silver, the glass forms a layer on the silicon solar cell. Dissolution of silver in glasses used for the preparation of silver front metallization was reported by Prudenziati *et al.* (1989a).

Layers of glass on silicon solar cells were reported by Ballif *et al.* (2003; 1989b), Nakajima *et al.* (1983); Prudenziati *et al.* (1986b); Schubert *et al.* (2006); Thuillier *et al.* (2000), and in citations quoted in Schubert *et al.* (2006).

Since the glass wets the silver and forms a layer on the silicon, the electrons have to tunnel through the glass from the silicon (Nakajima *et al.*, 1983; Prudenziati *et al.*, 1996). The glass is a dielectric material and even with a dissolution of 1–3 wt% of Ag during the short thermal processing cycle, it can be argued (Sopori *et al.*, 2007) that its conductivity is not high enough to support transport. Moreover, most of the silver in the glass is ionic and the volume fraction of metallic silver is too low to make the glass sufficiently conducting. These arguments of the low solubility and low volume fraction of Ag have to be contrasted with the vitreous enamel resistance material developed by Janakirama-Rao and Murphy (1964). These authors have shown (see Chapter 2 for a detailed discussion) that by the introduction of ionic silver into the glass, the conductivity of the conductor was increased by several orders of magnitude compared to a conductor that contains the same glass but without ionic silver.

Improvement of the photovoltaic performance of silicon-based solar cells can be accomplished by increasing the light absorption area. Special Ag front metallization compositions need to be developed that will allow the deposition of very fine conductor lines. The new compositions will probably be based on very fine solid ingredients, such as nanoparticles of silver and dielectric materials, and organic ingredients, which will allow deposition of fine conductor lines by conventional thick-film techniques and other methods such as ink-jet printing. Other important future issues are to decrease the cost of materials and processing.

© Woodhead Publishing Limited, 2012

4.4 Dielectrics

4.4.1 Applications

Thick-film dielectrics find applications in a variety of different areas. They encompass the traditional dielectrics for hybrid microelectronics to the more recent areas of sensors, actuators, MEMS, optoelectronic devices (displays), heaters and energy converters (e.g. fuel cells). Thus a wide range of thick-film inks is available today. Specific properties for some of the applications will be delineated in the following sections, with reference to the related literature.

The general basic requirements for thick-film dielectrics are the same for any dielectric materials, such as appropriate dielectric strength, dielectric constant and loss, mechanical strength and environmental stability. However, additional features are associated with the printed film structure and processing; these are compatibility with other system elements, the sequence of depositions and firing operations.

The traditional thick-film dielectrics fall into three different classes: (1) crossover and multilayers, (2) overglaze and sealants, (3) capacitors. The specific functions and properties of these films have been reviewed by Bouchard, 1999; Dell'Acqua, 1994; Hoffman, 1984; Larry *et al.*, 1980; Vest 1991b.

Crossovers allow conductor lines to be printed over one another, through multiple firing steps, without 'flowing' in the refiring process. Crystallizable glasses, e.g. calcium zinc aluminosilicates, which precipitate celsian ($BaAl_2Si_2O_8$) or hardystonite on firing, are adequate composition for crossover. In multilayer circuits, a dielectric is printed over the entire first layer of printed and fired components, which are electrically connected through holes or vias in the dielectric. In this case, the composition may be similar to crossovers, but requirements to be met are more stringent to match the thermal expansion coefficient, reach high dielectric strength and inhibit ionic migration. Typical properties are: relative permittivity in the range 8–14, breakdown voltage 500–1000V/25 µm; insulation resistance $R > 10^{10}\ \Omega$·cm at 100 Volts DC.

Overglaze dielectrics provide passivation to underlying resistor and capacitor films. They are usually glasses that flow and coalesce at low temperature (e.g. 400 to 500 °C) to minimally change the properties of the underlying films.

Capacitor dielectrics need to exhibit as high a dielectric constant as possible. The past two decades have brought outstanding progress in the development of high-performing capacitors, by means of relaxor ceramics. These are ferroelectric perovskites typified by lead magnesium niobate ($PbMn_{1/3}Nb_{2/3}O_3$) with a ferroelectric transition at a temperature (the Curie temperature T_c or Curie point) near room temperature (Lejeune and Boilot, 1985). All the ferroelectric materials exhibit a maximum (peak) permittivity, often as high as 15 000–30 000, near T_c. Relaxors are characterized by their notable diffuse (50–100 °C around T_c) transition; moreover, T_c can be shifted to the optimum value for the envisaged operations by means of known changes of composition (e.g. solid solutions of different perovskites) and processes (including powder size, thermal processes). Relaxors, with their

© Woodhead Publishing Limited, 2012

complex physical and technological properties, are a very rich chapter of electronic ceramics (Swartz, 1990). Their applications in thick-films give us compounds with dielectric constants up to 10 000–15 000, and other excellent dielectric properties for films fireable in air with noble metal electrodes at 'standard' firing temperatures (850–950 °C). Hence, integral thick-film capacitors may be accomplished with capacitance density of up to 3000 pF/mm^2. For high integration and high volumetric efficiency (e.g. in cellular phones, computers), single-layer thick-film capacitors have been supplanted by MLCCs, i.e. structures in which many dielectric layers and internal electrodes are alternately stacked and the internal electrodes are connected in parallel. In the current technology, the number of layers is typically 500–700, and the areas are smaller than 1 mm^2. With this structure, noble metals for the internal electrodes are too expensive, and therefore are replaced by Ni. This latter has to be fired in reducing ambient because of its tendency to severely oxidize in air; this requirement in turn calls for a 'non-reducible' dielectric, in place of lead-based relaxors. Today the materials of choice for imbedded dielectrics in LTCC are variously doped $BaTiO_3$. A perovskite oxide, (k ~15.000), in which the dopants substitute for the A ion (Ba) or for the B ion (Ti) with proper charge, balance and stabilize the ideal perovskite structure ABO_3. They have to inhibit the decline of insulation resistance otherwise due to oxygen vacancies in the $BaTiO_3$ lattice. The development of this technology, which required a deep understanding of electronic defect phenomena in complex materials, today provides millions of units of MLCCs at prices of around 0.01 $/unit. The capacitance may be 1 to 100 μF in case sizes as small as 1.0 × 0.5 mm^2 (Kishi *et al.*, 2003).

While the majority of thick-film dielectrics are tailored to meet requirements for hybrid circuits, components and systems on alumina and LTCC, a variety of compositions for other applications and substrates have been developed, for example:

- Dielectric for multilayers and sealants designed to match the thermal expansion coefficient of AlN (e.g. Ferro Corporation, multilayer dielectric 10-054).
- High-temperature compositions for use in planar oxygen sensors (e.g. ESL 4492).
- Porous overcoat for planar oxygen sensors (e.g. ESL 4550).
- Pb- and Cd-free thick-film glass designed for sealing low thermal expansion substrates, such as silicon and soda lime, at reduced firing temperatures. For hermetic sealing of wafer-level, MEMS packaging and other micro-mechanical devices, such as vibration, SAW, accelerometer sensors and gyroscopes (Ferro Corporation).
- Glasses for the hermetic sealing on alumina, ceramic packages, glass optoelectronic displays and other applications calling for low glazing temperatures (T ~ 400 °C) (e.g. Ferro Corporation, 1161 HZ).
- Dielectrics-on-steel (e.g. DuPont QM42, ESL D4914, Heraeus IP-222-SL for sensors and heaters, Heraeus IP-211 for Cr-steel).
- Insulation of aluminium, for integral packaging of devices, such as high-emitting LEDs (e.g. ESL 4003 and 4604-A).

© Woodhead Publishing Limited, 2012

In each new product, challenges were addressed to meet one, or a variety of, specific requirements; tightness or porosity of the film, long-term stability at high operating temperatures, unusual low (or high) processing temperature or adhesion with the envisaged substrate.

4.5 References

Abe O. and Taketa Y., 1989, 'Mathematical relation between RuO_2 volume fraction and resistance of thick-film resistors', *J Phys D: Appl Phys* 22(11), 1777–1781.

Altenburg H., Plewa J., Plesch G. and Shpotyuk O., 2002, 'Thick-films of ceramic, superconducting, and electro-ceramic materials', *Pure Appl Chem* 74(11), 2083–2096.

Ballif C., Huljie D. M., Willeke G. and Hessler-Wyser A., 2003, 'Silver thick-film contacts on highly doped n-type silicon emitters: structural and electronic properties of the interface', *Appl Phys Lett* 82(12), 1878–1880.

BCC reports, 2010, 'Thick-film devices, processes and applications', Report Code: AVM046B.

Borland W., 2004, 'Ceramic thick-films process and materials', *in* R. C. Buchanan (ed.), *Ceramic Materials for Electronics*, 3rd edn, pp. 527–580.

Bouchard R. J., 1999, 'Thick-film technology: an historical perspective', *Ceramic Transactions 100 (Dielectric Ceramic Materials)*, pp. 429–442.

Cheng P. L., Leung S. Y. Y., Law T. W., Liu C. K., Chong J. I. T. *et al.*, 2007, 'Quantitative analysis of resistance tolerance of polymer thick-film printed resistors', *IEEE Trans Comp Packag Technol* 30(2), 269–274.

Coleman M. V., 1979, 'The effect of nitrogen and nitrogen–hydrogen atmospheres on the stability of thick-film resistors', *Proceedings of the International Microelectronics Symposium*, pp. 255–262.

Coleman M. V. and Winster A. E., 1981, 'Silver migration in thick-film conductors and chip attachment resins', *Microelectronics Journal* 12(4), 23–29.

Dell'Acqua R., 1994, 'Thick-film dielectric materials', *in* M. Prudenziati (ed.), *Thick-film Sensors*, Elsevier, Amsterdam, pp. 99–111.

Dell'Acqua R. and Prudenziati M., 1994, 'Thick-film resistors', *in* M. Prudenziati (ed.), *Thick-film Sensors*, Elsevier, Amsterdam, pp. 85–97.

Dell'Acqua R., Dell'Orto G., Simonetta A. and Canali C., 1982, 'Long term stability of thick-film resistors under strain', *Int J Hybrid Microel* 5, 82–84.

Dietrich S., Kretzschmar C., Partsch U. and Rebenklau L., 2009, 'Reliability and effective signal-to-noise ratio of RuO_2-based thick-film strain gauges: the effect of conductive and glass particle size', *32nd International Spring Seminar on Electronics Technology*, ISSE 2009, pp. 1–6.

Dziedzic A. and Golonka L., 1988, 'Electrical properties of conductive materials used in thick-film resistors', *J Mater Sci* 23(9), 3151–3155.

Dziedzic A., Kolek A., Ehrhardt W. and Thust H., 2006, 'Advanced electrical and stability characterization of un-trimmed and variously trimmed thick-film and LTCC resistors', *Microelectronics Reliability* 46(2–4), 352–35.

Emsley J., 1991, *The Elements*, 2nd edn, Clarendon Press, Oxford.

Fawcett N. and Hill M., 2000, 'A contribution to the debate on the resistance–temperature characteristics of thick-film resistor materials', *Sensors and Actuators A* 86(1–2), 52–57.

Finch R. G., 1969, 'Thick-film materials', *Thin Solid Films* 3(3), 189–199.

© Woodhead Publishing Limited, 2012

Flachbart K., Pavlìk V., Tomašovičová N., Adkins C. J., Somora M. *et al.*, 1998, 'Conduction mechanism in RuO_2-based thick-films', *Phys Stat Sol (b)*, 205(1), 399–404.

Hoffman L. C., 1984, 'An overview of thick-film hybrid materials', *Ceram Bull* 63(4), 572–576.

Jakubowska M. and Pitt K., 1995, 'Influence of the contacts and firing process on the properties of thick-film resistors on alumina and dielectrics', *J Mater Sci: Mater Electron* 6(2), 75–78.

Janakirama-Rao B. V. and Murphy R. M., 1964, 'Resistance material and resistor made therefrom', US Patent 3 154 503, October 27.

Kelemen D. G., 1970, 'Metallographic aspects of thick-film technology', *Metallurgical Transactions* 1, 667–677.

Kishi H., Mizuno Y. and Chazono H., 2003, 'Base-metal electrode-multilayer ceramic capacitors: past, present and future perspectives', *Jpn J Appl Phys* 42(1), 1–15.

Kubový A., 1995, 'Model of electric conductivity of thick-film resistors Part III. Temperature dependence of sheet resistivity', *Ceramics-Silikáty* 39(1), 30–33.

Kuo C. C. Y., 1992, 'Thick-film circuit materials', *Gongneng Cailiao* 23(5), 265–269.

Kurihara Y., Takahashi S., Yamada K., Endoh T. and Kanai K., 1991, 'Thick-film resistors for AlN ceramics', *IEEE Trans on Compon, Hybrids and Manufact Technol* 14(1), 199–203.

Lejeune M. and Boilot J. P., 1985, 'Low firing dielectrics based on lead magnesium niobate', *Mater Res Bull* 20(5), 493–499.

Larry J. R., Rosenberg R. M. and Uhler R. O., 1980, 'Thick-film technology: an introduction to the materials', *IEEE Trans on Compon, Hybrids and Manufact Technol* CHMT-3(2), 211–225.

Lin J. C. and Chan J. Y., 1996, 'On the resistance of silver migration in Ag-Pd conductive thick-films under humid environment and applied d.c. field', *Mater Chem Phys* 43(3), 256–265.

Lin J. C. and Chan J. Y., 1997, 'Resistance to silver electrolytic migration for thick-film conductors prepared from mixed and alloy powders of Ag-15Pd and Ag-30Pd, *J Electrochem Soc* 144(5), 1652–1659.

Listkjewicz E. and Kusy A., 1985, 'Computer simulation of thick resistive films as two component percolation systems; segregation of the conducting component', *Thin Solid Films* 130(1–2), 1–15.

Liu Y., Long J., Zhu X. and Liu W., 2011, 'Electrochemical migration characteristics of Ag-plated Cu powders in conductive thick-film', *Adv Mater Res* 146–147, 1070–1074.

Masoero A., Morten B., Prudenziati M. and Stepanescu A., 1990, 'An improved technique of measuring the contact noise in thick-film resistors', *in* A. Ambrozy (ed.), *Noise in Physical Systems*, Proceedings 10th International Conference, Akademia Kiado Budapest, pp. 561–564.

Mleczko K., Zawiślak Z., Stadler A. W., Kolek A., Dziedzic A. *et al.*, 2008, 'Evaluation of conductive-to-resistive layers interaction in thick-film resistors', *Microelectron Reliab* 48(6), 881–885.

Monneraye M., 1978, 'Les encres sérigraphiables en microélectronique hybride: les matériaux et leur comportement', *Acta Electron* 21(4), 263–281.

Morandi M., Morten B., Prudenziati M., Argentino E. and Ruffi M. G, 1991, 'Manganese in ruthenium-based thick-film resistors', *Materials Engineering* 2(3), 421–433.

Morten B. and Prudenziati M., 1983, 'Thermal aging of thick-film resistors', *Hybrid Circuits* 3, 24–26.

© Woodhead Publishing Limited, 2012

Morten B., Sirotti F., Prudenziati M. and Manfredini T, 1994, 'Evolution of ruthenate-based thick-film cermet resistors', *J Phys D: Appl Phys* 27(10), 2227–2235.

Naguib H. M. and MacLaurin B. K., 1979, 'Silver migration and reliability of Pd/Ag conductors in thick-film dielectric crossover structures', *IEEE Trans Comp, Hybrids, Manufact Technol* CHMT-2(2), 196–207.

Nakajima T., Kawakami A. and Tada A., 1983, 'Ohmic contact of conductive silver paste to silicon solar cells', *Intl J Hybrid Microelectron* 6(1), 580–586.

Pešić L., 1988, 'A review of thick-film glaze resistors', *Microelectr J* 19(4), 71–87.

Pike G. E. and Seager C. H., 1977, 'Electrical properties and conduction mechanisms of Ru-based thick-film (cermet) resistors,' *J Appl Phys* 48(12), 5152–5169.

Prudenziati M., 1981. 'Conduction mechanisms in thick-film resistors', *Procedings of 3rd European Hybrid Microelectron Conference Avignon*, pp. 1–10.

Prudenziati M. and Morten, B., 1983, 'Thermal aging and stability of thick-film resistors', *Int J Hybrid Microelectron* 6(1), 96–100.

Prudenziati M., Morten B., Ruffi G., Argentino E. and Iachetti C., 1989a, 'Size effect due to silver diffusion in RuO_2-based resistors', *7th European Hybrid Microelectron Conference*, Hamburg, May.

Prudenziati M., Moro L., Morten B., Sirotti F. and Sardi L., 1989b, 'Ag-based thick-film front metallization of silicon solar cells', *Active and Passive Electr Components* 13(3), 133–150.

Prudenziati M., Morten B., Olumekor L., Moro L. and Tombesi A., 1986. 'Interactions between terminations and thick-film (cermet) resistors: the role of bismuth', *J Phys D: Appl Phys* 19(2), 275–282.

Prudenziati M., Morten B. and Taroni A., 1981/82, 'Characterization of thick-film resistor strain gauges on enamel steel', *Sens Actuators* 2(1), 17–27.

Prudenziati M., Sirotti F., Sacchi M., Morten B., Tombesi A. *et al.*, 1991, 'Size effects in Ru-based thick-film resistors: RuO_2 vs. pyrochlore-based resistors', *Active and Passive Electro Components* 14(3), 163–173.

Rocak D., Belavic D., Hrovat M., Sikula J., Koktavy P. *et al.*, 2001, Low-frequency noise of thick-film resistors as quality and reliability indicator, *Microelectron Reliab* 41(4), 531–542.

Sato K., Watanabe M. and Seino T., 1993, 'Development of thick-film thermal print head for full color video printer', *Int J Microcircuits Electron Pack* 16(2), 145–160.

Schubert G., Fischer B. and Fath P., 2002, 'Formation and nature of Ag thick-film front contacts on crystalline silicon solar cells', *Proceedings of Photovoltaics in Europe Conference*, Rome, pp. 343–346.

Schubert G., Huster F. and Fath P., 2006, 'Physical understanding of printed thick-film front contacts of crysalline Si solar cells – review of existing models and recent developments', *Solar Energy Materials and Solar Cells* 90, 3399–3406.

Seager C. H. and Pike G. E., 1976, 'Electrical field induced changes in thick-film resistors', *Proc Int Microelectronics Symp* ISHM-USA, 115–122.

Sinnadurai N. and Wilson K. J., 1982, 'The aging behavior of commercial thick-film resistors', *IEEE Trans Comp, Hybrids Manufact Technol* CHMT-5(3), 308–317.

Sion R. P., Atkinson J. K. and Turner J. D., 1994, 'A novel model for the temperature characteristic of a thick-film piezoresistive sensor', *Sens Actuators A* 41–42, 460–464.

Sopori B., Mehta V., Rupnowski P., Appel J., Romero M. *et al.*, 2007, 'Fundamental mechanisms in the fire-through contact metallization of Si solar cells: a review', presented at *17th Workshop on Crystalline Silicon Solar Cells and Modules: Materials and Processes*, August 5–8, Vail Cascade Resort, Vail, Colorado USA.

© Woodhead Publishing Limited, 2012

Stanimirovi I., Jevti M. M. and Stanimirovi Z., 2006, 'Performances of conventional thick-film resistors after multiple high-voltage pulse stressing', *Proceedings of 25th International Conference On Microelectronics* (MIEL 2006), Belgrade, Serbia and Montenegro, May 14–17.

Stevens E., Gilbert D. and Ringo J., 1976, 'High-voltage damage and low-frequency noise in thick-film resistors', *IEEE Trans Part, Hybrids, Pack* 12(4), 351–356.

Swartz S. L., 1990, 'Topics in Electronic Ceramics', *IEEE Trans Electr Insul* 25(5), 935–987.

Tamborin M., Piccinini S., Prudenziati M. and Morten B., 1997, 'Piezoresistive properties of RuO_2-based thick-film resistors: the effect of RuO_2 grain size', *Sens Actuators A* 58(2), 159–164.

Thuillier B., Berger S., Boyeaux J. P. and Luagier A., 2000, 'Observation of mechanisms of screen-printed contact formation during heat treatment of multicrystalline silicon solar cells by transmission electron microscopy', in *Proceedings of 28th IEEE PVSC*, Ancorage, p. 411–413.

Tobita T. and Takasago H., 1991, 'New trimming technology of a thick-film resistor by the pulse voltage method', *IEEE Trans Comp, Hybrid Manufact Technol* 14(3), 613–617.

Totokawa M., Yamashita S., Morikawa K., Mitsuoka Y., Tani T. *et al.*, 2009, 'Microanalyses on the RuO_2 particle–glass matrix interface in thick-film resistors with piezoresistive effects', *Intl J Appl Ceram Technol* 6(2), 195–204.

Vest R. W., 1991a, 'A model for sheet resistivity of RuO_2 thick-film resistors', *IEEE Trans Comp, Hybrids, Manufact Technol* 14(2), 396–406.

Vest R. W., 1991b, 'Materials aspects of thick-film technology', *in* C. Buchanan (ed.), *Ceramic Materials for Electronics*, 2nd edn, Marcel Dekker Inc., pp. 435–488.

Vionnet-Menot S., Grimaldi C., Maeder T., Ryser P. and Strässler S., 2005, 'Study of electrical properties of piezoresistive pastes and determination of the electrical transport', *J Eur Ceram Soc* 25(12), 2129–2132.

Walton B., 1975, 'Principles of thick-film materials formulation', *Radio Electron Eng* 45(3), 139–143.

Wang S. F., Dougherty J. P., Huebner W. and Pepin J. G., 1994, 'Silver-palladium thick-film conductors', *J Am Ceram Soc* 77(12), 3051–3072.

Weast, R. C. (ed.) 1987/88, *Handbook of Chemistry and Physics*, 68th edn., CRC Press Inc, Boca Raton, Florida.

Wheeler, J. M., 1985, 'Thick-film conductors and resistors on dielectrics for high reliability applications', *Hybrid Circ* 8, 24–27.

White N., 2006, 'Thick-films', *Springer Handbook of Electronic and Photonic Materials*, Springer, New York, pp. 717–731.

White N. M. and Turner, J. D., 1997, 'Thick-film sensors: past, present and future', *Meas Sci Technol* 8(1), 1–20.

Yang P., Dimos D., Rodriguez M. A., Huang R. F., Dai S. *et al.*, 1999, 'Direct-write precision resistor for ceramic packages', *Mater Res Soc Symp Proc* 542 (Solid Freeform and Additive Fabrication), 159–164.

© Woodhead Publishing Limited, 2012

5

Conduction mechanisms in printed thick-film resistors

C. GRIMALDI, École Polytechnique Fédérale de Lausanne, Switzerland

Abstract: The current theoretical understanding of the electron transport mechanism in thick-film resistors is reviewed and critically discussed in relation to the transport problem for other classes of conductor–insulator composites. The filler concentration and temperature dependencies of transport are analysed in terms of both percolation and tunnelling (i.e. hopping) processes. In particular, this chapter points out that, since inter-particle tunnelling is the predominant mechanism of transport in thick-film resistors, the percolation theory is not well suited to describe the filler concentration dependence of transport, while a hopping-like approach is more physically sound.

Key words: conductor–insulator composites, transport, percolation, tunnelling, hopping.

5.1 Introduction

Thick-film resistors (TFR) are composite systems that typically contain a conductive metallic phase dispersed in an insulating and continuous glass matrix. By borrowing a terminology more pertinent to the physics of fluids, TFR may then be regarded as 'colloidal composites', to be distinguished from the class of granular composites that are formed by mixtures of conducting and insulating particles. Among the important factors influencing the electrical conduction in TFR are the concentration and distribution of conductive particles in the glass matrix, the glass wetting, the diffusion from conductive nanometric particles into the glassy interfaces, the chemical interactions between conductive particles and the glass, and the conditions during the TFR fabrication. Composites based on metallic oxides such as RuO_2, $Bi_2Ru_2O_7$, $Pb_2Ru_2O_6$, dispersed into a glass phase of typically lead borosilicate type, represent the most common TFR systems found in various applications exploiting their quite large change in bulk conductivity when subjected to applied deformation.

The electrical transport properties of TFR have aspects in common with those of other types of conductor–insulator composites. Namely, the conductivity displays a strong dependence upon the volume fraction ϕ of the metallic phase characterized by a sharp increase once a 'critical' value ϕ_c is reached. As a function of the temperature T, the conductivity follows a stretched exponential behaviour at low T, which indicates tunnelling-assisted hopping between the conducting

© Woodhead Publishing Limited, 2012

particles, and which is found in many other classes of composites in the so-called 'dielectric' regime. Furthermore, the rather strong piezoresistive response, i.e. the relative change of the resistivity upon an applied mechanical strain or stress, is comparable to that of polymer-based composites, and is also an indication of a prominently inter-particle tunnelling conduction mechanism.

What makes TFR rather peculiar among the different classes of composites is their marked non-homogeneous dispersion of the conducting phase into the insulating continuum matrix. TFR indeed are fabricated starting from glassy grains whose mean size prior to the thermal processing (firing) is typically of the order of 1–5 μm, which is much larger than that of the conducting particles (from 10 to about 500 nm). The large insulating grains prevent a homogeneous dispersion of the conducting particles in the composites, and the resulting microstructure (commonly referred to as segregated or, less often, cellular) is characterized by large regions depleted of conducting particles, surrounded by areas with a much higher concentration of the conducting phase. An example of this segregated microstructure is shown in Fig. 5.1 for a RuO_2-based TFR (Vionnet-Menot, 2005).

As will be discussed in more detail in the remainder of this chapter, the main effect of segregation is that of reducing the 'critical' volume fraction ϕ_c below which the composite conductivity is negligible compared to that at larger concentrations. For example, for the TFR of Fig. 5.1, the value of ϕ_c estimated from conductivity measurements was found to be $\phi_c \approx 0.05$ (Vionnet-Menot *et al.*, 2005), and even lower values have been reported in the literature (for a short review on ϕ_c values in TFR see: Dziedzic, 2001). These values of ϕ_c must be compared with those resulting from homogeneous dispersions of impenetrable spheres in the continuum, for which the percolation threshold coincides with the random close packed value 0.64, or with close-packed mixtures of conducting and insulating spheres, for which $\phi_c \approx 0.16$ (Scher and Zallen,1970). By varying the relative sizes of the conducting and insulating particles it has been shown that ϕ_c can be systematically lowered when finer conducting particles are employed in the composite (Carcia *et al*., 1982; Tamborin *et al*., 1997). Conversely, TFR fabricated under stirring displays larger ϕ_c values than the unstirred ones (Pflieger *et al*., 2009), due to the more homogeneous dispersion of the conducting fillers under stirring conditions.

Another peculiarity of TFR is of historical nature. Indeed, by fitting the conductivity σ versus ϕ data with the power–law relation:

$$\sigma \approx \sigma_0 (\phi - \phi_c)^t, \qquad [5.1]$$

which is predicted by percolation theory (Kirkpatrick, 1973; Sahimi, 2003; Stauffer and Aharoni, 1992), Ru-based TFR were among the first materials showing deviations from the universal value $t \approx 2$ of the transport exponent (Pike, 1978). This was expected to hold true for all three-dimensional percolating systems. Subsequent studies have confirmed the non-universality of the transport

© Woodhead Publishing Limited, 2012

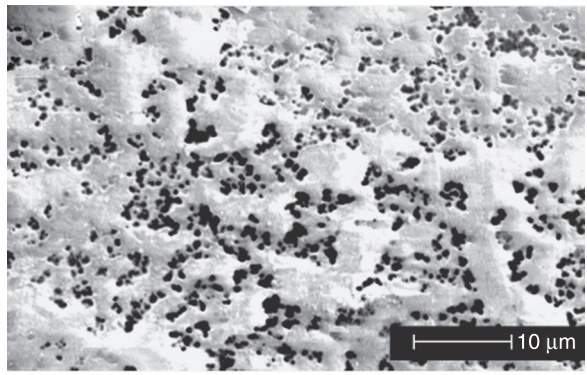

(a)

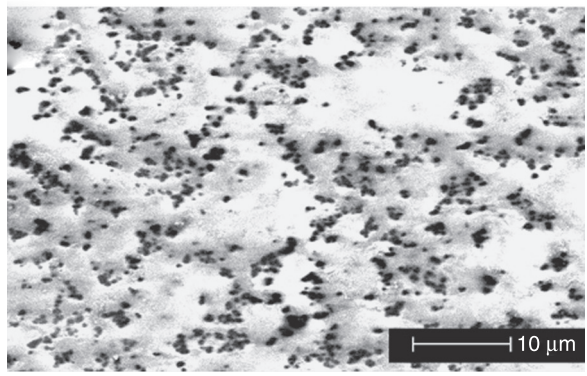

(b)

5.1 Scanning electron microscopy images of the surfaces of RuO_2-glass TFR with RuO_2 volume fraction $\phi = 0.08$ and nominal RuO_2 grain size of 40 nm for different firing temperatures: (a) 550°C and (b) 600°C (Vionnet-Menot *et al.,* 2005).

exponent for TFR as well as for many other types of composites (see Fig. 5.2 for a collection of data), and no definite explanation has yet been proposed to account for it (for a short review see: Vionnet-Menot *et al.*, 2005).

5.2 Current understanding of the conduction mechanism in thick-film resistors

As already pointed out in the introduction, TFR may be regarded as belonging to the general class of colloidal composite, where the conducting particles are dispersed into a continuous insulating matrix. Thermal processing in the fabrication of TFR has the primary effect of softening the glassy phase so as to induce wetting of the conducting particles. As a result, there is usually no physical

© Woodhead Publishing Limited, 2012

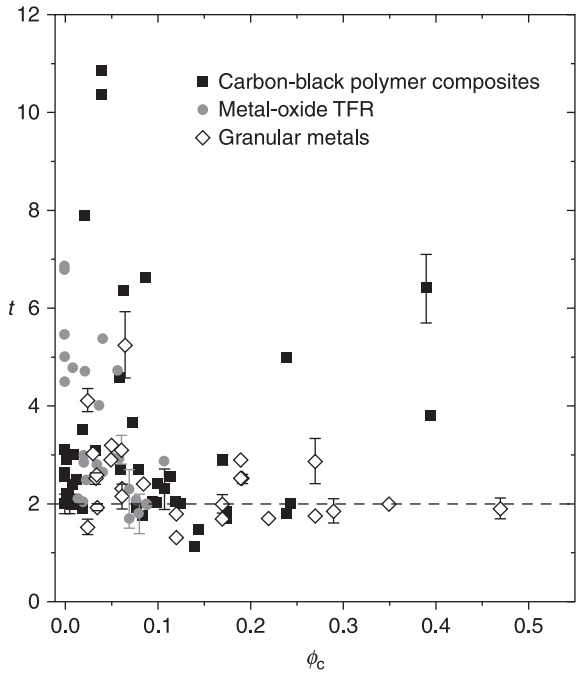

5.2 Collection of the transport critical exponent *t* as a function of the critical volume fraction ϕ_c for various conductor–insulator composites. For the complete list of references from which the data have been collected see Vionnet-Menot *et al.* (2005).

contact between adjacent conducting fillers, which instead are separated from each other by a thin glassy layer (Chiang *et al*., 1994). In this situation, electron tunnelling processes dominate the inter-particle conductance g_{ij} which, if for the moment we neglect charging energy effects, is given by:

$$g_{ij} = g_0 e^{-2\delta_{ij}/\xi}, \qquad [5.2]$$

where g_0 is a constant 'contact' conductance, ξ is the characteristic tunnelling decay length and δ_{ij} is the minimal distance between the surfaces of two particles i and j. For spherical particles of diameter D, $\delta_{ij} = r_{ij} - D$, where r_{ij} is the centre-to-centre distance. In principle, Eq. [5.2] applies to two-phase composites with sharp interfaces separating the conducting and insulating phases, and the tunnelling factor ξ depends on the potential barrier height provided by the glass. However, chemical interactions between the two phases may set in, as is generally the case when high firing temperatures are used in the fabrication process, giving rise to chemical species that can alter the local transport properties (Adachi and Kuno, 1997; Hrovat *et al*., 2001). For example, in ruthenate-based TFR, the interaction with the glass phase may lead to the formation of

© Woodhead Publishing Limited, 2012

RuO_2 particles, possibly resulting from a decomposition-precipitation process. Furthermore, when the conducting grains are made of particle agglomerates, the firing process may disperse a fraction of particles of the aggregate, leading to less sharp conductor–insulator interfaces. In these cases, the resulting changes in the local chemical and physical properties can be tentatively described by considering the conducting particles as coated by a third, thin, phase that changes the local charge distribution. In this case, the tunnelling decay length ξ appearing in Eq. [5.2] is an effective one that takes into account the changes in the local dielectric constant.

In the following, we shall review the current theoretical understanding of the filler concentration and temperature dependencies of transport in TFR in order to assess the role played by various important microscopic factors in the overall conductivity behaviour, and to tentatively provide a theoretical framework for the understanding of the transport properties in TFR as a particular class of resistive colloidal composites.

5.2.1 Filler concentration dependence of the conductivity: percolation interpretation

The theoretical framework that has guided much of the understanding of the conducting filler dependencies of the conductivity in TFR, in particular, and in conductor–insulator composites, in general, is based on the concept of percolation (Kirkpatrick, 1973; Sahimi, 2003; Stauffer and Aharoni, 1992). In this picture, the conducting particles are either electrically connected (with some nonzero inter-particle conductance g_{ij}) or disconnected ($g_{ij} = 0$). For sufficiently low values of the conducting particle volume fraction ϕ ($\phi = \rho v$, where ρ is the particle density and v is the volume of a single particle), the connected particles form only isolated clusters in the system which prevent the flow of the current from one side of the sample to the opposite side. In this situation, the macroscopic conductivity σ is either zero or equal to the intrinsic conductivity of the insulating phase. As ϕ increases, new connections are added until, at a critical value ϕ_c (i.e. the percolation threshold), a cluster of connected particles spanning the entire sample first forms, giving rise to a sharp increase of σ. As more connections are added for $\phi > \phi_c$, percolation theory predicts that the conductivity follows in the vicinity of ϕ_c the power–law behaviour of Eq. [5.1], where σ_0 is a pre-factor independent of ϕ and t is the dc critical exponent which has the universal value $t \approx 2$ for three-dimensional systems (Sahimi, 2003; Stauffer and Aharoni, 1992). Equation [5.1] and its generalization, which includes the effect of a finite conductivity of the insulating matrix, has been applied to several classes of conductor–insulator composites and represents, besides its fundamental signification, a useful tool for characterizing the filler dependencies of real composites. Indeed, apart from the specific value of the exponent t, which will be discussed in more detail below, the most important ingredient of Eq. [5.1] is the explicit dependence of σ on the percolation threshold

© Woodhead Publishing Limited, 2012

ϕ_c. Its specific value depends on several factors such as the shape of the conducting fillers, their orientation (in the case of anisotropic filler shapes) and their arrangement or distribution in the composite. Hence the value of ϕ_c extracted from fits to Eq. [5.1] of experimental σ vs. ϕ data gives important insights on the microscopic properties of the composite.

There are two main theoretical approaches in the study of charge conduction in percolating systems. In the lattice percolation approach, the conducting fillers occupy a fraction p of the sites of a regular or topologically disordered lattice (site percolation model), while the remaining fraction $1 - p$ of sites is occupied by the insulating particles. The conductance between two neighbouring sites is non-zero only if both of such sites are occupied by the conducting particles. In the bond percolation variant, the percolating elements are the bonds connecting two given (neighbouring) lattice sites. The percolation threshold values p_c arising from these lattice models depend on the lattice topology and dimensionality, and have relevance for composite with granular microstructure.

In the second approach to percolation, the positions of the conducting elements are not restricted to occupying the sites of a particular lattice, but rather are continuous variables that can span the entire sample volume. Compared to the lattice percolation construction, this continuum percolation approach therefore constitutes a better description of percolation in colloidal composites. Within this framework, the inter-particle tunnelling mechanism of Eq. [5.2] is taken into account by treating the conducting fillers as core–shell objects, where the impenetrable hard core represents the physical particle and the thickness of the concentric penetrable shell is basically identified with the tunnelling decay length ξ (Berhan and Sastry, 2007; He and Ekere, 2004; Jing *et al*., 2000; Wang and Ogale, 1993). In light of this tunnelling-percolation model, two spherical fillers are considered electrically connected only if their penetrable shells overlap, so that the resulting percolation threshold scales by a factor approximately proportional to $D^3/(D + \xi)^3$, where D is the mean diameter of the conducting filler (Heyes *et al*., 2006). Although the specific values of ξ depend on the characteristics of the insulating phase, they typically fall between a fraction and a few nanometers, so that the reduction factor $D^3/(D + \xi)^3$ affects prevalently composites with fillers of nanometric sizes.

As already pointed out in the introduction, typical TFR composites have a segregated microstructure that must be taken into consideration in order to understand their low values of ϕ_c. Qualitatively, the reduction of ϕ_c can be understood by realizing that, in segregated composites, the conducting phase is constrained to fill the space between the large insulating regions, and that therefore, compared to a homogeneous dispersion, lower amounts of conducting fillers are needed to establish percolation. On a more quantitative level, however, the study of the percolation problem in continuum segregated systems has been pursued at a much lower rate than the more classical percolation problem for homogeneous dispersions. It is illuminating in this respect to realize that, even though the first

© Woodhead Publishing Limited, 2012

work on segregated systems was published in 1971 (Malliaris and Turner, 1971), the first Monte Carlo simulations on continuum segregated percolation appeared only in 2002 and in 2004 for two- and three-dimensional cases, respectively (He and Ekere, 2002, 2004). The literature on the subject, indeed, consists almost completely of lattice representations and of discrete approaches to the problem of segregation.

For example in the first model of 1971 (Malliaris and Turner, 1971), formulated to explain the low percolation thresholds of polyethylene–nickel aggregates, the insulating phase was assimilated to large spheres occupying the sites of a cubic lattice and coated with much smaller conducting spheres. Subsequent refinements of this model were aimed to adjust the far too low values of the percolation threshold compared to the experiments by allowing the conducting particles to occupy preferably the interstices between the large insulating spheres (Kusy, 1977). Other lattice models were defined by using cubes and spheres of different sizes to represent respectively the insulating and conducting phases (Kubový, 1986; Pike, 1978; Youngs, 2003), with one or more layers separating the faces of two nearest-neighbour insulating cubes (Lebovka *et al*., 2006), or small circles occupying the edges of a honeycomb lattice for the description of a two-dimensional segregated structure (Kim *et al*., 1998). Similar lattice constructions were presented in Grimaldi *et al*. (2003), where conducting small spheres were allowed to occupy random positions along the edges of a cubic lattice.

A semi-continuum approach was described in Kusy (1997), where sites of a cubic lattice were occupied by conducing spheres of a given diameter, and a segregated structure was generated by removing large spherical volumes randomly according to an overlapping spheres model. At the limit of the zero conducting particle diameter, the conducting phase can be regarded as a continuum, and the segregated construction reduces to the random–void model (Feng *et al.*, 1987). At this limit, the volume fraction at the percolation threshold can be obtained via an exact mapping to a random bond model, where the edges arise from a Voronoi tessellation of the original continuum random–void model. Apart from this particular limit, continuum segregated percolation with finite size ratios of the two species of objects has been considered in He and Ekere (2002, 2004) for a random packing of impenetrable disks and spheres.

All these models provide a general understanding of the role of segregation in lowering the percolation threshold, and so can account for the values of ϕ_c extracted from the fits of the experimental σ versus ϕ curves to the percolating behaviour of Eq. [5.1]. However, as already noticed above, the values of the transport exponent t extracted from the same fits result to be generally larger or much larger than the universal value $t \approx 2$ expected from percolation theory (see Fig. 5.2).

This incongruence is not limited to TFR composites, but it is also shared by other classes of conductor–insulator materials, and its origin has been the subject of several theoretical studies (for a short review, see Vionnet-Menot, 2005). In Heaney (1995) it was argued that long-range interactions could drive the system

© Woodhead Publishing Limited, 2012

towards the mean-field regime for which $t = t_{mf} = 3$. This interpretation cannot however explain the observation of critical exponents much larger than t_{mf}, such as those of carbon–polymer composites or TFR that display values of t as high as $t = 5 - 10$. Feng, Halperin and Sen (Feng *et al*., 1987) introduced the random–void model of continuum percolation where current flows through a conducting medium embedding insulating spheres placed at random, thus resembling the situation for an extremely segregated composite (Kusy, 1997). By using an earlier result (Kogut and Straley, 1979) they were able to show that for this model d.c. transport is described by a universality class different from that of the standard percolation model on a lattice. However, the resulting critical exponent was found to be $t \approx 2.4$ for three-dimensional systems, which is again a value too small to account for the experimental results.

Within a tunnelling–percolation approach, Balberg (1987) proposed a model of transport non-universality by explicitly taking into account the exponential tunnelling decay of Eq. [5.2] between particles with mutual distances lower than a given cut-off. Within this picture, if the distribution function of the nearest-neighbour inter-particle distances decays much more slowly than the tunnelling decay length ξ, then the critical transport exponent t becomes dependent on the mean inter-particle distance and in principle has no upper bound. The appeal of this model resides in the fact that it considers explicitly the tunnelling inter-particle processes and the statistical properties of the conducting filler distribution in the composite. However, more detailed studies of this model have also evidenced that, actually, very close to the percolation threshold the transport exponent is expected to be universal, while away from ϕ_c it acquires a strong filler concentration dependence such that $t(\phi) > 2$ (Grimaldi and Balberg, 2006). In other words, the critical region in a tunnelling–percolation model is shrunk to a very small region around ϕ_c, so that the observed non-universality reported in Fig. 5.2 could arise when the composite conductivity data are fitted to Eq. [5.1] by forcing the exponent t to be independent of ϕ outside the region of criticality. Recent Monte-Carlo calculations on homogeneous dispersions of core–shell particles with the tunnelling processes of Eq. [5.2] have evidenced that this 'apparent' non-universality is a rather general feature, and that it is not limited to segregated composites (Johner *et al*., 2008). From a practical point of view, however, the low values of ϕ_c in segregated systems such as TFR enhance the possibility of measuring large 'apparent' t values because of the difficulty of sampling the conductivity behaviour in the vicinity of ϕ_c when $\phi_c << 1$.

5.2.2 Filler concentration dependence of the conductivity: the global tunnelling network approach

As pointed out above, in TFR as well as in other classes of colloidal composites in the dielectric regime, the conducting particles are embedded in a continuous insulating matrix and they do not physically touch each other, with the results that

© Woodhead Publishing Limited, 2012

the electrical connectedness is established through tunnelling between the conducting filler particles. In this situation, the basic assumptions of percolation theory are, in principle, at odds with the inter-particle tunnelling mechanism. Indeed, while percolation requires the introduction of some sharp cut-off in the inter-particle conductances, i.e. the particles are either connected or disconnected (Sahimi, 2003; Stauffer and Aharoni, 1992), the tunnelling of Eq. [5.2] between particles is a continuous function of inter-particle distances and, hence, it does not imply any sharp cut-off or threshold.

Quite surprisingly, this fundamental incompatibility has hardly been discussed in the literature and basically all the measured conductivity dependencies on the fractional volume content of the conducting phase, $\sigma(\phi)$, have been interpreted in terms of Eq. [5.1] assuming the 'classical' percolation behaviour. Even more surprising is also the fact that, instead, the temperature dependence of composites in the dielectric regime is commonly described by allowing tunnelling with particles far away from each other (i.e. hopping beyond the first nearest-neighbours), which implicitly assumes that no sharp cut-off exists in the inter-particle conductance. Hence, besides a few cases (e.g. Hu and Shklovskii, 2006; Levin, 1986), basically in all the scientific literature the filler concentration and the temperature dependences are interpreted in terms of, respectively, percolation and hopping processes, which are two mutually incompatible descriptions of the transport mechanisms in composites.

A formulation that goes beyond the percolation description for $\sigma(\phi)$ and is therefore compatible with the tunnelling (or hopping) nature of the microscopic transport processes in dielectric composites is the global tunnelling network (GTN) model, in which each conducting filler particle is connected to all others via the tunnelling conductance of Eq. [5.1], and so without imposing the restrictive hypothesis on which the usual core–shell model is based (Ambrosetti *et al*., 2009, 2010a, 2010b). For a system composed of N conducting particles dispersed into a continuous insulating matrix, the GTN model is equivalent to a weighted disordered network with N nodes, each with coordination number N–1. However, contrary to the usual models of weighted networks (Li *et al*., 2007), each link weight is not uncorrelated but it is given by Eq. [5.2], which depends on the particular arrangement of the conducting fillers in the composites. This characteristic of the model permits one in principle to describe the ϕ dependence of the conductivity for many different classes of composites with different statistical properties of the microstructures.

When applied to equilibrium dispersions of (impenetrable) particles with different shapes, ranging from spherical ones to rod-like and plate-like geometries, so to simulate systems of recent interest such as nanotubes nanofibres and nanosheets composites (Ambrosetti *et al.*, 2010a), the GTN model is able to reproduce the strong reduction for decreasing the volume fraction ϕ of the conductivity, which is a direct consequence of the fact that as ϕ is reduced the inter-particle distances get larger, leading in turn to a reduction of the local

© Woodhead Publishing Limited, 2012

inter-particle conduction g_{ij} of Eq. [5.2]. Furthermore, such reduction depends strongly on the shape of the conducting fillers in such a way that stronger filler shape anisotropies entail conductivity drops for lower values of ϕ, as commonly observed in real composite materials.

Another important point of the GTN model applied to such colloidal dispersions is that, by construction, there is not an imposed cut-off and so the system does not display a true percolation threshold. Although at first sight this appears to be in contradiction with the observed behaviour, one must recognize that actually in real composites the lowest measured conductivity σ_{min} is limited by either the experimental setup or by the intrinsic (prevalently of ionic origin) conductivity of the insulating matrix. Hence, in the present picture ϕ_c can be identified with the value of the volume fraction such that $\sigma(\phi_c) \approx \sigma_{min}$, which represents a (more or less smooth) crossover between the region at $\phi > \phi_c$, where σ is dominated by inter-particle tunnelling and $\phi < \phi_c$, where the transport is prevalently sustained only by the insulating phase. This interpretation represents a radical change in perspective with respect to the classical percolation picture, which naturally explains the observed shift of ϕ_c upon the change of σ_{min} (Pflieger *et al*., 2009).

Although for the case of colloidal dispersion the tunnelling network conductivity does not follow the percolation-like behaviour of Eq. [5.1], concepts and quantities pertinent to percolation theory are nevertheless very effective and useful in describing the filler dependencies of transport. Indeed, the ϕ-dependence of the conductivity of colloidal composites can be very well approximated by the critical path (CP) approximation, which was originally introduced to study the temperature dependence in amorphous semiconductors (Ambegaokar *et al*., 1971). When applied to conducting colloidal dispersions, the CP approximation states that the conductivity behaviour is well captured by:

$$\sigma = \sigma_0 e^{-2\delta_c(\phi)/\zeta}, \qquad [5.3]$$

where, for a given ϕ, $\delta_c(\phi)$ (which depends also on the particle size and anisotropy) is the minimum value of δ such that a cluster of connected core–shell particles with penetrable shell thickness $\delta/2$ spans the sample. The study of how the critical distance δ_c depends on ϕ and on the geometrical characteristics of the fillers has permitted us to identify approximate but yet accurate formulas for δ_c (and consequently for σ through Eq. [5.3]), valid for many regimes of interests of colloids with spherical as well as rod-like and plate-like particles. By reinterpreting the many published experimental results on nanospheres, nanotubes, nanofibres and nanosheets in terms of δ_c, it has been possible to extract the values of the tunnelling decay length ξ, which has been found to fall between 0.1 nm and 10 nm, in accord therefore with the expected value range (Ambrosetti *et al*., 2010a).

In order to describe TFR composites, or more generally colloidal systems in the segregated regime, the GTN model has been recently generalized to non-homogeneous dispersions of conducting fillers (Nigro *et al*., 2011). A realistic model of a segregated conductor–insulator composite is schematically illustrated

© Woodhead Publishing Limited, 2012

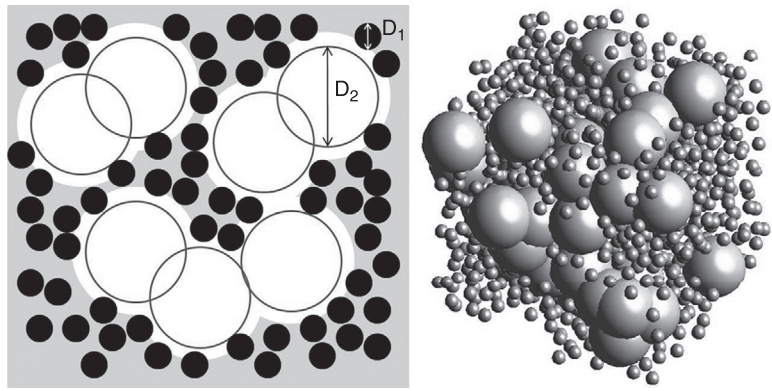

5.3 (a) Schematic representation of a segregated dispersion of conducting particles in the continuum. The insulating (conducting) particles are represented by open (filled) circles of diameter D_2 (D_1). (b) Example of a segregated distribution for $D_2/D_1 = 4$ generated from Monte Carlo.

in Fig. 5.3, where the spherical particles of diameter D_2 represent the insulating inclusions (e.g. the glassy frit particles in RuO_2 TFR), while the conducting particles are modelled as hard spheres of diameter D_1. The two kinds of particles are mutually impenetrable and, furthermore, the D_2 spheres are assumed to penetrate each other in order to simulate sintering and softening of the insulating grains (Johner *et al*., 2009). Typically, as in RuO_2 TFR composites, D_2 is as large as a few micrometres while D_1 ranges from tens to hundreds of nanometres, so that the regime $D_2 >> D_1$ is the one of practical interest.

The overall conductivity arising from the segregated system described above is obtained by solving numerically the tunnelling network equations applied to the subset of D_1 particles in the composite. The results are presented in Fig. 5.4(a), where the conductivity σ (symbols) is plotted as a function of the concentration ϕ_1 of the conducting particles for $D_2/D_1 = 8$ and $D_1/\xi = 50$. In the figure, the different sets of data have been obtained by changing the concentration ϕ_2 of the insulating spheres, which, for fixed D_2/D_1, is equivalent to changing the degree of segregation in the model composite. The reduction in σ for decreasing ϕ_1, which is a direct consequence of the fact that as ϕ_1 is reduced the inter-particle distances δ_{ij} in Eq. [5.2] get larger, is strongly mitigated by the segregation which, as will be clarified below, tends instead to decrease δ_{ij}. One has therefore that, for fixed tunnelling decay length ξ, as the segregation (i.e. ϕ_2) is enhanced, the threshold value of ϕ_1 required to achieve a given σ decreases considerably. By combining this result with the presence of a lower measurable conductivity σ_{min}, identified by (for example) the ionic conductivity of the glassy matrix, one obtains that more segregated systems entail lower values of ϕ_c, in agreement with the observed trends.

© Woodhead Publishing Limited, 2012

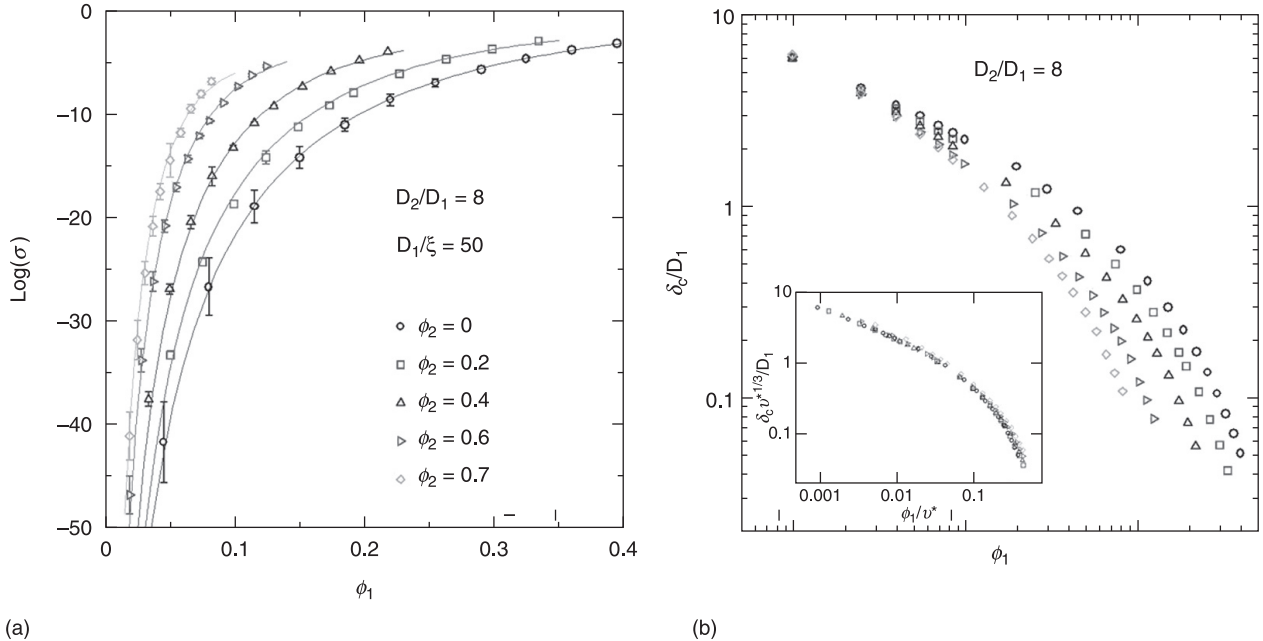

5.4 (a) Calculated conductivity (symbols) as a function of the volume fraction f1 of the conducting spheres with diameter D_1 for $D_1/\xi = 50$ and for different values of the volume fraction ϕ_2 of the insulating spheres with diameter $D_2 = 8D_1$. The solid lines are fits with Eqs. (3) and (4). (b) Critical distance δ_c dependence on ϕ_1 for the same parameter values of (a). Inset: the same data plotted according to the scaling relation of Eq. [5.4].

© Woodhead Publishing Limited, 2012

The numerical results of Fig. 5.4(a) find a straightforward interpretation by employing the CP approximation of Eq. [5.3]. Indeed, as shown in Fig. 5.4(b) for the same parameters values of (a), the calculated critical tunnelling distances δ_c decrease as the degree of segregation is enhanced. This decrease can be understood by noticing, as illustrated in Fig. 5.3, that the main effect of the large insulating spheres is that of confining the conducting particles within the volume left over from the insulating D_2 spheres, thereby reducing the mutual distances δ_{ij}, and so δ_c, of the conducting fillers.

This reasoning can be put in more quantitative terms by introducing the available volume fraction υ^*, which is defined as the ratio between the volume, which can be spanned by the centres of the conducting D_1 spheres (i.e.: the gray region in Fig. 5.3(a)), and the total volume of the system. For the particular model of segregation in Fig. 5.3, the available volume fraction reduces to $\upsilon^* = (1-\phi_2)^{(1 + D_1/D_2)3}$ (Johner *et al.*, 2009; Nigro *et al.*, 2011), but it can be defined also for other kinds of segregation (like those resulting from non-spherical, polydispersed and semipenetrable insulating particles, for example). By assuming that the only relevant variable for describing segregation is υ^*, and that consequently the critical distance for a segregated system is a function of only ϕ_1 and υ^*, then it appears rather natural to argue that the critical distance $\delta_c(\phi_1,\upsilon^*)$ for $\upsilon^* < 1$ is proportional to that of a homogeneous system at the effective concentration ϕ_1/υ^*, i.e. $\delta_c(\phi_1/\upsilon^*,1)$. From dimensional considerations one therefore obtains that:

$$\delta_c(\phi_1,\upsilon^*) = (\upsilon^*)^{-1/3\delta_c}(\phi_1|\upsilon^*,1), \qquad [5.4]$$

which, as shown in the inset of Fig. 5.4(b), gives a nearly perfect collapse of all the δ_c data for different ϕ_2 values into a single curve. Thus, from Eqs. [5.3] and [5.4], the full ϕ_1 dependence of the calculated σ of Fig. 5.4(a) can be expressed in terms of the critical distance of a corresponding homogeneous system. This is illustrated by the solid lines in Fig. 5.4(a), which have been obtained by using in Eq. [5.4] the fitting formula for $\delta_c(x,1)$ given in Ambrosetti *et al*. (2009).

The procedure described above can be used to reinterpret the filler concentration dependence of the conductivity in real segregated composites, in the same spirit as what has been previously done for homogeneous conductor–insulator systems. In order to illustrate how the theory applies to real composites, let us consider the conductivity data of RuO_2-based TFR, which were already reported in Vionnet-Menot *et al*. (2005). In particular, two series of samples were constituted by RuO_2 conducting particles of mean sizes $D_1 \sim 40$ nm and $D_1 \sim 100$ nm, dispersed in a borosilicate glass. The glassy grains prior to thermal processing (firing) had an average size of about 3 μm, so that for both series of composites $D_2/D_1 >> 1$. The two series of samples were fired following identical thermal cycles so that, in principle, they differ only in the mean size D_1 of the conducting particles. It should be noted, however, that although the finer RuO_2 powders were constituted by nearly spherical and mono-dispersed particles, the series of samples with

© Woodhead Publishing Limited, 2012

coarser powders ($D_1 \sim 100$ nm) had actually rather dispersed particle sizes, with less regular shapes. The measured conductivity as a function of RuO_2 volume fraction ϕ_1 is plotted in Fig. 5.5(a) for both series of TFR composites. In Vionnet-Menot *et al*. (2005) these same data were interpreted in the framework of percolation theory and were fitted with the power–law relation of Eq. [5.1]. The resulting low percolation threshold values, $\phi_c \sim 0.07$–0.05, were found to be consistent with the segregated distribution of the RuO_2 conducting phase observed in the microstructure, while the large transport exponent values, $t \sim 3$–4, were concluded to arise from the non-universality of the critical behaviour as predicted by the tunnelling–percolation model of Balberg (1987) discussed above. Here, an alternative interpretation of these data based on the GTN theory is offered which, as explained in this chapter, is more justified on physical grounds than the percolation-based one of Vionnet-Menot *et al*. (2005).

Let us start by re-plotting the conductivity data of Fig. 5.5(a) in terms of the critical distance $\delta_c(\phi_1,\upsilon^*)$ by using the scaling relation of Eq. [5.4] with the functional form of $\delta_c(\phi_1/\upsilon^*,1)$ published in Ambrosetti *et al*. (2009). The available volume fraction υ^* is treated as an adjustable parameter. The resulting $\ln(\sigma)$ vs δ_c plots for two different values of υ^* are shown in Fig. 5.5(b) and Fig. 5.5(c) for the

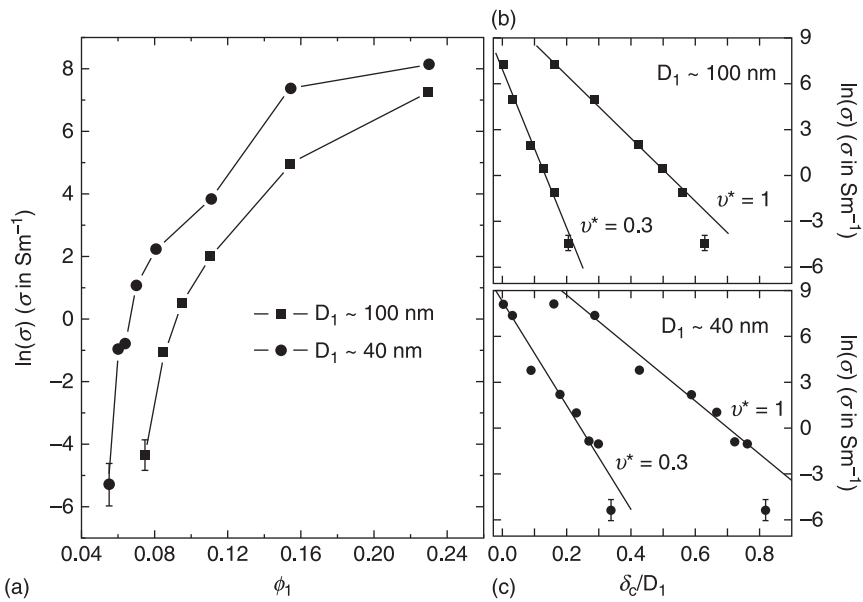

5.5 (a) Measured conductivity data for two series of RuO_2-based TFR as a function of RuO_2 volume fraction ϕ_1 (Vionnet-Menot *et al.*, 2005). The same data are re-plotted as a function of the corresponding critical distance δ_c for (b) $D_1 \sim 100$ nm and (c) $D_1 \sim 40$ nm for two different values of the available volume fraction υ^*. The solid lines in the figure have been obtained by fitting the data to Eq. [5.5].

© Woodhead Publishing Limited, 2012

$D_1 \sim 40$ nm and $D_1 \sim 100$ nm samples, respectively. In both cases, the data follow approximately a linear relation that can be fitted to:

$$\ln(\sigma) = \frac{2}{\xi}\delta_c + \ln(\sigma_0) \qquad [5.5]$$

which is obtained by taking the natural logarithm of both sides of the CP Eq. [5.3]. From Eq. [5.5], the slope $2/\xi$ directly gives the value of the tunnelling decay length independently of the specific σ_0 value used to fit the data. As apparent from the fits in Fig. 5.5(b) and Fig. 5.5(c), lower values of υ^* imply lower values of ξ (i.e. the slopes are larger). This is most clearly seen in Fig. 5.6 where the υ^* dependence of the so-obtained ξ values is plotted for both series of samples. Starting from the homogeneous limit at $\upsilon^* = 1$, the tunnelling decay length ξ of the $D_1 \sim 100$ nm series decreases by a factor of five when the available volume fraction is lowered to the minimum value $\upsilon^* = 0.2$ for which a fit Eq. [5.5] was possible, while the $D_1 \sim 40$ nm case displays a weaker decrease in the same range of υ^* due to the smaller RuO_2 grain size. By realizing that the tunnelling decay length should be independent of the size D_1 of the conducting particles, while the specific υ^* value could be different for the two series of composites, then ξ must be fall between the two horizontal dashed lines at 4.6 nm and 2.1 nm in Fig. 5.6. However, since the microstructure of both series of composites

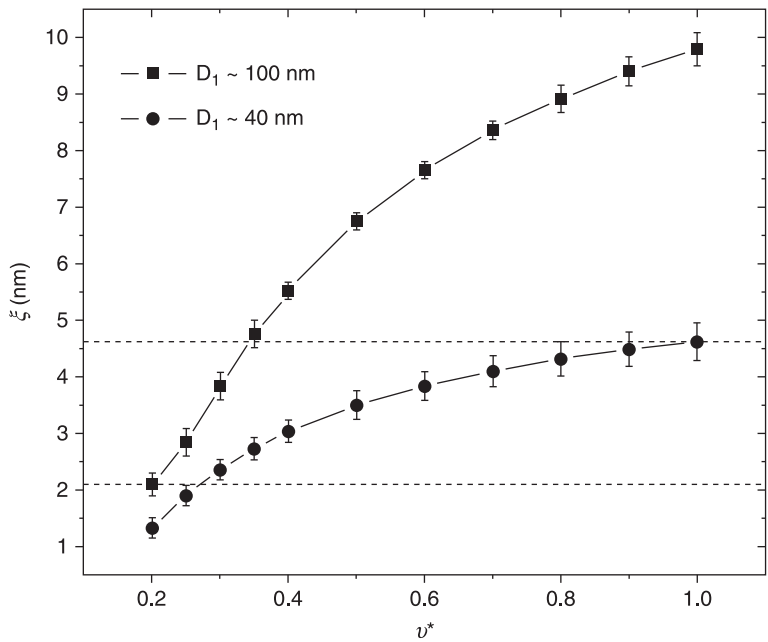

5.6 Values of the tunnelling decay distance ξ as a function of the available volume fraction υ^* extracted as explained in the text for the two series of sample in Fig. 5.5.

© Woodhead Publishing Limited, 2012

displays a marked segregated dispersion (Vionnet-Menot *et al*., 2005) then υ^* should be sensibly smaller than the unity, suggesting that the lower limit $\xi \sim 2\,\text{nm}$ is a more reliable estimate for ξ. This value is fully comparable to those extracted from other conductor–insulator composites (Ambrosetti *et al*., 2009, 2010a) and, specifically, agrees well with the results of microscopic investigations of TFR composites (Chiang *et al*., 1994).

The application of the GTN method to real segregated composites described above clarifies that the role of segregation is basically that of reducing the mean inter-particle distances, so that realistic values of ξ in the nanometre range can account for conducting particles' contribution to σ observed for very small ϕ values. From a more general perspective, the above example indicates that, for the ultimate understanding of the conducting filler dependencies of transport, a primary role is played by the statistical properties of the microstructure.

Before concluding this section, it is useful to discuss briefly what the GTN model predicts for the piezoresistive response, which is commonly exploited in Ru-based TFR for pressure and force sensing applications. The piezoresistive response Γ is the relative change of the resistivity upon the application of a mechanical strain ε. Without loss of generality, we assume that the same value of strain ε is applied to all the orthogonal directions x, y and z. From the CP formula of Eq. [5.3] one has therefore:

$$\Gamma = \frac{\partial \ln(\sigma^{-1})}{\partial \varepsilon} = \ln(\sigma_0 / \sigma)\frac{\partial \ln(\delta_c)}{\partial \varepsilon}. \qquad [5.6]$$

For fillers having the same elastic properties of the insulating matrix, the last term in Eq. [5.6] is unity, while for elastically rigid fillers this term can be rewritten as $[\partial \ln(\delta_c)/\partial \ln(\phi)]\, \partial \ln(\phi)/\partial \varepsilon$. Since $\partial \ln(\phi)/\partial \varepsilon = -1$ and given that, as ∂ can be inferred from Fig. 5.4, $\partial \ln(\delta_c)/\partial \ln(\phi)$ has a weak dependence on ϕ, the expected dominant dependence of Γ is thus of the form $\Gamma \propto \ln(1/\sigma)$, which agrees well with the behaviours observed in TFR composites (Tamborin *et al*., 1997). The $\Gamma \propto \ln(1/\sigma)$ dependence predicted by the GTN model contrasts with the power–law divergence at ϕ_c of Carcia *et al.* (1983) obtained from a percolation approach, but is consistent with the logarithmic behaviour $\Gamma \propto \ln(1/(\phi - \phi_c))$ reported in Vionnet-Menot *et al*. (2005).

5.2.3 Temperature dependence of the conductivity

As a function of the temperature T, the conductivity of TFR can often be characterized by two separate regimes at low and high temperatures. At low temperatures, resistivity ρ displays a negative temperature coefficient (i.e.: $d\rho/dT < 0$) which, as will be discussed in more detail below, is a signature of hopping-assisted transport, while at sufficiently high temperatures ρ has a 'metal-like' behaviour, i.e. it increases with T. The crossover between the two regimes is identified by a characteristic T_{min}, which is the temperature at which ρ has a minimum. In order to account for this behaviour, various explanations have been proposed which, although they basically

© Woodhead Publishing Limited, 2012

agree on the hopping-like origin of the $T < T_{min}$ regime, differ substantially in what concerns the large T behaviour at $T > T_{min}$. For example, Forlani and Prudenziati (1976) studied the effect of the temperature dependence of the prefactor σ_0 appearing in the hopping conductivity formula (see eq. [5.7] below) and noticed that it can provide a possible cause for the change of sign of the temperature coefficient. Pike and Seager (1977) interpreted the positive temperature coefficient as orginating from diffusive transport of the conductive grains. The $d\rho/dT > 0$ regime has also been explained in terms of the thermal expansion affecting the inter-particle tunnelling distances (Kubový, 1995), in analogy to what is observed in polymer composites (Costa *et al.*, 2011), or by invoking the temperature-induced strain due to the mismatch between the temperature expansion coefficients of the resistor and the substrate (Fawcett and Hill, 2000; Sion *et al*., 1994).

In order to explain the change in sign of the temperature coefficient of resistance (*TCR*)in TFR, and so the resistance minimum at T_{min}, two important points have to be taken into consideration. First, this temperature behaviour of transport is not unique to TFR, but it is also observed in other kinds of conductor–insulator composites, like co-sputtered granular metals (McAlister *et al.*, 1985; Peng *et al*., 1999; Savvides *et al.*, 1982), for example, or some polymer composites (Carmona and Mouney, 1992; Celzard *et al.*, 1998; Jović *et al.*, 2008), which may suggest that the mechanism responsible for the minimum of resistance is not necessarily linked to some specific characteristics of TFR. Second, generally T_{min} increases as the concentration of the conducting phase decreases (and at the same time, the negative temperature coefficient of the resistance becomes larger in absolute value), which indicates that the distribution of the conducting particles in the composite and the temperature behaviour of transport are intimately connected. Indeed, on average, larger volume fractions entail shorter tunnelling distances, so that hopping between neighbouring conducting particles, even in the presence of some activation energy, becomes increasingly favourable. In this respect, the crossover towards the positive temperature coefficient regime may be viewed as the tendency of the system to behave effectively as a dirt metal as ϕ increases, in some analogy to the situation encountered in co-sputtered granular metals on the verge of the percolation threshold of coalescing metallic particles (McAlister *et al.*, 1985; Savvides *et al*., 1982). This crossover is facilitated in composites with large conducting particles or aggregates because of the lower activation energies participating in the hopping processes.

Let us turn now to discuss in more detail the dielectric regime of TFR, i.e. the one characterized by $d\rho/dT < 0$. As in many other kinds of conductor–insulator composites, the low temperature dependence of the conductivity in TFR displays a stretched exponential dependence of the type:

$$\sigma \approx \sigma_0 exp\left[\left(\frac{T_0}{T}\right)^{\alpha}\right], \qquad [5.7]$$

where T_0 is a characteristic temperature and α is a dimensionless number. At sufficiently large temperatures $\alpha \approx 1$, which indicates activated behaviour, while at

© Woodhead Publishing Limited, 2012

low T the exponent is usually lower than the unity. In particular, both $\alpha = ¼$ and $\alpha = ½$ have been shown to provide reasonably good fits to the temperature dependence of σ, depending on the particular composite considered, although also values of α different from ¼ and ½ have been reported repeatedly.

The $\alpha = ¼$ law is reminiscent of the Mott variable-range hopping behaviour observed in amorphous semiconductors, while the Efros–Shklovskii $\alpha = ½$ case is the one usually observed to arise when Coulomb effects are important in semiconductors (Efros and Shklovskii, 1975). The origin of the $\alpha = ¼$ and $\alpha = ½$ behaviours in semiconductors stems from the energy E dependence of the density of states $\rho(E)$ in the vicinity of the Fermi level E = 0. When $\rho(E)$ is constant and different from zero about E = 0, Eq. [5.7] follows the Mott behaviour with $\alpha = ¼$ (for three-dimensional systems), while the soft Coulomb gap $\rho(E) \propto E^2$ arising from the long-range Coulomb interaction in charged unscreened impurities leads to the Efros–Shklovskii law $\alpha = ½$.

Although Eq. [5.7] provides a good understanding for the transport mechanism in doped semiconductors, its application to composite materials in general, and to TFR in particular, is still rather problematic. Indeed, even if the Efros–Shklovskii law with $\alpha = ½$ is the one that provides, on average, rather good fits to the low temperature dependence of σ in composites, its implications are non-trivial. For example, from the original work of Efros–Shklovskii, the parameter T_0 in Eq. [5.7] is expected to be $T_0 \approx e^2/\kappa\xi$, where e is the electron charge, κ is the dielectric constant and ξ is the tunnelling decay length (we have used units in which the Boltzmann constant K_B is unity). Typically, in TFR, T_0 is of the order of a fraction of meV, which implies for ξ values as large as 2 μm, which are clearly unphysical and too large if referred to as the direct tunnelling of electrons between conducting particles (Roman *et al*., 1997). Similar considerations apply also for those TFR composites showing the Mott $\alpha = ¼$ behaviour. For example, in Forlani and Prudenziati (1976), the values of ξ from the fits with the Mott law, where $T_0 \propto \xi^3/\rho$, have resulted to be of the order of 40–80 nm. In order to resolve this discrepancy, it has been argued that, actually, the glassy layer separating adjacent conducting grains is doped with hopping centres generated by the interaction between the insulating and the conducting phases. Alternatively, it has been proposed that the temperature behaviour of σ actually follows that of a fluctuation-induced tunnelling model, which predicts that $\sigma \propto \exp[-T_0(T + T_1)]$, where T_0 and T_1 are parameters depending on ξ and on the area and separation of the tunnelling barriers (Sheng *et al*., 1978). However, this model also predicts that, at $T \ll T_1$, the conductivity become temperature-independent, while TFR show no sign of such a behaviour down to millikelvin temperatures (Bat'ko *et al*., 1994).

If one considers the problem of the temperature dependence of σ of TFR from the more general perspective in which TFR are viewed as just a particular class of conductor–insulator composites, then one should also realize that this problem, although having attracted very wide attention for decades, is still open to debate and only recently has some real understanding been achieved. For example, although the Efros–Shklovskii regime with $\alpha = ½$ appears to be generic for both irregular and strictly periodic granular arrays, its manifestation has remained a

© Woodhead Publishing Limited, 2012

challenging puzzle for a long time. Now, it appears rather established that, in order to allow tunnelling with spatially remote and not only adjacent conducting grains (a condition necessary for the stretched–exponential behaviour of Eq. [5.7]), electrons use virtual electron levels in a sequence of grains (for a recent review on this matter, see Beloborodov *et al*., 2007). This co-tunnelling mechanism (Averin and Nazarov,1990), which can be both elastic and inelastic, leads to an effective tunnelling decay length ξ, which can be much larger than the decay length ξ_0 of direct inter-particle tunnelling processes. For example, for a row of spherical particles of diameter D separated by insulating layers of thickness δ, the effective decay length for elastic co-tunnelling scales approximately as $\xi \propto \xi_0 D/\delta$ (Zhang and Shklowskii, 2004). Hence, the large tunnelling decay length values extracted from fits to Eq. [5.7] with $\alpha = ½$ in TFR appear more realistic if interpreted in terms of an effective ξ, as resulting from the co-tunnelling mechanism.

As pointed out at the beginning of this section, TFR display low-temperature stretched exponential behaviours also with α different from ¼ and ½. In part, this could result from the experimental limitation to accurately determine the coefficient α, which accurately account for the data, but it could also arise from the effect of the statistical properties of the conducting phase dispersion into the insulating host matrix. In this respect, not much has been done without invoking *ad hoc* assumptions, and much work still has to be done in order to fully understand the origin of such α values.

5.3 Conclusion and future trends

As discussed above, the general behaviour of transport in TFR does not deviate from that of other classes of conductor–insulator composites, although some peculiarities in their microstructure or other local properties are certainly responsible for features that are characteristic of TFR, like for example their high level of conductivity for low or very low contents of the conducting phase driven by the segregated microstructure. In this respect, the theoretical understanding of the transport properties in TFR as well as in other classes of conductor–insulator composites will certainly profit if the temperature and the concentration dependencies of σ are considered in conjunction, instead of being studied separately as has been generally done in the literature. It is indeed worth remembering that, as a result of these separate approaches, the ϕ and T dependences are commonly interpreted in terms of, respectively, percolation and hopping mechanisms that, as already stressed above, are in principle two incompatible representations of the transport mechanism in conductor–insulator composites.

5.4 References

Adachi K. and Kuno H. (1997), 'Decomposition of ruthenium oxides in lead borosilicate glass', *J Am Ceram Soc*, 50, 1055–1064.

© Woodhead Publishing Limited, 2012

Ambegaokar V., Halperin B. I. and Langer J. S. (1971), 'Hopping conductivity in disordered systems', *Phys Rev B*, 4, 2612–2620.

Ambrosetti G., Johner N., Grimaldi C., Maeder T., Ryser P. *et al.* (2009), 'Electron tunnelling in conductor–insulator composites with spherical fillers', *J Appl Phys*, 106, 016103.

Ambrosetti G., Grimaldi C., Balberg I., Maeder T., Danani A. *et al.* (2010a), 'Solution of the tunnelling–percolation problem in the nanocomposite regime', *Phys Rev B*, 81, 155434.

Ambrosetti G., Balberg I. and Grimaldi C. (2010b), 'Percolation-to-hopping crossover in conductor–insulator composites', *Phys Rev B*, 82, 134201.

Averin D. V. and Nazarov Y. V. (1990), 'Virtual electron diffusion during quantum tunnelling of the electric charge', *Phys Rev Lett*, 65, 2446–2449.

Balberg I. (1987), 'Tunneling and nonuniversal conductivity in composite materials', *Phys Rev Lett*, 59, 1305–1308.

Bat'ko I., Flachbart K., Somora M. and Vanický D. (1994), 'Design of RuO_2-based thermometers for the millikelvin temperature range', *Cryogenics*, 35, 105–108.

Berhan L. and Sastry A. M. (2007), 'Modeling percolation in high-aspect-ratio fiber systems. I. Soft-core versus hard-core models', *Phys Rev E*, 75, 041120.

Beloborodov S., Lopatin A. V., Vinokur V. M. and Efetov K. B. (2007), 'Granular electronic systems', *Rev Mod Phys*, 79, 469–518.

Carcia P. F., Ferretti A. and Suna A. (1982), 'Particle size effects in thick-film resistors', *J Appl Phys*, 53, 5282–5288.

Carcia P. F., Suna A. and Childers W. D. (1983), 'Electrical conduction and strain sensitivity in RuO_2 thick-film resistors', *J Appl Phys*, 54, 6002–6008.

Carmona F. and Mouney C. (1992), 'Temperature-dependent resistivity and conduction mechanism in carbon particle-filled polymers', *J Mater Sci*, 27, 1322–1326.

Celzard A., McRae E., Marêché J. F. and Furdin G. (1998), 'Conduction mechanisms in some graphite–polymer composites: effects of temperature and hydrostatic pressure', *J Appl Phys*, 83, 1410–1419.

Chiang Y.-M., Silverman L. A., French R. H. and Cannon R. M. (1994), 'Thin glass film between ultrafine conductor particles in thick-film resistors', *J Am Ceram Soc*, 77, 1143–1152.

Costa L. C., Chakki A., Achour M. E. and Graça M. P. F. (2011), 'PTCR effect in carbon black/copolymer composites', *Physica B: Condensed Matter*, 406, 245–249.

Dziedzic A. (2001), 'Percolation theory and its application in materials science and microelectronics. (Part II – Experiments and numerical simulations)', *Inform. MIDEM*, 31, 141–152.

Efros A. L. and Shklovskii B. I. (1975), 'Coulomb gap and low temperature conductivity of disordered systems', *J Phys C*, 8, L49–L51.

Fawcett N. and Hill M. (2000), 'A contribution to the debate on the resistance–temperature characteristics of thick-film resistor materials', *Sensors and Actuators*, 86, 52–57.

Feng S., Halperin B. I. and Sen P. N. (1987), 'Transport properties of continuum systems near the percolation threshold', *Phys Rev B*, 35, 197–214.

Forlani F. and Prudenziati M. (1976), 'Electrical conduction by percolation in thick-film resistors', *Electrocomp Sci Technol*, 3, 77–83.

Grimaldi C., Maeder T., Ryser P. and Strässler S. (2003), 'Segregated tunneling–percolation model for transport nonuniversality', *Phys Rev B*, 68, 024207.

Grimaldi C. and Balberg I. (2006), 'Tunneling and nonuniversality in continuum percolation systems', *Phys Rev Lett*, 96, 066602.

© Woodhead Publishing Limited, 2012

He D. and Ekere N. N. (2002), 'Two dimensional percolation and cluster structure of the random packing of binary disks', *Phys Rev E*, 65, 061304.
He D. and Ekere N. N. (2004), 'Effect of particle size ratio on the conducting percolation threshold of granular conductive-insulating composites', *J Phys D: Appl Phys*, 37, 1848–1852.
Heaney M. B. (1995), 'Measurement and interpretation of nonuniversal critical exponents in disordered conductor–insulator composites', *Phys Rev B*, 52, 12 477–12 480.
Heyes D. M., Cas M. and Brańca A. C. (2006), 'Percolation threshold of hard-sphere fluids in between the soft-core and hard-core limits, *Mol Phys*, 104, 3137–3146.
Hrovat M., Samardžija Z. and Holc J. (2001), 'Microstructural and electrical characteristics of some overfired thick-film resistors', *J Mater Sci Lett*, 20, 347–351.
Hu T. and Shklovskii B. I. (2006), 'Theory of hopping conductivity of a suspension of nanowires in an insulator', *Phys Rev B*, 74, 054205.
Jing X., Zhao W. and Lan L. (2000), 'The effect of particle size on electric conducting percolation threshold in polymer/conducting particle composites', *J Mater Sci Lett*, 19, 377–379.
Johner N., Grimaldi C., Balberg I. and Ryser P. (2008), 'Transport exponent in a three-dimensional continuum tunnelling-percolation model', *Phys Rev B*, 77, 174204.
Johner N., Grimaldi C., Maeder T. and Ryser P. (2009), 'Optimal percolation of disordered segregated composites', *Phys Rev E*, 79, 020104(R).
Jović N., Dudić D., Montone A., Vittori Antisari M., Mitrić M. *et al.* (2008), 'Temperature dependence of the electrical conductivity of epoxy/expanded graphite nanosheet composites', *Scripta Materialia*, 58, 846–849.
Kim W. J., Taya M., Yamada K. and Kamiya N. (1998), 'Percolation study on electrical resistivity of SiC/Si_3N_4 composites with segregated distribution', *J Appl Phys*, 83, 2593–2598.
Kirkpatrick S. (1973), 'Percolation and conduction', *Rev Mod Phys*, 45, 574–588.
Kogut P. M. and Straley J. P. (1979) 'Distribution-induced non-universality of the percolation conductivity exponents', *J Phys C*, 12, 2151–2159.
Kubový A. (1986), 'A percolation model of the conduction threshold in thick-film resistors: segregated structures', *J Phys D: Appl Phys*, 19, 2171–2183.
Kubový A. (1995), 'Model of electric conductivity of thick-film resistors Part III. Temperature dependence of sheet resistivity', *Ceramics-Silikáty*, 39, 1–40.
Kusy R. (1977), 'Influence of particle size ratio on the continuity of aggregates', *J Appl Phys*, 48, 5301–5305.
Kusy A. (1997), 'Classical percolation threshold and resistance versus temperature behaviour of RuO_2-glass films', *Physica B*, 240, 226–241.
Lebovka N., Lisunova M., Mamunya Ye P. and Vygornitskii N. (2006), 'Scaling in percolating behaviour in conductive–insulating composites with particles of different sizes', *J Phys D: Appl Phys*, 39, 2264–2271.
Levin G. A. (1986), 'Concentration dependence of hopping conductivity in granular metals', *Phys Rev B*, 34, 6318–6321.
Li G., Braunstein L. A., Buldyrev S. V., Havlin S. and Stanley H. E. (2007), 'Transport and percolation theory in weighted networks', *Phys Rev E*, 75, 045103(R).
Malliaris A. and Turner D. T. (1971), 'Influence of particle size on the electrical resistivity of compacted mixtures of polymeric and metallic powders', *J Appl Phys*, 42, 614–618.
McAlister S. P., Inglis A. D. and Kayll P. M. (1985), 'Conduction in cosputtered Au-SiO_2 films', *Phys Rev B*, 31, 5113–5120.

© Woodhead Publishing Limited, 2012

Nigro B., Ambrosetti G., Grimaldi C., Maeder T. and Ryser P. (2011), 'Transport properties of nonhomogeneous segregated composites', *Phys Rev B*, 83, 064203.

Peng D. L., Sumiyama K., Konno T. J., Hihara T. and Yamamuro S. (1999), 'Characteristic transport properties of CoO-coated monodispersive Co cluster assemblies', *Phys Rev B*, 60, 2093–2100.

Pflieger R., Malki M., Guari Y., Larionova J. and Grandjean A. (2009), 'Electrical conductivity of RuO_2-borosilicate glasses: effect of the synthesis route', *J Am Ceram Soc*, 92, 1560–1566.

Pike G. E. (1978), 'Conductivity of thick-film (cermet) resistors as a function of metallic particle volume fraction', *in* Garland J. C. and Tanner D. B. (eds), *Electrical transport and optical properties of inhomogeneous media*, New York, American Institute of Physics, 366–371.

Pike G. E. and Seager C. H. (1977), 'Electrical properties and conduction mechanisms of Ru-based thick-film (cermet) resistors', *J Appl Phys*, 48, 5152–5169.

Roman J., Pavlik V., Flachbart K., Adkins C. J. and Leib J. (1997), 'Electronic transport in RuO_2-based thick-film resistors at low temperatures', *J Low Temp Phys*, 108, 373–382.

Sahimi M. (2003), *Heterogeneous Materials*, New York, Springer.

Savvides N., McAlister S. P., Hurd C. M. and Shiozaki I. (1982), 'Localization in the metallic regime of granular Cu-SiO_2 films', *Solid State Comm*, 42, 143–145.

Scher H. and Zallen R. (1970), 'Critical density in percolation processes', *J Chem Phys*, 53, 3759–3761.

Sheng P., Sichel E. K. and Gittleman J. I. (1978), 'Fluctuation-induced tunnelling conduction in carbon–polyvinylchloride composites', *Phys Rev Lett*, 40, 1197–1200.

Sion R. P., Atkinson J. K. and Turner J. D. (1994), 'A novel model for the temperature characteristic of a thick-film piezoresistive sensor', *Sensors and Actuators A*, 41–42, 460–464.

Stauffer D. and Aharoni A. (1992), *Introduction to Percolation Theory*, Taylor & Francis, London.

Tamborin M., Piccinini S., Prudenziati M. and Morten B. (1997), 'Piezoresistive properties of RuO_2-based thick-film resistors: the effect of RuO_2 grain size', *Sensors and Actuators A*, 58, 159–164.

Vionnet-Menot S., Grimaldi C., Maeder T., Strässler S. and Ryser P. (2005), 'Tunneling-percolation origin of nonuniversality: theory and experiments', *Phys Rev B*, 71, 064201.

Wang J. F. and Ogale A. A. (1993), 'Simulation of percolation behavior of anisotropic short-fiber composites with a continuum model and non-cubic control geometry', *Compos Sci Technol*, 46, 389–398.

Youngs I. J. (2003), 'A geometrical pecolation model for non-spherical excluded volumes', *J Phys D: Appl Phys*, 36, 738–747.

Zhang J. and Shklovskii B. I. (2004), 'Density of states and conductivity of a granular metal or an array of quantum dots', *Phys Rev B*, 70, 115317.

© Woodhead Publishing Limited, 2012

6

Multilayer low-temperature co-fired ceramic systems incorporating a thick-film printing process

M. SOBOCINSKI, J. PUTAALA and H. JANTUNEN,
University of Oulu, Finland

Abstract: Since the first application of low-temperature co-fired ceramics (LTCC) – a radar chip manufactured by DuPont and Hughes – in the 1980s, LTCC has gone through many changes, evolving from a simple multilayer substrate technology to a complex microelectronic system suitable for 'intelligent' packages with buried passive components, heat sinks, sensors, actuators, energy harvesters and even microsystems. Moreover, novel materials and enhanced processes have been introduced constantly. This chapter presents LTCC technology, starting from material development followed by processing steps and proposed applications. Future trends and challenges are discussed, and literature containing more detailed descriptions is listed.

Key words: ceramic, multilayer, LTCC, low-temperature co-fired ceramics.

6.1 Introduction

The introduction in 1947 of a tape casting-method for ceramic materials by Glenn Howatt (Howatt *et al.*, 1947) opened up the possibility of fabricating multilayer ceramic devices with embedded electrodes. High-temperature co-fired ceramic (HTCC) technology, in particular, was utilised in the very beginning to fabricate multilayer ceramic capacitors. Components were made of common ceramic compositions like Al_2O_3 or $BaTiO_3$, and since they required a moderately high sintering temperature (well over 1100 °C), refractory metals like tungsten were used for electrodes. Although nowadays HTCC technology is also utilised in broader application areas like radio frequency devices (RF) or microelectromechanical systems (MEMS), novel substrates capable of handling large numbers of signal lines or substrates enabling higher-conductivity electrodes were needed in modern electronics. This was achieved with low-temperature co-fired ceramics (LTCCs), in which the ceramic materials employ a lower sintering temperature (<1000 °C) and embedded electrodes are made of silver or copper.

LTCC technology is based on the simple idea of printing conductive patterns using pastes on tape-cast unsintered ('green') ceramic sheets, which are then stacked and joined together in a lamination process, forming a solid bulk body after sintering at about 850 °C. A huge amount of LTCC products have been introduced, especially for automotive, military, space and telecommunication

© Woodhead Publishing Limited, 2012

Table 6.1 Some commercially available LTCC materials and their properties

LTCC system	DuPont 951	DuPont 9k7	Heraeus HeraLock 2000	Heraeus CT 2000	ESL 41010	Ferro A6-M	Kyocera GL330
Dielectric constant ε @2–3 GHz	7.8	7.1	7.3	9.1	7.3	5.9	7.8
Loss tangent @2–3 GHz	0.006	0.0010*	0.0026	0.002	0.0057	0.002	0.0004
Electrical strength (V/μm)	>39	44000	17–23	>40	>72	>39	–
Shrinkage x–y (%)	12.7	9.1	0.2	10.6	13	15	–
Shrinkage z (%)	15	11.8	32–44**	16	17	24	–
Thermal conductivity (W/mK)	3	4.6	–	–	3	2	4.3
CTE (ppm/K)	5.8	4.4	6.1	5.6	7	7	832

Notes:

*At 10 GHz.

**Depends on tape thickness.

purposes. Table 6.1 shows some commercially available LTCC materials and their most important properties. These systems have a fully conductive paste series for embedded and post-fired electrodes, and many vendors provide dielectric and resistive pastes as well.

The largest suppliers of LTCC systems that include LTCC tapes and pastes are Du Pont, Heraeus, ESL and Ferro. However, many companies manufacture LTCC only for their own purposes. The popularity of LTCC technology, resulting from its superb electrical and mechanical properties together with its relatively low cost, can be easily seen in Fig. 6.1, which shows the number of publications dealing with this topic.

Properties like excellent mechanical and electrical stability even in harsh environments and at high temperatures, good dielectric properties at high frequencies, together with a coefficient of thermal expansion (CTE) matching that of silicon and resistance to different chemicals, make LTCC technology very competitive in comparison with, for example, printed circuit boards (PCBs) made of polymer materials (Table 6.2). LTCC technology is also used to fabricate hermetic packages. Additionally, the fact that the structures are co-fired makes parallel processing possible, which greatly reduces manufacturing times. Also, computer aided design (CAD) and short process times make LTCC a perfect technology for rapid prototyping, ensuring fast turnarounds in production and short time-to-market.

© Woodhead Publishing Limited, 2012

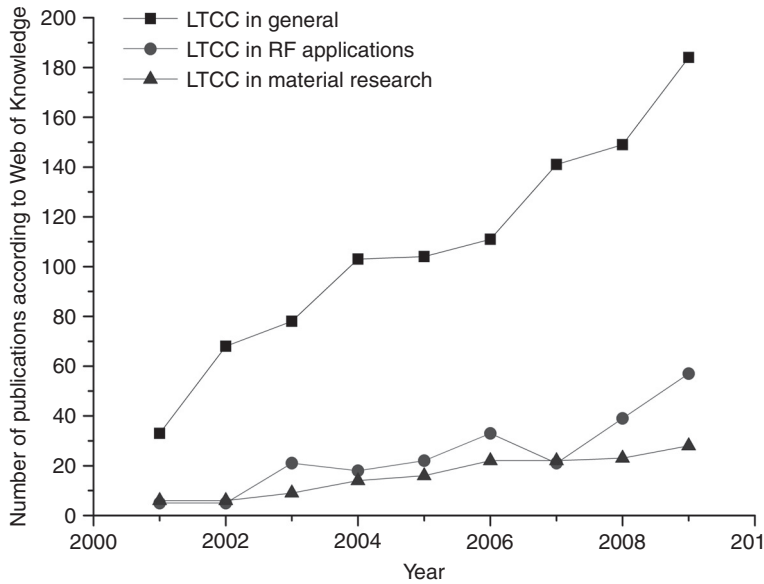

6.1 LTCC publications introduced since 2001, based on Web of Knowledge (http://wok.mimas.ac.uk).

Table 6.2 Comparison of different technologies

	LTCC	Thin film	FR4
Thermal performance	++	+	–
Electrical performance	++	+	–
Resistors	+	+	–
Integral passives	++	–	–
3D structures	++	–	–
Interconnection density	+	+	–

Source: Golonka (2001).

6.2 Low-temperature co-fired ceramics (LTCC) compositions

The main objective of LTCC research has been to enable the manufacture of multilayer ceramic structures with highly conductive embedded electrodes, thereby challenging polymer-based structures. For dielectric compositions the objective has been (1) to make electrical circuits for hazardous environments (automotive industry) and (2) to form modules with extremely low losses (telecommunication industry), both providing improved thermomechanical and electrical performance. However, in order to fabricate multifunctional ceramic multilayer modules, not

© Woodhead Publishing Limited, 2012

available with polymer materials, non-linear LTCCs also need to be developed. This chapter discusses the approaches used to reach these goals.

6.2.1 Dielectric LTCCs

LTCC compositions widely used today in industrial products are mostly dielectric. LTCCs commercially available in tape form and have a relative permittivity value ranging from 4 up to 20, with a very competitive dielectric loss even at GHz frequencies, thus being compatible with silver/copper paste systems used to form embedded electrodes (Sebastion and Jantunen, 2008). In practice, these materials are developed either by adding low softening point glass to crystalline dielectric powder, or by utilising a fully glass system as a starting material. In the first approach, a high sintering temperature dielectric crystalline powder, like Al_2O_3, TiO_2 or SiO_2, is used as a starting material to which low softening point glass is added to form a matrix that enables the use of a lower sintering temperature (Knickerbocker *et al*., 1993; Imanaka, 2005). The sintering process can be non-reactive or reactive, depending on whether the glass material serves only as a bonding agent or reacts with the dielectric filler. These compositions are also commonly made of several different phases, especially when advanced glasses are developed to manage properties such as glass fluidity, crystallisation, softening point or foaming. Several commercial dielectric LTCCs follow this route, for example DuPont 951, which is composed of Al_2O_3, $CaZrO_3$ and glass (Steinberg *et al*., 1998).

In the second approach, the starting material is mainly in the glassy phase, which devitrifies during the sintering process, forming as fully crystalline structure as possible, with high density, to achieve the desired electrical properties. To enhance the crystallisation it is also common to add some nucleating agents. Commercial LTCC from Ferro A6-M follows this procedure, using CaO-SiO_2-B_2O_3 glass as a starting material, devitrifying it to wollastonite crystal surrounded by a small amount of borosilicate glass.

However, in both of these approaches the main objective is to achieve a dense structure with a low amount of glassy phases, which commonly reduce the thermomechanical and electrical properties of the final composition. This is the main reason several versatile methods for developing LTCC compositions have also been introduced. It is possible to use a mixture of the approaches mentioned above: decrease particle size (Marques *et al*., 2006), utilise materials with a low sintering temperature (Udovic *et al*., 2004) or use a chemical process where the ceramic dissolves in flux forming crystalline oxides (Jean and Lin, 2000). Two-step processes have also been found to be an effective method for decreasing the amount of glassy phases and thus keeping the original electrical properties as far as possible. Hsi *et al.* (2008) reported that a $BaTiO_3$-based LTCC composition sintered at 850 °C had high relative permittivity (1700), being close to the high sintering temperature composition value (Hsi *et al*., 2008). This was performed with a two-stage process using calcium boron silicate glass with a LiF coating (Fig. 6.2).

© Woodhead Publishing Limited, 2012

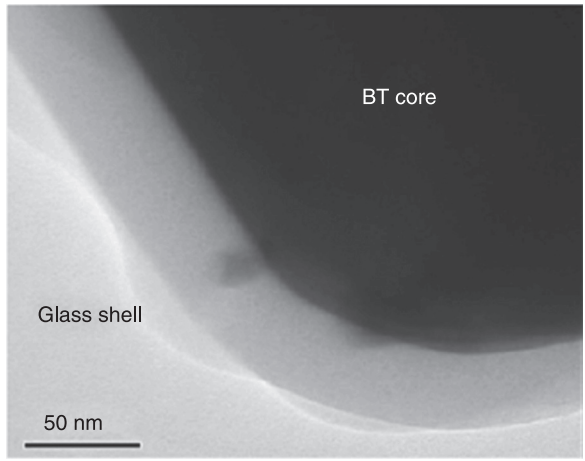

6.2 Transmission electron microscopy (TEM) bright field image of Barium Titanate (BT) particle coated with calcium boron silicate glass with LiF (Hsi *et al.*, 2008).

One very effective approach to developing LTCCs that enable advanced electrical properties is to use sintering aids. This approach has been widely used for high-permittivity dielectrics reaching values of relative dielectric constant close to 500 at GHz frequencies (Kim *et al*., 2002). Commonly used sintering aids are oxides like B_2O_3, LiF, CuO, V_2O_5 or Bi_2O_3, and the amount added is in the region of a few wt% (Kim *et al*., 1999; Lee *et al*., 2003; Yokoi *et al*., 2005; Zhang *et al*., 2006). The main reason for the success of this approach is that a minimum amount of glassy phases or even glass-free microstructures can be achieved, thus enabling the preservation of the original dielectric properties of the starting material. Additionally, it is clear that if different LTCC materials could be developed with this approach, this would allow the use of similar sintering mechanisms for all compositions enabling their co-firing in multifunctional applications.

Although the first challenge in the development of LTCC compositions is to decrease the sintering temperature close to 900 °C, the work itself is far more complicated when commercial products for industrial purposes are targeted. Devitrification, sintering and liquification mechanisms and rates, viscous flow mechanisms, wetting, chemical reactions, phase formation, glass fabrication routes, etc. should be well managed during the sintering process. Slurry compositions that enable tape casting also create their own requirements, since they contain organic additives that should be burned out before densification so that a minimum amount of carbon remains in the microstructure (Tummala, 1991). In addition, to achieve the desired electrical performance, sintering behaviour, thermomechanical properties, chemical compatibility together with production and material cost as well as repeatability should be taken into account. Furthermore, multilayer LTCC structures fabricated with embedded electrodes

© Woodhead Publishing Limited, 2012

also require that the LTCC composition be compatible with the conductive paste; this issue should be analysed at a very early stage. This is a major challenge, because LTCC compositions are commonly complicated, and in fact all commercially available systems include pastes meant just for these compositions, enabling embedded, post-fired or bonding electrodes.

A very comprehensive review of developed dielectric LTCC compositions and process requirements is presented by Sebastian and Jantunen (2008) and Imanaka (2005).

6.2.2 Non-linear LTCCs

If all the benefits available within LTCC technology are to be utilised, process-compatible non-linear ceramics should also be developed in addition to dielectric ones. Electroceramics including compositions from the highly insulating end of electrical performance up to superconductors should be considered. Especially interesting are sensors, actuators and energy-harvesting applications made of piezoelectrics, frequency-tuning elements made of ferroelectrics, non-linear resistors for varistor applications, and magnetic/ferrite compositions. So far, the main interest has been in magnetic/ferrite compositions made primarily from NiZn, NiCuZn, MnZn, CoZn and LiZn compounds, Ba- or Sr-based hexagonal ferrites or YIG garnets using sintering aids like V_2O_5 or Bi_2O_3 and Ag_2O, or a small addition of glass like Bi_2O_3-B_2O_3-SiO_2-ZnO (Yan *et al*., 2006; Matz *et al*., 2009). Especially interesting compositions have been reported by Ganne *et al.* (2007) and Lisjak and Drofenik (2007), based on $Y_{3-2x/3}Cu_xFe_5O_{12}$ and $Ba_3Co_{1.4}Cu_{0.6}Fe_{24}O_{41}$, respectively. Suitability for GHz frequency applications is one of the main challenges with these materials. A good example of the power of this kind of research is the solenoid transformer introduced by Shamim *et al.* (2007), or ferrites integrated in high-frequency antenna structures that provide self-biased structures, enabling miniaturisation of the devices to a great extent (Sun *et al*., 2007).

$BaSrTiO_3$ in the ferroelectric or paraelectric state is also a very interesting material. In the ferroelectric state, this material is used for memory devices. In the paraelectric state, no domains exist and lower losses are achieved, which is why these compositions are used to tune the frequency or phase of telecommunication devices. All related LTCC compositions are based on $BaSrTiO_3$, having different portions of Ba/Sr to adjust the Curie temperature. Several glass compositions like the ones based on SiO_2, Al_2O_3, B_2O_3 and BaO have been studied to decrease the sintering temperature, but the most successful compositions are made using sintering aids. In 2004, Valant and Suvorov, and Jantunen *et al.* introduced compositions that utilise a very small addition of LiF and $B_2O_3 + Li_2O$, respectively (Valant and Suvorov, 2004; Jantunen *et al*., 2004). Since then, LTCC modules made of these materials have been reported (Deleniv *et al*., 2005). One interesting study mentioned earlier is a $BaTiO_3$-based LTCC-compatible composition (Fig. 6.2). Tunability ((C(0) – C(E))/C(0)) (where C(0) is the capacitance with 0 V

© Woodhead Publishing Limited, 2012

applied field, and C(E) is capacitance with applied field equal to E) achieved with E = 4 V/μm was 50%, being very close to the values achieved with a pure composition fabricated with thin-film processes (Hsi *et al*., 2008).

In recent years, development related to piezoelectric ceramics has been concentrated on the important topic of lead-free compositions. These compositions are commonly based on $K_{0.5}Na_{0.5}NbO_3$, first introduced by Jaeger (Jaeger and Egerton, 1962) and Haertling (Haertling, 1967). Since then, these materials have been developed to enable more controlled and lower-temperature sintering by modifying their main composition, using sintering aids like MnO_2 or Bi_2O_3 (Nagata, 2008; Takao *et al*., 2006) and utilising advanced processing methods like spark plasma sintering (Li *et al*., 2006). Although this field of science is still waiting for major progress before true LTCC integrations are performed, LTCC-compatible piezoelectric compositions are able to provide a very wide range of applications like frequency-tunable elements for telecommunication purposes, already proposed by Joshi *et al.*, (Joshi *et al*., 2007) and piezoelectric films on LTCC (Hrovat *et al*., 2006).

Additional application examples that could be useful if embedded in LTCC structures are varistors. These components are commonly based on ZnO, SiO_2, TiO_2 or SnO_2, with different performance-modifying additives (MnO_2, Sb_2O_3 with a two-step process, semiconductive glass) used to lower the sintering temperature (Zhao *et al*., 2007; Nehm, 2008; Honkamo *et al*., 2007). In addition to simple high-voltage protection devices in low-voltage automotive and semiconductor electronic devices, applications could include, for example, a circuit comprised of an antenna input, a signal input and output and a switching unit, wherein the antenna input is connected to a device that protects against electrostatic discharges (Block *et al*., 2008).

These kinds of multi-material integrations enable the creation of applications not available in any way other than by utilising advanced LTCC compositions.

6.2.3 Pastes for LTCC systems

All LTCC tape manufacturers provide a wide selection of system-compatible Ag, Ag-Pt, Ag-Pd, Pt and Au thick-film pastes for embedded electrodes, conductive vias and post-fired surface electrodes enabling also soldering or bonding. However, efficient packaging through the multilayer structure is only achieved if capacitors, resistors and non-linear structures like sensors or heaters can be also seamlessly integrated. Since the commercial LTCC tapes have commonly low relative permittivity (<10) and the tape thickness is relatively high (>50 um), other methods to embed large capacitors are needed. For embedded structures, high permittivity pastes have been introduced. ESL, for example, provides pastes with dielectric constant between 50 and 250, fulfilling the Electronic Industries Alliance X7R standards (±15% Δc over –55ºC ~ +125ºC) (Feingold *et al*., 2003). Also, other structures are proposed to be fabricated with LTCC-compatible pastes. The challenge with embedded resistors in LTCC is the high resistance tolerance, normally 20–30%,

© Woodhead Publishing Limited, 2012

and several groups have investigated this problem through modelling, resistor materials' development and careful processing control (Hsi *et al*., 2003; Horvth, 2008; Birol *et al*., 2005, 2006). Wang *et al.* (2002), for example, have estimated that to reach the 10% resistance tolerance goal, the print thickness of the resistor tolerance must be no more than 8%. However, there is still much work to be done to enable accurate and reliable embedded resistors in LTCC modules.

In addition to embedded passive elements, varistors, temperature sensors, heaters and frequency-tuning elements utilizing thick-film pastes have also been proposed. One example is a Zn-based varistor using thick-film LTCC pastes suitable for electronic circuits protecting semiconductive devices, for example, for high voltages (Mis *et al*., 2009). The structures, co-fired at 850 or 950 °C, showed nonlinearity coefficient α up to 23 with capacitor-like varistors having Pt terminations. Additionally e.g. temperature sensors (Vanek *et al*., 2009), heaters (Kim *et al*., 2010), pressure sensors (Hrovat *et al*., 2008) and antenna tuning (Tick *et al*., 2008) embedded to LTCC modules using compatible thick-film pastes have been reported.

Although over 200 articles related to thick-film materials and structures for LTCC systems have been reported, e.g. including, most recently, on multisensors for compressed air diagnostics (Fournier *et al*., 2010), ultra low gas concentration sensors (Karioja *et al*., 2010) and piezoelectric cantilevers for energy harvesting (Kok *et al*., 2009), pastes are one interesting option for advanced research in LTCC modules.

6.3 LTCC manufacturing methods

6.3.1 Design of LTCC products

Before introducing the LTCC fabrication process, an overall design guideline for LTCC products is given. The first challenge is to manage tape shrinkage. In general, this means that if a new tape is taken into production, shrinkage in all directions (x, y and z) should be measured using structures closely mimicking the modules to be fabricated. Many tape systems have almost the same shrinkage in all directions (5–20%), but so-called zero shrinkage systems can also be selected where horizontal (x–y) dimensional change is only 0.20% ± 0.04% (see Table 6.1). However, it is important to remember that the next fabrication steps, like lamination, can affect shrinkage. The general structural design rules that enable production of quality LTCC products with commonly available processes are presented in Table 6.3 and Fig. 6.3. The dimensions given are suggestive, and are based on feasible dimensions with safety margins. As with other thick-film methods, careful design is a prerequisite for a functioning LTCC product. The main limitations are caused by the thick-film printing process and the method of fabricating vias. The limitations of the latter also depend on the thickness of the tape itself. The shrinkage behaviour of the ceramic tapes is also a challenge: it depends especially on the selected LTCC system, as shown in Table 6.1.

© Woodhead Publishing Limited, 2012

Table 6.3 General dimension guidelines for an LTCC product

Key	Meaning	Minimum dimension (μm)*
A	Distance between soldering base and module edge (see also key M)	125
B	Distance between conductor and via	175
C	Distance between an SMD (surface-mount device) and conductor	200
D	Conductor width	150
E	Distance between two conductors	150
F	Distance between conductor and module edge	300
G	Distance between conductors in a meshed ground plane	550
H	Distance between ground plane and via	300
I	Meshed ground plane conductor width	250
J	Via diameter	200
K	Smallest distance between adjacent vias in same tape layers	2.5 × ø(via)
L	Minimum distance between staggered vias in successive tape layers	2 × ø(via)
M	Minimum distance of a via to the edge of the module	3 × ø(via)

Notes:

Key parameters from A to M are illustrated in Fig. 6.3.

*These are suggestive dimensions based on current proofed technology.

Additionally, large conductive planes, like ground planes, should be implemented as a meshed structure. To reduce the possibility of delaminating tape layers and to reduce bending of the ceramic during sintering, the area of the conductive surface should be less than 50% of the total surface area of the layer. The main reason for this is the differences in the shrinkage behaviour of ceramic tape and thick-film printed paste. Additionally, sintering of symmetrical structures to form flat, dense structures should be selected, if possible. However, several manufacturers use device-oriented tape designs and tape thicknesses, two-step lamination processes, etc., thus enabling clearly smaller dimensions than presented here. The state-of-the-art in LTCC process capabilities is presented in the design guidelines of each LTCC tape manufacturer and in related publications (see the reference list at the end of the chapter).

6.3.2 General LTCC manufacturing methods

The general LTCC fabrication process is presented in Fig. 6.4, which introduces the process from mixing of the raw materials to final inspections of the LTCC products.

One can select ready-cast tapes on reels or sheets from a manufacturer and compatible conductive paste or start from fabrication of the ceramic material

© Woodhead Publishing Limited, 2012

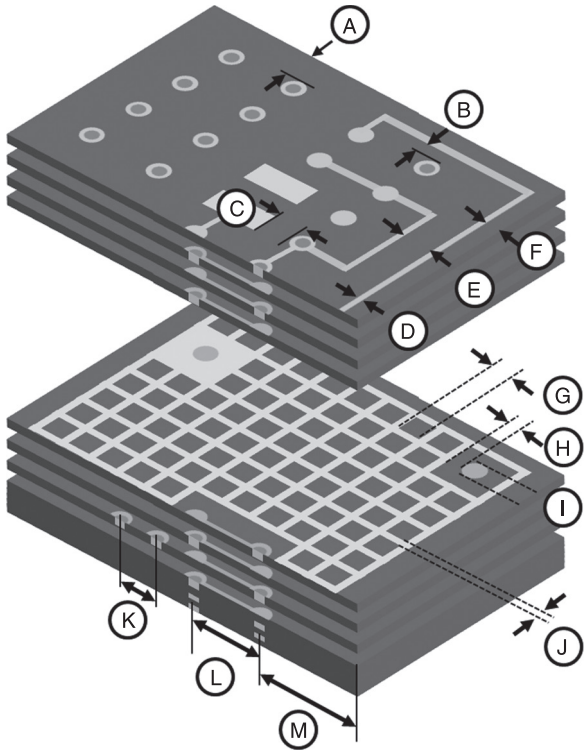

6.3 Dimensioning of an LTCC product.

itself. However, if commercial tapes are used, understanding the method of producing the green tapes enables better management of the whole process. The tape fabrication method explained briefly here is described in detail, e.g. by Mistler and Twiname (2000).

After choosing the LTCC composition, as explained in Chapter 2, the slurry from which the green tape is cast is prepared. This includes mixing of the LTCC composition with solvents and organic additives. This is commonly performed in several steps, starting with addition of solvents and dispersants, followed by mixing binders, plasticiser, etc. All the additives have their own special role in enhancing the mixing or casting processes or tape properties, as listed below (Imanaka, 2005):

- binder helps to keep the green tape together during processing;
- plasticiser increases flexibility and thus helps to make the material easier to shape;
- deflocculant/dispersant ensures that the particles do not become agglomerated (i.e. it prevents the formation of flocks) and that they are dispersed uniformly in the cast tape (i.e. to result in a homogenous suspension);

© Woodhead Publishing Limited, 2012

- antifoaming agents help during the tape casting process to ensure that the slurry does not foam, which would result in voids within the produced tape;
- surface treatment coupling agents;
- organic solvents.

The tapes are then fabricated by doctor blade or knife casting in the desired thickness using a carrier tape, usually made of cellulose acetate, Teflon®, Mylar® or cellophane (Gongora-Rubio *et al*., 2001). Drying the tapes in ambient conditions

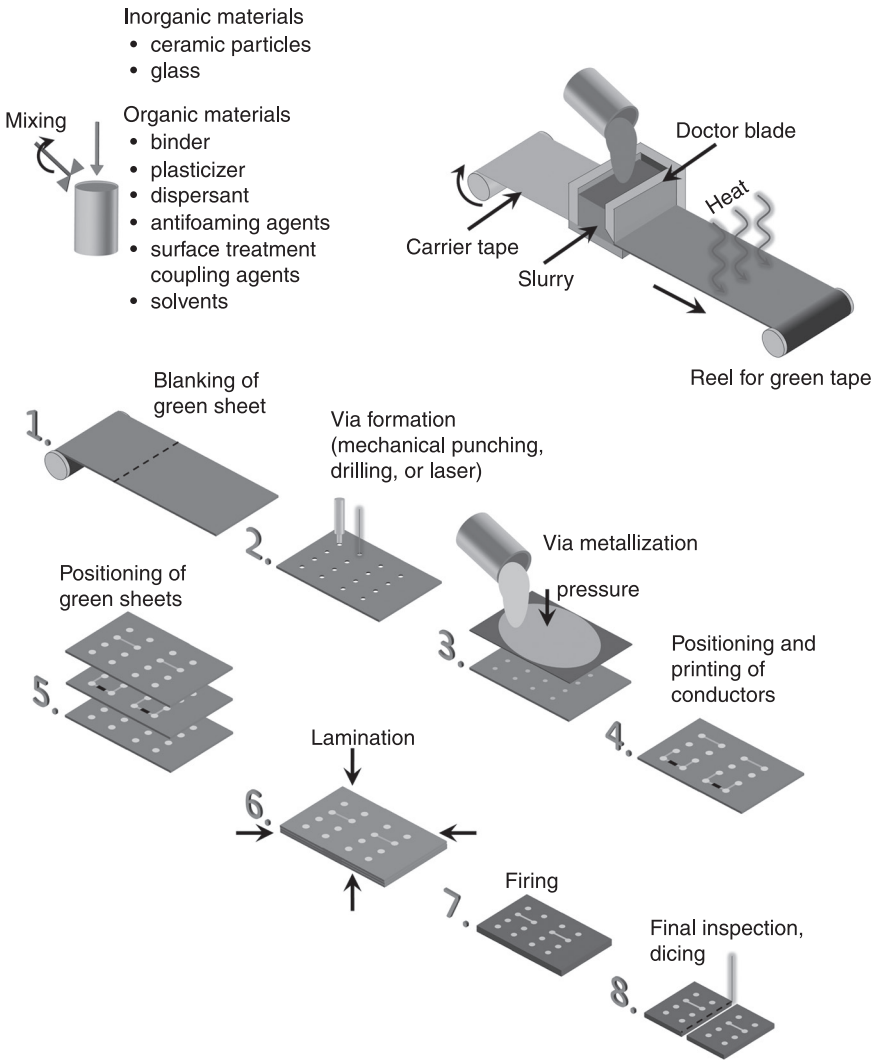

6.4 The general LTCC fabrication process.

© Woodhead Publishing Limited, 2012

or by heating results in solid, flexible tapes that can be stored on reels and cut into sheets. The thickness of commercially available tapes generally ranges from 50 to 500 μm, while available widths are roughly from 20 to 30 cm (8 to 12 inches).

Blanking the green sheet (step 1 in Fig. 6.4) to the desired shape can be done, e.g. with a professional paper cutter or a laser. The tape casting direction (i.e. the direction in which the tape carrier was moved during casting) must be known and marked on the tape (this direction is always marked on commercially sold sheets). The reason for this is that the tape shrinks differently in different horizontal directions. To balance shrinkage, each consecutive tape layer should be rotated 90 ° when stacking the green sheets. After blanking, the tape is heated in an oven, typically at 120 °C, for five minutes to release mechanical stresses (induced in the tape cutting) that affect shrinkage of the green tape.

Vias (step 2 in Fig. 6.4) are used to link two layers of conductors vertically through ceramic material or to form channels or cavities. So far, the minimum diameters of vias in LTCC technology are in the range of 30–50 μm with a mechanical punching machine (Hagen and Rebenklau, 2006), and in the same range using laser micromachining (Wang *et al*., 2006). These two methods are the main via formation methods, but other methods are also available, such as milling, which currently yields dimensions larger than 100 μm. In the past, electron beam machining has also been proposed. (Yau *et al*., 1991, 1993)

Currently, some of the main challenges in via formation by punching are burr formation, edge breakout during punching, and carrier tape intrusion into the tape (Rhim *et al*., 2006; Imanaka, 2005). A combination of tape properties (tape thickness, material composition, i.e. its mechanical properties) and process properties (punching speed, tool clearance) mainly affect these. Because the green tape also includes hard ceramic particles, abrasion of the punching tool needs to be taken into account (Imanaka, 2005).

Via formation by laser processing enables formation of high aspect ratio (i.e. thickness/diameter) vias. Also, as no mechanical damage is inflicted on the surrounding green tape, a shorter pitch between vias can be used than with a mechanical puncher (Yau *et al*., 1993). However, problems with lasering include tapering of the vias and softening or melting of the glass phase, which may fill up the via hole.

With laser processing, the amount of glass in the green tape affects its processability; namely, the more glass there is compared with the ceramic phase, the more likely it will soften or melt during processing and fill the via partly or fully (Kita *et al*., 2002). The wavelength of the laser and the absorption wavelength of the green tape often differ, but in an ideal case all the energy of the laser is absorbed by the green tape, resulting in fast sublimation of the material. If the structure is to include cavities or channels, they are also formed in this phase. Finally, alignment holes for further processing steps are made in the tape, enabling accurate printing of conductors and stacking of green sheets in the later phases.

© Woodhead Publishing Limited, 2012

Via metallization (step 3 in Fig. 6.4) is a critical process during LTCC manufacturing. Besides electrical/thermal conductor material, the vias may be filled with dielectric, resistive or functional material (see section 6.3.3). Vias are filled using a screen-printing machine or a via filler machine. With a via filler machine, pressure is applied on top of a stencil that has filled via paste, forcing it to flow through stencil openings located in the corresponding places to via holes in the green tape. To avoid contamination of the areas near the vias, paste filling should be done through the carrier tape side. Another way to fill vias is with a screen-printing machine. The green tape is placed on a flat surface (a porous plate) and suction is applied to keep the tape in place whilst printing the paste. The paste printing process, which is applicable also in via filling, is presented in the next section. However, by using a via filler machine it is possible to use higher pressure in the filling process, which allows filling large aspect ratio vias. In addition to via paste, powder can also be used in the filling process, but this includes a risk of voids due to the lower fluidity of powder compared with a material in paste form (Imanaka, 2005).

The success of the filling depends on process variables like pressure and time, material variables like viscosity of the paste, chemistry, and geometrical variables including the shape of the via or its aspect ratio. At the same time, the process is very delicate; adjusting some parameter may result in underfilling or overfilling of the vias, damage to the tape, etc. If the vias are filled with the supporting carrier tape, as is usually the case, there will often be extra via paste left when removing the carrier tape before possible printing of catch pads and lamination. Added to this, the shrinkage of via metallization materials is typically much less than that of the LTCC. This results in a bumpy profile in the fired structure (Sunppan *et al*., 2006), bringing challenges to the component attachment phase, for example. Structural design modifications (e.g. staggered vias) and material selection are needed to avoid this effect.

Metallization of microvias (<100 μm in diameter) is especially sensitive to different parameters; the most likely problem is that the aspect ratio is too high, which results in underfilled vias. On the other hand, vias that are too large cause problems afterwards because the via material might not stay in place during handling of the tape.

After filling of the vias, a screen-printing machine is used to print the conductors, resistors, dielectrics, etc. on the tape (step 4 in Fig. 6.4). The screen-printing method commonly used in LTCC manufacturing, also known as gap printing, is an off-contact method, where the screen makes contact with the green tape only at the point where the squeegee pushes the paste through the mesh openings (see Fig. 6.5).

A print screen with a pattern is used to print the paste on top of the green sheet. The screen is commonly made of metal or nylon wires meshed together. The screen includes a photoreactive emulsion which is exposed to UV light with an exposure mask that includes the desired pattern. Typically, the emulsion thicknesses used are around 10–30 μm. In LTCC screen printing, the mesh count usually varies from 200 to 400 holes per square inch, with a higher mesh count

© Woodhead Publishing Limited, 2012

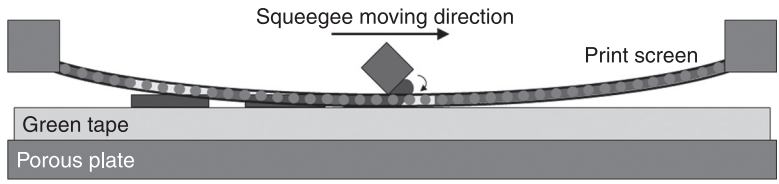

6.5 Printing of paste with screen-printing method.

able to produce finer detail, but also increasing the possibility of clogging. Both the emulsion thickness and the mesh size needed depend on the paste properties (viscosity, particle size, etc.). The printing paste is a non-Newtonian, more specifically, thixotropic substance, meaning that its viscosity drops as the shear rate increases. Another important property of the paste is its recovery time, which indicates how quickly the viscosity of the paste is restored (Imanaka, 2005).

Four main factors affecting the quality of printing are:

- paste properties (viscosity, particle size);
- screen properties (mesh, emulsion thickness/opening size);
- tape properties (material, surface roughness: the carrier tape side is smoother);
- printing parameters (squeegee speed and pressure, printing gap size, etc.).

Both sides of the green tape can be printed; i.e. after printing the top side, the tape is dried in an oven (typically at 120 °C for 5 minutes), the carrier tape is removed and printing is done on the underside. Minimum conductor width in a typical process is 150 μm, but by using specialised techniques such as direct gravure printing or photoimageable inks (e.g. Du Pont's Fodel®), for example, conductors less than 50 microns in diameter can be created (Kittilä *et al*., 2004; Wang *et al*., 2000). The conductor layer print screen also has openings for the via catch pads that are used to ensure an electrical connection between vias and printed pattern. A rough rule of thumb is that the size of the catch pad should be about 50–100 microns larger in diameter than that of the via if the via is to be smaller than 200 microns in diameter, although recently there have been examples of microvias without catch pads (Wang *et al*., 2006).

With screen printing, basic elements such as resistors can be integrated in the product. It must be noted, however, that the absolute value of the resistor may deviate from the designed value by tens of percents, especially when making resistors embedded in the structure due to shrinkage, burn-out leftovers and so on.

After the printing phase, the carrier tapes are removed and the green sheets are stacked together using a mechanical or optical aligner (step 5 in Fig. 6.4). In a mechanical alignment system, the green tape, which includes holes for this purpose, is aligned with the substrate, which again has pins in the corresponding positions. In an optical aligning system, the alignment is done with the aid of a camera. Although mechanical aligning is generally used, the optical system is

© Woodhead Publishing Limited, 2012

more accurate. As mentioned above, stacking should be done so that the consecutive tape layers are rotated (90°) in order to minimise the difference in shrinkage in the x and y directions.

To improve the adhesion of the tape layers and thus facilitate handling of the tape at this phase, some drops of ethanol may be spread on the edges of each tape layer, e.g. with a needle. After stacking, the pack is dried in an oven (90 °C for 30 minutes) to evaporate the ethanol. Another way to ensure that tapes stay aligned during handling before lamination is to use hot iron for punctual joining on the edges of the structure. This step can be automated by using so-called stack and tack machines.

In the lamination phase (step 6 in Fig. 6.4), the tape layers are attached together by thermocompression, i.e. by applying heat and pressure to the green tape stack. It was reported in 2001 by Gongora-Rubio *et al.* (2001) that the highest number of laminated layers can be close to 80. However, four years later, Peterson *et al.* (2005) showed structures with up to 300 layers.

Uniaxial lamination is perhaps the most commonly used method where, after attaching a stress release foil to both sides of the LTCC stack and installing a silicon mat to equalise pressure everywhere, the stack is placed between two heating plates that compress the tape in the z direction. Typically, the lamination is done at a temperature of around 70–80 °C and a pressure of 20–30 MPa (200–300 bar, i.e. 2900–4350 psi) for 10–20 minutes, depending on the tape used. Isostatic lamination is used to enhance the adherence of the green tapes and the shrinkage behaviour. It is very important for the lamination phase to be successful, since it affects final properties, sintering shrinkages and the probability of later delaminations.

If cavities are used in the stack, some form of support is generally needed during lamination to reduce bending of the stack, rounding of the corners, etc. In the case where the cavities are located on the substrate, rubber inserts can normally be used. However, if the cavities are inside the LTCC module, fugitive or sacrificial materials are needed. (Khoong *et al*., 2010)

Sintering, i.e. firing (step 7 in Fig. 6.4) is the phase where the laminated green tape package is taken to such a high temperature that neighbouring particles are bonded together by atomic diffusion. This results finally in a monolithic structure. Firing is usually done in a box oven because the temperature can be controlled more accurately, but belt ovens are also used in mass production.

The laminated package is placed on a flat surface, such as a thick Al_2O_3 plate. A typical LTCC sintering profile is depicted in Fig. 6.6. First, the temperature is raised to 400–450 °C at a rate of a few degrees per minute, after which the organics are burned out. Then the temperature is swiftly raised to 850–875 °C, which is kept for 10–20 minutes. Finally, the temperature is allowed to settle down to room temperature. The whole sintering phase takes about eight hours. During sintering, densification of the basic LTCC composition takes place, resulting in typical green tape shrinkage of 5–20% compared with the sintered product.

Depending on the LTCC system and the materials used, sintering is done in either an oxidizing or a reducing atmosphere. Especially if copper conductors are

© Woodhead Publishing Limited, 2012

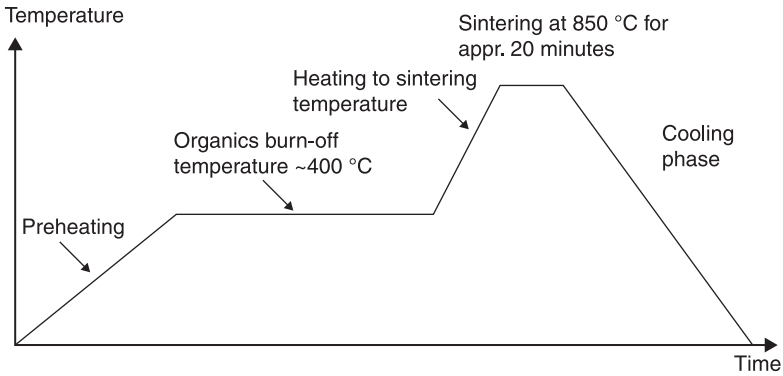

6.6 A typical sintering profile in LTCC manufacturing.

used, a reducing or neutral atmosphere is preferred in order to achieve adequate conductivity (Gongora-Rubio *et al*., 2001; Imanaka, 2005).

After the co-firing phase, some post-processing, like printing of post-fire conductors, may be performed on the fired package. The post-firing profile may differ from the co-firing profile, depending on the material used, but it never exceeds the highest temperature used in the co-firing process.

Next, the monolithic LTCC package is inspected (step 8 in Fig. 6.4) with an optical, acoustic or X-ray microscope, followed by functionality testing with electrical probing, for example. Finally, the structure is diced using a diamond saw or a laser.

6.3.3 Advanced methods for manufacturing and future trends

LTCC process technology has developed tremendously since it was first introduced. Experiments are showing, for example, that piezoelectric cantilevers (Heionen *et al*., 2007) and optical fibres (Sobocinski *et al*., 2008) can be integrated into the LTCC even before co-firing. Also thermal management will become more and more important in the future due to increasing packing density. Thermal loads can be dealt with, for instance, using thermal vias (Zampino *et al*., 2002) or liquid cooling (Barlow *et al*., 2009). This has already resulted and will surely further result in modifications of the common LTCC process. The possibilities of LTCC technology have been enhanced by ingenious inventions in the following areas:

- Fabrication of complex 3D microstructures by lasering and mechanical (hot) embossing tools (e.g. cavities and microchannels on the scale of a few dozen microns, for micro-opto-electromechanical systems (MOEMS), microfluidistics, waveguides, etc.) (Andrijasevic *et al*. 2007; Maw *et al*. 2007; Rabe *et al*. 2007).

© Woodhead Publishing Limited, 2012

- Shape-preserving buried cavities are created during sintering, e.g. by printing conductors on the opposite sides of the green tape (Espinoza-Vallejos *et al*., 1998).
- Process modification to create cavities without the need for (carbon-based) sacrificial volume material (SVM) (Barlow *et al*., 2009).
- Other lamination techniques to create 3D structures (sacrificial material (does not decompose or decomposes partly during sintering), fugitive material (decomposes fully during sintering), etc.)
- Photolithography of LTCC conductors (e.g. Du Pont's Fodel® paste) with the use of a laser to create fine lines down to 10 μm in width. (Corbett *et al*., 2005)
- Patterning of LTCC by etching partially sintered tapes, (Park *et al*., 1998; Espinoza-Vellejos and Santiago-Aviles, 2000; Gongora-Rubio *et al*., 2001).
- Via fabrication by acetone jet. With this method, Park *et al.*, 1998, for example, have manufactured microvias of 25 microns in diameter (Park *et al*., 1998; Gongora-Rubio *et al*., 2001).
- Room temperature lamination with the aid of an adhesive tape (Piwonski and Roosen, 1999; Roosen, 2001), by gluing, (Gurauskis *et al*., 2005), or otherwise chemically (Jurkow *et al*., 2009).
- Embedding optical fibres in LTCC (Golonka *et al*., 2005; Sobocinski *et al*., 2008).
- Technological development to achieve zero shrinkage horizontally (pressure-assisted sintering, use of sacrificial tapes, zero-shrinking tape) in order to fabricate products with great uniformity (Mikeska *et al*., 1992; Rabe *et al*., 2005).
- Embedded functional materials used in applications such as varactors (Tick *et al*., 2008).

6.4 An overview of LTCC applications

6.4.1 LTCC in packaging and microelectronics

When LTCC was introduced to the market, no one expected the variety of applications within which it is used today. Evolution of the technology allowed it to broaden its margins from simple multilayer substrates to complex 'intelligent' packages, sensors, microsystems and more. Each new feature presented to the technology – co-fired resistor pastes, co-strained tapes or co-fireable functional materials – opened new possibilities, but also issued new challenges. Nowadays, LTCC technology is commonly used in RF technologies, wireless communication and packaging. New applications include sensors, actuators and microsystems together with microfluidic lab-on-chips. High yield, fast prototyping and turnaround, flexibility of design, high reliability and relatively low cost have made LTCC the cornerstone of modern electronics.

The first LTCC applications, a radar chip for the F-22 jet fighter and a multilayer substrate for IBM and Fujitsu mainframe computers, were presented in the 1980s

© Woodhead Publishing Limited, 2012

(Imanaka, 2005; Golonka, 2001). At that time, LTCC was used mainly as a multilayer PCB. The ability to implement signal lines on different levels within the substrate allowed reaching packaging levels unavailable to standard PCBs. Multilayer composition made it possible to separate ground planes from signal lines, wirings from passives, receivers from transmitters and so on, for ease of designing, inspection and better properties. Furthermore, LTCC's superb microwave properties, such as low-loss and low-resistivity conductors, made it a perfect solution for RF devices (Golonka, 2001; Jantunen *et al*., 2003). Microwave strip lines, switches, antennas and baluns can be easily manufactured, either as discrete elements of very small size or embedded between thin sheets of LTCC. The possibility of integrating passive elements within the substrate, together with bare dice mounting, allows manufacturing of complete high-frequency devices with excellent properties at relatively low cost.

Applications in the area of RF modules vary from singe/dual/triple-band Global System for Mobile Communications (GSM) transceivers and Global Positioning System (GPS) devices to Bluetooth, Wi-Fi wireless communications and others (Lim *et al*., 2002; Lin *et al*., 2004; Ohata *et al*., 2003). Figure 6.7 presents a RF module and its schematic cross-section, manufactured by Kyocera. Embedding passive functions inside the module allowed a 30% reduction in size compared with the previous built-up substrate approach (Kyocera, 2007).

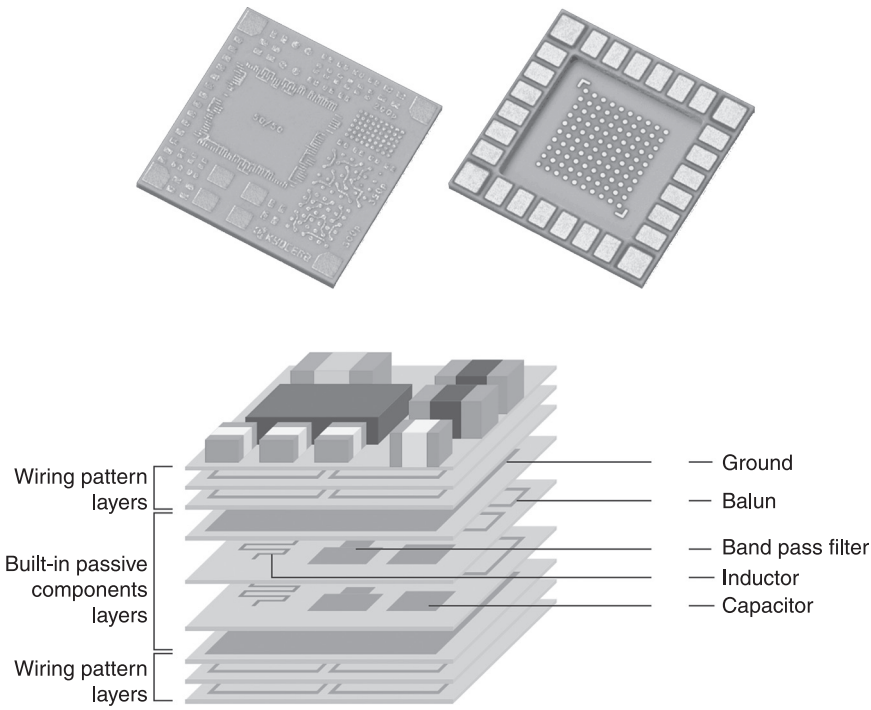

6.7 Multilayer RF structure manufactured by Kyocera (courtesy and copyright of Kyocera).

© Woodhead Publishing Limited, 2012

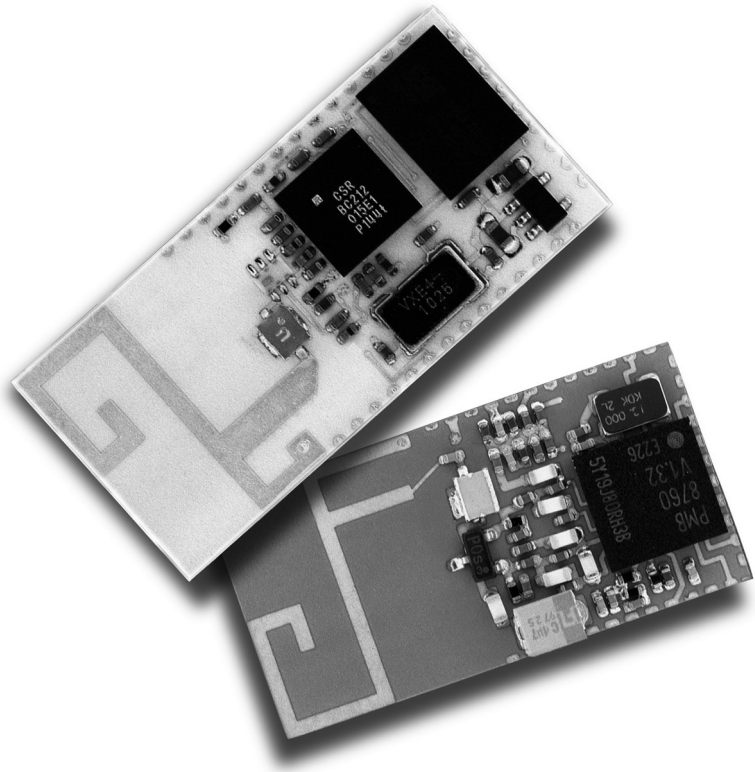

6.8 An example of a Bluetooth device with integrated antenna (courtesy and copyright of IMST GmbH).

A common element in smartphones and notebooks – the Bluetooth module – is presented in Fig. 6.8, in this case manufactured by IMST. This second-generation Bluetooth module has an integrated, inverted-F antenna structure, which has proved to have better performance than surface-mount device (SMD) solutions (Kulke *et al*., 2003).

Figure 6.9 presents a Wireless Local Area Network (WLAN) module fully integrated by EPCOS into one SMD chip ready to be mounted in a telephone, MP3 player, laptop or any other portable device. This 8.2 mm × 5.5 mm × 1.4 mm single package contains a RF front end, a power amplifier, a low-noise amplifier and a WLAN radio Integrated Circuit (IC) (Transceiver, Baseband/MAC), and compared to discrete solutions, saves around 80% in PCB space (EPCOS AG, 2006).

An example of planar, liquid-cooled and electronically steerable antennas for mobile applications, including satellite communications in the Ka band on ships, cars and airplanes, manufactured by IMST, is presented in Fig. 6.10. This application

© Woodhead Publishing Limited, 2012

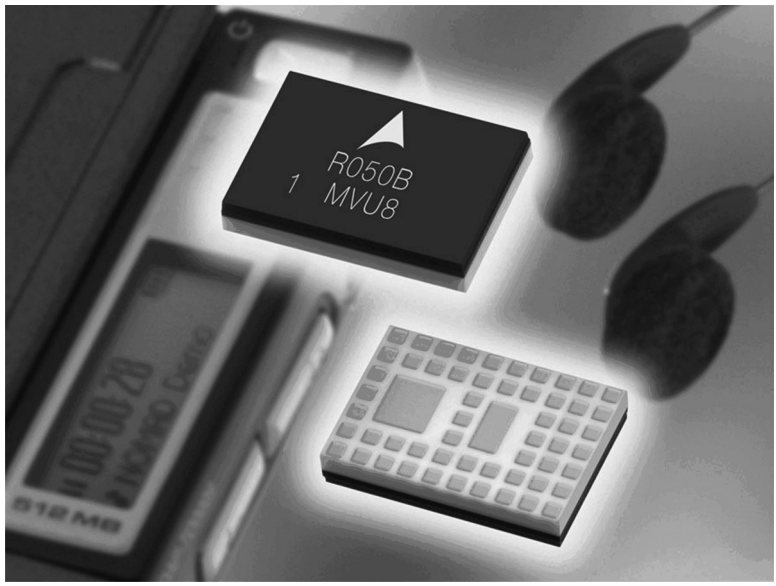

6.9 A WLAN module with integrated RF front end, power amplifier, low-noise amplifier and radio IC (courtesy and copyright of TDK-EPC).

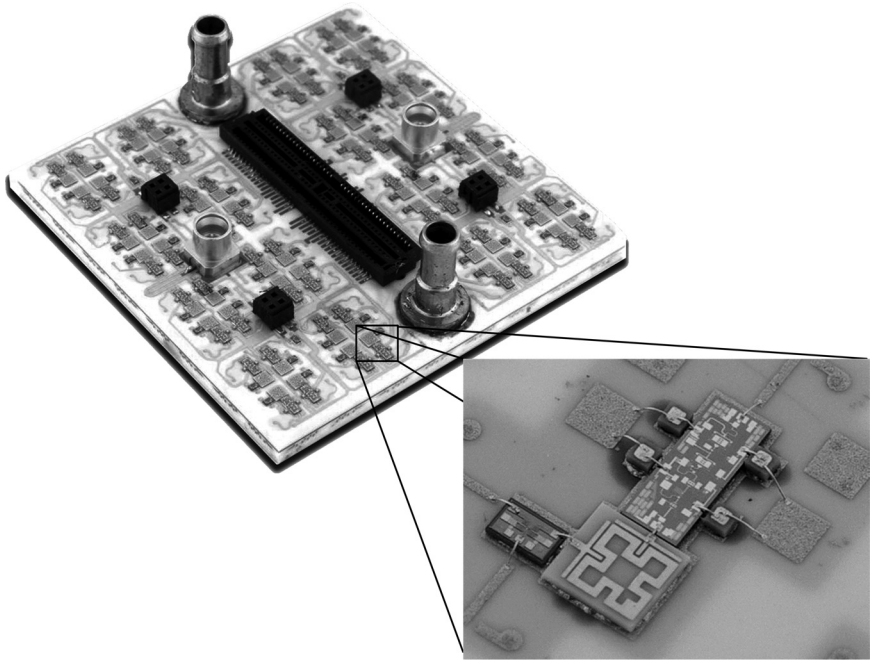

6.10 A planar, liquid-cooled electronically steerable antenna for Ka-band communication (courtesy and copyright of IMST GmbH).

© Woodhead Publishing Limited, 2012

shows that the possibility of embedding microfluidic channels inside circuit boards for active cooling has already come to realisation in LTCC technology.

Due to its high reliability and resistance to harsh environments, LTCC is used where normal methods fail – i.e. in engine control units, transmission control, electric power steering, electronic stability control, or dual-clutch transmissions (Murata, 2006). A mass-flow sensor for fuel injection control was presented (Schmid, 2002), as well as a pressure sensor (Fonesca *et al*., 2002) capable of working at high temperatures. Other LTCC applications in the automotive industry include on-board electronics such as sound and television systems, telecommunication, global positioning systems, but also a short-range radar system for driving assistance.

LTCC structures have also gone many times into space, including voyages to Mars and Jupiter (Scrantom and Gravier, 2000). They are used for satellite communications (Kulke *et al*., 2009) and many scientific space programmes (Barry LTCC, 2010).

6.4.2 Other areas of application

While industry is already quite familiar with LTCC technology, scientists are constantly working on new applications. Currently, such areas as microsystem packaging, microfluidics, sensors and actuators, optoelectronics and even micro-propulsion are being investigated.

Recent developments in microsystem technologies, mainly in silicon-based chips, have created a need for versatile packaging technology that could connect the chip in all ways necessary, still ensuring good mechanical stability and hermetic sealing. LTCC technology provides the answer to that problem, as it allows not only fine-line electrical connections, but also buried channels, valves and micropumps, freestanding cantilevers, membranes and even optical features. An example of using LTCC technology for silicon microfluidic packaging was presented by Sandia National Laboratories (2007). The connection between silicon and LTCC was secured with screen-printed O-ring seals, which ensured that no fluid leaks out from the joint, while the buried channels allowed a smooth transfer from microscale to standard fluidic connections.

LTCC technology is also feasible for manufacturing different sensors and actuators. Sensors such as flow sensors (Gongora-Rubio *et al*., 1999), millinewton force sensors (Birol *et al*., 2007) and temperature sensors (Hrovat *et al*., 2005) can be manufactured in LTCC. It is also possible to manufacture more complicated structures such as heavy metal detection sensors (Gongora-Rubio *et al*., 2004), chloride detection sensors (Ibañez-Garcia *et al*., 2006), phenolic compound sensors (Goldbech *et al*., 2006) or urea detection sensors (Malecha *et al*., 2009). Moreover, this technology allows integration of different sensors on one substrate, creating complex lab-on-chip modules (Smetana *et al*., 2007).

In some cases, valves and pumps are needed to manage the flow correctly. An example of a flow injection analysis LTCC module is presented in Fig. 6.11.

© Woodhead Publishing Limited, 2012

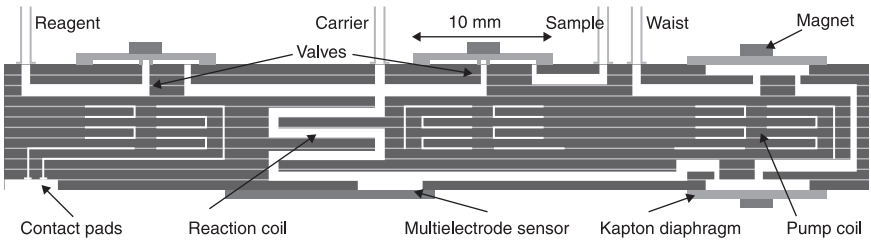

6.11 An example of flow injection analysis LTCC module (Gongora-Rubio *et al.,* 2001).

The presented structure includes reagent, sample and carrier inlets, a reaction coil and a multielectrode sensor for electrochemical measurement. Equipped with electromagnetic valves and a pump, this structure is capable of dosing reagents in the right proportions, mixing them and measuring the product of the reaction. Benefits of using LTCC-based microlaboratories include shorter analysis times as well as a smaller amount of reactants and waste.

Actuator applications in LTCC usually employ the piezoelectric effect or the electromagnetic effect to convert an electrical signal into mechanical displacement, although other structures that harness, e.g. electrostatic force, have been presented. Actuator applications include leaf spring actuators (Newborn *et al*., 2006), piezoelectric unimorph valves (Sobocinski *et al*., 2009), piezoelectric cantilevers (Heionen *et al*., 2007), piezoelectric optical fiber aligning devices (Park *et al*., 2010), electromagnetic hybrid valves (Gongora-Rubio *et al*., 1999), micropumps (Gongora-Rubio *et al*., 2001) and electrostatic valves (Klumbies *et al*., 2009).

New applications for space technology include solid-state micropropellers (Zhang *et al*., 2005; Thakur *et al*., 2010). Ignition by electrical impulse produces a large amount of gases to propel the structure. Thanks to their small size and low cost, arrays of these devices can be mounted on spacecrafts for position corrections. Further investigations will include possibilities of refills.

Energy harvesting structures based on LTCC are also being investigated. A multilayer coil inducer in a vibration-based electromagnetic meso-generator was presented by Hwang *et al.* (2010). The structure consisted of suspended thick-film multilayer coils with a seismic mass in the centre and a rare-earth magnet attached to the bottom of the structure. Under external vibrations, the seismic mass moved the coils up and down in the static magnetic field of the permanent magnet, generating a current in the coil circuit. An output of 6.46 $\mu W/mm^3$ was generated with 1 g (9.81 m/s^2) acceleration.

Progress has been made in introducing optical components into LTCC, such as transparent glass windows (Tan *et al*., 2007; Sandia National Laboratories, 2007), co-fired optical fibres (Lautzenhiser and Amaya, n. d.) and others. An example of such application is shown in Fig. 6.12. A liquid-cooled, fibre-pigtailed package for a high-power laser diode was manufactured by VTT. Passive

© Woodhead Publishing Limited, 2012

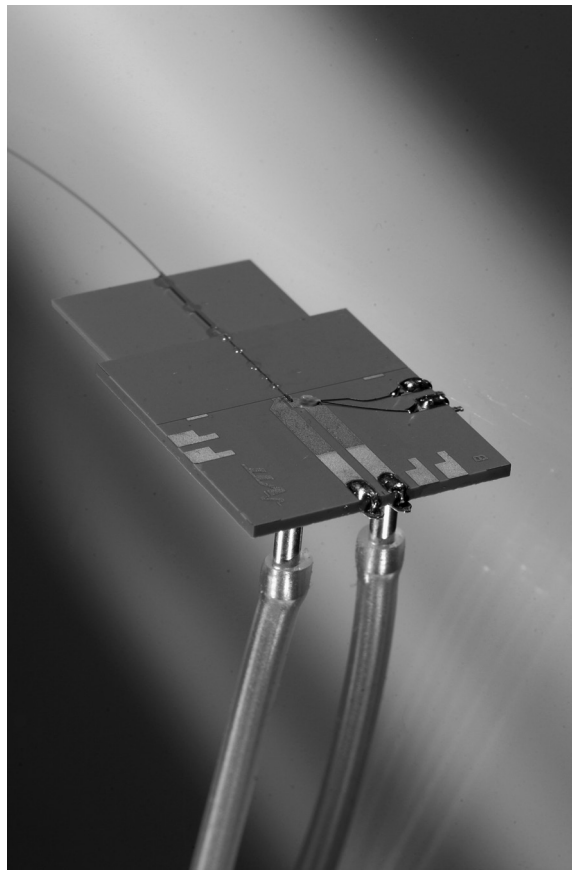

6.12 A liquid-cooled, fiber-pigtailed high-power laser diode (courtesy and copyright of VTT).

alignment methods allowed average coupling efficiency at a level of 0.31 with multimode optical fibre.

Another interesting application, presented by Sandia National Laboratories, is an ion mobility spectrometer, presented in Fig. 6.13. In this case, LTCC sheets were rolled after screen printing and laminated into a tube, forming a 3D structure. This solution allowed the use of only three layers instead of 300 (Sandia National Laboratories, 2007). The complete structure included an ioniser, a precise voltage divider, an ion drift chamber, an embedded thick-film heater for ensuring the right operating temperature and a nickel-plated kovar target. The tube ensured hermeticity, proper gas handling and shielding from radioactive material used in the ioniser.

As shown in this chapter, thanks to its advantages, LTCC technology covers a large range of applications in both everyday use and specially tailored applications.

© Woodhead Publishing Limited, 2012

6.13 Portable ion mobility spectrometer (Sandia National Laboratories, 2007).

The constant evolution of this technology makes new applications possible and improves those already existing.

6.5 Future trends

Recent development in LTCC technology has been enormous. Particularly interesting possibilities will be created by novel functional LTCC materials, enhanced processes and constantly widening application areas. However, further research is needed to manage the chemical, physical and electrical properties of the materials, i.e. modifying the compound with better chemistry without degrading either physical or electrical properties. Process enhancement may include even lower processing temperatures, tightly controlled shrinkage, higher tolerances of conductors, vias, etc. without increasing processing time. Application areas should spread to MEMS, lab-on-chips, highly integrated systems-on-a-package, autonomous sensors and energy harvesting, among others.

6.6 Sources of further information

The interested reader is guided to the following literature, which provides more information on LTCC technology. This is not a complete list (there are far too many other excellent publications available), but it quite neatly summarises the area of LTCC:

- Imanaka, *Multilayered Low Temperature Cofired Ceramics (LTCC) Technology*, 2005.
- Mistler and Twiname *Tape Casting, Theory and Practice*, 2000
- http://ltcc-consulting.com/
- http://www.electroscience.com
- www.dupont.com

© Woodhead Publishing Limited, 2012

- www.epcos.com
- www.heraeus.com
- www.kyocera.com
- www.ltcc.de – homepage of IMST Gmbh
- www.murata.com

6.7 References

Andrijasevic, D., Smetana, W., Zehetner, J., Zoppel, S. and Brenner, W., 2007. Aspects of micro structuring low temperature co-fired ceramic (LTCC) for realization of complex 3D objects by embossing. *Microelectronic Engineering*, 84, 1198–1201.

Barlow, F., Wood, J., Elshabini, A., Stephens, E. F., Feeler, R. *et al.*, 2009. Fabrication of precise fluidic structures in LTCC. *International Journal of Applied Ceramic Technology*, 6, 18–23.

BarryLTCC, 2010. *MetroGroup USA*. Available at: http://www.barryltcc.com (accessed 26 August 2010).

Birol, H., Maeder, T., Jacq, C. and Ryser, P., 2005. Investigation of interactions between co-fired LTCC components. *Journal of the European Ceramic Society*, 25, 2065–2069.

Birol, H., Maeder, T. and Ryser, P., 2006. Influence of processing and conduction materials on properties of co-fired resistors in LTCC structures. *Journal of the European Ceramic Society*, 26, 1937–1941.

Birol, H., Maeder, T., Nadzeyka, I., Boers, M. and Ryser, P., 2007. Fabrication of a millinewton force sensor using low temperature co-fired ceramic (LTCC) technology. *Sensors and Actuators A: Physical*, 334–338.

Block, C., Fluhr, H., Wiesbauer, K., Riedler, J., Ragossnig, H. *et al.*, 2008. Circuit, switching module comprising the same, and use of said switching module. United States Patent 7 343 137.

Corbett, S., Strole, J. and Johnston, K., 2005. Direct-write laser exposure of photosensitive conductive inks using shaped-beam optics. *International Journal of Applied Ceramic Technology*, 2, 390–400.

Deleniv, A., Gevorgian, S., Jantunnen, H. and Hu, T., 2005. LTCC compatible ferroelectric phase shifters. *Microwave Symposium Digest, 2005*. IEEE MTT-S International, Long Beach, CA.

EPCOS AG, 2006. *Components Magazine – EPCOS AG*. Available at: http://www.epcos.com/web/generator/Web/Sections/Components/Page,locale=en,r=247996,a=367940.html (accessed 19 July 2010).

Espinoza-Vallejos, P. and Santiago-Aviles, J., 2000. Photolithographic feature fabrication in LTCC. *International Journal of Microcircuits and Electronic Packaging*, 23, 286–292.

Espinoza-Vallejos, P., Zhong, J., Gongora-Rubio, M., Sola-Laguna, L. and Santiago-Aviles, J. J., 1998. Meso (intermediate)-scale electromechanical systems for the measurement and control of sagging in LTCC structures. *Materials Research Society Symposium Proceedings*, San Francisco.

Feingold, A. H., Heinz, M., Wahlers, R. L. and Stein, M. A., 2003. Materials for capacitive and inductive components integrated with commercially available LTCC systems. *Proceedings of the 3rd Annual Conference on Microelectronics and Packaging, IMAPS*. Herzelia.

© Woodhead Publishing Limited, 2012

Fonseca, M. A., English, J. M., von Arx, M. and Allen, M. G., 2002. Wireless micromachined ceramic pressure sensor for high-temperature applications. *Journal of Microelectromechanical Systems*, 11(4), 337–343.

Fournier, Y., Maeder, T., Boutinard-Rouelle, G., Barras, A., Craquelin, N. *et al.* 2010. Integrated LTCC pressure/flow/temperature multisensor for compressed air diagnostics. *Sensors*, 10, 11 156–11 173.

Ganne, J.-P., Lebourgeois, R., Paté, M., Dubreuil, D., Pinier, L. *et al.* 2007. The electromagnetic properties of Cu-substituted garnets with low sintering temperature. *Journal of the European Ceramic Society*, 27, 2771–2777.

Goldbach, M., Axthelm, H. and Keusgen, M., 2006. LTCC-based microchips for the electrochemical detection of phenolic compounds. *Sensors and Actuators B: Chemical*, 120, 346–351.

Golonka, L., 2001. *Zastosowanie Ceramiki LTCC w Mikroelektronice*. Wroclaw.

Golonka, L. J., Roguszczak, H., Zawada, T., Radojewski, J., Grabowska, I. *et al.*, 2005. LTCC based microfluidic systems with optical detection. *Sensors and Actuators B*, 111–112, 396–402.

Gongora-Rubio, M. R., Espinoza-Vallejos, P., Sola-Laguna, L. and Santiago-Avilés, J. J., 2001. Overview of low temperature co-fired ceramics tape technology for meso-system technology (MsST). *Sensors and Actuators A: Physical*, 89, 222–241.

Gongora-Rubio, M. R. Fontes, M. B. A., Rocha, Z. M. d., Richter, E. M. and Angnes, L., 2004. LTCC manifold for heavy metal detection system in biomedical and environmental fluids. *Sensors and Actuators B: Chemical*, 103, 468–473.

Gongora-Rubio, M. R., Solá-Laguna, L. M., Moffett, P. J. and Santiago-Avilés, J. J., 1999. The utilization of low temperature co-fired ceramics (LTCC-ML) technology for meso-scale EMS, a simple thermistor based flow sensor. *Sensors and Actuators A: Physical*, 73, 215–221.

Gongora-Rubio, M. R., Solá-Laguna, L. M., Smith, M. and Santiago, J. J. A., 1999. A meso-scale electromagnetically actuated normally closed valve realized on LTCC tapes. *Proceedings of SPIE Conference on Microfluidic Devices and Systems II*, SPIE, Santa Clara.

Gurauskis, J., Sanchez-Herencia, A. J. and Baudin, C., 2005. Joining green ceramic tapes made from water-based slurries by applying low pressures at ambient temperature. *Journal of the European Ceramic Society*, 25, 3403–3411.

Haertling, G. H., 1967. Properties of hot-pressed ferroelectric alkali niobate ceramics. *Journal of the American Ceramic Society*, 50, 329–330.

Hagen, G. and Rebenklau, L., 2006. Fabrication of smallest vias in LTCC tape. *Electronics System Integration Technology Conference*, Dresden.

Heinonen, E., Juuti, J. and Jantunen, H., 2007. Characteristics of piezoelectric cantilevers embedded in LTCC. *Journal of the European Ceramic Society*, 27, 4135–4138.

Honkamo, J., Hannu, J., Jantunen, H., Moilanen, M. and Mielcarek, W. 2007. Microstructural and electrical properties of multicomponent varistor ceramics with PbO–ZnO–B_2O_3 glass addition. *Journal of Electroceramics*, 18, 175–181.

Horvth, E., 2008. Embedded thick-film resistors applied in low temperature co-fired ceramic circuit substrates. *Periodica Polytechnica, Electrical Engineering*, 52, 45–57.

Howatt G. N., Breckenridge R. G. and Brownlow J. M. 1947. Fabrication of thin ceramic sheets for capacitors. *Journal of the American Ceramic Society*, 30, 237–242.

Hrovat, M., Belavič, D., Kita, J., Cilenšek, J., Golonka, L. *et al.* 2005. Thick-film temperature sensors on alumina and LTCC substrates. *Journal of the European Ceramic Society*, 3443–3450.

© Woodhead Publishing Limited, 2012

Hrovat, M., Holc, J., Drnovšek, S., Belavič, D., Cilenšek, J. *et al.* 2006. PZT thick-films on LTCC substrates with an interposed alumina barrier layer. *Journal of the European Ceramic Society*, 26, 897–900.

Hrovat, M., Belavic, D., Ursic, H., Kita, J., Holc, J. *et al.*, 2008. An investigation of thick-film materials for temperature and pressure sensors on self-constrained LTCC substrates. *Second Electronics System-Integration Technology Conference*, ESTC, Greenwich, 2008.

Hsi, C.-S., Chen, Y.-C., Jantunen, H., Wu, M.-J. and Lin, T.-C., 2008. Barium titanate based dielectric sintered with a two-stage process. *Journal of the European Ceramic Society*, 28, 2581–2588.

Hsi, C.-S., Chen, D.-F., Shieh, F.-M. and Fu, S.-L., 2003. Processing of LTCC with embedded RuO_2-based resistors. *Materials Chemistry and Physics*, 78, 67–72.

Hwang, Y. M., Lu, W. L. and Pan, C. T., 2010. Development and fabrication of an LTCC multilayer coil inducer in a vibration-based electromagnetic meso-generator. *Microelectronics Journal*, 41, 338–346.

Ibañez-Garcia, N., Gonçalves, R. D. M., Rocha, Z. M. d., Góngora-Rubio, M. R., Seabra, A. C. *et al.* 2006. LTCC meso-analytical system for chloride ion determination in drinking waters. *Sensors and Actuators B: Chemical*, 118, 67–72.

Imanaka, Y., 2005. *Multilayered Low Temperature Cofired Ceramics (LTCC) Technology*. Springer, USA.

Jaeger, R. E. and Egerton, L., 1962. Hot pressing of potassium-sodium niobates. *Journal of the American Ceramic Society*, 45, 209–213.

Jantunen, H., Kangasvieri, T., Vähäkangas, J. and Leppävuori, S., 2003. Design aspects of microwave components with LTCC technique. *Journal of the European Ceramic Society*, 23, 2541–2548.

Jantunen, H., Hu, T., Uusimäki, A. and Leppävuori, S., 2004. Ferroelectric LTCC for multilayer devices. *Journal of Ceramic Society of Japan*, 112, 1552–1556.

Jean, J.-H. and Lin, S.-C., 2000. Low-fire processing of ZrO_2–SnO_2–TiO_2 ceramics. *Journal of the American Ceramic Society*, 83, 1417–1422.

Joshi, H., Sigmarsson, H. H., Peroulis, D. and Chappell, W. J., 2007. Highly loaded evanescent cavities for widely tunable high-Q filters. *Microwave Symposium*, IEEE/MTT-S International.

Jurkow, D., Roguszczak, H. and Golonka, L., 2009. Cold chemical lamination of ceramic green tapes. *Journal of the European Ceramic Society*, 29, 703–709.

Karioja, P., Keränen, K., Kautio, K., Ollila, J., Heikkinen, M. *et al.*, 2010. LTCC-based differential photo acoustic cell for ppm gas sensing. *Proceedings of the SPIE*, San Francisco.

Khoong, L. E., Tang, Y. M. and Lam, Y. C., 2010. Overview on fabrication of three-dimensional structures in multi-layer ceramic substrate. *Journal of the European Ceramic Society*, 30, 1973–1987.

Kim, B.-Y., Han, D.-B. and Jeong, C.-W., 2010. Preparation of screen printable conductive $MoSi_2$ thick-films for ceramic sheet heater. *Journal of the Korean Ceramic Society*, 47, 319–324.

Kim, D.-W., Kim, T.-G. and Hong, K. S., 1999. Low-firing of CuO-doped anatase. *Materials Research Bulletin*, 34, 771–781.

Kim, H., Shrout, T., Rindall, C. and Langan, M., 2002. Low temperature sintering and properties of $Ag(Nb,Ta)O_3$ composite ceramics. *Journal of the American Ceramic Society*, 85, 2738–2744.

Kita, J., Dziedzic, A., Golonka, L. J. and Zawada, T., 2002. Laser treatment of LTCC for 3D structures and elements fabrication. *Microelectronics International*, 19, 14–18.

© Woodhead Publishing Limited, 2012

Kittilä, M., Hagberg, J., Jakku, E. and Leppävuori, S., 2004. Direct gravure printing (DGP) method for printing fine-line electrical circuits on ceramics. *IEEE Transactions on Electronics Packaging Manufacturing*, 27, 109–114.

Klumbies, H., Partsch, U., Goldberg, A. and Gebhardt, S., 2009. Actuators to be integrated in low temperature cofired ceramics. *ISSE 2009 thirty-second International Spring Seminar on Electronics Technology*, Brno, Czech Republic.

Knickerbocker, S. H., Kumar, A. H. and Herron, L. W., 1993. Cordierite glass–ceramics for ceramic packaging. *American Ceramic Society Bulletin*, 72, 90–95.

Kok, S. L., White, N. and Harris, N., 2009. Fabrication and characterisation of free-standing thick-film piezoelectric cantilevers for energy harvesting. *Measurement Science and Technology*, 20, 124 010–124 023.

Kulke, R., Wahle, V., Sollbach, D., Uhlig, P., Rittweger, M. *et al.*, 2003. High level of integration for Bluetooth modules on LTCC. *Fourteenth European Microelectronics and Packaging Conference and Exhibition*, Friedrichshafen.

Kulke, R., Möllenbeck, G., Günner, C., Uhlig, P., Drüe, K. H. *et al.*, 2009. Ceramic microwave circuits for satellite communication. *Journal of Microelectronics and Electronic Packaging*, 6, 27–31.

Kyocera, 2007. *LTCC Packages for RF Modules | Semiconductor Components | Products | KYOCERA*. Available at: http://global.kyocera.com/prdct/semicon/semi/ltcc/index.html (accessed 19 July 2010).

Lautzenhiser, F. and Amaya, E. 2002, *HeraLock 2000 Self-constrained LTCC Tape*. Heraeus CMD.

Lee, Y.-C., Lin, C.-H. and Lin, I.-N., 2003. Bi-Zn-Nb-O microwave dielectric materials for multilayer filter application. *Materials Chemistry and Physics*, 79, 124–128.

Li, J.-F., Wang, K., Zhang, B.-P. and Zhang, L.-M., 2006. Ferroelectric and piezoelectric properties of fine-grained $Na_{0.5}K_{0.5}NbO_3$ lead-free piezoelectric ceramics prepared by spark plasma sintering. *Journal of the American Ceramic Society*, 89, 706–709.

Lim, K., Pinel, S., Davis, M., Sutono, A., Lee, C.-H. *et al.*, 2002. RF-System-on-package (SOP) for wireless comunnications. *IEEE Microvawe Magazine*, 3(1), 88–94.

Lin, Y.-S., Liu, C.-C., Li, L.-M. and Chen, C.-H., 2004. Design of an LTCC tri-band transceiver module for GPRS mobile applications. *IEEE Transactions on Microwave Theory and Techniques*, 52, 2718–2724.

Lisjak, D. and Drofenik, M., 2007. Influence of Ag on the composition and electromagnetic properties of low-temperature cofired hexaferrites. *Journal of the American Ceramic Society*, 90, 3121–3126.

Malecha, K., Pijanowska, D. G., Golonka, L. J. and Torbiczb, W., 2009. LTCC microreactor for urea determination in biological fluids. *Sensors and Actuators B: Chemical*, 141, 301–308.

Marques, V. M. F., Tulyaganov, D. U., Agathopoulos, S., Gataullin, V. K., Kothiyal, G. P. *et al.*, 2006. Low temperature synthesis of anorthite based glass-ceramics via sintering and crystallization of glass-powder compacts. *Journal of the European Ceramic Society*, 26, 2503–2510.

Matz, R., Götsch, D., Karmazin, R., Männer, R. and Siessegger, B., 2009. Low temperature cofirable MnZn ferrite for power electronic applications. *Journal of Electroceramics*, 22, 209–215.

Maw, H. P., Wai, S. C., Tjeung, R. T., Wai, L. C., Keng, L. B. *et al.*, 2007. Microembossing of LTCC (low temperature co-fired ceramic) green substrates. *Ninth Electronics Packaging Technology Conference*, Singapore.

© Woodhead Publishing Limited, 2012

Mikeska, K. R., Schaefer, D. T. and Jensen, R. H., 1992. Method for reducing shrinkage during firing of green ceramic bodies. United States Patent No. 5085720.

Mis, E., Dziedzic, A. and Mielcarek, W., 2009. Microvaristors in thick-film and LTCC circuits. *Microelectronics Reliability*, 49, 607–613.

Mistler, R. E. and Twiname, E. R., 2000. *Tape Casting, Theory and Practice*. Westerville: American Ceramic Society.

Murata, 2006. (Press release) Making great contributions to realize the intelligent cars. *('Technologies of Murata') Tech-On!* Available at: http://www.murata.com/auto/techon/solution_5–5.html (accessed 19 July 2010).

Nagata, H., 2008. Electrical properties and tracer diffusion of oxygen in some Bi-based lead-free piezoelectric ceramics. *Journal of the Ceramic Society of Japan*, 116, 271–277.

Nahm, C.-W., 2008. Effect of sintering temperature electrical properties of ZNR doped with Pr–Co–Cr–La. *Ceramics International*, 34, 1521–1525.

Newborn, C. H., English, J. M. and Coe, D. J., 2006. LTCC fabrication for a leaf spring vertical actuator. *International Journal of Applied Ceramic Technology*, 3, 61–67.

Ohata, K., Maruhashi, K., Ito, M., Kishimoto, S., Ikuina, K. *et al.*, 2003. 1.25 Gbps wireless Gigabit Ethernet link at 60 GHz-band. *IEEE MTT-S International Microwave Symposium Digest*, Philadelphia.

Park, S.-H., Baker, A., Eitel, R. E., Randall, C. A. and Uchino, K., 2010. Active optical fiber alignment with a piezoelectric ultrasonic motor integrated into low temperature cofired ceramics. *Journal of Intelligent Material Systems and Structures*, 21, 469–479.

Park, J., Espinoza-Vallejos, P., Sola-Laguna, L. and Santiago-Aviles, J., 1998. Etching and exfoliation techniques for the fabrication of 3-D meso-scale structures on LTCC tapes. *Proceedings SPIE 3582 (International Society for Optical Engineering)*, San Diego.

Peterson, K. A., Patel, K. D., Ho, C. K., Rohde, S. B., Nordquist, C. D. *et al.*, 2005. Novel microsystem applications with new techniques in low-temperature co-fired ceramics. *International Journal of Applied Ceramic Technologies*, 2, 345–363.

Piwonski, M. A. and Roosen, A., 1999. Low pressure lamination of ceramic green tapes by gluing at room temperature. *Journal of the European Ceramic Society*, 19, 263–270.

Rabe, T., Kuchenbecker, P. and Schulz, B., 2007. Hot embossing: an alternative method to produce cavities in ceramic multilayer. *International Journal of Applied Ceramic Technology*, 4, 38–46.

Rabe, T., Schiller, W. A., Hochheimer, T., Modes, C. and Kipka, A., 2005. Zero shrinkage of LTCC by self-constrained sintering. *International Journal of Applied Ceramic Technology*, 2(5), 374–382.

Rhim, S. H., Shin, S. Y., Joo, B. Y. and Oh, S. I., 2006. Burr formation during micro via-hole punching process of ceramic and PET double layer sheet. *International Journal of Advanced Manufacturing Technologies*, 30, 227–232.

Roosen, A., 2001. New lamination technique to join ceramic green tapes for the manufacturing of multilayer devices. *Journal of the European Ceramic Society*, 21, 1993–1996.

Sandia National Laboratories, 2007. *Macro–Meso–Microsystems Integration in LTCC LDRD*, Sandia National Laboratories, Albuquerque.

Schmid, U., 2002. A robust flow sensor for high pressure automotive applications. *Sensors and Actuators A: Physical*, 97–98, 253–263.

Scrantom, C. and Gravier, G., 2000. *LTCC Technology. Where We Are and Where We're Going IV*, Costa Mesa, California.

Sebastian, M. and Jantunen, H., 2008. Low loss dielectric materials for LTCC applications: a review. *International Materials Reviews*, 53, 57–90.

© Woodhead Publishing Limited, 2012

Shamim, A., Bray, J., Roy, L., Hojjat, N., Abou Elasoued, R. *et al.* 2007. Microwave and magnetostatic characterization of ferrite LTCC for tunable and reconfiguarable SiP applications. *Microwave Symposium*, IEEE/MTT-S International, Honolulu.

Smetana, W., Balluch, B., Stangl, G., Gaubitzer, E., Edetsberger, M. *et al.* 2007. A multi-sensor biological monitoring module built up in LTCC-technology. *Microelectronic Engineering*, 84, 1240–1243.

Sobocinski, M., Juuti, J., Jantunen, H. and Golonka, L., 2009. Piezoelectric unimorph valve assembled on an LTCC substrate. *Sensors and Actuators A: Physical*, 149, 315–319.

Sobocinski, M., Tadaszak, R. and Golonka, L., 2008. Cofired optical fiber in LTCC. *Thirty-second International IMAPS-IEEE CPMT Poland Conference*.

Steinberg, J. I., Horowitz, S. J. and Bacher, R. J., 1998. Low-temperature co-fired tape dielectric material systems for multilayer interconnections, advances in ceramics. *Multilayer Ceramic Devices*, 19, 31–39.

Sun, N. X., Wang, J. W., Daigle, A., Pettiford, C., Mosallaei, H. *et al.* 2007. Electronically tunable magnetic patch antennas with metal magnetic films. *Electronics Letters*, 43, 434–436.

Sunppan, V. Vadiveloo, P. L., Wai, L. L., Fan, W. and Lu, C. W., 2006. Processing and electrical characterization of co-sintered composite glass ceramics. *Eighth Electronics Packaging Technology Conference*, Singapore.

Takao, H., Saito, Y., Aok, Y. and Horibuchi, K., 2006. Microstructural evolution of crystalline-oriented $(K_{0.5}Na_{0.5})NbO_3$ piezoelectric ceramics with a sintering aid of CuO. *Journal of the American Ceramic Society*, 89, 1951–1956.

Tan, Y. M., Khoong, L. E., Lam, Y. C. and Lu, C. W., 2007. Integration of glass layer for meso and micro-system applications. *Ninth Electronics Packaging Technology Conference*, Singapore.

Thakur, J., Pratap, R., Fournier, Y., Maeder, T. and Ryser, P., 2010. Realization of a solid-propellant based microthruster using low temperature co-fired ceramics. *Sensors and Transducers Journal*, 117, 29–40.

Tick, T., Palukuru, V., Komulainen, M., Peräntie, J. and Jantunen, H., 2008. Method for manufacturing embedded variable capacitors in low-temperature cofired ceramic substrate. *Electronics Letters*, 44, 94–95.

Tummala, R. R., 1991. Ceramic and glass-ceramic packaging in the 1990s. *Journal of the American Ceramic Society*, 74, 895–908.

Udovic, M., Valant, M. and Suvorov, D., 2004. Phase formation and dielectric characterization of the Bi_2O_3–TeO_2 system prepared in an oxygen atmosphere. *Journal of the American Ceramic Society*, 87, 591–597.

Valant, M. and Suvorov, D., 2004. Low-temperature sintering of $(Ba_{0.6}Sr_{0.4})TiO_3$. *Journal of the American Ceramic Society*, 87, 1222–1226.

Vanek, J., Smetana, W., Weilguni, M. and Szendiuch, I., 2009. Characterization of PTC resistor pastes applied in LTCC technology. *Proceedings of the European Microelectronics and Packaging Conference EMPC*, Rimini.

Wang, G., Barlow, F. and Elshabini, A., 2002. Modeling and control of resistance tolerance for embedded resisotrs in LTCC. *Proceedings of Fifty-Second Electronic Components and Technology Conference*, San Diego.

Wang, G., Folk, E. C., Barlow, F. and Elshabini, A., 2006. Fabrication of Microvias for Multilayer LTCC Substrates. *IEEE Transactions on Electronics Packaging Manufacturing*, 29, 32–41.

Wang, Y. L., Ollivier, P. J. and Skurski, M. A., 2000. Photoformed thick-film materials and their application to fine feature circuitry. *HDI Conference*, Denver.

© Woodhead Publishing Limited, 2012

Yan, M., Hu, J., Luo, W. and Zhang, W. Y., 2006. Preparation and investigation of low firing temperature NiCuZn ferrites with high relative initial permeability. *Journal of Magnetism and Magnetic Materials*, 303, 249–255.

Yau, Y.-W., Booke, M. A., Sandhu, N. S. and Fulton, J. J., 1991. Microelectronics packaging processing using focused high power electron beams. *Proceedings of Forty-First Electronic Components and Technology Conference*, Atlanta.

Yau, Y.-W., Long, D. C., Grant, W. T., Sandhu, N. S. and Fulton, J. J., 1993. Overview of via formation technologies for ceramic packaging manufacturing. *Proceedings of Forty-Third Electronic Components and Technology Conference*, Orlando.

Yokoi, A., Ogawa, H. and Kan, A., 2005. Microwave dielectric properties of $Mg_4Nb_2O_9$–3.0 wt.% LiF ceramics prepared with $CaTiO_3$ additions. *Journal of the European Ceramic Society*, 25, 2871–2875.

Zampino, M. A., Kandukuri, R. and Kinzy Jones, W., 2002. High performance thermal vias in LTCC substrates. *Proceedings 2002 Inter Society Conference on Thermal Phenomena*, San Diego.

Zhang, K. L., Chou, S. K. and Ang, S. S., 2005. Development of a low-temperature co-fired ceramic solid propellant microthruster. *Journal of Micromechanics and Microengineering*, 15, 944–952.

Zhang, Q.-L., Yang, H. and Tong, J.-X., 2006. Low-temperature firing and microwave dielectric properties of $MgTiO_3$ ceramics with Bi_2O_3–V_2O_5. *Materials Letters*, 60, 1188–1191.

Zhao, F., Yue, Z., Lin, Y., Gui, Z. and Li, L., 2007. Phase relation and microwave dielectric properties of $xCaTiO_3$–$(1–x)TiO_2$–$3ZnTiO_3$ multiphase ceramics. *Ceramics International*, 33, 895–900.

© Woodhead Publishing Limited, 2012

7

Printed resistive sensors for physical quantities

M. PRUDENZIATI, University of Modena and Reggio Emilia, Italy

Abstract: This chapter reviews commonly used and state-of-the-art versions of resistive sensors for physical quantities such as temperature, strain, radiant energy and magnetic field, relying on printed films. An outline is given for the properties of the films on which these sensors operate with a mention of their structure and applications.

Key words: resistive sensors, physical sensors, piezoresistivity, magnetoresistivity, thermoresistivity, thick-films, structure–properties relations.

7.1 Introduction

Academic and technical communities started to recognize the potential of thick-film technology in the field of solid state sensors about 40 years ago. Research and development efforts resulted in a notable impact of thick-films in measuring systems (Prudenziati, 1994; White and Turner, 1997). Nowadays, thick-film resistive sensors are well assessed especially in applications where high reliability and long-term stability in very demanding environments are requisites to be complied with economically, such as in large market sectors like automotive applications (Wada *et al.*, 1997), or in uncommon operations (e.g. appropriate performance in large facilities) or disposable devices. The innovations achieved in the 1980s with traditional thick-film materials and processes were extended during the next two decades with low-temperature co-fixed ceramics (LTCC) technology for Micro Electro-Mechanical Systems based on structured Ceramic materials (C-MEM) and micro-machined Micro Electro-Mechanical Systems based on micro-machined Silicon (Si-MEMS). Recently, some researchers have been exploring the new frontiers of fine-line printing technologies, such as ink-jet printing for mesoscale sensor systems. This chapter reviews commonly used and state-of-the-art versions of resistive sensors for physical quantities, i.e. temperature, strain, radiant and magnetic field-related quantifiers. Also applications of potentiometric thick-films will be briefly mentioned. An outline is given for the properties on which these sensors operate with a mention of their structure and applications. Thick-film physical sensors relying on capacitive devices and pyro–piezo electric thick-films materials are covered in chapters 8 and 9 respectively; thick-film chemical sensors are dealt with in chapters 10 and 11; biosensors are in chapter 13. Finally physical sensors relying on non-resistive thick-films forming parts of MEMS are described in chapter 10 of this book. The references quoted here are merely a sample of the huge quantities of studies published on resistive printed sensors and their applications.

© Woodhead Publishing Limited, 2012

7.2 Temperature sensors

Thick-film materials can be used for temperature measurements. A major advantage of this technique is its capability to integrate the temperature sensing function with the sensor signal conditioning circuitry. These thick-film sensors, when formed on ceramic or insulated metal substrates, can withstand much greater abuse and handling than the normal metallic wire thermocouples. This class of sensors includes: resistive temperature detectors (RTD), positive temperature coefficient sensors (also denoted as PTC thermistors), negative temperature-coefficient (NTC) thermistors, thick-film thermocouples, thermo-switches, cryogenic and low temperature detectors.

7.2.1 Resistive temperature detectors

Thick-film conductors, either simple metals or alloys (typical sheet resistance from 1.5 to 200 mΩ/□) exhibit thermoresistive properties *similar* to those of their bulk counterparts, that is to say that their electrical transport is governed mainly by electrons scattered from lattice defects and vibrations. The latter phenomenon (also denoted as phonon scattering) is the most influential at temperatures not too far from room temperature, resulting in a quasi-linear temperature dependence of resistivity and consequently of the resistance. The $R(T)$ vs. T relation over a temperature span of many hundreds of degrees is in fact:

$$R(T) = R_0(1 + \alpha T + \beta T^2), \qquad [7.1]$$

where T is temperature in degrees Centigrade and R_0 denotes resistance at a reference T, e.g. 0 °C. Alternatively, the simpler linear equation,

$$R(T) = R_0(1 + \alpha T), \qquad [7.2]$$

may be used to represent the sensor response, typically in a range from −55 to 125 °C.

The temperature coefficient of resistance (TCR) = α assumes values as high as 7000 ppm/°C in pure Ni and 3850 ppm/°C in pure Pt. These two metals are in fact the basic elements of the well-known wire-wound and thin-film RTD sensors.

Thick-film versions of RTDs were introduced starting with various conductive thick-film inks (Arima, 1994). The addition of glass or oxide binders (required to promote sintering and adhesion, as discussed in Chapter 4) is responsible for an added contribution to the electron scattering, or, in practice, to an increase of resistivity and decrease of TCR values. Hence, it is not surprising that these performance characteristics are affected by the preparation conditions, including the firing temperature and dwell time: all of the conditions promoting increased densification and grain growth of metal particles result in performance approaching that of the parent metal. Similarly, larger TCR values are displayed by fritless thick-film RDT than their glass-bonded counterparts. Therefore reproducibility of results requires close control of paste composition and preparing process.

© Woodhead Publishing Limited, 2012

Although Ni and several precious metal-based inks are of interest in manufacturing RTDs, it is Pt that plays a dominant role in thick-film RTD thermometry. A multipurpose RTD Pt-based sensor has been manufactured by Matthew Electronics since 1975, and commercially available under the trademark Thermafilm®, with a 100 Ω resistance at 0 °C and a *TCR* of 3850 ppm/°C. It meets the BS 1904 and DIN 43 760 standards, providing direct replacement for conventional wire-wound temperature detectors, with operating temperatures up to 600 °C and excellent stability (e.g. temperature error <1 °C at 600 °C/6000 h; Evans, 1981). In addition, in thick-film sensing systems for other physical, chemical and biological quantities, screen-printed temperature sensors are essentially omnipresent, and often Pt-based elements are chosen not only for their high-temperature sensitivity but also for their stability in a variety of harsh environments without degradation.

A common drawback of metal-based thick-film conductors is the relatively low sheet resistance of the fired layers. Thus high aspect–ratio configurations are required for yielding easily measurable resistance of the elements. A partial remedy is the use of metal–organic-based pastes, resulting in thinner (0.1–0.3 μm) fired films with higher sheet resistance (e.g. 1 to 3 Ω/□) than conventional thick-film materials, without sacrifice of *TCR* (e.g. Pt-based Heraeus RP 10003). For these films the substrate has to be glazed or very smooth, and several multiple layers are deposited and separately fired. RTDs of about 3 × 9 mm with a resistance of 100 Ω have been obtained in this way (Reynolds and Norton, 1986). Another route to increase the sensor resistance is to pattern fine (10–20 μm wide) lines, a procedure early executed with YAG-laser trimming of the deposited films; now micropen deposition or ink-jet printing processes are promising methods, that are currently under scrutiny (Cai *et al*., 2009). However, the most common way to cope with the main requirements of high sensitivity, small size and easily measurable resistance in temperature detectors is the use of cermet thick-film materials referred to as thermistors.

7.2.2 Positive temperature coefficient thermistors

Thick-film compositions for PTC thermistors with sheet resistances from 10 to 1000 Ω/□ have been developed (e.g. PTC 2100 or 2600 by ESL and 5090 by DuPont). The linear $R(T)$ vs. T relation in eq. [7.2] is representative of the sensor response with *TCR* values spanning from 2500 ppm/°C to 4500 ppm/°C. A possible way to prepare PTC sensors is to start from resistive inks comprising an adequate glass frit and a fine powder of complex perovskite oxides such as $CaCu_3Ru_4O_{12}$ and/or $LaCu_3Ru_4O_{12}$ (Burkhardt *et al.*, 1993) resulting in thermistors with sheet resistances from about 50 to 500 Ω/□ and *TCR* from 1000 to 2000 ppm/°C in the temperature range −25 to +125 °C. Another way is to 'load' the glass phase with a large fraction of RuO_2. The relatively low specific resistivity of RuO_2 and its metallic-like temperature dependence $P(T)$ with a *TCR* of a few 1000 ppm/°C

© Woodhead Publishing Limited, 2012

allows designers to create PTC sensors with α values typically in the range from 1000 to 1500 ppm/°C with sheet resistance around 1–10 Ω/□ (see Chapter 4, section 4.1, for sheet resistance definition). Likewise, Kuzel *et al.* (1993) successfully prepared cermets compositions based on $Bi_2Ru_2O_7$, CdO and two types of glass for sensors with sheet resistance of 0.5–3 kΩ/□ and *TCR* of 2200–2600 ppm/°C.

A very special composition (and microstructure) for PTC sensors is represented by the resistive series DuPont 5090D with sheet resistance ranging from 10 to 1 KΩ/□ and *TCR* of about 3500 ppm/°C. The member 5091D, 10 Ω/□, is claimed to exhibit a Pt-like behaviour e.g. to match exactly the α and β coefficients of the linear and quadratic terms in the $R(T)$ vs. T response (eq. [7.1]) of platinum standard sensors. These sensors are due to Cu_2O added to ruthenate-based pyrochlores in high-lead glass promoting the dissociation of the ruthenate compound, e.g. $Pb_2Ru_2O_{6,5}$ (Hormadaly, 1990; Jiang *et al.*, 2000) or $(Gd,Bi)_2Ru_2O_7$ (Hrovat *et al.*, 2007), which partially transforms during firing in needle-like RuO_2 grains (Fig. 7.1).

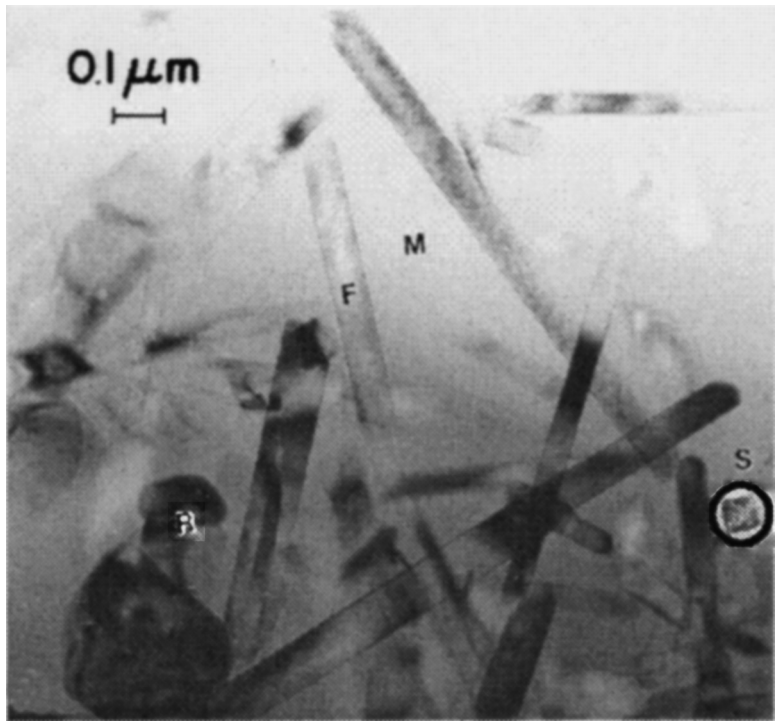

7.1 The ruthenate conductive phase in thick-film resistors decomposes due to interactions with a glass phase into RuO_2. Due to added copper oxide, the RuO_2 crystallizes in the form of needle-like grains. Bright field Transmission Electron Microscopy (TEM) micrograph of 5093 thermistor: RuO_2 elongated particles are denoted F, RuO_2 equiaxed particles are denoted R, M is a matrix region and a cross-section is circled at S (after Jiang *et al.*, 2000).

© Woodhead Publishing Limited, 2012

7.2.3 Negative temperature coefficient thermistors

NTC thermistors' compositions (e.g. ESL-NTC 2100 (http://www.electroscience.com/pdf/NTC-2100.pdf), Ferro-4900 (http://www.ferro.com/non-cms/EMS/EPM/HIC//HIGH-VOLTAGE/4900-thermistors.pdf), e.g. the former DuPont NTC40 and NTC50, complement the chances offered to designers of thick-film circuits and systems with NTC components.

Thick-film NTC compositions differ from those of NTC-thermistors manufactured in ceramic technology at least in one of the following features: (1) glass is added to the functional material to promote adhesion at the substrate/film interface, (2) a metal-like powder is added to control the sheet resistance, (3) the form of the functional material: it may be present in the ink either as a powder of the final oxide or as precursors that react during the thermal annealing to form the sensitive oxide, (4) lower peak temperature and dwell time for the sintering process. However, in both types of NTC thermistors (thick-films and ceramic), the functional material is a solid solution of transition metal oxides, such as Mn_3O_4, Co_3O_4, NiO, with the spinel structure (general formula AB_2O_4; Arima, 1994). It is generally accepted that their conductivity is due to a thermally activated phonon-assisted hopping of charge carriers between cations of differing oxidation state on the octahedral sites of the spinel structure (Park and Bang, 2003). The specific resistance ρ vs. temperature is described by the Arrhenius equation:

$$\rho = \rho_0 \times \exp B/T, \qquad [7.3]$$

where ρ_0 is the resistivity (Ω cm) at 'infinite' temperature, T is the absolute temperature and $B = E_a/k_B$ is the thermistor constant (also called the beta factor or the coefficient of temperature sensitivity), E_a is the activation energy for electrical conduction and k_B is the Boltzmann constant.

The values of the resistivity and the beta factors of NTC materials depend not only on the composition (ratio between the main oxides, minor addition of other oxides, e.g. Cu_2O, Fe_2O_3), but also on the sintering temperature and annealing treatments. The resistivity of the spinel compounds at room temperature ranges from a few hundreds of Ω cm to a few tens of KΩ cm, the beta factors from 2500 – 4000 K and the temperature coefficients of expansion from 8.5×10^{-6}/°C to 14.3×10^{-6}/°C (Arima, 1994).

Since screen-printed and fired films are usually 10 to 20 μm thick, the numerical value of the sheet resistance R_s (Ω/□) of the film turns out to be two and three orders of magnitude higher than the resistivity (Ω cm) of the material (according to the 'rule': $R_s = \rho/t$, where t is the thickness: see section 4.2.1, Chapter 4), resulting in resistances too high for practical applications. In order to overcome this shortcoming, enhanced by the presence of the glass phase, a further phase with a low specific resistance is added to the ink. The latter is often RuO_2. In appropriate amounts, this also serves to decrease the current noise and improve the stability of the sensors. However, due to the high positive TCR of RuO_2, it also decreases the beta factor.

© Woodhead Publishing Limited, 2012

Like the majority of thick-film resistors, PTC and NTC thick-film thermistors were developed for firing on relatively inert alumina substrates. The compatibility of existing pastes with LTCC systems is far from being straightforward. Because of shrinkage, mismatch and difference in thermal expansion coefficients, the tapes may cause the thermistors to deform during the firing process and vice versa. Moreover, physicochemical interactions between the paste and the tape may affect the thermistor characteristics. Investigations carried out on films prepared with the same paste and fired on 96%-Al_2O_3 and on (or between adjacent) LTCC tapes either co-fired or post-fired (Hrovat *et al.*, 2005, 2009; Zhong and Bau, 2001) not surprisingly showed different microstructures and electrical properties (sheet resistance, calibration curves, noise), but only in a few circumstances were the changes found to be detrimental for the use of the sensor/LTCC multilayer. Adverse results, such as delaminations, were observed with thermistors buried inside the LTCC structure forming cavities between adjacent LTCC tapes, when a significant mismatch in sintering rate of the thermistor and LTCC was allowed (Hrovat *et al.*, 2009). With accurate matching of thermistors–tape composition and process parameters (preferably Ag-free terminations, optimum firing cycle and deposition on top of the LTCC structure), close tolerance in resistance and *TCR* (e.g. <10% and 2%, respectively) were achieved (Birol *et al.*, 2004). Otherwise, for precise temperature readings, individual calibrations are required.

Direct laser trimming of thick-film thermistors on their support adds to thick-film thermistors the potential benefit of devices with tightly matched reference resistance; however, great care has to be taken in setting the proper trimming parameters in order to limit the inevitable heating, resulting in a lack of control of the target resistance value (A. M. Stein, private communication).

Thick-film thermistors are incorporated in the design of a variety of hybrid circuits and sensors for thermal compensation. Thick-film RTDs are almost omnipresent with printed thick-film gas sensors (either as an integrated component to measure and assist the control of the operation temperature, or with the simultaneous functions of heater and temperature detector). In several microfluidic devices that monitor flow-rate, and in minute chemical and biological reactors, thermistors play a critical role (Jurków and Golonka, 2009). In addition, RTDs are present in humidity sensors (Nicolics and Smetana, 1991), water quality control, in inclinometers (Birol, 2007), microwave circuit control (Feingold *et al.*, 1998) and flow sensors (Wada *et al.*, 1997), (Fig. 7.2), etc.

7.2.4 Thermocouples

Thermocouples and thermopiles operate on the thermoelectric (Seebeck) effect: an electromotive force (e.m.f.:voltage) appears when two different conductors are joined and the junctions are exposed to different temperatures. The e.m.f. is

© Woodhead Publishing Limited, 2012

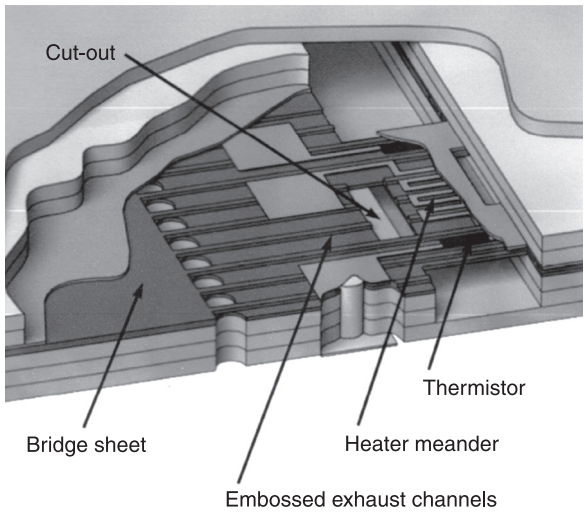

7.2 Sensor design of a thick-film flow sensor for biological microsystems, with thermistor compositions printed on a free-standing bridge and encapsulated to ensure biological compatibility (after Bartsch de Torres *et al.*, 2010).

proportional to the temperature difference ΔT, via a Seebeck coefficient σ_{ab}. Therefore, thermocouples and thermopiles are not 'resistive' sensors, strictly speaking; also, they are not widely used as temperature-sensing elements but in other interesting applications such as in planar, cheap infrared thermal detectors, laser power detectors (Smetana and Reicher, 1997), thermoelectric generators (Markowski and Dziedzic, 2008; Ohta *et al.*, 1990; Weber *et al.*, 2006) and thermoelectric coolers. Also, the measurement of the Seebeck voltage (sometimes in conjunction with the resistive response) has been found to be effective in improving the selectivity of chemoresistive printed gas sensors (e.g. Ionescu, 1998).

Relative Seebeck coefficients (σ_{ab}) for couples of selected commercial conductive pastes are in the range of 5 to 20 μV/K, whereas σ_{ab} up to 450 μV/K for $(Sb_2Te_3)_{72}(Bi_2Te_3)_{25}(Sb_2Te_3)_3$–$(Bi_2Te_3)_{95}(Sb_2Se_3)_5$ have been reported (Ohta *et al.*, 1990).

7.2.5 Low-temperature, cryogenic sensors

Thick-film cermet resistors made from RuO_2 or bismuth ruthenate pastes, introduced as cryogenic sensors in the early 1980s, are today typically referred to as ruthenium oxide (chip) RTDs (Postma, 1994; Rubin, 1991). These RTDs are essentially the same, in composition and manufacturing processes, as the TFRs exhibiting a near-zero *TCR* at 300 K. Yet, their resistance starts to increase

© Woodhead Publishing Limited, 2012

sharply below liquid nitrogen temperature, making them useful low-temperature sensors. Moreover, their outstanding low magneto-resistance and the possibility of predicting low R(T) behaviour from the room temperature resistance (Willekers *et al.*, 1990), render them a strong competitor to other known RTDs, especially from 40 K down to 10 mK. In fact, these devices have the lowest magneto-resistance below 1 K of any commercially available RTD (Affronte *et al.*, 1998; Watanabe *et al.*, 2001; Yeager and Courts, 2001). These characteristics, in addition to good immunity to ionizing radiation, recently found thick-film RTDs' application in the critical temperature control of the superconducting magnets in CERN's Large Hadron Collider (Ylöstalo *et al.*, 1996). They were also used as cryogenic sensors in the ARCADE experiment investigating the cosmic microwave background radiation (Fixsen *et al.*, 2002; Kogut *et al.*, 2004).

Suppliers of commercial thick-film RuO_2-chips (e.g. Oxford Instruments, UK and Scientific Instruments, USA) resort to special mounting strategies to accomplish optimum thermal contact, stability, wiring and measurement accuracy. Integrated small calorimeters for measurements at cryogenic temperatures have been also designed and tested (Mach *et al.*, 2003).

7.3 Piezoresistive properties and related sensors

Sensors of strain-related mechanical quantities relying on the piezoresistive properties of thick-film resistors (TFRs) are actually one of the most successful areas of application for printed sensors. Strain, load, force, acceleration and pressure are measured with thick-film piezoresistors, mainly based on ruthenium dioxide (RuO_2) or ruthenates as conductive phases. Resistance changes in TFRs were first noticed in the early 1970s, as described by Holmes, but the effect was considered to be more of a hindrance because of the induced stresses when circuits were potted in resins (Holmes, 1973). Holmes makes no mention of the potential of using the effect as a sensing mechanism in the form of a strain gauge. A few years later, the first studies of piezoresistive effects emerged while researchers were trying to collect a comprehensive picture of the physical properties in TFRs, which could fit in a suitable electrical transport model for this type of cermet resistor (Canali *et al.*, 1980; Morten *et al.*, 1977; Pike and Seager, 1977). The decisive step in exploitation of the effects may be recognized in the patent filed by F. I. Marelli in 1979, followed soon by the industrial production of pressure sensors for automotive applications (Cattaneo *et al.*, 1980). Since then, piezoresistive properties of TFRs have attracted a great deal of scientific and technological interest and applications have rapidly spread in many diversified areas (Morten and Prudenziati, 1994). According to concepts, materials and methods of the current thick-film technology, devices were first prepared on alumina substrates; it is interesting to note that the term 'ceramic sensors' was coined for these devices to recognize the contribution given by alumina to the

© Woodhead Publishing Limited, 2012

sensors' performance due to its corrosion resistance in aggressive media, refractory nature and low cost.

Figure 7.3 is a schematic of a typical pressure sensor based on a ceramic diaphragm and body (base plate). Thick-film conductors, resistors and sealing glasses are printed and fired to make the sensor. The four piezoresistors form a bridge on the diaphragm. Applying pressure deflects the diaphragm, thus resulting in an imbalance in the bridge network and in a corresponding proportional output signal. With minor modifications in the size (4–15 mm diameter) and thickness (0.25–1.3 mm) of the diaphragm, it is possible to cover a pressure range from about 0.1 to 50 MPa with an accuracy better than 1–2% (Dell'Acqua and Dell'Orto, 1986). This type of design can be used to produce all three types of pressure sensors: absolute, differential and relative. A variety of other substrates were considered in further designs, including other ceramic materials such as zirconia (Chitale *et al.*, 1992), enamelled steel (Prudenziati *et al.*, 1981/1982), insulated steel (Brignell *et al.*, 1988, Marioli *et al.*, 1993; White 1989), aluminium and titanium (Jacq *et al.*, 2004a, 2004b) and LTCC (Hrovat *et al.*, 2003, 2006).

Alumina is superior to all of these substrates in terms of dielectric strength, corrosion resistance and the matching of the thermal expansion coefficient with that of the largely available TFRs. However, alumina is surpassed by other substrates in terms of flexural strength and elastic modulus (Table 7.1).

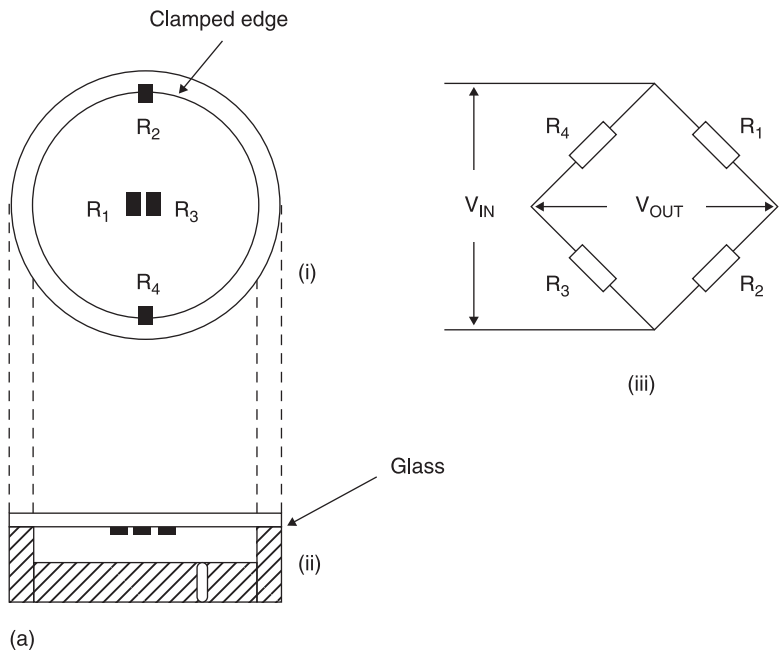

7.3 (a) Schematic drawing of a thick-film ceramic pressure sensor. (i) sensing resistors on the diaphragm; (ii) set up of the diaphragm on the body; (iii) Wheatstone bridge configuration.

© Woodhead Publishing Limited, 2012

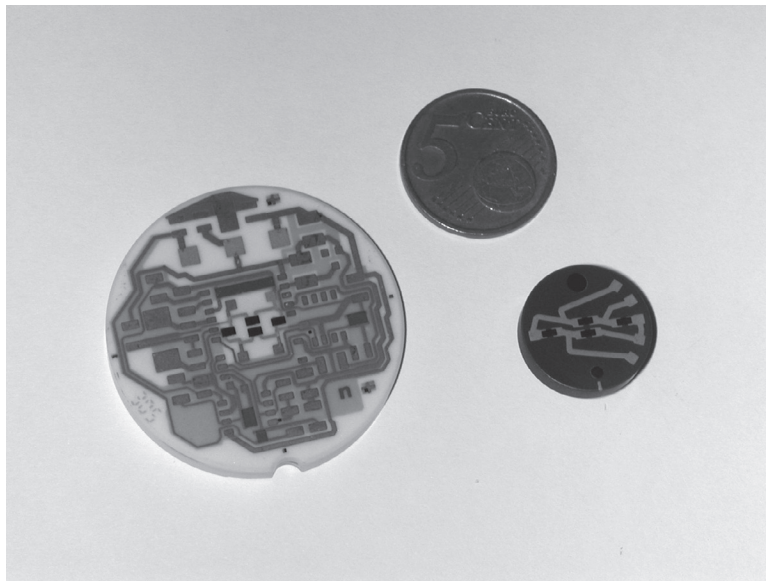

(b)

7.3 Continued (b) Two realized designs: on the left, a sensor based on ceramic diaphragm and body (courtesy of Hybritec International, Italy); on the right, insulated steel membrane on steel body (courtesy of Gefran, Italy).

Table 7.1 Properties of materials for piezoresistive thick-film sensors

Property	96% Al_2O_3	DuPont LTCC 951 (fired)	Yttrial-stabilised zirconia (YSZ)	Ferritic steel 1.40016
Elastic modulus (GPa)	250–330	152	200	226
Flexural strength (MPa)	280–300	320	200–500	–
Available thickness (mm)	0.25–1	0.04–0.21	–	Any
TCE (ppm/°C)	7.5	5.8	7.5–10.5	20–25

In addition, insulated metals and LTCC are very easily machined, formed and processed in a workshop. Particularly interesting in this picture are LTCC tapes for their low elastic modulus, which is about three times lower than that of standard alumina substrates, and their otherwise comparable elastic and electrical properties. One example of applications taking advantage of these properties is represented by the successful implementation of millinewton load sensors down to 100 mN full scale (Birol *et al.*, 2007).

City Sensor, France; WIKA, Germany; Impress Sensors & Systems, England; DJ Instruments, USA; Metallux Electronic, Switzerland; Hybritec International,

© Woodhead Publishing Limited, 2012

Italy; Baumer, USA; Gefran, Italy; and Hipot, Slovenia, are among the companies that manufacture commercial devices based on thick-film piezo-resistors. I could not confirm whether Fiat Italy is still active in manufacturing this type of sensor for applications for their own internal use.

Features that render thick-film piezo-resistors attractive from a technical as well as a speculative point of view, encompass:

- Strain responses $\Delta R/R$ vs. ε (where $\Delta R/R$ is the relative change of resistance due to the applied strain ε) linear, symmetrical (for tensile and compressive strains), hysteresis-free (at least up to about 1000 $\mu\varepsilon$, i.e. the breaking point of alumina substrates and near the upper limit of elastic behaviour of insulated metal substrates), with the following features:
- Gauge factors ($GF \equiv \Delta R/R\ \varepsilon$) in the range from 2 to 35, according to the composition of the paste, firing cycle, terminations, substrate; hence a gauge factor intermediate between those of metal and semiconductor strain gauge, accompanied by:
- The low temperature coefficient of resistance ($TCR \equiv \Delta R/R\Delta T$) and of gauge factor ($TCGF \equiv \Delta GF/GF\Delta T$, of a few hundreds ppm/°C);
- Negligible changes of resistance under (even very intense) magnetic fields, light intensity, electric fields, nuclear radiation;
- A good stability up to comparatively high temperatures (125–150 °C);
- Large immunity to severe conditions, thermal shock, vibrations, acceleration.

Investigations aimed at identifying the best materials and processes have been performed on either commercial pastes or model systems. The picture emerging from studies on RuO_2-based and ruthenate-based resistors shows the following properties.

The measured longitudinal gauge factor GF_l (strain ε parallel to the current I) and transverse gauge factor GF_t (ε perpendicular to I) are both positive (i.e. R increases in tensile stress) with $GF_l > GF_t$, being frequently $GF_l - GF_t \sim 2\,(1 + v)$, where v is the Poisson's ratio of the substrate, just as expected, under simplifying assumptions, for isotropic materials (Fawcett and Hill, 1999).

TFRs of the same series (i.e. based on the same conductive phase and the same or similar dielectric matrix) exhibit increasing strain sensitivity (GF values) at decreasing conductive volume fraction, i.e. at increasing sheet resistance R_s (Canali *et al.*, 1980; Tamborin *et al.*, 1997).

TFRs having the same Rs but coarser conductive particles exhibit larger GF values shown in Figure 7.4 (Tamborin *et al.*, 1997).

Model resistors prepared with $Bi_2Ru_2O_7$, RuO_2, $CaIrO_3$, IrO_2 powders of similar size were compared (Prudenziati *et al.*, 1997); the strain sensitivity appeared to be unaffected by the nature of the conductive oxides except for samples fired at high temperatures (e.g. 850–950 °C) where the compositions of the glassy matrix changed as a result of interactions with the conducting phase. The role of the glass composition remains unclear. It was suggested that addition of oxides (e.g. $BaTiO_3$,

© Woodhead Publishing Limited, 2012

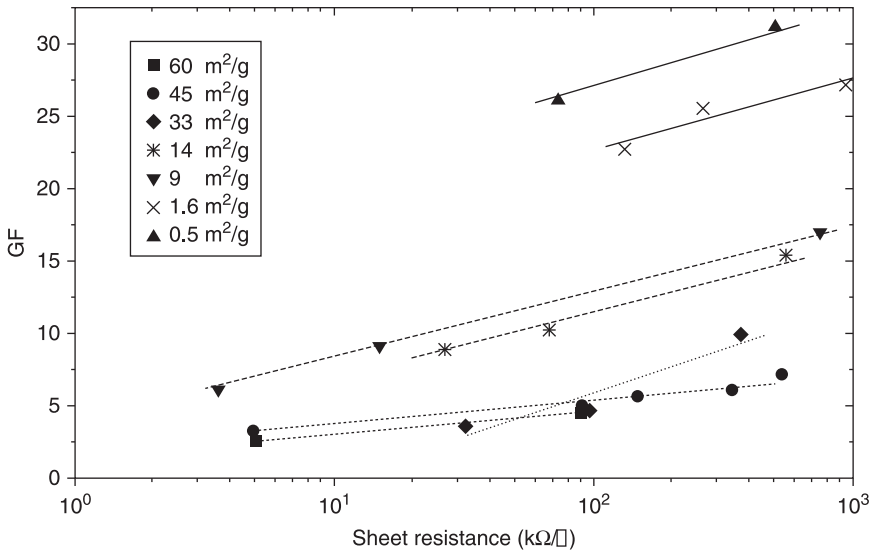

7.4 Strain sensitivity of RuO_2-based TFRs prepared with powders of various sizes, as a function of the sample sheet resistance.

MoO_3) and metal (e.g. Mo, K, Fe) provide 'super *GF* factors', i.e. *GF* values larger than 30, up to 200–300 (Abe and Takeda, 1986). Unfortunately these modifiers are responsible for asymmetric responses under compressive and tensile stresses, lack of linearity in ΔR vs. ε response, very high noise levels and crack lines running on the resistor's surface. Moreover, it was shown that the artificial (false) 'super-gauge factors' are to be ascribed to defects (cracks and fissures) in the glassy matrix: when these defects are 'healed' (closing them with glues) the asymmetric response disappears and 'normal' *GF* values are recovered (Prudenziati *et al.*, 1989).

Correlations between compositions, sheet resistance, gauge factors, *TCR* and excess noise have been studied in model systems prepared with the same glass frit and RuO_2 powders covering a range of particle sizes from a few nanometers to micrometers (Tamborin *et al.*, 1997), resulting in samples with sheet resistance R_s in the range from 200 Ω/□ to 3 MΩ/□. At a selected R_s value, the GF_1 increases linearly with the logarithm of RuO_2 grain size, while the *TCR* and excess noise do not significantly depend on the RuO_2 powder size. Similar investigations by researchers in Dresden (Dietrich *et al.*, 2009) opted for the conductive/glass size–particle ratio as the parameter for RuO_2-based resistors with the same sheet resistance (10 KΩ/□). In addition, the ageing stability was also measured. The increase of *GF* values by increasing the RuO_2 particle size was confirmed, whereas the results on *TCR* and noise index were in substantial disagreement (probably because of the different composition of the glassy phase, although in both studies it was a lead–silicate glass).

© Woodhead Publishing Limited, 2012

In all TFRs, either prepared with commercial pastes (bearing ruthenates, RuO_2 a mixture of these compounds) or model systems, the best compromise between the strain sensitivity and noise spectral density, hence the optimum signal-to-noise ratio of piezoresistors, can be achieved with resistors of intermediate sheet resistances, e.g. R_s in the 10 KΩ/□ (Hrovat *et al.*, 2001).

Considerably less copious is the harvest of data available on piezo effects in TFRs based on a conductive phase other than a Ru-compound. Ir O_2-based resistors with lead–silicate glass offer similar behaviour in terms of sensitivity and *TCR*, with the additional benefit of higher stability up to 175°C but also higher cost (Tankiewicz *et al.*, 2002).

Sensitivity to stress applied normally to the printed piezoresistor is about twice that experienced with uniaxially applied stress, in accordance with the resolved components of the stress and the low stiffness of the film as compared with its substrate (Fawcett and Hill, 1999; Puers *et al.*, 1987). Thick-film piezoresistors under hydrostatic pressure invariably exhibit $\Delta R/R\Delta p$ of the order of 20–30 (Fawcett and Hill, 1999). Also notable is the persistence of the high gauge factors down to liquid helium temperatures (Ferrero *et al.*, 1990).

No systematic study has been performed with lead-free thick-film piezoresistors. However, in some explorative investigations, no interesting strain sensitivity was experienced so far in either RuO_2-based (Morten *et al.*, 1991) or $CaRuO_3$-based systems (Rane *et al.*, 2007).

A deeper knowledge of the resistors' microstructure and advanced computational methods for modelling these complex phenomena are paving the way for a satisfactory interpretation of the physical origin of the mentioned effects. A separate contribution in this volume (Grimaldi, Chapter 5) describes the approaches used and the actual level of understanding of the mechanisms of electrical transport and mechanical–electrical phenomena occurring in cermet TFRs. In brief, the results show that the coexistence of electron tunnelling and percolation phenomena, together with the heterogeneity of the microstructure, are responsible for the strain sensitivity of the resistors. Their segregated structure is responsible for the non-marked difference in GF_l and GF_t, whereas a gauge factor (GF) enhancement results from the highly heterogeneous dispersion of conducting phases, which are stiffer than the insulating one. Therefore, the local strains within the matrix are enhanced with respect to the averaged macroscopic strain.

Polymer-based TFRs, such as carbon resistors, offering the chance of thermal *cure* at low temperatures (typically 125–150 °C) and consequently the possibility of printing on *flexible* organic substrates, were promising for sensors envisaged for low pressure and/or low load sensors. However, no suitable materials were identified. The resistors were generally characterized by lack of linearity, significant hysteresis, high *TCR* and low sensitivity. Pseudo-plastic effects of the substrates (e.g. Mylar) and the matrix of the carbon-conducting phase were signalled as responsible for this deluding performance (Arshak *et al.*, 1995).

© Woodhead Publishing Limited, 2012

7.4 Magnetoresistive effects and sensors

Contactless sensors relying on magnetoresistive properties of screen-printed and fired films based on either metal ferromagnetic materials and perovskite oxides have been realized. Properties of the materials and films, choice of structure and sensor type are briefly delineated here.

In ferromagnetism, close relationships exist between electrical transport and magnetization, resulting in the dependence of the resistivity on the direction of the magnetization vector: measurements of the resistivity with the current I parallel ($\rho//$) or perpendicular ($\rho\perp$) to the magnetization direction provide different figures, with $\rho// > \rho\perp$ in most cases, as a consequence of the anisotropic scattering of the conduction electrons. The quantity:

$$\Delta\rho/\rho \equiv (\rho// - \rho\perp)/\rho_o, \qquad [7.4]$$

where $\rho_o = (\rho// + \rho\perp)/2$, is defined as anisotropic magneto-resistance (AMR) and assumes typical values of a few percentage points. In the more general case of the current flowing at a θ angle with respect to M, the expression of ρ reads as:

$$\rho(\theta) = \rho\perp + (\rho// - \rho\perp)\ cos\ 2\theta. \qquad [7.5]$$

This property is the basis of a variety of many thin film sensors. In thin films, vapour deposited or sputtered, the saturation magnetization direction is 'entailed' by an external magnetic field applied parallel to the plane of the substrate during the deposition process or in the next annealing, and 'constricted' on the film plane because of the large demagnetizing field normal to the film plane. The most common composition for these films is $Ni_{81}Fe_{19}$, which does not exhibit magnetostrictive effects, exhibits a relative high Curie temperature of 850 °C, and, according to a general rule for alloys, a *TCR* much lower than that of the parent elements (Bozorth, 1993; Dibbern, 1986).

A search for magneto-resistive properties of ferromagnetic-metal based screen-printed films was performed first in films prepared with commercial *air-fireable* Ni-based pastes, developed for non-sensing applications (e.g. cathodes in gas discharge displays). In these pastes, the strong tendency of Ni to get consistently oxidized at high firing temperatures is contrasted by a 'passivation effect' provided by boride glassy and crystalline phases, e.g. $AlB_{10}Ni_3(BO_3)_2$ and/or boron–lead silicate glassy phases (Sirotti *et al.*, 1990). The complex microstructure of the films, with Ni accounting for only 70 to 80%wt in the fired layer, and limited growth of Ni grains even after treatments up to 900 °C, result in: (1) resistivity and *TCR* values not too dissimilar to those of Ni-bulk, (2) poor AMR ratio (Morten *et al.*, 1990).

Nevertheless, special designs, aimed at achieving a reasonable degree of immunity to thermo-resistive effects, allowed designers to realize prototypes of interesting contactless sensors for linear position, speed of rotation and linear distance measurements (Morten *et al.*, 1997).

© Woodhead Publishing Limited, 2012

Improved properties were looked for with the development of nitrogen-fireable pastes based on NiCo alloys. Two approaches where followed: either in situ alloy formation (and sintering) from fine powders (1–5 μm) of Ni and Co in the ratio Ni:Co = 4:1 (samples referred to as Ni/Co-based films) or the sintering of a $Ni_{80}Co_{20}$ powder (1–1.5 μm particles) obtained by co-reduction of Ni(II) and Co(II) acetates with a polyol process (samples referred to as $Ni_{80}Co_{20}$; Bianco *et al.*, 2000; Gusmano *et al.*, 1996). The pastes, with no other constituents but the organic vehicle, were printed and fired in N_2, on alumina substrates previously glazed with a calcium–silicate glass layer fired in air at 1000 °C to achieve adequate adhesion. Films prepared at increasing firing temperatures (750 °C–1000 °C) exhibit increasing magnetic polarization M_s(Masoero *et al.*, 1999) and a decrease of the coercive field H_c, which are interpreted as natural consequences of perfected sintering and alloy formation in Co-Ni phase in one type of films and sintering of $Ni_{80}Co_{20}$ fine powders in the other films (Table 7.2).

The microstructure exhibited carbonaceous residues due to incomplete burning of the organic vehicle, as well as porosities and oxidized regions due to residual oxygen partial pressure in the firing furnaces; these contribute to making the films magnetically harder than a corresponding bulk alloy. The temperature dependence of the saturation magnetization is very weak until at least 200 °C and follows the Curie–Weiss behaviour with a Curie temperature of 697 °C. Compared with Ni-based magneto-resistors, the new ferroelectric thick-film compositions exhibit a notably improved AMR value (Fig. 7.5 and Table 7.3) due to the enhanced longitudinal response added to the very low (essentially negligible) transverse response. Also a sensitivity S of the longitudinal response for $H > H_{sat}$ is of interest for application purposes. However, the major actual drawback of these systems is due to the remarkable deterioration of the magneto-response at increasing ambient temperature. For example, the maximum $\Delta R/R_{long}$ at H_{sat} in $Ni_{80}Co_{20}$ films fired at 950 °C follows the trend shown in Table 7.4.

The ferromagnetic properties of the films do not justify this result (according to the M_s vs. T behaviour) but the high TCR values of the Thick-Film-Magnetoresistors (*TF-MR*s) do (Table 7.3): the large increase in R_0 makes the $\Delta R/R_0$ progressively lower at increasing T values.

Table 7.2 Magnetic properties of NiCo-based thick-films prepared at various peak firing temperatures T_f, M_s and remanent magnetization BV, in Tesla, coercive field H_c in kA/m

Sample/T_f (°C)	Magnetic polarization M_s (T) at H_{max} = 200 kA/m	Br and H_c at H_{max} = 20 kA/m, f = 100 Hz B_r (T) H_c (kA/m)	
T1/750	0.280	0.015	2.45
T2/800	0.295	0.031	3.30
T3/850	0.305	0.042	3.77
T4/900	0.297	–	–
T5/950	0.435	0.120	1.84

© Woodhead Publishing Limited, 2012

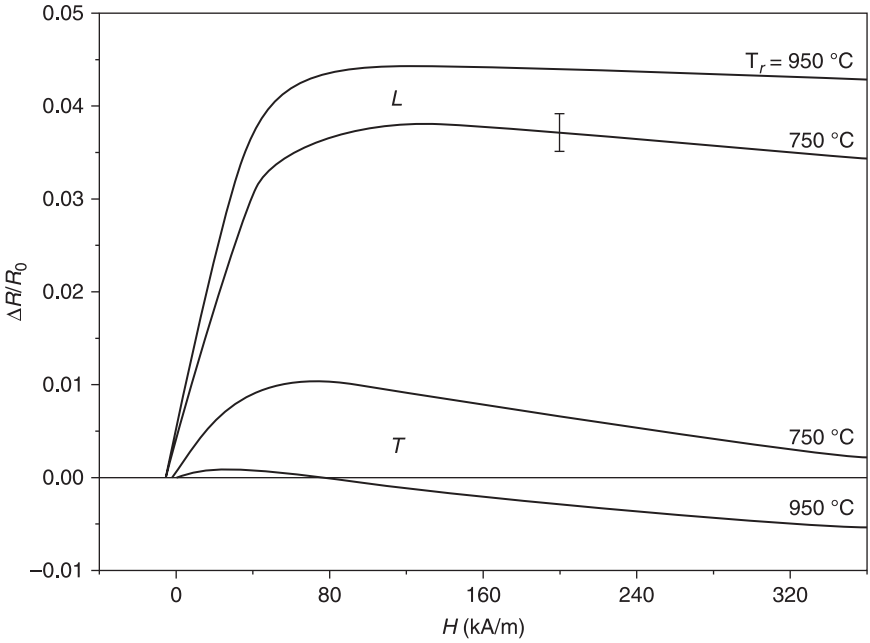

7.5 Comparison of the longitudinal (*L*) and transverse (*T*) magnetoresistance of two layers of Ni/Co = 70/30 alloy prepared with different peak firing temperatures (T_f) and measured at room temperature, as a function of field *H*. R_0 is the resistance measured in zero field.

Table 7.3 Properties of thick-film magneto-resistors based on Ni and Ni-Co alloys, fired at 950 °C

Material	Resistivity (μΩ cm)	TCR (ppm °C^{-1})	AMR (%)	Sensitivity at $H = 0.32\ 10^5$ A m^{-1} (ppm A^{-1} m^{-1})
Ni air fireable	35	5340	0.55	0.05–1
Ni/Co	27	3200	2.40	0.8
$Ni_{80}Co_{20}$	15	4700	4.60	1.08

Table 7.4 Temperature dependence of the maximum $\Delta R/R$ (at H_{sat}) measured in the longitudinal response of $Ni_{80}Co_{20}$-based *TF–MR*s

Temperature (°C)	20	50	80	110
$\Delta R/R$ (%)	4.3	3.7	3.05	2.2

© Woodhead Publishing Limited, 2012

Nowadays the same drawback afflicts the second family of printed magneto-resistors described in the literature, i.e. ferromagnetic screen-printed perovskites. This class of materials, chiefly manganites (notably La-A-Mn-O with A = Ca, Ba, Sr manganites), is a subject of very active research since the discovery of their anomalous high magneto-resistance *close* to the Curie temperature T_c. In addition, this effect is enhanced and extended to a wider temperature range in polycrystalline materials (Fig. 7.6).

Magneto-resistance ratio MRR (defined as MRR = $(\rho_H - \rho_0)/\rho_0$, where ρ_0 and ρ_H are the resistivity measured at zero and H fields, respectively) as large as 90% have been observed at low temperatures (Viret *et al.*, 1997) and the application of relatively low magnetic fields promotes a substantial reduction of the resistivity (low-field MRR, LFMR). This effect can be enhanced by using submicroscopic particles and LFMR values of about 30% can be routinely obtained, e.g. at low temperature in the range of field of 10^4 A/m. It has been found that the magneto-transport behaviour in manganites can be attributed to a double exchange mechanism between pairs of Mn^{3+} and Mn^{4+} ions. In this mechanism, a parallel alignment of the manganese spins is required before the electron can transfer between the ions to give charge transport. Application of an external magnetic field enhances the spin ordering and thus suppresses the resistivity. With a *decrease* of temperature there is a natural increase in alignment of spins, the

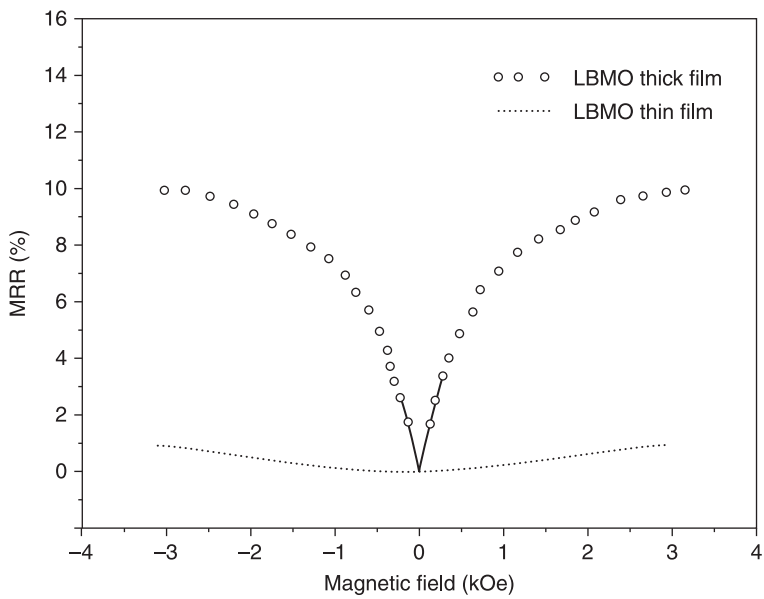

7.6 Variation of magneto-resistance ratio (MRR) for screen-printed and epitaxial thin film of $La_{0.67}Ba_{0.33}MnO_3$ (LBMO) with magnetic field. The field is varied from zero to 3 koe (240 A/m) and back to zero (adapted from Khare *et al.* 2004).

© Woodhead Publishing Limited, 2012

resistivity decreases and the MRR vanishes, as observed in epitaxial films. On the other hand, in polycrystalline samples, such as screen-printed films, there is an additional source of MRR due to grain boundaries. A sharp increase in MRR at low field is attributed to spin-polarized tunnelling across the boundaries. The boundaries provide a kind of thin insulating barrier for electron tunnelling together with a magnetic decoupling of grains. Application of a small magnetic field aligns the randomly oriented grains and thus increases the tunnelling with the consequent decline in resistivity. Furthermore, the magnetic field applied at low temperatures ($T < T$c) reduces the spin-dependent grain-boundary scattering of charge carriers (Khare *et al.*, 2004).

This substantial LFMR has been used to design magneto-resistive magnetic thick-film sensors, e.g. a magnetic position sensor (Balcells *et al.*, 1996), a magnetic potentiometer (Balcells *et al.*, 2000), an angular position sensor, an on–off switch (Rubi *et al.*, 2006). However, applications at or above room temperature are dampened by the fact that the LFMR decays rather fast with temperature and becomes almost negligible (<0.05%) already below the Curie temperature (T_c < 360 K in $La_{1-x}A_xMnO_3$). The proposed alternative was to use the LFMR exhibited by the Sr_2FeMoO_6 oxides (T_c > 410 K). The synthesis of these materials resulted in a variety of subtle problematic issues related to stoichiometry, purity and disorder (Fe/Mo antisites), which was progressively overcome (Fontcuberta *et al.*, 2002). The second alternative to overcome the issue of decay in LFMR(T) of manganese perovskites was recognized in the presence of the anisotropic magneto-resistance (AMR), which offers a relative resistance change of about 0.25% and 0.1% at 300 K and 350 K respectively, for a magnetic field H = 100 Oe (about 6×10^3 A/m) parallel to the film plane (Balcells *et al.*, 2002). The prospects for further progress in both materials preparation and opportunities for new oxides with still higher Curie temperatures are discussed in Foncutberta *et al*. (2002).

7.5 Radiant sensors

Already in 1995 researchers in RCA Laboratories at Princeton, USA (Nicoll and Kazan, 1955; Thomsen and Bube, 1955) were applying thick-film technology just as a cost-effective production process for solid state sensors. In fact, R. H. Bube (Thomsen and Bube 1955) describes highly sensitive photoconductive layers prepared, 'by a "paint" of cadmium sulfide or selenide (a water mixture of sulfide or selenide with chloride and copper) onto a suitable surface, and firing the surface with its dried layer to form a polycrystalline sintered layer'. Thick-film photoconductors based on CdS, CdSe and CdInSe have been intensively studied in the past 45 years. The main changes in electrical and optical characteristics resulting from oxygen chemisorptions, residual Cu and Cl ions, sintering atmosphere and firing cycles have been understood and a lot of knowledge accrued in studies performed in several research centres, e.g. in India (Amalnerkar *et al.*, 1980); Germany (Battelle Institute), Belgium (Ghent State University), Japan

© Woodhead Publishing Limited, 2012

(Matsushita and Toshiba), UK (Southampton University), to cite a few. A review of thick-film CdS-based sensors has been provided by Setty and Amalnerkar (1994) and new applications of CdS-CdSe-based thick-films described by Ross (Ross 1995). In addition, the search for cheap production techniques for solar energy conversion devices has triggered the development of printed photovoltaic cells. This field also has been addressed in many countries, with the most intense activities in the decade between 1980 and 1990. Thick-film CdS/CdTe heterojunctions appear to be the most promising candidate and a conversion efficiency of around 10% has been demonstrated (Ikegami and Uda, 1994; Uda *et al.*, 1997).

Photoconductive cells have seen a long, prosperous life on the market. Hamamatsu Photonics has manufactured and supplied CdS photo-cells for decades, until it recently (2006) ceased this production as a direct result of the Restriction of Hazardous Substances in Electrical and Electronic Equipment (RoHS) Directive, which restricts the import of Col-containing products to the European Union (http://hamamatsu.com). The commercial production of screen-printed and sintered CdS/CdTe solar cells by Matsushita Battery Industrial Company started in January 1986 (Ikegami and Uda, 1994) and modules for different applications appear in the *Panasonic Solar Cell Handbook* (August 1998; see http://downloads.solarbotics.com/PDF/sunceramcat.pdf) under the tradename SunCeram II. We cannot confirm that production is continuing in this case.

7.6 Potentiometric sensors

As the name indicates, the potentiometric sensor consists in a variable resistance and wiper device. The primary design elements of such a system are a resistor and a wiping contact enclosed in a suitable package. The voltage drop across a potentiometer or variable resistor is monitored to achieve the desired control. The ratiometric output signal is proportional to the angular or linear position of the wiping contact (wiper). Both, linear and non-linear types of output signals can be obtained by appropriate design of the variable resistor. Applications of such systems include fluid level gauges (Fig. 7.7) and flow meters, while in addition, in automotive applications they are found in brake wear life gauges and position sensors to monitor valves and suspension and/or steering components. Automotive subsystems utilizing this type of sensor include electronic fuel injection, active suspension and exhaust gas recirculation (Wada *et al.*, 1997).

Depending on the application, the thick-film material can be of cermet or polymer composition. Typical wiping contacts are metallic and are designed to complement the device performance. The high reliability greatly overshadows the relatively low accuracy (0.5–2%) of devices based on thick-film materials. The thick-film materials offer the required fine line definition, accurate trimming, linearity, low noise, high abrasion and corrosion resistance for these types of devices.

© Woodhead Publishing Limited, 2012

© Woodhead Publishing Limited, 2012

(a)

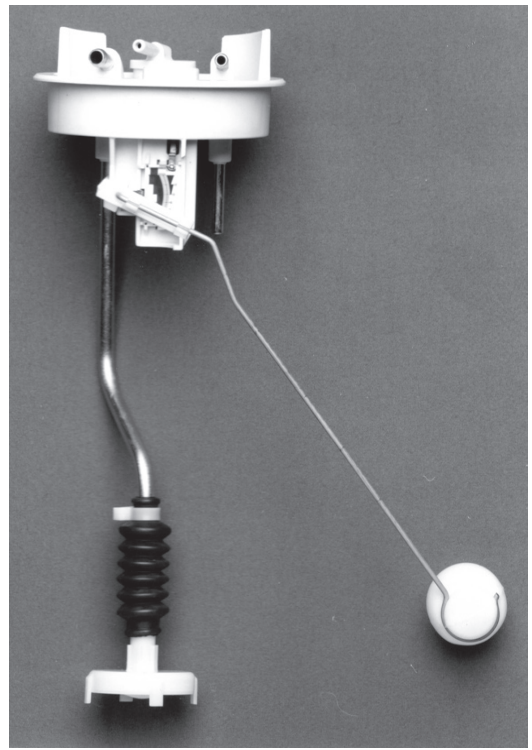

(b)

7.7 A fluid level sensor: the wiper of a thick-film potentiometer is connected to a lever arm (a). Any change in fluid level causes a change in the float lever arm assembly (b) thus providing an output signal proportional to the position of the wiper on the resistor track.

7.7 Conclusion and future trends

The driving force of development in resistive thick-film physical sensors has been the need for cheap, reliable, stable devices and systems for harsh environments. As shown in this chapter and in the vast literature on the subject, a variety of successful products and applications has been accomplished. Future markets can be envisaged however, in which other demands, such as a reduction in size, integration with printed electronics and very large-scale mass production, will be the priorities. Therefore efforts might be at a premium in the evaluating printing methods such as MicroPen® and ink-jet printing, with the related issue of ink composition. Likely studies of interactions between both cermets and polymer-based inks and new, mostly flexible, substrates have to be addressed. These approaches should also be promising for the introduction of thick-film physical sensors into new market sectors such as in biomedical instrumentation and diagnostic devices and in portable electronic devices. Of course, a deeper and clearer understanding of electrical transport in cermet resistors and research into the electrical properties of complex oxides would support the advanced performance of devices already present in the actual panorama of thick-film physical sensors.

7.8 References

Abe O. and Takeda Y., 1986, Strain characteristics of thick-film resistors and its application to a strain sensor, *IMC 1986 Proceedings*, Kobe, Japan, May, pp. 282–284.

Affronte M., Campani M., Morten B., Prudenziati M. and Laborde O., 1998, Magnetoresistance of RuO_2-based thick-film resistors, *Journal of Low Temperature Physics*, 112, 355–371.

Amalnerkar D. P., Setty M. S., Pavaskar N. R. and Sinha A. P. B., 1980, Studies on thick-films of photoconducting cadmium sulphide, *Bulletin of Material Science*, 2 (4), 251–264.

Arima H., 1994, Thick-film thermistors and RTDs, in *Handbook of Sensors and Actuators, 1 (Thick-film Sensors)*, Elsevier, UK, pp. 127–150.

Arshak K. I., Ray A. K., Hogarth, D. G., Collins C. A. and Ansari F., 1995, An analysis of polymeric thick-film resistors as pressure sensors, *Sensors and Actuators*, A49 (1–2), 41–45.

Balcells L., Calvo E. and Fontcuberta J., 2002, Room-temperature anisotropic magnetoresistive sensor based on manganese perovskite thick-films, *Journal of Magnetism and Magnetic Materials*, 242–245, 1166–1168.

Balcells L., Enrich R., Mora J., Calleja A., Fontcuberta J. *et al.*, 1996, Manganese perovskites: thick-film based position sensors fabrication, *Applied Physics Letters*, 69 (10), pp. 1486–1488.

Balcells L., Carrillo A. E., Martinez B., Sandiumenge F. and Fontcuberta J., 2000, Room temperature magnetoresistive sensor based on thick-films manganese perovskite, *Journal of Magnetism and Magnetic Materials*, 221, 224–230.

Bartsch de Torres H., Rensch C., Fischer M., Schober A., Hoffmann M. *et al.*, 2010, Thick-film flow sensor for biological microsystems, *Sensors and Actuators A*, 160 (1–2), 109–115.

© Woodhead Publishing Limited, 2012

Bianco A., Gusmano G., Montesperelli G., Morten B., Prudenziati M. *et al.*, 2000, Microstructure and surface composition of ferromagnetic thick-films prepared with NiCo Polyol derived powders, *Thin Solid Film*, 359, 21–27.

Birol H., 2007, Doctoral thesis, Fabrication of low temperature co-fired ceramic (LTCC)-based sensor and micro-fluidic structures, École Polytechnique Federale De Lausanne.

Birol H., Maeder T., Jacq C. and Ryser P., 2004, Effects of firing conditions on thick-film ptc thermistor characteristics in LTCC Technology, *IMAPS Conference on Ceramic Interconnect Technology*, pp. 106–109.

Birol H., Maeder T., Nadzeyka I., Boers M. and Ryser P., 2007, Fabrication of a millinewton force sensor using low temperature co-fired ceramic (LTCC) technology, *Sensors and Actuators, A: Physical*, A134 (2), 334–338.

Bozorth R. M., 1993, *Ferromagnetism*, IEEE, New York.

Brignell J. E., White N. M. and Cranny A. W. J., 1988, Sensor applications of thick-film technology, *IEE Proceedings*, 135, 77–84.

Burckhardt H.-G., Gora F., Guldner K.-H., Dehoust J., Modes C. *et al.*, US Patent No. 5 244 601 (14 September 1993).

Cai Z., Li X., Hu Q. and Zeng X., 2009, Laser sintering of thick-film PTC thermistor paste deposited by micro-pen direct-write technology , *Microelectronic Engineering*, 86, 10–15.

Canali C., Malavasi D., Morten B., Prudenziati M. and Taroni A., 1980, Piezoresistive effects in thick-film resistors, *Journal of Applied Physics*, 51, 3282–3288.

Cattaneo A., Dell'Acqua R., Dell'Orto G., Pirozzi L. and Canali C., 1980, A practical utilization of the piezoresistive effect in thick-film resistors: a low cost pressure sensor, *Proceedings of the International Microelectronics Symposium*, pp. 221–228.

Chitale S. M., Huang C. Y. D., Stein S. J. and Wada T., 1992, Piezoresistivity in high thick-film resistors: sensor design and very thin YSZ substrates, *Proceedings of 7th International Microelectron Conference*, Yokohama, Japan, pp. 561–570.

Dell'Acqua R. and Dell'Orto G., 1986, High pressure thick-film monolithic sensors, SAE Paper 860474, Detroit.

Dibbern U., 1986. Magnetic field sensors using the magnetoresistive effect, *Sensors and Actuators*, 10 (1–2), 127–140.

Dietrich S., Kretzschmar C., Partsch U. and Rebenklau L., 2009, Reliability and effective signal-to-noise ratio of RuO_2-based thick-film strain gauges: the effect of conductive and glass particle size, *32nd International Spring Seminar on Electronics Technology*, ISSE 2009, pp. 1–6.

Evans W. D. J., 1981, Thick-film platinum resistance temperature detectors. The development and manufacture of advanced types for industrial and domestic applications. *Platinum Metals Review*, 25 (1), 2–11.

Fawcett N. and Hill M., 1999, The electrical response of thick-film resistors to hydrostatic pressure and uniaxial stress between 77 and 535 K, *Sensors and Actuators A*, 78 (2–3), 114–119.

Feingold A., Wahlers R. L., Amstutz P., Huang C., Stein S. J. *et al.*, 1988, New microwave applications for thick-film thermistors, Proc SPIE, Vol. 3582, *Proceedings of the 1998 International Symposium on Microelectronics*, assembled and edited by the 1998 Technical Program Committee and IMAPS Staff, pp. 179–184.

Ferrero C., Marinari C., Masoero A., Morten B. and Prudenziati M., 1990, Performance of thick-film strain gauges at cryogenic temperatures, *Cryogenics*, 30, 726–729.

Fixsen D. J., Mirel P. G. A., Kogut A. and Seiffert M., 2002, A low noise thermometer readout for ruthenium oxide resistors, *Review of Scientific Instruments*, 73 (10), 3659–3663.

© Woodhead Publishing Limited, 2012

Fontcuberta J., Balcells L., Bibes M., Navarro J., Frontera C. *et al.*, 2002, Magnetoresistive oxides: new developments and applications, *Journal of Magnetism and Magnetic Materials*, 242–245, 98–104.

Gusmano G., Bianco A., Montesperelli G., Morten B., De Cicco G. *et al.*, 1996, Preparation and properties of new thick-film magnetoresistive materials, *Sensors and Actuators A*, 52, 161–165.

Holmes P. J., 1973, Changes in thick-film resistor values due to substrate flexure, *Microelectronics Reliability*, 12, 395–396.

Hormadaly J., Thermistor composition, US Patent 4 961 999 (9 October 1990).

Hrovat M., Belavič D., Samardzija Z. and Holc J., 2001, A characterization of thick-film resistors for strain gauge applications, *Journal of Materials Science*, 36, 2679.

Hrovat M., Belavič D., Bencan A., Bernard J, Hole J. *et al.*, 2003, Thick-film resistors on various substrates as sensing elements for strain gauge applications, *Sensors and Actuators A*, 107, 261–272.

Hrovat M., Belavič D., Kita J., Cilenšek J., Golonka L. *et al.*, 2005, Thick-film temperature sensors on alumina and LTCC substrates, *Journal of the European Ceramic Society*, 25, 3443–3450.

Hrovat M., Belavič D., Kita J., Holc J., Drnovšek S. *et al.*, 2006, Thick-film strain and temperature sensors on LTCC substrates, *Microelectronics International*, 23(3), 33–41.

Hrovat M., Belavič D., Kita J., Holc J., Cilenšek J. *et al.*, 2007, Thick-film PTC thermistors and LTCC structures: the dependence of the electrical and microstructural characteristics on the firing temperature, *Journal of the European Ceramic Society*, 27, 2237–2243.

Hrovat M., Belavič D., Kita J., Holc J., Cilenšek J., Drnovšek S., 2009, Thick-film NTC thermistors and LTCC materials: the dependence of the electrical and microstructural characteristics on the firing temperature, *Journal of the European Ceramic Society*, 29, 3265–3271.

http://sales.hamamatsu.com/en/products/solid-state-division/compound-semiconductors/cds.php

Ikegami S. and Uda H., 1994. Screen-printed CdS/CdTe solar cells, *in* Prudenziati M. (ed.) *Thick-Film Sensors*, Elsevier, Amsterdam.

Ionescu R., 1998, Combined Seebeck and resistive SnO_2 gas sensors, a new selective device, *Sensors and Actuators B*, 48, 392–394.

Jacq C., Maeder T. and Ryser P., 2004a, High-strain response of piezoresistive thick-film resistors on titanium alloy substrates, *Journal of the European Ceramic Society*, 24 (6), 1897–1900.

Jacq C., Vionnet S., Maeder T. and Ryser P., 2004b, Integrated thick-film hybrid microelectronics on aluminium substrates, *Proceedings of the European Microelectronics and Packaging Symposium*, Prague.

Jiang J. C., Crosbie G. M., Tian W., Cameron K. K., and Pan X. Q., 2000, Transmission electron microscopy structure and platinum-like temperature coefficient of resistance in a ruthenate-based thick-film resistor with copper oxide, *J Appl Phys*, 88 (2), 1124–1128.

Jurków D. and Golonka L., 2009, Novel cold chemical lamination bonding technique, a simple TCC thermistor-based flow sensor, *Journal of the European Ceramic Society,* 29 (10), 1971–1976.

Khare, N., Moharil U. P., Singh B. and Gupta, A. K., 2004, Study of low field magneto-resistance in $La_{0.67}A_{0.33}MnO_3$ (A ≡ Ca, Ba, Sr) screen-printed films, *Indian Journal of Pure and Applied Physics*, 42 (1), 62–66.

© Woodhead Publishing Limited, 2012

Kogut A., Wollack E., Fixsen D. J., Limon M., Mirel P. *et al.*, 2004, Design and calibration of a cryogenic blackbody calibrator at centimeter wavelengths, *Review of Scientific Instruments*, 75, 5079–5083.

Kuzel R., Koprivova E. and Broukal J., 1993, Thick-film resistors with high *TCR, Microelectronics International*, 4 (1), 28–31.

Mach M., Pietriková A., Gabàni S., Pavlìk V., Flachbad K., *et al.*, 2003, Low temperature micro-calorimeters based on thick-film resistors, *26th International Spring Seminar on Electronics Technology*, Stará Lesná, Slovak Republic.

Marioli D., Rolla P. and Taroni A., 1993, Insulated metal substrates for thick-film sensors applications, *Proceedings of 9th European Hybrid Microelectronics Conference (Nice)*, pp. 261–268.

Markowski P. and Dziedzic A., 2008, Planar and three-dimensional thick-film thermoelectric microgenerators, *Microelectronics Reliability*, 48, 890–896.

Masoero A., Morten B., Olcese G. L., Prudenziati M., Tango F. *et al.*, 1999, Magnetic properties of Ni-Co thick-film magnetoresistors, *Thin Solid Films*, 350, 214–218.

Morten B. and Prudenziati M., 1994, Piezoresistive thick-film sensors, *in* Prudenziati M. (ed.), *Thick-film Sensors*, Elsevier, Amsterdam, pp. 189–208.

Morten B., Prudenziati M. and Taroni A., 1977, Piezoresistenza in resistori a film spesso depositati per serigrafa, *Digest AEI Conference* (unpublished).

Morten B., Prudenziati M., Sirotti F., DeCicco G., Alberigi-Quaranta A. *et al.*, 1990, Magnetoresistive properties of Ni-based thick-films, *Journal of Materials Science: Materials in Electronics*, 1, 118–122.

Morten B., Ruffi G., Sirotti F., Tombesi A., Moro L. *et al.*, 1991, Lead-free ruthenium-based thick-film resistors: a study of model-systems, *Journal of Materials Science: Materials in Electronics*, 2 (1), 46–53.

Morten B., Prudenziati M., De Cicco G., Bianco A., Montesperelli G. *et al.*, 1997, Thick-film magnetoresistors and related sensors, *Measurment Science* and *Technology*, 8, 21–28.

Nicolics J. and Smetana W., 1991, A laser power detector built up by application of thick-film technology, *Sensors and Actuators A*, 25–27, 235–239.

Nicoll F. H. and Kazan B., 1955, Large area high-current photoconductive cell using cadmium sulphide powder, *Journal of the Optical Society of America*, 45, 647–650.

Ohta T., Kajikawa T. and Kumashiro Y., 1990, Characteristics of $(Bi,Sb)_2(Te,Se)_3$-based thick-film thermoelectric elements for power generation, *Electrical Engineering in Japan*, 110, 14–23.

Park K. and Bang D. Y., 2003, Electrical properties of Ni–Mn–Co–(Fe) oxide thick-film NTC thermistors prepared by screen printing, *Journal of Materials Science: Materials in Electronics*, 14 (2), 81–88.

Pike G. E. and Seager G. H., 1977, Electrical properties and conduction mechanisms of Ru-based thickfilm (cermet) resistors, *Journal of Applied Physics*, 48, 5152–5169.

Postma H., 1994, Thermometers for cryogenic temperatures, *in* M. Prudenziati (ed.), *Handbook of Sensors and Actuators (Vol. 1) Thick-film Sensors,* Elsevier, pp. 127–150.

Prudenziati M., Device for pressure measurement using a resistor strain gauge. U.S. 4-311-980 patent issued Jan 19, 1982, on application filed by Fabbrica Italiana Magneti Matelli in Sept 21, 1979.

Prudenziati M., Morten B., Cilloni F. and Ruffi G., 1989, Very high strain sensitivity in thick-film resistors: real and false super gauge factors, *Sensors and Actuators*, 19, 401–414.

Prudenziati M., Tankiewicz S., Morten B., Piccinini S. and Golonka L, 1997, Piezoresistive effects in thick-film piezoresistors: the effect of the conductive phase, *Proceedings of International Spring Seminar on Electronic Technology*, ISSE'97, Poland, pp. 76–81.

© Woodhead Publishing Limited, 2012

Prudenziati M. (ed.), 1994, *Thick-film Sensors*, Elsevier, Amsterdam.
Prudenziati M., Morten B. and Taroni A., 1981/82, Characterization of thick-film resistor strain gauges on enamel steel, *Sensors and Actuators*, 2, 17–27.
Puers B., Sansen W. and Paszczynski S., 1987, Assessment of thick-film fabrication methods for force (pressure) sensors, *Sensors and Actuators*, 12, 57–76.
Rane S., Prudenziati M. and Morten B., 2007, Environment friendly Perovkite ruthenate-based thick-film resistors, *Materials Letters*, 61, 595–599.
Reynolds Q. M. and Norton M. G. 1986, Thick-film platinum temperature sensors, *Hybrid Circuits*, 9, 33–35.
Ross J. N., 1995, Thick-film photosensors, *Measurement Science and Technology*, 6, 405–409.
Rubi D., Fontcuberta J., Lacaba M., Gonzalez A. M., Baztan J. *et al.*, 2006, On–off magnetoresistive sensor based on screen-printed $La_{2/3}Sr_{1/3}MnO_3$ manganite, *Sensors and Actuators A*, 132, 52–55.
Rubin L. G., 1991, Cryogenic thermometry: a review of progress since 1982, *Cryogenics*, 31, 341–356.
Setty M. S. and Amalnerkar D. P., 1994, CdS based photoconducting sensors, *in* M. Prudenziati (ed.) *Thick-Film Sensors*, Elsevier, Amsterdam, pp. 359–377.
Sirotti F., Prudenziati M., Giardullo B., Anzolin W. and Manfredini T., 1990, Ni-based air-fireable thick-film conductors, *Journal of Materials Science*, 25, 4688–4693.
Smetana W. and Reicher R., 1997, Designing the performance of a thick-film laser power detector by means of a heat-transfer analysis using finite-element method, *Sensors and Actuators A: Physical*, A58(3), 213–218.
Tamborin M., Piccinini S., Prudenziati M. and Morten B., 1997, Piezoresistive properties of RuO_2-based thick-film resistors: the effect of RuO_2 grain size, *Sensors and Actuators A*, 58, 159–164.
Tankiewicz S., Morten, B., Prudenziati M. and Golonka L. J., 2002, IrO_2-based thick-film resistors, *Journal of Applied Physics*, 91, 4261–4266.
Thomsen S. M. and Bube R. H., 1955, High-sensitivity photoconductor layers, *Review of Scientific Instruments*, 26, 664–665.
Uda, H., Sonomura, H. and Ikegami S., 1997, Screen-printed CdS/CdTe cells for visible-light-radiation sensor, *Measurement Science and Technology*, 8 (1), 86–91.
Viret M., Drouet M., Nassar J., Contour J. P., Fermon C. *et al.*, 1997, Low-field colossal magnetoresistance in manganite tunnel spin valves, *Europhysics Letters*, 39 (5), 545–549.
Wada T., Stein S. J., Stein M. A. and Chitale S. M, 1997, The state-of-the-art of thick-film technology for automotive sensors, *Proceedings IEMT/IMC*, pp. 41–46.
Watanabe M., Morishita M. and Ootuka Y., 2001, Magnetoresistance of RuO_2-based resistance thermometers below 0.3 K, *Cryogenics*, 41, 143–148.
Weber J., Potje-Kamloth K., Haase F., Detemple P., Volklein F. *et al.*, 2006, Coin-size coiled-up polymer foil thermoelectric power generator for wearable electronics. *Sensors and Actuators A*, 132, 325–330.
White N. M., 1989, An assessment of thick-film piezoresistors on insulated steel substrates, *Hybrid Circuits*, 20, 23–27.
White N. M. and Turner J. D., 1997, Thick-film sensors: past, present and future, *Measurement Science and Technology*, 8, 1–20.
Willekers R. W., Mathu F., Meijer H. C. and Postma H., 1990, Thick-film thermometers with predictable R-T characteristics and very low magnetoresistance below 1 K, *Cryogenics*, 30 (4), 351–355.

© Woodhead Publishing Limited, 2012

Yeager C. J. and Courts S. S., 2001, A review of cryogenic thermometry and common temperature sensors, *IEEE Sensors Journal*, 1 (4), 352–360.
Ylöstalo J., Berglund P., Niinikoski T. O. and Voutilainen R., 1996, Cryogenic temperature measurement for large applications, *Cryogenics*, 36, 1033–1038.
Zhong J. and Bau H. H., 2001, Thick-film thermistors printed on LTCC tapes, *American Ceramic Society Bulletin*, 80 (10), 39–42.

© Woodhead Publishing Limited, 2012

8

Printed thick-film capacitive sensors

V. FERRARI, University of Brescia, Italy and
M. PRUDENZIATI, University of Modena
and Reggio Emilia, Italy

Abstract: Capacitive sensors and microsystems based on films printed on different substrates, including alumina, steel and silicon, are reviewed. Screen printing is the prevalent film deposition method considered, though other techniques based on direct writing are also referred to. Principles and configurations of capacitive sensors based on geometrical and permittivity variations are described, and examples are given of thick-film sensors for the measurement of physical and chemical quantities.

Key words: thick-film sensors, capacitive sensors, pressure sensors, interdigitated electrodes.

8.1 Introduction

Capacitive sensors can detect and measure a large variety of physical and chemical quantities such as strain, displacement and motion, acceleration, pressure, flow, temperature, humidity, concentration of gases and chemical species and many other variables, and can be used in a wide range of applications (Puers, 1993). Compared with competing alternatives such as optical, inductive, and piezoresistive sensors, capacitive sensors may offer a number of advantages, including high resolution, low power consumption, potential for reduced fabrication cost and moderate temperature influence on the output, while stability and reproducibility are mainly related to the materials and construction layout. Capacitive sensors are generally combined with electronic circuitry, or in specific cases integrated with microelectronics into a single silicon chip or package, forming active transducers. In addition, they also offer the opportunity to become part of inductive–capacitive (LC) resonant circuits that can be operated as passive sensors with wireless interrogation.

Nevertheless, for a long time these benefits have not been fully exploited or the technologies used have been inadequate to leverage them. One possible explanation of critical importance is that improperly designed capacitive sensing systems, comprising the sensing element(s) and signal-conditioning electronics, are affected by issues such as stray capacitances and sensitivity to interference, which can significantly impair performances. In practical systems, the capacitance to be sensed usually ranges from few picofarads, or less, to hundreds of picofarads in the case of air or higher-permittivity dielectrics, respectively. The sensor impedance is typically very high, reaching about 160 MΩ at 1 kHz for a 1-pF

© Woodhead Publishing Limited, 2012

sensor. Hence, very high input impedance is needed in voltage amplifiers to avoid shunting the signal, or other configurations such as transimpedance input stages have to be used. In all cases, special caution in signal readout is required to minimize electromagnetic interference pick-up and noise. Capacitance variations as low as 1 fF may need to be detected in some cases, which requires very careful system layout to keep the stray capacitances as low as possible and adequate circuit techniques to reduce their effect when they are comparable with or larger than the sensor capacitance.

The current renewed interest in capacitive sensors may be ascribed to one or more of the following reasons:

- Availability at low cost of electronic techniques and circuits for high-performance interfacing to the sensing element(s), in some cases also enabling integration into micro-electro-mechanical systems made with micromachined silicon (Si-MEMS or simply MEMS) or with ceramic materials (C-MEMs), e.g. by low temperature co-fired ceramic (LTCC) technology.
- Interest in resonant capacitive–inductive circuits and thus potential use of sensors for both passive and active wireless applications, e.g. in medical applications for implanted devices, automotive, aerospace, radio-frequency identification (RFID) systems.
- Interest for applications in temperature ranges where other classes of sensors are more sensitive to thermal effects and ageing.

In this framework, materials and processes of thick-film technology (TFT) may contribute: low cost of infrastructure, processing and materials; good degree of miniaturization on different substrates; wide choice of conducting printable materials; and ability to maintain low manufacturing cost also in small production volumes.

Capacitive sensors based on screen-printed thick-films are reviewed in this chapter. Alternative processes for film deposition, other than conventional screen printing, are also briefly mentioned, such as direct-writing techniques. Device and system issues are considered in more detail, such as theory of operation, transduction characteristics, coupling to electronic circuitry for signal readout, and examples of applications. Extensive reference to literature is made throughout the chapter to provide sources of information and point to updated research results that belong to the state of the art in the field.

8.2 General concepts

The capacitance C between two electrodes (plates) separated by a dielectric medium expresses the amount of charge induced on each plate by a unit potential difference applied to the electrodes. Irrespective of the specific configuration of the considered system, capacitance generally increases by raising either the medium dielectric permittivity or the equivalent overlap area between the electrodes, whereas it decreases by augmenting their separation distance.

© Woodhead Publishing Limited, 2012

In the simplest case of two parallel plates of area A separated by a gap g, much smaller than the plate dimensions, filled with a dielectric medium, the capacitance C is given by:

$$C = \varepsilon \frac{A}{g}, \qquad [8.1]$$

where $\varepsilon = \varepsilon_0 \varepsilon_r$, with $\varepsilon_0 = 8.85 \times 10^{-12}$ F/m being the dielectric permittivity of free space and ε_r the relative dielectric constant of the medium.

In the small increment limit, the fractional capacitance variation dC/C can be expressed by the relation:

$$\frac{\mathrm{d}C}{C} = \frac{\mathrm{d}\varepsilon}{\varepsilon} + \frac{\mathrm{d}A}{A} - \frac{\mathrm{d}g}{g}, \qquad [8.2]$$

which again shows that C increases by increasing ε or A, or decreasing g.

Capacitive sensors rely on the changes of capacitance arising from variations in the geometry (A and g) or the medium physical property (ε_r) affected by the quantity to be measured, i.e. the measurand.

Ideal capacitive sensors, having a purely reactive impedance $Z_C = 1/(2\pi f C)$, do not dissipate static power; therefore they are immune from self-heating and the associated thermal drift, and do not display thermal noise. The influence of temperature on capacitance can be minimized by a suitable choice of geometry to reduce the effect of thermal expansion and, when possible, by selecting a dielectric with a low temperature coefficient of permittivity. Long-term stability and aging, provided that unintentional mechanical deformations do not occur, are related mostly to material and fabrication features, such as electrode surface finishing, stability of the dielectric medium and protection of the capacitor against humidity and moisture.

Among the drawbacks of capacitive sensors is their propensity to interference pick-up and parasitic effects, mostly due to the large reactive impedance Z_C, which typically amounts to 10–20 MΩ for C around 10 pF at 1 kHz. Therefore, the request arises for proper design of the sensor element with adequate use of shielding, and special caution in signal readout and amplification. Currently, properly designed electronic interface circuits can provide high values of signal-to-noise ratio, thereby making capacitive sensing a high-precision technique. A comprehensive treatment of electronic techniques and circuits for capacitive sensors is given in Baxter (1996).

8.3 Configurations and technologies

Capacitive sensors in general do not require bulk conductors, since capacitance derives from faced surfaces. High capacitance values call for large surface area/thickness ratios. Therefore, film technologies are in principle especially suited and attractive to manufacture capacitive sensors (Puers, 1993).

The faced plate geometry of Fig. 8.1(a) provides the largest capacitance at parity of electrode spacing and area, since it maximizes surface overlap. It also

© Woodhead Publishing Limited, 2012

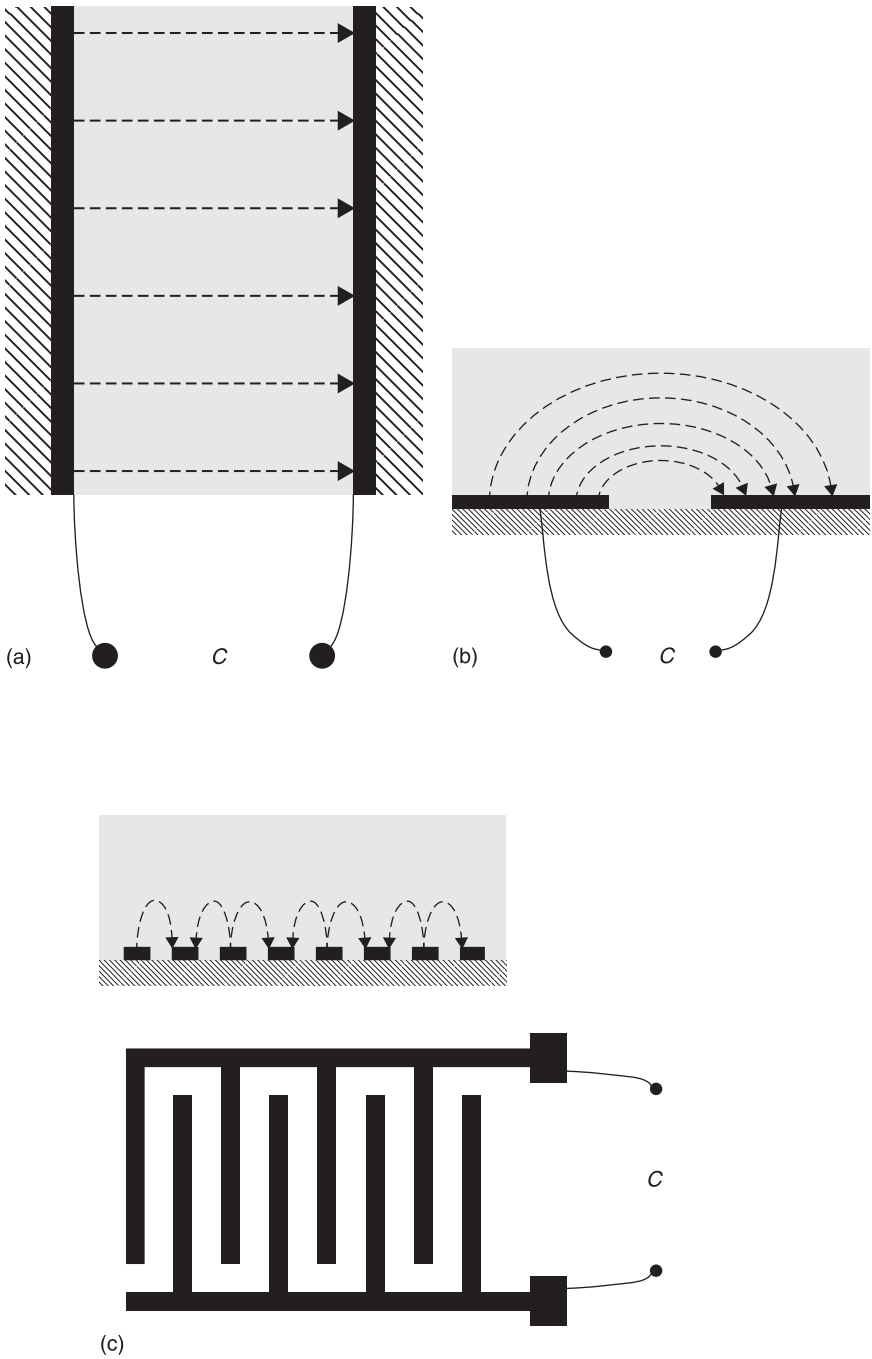

8.1 Configurations of capacitive sensors: (a) faced electrodes in a planar plate capacitor; (b) coplanar electrodes; (c) interdigitated electrodes.

© Woodhead Publishing Limited, 2012

offers electromagnetic shielding due to the 'closed' configuration. The alternative option is an 'open' configuration based on coplanar electrodes interacting by means of fringing fields, as shown in Fig. 8.1(b). Also, the basic coplanar electrode pair can be replicated in the interdigitated (IDT) structure of Fig. 8.1(c), which results in the interdigitated capacitor (IDC).

In the following, the attention is focused on sensors implemented in TFT, i.e. applying screen printing or closely related processes stemmed therefrom (Prudenziati, 1994; White and Turner, 1997).

The configuration of Fig. 8.1(a) can be implemented in multilayer structures on a single side of the substrate with conductive films separated by dielectric layers in a stacked arrangement. When air, or another fluid, is the dielectric medium, the supporting solid surface for the top electrode is missing: therefore an additional substrate becomes necessary to host the top electrode, such as in diaphragm pressure sensors. This can be typically obtained by assembling plane substrates in combination with spacing layers or frames to create suspended configurations or laterally supported arrangements.

This result can be directly accomplished in LTCC technology, where ceramic green tapes are shaped, provided with necessary screen-printed films, stacked, laminated and co-fired at 800–900 °C (Golonka, 2006). Moreover, LTCC combined with standard TFT and silicon micromachining have introduced a hybrid or heterogeneous integration (Gongora-Rubio *et al.*, 2001). In the field of sensor implementation, a particularly appreciable variety of three-dimensional (3D) microstructures is achievable with LTCC technology by means of vias and cavities created in the multilayer stack. Mechanical punching or laser scribing are typically used to form vias, cavities and cutouts in the individual green sheets before lamination and co-firing (Peterson *et al.*, 2005).

When the thicknesses of commercially available green tapes of LTCC are a limitation for the design of feature sizes, including cavity airgap distance and diaphragm thickness of capacitive sensors, a viable option is to accomplish accurately designed structures by means of sacrificial layers. For instance, a layer of carbon-based paste can be printed to act as stable mechanical support for a subsequently printed electrode. During the next firing process, the carbon-based layer is burnt out, thereby releasing the active layer from the substrate and leaving it partially self-supported (Lucat *et al.*, 2008). Other 'fugitive phases' and sacrificial volume materials (SVM) which create temporary inserts can be deposited and thermally removed to create freely-supported beams, plates and bridges (Gongora-Rubio *et al.*, 2001; Peterson *et al.*, 2005). Otherwise a screen-printed metal film is co-fired with the desired structure and chemically etched away, in the post-firing process, with a strong acid solution (Sippola and Ahn, 2006) or, similarly, a strontium-carbonate layer is applied which can be removed with a weak acid solution (Lucat *et al.*, 2008).

Coplanar and IDT electrodes represented in Fig. 8.1(b,c) provide the most straightforward means to create capacitive sensors on a single side of the substrate.

© Woodhead Publishing Limited, 2012

Substrates may be the most traditional rigid or flexible materials, ceramics or polymers (Prudenziati, 1994), but also increasing interest is addressed to new unconventional materials, such as paper, plastics and textiles. Representative examples are IDT capacitors and other patterned components screen-printed on fabrics, whose feasibility was recently demonstrated for applications in functional clothes with embedded sensors (Kim *et al.*, 2010) and in instrumented textiles for healthcare applications (Kang *et al.*, 2006).

8.4 Capacitive sensing based on geometrical variations

With reference to the sufficiently general case described by Eqs. [8.1] and [8.2], the geometrical parameters influencing capacitance are the armature gap g and overlap area A. Therefore, any physico–chemical quantity, e.g. pressure, force or acceleration, acting on capacitor plates to vary g or A is potentially measured with a capacitive sensor. Three cases will be illustrated in the following, where, respectively, *g, A* or both vary under the measurand action.

8.4.1 Sensing relying on changes of distance

Let us suppose that a parallel plate capacitor, as shown in the inset of Fig. 8.2, has initial gap g_0 and capacitance C_0. When one plate is rigidly moved and the gap is changed to g, the capacitance as a function of the gap $C(g)$ can be conveniently expressed as the normalized capacitance $C(g)/C(g_0) = C(g)/C_0 = c(x)$, where $x = g/g_0$. It follows that $c(x) = 1/x$ and the normalized sensitivity can be defined as $k(x) = \mathrm{d}c/\mathrm{d}x$ resulting in $k(x) = -1/x^2$. Furthermore, the normalized nonlinearity, i.e. the departure from a constant-sensitivity value, defined as $\mathrm{d}k(x)/\mathrm{d}x$, will be $\mathrm{d}k(x)/\mathrm{d}x = 2/x^3$.

The plots of these quantities, given in Fig. 8.2, make evident the advantage of a narrow gap in obtaining high sensitivity, but at the expense of a large nonlinearity. On the contrary, wide gaps improve linearity but reduce sensitivity and also result in a decrease of capacitance, which can be therefore swamped by parasitic effects in practical cases. Moreover, if the initial spacing g_0 is set too small, a reduced span for the plate displacement remains possible before the plates touch each other, thus limiting the measurement range. The choice of g_0 will necessarily be a trade off among the different requirements.

If the gap g itself is the measurand, i.e. the sensor is applied to measure distance or displacement, then a linear output can be attained by an electronic readout, which provides an output signal directly proportional to the sensor impedance $|Z_C|$. Since $|Z_C| = 1/\omega C$, the output signal will be proportional to g at a given angular frequency ω. Alternatively, the capacitor can be inserted into a relaxation oscillator circuit whose frequency, proportional to the sensor capacitance, is taken as the output signal. A further limitation to linearity comes from the fringing effect

© Woodhead Publishing Limited, 2012

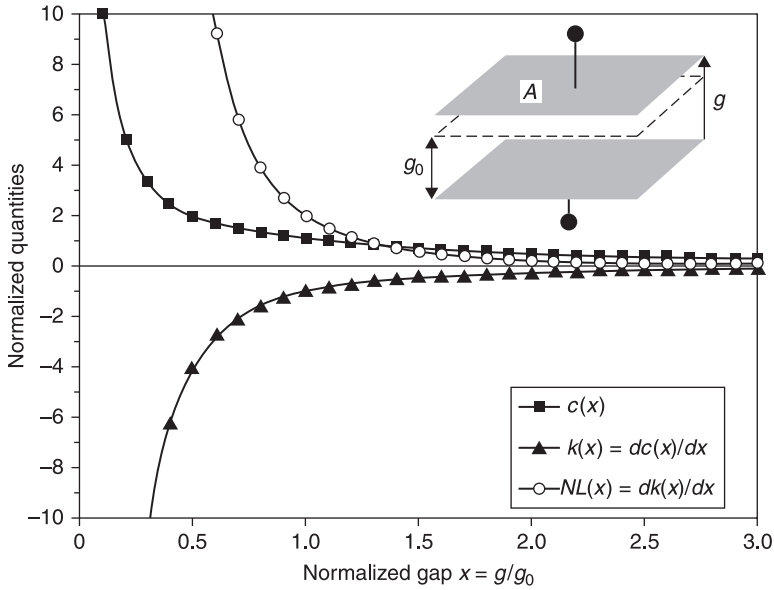

8.2 Normalized capacitance *c,* sensitivity *k* and nonlinearity *NL* as a function of the normalized gap size $x = g/g_0$ for a parallel plate capacitor as shown in the inset.

caused by the electric field lines diverting from being parallel at the edge of the sensor electrodes due to their finite dimension. To counteract this effect, properly driven guard electrodes can be adopted to steer the electric field as parallel as possible between the sensor electrodes (Baxter, 1996).

With bending plates, such as diaphragms in pressure sensors, the spacing g, or equivalently the plate deflection z, is a function of position on the plate. For example, the deflection z of a disc diaphragm (inset of Fig. 8.3) having thickness t and radius R, rigidly clamped at the edge, for $z<<t$, is given by (Taroni, 1994):

$$z(p, r) = \frac{3(1-v^2)}{16Et^3} p(R^2 - r^2)^2, \qquad [8.3]$$

where p is the uniform pressure applied to the disc, r is the radial distance from the center, v and E are the Poisson's ratio and Young's modulus of the diaphragm material, respectively.

Therefore, the transduction function of a capacitive pressure sensor formed by a pair of electrodes placed respectively on a bending circular diaphragm and a faced rigid plane is:

$$C(p) = \int_0^R \frac{2\pi\varepsilon r}{g_0 - z(p,r)} \mathrm{d}r = \frac{C_0}{R^2\sqrt{Kp}} \tanh^{-1}\left[R^2\sqrt{Kp}\right], \qquad [8.4]$$

© Woodhead Publishing Limited, 2012

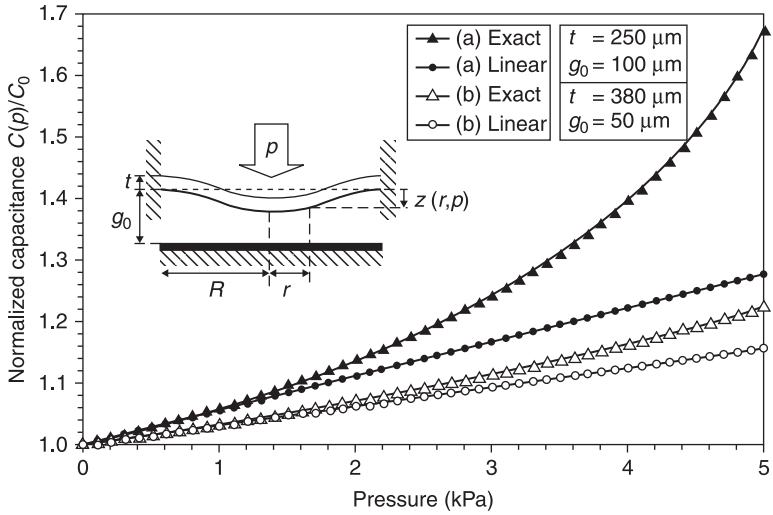

8.3 Normalized capacitance versus applied pressure for a deformable diaphragm sensor as shown in the inset; data calculated for $E = 330$ GPa (alumina), $R = 7.5$ mm and different values of diaphragm thickness t and gap g_0. Exact and linearized plots refer to Eqs. (8.4) and (8.6), respectively.

where $\varepsilon = \varepsilon_0\varepsilon_r$ is the permittivity of the dielectric medium, with $\varepsilon \approx \varepsilon_0$ in case of air, and:

$$C_0 = \frac{\pi\varepsilon R^2}{g_0};\ K = \frac{3(1-\nu^2)}{16Et^3g_0}. \qquad [8.5]$$

For small deflections so that $z/g_0 << 1$, Eq. [8.4] can be approximated as in Taroni (1994):

$$C(p) = \int_0^R \frac{2\pi\varepsilon r}{g_0 - z(p,r)}\,\mathrm{d}r \cong \frac{2\pi\varepsilon}{g_0}\int_0^R \left(1 + \frac{z(p,r)}{g_0}\right) r\mathrm{d}r = C_0\left(1 + \frac{KR^4}{3}p\right). \qquad [8.6]$$

With a diaphragm homogeneous in thickness and composition, the maximum deflection z_{max} occurs at the centre ($r = 0$) and is constrained to be $z_{max}(0) \le g_0$. Accordingly, the allowed full-scale pressure p_{max}, in deflection mode, is:

$$p_{max} = \frac{16Et^3}{3(1-\nu^2)} \times \frac{g_0}{R^4}, \qquad [8.7]$$

provided that it would not cause the flexural strength limit of the material σ_{lim} to be exceeded, in which case the full scale is bounded by the limit pressure $p_{lim} \cong 4t^2\sigma_{lim}/(3R^2)$.

© Woodhead Publishing Limited, 2012

Equations [8.4] to [8.6] show that the transduction characteristic $C(p)$ becomes notably nonlinear at increasing pressures, but a proper design, with careful choice of g_0, t and R of the diaphragm and of its elastic properties, together with operating the sensor in the lower part of the pressure range, can mitigate this effect. The plots of $C(p)/C_0$ versus p are shown in Fig. 8.3 for a sensor with an alumina circular diaphragm as the results of computations for two different values of thickness t and gap g_0. The exact and linearized expressions of Eqs. [8.4] and [8.6], respectively, are compared in the plots, showing that the 250 μm thick diaphragm provides higher sensitivity but larger nonlinearity. A marked improvement in linearity at parity of pressure is obtained for the 380 μm thick diaphragm, but in this case the gap g_0 has been reduced from 100 μm to 50 μm in order to counteract, at least partially, the decrease in sensitivity caused by the thicker diaphragm.

An improvement in linearity with respect to uniform-thickness diaphragms could be achieved with bossed diaphragms, e.g. a disk thicker in the central portion to increase its rigidity there, or diaphragms provided with corrugations around the edge to increase the compliance there, which flatten the deflection profile and enable larger displacements. Both expedients, however, require tridimensional shaping, which is easier in silicon micromachining than in TFT.

In practical implementations of capacitive pressure sensors, often an additional electrode (3) is placed around the edge of the sensing electrode (2) of $C(p)$, resulting in the three-electrode configuration shown in Fig. 8.4. The additional electrode (3) and the electrode (1) on the faced plate form a reference capacitor C_{ref} which is essentially unaffected by the applied pressure because of the

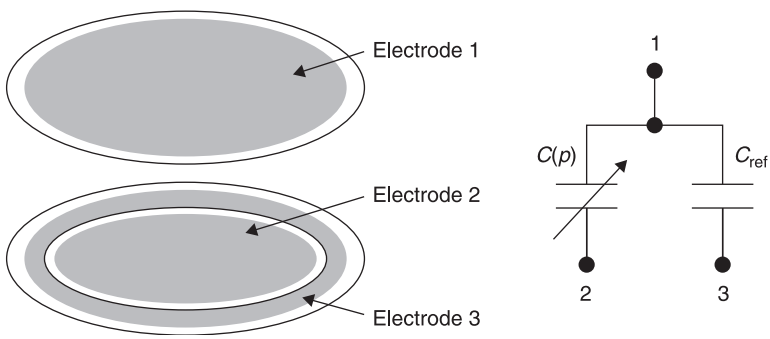

8.4 Three-electrode configuration for capacitive pressure sensor: the capacitance $C(p)$ between electrodes 1 and 2 is sensitive to pressure, the capacitance C_{ref} between electrodes 1 and 3 is virtually unaffected by pressure and can be used as a reference for compensation of permittivity variations and thermal effects.

© Woodhead Publishing Limited, 2012

negligible diaphragm deflection in the edge region. Both $C(p)$ and C_{ref} are equally sensitive to perturbing factors such as thermal effects and environmental changes. Therefore, the three-electrode configuration can be applied to compensate for interfering factors if the ratio $C(p)/C_{ref}$ is measured. Similar compensation effects are accomplished in differential capacitive pressure sensors.

8.4.2 Sensing relying on changes of area

Sensors in which the measurand changes the overlapping area A between electrodes benefit from the linear dependence of capacitance C versus A, provided that stray capacitances due to fringing effects are negligible.

This can be obtained if faced electrodes are made to displace relative to each other in the direction parallel to their surface while keeping the separation gap constant, resulting in a capacitance variation proportional to displacement. This characteristic has been applied for instance in the design of a capacitive torque sensor based on changes in area of two faced serrated teeth (Turner, 1989).

The variable-area principle can also be exploited in bending diaphragm capacitive pressure sensors. By applying a pressure p higher than the pressure p_{max} at which the diaphragm touches the bottom plate, capacitive pressure sensors can be operated in contact mode. The pressure causes increasingly larger regions of the diaphragm to touch (contact) the lower plate; therefore, provided that the electrode surfaces are electrically insulated, the capacitance is nearly proportional to the contact area, which in turn exhibits good linearity with respect to the applied pressure. This holds true over a wide range of pressures. However, this linearity comes at the expense of decreased sensitivity with respect to the deflection mode (Eaton and Smith, 1997).

8.4.3 Sensing relying on deformation

Both the distance and overlap area of electrodes can vary in a capacitive sensor when the measurand acts on the sensor volume in such a way to cause deformation. An example is shown in Fig. 8.5, where a planar capacitor formed by a dielectric film sandwiched between two conductor layers deforms under the effect of a longitudinal strain $S = \mathrm{d}l/l$ applied normal to the lateral surface. This structure works as a capacitive strain gauge, where strain induces a variation of capacitance through changes in dimensions due to stretching.

Assuming that the conductor films have negligible thickness, the fractional capacitance variation is:

$$\begin{aligned}\frac{\mathrm{d}C}{C} &= \frac{\mathrm{d}\varepsilon}{\varepsilon} + \frac{\mathrm{d}A}{A} - \frac{\mathrm{d}h}{h} = \frac{\mathrm{d}\varepsilon}{\varepsilon} + \frac{\mathrm{d}l}{l} + \frac{\mathrm{d}w}{w} - \frac{\mathrm{d}h}{h} \\ &= \frac{\mathrm{d}\varepsilon}{\varepsilon} + S - \nu S + \nu S = \frac{\mathrm{d}\varepsilon}{\varepsilon} + S,\end{aligned} \qquad [8.8]$$

© Woodhead Publishing Limited, 2012

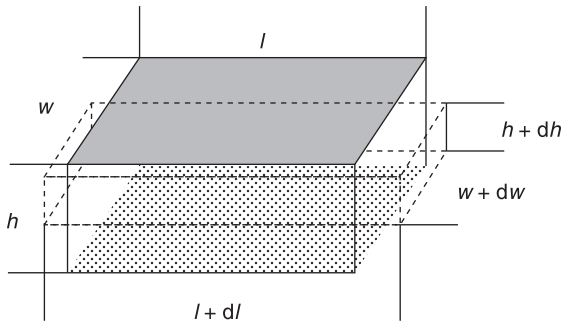

8.5 Capacitive strain gauge with strain applied along the length *l* normal to the top and bottom electrode faces causing longitudinal stretching and transverse contraction.

where v is the Poisson's ratio of the dielectric medium. The gauge factor GF, defined as $GF = (\mathrm{d}C/C)/S$, is then:

$$GF = \frac{\mathrm{d}C/C}{S} = 1 + \frac{\mathrm{d}\varepsilon/\varepsilon}{S}. \qquad [8.9]$$

The unity term comes from geometrical factors, while the second term accounts for the strain dependency of the dielectric permittivity and it is sometimes referred to as the 'piezocapacitive' effect in analogy with the corresponding effect in piezoresistors. A different configuration based on IDT electrodes can be used. The operating principle is similar but, in this case, closed form expressions for the capacitance variation and gauge factor are more complex to derive.

8.5 Capacitive sensing based on permittivity variations

Capacitive sensing of physical and chemical quantities, such as temperature, gas concentration, relative humidity as well as biosensors, frequently rely on changes in the dielectric permittivity of fluids or solid media. Also mechanical effects such as a pressure applied over the surface area of planar capacitors can produce capacitance variations related to permittivity changes (Arshak, K. *et al.*, 2005).

The majority of capacitive sensors in chemical and bio-chemical applications have the open electrode configuration of Fig. 8.1(c) with coplanar IDT electrodes covered by the dielectric medium made by a bio-chemically-sensitive film facing the environment for maximum interaction. Optimization of the system requires the choice of the best dielectric film for sensing the target species together with the optimal choice of electrode configuration.

A rather general analysis of planar IDT capacitive sensors can be made with reference to the simplified three-medium model illustrated in Fig. 8.6; the model

© Woodhead Publishing Limited, 2012

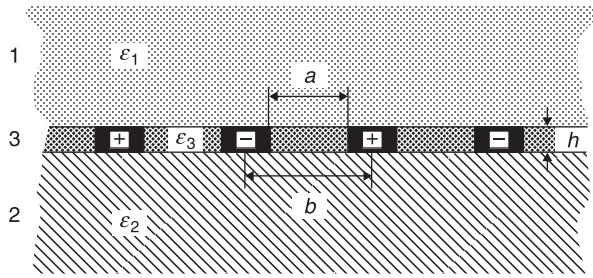

8.6 Three-medium model for an IDT capacitor after Endres and Drost (1991).

comprises the sensed medium (1), the substrate (2) and the inter-electrode space (3), each medium *i* with its dielectric permittivity ε_i, while the electrodes are assumed to be perfect conductors (Endres and Drost, 1991).

Neglecting edge effects, the sensor capacitance C can be computed from the capacitance per unit length C_{UC} of a two-dimensional cell formed by an electrode pair, yielding:

$$C = C_{UC}\,(N-1)L, \qquad [8.10]$$

where N and L are the number and length of the finger electrodes, respectively.

The capacitance of the unit cell C_{UC} is given by the approximated expression:

$$C_{UC} = C_1 + C_2 + C_3 = \frac{(\varepsilon_1 + \varepsilon_2)}{2} \times \frac{K\left[\sqrt{1-\left(\frac{a}{b}\right)^2}\right]}{K\left[\frac{a}{b}\right]} + \frac{\varepsilon_3 h}{a}, \qquad [8.11]$$

where a, b and h are the finger spacing width, distance (pitch) and thickness, respectively. $K[x]$ is the complete elliptic integral of the first kind (Bronshtein *et al.*, 2007), given by:

$$K\left[x\right] = \int_0^{\pi/2} \frac{1}{\sqrt{1-x^2\sin^2\theta}}\,\mathrm{d}\theta, \qquad [8.12]$$

and C_1 and C_2 are the contributions of the upper medium and substrate permittivities, and C_3 that of the inter-electrode film. If the medium 3 is a single overlaying film that entirely buries the IDT electrodes, as it often happens with TFT sensors, then $\varepsilon_3 = \varepsilon_1$ in Eq. [8.11].

An expression slightly different from Eq. [8.11], yet substantially equivalent, was presented for capacitive humidity sensors in Smetana and Wiedermann (1987). A review of IDT sensors and transducers is given in Mamishev *et al.*, (2004).

© Woodhead Publishing Limited, 2012

8.6 Examples of devices and their applications

Several studies have been carried out on design and implementation methods of thick-film capacitive pressure sensors. With respect to the more usual piezoresistive devices, capacitive sensors call for less extensive processing, are less susceptible to misalignment errors and are potentially more stable at high temperature. On the other hand, a much closer control of inter-electrode distance is mandatory in design and manufacture of capacitive devices for reproducible behaviour.

The cross-section of the differential capacitance pressure sensor described in Dargie and Hughes (1994) is shown in Fig. 8.7.

It represents a successful application of traditional TFT methods and materials. The circular alumina diaphragm (250 μm thickness and 15 mm diameter) with electrodes on its upper and lower surfaces is sandwiched between two outer fixed plates forming top (T) and bottom (B) electrodes. The electrodes on the three plates together give rise to two capacitances C_T and C_B that, under applied pressure, vary in an opposite way in a push–pull operation. The outer electrodes are driven with anti-phase voltage signals so that the voltage between the inner electrodes and ground depends on the normalized capacitance difference $(C_T - C_B)/(C_T + C_B)$. This ensures good common-mode rejection of unwanted signals due to changes in temperature and dielectric constant, while it also improves linearity due to partial compensation between the nonlinearities of C_T and C_B. The measured sensitivity was 0.63 mV kPa^{-1} with a nonlinearity lower than 3% FS (full scale) over the pressure range 0 ÷ 207 kPa (0 ÷ 30 psi).

The co-design of a peculiar electrode shape and a tailored frequency–output electronic interface were described in Crescini *et al.* (1997) for a capacitive pressure sensor that exhibits a linearity error lower than 2% FS over an extended

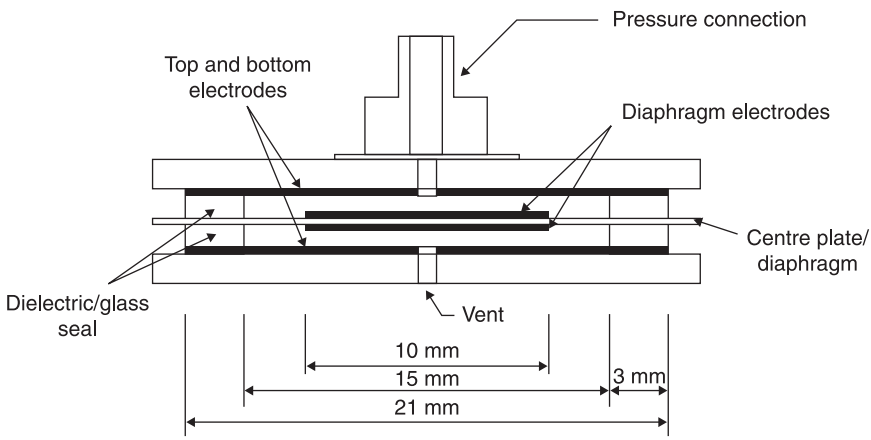

8.7 Cross-section of a thick-film capacitive differential pressure sensor after Dargie and Hughes (1994).

© Woodhead Publishing Limited, 2012

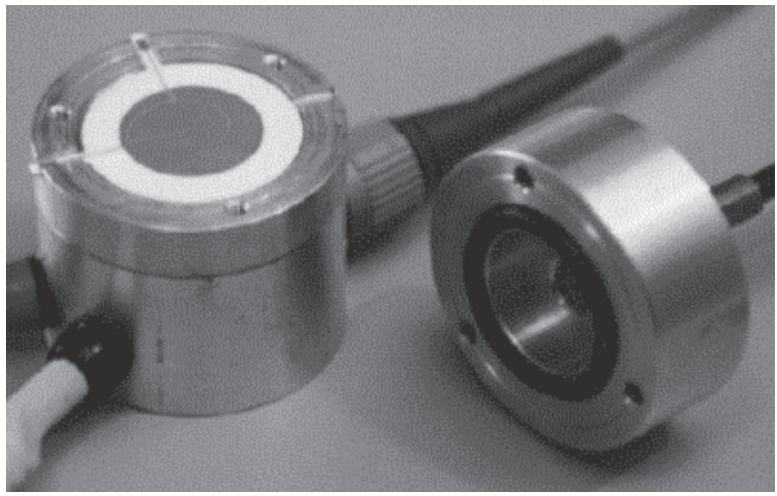

(a)

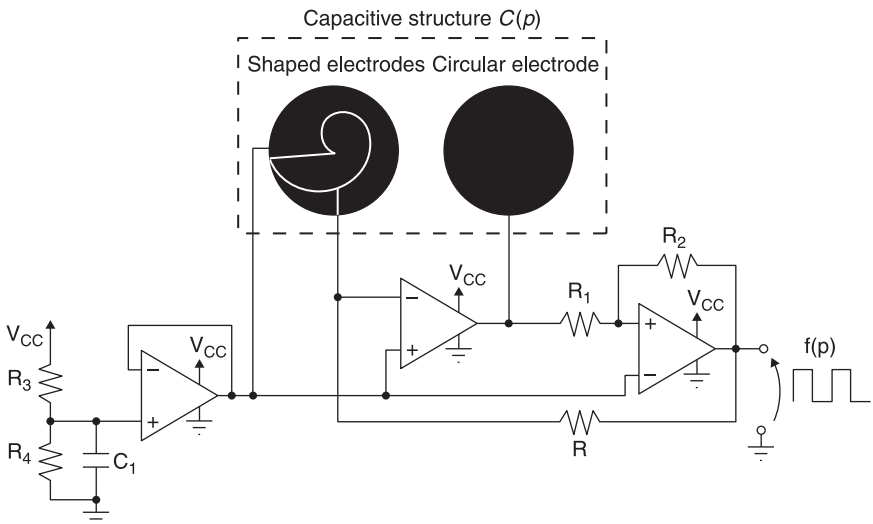

8.8 Capacitive pressure sensor with improved linearity after Crescini *et al.* (1997): (a) view of the sensor with shaped electrode; (b) signal conditioning electronic circuit for conversion from capacitance to frequency output.

pressure range (0 ÷ 600 kPa), with a sensitivity of 12 Hz kPa^{-1} and the output virtually independent of the power supply. As shown in Fig. 8.8(a), the sensor applies screen-printed electrodes on circular alumina plates, one of which is a fixed substrate, while the other is a 500 µm thick diaphragm that deflects under applied pressure p. While the substrate electrode is circular, the diaphragm

© Woodhead Publishing Limited, 2012

electrode has a specific spiral shaping that is surrounded by a guard electrode. As shown Fig. 8.8(b), the sensor is connected to an electronic circuit based on a relaxation oscillator which interfaces to the sensor capacitance C, drives the guard electrode and outputs a square-wave signal whose frequency f is proportional to $1/C(p)$. The combination of the electrode shaping and the capacitance to frequency conversion optimizes linearity of the overall pressure-to-frequency transduction function.

Capacitive pressure sensors in standard thick-film technology are manufactured, among others, by Endress+Hauser (www.endress.com) and Kavlico (www.kavlico.com). Endress+Hauser offers a gauge sensor that takes advantage of the three-electrode configuration illustrated in Fig. 8.4, as well as a differential pressure sensor, as shown in Fig. 8.9(a, b), respectively. Kavliko manufactures the capsule shown in Fig. 8.10, available either as a gauge or absolute pressure

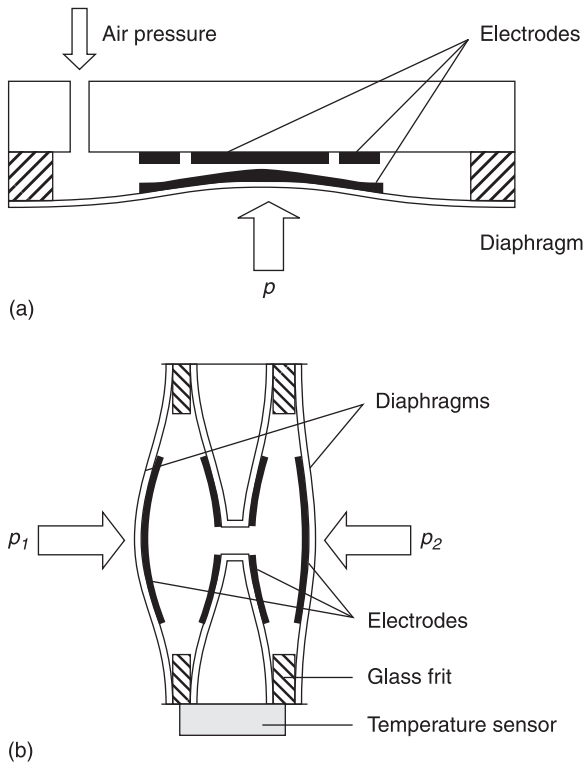

8.9 Schematic view of ceramic capacitive pressure sensors manufactured by Endress+Hauser: (a) gauge pressure sensor, model Cerabar PMC71, adapted from Endress+Hauser A; (b) differential pressure sensor, models Deltabar PMD70 and FMD76, adapted from Endress+Hauser B.

© Woodhead Publishing Limited, 2012

8.10 Ceramic capacitive pressure sensor manufactured by Kavlico, model PS312, adapted from Kavlico: (a) view of the arrangement where the hybrid electronic circuit is fitted behind the sensing diaphragm 33 mm in diameter; (b) picture of the sensor capsule.

sensor, with the hybrid signal-conditioning electronics fitted behind the diaphragm.

A capacitive pressure microsensor was recently described in Sippola and Ahn (2006). This device applies thick-film electrodes separated by a thin airgap created by a sacrificial layer process, resulting in a hybrid micro-fabrication technique. The

© Woodhead Publishing Limited, 2012

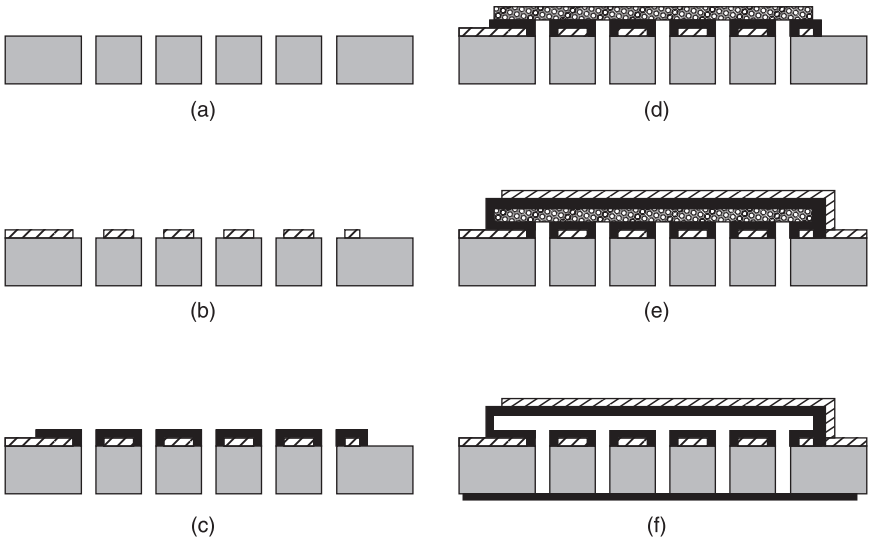

8.11 Ceramic capacitive pressure sensor after Sippola and Ahn (2006); the fabrication steps for achieving the cavity are: (a) laser drilling of vias; (b) screen-printing of bottom electrode; (c) screen-printing of bottom dielectric layer; (d) screen-printing of sacrificial layer; (e) screen-printing of top dielectric diaphragm and top electrode; (f) etching of sacrificial layer and screen-printing of backside sealing dielectric.

structure and fabrication steps of the sensor are shown in Fig. 8.11: a bottom gold electrode is printed on 96% alumina into which vias have been previously drilled by laser to create access to Au-based thick-film paste and permit chemical etchant penetration. The electrode is protected by a dielectric film over which the sacrificial layer made by a gold film is screen-printed. A top protection dielectric and electrode replicate the bottom structure. A backside-sealing layer completes the fabrication. Sacrificial layer thicknesses of 12 and 22 µm were used to create two different cavity airgap distances, resulting in the capacitance at zero gauge pressure of about 8 and 6 pF, respectively. The sensor was intended for high temperature and a harsh environment, and showed hermeticity up to 500 °C. In the characterization up to 300 °C in a pressure range of 0 to 345 kPa, the average sensitivity for the sensor with a 12 µm airgap was 1.3 fF kPa^{-1}. The temperature coefficient of capacitance (TCC) was 97 ppm $°C^{-1}$ over the temperature range of 25 to 300 °C.

Capacitive pressure sensors using thick-film and LTCC technologies have been reported in Belavič *et al.* (2008), Fonseca *et al.* (2002), Meijerink *et al.* (2005), Plumlee *et al.* (2002), Radosavljević *et al.* (2009) and Tamas *et al.* (2010).

Particularly relevant is the design described in Fonseca *et al.* (2002), which implemented concepts developed by English and Allen (1999) for a capacitive pressure sensor with wireless readout for high-temperature applications. The

© Woodhead Publishing Limited, 2012

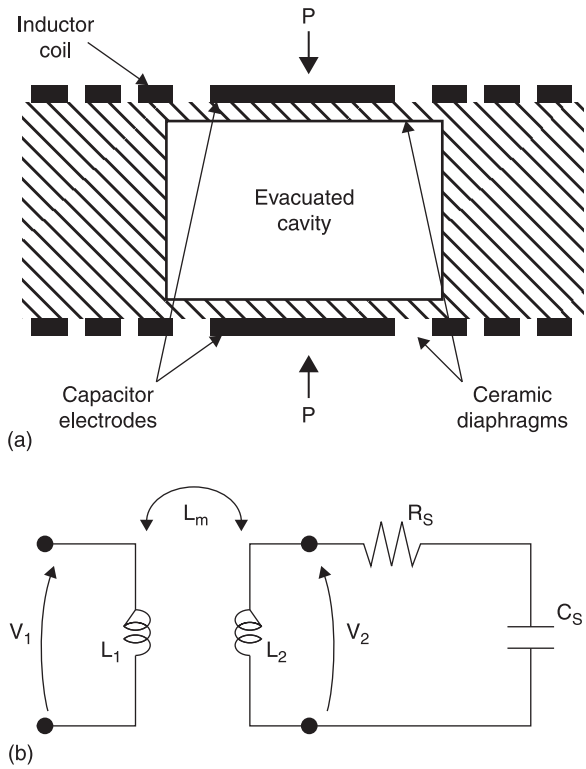

8.12 Capacitive absolute pressure sensor with contactless readout for high-temperature applications after Fonseca *et al.* (2002): (a) schematic view of the sensor structure with sensing capacitor and integrated inductor coil on ceramics; (b) equivalent circuit of the resulting *LC* resonator and external loop antenna for readout.

sensor consists in a sealed cavity; its top side supports a passive *LC* resonator comprised of a movable diaphragm capacitor and a fixed inductor, as shown in Fig. 8.12, thereby causing the sensor resonant frequency of around 18 MHz to be dependent on pressure. The sensor signal is read by an external loop antenna. The passive nature of the sensor removes the need for on-board electronics, power supply, or contacts to withstand high operating temperature up to 400 °C. In a pressure range from 0 to around 700 kPa the average sensitivity was 1.41 Hz kPa^{-1}.

A thick-film capacitive sensor as a part of a resonant circuit, excited by means of induction coupling across an air-gap, had been already successfully implemented by Turner (1989) for a contactless shaft torque sensor for automotive applications (Turner and Austin, 2000). The realization comprised two unusual technological features: the use of printing process on curved surfaces and application of dielectric and conductive inks curable at low temperature on steel. Either the

© Woodhead Publishing Limited, 2012

change in the resonance frequency of the circuit or the change in reflected impedance measured at the exciting coil could be taken as the response signal for the torque measurement.

Capacitive strain sensors based on TFT have been studied (Arshak, A. *et al.*, 2005; Arshak *et al.*, 2000) in both sandwich and planar configurations that are illustrated in Figs. 8.13(a) and 8.13(b), respectively. In the former case, two types of dielectric were used: lead zirconate titanate (PZT) and polyvinylidene fluoride (PVDF). PZT offers higher permittivity than PVDF. Sensors, tested in the range 0–350 $\mu\varepsilon$ over the frequency range 1–100 kHz, have shown that PZT-based capacitors provide higher gauge factor of 6 as compared to 3.5 for PVDF-based capacitors, but higher TCC of around 4000 ppm $°C^{-1}$ instead of 2500 ppm $°C^{-1}$ for PVDF at 25°C. Both strain sensors showed low values of dissipation factor but the gauge factor of the PZT-based sensor was frequency-dependent.

The comparison between planar sandwich and IDC configurations for strain

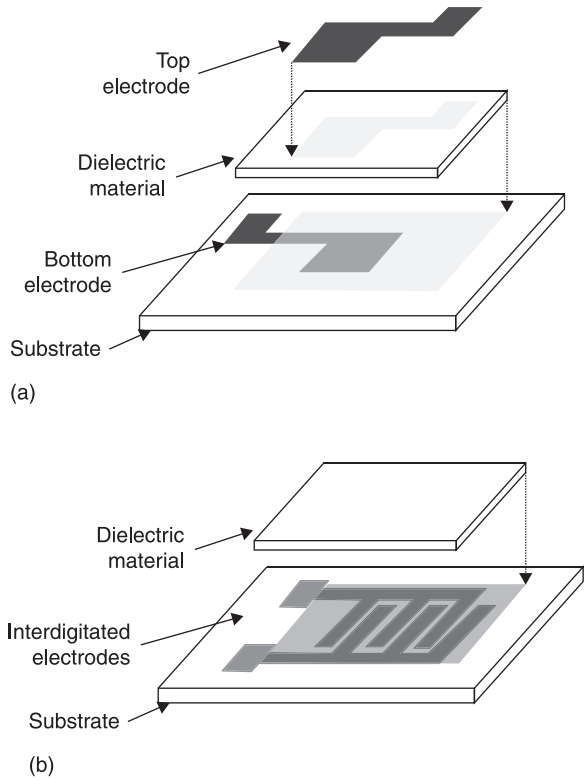

8.13 Configurations of capacitive strain sensors: (a) planar sandwich structure; (b) interdigitated structure.

© Woodhead Publishing Limited, 2012

sensors was reported in Arshak A., *et al.* (2005) on samples prepared with a blend of TiO_2 powder in a polymeric binder. The screen-printed capacitors were cured at 120 °C. Ag-based conducting electrodes and a glass substrate were the other parts of the sensors. They were tested under strains up to beyond 300 με. Gauge factors of 5 and 30 were recorded for interdigitated and sandwich capacitors, respectively. The higher sensitivity of the sandwich-type device was ascribed to the larger contribution of the geometrical factor. However, the sandwich sensor suffered from hysteresis and repeatability errors (7 and 18% FS, respectively) of about an order of magnitude higher than those of the IDT-type sensor. The formulated dielectric paste resulted in a TCC of about 1000 ppm/°C at room temperature for both the sandwich and IDT sensors, with a marked increase with increasing temperature.

Interdigitated capacitive strain gauges that can be integrated directly onto engineering components fabricated using *direct-write thermal spray* (DWTS) and intended for operation in harsh environments over an extended temperature range have been described by Li *et al.* (2007). Sensor elements were fabricated on polyethylene, etherester amide (EEA), graphite composite, fibreglass reinforced epoxy (FR4) composite, and alumina substrates. Gauge factors ranging from 0.9 to 20 have been measured, and the gauge factor was found to depend strongly on the underlying substrate material.

A proper selection of the dielectric material and the sensor design enabled the construction of a miniature frequency-output thick-film temperature sensor proposed in Leppävuori *et al.* (1983). The selected dielectric is a $SrTi0_3$-$BaTi0_3$ solid solution, whose composition determines the transition to paraelectric behaviour at $T_c = -47$ °C; therefore its permittivity is a linear decreasing function of temperature at $T > T_c$, according to the Curie–Weiss law. The sensor is a planar sandwich capacitor whose capacitance varied from about 1000 to 100 pF in the range from −30 to +80 °C, with a sensitivity of 1.3% $°C^{-1}$ at 25 °C, while the spread across the batch was as low as 0.02% $°C^{-1}$. When the sensor was coupled to a complementary metal-oxide-semiconductor (CMOS) oscillator, an output frequency was obtained linearly increasing with temperature from −25 to 85 °C, with a sensitivity of 20 Hz $°C^{-1}$ and a linearity error of 0.4 °C.

Capacitive IDT thick-film sensors for the measurement of humidity have been known for a long time. They were proposed for instance in Smetana and Wiedermann, (1987), where the permeation and adsorption of water in various dielectric thick-film compositions were studied, and even earlier in Lucas *et al.* (1976) for the measurement of moisture content in soil.

An interesting structure of thick-film capacitive relative humidity (RH) sensors is a hybrid between the sandwich and IDT configurations described in Qu and Meyer (1997). The idea is to compensate for the rather slow response of the highly sensitive sandwich humidity sensors with the much faster response of IDT sensors, which, however, are typically less sensitive. Fig. 8.14 shows the hybrid structure designed to implement this approach. A 40 μm porous $MnWO_4$ ceramic layer is sandwiched between two 10 μm polarity-reversed, IDT Pt films. A negative

© Woodhead Publishing Limited, 2012

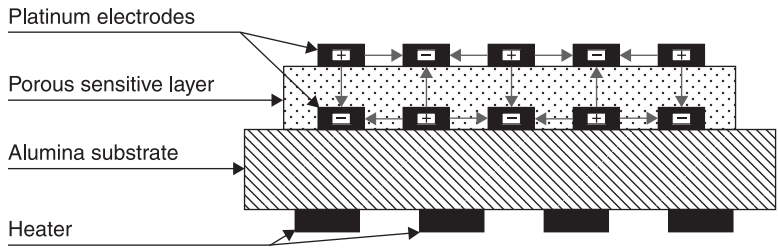

8.14 Structure of thick-film capacitive humidity sensor after Qu and Meyer (1997); the design is a hybrid between the sandwich and IDT configurations.

temperature cuefficient (NTC) thick-film sensor to compensate for thermal effects and a Pt refresh heater on the back-side of the alumina substrate complete the device. Variations of capacitance and resistance over three orders of magnitude were observed in the range from 25 to 95% RH with a response time of 10 s.

Innovative solutions under study include ink-jet-printed capacitive humidity sensor tags for passive RFID systems (Virtanen *et al.*, 2011) and screen-printed films using multiwall carbon nanotube and SiO_2 powders (Chen *et al.*, 2009).

Raindrops can be sensed by capacitive methods implemented in TFT. A capacitive rain sensor based on silver-based polymeric paste screen-printed on sodocalcic glass and cured at 120 °C was presented in Bord *et al.* (2006). There is no sensitive dielectric layer in the capacitor, therefore potential problems of reliability and stability due to dielectric poisoning and ageing are circumvented. The sensor is made of three protected coplanar electrodes that define a differential configuration with a sensitive element with capacitance C_1 affected by water, and a reference element with capacitance C_2. In dry conditions, $C_1 = C_2$, whereas an imbalance between C_1 and C_2 reveals the presence of water on the sensor; the sensor time response is negligible, making real-time monitoring achievable.

A commercially available ceramic capacitive rain sensor produced by Telecontrolli (www.telecontrolli.com) is shown in Fig. 8.15. The sensor has IDT electrodes on one side of the alumina substrate, while a refresh resistive heater and a temperature sensor are placed on the opposite side.

As an extension of capacitive sensing, discrimination among the various possible contributions (physi-sorption, chemi-sorption, condensation in pores, etc.) of dielectric media to the response of RH sensors can benefit from impedance spectroscopy, through the study of the complex impedance spectra collected in various environmental conditions. Examples of such studies have been reported for a sensor consisting in TiO_2-based ink spin-coated on top of IDT electrodes on alumina (Faia *et al.*, 2004) and a 20 nm grain-size ZrO_2-based ink screen-printed on gold IDT electrodes deposited on a silicon substrate (Wang *et al.*, 2009). Similar impedance-spectroscopy investigations are well known in the field of chemical gas sensors (Malagù *et al.*, 2005) and bio-sensors (Lucarelli *et al.*, 2005).

© Woodhead Publishing Limited, 2012

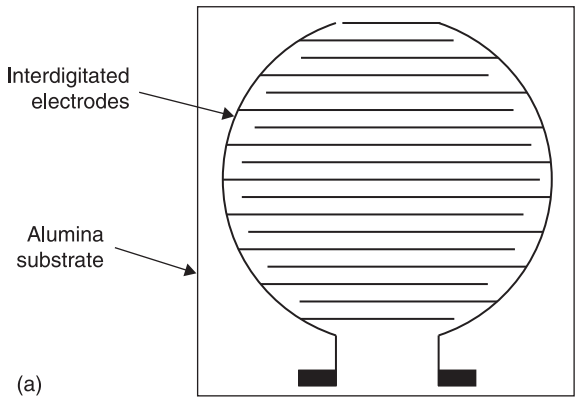

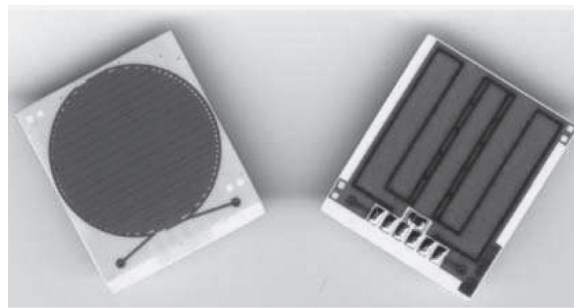

(b)

8.15 Ceramic capacitive rain sensor available from Telecontrolli, adapted from Telecontrolli: (a) schematic view of the interdigitated sensor structure on alumina substrate; (b) picture of the sensor seen from top and bottom faces.

Each of these application fields is a wide and diverse sector by itself (Galán-Vidal *et al.*, 1995) and will not be covered here.

A further wide field of hybridization of technologies on one side and capacitive sensors on the other side is represented by μTAS (micro total analysis systems) and LabOnChip systems for biochemical applications, one specific sector being that of microfluidics. Special emphasis is posed in developing efficient and cost-effective methods and technologies to provide microfluidic systems with embedded actuating and sensing capabilities. An important role in this scenario is played by TFT and LTCC (Golonka, 2006; Peterson *et al.*, 2005), due to their flexibility and typical feature sizes compatible with the required dimensions of microfluidic systems.

One example of these opportunities is the device described in Demori *et al.* (2011), which combines PDMS (polydimethylsiloxane) soft photolithography and screen-printing techniques. The device goal is to discriminate and characterize fluids in a microchannel on the basis of their dielectric permittivity. Fig. 8.16

© Woodhead Publishing Limited, 2012

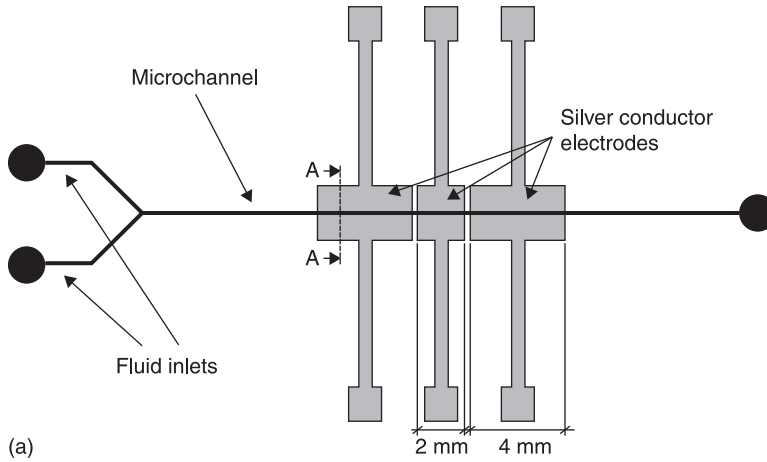

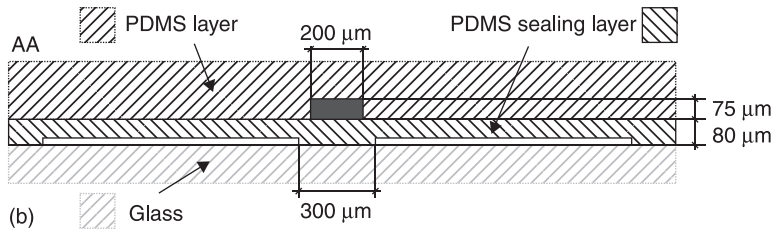

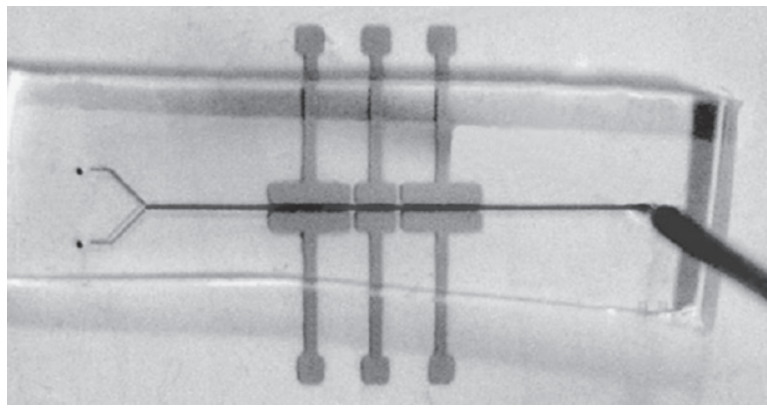

(c)

8.16 Screen-printed capacitive sensor embedded into a microfluidic device after Demori *et al.* (2011): (a) top view with microchannel and electrodes; (b) cross-section; (c) device picture where a liquid is visible in the microchannel.

© Woodhead Publishing Limited, 2012

shows the device structure formed by the microchannel with three pairs of electrodes screen-printed alongside from an Ag polymeric ink (DuPont 5000) and buried into the PDMS on a glass substrate. The microchannel is thus placed in the fringe field of the electrodes. The inner electrode pair work as a sensing capacitor while the two outer pairs act as guarding sections. The sensing capacitance is around 80 fF with a variation of few per cent between air and water in the microchannel. A tailored electronic interface system has been developed that drives the sensing and guard capacitors with a sinusoidal voltage signal and reads the sensor current with a synchronous detection technique to obtain bandwidth narrowing and improve the signal-to-noise ratio. A capacitance resolution of 0.06 fF is obtained over a bandwidth of 10 Hz. The sensor is able to distinguish clearly between continuous water flow and air–water segmented flow in the microchannel. In terms of capacitance, the air-filled and water-filled conditions differ by about 10 fF. The ability to reliably discriminate between various fluids with different permittivities has been demonstrated, as shown in Fig. 8.17.

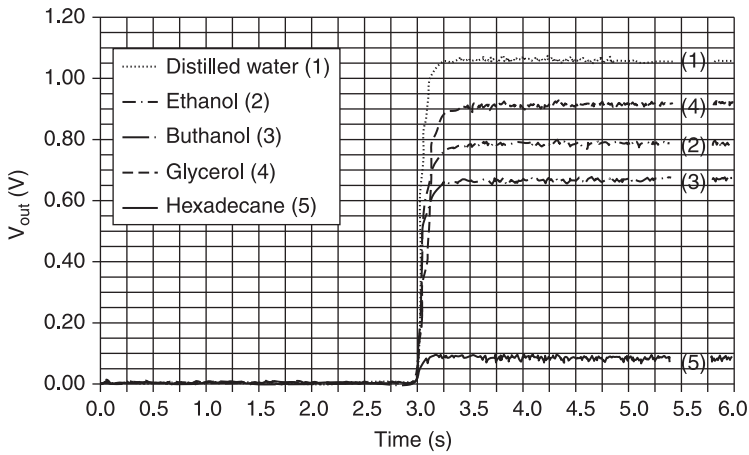

8.17 Measured output signal versus time of the capacitive sensor system of Fig. 8.16 due to step injections of fluids with different dielectric permittivity. The signal traces are superimposed in time for better comparison.

8.7 Conclusion and future trends

Capacitive sensors relying on geometrical variations can in general be considered mature devices, though continuing developments will most likely take place in new designs. For measuring mechanical quantities, capacitive sensors, together with piezoresistive sensors, are expected to remain among the prevalent technologies in the near future (AMA, 2010). Capacitive thick-film sensors will in

© Woodhead Publishing Limited, 2012

many cases evolve towards miniaturization through a convergence of different technologies like LTCC and microfabrication, such as in the devices described in Belavič *et al.* (2008), Meijerink *et al.* (2005) and Sippola and Ahn (2006).

Ceramic-based capacitive sensors will further develop their ability to operate in hostile environments, such as over extended temperature ranges. Improvements can be expected in coupling capacitive sensors with tailored electronic circuits, which are increasingly capable of ensuring high accuracy with small capacitance values and variations. This, combined with suitable signal processing techniques as allowed by new-generation processors, will result in increased performance and functionality, yet reduced power consumption.

Capacitive sensors relying on permittivity changes will most likely experience significant expansion. Especially for chemical sensing, they are expected to take advantage of material developments and processing technologies.

Capacitive sensors on plastic and flexible substrates are attracting increasing attention to reduce cost and develop, for instance, smart labels or multi-sensor devices for environmental monitoring such as in Oprea *et al.* (2009) and Courbat *et al.* (2009). Printed-film technologies, though not necessarily screen-printing, have the potential to play a significant role in this rapidly-evolving scenario.

Also based on the variable-permittivity principle are capacitive touch sensors. They represent a field where significant expansions are expected. Capacitive touch sensors are gradually replacing mechanical switches and buttons in a wealth of applications due to their superior aesthetics, flexibility and reliability. Capacitive sensors also enable sliders, trackpads and, thereof, advanced human–machine-interface components and functions. Additionally, capacitive sensors are used for proximity sensing where no contact is required between the sensor and the target, without line-of-sight constraints. This in turn opens other possibilities, such as fluid level measurement. Important markets exist, such as the consumer and automotive sectors, and dedicated integrated circuits are increasingly available from semiconductor manufacturers, which is contributing to the penetration of the capacitive technology (Arora and Verma, 2010). Here, there is room for research and development on printed-film capacitive sensors, which can offer flexibility in design, materials and configurations, and low cost even at medium production volumes.

8.8 Sources of further information

- *IEEE Instrumentation and Measurement Society (IMS)* Society dedicated to research concerning the theory, methodology and practice of measurement, and in the design, development and evaluation of instrumentation and associated measurement systems (http://www.ieee-ims.org).
- *IEEE Sensors Council* Council dedicated to research on the theory, design, fabrication, manufacturing and application of devices for sensing and

© Woodhead Publishing Limited, 2012

transducing physical, chemical, and biological phenomena, with emphasis on the electronics, physics and reliability aspects of sensors and integrated sensor-actuators (http://www.ieee-sensors.org).

- *International Microelectronics and Packaging Society (IMAPS)* Society dedicated to the advancement and growth of microelectronics and electronics packaging technologies through professional education (http://www.imaps.org/default.asp).

8.9 References

AMA (2010), *Sensor Trends 2014: Trends in Future-Oriented Sensor Technologies*, Association for Sensor Technology, Berlin, Germany. Available from: http://www.ama-sensorik.de

Arora P. and Verma M. (2010), 'Emerging trends in automotive capacitive touch-sensing', *Electronic Products*, November 2010. Available from: http://www2.electronicproducts.com

Arshak A., Arshak K., Morris D., Korostynska O. and Jafer E. (2005), 'Investigation of TiO_2 thick-film capacitors for use as strain gauge sensors', *Sensors and Actuators A*, 122, 242–249.

Arshak K. J., McDonagh D. and Durcan M. A. (2000), 'Development of new capacitive strain sensors based on thick-film polymer and cermet technologies', *Sensors and Actuators A*, 79, 102–114.

Arshak K., Jafer E. and Fox A. (2005), 'Design of a new thick-film capacitive pressure and circuitry interface', *Composites Science and Technology*, 65, 757–764.

Baxter L. (1996), *Capacitive Sensors: Design and Applications*, Wiley-IEEE Press, New York.

Belavič D., Zarnik M. S., Macek S., Jerlah M., Hrovat M. *et al.* (2008), 'Capacitive pressure sensors realized with LTCC technology', *International Spring Seminar on Electronics Technology, 2008. ISSE'08*, Budapest, May 7–11, 2008, pp. 269–272.

Bord I., Tardy P. and Menil F. (2006), 'Influence of the electrodes configuration on a differential capacitive rain sensor performances', *Sensors and Actuators B*, 114, 640–645.

Bronshtein I. N., Semendyayev K. A., Musiol G. and Muehlig H. (2007), *Handbook of Mathematics*, Springer-Verlag, Berlin Heidelberg.

Chen W. P., Zhao Z. G., Liu X. W., Zhang Z. X. and Suo C. G. (2009), 'A capacitive humidity sensor based on multi-wall carbon nanotubes (MWCNTs)', *Sensors*, 9, 7431–7444.

Courbat J., Briand D., Oprea A., Bârsan N., Weimar U. *et al.* (2009), 'Multi sensor platform on plastic foil for environmental monitoring', *Procedia Chemistry*, 1, 597–600.

Crescini D., Ferrari V., Marioli D. and Taroni A. (1997), 'A thick-film capacitive pressure sensor with improved linearity due to electrode shaping and frequency conversion', *Measurement Science and Technology*, 8, 71–77.

Dargie P. G. and Hughes S. T. (1994), 'A thick-film capacitive pressure transducer', *Measurement Science and Technology*, 5, 1216–1220.

Demori M., Ferrari V., Poesio P. and Strazza D. (2011), 'A microfluidic capacitance sensor for fluid discrimination and characterization', *Sensors and Actuators A*, 172, 212–219.

Eaton W. P. and Smith J. H. (1997), 'Micromachined pressure sensors: review and recent developments', *Smart Materials and Structures*, 6, 530–539.

© Woodhead Publishing Limited, 2012

Endres H. E. and Drost S. (1991), 'Optimization of the geometry of gas-sensitive interdigital capacitors', *Sensors and Actuators B*, 4, 95–98.

Endress+Hauser A, *Technical Information Cerabar S PMC71, PMP71, PMP75*, TI383PEN_0510.pdf. Available from: http://www.endress.com

Endress+Hauser B, *Technical Information Deltabar S PMD70/75, FMD76/77/78*, TI382PEN_0510.pdf. Available from: http://www.endress.com

English J. M. and Allen M. G. (1999), 'Wireless micromachined ceramic pressure sensors', *Proceedings of the 12th IEEE Microelectromechanical Systems Conference*, Orlando, Florida, USA, 17–21 January, pp. 511–516.

Faia P. M., Furtado C. S. and Ferreira A. R. (2004), 'Humidity sensing properties of a thick-film titania prepared by a slow spinning process', *Sensors and Actuators B*, 101, 183–190.

Fonseca M. A., English J. M., von Arx M. and Allen M. G. (2002), 'Wireless micromachined ceramic pressure sensor for high-temperature applications', *Journal of Microelectromechanical Systems*, 11, 337–343.

Galán-Vidal C. A., Muñoz J., Domínguez C. and Alegret S. (1995), 'Chemical sensors, biosensors and thick-film technology', *Trends in Analytical Chemistry*, 14, 225–231.

Golonka L. J. (2006), 'Technology and applications of low temperature cofired ceramic (LTCC) based sensors and microsystems', *Bulletin of the Polish Academy of Sciences: Technical Sciences*, 54, 224–231.

Gongora-Rubio M. R., Espinoza-Vallejos P., Sola-Laguna L. and Santiago-Avilés J. J. (2001), 'Overview of low temperature co-fired ceramics tape technology for meso-system technology (MsST)', *Sensors and Actuators A*, 89, 222–241.

Kang T. H., Merritt C., Karaguzel B., Wilson J., Franzon P. *et al*. (2006), 'Sensors on textile substrates for home-based healthcare monitoring', *Proceedings of the 1st Distributed Diagnosis and Home Healthcare (D2H2) Conference*, Arlington, Virginia, USA, 2–4 April.

Kavlico, *OEM Pressure Modules: Ceramic Capacitive – Gage and Absolute Pressures*, OEM_Sensor_Modules.pdf. Available from: http://www.kavlico.com

Kim Y., Kim H. and Yoo H. J. (2010), 'Electrical characterization of screen-printed circuits on the Fabric', *IEEE Transaction on Advanced Packaging*, 33, 196–205.

Leppävuori S., Niemela P., Piila T. and Uusimäki A. (1983), 'Miniature frequency-output temperature transmitter based on a ceramic capacitive sensor', *Sensors and Actuators*, 4, 573–580.

Li J., Longtin J. P., Tankiewicz S., Gouldstone A. and Sampath S. (2007), 'Interdigital capacitive strain gauges fabricated by direct-write thermal spray and ultrafast laser micromachining', *Sensors and Actuators A*, 133, 1–8.

Lucarelli F., Marrazza G. and Mascini M. (2005), 'Enzyme-based impedimetric detection of PCR products using oligonucleotide-modified screen-printed gold electrodes', *Biosensors and Bioelectronics*, 20, 2001–2009.

Lucas M. S. P., Stephens L. E., Dawess W. H. and Casey M. R. (1976), 'Thick-film sensors for agricultural applications', *Journal of Agricultural Engineering Research*, 21, 1–8.

Lucat C., Ginet P., Castille C., Debéda H. and Ménil F. (2008), 'Microsystems elements based on free-standing thick-films made with a new sacrificial layer process', *Microelectronics Reliability*, 48, 872–875.

Malagù C., Carotta M. C., Gherardi S., Guidi V., Vendemmiati B. *et al.* (2005), 'AC measurements and modeling of WO_3 thick-film gas sensors', *Sensors and Actuators B*, 108, 70–74.

© Woodhead Publishing Limited, 2012

Mamishev A. V., Sundara-Rajan K., Yang F., Du Y. and Zahn M. (2004), 'Interdigital Sensors and Transducers', *Proceedings of the IEEE*, 92, 808–845.

Meijerink M. G. H., Nieuwkoop E., Veninga E. P., Meuwissen M. H. H. and Tijdink M. W. W. J. (2005), 'Capacitive pressure sensor in post-processing on LTCC substrates', *Sensors and Actuators A*, 123–124, 234–239.

Oprea A., Courbat J., Bârsan N., Briand D., de Rooij N. F. *et al.* (2009), 'Temperature, humidity and gas sensors integrated on plastic foil for low power applications', *Sensors and Actuators B*, 140, 227–232.

Peterson K. A., Patel K. D., Ho C. K., Rohde S. B., Nordquist C. D. *et al*. (2005), 'Novel microsystem applications with new techniques in low-temperature co-fired ceramics', *International Journal of Applied Ceramic Technology*, 2, 345–363.

Plumlee D. G., Morales Y., Cheek B., Paris A. J., Ackler H. A. *et al*. (2002), 'Pressure sensors built in low temperature co-fired ceramic materials', *Proceedings of IMAPS Advanced Technology Workshop on Packaging of MEMS and Related Micro Integrated Nano Systems*, Denver, Colorado, USA, September 6–8.

Prudenziati M. (1994), *Thick-Film Sensors*, Elsevier, Amsterdam.

Puers R. (1993), 'Capacitive sensors: when and how to use them', *Sensors and Actuators A*, 37–38, 93–105.

Qu W. and Meyer J. U. (1997), 'A novel thick-film ceramic humidity sensor', *Sensors and Actuators B*, 40, I75–I82.

Radosavljević G. J., Živanov L. D., Smetana W., Marić A. M., Unger M. *et al.*, (2009), 'A wireless embedded resonant pressure sensor fabricated in the standard LTCC technology', *IEEE Sensors Journal*, 9, 12, 1956–1962.

Sippola C. B. and Ahn C. H. (2006), 'A thick-film screen-printed ceramic capacitive pressure microsensor for high temperature applications', *Journal of Micromechanics and Microengineering*, 16, 1086–1091.

Smetana W. and Wiedermann W. (1987), 'Using integrated capacitive humidity sensors in thick-film technology', *Sensors and Actuators*, 11, 329–337.

Tamas C., Marghescu C., Ionescu C. and Vasile A. (2010), 'Implementing a capacitive pressure sensor realized on LTCC', *Proceedings of SPIE*, p. 7821.

Taroni A. (1994) 'Capacitive sensors', *in* Prudenziati M. (ed.), *Thick-Film Sensors*, Elsevier, Amsterdam, pp. 245–258.

Telecontrolli, *Rain Sensor*, RAIN_SENSOR.pdf. Available from: http://www.telecontrolli.com

Turner J. D. (1989), 'The development of a thick-film non-contact shaft torque sensor for automotive applications', *Journal of Physics E: Scientific Instruments*, 22, 82–88.

Turner J. D. and Austin L. (2000), 'Sensors for automotive telematics', *Measurement Science and Technology*, 11, 58–79.

Virtanen J., Ukkonen L., Björninen T., Elsherbeni A. Z. and Sydänheimo L. (2011), 'Inkjet-printed humidity sensor for passive UHF RFID systems', *IEEE Transactions On Instrumentation and Measurement*, 60, 8, 2768–2777.

Wang J., Su M. Y., Qi J. Q. and Chang L. Q. (2009), 'Sensitivity and complex impedance of nanometer zirconia thick-film humidity sensors', *Sensors and Actuators B*, 139, 418–424.

White N. M. and Turner J. D. (1997), 'Thick-film sensors: past, present and future', *Measurement Science and Technology*, 8, 1–20.

© Woodhead Publishing Limited, 2012

9

Printed thick-film piezoelectric and pyroelectric sensors

V. FERRARI, University of Brescia, Italy

Abstract: The composition, structure and properties of piezoelectric and pyroelectric thick-films on ceramic and silicon substrates are surveyed. With particular focus on screen-printed films of ferroelectric ceramics in the family of lead zirconate titanate (PZT), applications in sensors and microsystems, actuators and energy harvesting are outlined and possible future trends delineated.

Key words: thick-film sensors, piezoelectric sensors, pyroelectric sensors, acoustic-wave sensors, resonant sensors, energy harvesting.

9.1 Introduction

The introduction of printed piezoelectric and pyroelectric films in the second half of the 1980s was an important step forward in the traditional thick-film technology (TFT), extending the choice of printable pastes beyond the most commonly available conductive, resistive and dielectric formulations used in hybrid microelectronic circuits. The times were ready for evaluation of the feasibility of new paste compositions for functional films that could replace more expensive crystalline materials, as well as polycrystalline ceramics less flexible to adapt in tailored shape and size.

The feasibility of screen-printed and fired piezoelectric thick-films based on the reported composition $Pb_{0.9875}[(Zr_{0.52}Ti_{0.48})_{0.975Nb0.025}]O_3$ was described in Fu *et al.* (1985), where the films were operated as acoustic transducers (buzzers). A similar application was apparently the motivation for the studies on $BaTiO_3$-based thick-films in Philips Lab. Eindhoven (Baudry, 1987), whereas in Morten *et al.* (1989) the interest in lead zirconate titanate (PZT) films started to be oriented to sensors. All of these studies were carried out on films printed on alumina, and showed the potential of piezoelectric thick-films for both actuators and sensors in terms of operating at lower voltages than bulk piezoelectric ceramics yet with satisfactory performances. Not less importantly, printed piezoelectric films advantageously offered flexibility in material composition and adequate miniaturization with patterning options for device layout, preserving mechanical robustness.

These promising characteristics soon determined an increasing interest for applications in micro-electromechanical systems (MEMS). In fact, printed films have thicknesses in the range from 10 to 100 μm, which offers the attractive perspective of producing microfabricated sensors, actuators and transducers without

© Woodhead Publishing Limited, 2012

resorting to the impractical, difficult and expensive processes of thinning, machining and bonding bulk piezo-ceramics. This led to investigations on piezoelectric printed films in MEMS made by micromachining silicon, hereafter denoted as Si-MEMS, mostly employing PZT-based thick-films (Dorey and Whatmore, 2004).

Despite the issues faced, the results prompted a great deal of research into making PZT films compatible with silicon technology and developing applications in several areas with an emphasis on sensors. The past two decades have yielded an understanding of the reasons why piezoelectric thick-films exhibit properties different from their ceramic counterparts, such as higher porosity and influence of clamping by the substrate. A better knowledge of procedures to obtain dense films and buffer layers as interdiffusion barriers has been achieved.

Significant research efforts have been also devoted to developing piezoelectric thick-films on MEMS made with low-temperature co-fired ceramic (LTCC) technology, hereafter denoted as C-MEMS, which appear promising in a wide range of applications such as microsensors, microfluidic systems and miniature reactors. The first examples of piezoelectric Si- and C-MEMS are recently moving towards commercial availability for selected applications such as accelerometers (InSensor) and pressure sensors (Zarnik *et al.*, 2009).

Thanks to the ferroelectric nature of PZT and the derived perovskites, PZT-based thick-films also exhibit pyroelectric properties which have been studied since the 1990s, for instance in Leppävuori *et al.* (1995) and Lucat *et al.* (1997), and applied in visible and infrared radiation sensors.

An emerging field of investigation of piezoelectric and pyroelectric elements is in energy harvesting, i.e. the conversion from mechanical and thermal energy sources to the electrical domain in order to supply power for instance to the sensor and microsystems, making them autonomous. PZT-based thick-films are attracting significant attention in this field, again for their favorable properties and achievable thickness range.

In this scenario, the present chapter describes the use of screen-printed thick-films to fabricate piezoelectric and pyroelectric devices. The chapter focuses on applications in sensors and microsystems. Material issues are treated only in those aspects, mostly related to technology, that are of interest to device designing. Processes for film deposition alternative to conventional screen printing, such as direct-writing techniques, are mentioned only briefly. Device and system issues in particular are covered, including transduction characteristics, modelling, impact on electronic signal readout, and examples of devices and their applications. Extensive reference to published literature is made, with the intention of providing a view on the state of the art in the field.

9.2 Piezoelectricity, pyroelectricity and ferroelectricity

Piezoelectricity, discovered in 1880 by the Curie brothers, is a property exhibited by a group of materials in which an imposed mechanical stress induces an electric

© Woodhead Publishing Limited, 2012

charge/polarization (direct effect), and vice versa, an applied electric field develops a mechanical strain/deformation (converse effect) (ANSI/IEEE, 1987; Ikeda, 1989).

Piezoelectricity is a linear and reversible effect, i.e. polarization is proportional to strain and when the former changes from negative to positive or vice versa, then the latter also changes sign – unlike electrostriction, which is present in all dielectrics to various degrees, where the induced strain is proportional to the electric field squared.

The piezoelectric effect is exploited in a variety of applications that can be broadly grouped as sonic and ultrasonic wave generation and detection, and electromechanical or mechanoelectrical conversion. The former category comprises sensors and transducers, filters and resonators. The latter includes actuators and motors, nebulizers, transformers, gas igniters, energy harvesting generators, and more.

Pyroelectricity, named in 1824 by Brewster but known as a phenomenon since before that date, is the response of polar materials that display a spontaneous electrical polarization as a function of temperature, which results in the appearance of surface charges proportional to a temperature change ΔT (Lang, 2005; Whatmore, 1986). The polarization is along a unique axis called the polar axis.

Pyroelectricity finds applications in thermal radiation detectors (Muralt, 2001), i.e. those in which the incident radiation is indirectly converted into an electric signal by detecting the temperature increase due to the radiation absorption, unlike photon detectors, i.e. semiconductor-based quantum devices, where the radiant energy is directly converted into the electrical domain through the photovoltaic or photoconductive effects.

Pyroelectric detectors generally have a wide spectral response and require no cooling to improve the signal-to-noise ratio. Applications of pyroelectrics are in occupancy detection systems, contactless temperature measurement (pyrometers), infra-red cameras and vidicons, gas analysers, laser power meters, to cite a few.

In the piezoelectric and pyroelectric effects, steady inputs, i.e. constant stress and temperature, respectively, determine static polarization states in which the induced charges do not last indefinitely but are eventually neutralized by losses due to finite material resistivity. Therefore, in practice, only dynamic stress and time-varying temperature can be detected. This is often expressed by saying that piezoelelctric and pyroelectric sensors are AC-responding devices.

The origin of piezoelectric and pyroelectric behaviours in inorganic materials lies in the nature of the chemical bonding and the associated degree of structural symmetry (Damjanovic, 1998; Newnham, 2005), according to Fig. 9.1.

Out of the 32 crystal classes (point groups) into which crystals can be classified, 11 are centrosymmetric, therefore they posses no polar properties and are not piezoelectric nor pyroelectric. The remaining 21 classes are noncentrosymmetric, i.e. they lack a centre of symmetry, and 20 of them have asymmetries that lead to piezoelectricity.

© Woodhead Publishing Limited, 2012

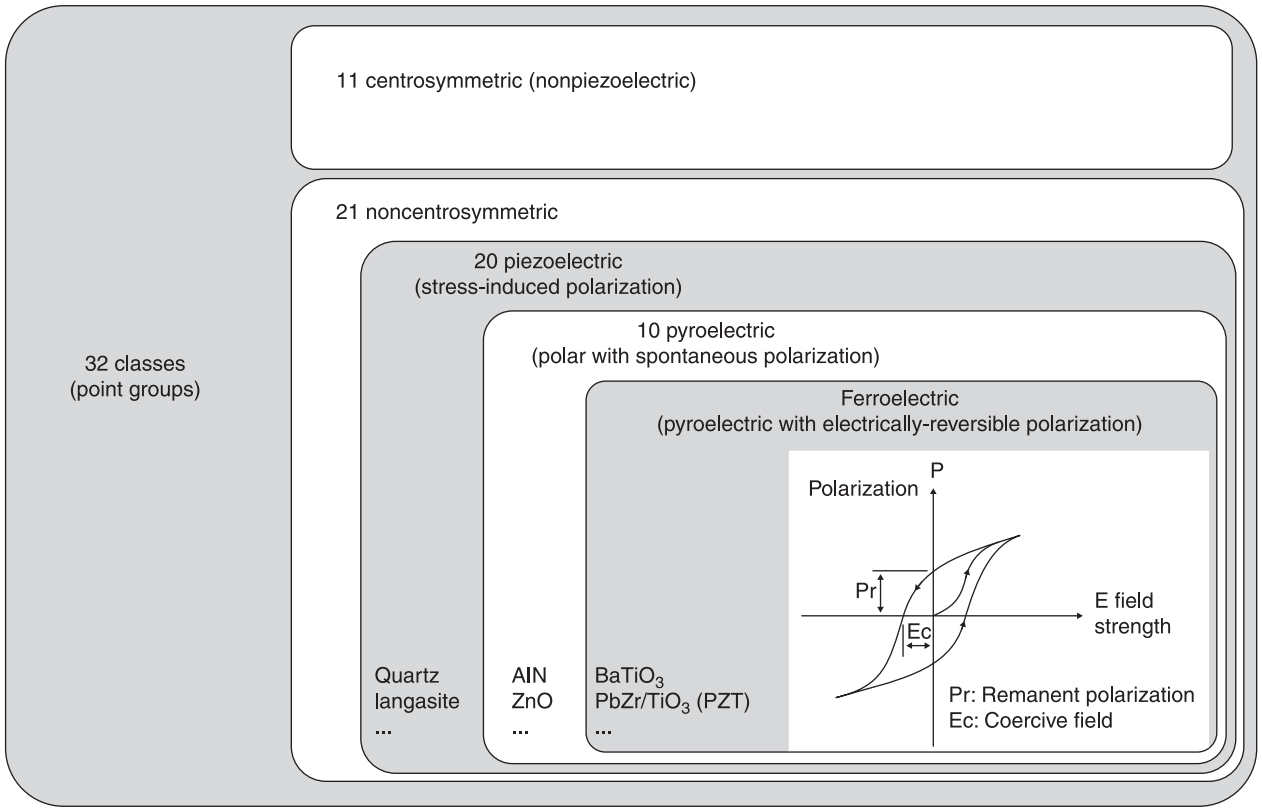

9.1 Crystallography point groups and material properties.

© Woodhead Publishing Limited, 2012

Out of 20 such classes, ten are spontaneously polarized, within a given temperature range, along a unique polar axis, therefore they are pyroelectric. Finally, a subclass of pyroelectrics in which polarization can be reoriented and reversed under an applied electric field is performed by the materials known as ferroelectrics. Ferroelectric materials generally exhibit strong piezoelectric and pyroelectric effects. Ferroelectrics can be either monocrystals, such as Rochelle salt or lithium niobate, or polycrystals, such as barium titanate or PZT ceramics (Haertling, 1999; Waanders, 1991).

In a ferroelectric material, spontaneous electric polarization depends on temperature and decreases upon heating. Above a certain temperature specific for the material, called the Curie temperature T_C, the polarization vanishes and a phase transition occurs from the ferroelectric state to the higher-symmetry paraelectric state.

In ferroelectrics, no matter if crystalline or polycrystalline such as PZT ceramics, the electrical dipoles are arranged in different regions, called domains, each with homogeneous polarization. In an untreated material the domains are randomly oriented thus they average out and produce a zero net polarization. Therefore, even below T_C, the presence of individual microscopic dipoles nevertheless results in the absence of significant macroscopic polarization.

To achieve a macroscopic polarization P, a process called poling is performed by applying an external electric field E, usually at a temperature higher than room temperature. Typically, the applied field is removed only when the material is again back at room temperature. The process is illustrated in Fig. 9.2.

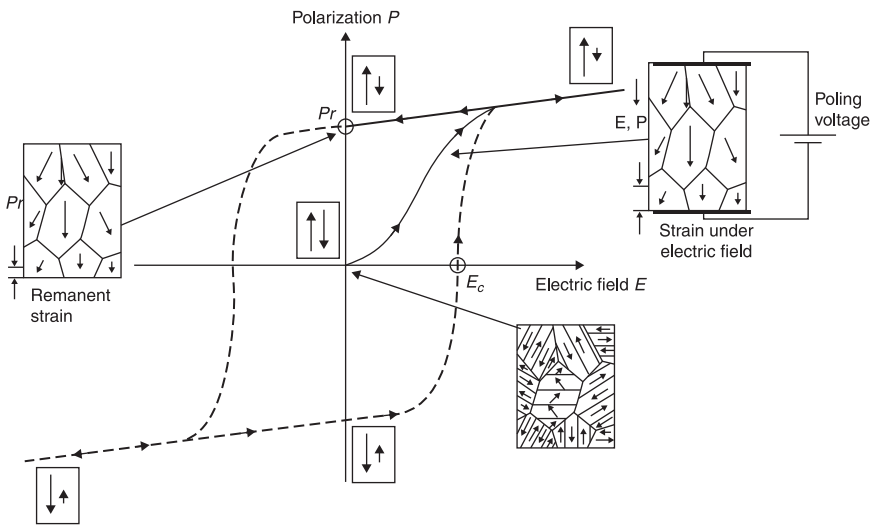

9.2 Poling of ferroelectrics and hysteresis loop.

© Woodhead Publishing Limited, 2012

Starting from $P = 0$, where randomly oriented domains prevail, the external field E promotes their alignment in the field direction with a corresponding increase in P which tends to a maximum. When the field is removed, the material retains a remanent polarization P_r along the poling axis and thereby exhibits both the piezoelectric and pyroelectric effects. Domain orientation brings about an associated strain during poling, a fraction of which stays as remanent strain after the poling field has been removed. Poled ferroelectrics must operate at a temperature well below their T_C, to contrast the tendency of structural transitions and thermal depoling.

If the applied field is changed in intensity and reversed at $T < T_C$, domain switching can occur. In this case, the E–P plot describes a hysteresis loop where P becomes a two-valued function of E in the range between $\pm E_c$, where E_c is defined the coercive field.

9.3 Basic theory and relationships of the piezoelectric effect

The interaction between the electrical and mechanical domains involved in piezoelectricity can be described by linear piezoelectric constitutive equations (Arnau, 2008; Ikeda, 1989).

There are different options for constitutive equations, depending on which of the electrical and mechanical quantities are chosen as the independent and dependent variables. In the monodimensional simplified hypothesis, the following four formulations are possible:

$$\begin{cases} S = s^E T + dE \\ D = dT + \varepsilon^T E \end{cases} \quad [9.1a]$$

$$\begin{cases} S = s^D T + gD \\ E = -gT + D/\varepsilon^T \end{cases} \quad [9.1b]$$

$$\begin{cases} T = c^E S - eE \\ D = eS + \varepsilon^S E \end{cases} \quad [9.1c]$$

$$\begin{cases} T = c^D S - hD \\ E = -hS + D/\varepsilon^S \end{cases} \quad [9.1d]$$

where S represents the strain [m/m], T the stress [N/m^2], D the dielectric displacement [C/m^2] that can be assimilated to polarization, E the electric field [V/m]. The coefficients s^x, $c^x = 1/s^x$, and ε^x are respectively the elastic compliance [m^2/N], elastic stiffness [N/m^2] and dielectric permittivity [F/m], each considered for a constant value of the variable x. The terms d, e, g and h are called the piezoelectric constants. The first and second equations in the four pairs in Eqs. [9.1] describe the converse and direct effects, respectively.

© Woodhead Publishing Limited, 2012

The piezoelectric constants, elastic stiffness and compliance, and dielectric permittivity are linked as:

$$\begin{aligned} d &= \varepsilon^T g = s^E e = [\mathrm{C/N}] = [\mathrm{m/V}], \\ e &= \varepsilon^S h = c^E d = [\mathrm{C/m}^2] = [\mathrm{N/mV}], \\ g &= d/\varepsilon^T = s^D h = [\mathrm{m}^2/\mathrm{C}] = [\mathrm{Vm/N}], \\ h &= e/\varepsilon^S = c^D g = [\mathrm{N/C}] = [\mathrm{V/m}], \\ \varepsilon^T &= \varepsilon^S + de \quad ; \quad c^D = c^E + he. \end{aligned} \qquad [9.2]$$

The energy transfer across the electrical and mechanical domains is expressed by the electromechanical coupling factor κ:

$$\kappa^2 = \frac{e^2}{c^D \varepsilon^S} = \frac{d^2}{s^E \varepsilon^T}. \qquad [9.3]$$

In the more general case of a tridimensional nonisotropic medium, the tensor notation becomes necessary for generalizing Eqs. [9.1] and to relate properties along different orientations of the material (Auld, 1973). The electric field and dielectric displacement are represented by three-dimensional vectors, while stress and strain, as second-rank symmetric tensors, can be represented by 3 × 3 matrices or six-dimensional vectors in the reduced-index Voigt notation.

The piezoelectric coefficients therefore become matrices where each entry has a pair of subscripts of which, in the conventional notation, the first one refers to the electrical direction (electric field or dielectric displacement) and the second one to the mechanical direction (stress or strain). For poled ferroelectrics, the axis 3 of a Cartesian reference frame is typically taken along the poling direction that usually is also parallel to the thickness of the sample or film. Therefore d_{33} describes the induced charge areal density on the surfaces of a film normal to the poling axis for unit stress applied along the same direction of poling. On the other hand, d_{31} describes the strain experienced by the film in a direction normal to the poling axis for unit electric field applied along the same poling direction.

For piezoelectric films the three-dimensional analysis is especially relevant in deriving the relationships between the material constants of the free element, e.g. an unclamped ceramic disk, and a film, thin or thick, adhering to a substrate. The difference between the two sets of constants is due to the clamping effect exercised by the substrate, which acts as a rigid base that affects the film behaviour both in the direct and converse piezoelectric effects (Damjanovic, 1998; Gwirc and Negreira, 2006; Lefki and Dormans, 1994; Muralt, 2008a; Torah *et al.*, 2004). For example, the effective piezoelectric coefficients d_{33eff} of a piezoelectric film on an isotropic substrate in the converse and direct effects, respectively, are related to the unconstrained coefficient d_{33} according to:

$$\left.\frac{S_3}{E_3}\right|_T \equiv d_{33eff} = d_{33} - 2d_{31}\frac{s_{13}^E}{s_{11}^E + s_{12}^E}, \qquad [9.4a]$$

© Woodhead Publishing Limited, 2012

$$\left.\frac{D_3}{T_3}\right|_E \equiv d_{33eff} = d_{33} - 2d_{31}\frac{v_{sub}/Y_{sub} + s_{13}^E}{s_{11}^E + s_{12}^E}, \qquad [9.4b]$$

where v_{sub} and Y_{sub} are the Poisson's ratio and Young's modulus of the substrate, respectively. Considering the signs of the coefficients, d_{33eff} results in both cases to be lower than the nominal d_{33} with reductions of 30 to 70%, which means that the films are significantly less piezoelectrically active than their free counterparts.

9.4 Thick-films based on ferroelectric inorganic compounds

Among the vast spectrum of interesting ferroelectric materials studied for their piezoelectric and pyroelectric properties (Heywang *et al.*, 2008; Muralt, 2008b), PZTs are used in the majority of applications in thick-film based sensors, actuators and microsystems.

PZTs are polycrystalline solid solutions of two perovskite oxides, whose general formula is ABO_3, namely lead zirconate ($PbZrO_3$) and lead titanate ($PbTiO_3$) in different relative amounts leading to $Pb(Zr_xTi_{1-x})O_3$, and they represent a family of materials with a Curie temperature T_C around 250–350°C, according to the Zr/Ti ratio (Ikeda, 1989). Above T_C the structure is cubic, therefore, due to the associated symmetry, polar behaviour is precluded. Below T_C the structure is asymmetric, either rhombohedral or tetragonal, hence the polar behaviour results. Attractive properties of PZT materials for sensing and actuating applications are the large piezoelectric and pyroelectric coefficients, high electromechanical coupling and the fairly high Curie temperature.

PZT powders are commercially available in various compositions with different grades and denominations, such as PZT-4, PZT-5, PZT-5H. Another commercial name of PZT is PXE, standing for piezoxide (Waanders, 1991). Small quantities of additives can be included to tailor the properties of the basic solution. A distinction is often made between 'soft' and 'hard' PZT compositions, which differ in the type of added dopants and the resulting macroscopic properties (Damjanovic, 1998).

Soft PZTs are characterized by high permittivity, high dielectric loss, large piezoelectric coefficients, high values of dielectric dissipation factors, and are easily poled but also more susceptible to depolarization. Hard PZTs have characteristics generally opposite to those of their soft counterparts, including low permittivity and dielectric losses, large mechanical quality factors, yet typically lower piezoelectric charge constants. They also are more difficult to polarize or depolarize.

PZT films can be advantageously deposited by screen printing as reported and reviewed in Baudry (1987), De Cicco *et al.* (1994a), V. Ferrari (2004), Fu *et al.* (1985) and Torah *et al.* (2007). Screen printing enables film thickness in the range from 10 to 100 μm using a sequence of a few printing/drying steps; on the contrary, less than 5 μm/layer is deposited with a typical sol-gel process. Such a comparatively high film thickness is often desirable for actuating and sensing

© Woodhead Publishing Limited, 2012

purposes. Also, the film deposition process is simple, cost-effective and capable of defining feature sizes normally in the range of few hundred microns.

In typical PZT screen-printable pastes a PZT powder with average grain size in the micron range is used as the functional part. A PbO powder is often added (5 to 20% wt); it supplies an overpressure of Pb (or PbO) which, during the firing process at temperatures higher than 850 °C, counteracts the Pb volatilization from the active grains, compensates for the Pb lost in interactions with the substrate and acts like a sintering aid. A glass frit, e.g. a lead borosilicate, can be used as a binder to promote adhesion. Binderless PZT thick-films have also been studied (Cotton *et al.*, 2007). As an organic vehicle to provide proper printability, a solution of in ethylcellulose terpineol leads to adequate rheology, but commercial thinners are used as well. Grinding of the powder mixture and wet ball-milling of the paste can be performed to improve homogeneity. The obtained PZT paste is then screen-printed on the substrate, which can be alumina (Al_2O_3), insulated metals, LTCC tapes or silicon.

For PZT layers in a planar sandwich configuration, the nature and composition of the bottom electrode, usually made by a thick-film conductor as well, may affect the properties of the overlaying layer, acting as a barrier to interactions between the film and the substrate. Lead diffusion from the PZT film into the substrate, either Si (Torah *et al.*, 2007) or LTCC tapes (Belavič *et al.*, 2009), may be a key issue in applications. The composition and deposition process for the top electrode on the fired films is much less critical. Screen-printed conductor layers or evaporated metal films are the most common solutions, while silver–polymer conductors have been used for characterizing the films and testing device prototypes.

After suitable drying and levelling steps, the printed layer is fired at a peak temperature in the range between 900 and 1000 °C for 20–30 min. Poling is then performed, typically under applied field of 2 to 5 MV/m at T ≥150 °C for about 30 min.

PZT thick-films differ from their bulk counterparts in density and grain size, as well as in elastic, dielectric and piezoelectric properties. For instance, the mass densities are about one-third lower while Young's modulus, dielectric permittivity and piezoelectric coefficients can be several tens of percents lower in thick-films derived by the same powder than the ceramic material (Lou-Moeller *et al.*, 2007). Such differences can be ascribed partially to the porosity of the films, found to span from 5 to even 60% according to the composition and process (Park *et al.*, 2010; Walter *et al.*, 2002), but the substrate clamping effect also plays an important role (Gwirc and Negreira, 2006).

To reduce the porosity and improve the overall characteristics of the films, a high isostatic pressure can be applied on the dried but yet unfired film (Hindrichsen *et al.*, 2010a; Lucat *et al.*, 1997; Yao and Zhu, 1998). In addition, sol infiltration of $Pb(Zr_{1-x}Ti_x)O_3$ can be used to reduce the porosity (Dauchy and Dorey, 2007; Park and Park, 2011).

Correlations among composition, processing, microstructural features and properties of PZT thick-films have been analysed in Torah *et al.*, (2005). Enhanced

© Woodhead Publishing Limited, 2012

performances in screen-printed films obtained from a paste prepared with a mixed powder of both nano- and micro-sized piezoelectric particles without sol infiltration have been reported in Kwon *et al.* (2007).

A comparison of the properties of PZT thick-films with those of the ceramic counterparts made with the same PZT powder is reported in Table 9.1, which confronts the values extracted from the data sheets for thick-films from InSensor (www.insensor.com) and PZ26 hard-type bulk ceramic from Ferroperm (www.ferroperm-piezo.com).

Currently, deviations from the 'standard' PZT thick-films described above are many. They include printed films on LTCC tapes for sensors and microsystems. The degradation of properties observed in films fired on LTCC, compared to the same compositions on Al_2O_3, are partially mitigated introducing proper interaction barriers (Belavič *et al.*, 2007, 2009; Hrovat *et al.*, 2003; Uršič *et al.*, 2008). Also films directly printed on metals have been studied, including steel (Fu *et al.*, 1985). In both cases, LTCC and metal, issues may arise from thermal expansion mismatch, a possible source of cracks (Dorey and Whatmore, 2004). Nevertheless, piezoelectric activity suitable for sensors and actuators has been obtained.

Attractive variants for the production of PZT thick-films were studied, such as the use of binders that allow for low-temperature curing (Clegg *et al.*, 1997; M. Ferrari *et al.*, 2010a) and piezoelectric paints that can lead to films for coatings on plastics and flexible substrates (Egusa and Iwasawa, 1994; Payo and Hale, 2010). However, currently the properties exhibited by such low-curing temperature PZT compositions are poorer than those of conventional thick-films with typical values of d_{33} ranging in the order of magnitude of one-tenth of that of the parent compound.

Table 9.1 Comparison between the properties of screen-printed PZT thick-films from paste TF2100 by InSensor, taken from 'InSensor', and bulk ceramic of the same powder composition used for the paste, namely PZ26 hard-type from Ferroperm, taken from Ferroperm".

Property	Symbol	Unit	Bulk ceramic	Thick-film
Relative dielectric constant at 1 kHz	$\varepsilon_{33}^T/\varepsilon_o$	–	1300	520
Dielectric dissipation factor at 1 kHz	$\tan\delta$	–	3×10^{-3}	8×10^{-3}
Piezoelectric charge coefficient	d_{33}	pC/N	328	200
Piezoelectric charge coefficient	d_{31}	pC/N	–128	–50
Curie temperature	T_C	°C	>330	
Mechanical quality factor	Q_m	–	>1000	100
Density	ρ	g/cm^3	7.7	5 (*)
Young's modulus	Y_{33}^D	GPa	95.6	70 (**)

Notes:
* Taken from Ferrari *et al.* (2001).
** Taken from Hindrichsen *et al.* (2010a).

© Woodhead Publishing Limited, 2012

A different matter is the deposition of piezoelectric films on silicon for MEMS. Screen printing has received significant attention despite the various issues encountered. Pb-Si interactions have been circumvented with adequate diffusion barriers to separate the silicon and lead-containing materials and to prevent the migration of atomic species with successful implementations in thin films and thick-films as well (Chen *et al.*, 1995; Dorey and Whatmore, 2004; Hindrichsen *et al.*, 2010a; Gebhardt *et al.*, 2007). Also, modified firing profiles have been studied to minimize the interactions and preserve film properties (Glynne-Jones *et al.*, 2000), while set-ups were developed to print on thin fragile silicon membranes (Chapter 10).

Nevertheless, current research is still ongoing to find deposition methods of thick PZT films on Si enabling improvements in performances and feature resolution at lower processing temperatures than thick-film technology. Investigations comprise aerosol (Wang *et al.*, 2008), sol-gel spinning plus sol infiltration and photoresist-assisted pattern etching (Corkovic *et al.*, 2007; Dauchy and Dorey, 2007; Frood *et al.*, 2007), electrophoretic deposition and direct-writing techniques (Dorey and Whatmore, 2004). An example of low-curing temperature PZT films deposited on silicon MEMS is shown in Fig. 9.3 (Baù *et al.*, 2011).

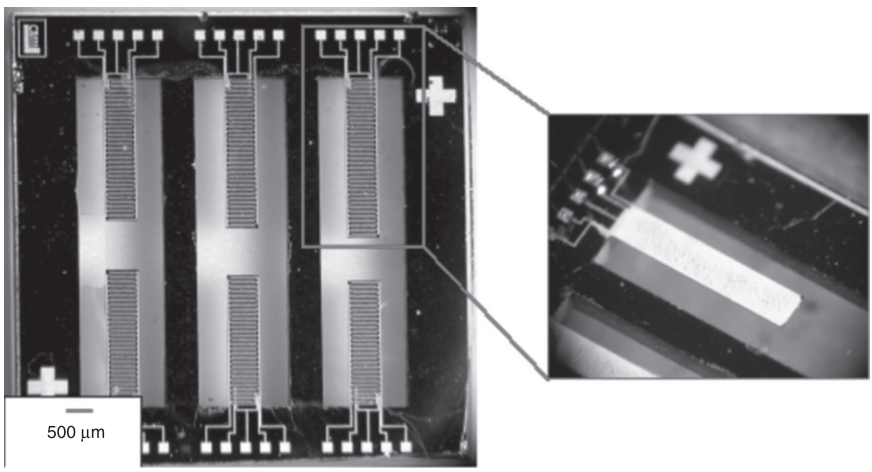

9.3 Example of low-curing temperature PZT films deposited by screen printing on a silicon MEMS cantilever after Baù *et al.* (2011).

9.5 Piezoelectric sensors

9.5.1 Modelling and configurations of piezoelectric transducers

If a piezoelectric prism of area A and thickness b is considered and harmonic regime at angular frequency ω is assumed, under the hypothesis that stress and strain do not depend on position along the thickness, the element behaves as

© Woodhead Publishing Limited, 2012

© Woodhead Publishing Limited, 2012

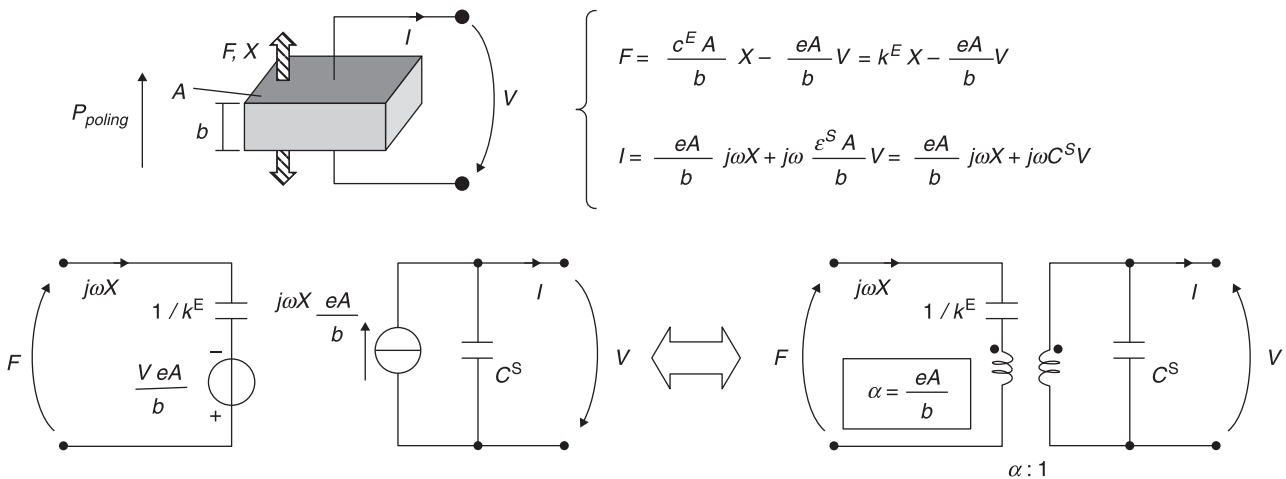

9.4 Equivalent circuit lumped-element model based on the electromechanical analogy at low frequency for a piezoelectric transducer under the mono-dimensional assumption.

mechanically concentrated. Under the mono-dimensional assumption, starting from Eq. [9.1c] and passing to the global variables tensile force F, outward displacement X, voltage V and current I, the equivalent electromechanical lumped-element model of Fig. 9.4 can be derived. The terms k^{E} and C^{S} represent mechanical stiffness at constant field and electrical capacitance at constant strain, respectively. This model is quasi static, being valid for frequencies lower than the first resonance of the piezoelectric element. Mechanical and electrical losses are not accounted for in the model. The circuits can be seen as the low-frequency limit of the Mason's model corresponding to the same force applied at the two faces of the transducer (Mason, 1948).

The ideal DC-responding transformer with turn ratio α:1 represents the linear coupling between the electrical and mechanical domains. The electromechanical coupling factor κ can be derived from the model by reflecting the impedances through the transformer ports, leading to the following expression consistent with Eq. [9.3]:

$$\kappa^2 = \frac{\alpha^2}{\alpha^2 + k^E C^S} = \frac{e^2}{c^D \varepsilon^S} = \frac{d^2}{s^E \varepsilon^T}. \qquad [9.5]$$

While the transformer ratio α depends on dimensions, the electromechanical coupling factor κ is only related to specific material properties. Typical nominal values of κ for PZT ceramics range between 0.3 and 0.7.

Different types of piezoelectric transducers can be obtained depending on the configurations in which piezoelectric elements are arranged. Fig. 9.5 summarizes four general cases.

Figure 9.5(a) shows the electromechanical (EM) conversion where the input signal is the electrical (E) stimulus to the piezoelectric element, and the output signal is the mechanical (M) response. In this configuration the piezoelectric element acts as an actuator. Examples of this type are micropositioners, motors, sonic or ultrasonic emitters.

Figure 9.5(b) represents the opposite case, where the input signal is the mechanical stimulus to the piezoelectric element and the output signal is the electrical response; this configuration gives a mechanoelectrical (ME) conversion and the piezoelectric transducer works as a sensor. Examples of this type are vibration pick-ups, sonic or ultrasonic receivers. When power, rather than current or voltage, is taken as the electrical output, the device is intended to perform mechanoelectrical energy conversion, such as in energy harvesting from mechanical vibrations.

Figure 9.5(c) represents a sensor configuration based on an EM–ME open loop conversion. An electrical stimulus to an input piezoelectric element generates a mechanical effect in a medium that is converted back into an electrical response by a second piezoelectric element. The input quantity, i.e. the one to be measured, modulates some property of the mechanical propagation path between the two piezoelectric elements, thus it is transduced into the output signal in the form of a

© Woodhead Publishing Limited, 2012

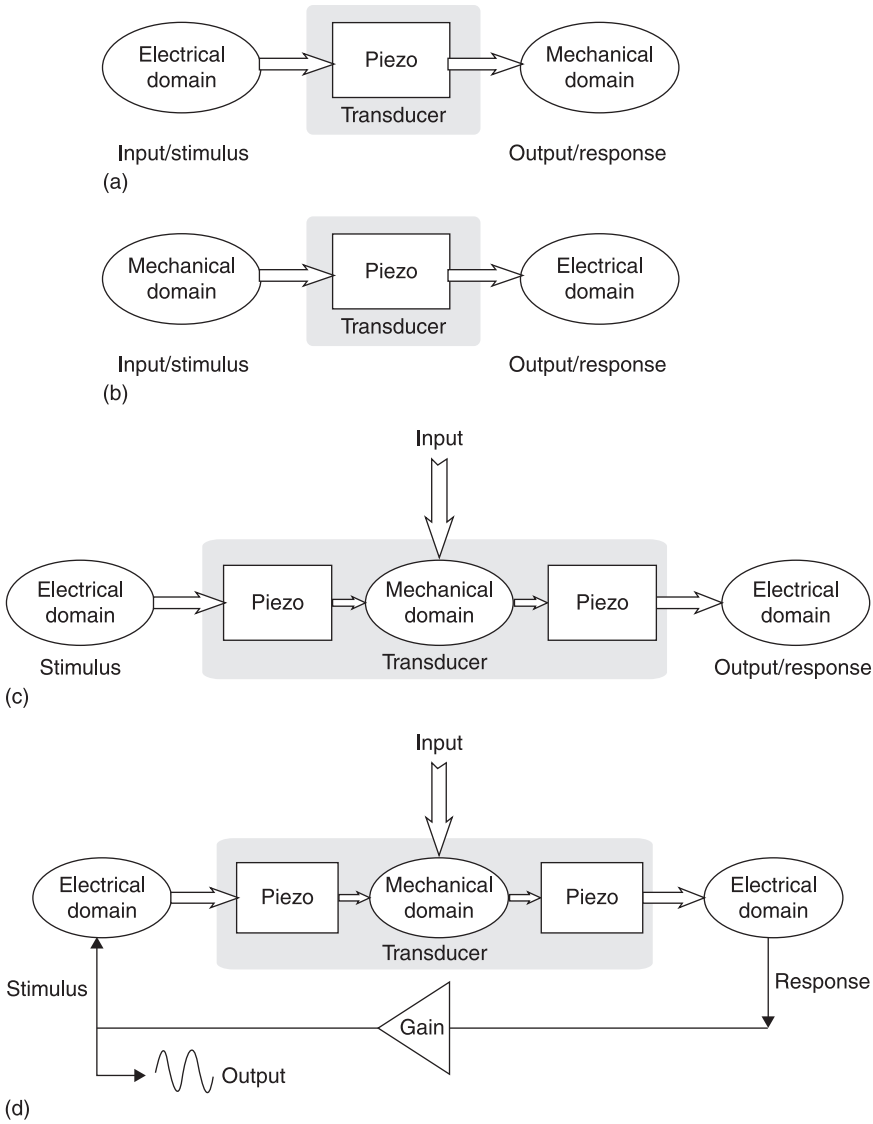

9.5 Configuration types of piezoelectric transducers: (a) electromechanical (EM) conversion; (b) mechanoelectrical (ME) conversion; (c) EM–ME conversion; (d) closed-loop EM–ME conversion.

perturbation of the electrical transfer function between stimulus and response. The mechanical propagation path can be external to the transducer or be an integral part of the transducer itself. In the latter case, the transducer sustains the propagation of mechanical elastic vibrations, i.e. acoustic waves, and the sensor can be referred to as an acoustic-wave (AW) sensor (Ballantine *et al.*, 1997). The

© Woodhead Publishing Limited, 2012

presence of two separate piezoelectric elements as input and output devices is not strictly required, since a single element can be used as well. In this case, the mechanoacoustic propagation path becomes the piezoelectric element itself.

Figure 9.5(d) extends the concept of acoustic-wave sensors by inserting the configuration of Fig. 9.5(c) as the feedback element of an amplifier, therefore creating an EM–ME closed-loop conversion. If proper gain conditions are satisfied, the system can be made resonating at one of the natural frequencies of the mechanoacoustic propagation path that, in turn, depends on the input measurand quantity. Therefore, the resonant frequency can be conveniently taken as the output signal. The resulting device is called an acoustic-wave resonant sensor (Benes *et al.*, 1995; Hauptmann, 1991). AW resonant sensors offer a number of potential advantages such as high sensitivity, determined only by the mechanical properties of used materials and a response virtually unaffected by piezoelectric coefficients and amplifier gain. Good stability, resolution and high noise immunity are additional benefits, since the signal information is conveyed in the time scale rather than in the analogue amplitude. The 'quasi digital' nature of the frequency output facilitates the direct interfacing of resonant sensors to digital systems. Piezoelectric AW and resonant microsensors are comprehensively discussed in V. Ferrari and Lucklum (2008) and references therein.

9.5.2 Examples of devices and applications

Since the earliest investigations on piezoelectric printed films for buzzers (Fu *et al.*, 1985), loudspeakers (Baudry, 1987) and developments thereof (Morten *et al.*, 1989), piezoelectric films have been attracting a significant research interest for innovative applications in sensors and microsystems (Muralt, 2008b; Tadigadapa and Mateti, 2009).

Even limiting our attention to screen-printed films, the scenario of the investigated techniques and proposed devices is increasingly wide and diverse, with a growing tendency to migrate form traditional TFT substrates, such as alumina and possibly metal, to include silicon MEMS. This often implies deposition techniques and dimensional scales that are different from those of conventional screen printing, which in turn produces a range of ongoing developments and opportunities toward hybrid microfabrication technologies. For this reason, it was chosen to group the following examples according to the operating principles and configurations, as discussed in section 9.5.1, rather than divide them into technology categories, which are continuously evolving and increasingly interrelated.

A first implementation of an accelerometer (Morten *et al.*, 1990) makes use of two piezoelectric films of 5 mm × 5 mm poled along the thickness, mounted back-to-back on the opposite sides of the seismic mass. Therefore the output results in a differential signal and the common-mode effects, such as temperature, are minimized. A flat frequency response between 0.5 and 500 Hz was observed, with a sensitivity of about 2.5 V/g for an acceleration range of ±4 g and a temperature

© Woodhead Publishing Limited, 2012

sensitivity of 3. 10^{-3} *g*/°C. The device proposed by Crescini *et al.* (2001) applies a similar structure. The sensor consists of two PZT layers, with a thickness of 40–50 μm each, screen-printed on the opposite sides of an alumina substrate and connected with opposite polarity to allow for thermal compensation. The sensor works without added seismic mass. A low-noise, large-bandwidth charge amplifier sets the low-frequency limit in the sub-hertz region. Experimental tests demonstrate a d_{33} coefficient of the PZT layers around 180 pC/N when poled at 3 MV/m, a sensitivity of the device of about 60 mV/*g* over the bandwidth 0.7 Hz–40 kHz, with a resolution of 0.025% of the full scale (FS).

The piezoelectric accelerometer described in Beeby *et al.* (2001) is one of the early examples of migration of PZT screen-printed sensors from alumina to micromachined silicon. It consists of a micromachined square seismic mass 2 mm × 2 mm suspended by four silicon 750 μm × 975 μm beams where PZT films are screen-printed. The sensor is equipped with a microprocessor circuit that provides self-validation by driving the piezoelectric elements and reading the resulting output.

Efforts to integrate screen-printed piezoelectric PZT thick-films with silicon technology have recently led to the micromachined high-bandwidth triaxial accelerometer described in Hindrichsen *et al.* (2010b). The microsensor has a square 1.2 mm × 1.2 mm seismic mass suspended on four 600 μm × 800 μm beams onto which 30 μm thick PZT films are screen-printed (Chapter 10). The tests demonstrate that voltage sensitivity is 0.31 mV/*g* in the vertical direction, 0.062 mV/*g* in the horizontal directions and the first mode resonance frequency is 11 kHz.

Pressure sensors based on PZT thick-films and their evolution are a significant example of the flexibility of the technology and the capability to transfer different transduction principles into devices. Static pressure cannot be measured with piezoelectric elements, unless they are arranged in resonant sensor configurations as discussed in the examples presented later on in this section. Instead, dynamic pressure, or shock pressure waves, can be directly detected.

An example is the dynamic pressure sensor described in Crescini *et al.* (2002), which was designed for pressure peaks up to 100 MPa. The sensor consists of a 2 mm thick alumina substrate onto which a screen-printed PZT layer, 3 mm in diameter, is sandwiched between Pt-Au printed electrodes and poled through the thickness. The performance characteristics include a sensitivity of 80–110 pC/MPa, a linearity better than 2% FS in the range between 25 and 60 MPa, and a response time lower than 10 μs.

The use of PZT thick-films in slip sensors for the feedback control of prosthetic hands is illustrated in Cranny *et al.* (2005). Each stainless-steel fingertip of the hand, configured as a cantilever, is equipped with a sensor made by a poled PZT layer, about 100 μm thick, sandwiched between two gold electrodes overlapping over an area of 8 mm × 8 mm. The results of tests run with small masses dropped onto the surface of an inclined fingertip and allowed to slide over the top electrode indicate the potential of the sensor to detect the moment of first contact between the hand and an object, as well as its ability to detect the onset of slip.

© Woodhead Publishing Limited, 2012

A field of topical interest where piezoelectric thick-films can be used as both sensors and actuators is in piezoelectric micromachined ultrasound transducers (pMUT). A typical requirement is to decrease dimensions of the single transducer to make compact arrays. At the same time, piezoelectric films of comparatively high thickness are necessary to generate and detect sufficient acoustic power. To this purpose, the combination of Si-MEMS technology with piezoelectric thick-films is attractive.

Arrays of pMUTs made by PZT films screen-printed on silicon are reported in Hirsch *et al.* (2005). As illustrated in Fig. 9.6, the configuration consists of a transducer matrix on top of a micromachined membrane. Since the PZT transducers were intended to operate as thickness-mode resonators instead of as actuators for the eigenfrequencies of the silicon membrane, they were designed so that there is no overlap between the resonance frequencies of PZT elements and membrane, respectively. A multi stage screen-printing process with firing at 950 °C allowed the creation of layers of PZT with a final thickness variable between 30 and 110 μm. In this latter case, a resonance peak at 4.9 MHz has been measured with a quality factor improvement over commercial bulk ceramics.

A two-dimensional pMUT array based on PZT films is described in Wang *et al.* (2006). The considered films range in thickness between 2 and 50 μm. It is recognised that they occupy a technological region between the processing capabilities of thin film and machining of bulk ceramics. To avoid the high firing temperature usually required for conventional thick-film pastes, a composite thick-film deposition technique is described. The process uses composite slurry consisting of a ceramic powder and an oxide ceramic producing sol. The composite slurry is then deposited using a spin coating process whereby the electroded substrate wafer is coated with the slurry spun at high speed to yield a thick-film. The final thermal treatment is at 600 °C, which is lower than the conventional firing temperatures.

In the field of piezoelectric acoustic-wave and resonant sensors, one early example in TFT is the pressure sensor reported in Morten *et al.* (1992), which, thanks to the resonant principle, allows the measurement of static pressure. The

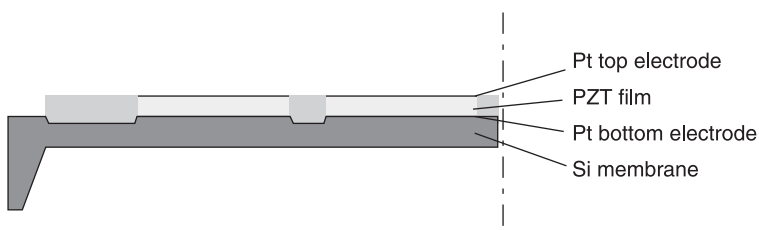

9.6 Cross-sectional diagram of piezoelectric micromachined ultrasound transducers (pMUT) made by PZT screen-printed on silicon membranes after Hirsch *et al.* (2005).

© Woodhead Publishing Limited, 2012

sensor has a two-port resonator configuration based on an alumina circular diaphragm where an annular interdigitated actuator and a central sandwich sensor made by screen-printed PZT films are deposited. The diaphragm is excited in flexural resonance at its third vibration mode by properly applying feedback across the driving and reading PZT elements by means of a phase-locked loop (PLL) electronic circuit forming a pressure-controlled oscillator. The differential pressure applied across the diaphragm deforms it and generates a radial tension. This in turn increases the diaphragm equivalent stiffness, therefore the resonant frequency rises and the sensor is thus able to measure static pressure. The reported sensitivity is around 150 Hz/mmHg at a frequency of 57.8 kHz.

A hydrostatic pressure resonant sensor based on a rectangular alumina beam excited in flexural resonance by two PZT thick-film elements is described in V. Ferrari (2004). The beam was mounted in a dual-in-line (DIL) package supported by the bonding wires in an approximately free-free condition that provided a marked resonance at the fifth flexural mode located at 198 kHz. The hydrostatic pressure of a surrounding gas results in the increase of the beam inertia and the resonant frequency decreases accordingly. A linear behaviour up to 4 bar has been measured, with a sensitivity of around –35 Hz/bar in air. This sensor configuration has an extended measuring range and a high overload capability since no deformable diaphragms are present that may fracture. On the other hand, the sensitivity depends on the particular gas.

An intense activity on the development and applications of PZT printed films has been carried out at Fraunhofer Institute of Ceramics in Dresden (Gebhardt *et al.* (2004). Here the development of many sensors has also comprised piezoelectric resonant pressure sensors realized in LTCC technology (Partsch *et al.*, 2003).

The Jožef Stefan Institute in Slovenia has also been very active in the development and applications of PZT thick-films. In particular, resonant pressure sensors with diaphragms less than 10 mm × 10 mm in size realized in LTCC technology for different pressure ranges in collaboration with HIPOT-RR are reported in Zarnik *et al.* (2009).

An early device relying on the acoustic-wave principle based on piezoelectric thick-films was described in White and Ko (1993). A plate-wave sensor structure was realized on a rectangular alumina substrate using two screen-printed PZT elements with interdigitated electrodes working as emitter and receiver, respectively, of acoustic waves along the substrate. The sensor is configured as a two-port delay line that, equipped with an electronic amplifier, behaves as an oscillator. A constant force applied in the centre of the substrate generates a strain, which in turn produces a decrease in the frequency. A frequency decrement of around 40 Hz for a load of 100 g was reported at a resonant frequency of 8 MHz.

Similarly, acoustic waves launched and detected by two pairs of PZT thick-films with interdigitated electrodes have been exploited to measure flow in a pipe as described in De Cicco *et al.* (1994b). The piezoelectric devices were realized on alumina substrates attached to the outside surface of a metal pipe where liquid flows. Flexural plate waves are generated by the PZT films through the substrates,

© Woodhead Publishing Limited, 2012

and guided into the pipe. The wave patterns propagate in opposite directions, while their velocities result to be affected by the liquid flow in the pipe. Two different flow-meter designs have been studied, operating in the megahertz region and below 100 kHz, respectively. Both designs were provided with an oscillator, which synchronously drives the two guides at the same frequency. The change in phase difference between the piezoelectric signals induced in the two receivers, due to the change of the flow velocity, is taken as the sensor output. A flow sensitivity in water of 17×10^{-2} deg/(mm/s) was measured for the second design over the range between 0 and 750 mm/s.

For the measurement of static force, Fig. 9.7 illustrates a PZT-on-steel resonant tuning fork sensor (Crescini *et al.*, 1996). On a steel beam, a dielectric insulation layer was screen-printed followed by three PZT thick-films with associate electrodes. The two elements at the beam-ends connected in parallel work as a

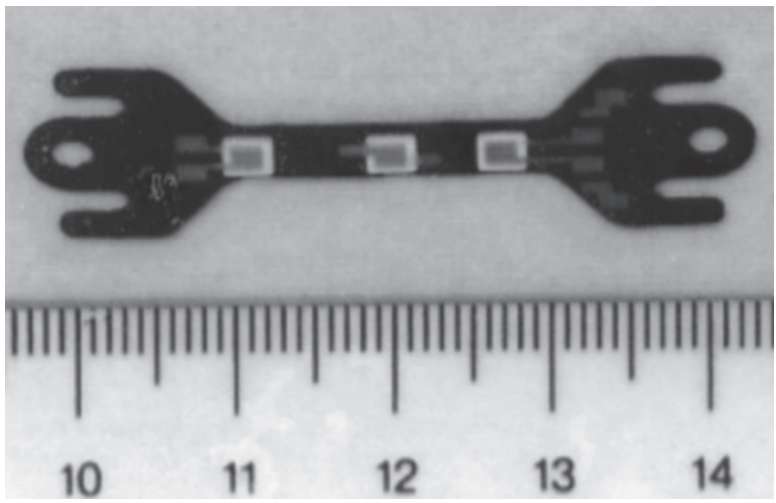

(a)

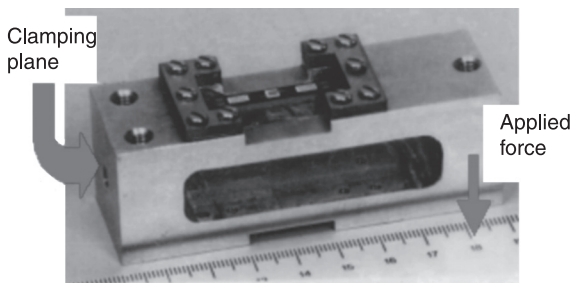

(b)

9.7 PZT-on-steel resonant tuning fork force sensor after Crescini *et al.* (1996): (a) picture of the fabricated sensor; (b) tuning fork sensor mounted on the supporting frame.

© Woodhead Publishing Limited, 2012

driver, and the central element as a sensor in a two-port configuration which, arranged in a feedback loop with an electronic amplifier, allows to excite the beam in flexural resonance. When the beam is clamped at both ends, an axial traction force increases the equivalent stiffness, therefore the resonant frequency rises. The relationship between frequency and applied force is linear for small forces. The beam was mounted on a clamped-free aluminium frame to transform an applied vertical force into beam strain. A sensitivity of 1.1 Hz/N at the resonant frequency of 35 kHz was measured, with a linear range reaching 800 N.

PZT thick-films allow the development of variable-mass AW sensors or, more generally, AW sensors responsive to an applied acoustic load (V. Ferrari and Lucklum, 2008). Variable-mass, also called gravimetric, AW sensors work as resonant microbalances. By functionalizing the surface with a sorption coating they can be used for chemical sensing.

PZT thick-films were first used for gravimetric sensing in diaphragm and cantilever resonator sensors with polymeric coatings for the detection of humidity in air (Morten *et al.*, 1993; V. Ferrari *et al.*, 1996). A significant increase in mass sensitivity was later obtained by using the PZT thick-film resonator itself as the microbalance, leading to a device named resonant piezo-layer (RPL) sensor (V. Ferrari *et al.*, 1997). As shown in Fig. 9.8(a), the structure of a thick-film RPL sensor is made by the superposition of a nonpiezoelectric substrate, specifically alumina, a bottom electrode layer, a PZT layer poled through its thickness and a top electrode layer. The PZT film is acoustically coupled to the substrate, leading to a thickness-expansion composite resonator, which can be used as a bulk acoustic wave sensor responsive to an acoustic surface load. Typical dimensions are 5 mm for the electrode diameter, and 250, 10 and 90 μm for the thickness of the substrate, electrodes and PZT, respectively. This results in a resonant frequency of around 7 MHz, while higher values can be achieved for thinner devices. A surface mass load on the top electrode determines a frequency decrement with a sensitivity higher than 500 Hz/μg at 7 MHz (V. Ferrari *et al.*, 2001).

A multisensor array of RPLs on the same substrate is shown in Fig. 9.8(b). The array also integrates a resistive heater driven in the constant-temperature mode, to minimize the thermal drift of the sensor resonant frequencies that can typically be as high as 500–1000 Hz/°C.

By the use of proper sorption coatings, the achieved mass sensitivity was suitable for gravimetric chemical sensing (M. Ferrari *et al.*, 2004; V. Ferrari *et al.*, 2000). To further increase the mass sensitivity, it is desirable to reduce the sensor dimensions. As a significant example, silicon microcantilever resonators based on PZT thick-films are described in Park *et al.* (2006). The thicknesses of the PZT and the silicon cantilever are approximately 22 μm and 12.3 μm, respectively. The reported estimated mass sensitivity for a 400 μm × 380 μm cantilever is nearly 32 kHz/μg at a resonant frequency of about 150 kHz.

A field of application of significant interest for piezoelectric materials is energy harvesting from mechanical sources, predominantly vibrations, to generate electrical

© Woodhead Publishing Limited, 2012

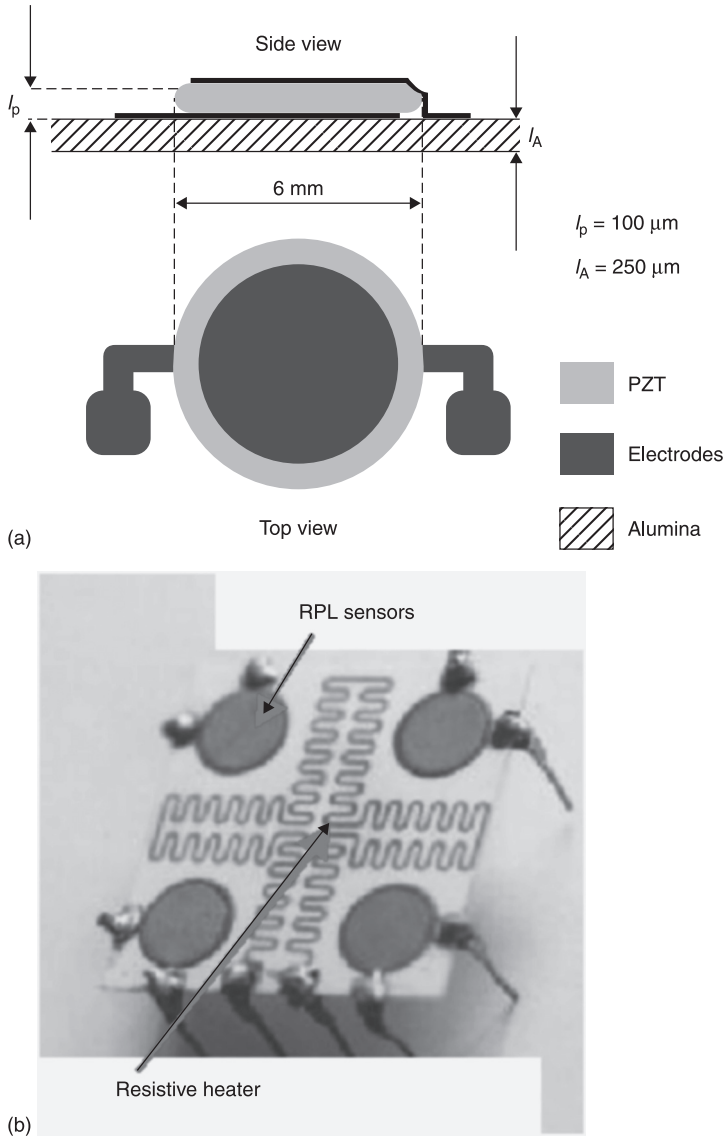

9.8 PZT-on-alumina resonant piezo-layer (RPL) sensor after V. Ferrari *et al.* (2000): (a) layout of the piezo-element; (b) array of four RPLs plus integrated resistive heaters.

supply for low-power sensor nodes (Kim *et al.*, 2009). In this context, thick-film devices could provide solutions at an intermediate dimensional scale, which is conveniently lower than bulk devices yet retaining a sufficient volume to collect enough mechanical energy, as opposed to fully miniaturized devices whose power

© Woodhead Publishing Limited, 2012

output inherently reduces due to decreasing size. A recent review of the potential of thick-films in the field of energy harvesting is given in Priya *et al.* (2009).

An energy harvester from vibrations based on PZT thick-films on metal substrate is reported in M. Ferrari *et al.* (2010b). Vibration harvesters typically are linear mass-spring-damper systems working at resonance. Therefore, they are narrow-band devices whose conversion effectiveness falls if the frequency varies across a comparatively wide range. A different approach is here proposed based on nonlinear converters that exploit stochastic resonance to extract energy from broadband excitation.

As shown in Fig. 9.9(a), the converter consists of a piezoelectric film on an elastic beam coupled to permanent magnets to create a bistable system. Under proper conditions, the system bounces between two stable states in response to random excitation, which significantly improves energy harvesting from

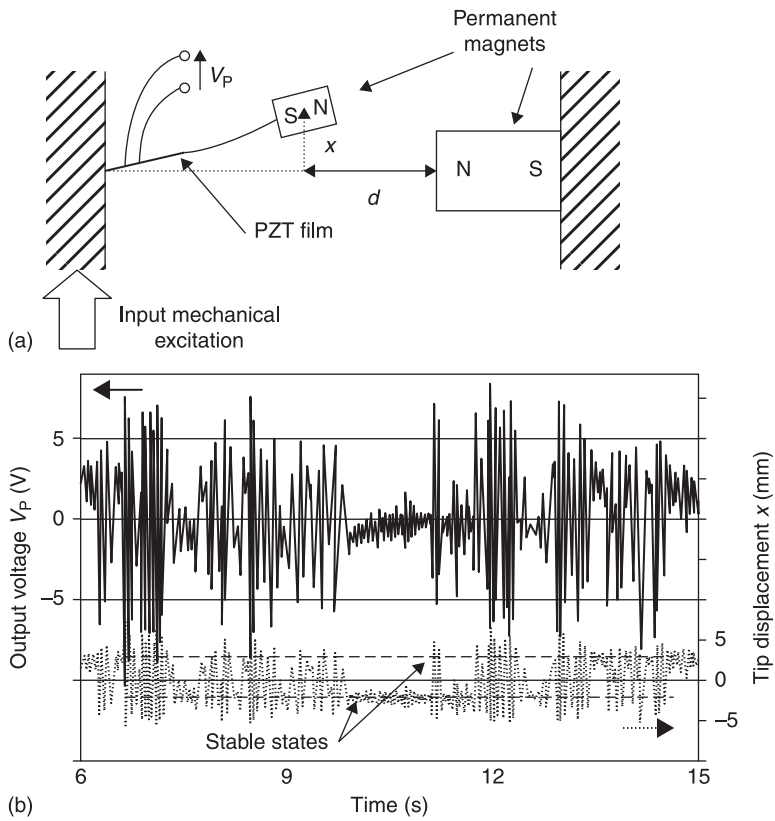

9.9 Nonlinear energy harvesting system formed by a piezoelectric cantilever beam and two permanent magnets after M. Ferrari *et al.* (2010b): (a) schematic diagram of the energy harvester; (b) harvester vibration displacement and output signal showing that when distance *d* is low enough, the cantilever bounces between two stable states.

© Woodhead Publishing Limited, 2012

wide-spectrum vibrations. Nonlinear converters were realized by screen-printing low-curing-temperature PZT films on steel cantilevers equipped with magnets. Experimental tests were performed by measuring both the beam deflection and the output voltage under excitation by random vibrations at varying degrees of nonlinearity added to the system. Typical plots of the beam displacement and corresponding output voltage are shown in Fig. 9.9(b). The obtained results demonstrate an increase of up to 88% in the rms output voltage at parity of mechanical excitation when the system is made bistable.

The same principle can be implemented in a simplified single-magnet configuration that exploits the ferromagnetic properties of the elastic beam over which PZT thick-films are screen-printed (M. Ferrari *et al.*, 2011).

9.6 Pyroelectric sensors

9.6.1 Basic theory and relationships of the pyroelectric effect

Pyroelectricity implies that the polarization P of a material is a function of temperature T. To avoid possible confusion with stress, in the present section temperature will be indicated with the symbol Θ.

In polar materials, P includes a spontaneous polarization P_S in addition to the field-induced polarization $P(E)$. In the scalar notation, the dielectric displacement D is therefore:

$$D = \varepsilon_0 E + P(E) + P_S = P_S + \varepsilon E. \qquad [9.6]$$

Assuming constant E, the derivative of D with respect to temperature Θ is:

$$\frac{\partial D}{\partial \Theta} = \frac{\partial P_S}{\partial \Theta} + E\frac{\partial \varepsilon}{\partial \Theta} = p + E\frac{\partial \varepsilon}{\partial \Theta} = p_G. \qquad [9.7]$$

The quantity p_G is called the generalized pyroelectric coefficient of the material (Damjanovic, 1998). It can be observed that p_G is made by two contributions: the first one, $p = \partial P_S/\partial\Theta$, is the so-called true pyroelectric coefficient, while the second contribution represents the induced pyroelectric effect. Sensors exploiting the induced pyroelectric effect are said to operate in the dielectric bolometer mode. They do not require poling and are not limited to work below the Curie temperature of the material, but need an applied electric field (Muralt, 2001).

The pyroelectric coefficients are affected by the mechanical boundary conditions, i.e. whether the material is considered in clamped (constant strain S) or free (constant stress T) conditions (Liu and Long, 1978). Under constant strain, the so-called primary pyroelectric effect occurs. When the material is free to undergo thermal expansion, i.e. at constant stress, an additional contribution results from the piezoelectrically induced charge. This second phenomenon is sometimes called the secondary pyroelectric effect (Muralt, 2001).

© Woodhead Publishing Limited, 2012

The expressions of p_G in the two cases can be derived by coupling Eq. [9.6] with the corresponding piezoelectric equations under either constant T or S, i.e. Eq. [9.1a] or Eq. [9. 1c], respectively. This results in:

$$p_G^T = p_G^S + \alpha e, \qquad [9.8]$$

where α is the linear coefficient of thermal expansion and e is the piezoelectric constant. In the case of films on a substrate, the partially-clamped boundary conditions and the given materials determine the effective value of e, and thereof the relative importance of the primary and secondary pyroelectric effects (Damjanovic, 1998; Muralt, 2001).

Limiting our attention to the true pyroelectric effect expressed by the coefficient p, if electrodes are placed normal to P in a material where temperature Θ is assumed to be uniform and they are wired in a circuit, a time variation of Θ induces a current I_p in the circuit, as shown in Fig. 9.10(a).

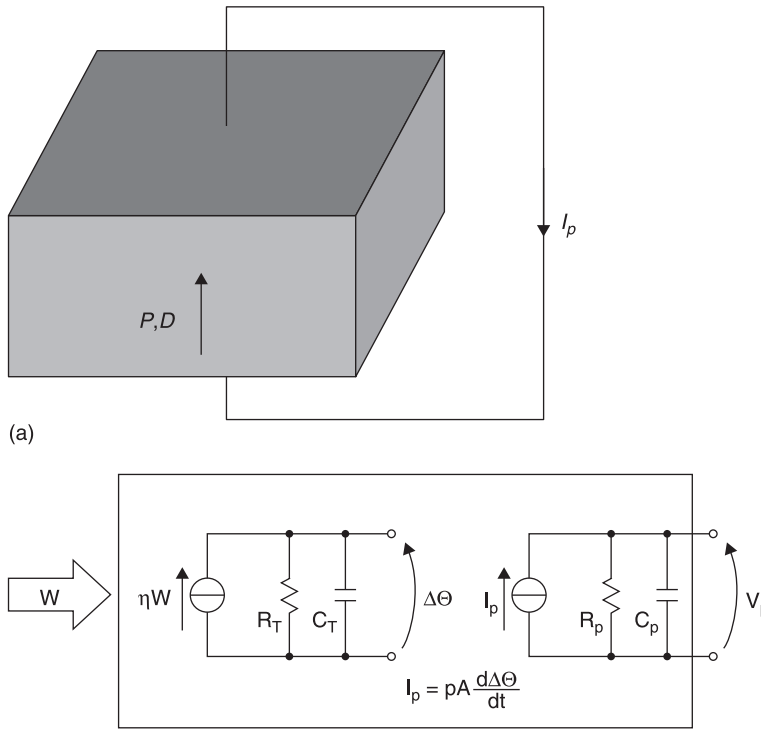

9.10 Pyroelectric sensor element: (a) simplified representation under short-circuit conditions; (b) electrothermal equivalent model under open-circuit conditions.

© Woodhead Publishing Limited, 2012

The electrical output can be related to the radiant energy input by means of the thermoelectrical equivalent model of Fig. 9.10(b), where R_T, R_P and C_T, C_P represent the thermal and electrical resistances and capacitances, respectively. Assuming an incoming radiant power W harmonic at the angular frequency ω, the voltage and current responsivities are respectively defined as (Whatmore, 1986):

$$R_v(\omega) = \frac{V_p(\omega)}{W(\omega)}, \qquad [9.9a]$$

$$R_I(\omega) = \frac{I_p(\omega)}{W(\omega)}. \qquad [9.9b]$$

The dynamic properties of a pyroelectric sensor can be analysed by considering the frequency responses of voltage and current responsivities, and including the effect of the input preamplifier. To first order, a thermal and an electrical corner frequencies are present, respectively given by $\omega_T = 1/R_T C_T$ and $\omega_E = 1/R_P C_P$. The relative positions of ω_T and ω_E depend on the material and geometrical parameters. For bulk materials generally $\omega_E > \omega_T$, whereas the opposite holds for thin films. The use of a transimpedance amplifier, due to its virtually zero input impedance, allows the tailoring of the electrical time constant by means of the external feedback components R_F and C_F, irrespective of R_P and C_P.

The simplified model of Fig. 9.10 becomes inadequate when the sensor has a multilayered structure and, therefore, the thermal profile along the thickness across the different materials is increasingly important (Samoilov and Yoon, 1998).

9.6.2 Examples of devices and applications

The reported pyroelectric coefficient p for PZT thick-films is typically between 1.2 and $1.5\times10^{-4}\,Cm^{-2}K^{-1}$, depending on paste composition and poling parameters, while it is around $3.8\times10^{-4}\,Cm^{-2}K^{-1}$ for PZT ceramics (Baudry and Delmas, 1991; De Cicco *et al.*, 1999).

Densification promoted by the application of isostatic pressure before firing has been proposed to increase p (Lucat *et al.*, 1997). Even though the pyroelectric coefficient of thick-films is low, their reduced dielectric permittivity favourably determines a voltage responsivity that can be similar or higher than for bulk ceramics.

Pyroelectric sensors using PZT or modified-PZT screen-printed thick-films have been reported as single-element detectors (De Cicco *et al.*, 1999; Leppävuori *et al.*, 1995; Lozinski *et al.*, 1997), as well as in multisensor arrays (Baudry and Delmas, 1991; Lozinski *et al.*, 1998).

In early works, measurements have been carried out mainly with relatively high-power light sources, such as lamps and lasers. For example, thick-films of lead lanthanum zirconate titanate (PLZT) were used to fabricate a linear array that was tested under a flash lamp excitation (Lozinski *et al.*, 1998). A pyroelectric detector

© Woodhead Publishing Limited, 2012

made by a PZT thick-film with buried electrodes was tested in response to an infrared (IR) chopped source with a peak power of 5.5 mW (De Cicco *et al.*, 1999).

Multi-element thick-film pyroelectric sensors were also proposed for wide spectral range radiation detection (from IR to ultraviolet (UV)), and laser beam alignment and profiling. An array of 3×3 pixels (Capineri *et al.*, 1998) and a four-quadrant detector (Capineri *et al.*, 2004) made by PZT thick-films on alumina intended for laser spot localization have been developed. The latter device is shown in Fig. 9.11 where the separation of the four quadrants obtained by sawing is visible.

More recently, it has been demonstrated that the pyroelectric signals from PZT thick-films can be detected even under excitation by low-power light sources, such as a light-emitting diode (LED) in the visible. If the LED is driven in amplitude modulation and the corresponding pyroelectric current is detected by synchronous

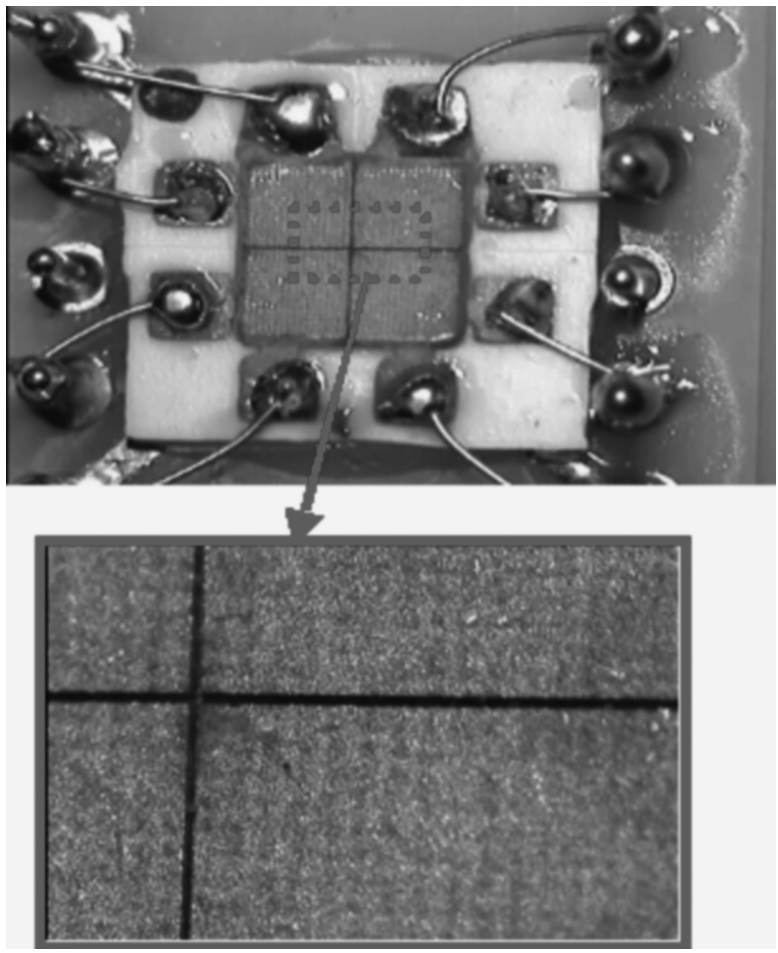

9.11 Pyroelectric four-quadrant detector after Capineri *et al.* (2004).

© Woodhead Publishing Limited, 2012

demodulation, a DC signal is obtained which depends on the fraction of the LED light intensity impinging on the pyroelectric film. Interferences from thermal and light background are rejected. The maximum responsivity is typically obtained for a modulation frequency in the region around 100 Hz. The typical pyroelectric signal corresponds to peak temperature variations in the PZT film between 50 and 100 mK.

Based on this principle, pyroelectric contactless displacement sensors were proposed. As shown in Fig. 9.12, a pyroelectric film coupled to a LED can work respectively as the reference element and the movable light-spot cursor of a contactless linear displacement sensor (V. Ferrari *et al.*, 2002). The sensor consists of a planar multi layer structure on alumina substrate where a rectangular film of PZT is enclosed between two PdAg electrode layers at the top and bottom. Each layer is in turn composed of a pair of triangular split electrodes (left, L, and right, R). The resulting four electrodes are combined in reverse-parallel with respect to the common poling direction, so that the pyroelectric signals from the R and L subsections subtract in a push-pull configuration producing a differential current. The LED spot position along the sensor length is converted into a suitably linear DC output by means of amplitude modulation of the LED and synchronous demodulation of the pyroelectric differential current. The readout method, combined with the differential configuration of the sensor, provides rejection of vibrations and microphonics caused by the piezoelectric response of PZT, as well as of external thermal and light sources. With a LED driving current of 33 mA at the stand-off distance of 3 mm, the measured sensitivity was 120 mV/mm over the range ±10 mm, with a resolution better than 1.5×10^{-3} of the span.

An extension of the same principle was proposed for biaxial position measurements by means of the pyroelectric sensor array shown in Fig. 9.13

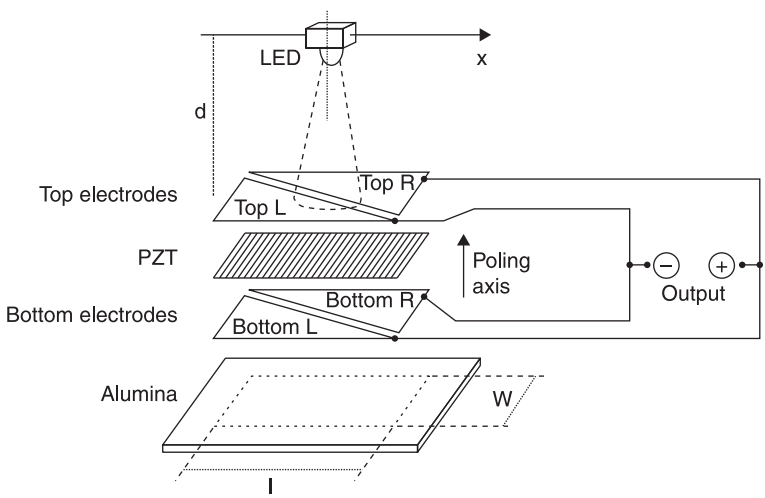

9.12 Contactless pyroelectric linear displacement sensor (after V. Ferrari *et al.*, 2002): sensor structure and operating principle with a LED cursor.

© Woodhead Publishing Limited, 2012

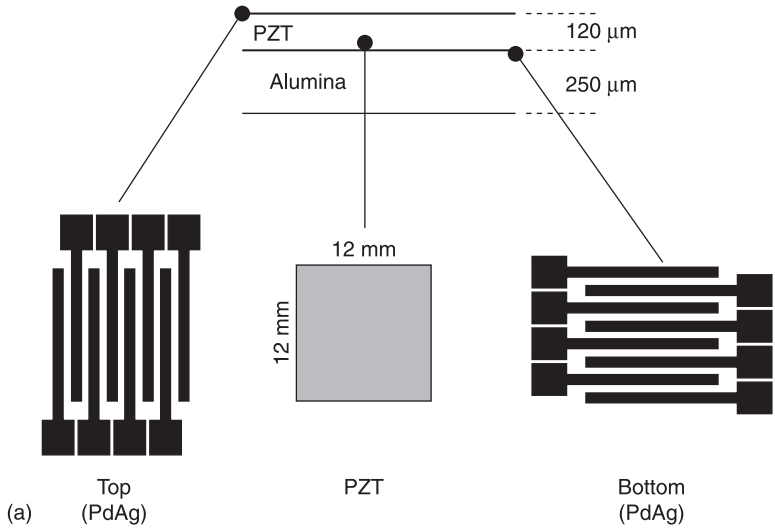

(a)

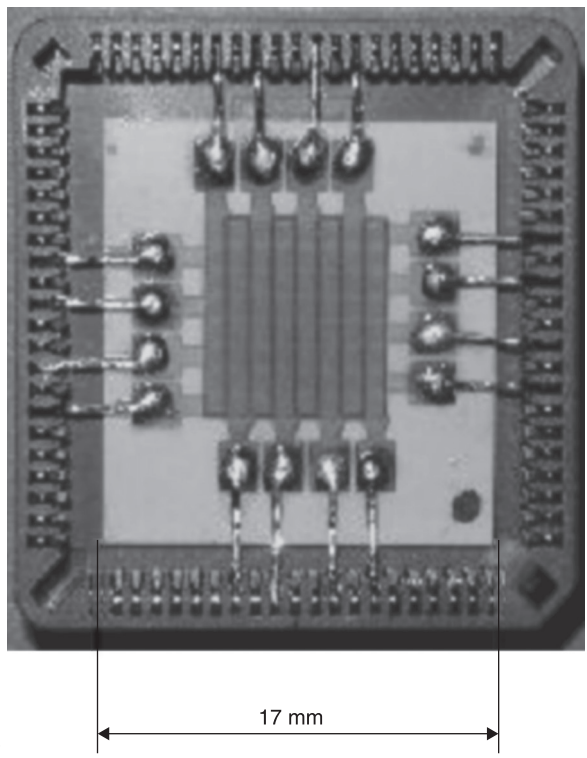

(b)

9.13 Pyroelectric array with 8 × 8 pixels for biaxial measurement of LED spot position after V. Ferrari *et al.* (2003): (a) array layout; (b) picture.

© Woodhead Publishing Limited, 2012

(V. Ferrari *et al.*, 2003). The sensor array is made by 8 × 8 pixels of PZT screen-printed on an alumina substrate. The electrodes are configured as eight columns and eight rows evenly spaced, whose respective crossings form the 64 pixels of the array. As shown in Fig. 9.14(a), with an amplitude-modulated LED placed in front of the array and movable in the XY plane parallel to the array surface, the array and the LED respectively work as the reference element and the contactless cursor of a biaxial position sensor. A tailored readout and processing technique based on weighted amplification of the column and row pyroelectric signals produces a continuous and linear dependence of the output voltages on the XY position of the LED cursor. The measured sensitivity was 1 V/mm over the range ±3.5 mm, with

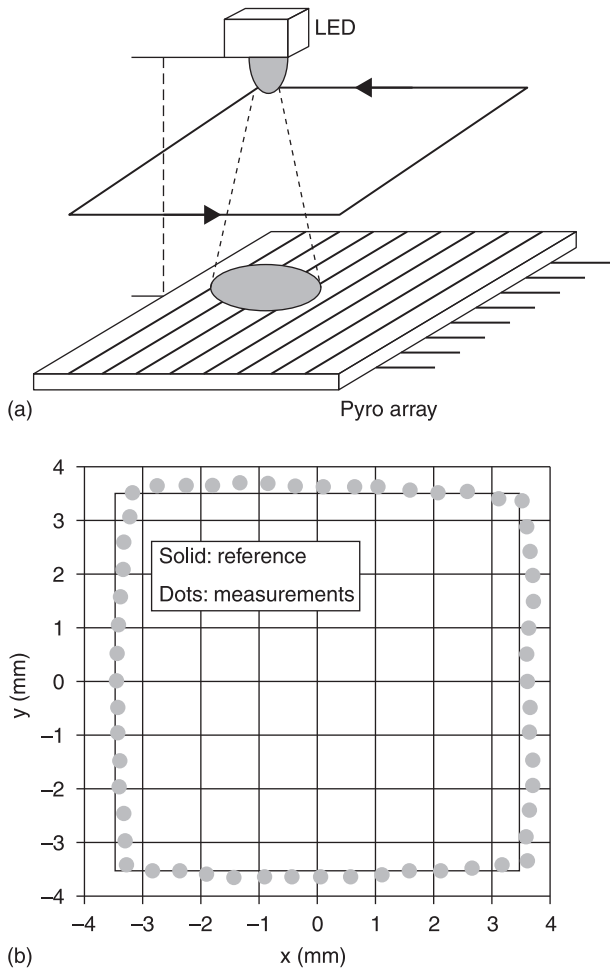

9.14 Characterization of the pyroelectric sensor array of Fig. 9.13: (a) test configuration; (b) measurement results along a square reference path.

© Woodhead Publishing Limited, 2012

nonlinearity within ±1% of the span. The resolution threshold was 4 µm, which is much better than the pixel pitch. Fig. 9.14(b) shows the results of biaxial measurements along the worst-case squared test path with side of 7 mm, i.e. on the borders of the linearity region. A good reconstruction of the LED trajectory can be observed.

Thick-film pyroelectric sensors for contactless displacement measurement offer low cost at large sensing areas when compared with semiconductor position-sensitive detectors. On the other hand, due to their limited frequency response with standard film and substrate thickness, they have been investigated for quasi-static applications so far.

Recently, the pyroelectric effect in PZT thick-films has started to be investigated for energy harvesting and possible use in generators for ultralow-power sensor modules. In Cuadras *et al.* (2010), PZT thick-films and commercial polyvinylidene fluoride (PVDF) elements were subject to thermal transients measuring currents and charges in the order of 10^{-7} A and 10^{-5} C, respectively, for temperature fluctuations from 300 to 360 K in a time period of the order of 100 s. Heating–cooling cycles were also investigated in order to accumulate energy. The pyroelectric current was rectified and the generated charge stored in a 1 µF capacitor up to an energy of 0.5 mJ.

In Dalola *et al.* (2010) sinusoidal temperature fluctuations were applied to screen-printed PZT films on alumina substrate. The charge extracted from the pyroelectric converter was stored into a capacitor using different rectifying circuits. The results of Fig. 9.15, where full-wave and voltage-doubler rectifiers are compared, show that after a few dozen heating–cooling cycles with a temperature

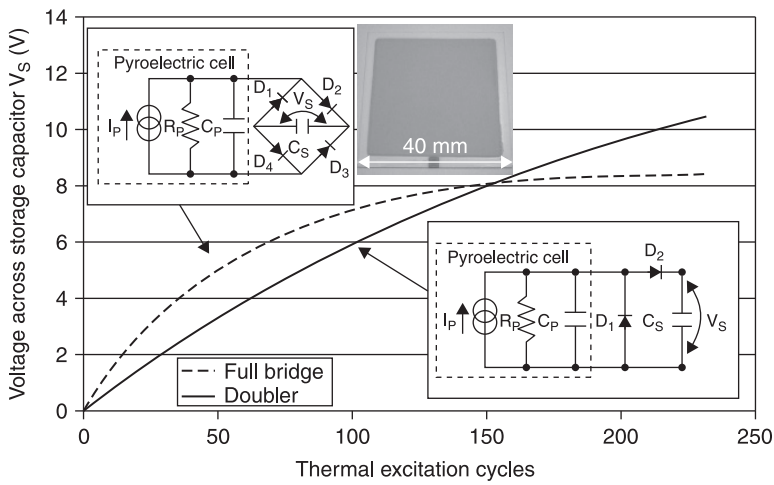

9.15 Pyroelectric elements on alumina used for thermal energy harvesting after Dalola *et al.* (2010): voltage across a 10 µF storage capacitor for different rectifiers with the sample, visible in the inset, excited with a sinusoidal temperature rate of 1.8 °C/s peak.

© Woodhead Publishing Limited, 2012

rate of 1.8 °C/s, voltages in the order of 5 V and more are reached on a 10 μF capacitor in either case. The corresponding harvested energy can be compatible with use in autonomous sensors working in low duty cycle intermittent mode.

9.7 Future trends

In the field of piezoelectric and pyroelectric thick-films, continuing research efforts are expected towards their integration with MEMS technology. While both silicon MEMS and electroceramics, in particular those with piezo- and pyroelectric properties, are successful technologies in their respective fields, their combination into devices amenable to manufacturing with repeatable and industrially-viable processes is still a matter of ongoing development. Piezo- and pyroelectric films of 10–100 μm thickness, such as obtainable by screen printing, can fill the gap between other deposition techniques and therefore will continue to be attractive. A large amount of technology and material aspects, applications and devices, including sensors and actuators, are comprehensively described in Setter (2005), which represents a valuable source of information and an overview on the current trends in electroceramic-based MEMS.

A key issue in the field of piezo- and pyroelectric devices is the requirement to progressively abandon PZT and look for lead-free materials. Due to the directive 2002/95/EC, commonly referred to as the Restriction of Hazardous Substances (RoHS) in the European Union and similar restrictions in other countries, the use of lead as well as other hazardous heavy metals is banned in the manufacture of electronic and electrical equipment. PZT typically contains a lead weight concentration around 60%, yet it has been granted a temporary exemption to RoHS, while the research for substitute materials has been encouraged (Rödel *et al.*, 2009). Considerable research efforts by industry and academia are ongoing on the topic, but at present a one-to-one replacement for PZT is still not available (Panda, 2009). Barium titanate (BT), modified sodium potassium niobate (KNN) and bismuth sodium titanate (BNT) are examples of lead-free materials that have attracted significant attention. All of them show stable piezoelectric response providing comparable performances to PZT in some respects, but important limitations in others (Aksel and Jones, 2010). Therefore, the development of lead-free piezoelectric films of adequate performances for sensors and transducers will be a topic of interest in material science that will impact in device development (Setter, 2008).

Another topic that is expected to attract increasing research interest in the near future is the deposition, by screen printing or other methods, of thick-films on nonconventional substrates such as plastics or textiles. The development of repeatable and cheap processes to obtain reliable sensors and interconnections on such diverse substrates is an ambitious goal that will bring advances in the broader research area of printed electronics. The timeliness of the topic is confirmed by recent projects funded by the EU such as, for example, 3Plast on printable, pyroelectrical and piezoelectrical large-area sensor technology (3Plast) and

© Woodhead Publishing Limited, 2012

Microflex on micro fabrication production technology for MEMS on new emerging smart textiles/flexibles (Microflex).

9.8 Sources of further information

- Energy Harvesting Network

Consortium of academic and industrial researchers and end-users of energy harvesting (EH) technology: http://eh-network.org.

- IEEE Instrumentation and Measurement Society (IMS)

Society dedicated to research concerning the theory, methodology and practice of measurement, and in the design, development and evaluation of instrumentation and associated measurement systems: http://www.ieee-ims.org.

- IEEE Sensors Council

Council dedicated to research on the theory, design, fabrication, manufacturing and application of devices for sensing and transducing physical, chemical, and biological phenomena, with emphasis on the electronics, physics and reliability aspects of sensors and integrated sensor-actuators: http://www.ieee-sensors.org.

- IEEE Ultrasonics, Ferroelectrics and Frequency Control Society (UFFC-S)

Society dedicated to promote the advancement of the theory and practice of ultrasonics, ferroelectrics, frequency generation and control, and allied arts and sciences: http://www.ieee-uffc.org.

- International Microelectronics and Packaging Society (IMAPS)

Society dedicated to the advancement and growth of microelectronics and electronics packaging technologies through professional education: http://www.imaps.org/default.asp.

- Piezo Institute

Consortium of academic and industrial researchers dedicated to the field of piezoelectric materials and devices: http://www.piezoinstitute.com.

9.9 Acknowledgments

The valuable contribution of Professor Maria Prudenziati in enriching the scope of the chapter, and the helpful discussions and inspiring advice by Professor Andrea Taroni are gratefully acknowledged.

9.10 References

3Plast, *Printable, Pyroelectrical and Piezoelectrical Large-Area Sensor Technology*, EU-FP7 project. Available from: http://www.3plast-sensor.eu

© Woodhead Publishing Limited, 2012

Aksel E. and Jones J. L. (2010), 'Advances in lead-free piezoelectric materials for sensors and actuators', *Sensors*, 10, 1935–1954.

ANSI/IEEE Std 176-1987 (1987), *IEEE Standard on Piezoelectricity*, Institute of Electrical and Electronic Engineers, New York.

Arnau A. (2008), *Piezoelectric Transducers and Applications*, 2nd edition, Springer-Verlag, Berlin, Heidelberg.

Auld B. A. (1973), *Acoustic Fields and Waves in Solids*. Vol. 1–2, John Wiley & Sons, New York.

Ballantine D. S., White R. M., Martin S. J., Ricco A. J., Zellers E. T. *et al.* (1997), *Acoustic Wave Sensors*, Academic Press, San Diego.

Baù M., Ferrari M., Tonoli E. and Ferrari V. (2011), 'Sensors and energy harvesters based on piezoelectric thick-films', *Proceedings of Eurosensors XXV*, Athens, Greece, September 4–7, in *Procedia Engineering*, 25, (2011) 737–744.

Baudry H. (1987), 'Screen printing piezoelectric devices', *Hybrid Circuits*, 14, 71–74.

Baudry H. and Delmas G. (1991), 'Thick-film pyroelectric sensor array', *Proceedings of 8th European Hybrid Microelectronics Conference*, pp. 227–235.

Beeby S. P., Grabham N. J. and White N. M. (2001), 'Microprecessor implemented self-validation of thick-film PZT/silicon accelerometer', *Sensors and Actuators A*, 92, 168–174.

Belavič D., Hrovat M., Hole J., Zarnik S. M., Kosec M. and Pavlin M. (2007), 'The application of thick-film technology in C-MEMS', *Journal of Electroceramics*, 19, 363–368.

Belavič D., Hrovat M., Zarnik M. S., Holc J. and Kosec M. (2009), 'An investigation of thick PZT films for sensor applications: a case study with different electrode materials', *Journal of Electroceramics*, 23, 1–5.

Benes E., Gröschl M., Burger W. and Schmid M. (1995), 'Sensors based on piezoelectric resonators', *Sensors and Actuators A*, 48, 1–21.

Capineri L., Ferrari V., Naldoni F., Masotti L., Marioli D. *et al.* (1998), '3 × 3 matrix of thick-film pyroelectric transducers', *Electronics Letters*, 34, 1486–1487.

Capineri L., Casotti L., Ferrari V., Marioli D., Taroni A. *et al.* (2004), 'Comparisons between PZT and PVDF thick-films technologies in the design of low-cost pyroelectric sensors', *Review of Scientific Instruments*, 75, 4906–4910.

Chen H. D., Udayakumar K. R., Cross L. E., Bernstein J. J. and Niles L. C. (1995), 'Dielectric, ferroelectric, and piezoelectric properties of lead zirconate titanate thick-films on silicon substrates', *Journal of Applied Physics*, 77, 3349–3353.

Clegg W. W., Jenkins D. F. L. and Cunningham M. J. (1997), 'The preparation of piezoceramic polymer thick-films and their application as micromechanical actuators', *Sensors and Actuators A*, 58, 173–177.

Corkovic S., Zhang Q. and Whatmore R. W. (2007), 'The investigation of key processing parameters in fabrication of $Pb(Zr_xTi_{1-x})O_3$ thick-films for MEMS applications', *Journal of Electroceramics*, 19, 295–301.

Cotton D. P. J., Chappell P. H., Cranny A. and White N. M. (2007), 'A new binderless thick-film piezoelectric paste', *Journal of Materials Science: Materials in Electronics*, 8, 1037–1044.

Cranny A., Cotton D. P. J., Chappell P. H., Beeby S. P. and White N. M. (2005), 'Thick-film force and slip sensors for a prosthetic hand', *Sensors and Actuators A*, 123–124, 162–171.

Crescini D., Ferrari V., Marioli D. and Taroni A. (1996), 'Thick-film resonant sensor for force measurement on stainless steel substrate', *Sensors and Microsystems: Proceedings*

© Woodhead Publishing Limited, 2012

of the First National Conference on Sensors and Microsystems AISEM, World Scientific Publishing, Singapore, pp. 256–260.

Crescini D., Marioli D., Sardini E. and Taroni A. (2001), 'Large bandwidth and thermal compensated piezoelectric thick-film acceleration transducer', *Sensors and Actuators A*, 87, 131–138.

Crescini D., Marioli D., Taroni A. and Romani M. (2002), 'Development of high pressure sensors using PZT-based thick-films', *Proceedings of 19th IEEE Intrumentation and Measurement Technology Conference*, Anchorage, AK, USA, May 21–23, pp. 1555–1558.

Cuadras A., Gasulla M. and Ferrari V. (2010), 'Thermal energy harvesting through pyroelectricity', *Sensors and Actuators A*, 158, 132–139.

Dalola S., Ferrari V. and Marioli D. (2010), 'Pyroelectric effect in PZT thick-films for thermal energy harvesting in low-power sensors', *Procedia Engineering*, 5, 685–688.

Damjanovic D. (1998), 'Ferroelectric, dielectric and piezoelectric properties of ferroelectric thin films and ceramics', *Reports on Progress in Physics*, 61, 1267–1324.

Dauchy F. and Dorey R. A. (2007), 'Patterned crack-free PZT thick-films for micro-electromechanical system applications', *International Journal of Advanced Manufacturing Technology*, 33, 86–94.

De Cicco G., Morten B. and Prudenziati M. (1994a), 'Piezoelectric Thick-film Sensors' *in* Prudenziati M. (ed.), *Thick-film Sensors*, Elsevier, Amsterdam, pp. 209–228.

De Cicco G., Morten B. and Prudenziati M. (1994b), 'A flowmeter operating with plate waves induced by piezoelectric thick-films', *Proceedings of IEEE Ultrasonics Symposium*, Cannes, France, November 1–4, pp. 1327–1331.

De Cicco G., Morten B., Dalmonego D. and Prudenziati M. (1999), 'Pyroelectricity of PZT-based thick-films', *Sensors and Actuators A*, 76, 409–415.

Dorey R. A. and Whatmore R. H. (2004), 'Electroceramic thick-film fabrication for MEMS', *Journal of Electroceramics*, 12, 19–32.

Egusa S. and Iwasawa N. (1994), 'Preparation of piezoelectric paints and application as vibration modal sensors', *J Intelligent Material Systems and Structures*, 5, 140–144.

Ferrari M., Ferrari V., Marioli D., Taroni A., Suman M. *et al.* (2004), 'Cavitand-coated PZT resonant piezo-layer sensors: properties, structure, and comparison with QCM sensors at different temperatures under exposure to organic vapors', *Sensors and Actuators B*, 103, 240–246.

Ferrari M., Ferrari V., Guizzetti M. and Marioli D. (2010a), 'Piezoelectric low-curing-temperature ink for sensors and power harvesting', *Sensors and Microsystems Lecture Notes in Electrical Engineering*, 54, Part 2, Springer-Verlag, Berlin, Heidelberg, pp. 77–81.

Ferrari M., Ferrari V., Guizzetti M., Andò B., Baglio S. *et al.* (2010b), 'Improved energy harvesting from wideband vibrations by nonlinear piezoelectric converters', *Sensors and Actuators A*, 162, 425–431.

Ferrari M., Baù M., Guizzetti M. and Ferrari V. (2011), 'A single-magnet nonlinear piezoelectric converter for enhanced energy harvesting from random vibrations', *Sensors and Actuators A*, 172, 287–292.

Ferrari V. (2004), 'Acoustic-wave piezoelectric and pyroelectric sensors based on PZT thick-films', *in* Yurish S. Y. and Gomes M. T. S. R. (eds), *Smart Sensors and MEMS*, Kluwer Academic, Dordtrecht, pp. 125–154.

Ferrari V. and Lucklum R. (2008), 'Overview of acoustic-wave microsensors', *in* Arnau Vives A. (ed.), *Piezoelectric Transducers and Applications*, 2nd edition, Springer-Verlag, Berlin, Heidelberg, pp. 39–62.

© Woodhead Publishing Limited, 2012

Ferrari V., Marioli D. and Taroni A. (1997), 'Thick-film resonant piezo-layers as new gravimetric sensors', *Measurement Science and Technology*, 8, 42–48.

Ferrari V., Marioli D. and Taroni A. (2001), 'Theory, modelling and characterization of PZT-on-alumina resonant piezo-layers as acoustic-wave mass sensors', *Sensors and Actuators A*, 92, 182–190.

Ferrari V., Marioli D. and Taroni A. (2002), 'Displacement sensor based on pyroelectric thick-films and contactless light-spot cursor', *IEEE Transactions on Instrumentation and Measurement*, 51, 819–823.

Ferrari V., Marioli D., Taroni A. and Ranucci E. (2000), 'Multisensor array of mass microbalances for chemical detection based on resonant piezo-layers of screen-printed PZT', *Sensors and Actuators B*, 68, 1–3, 81–87.

Ferrari V., Marioli D., Taroni A., Ranucci E. and Ferruti P. (1996), 'Development and Application of Mass Sensors based on Flexural Resonances in Alumina Beams', *IEEE Trans on Ultrasonics, Ferroelectrics, and Frequency Control*, 43, 601–608.

Ferrari V., Ghisla A., Marioli D. and Taroni A. (2003), 'Array of PZT pyroelectric thick–film sensors for contactless measurement of XY position', *IEEE Sensors Journal*, 3, 212–217.

Ferroperm, *Full Data Matrix*, Ferroperm Matdata.xls. Available from: http://www.ferroperm–piezo.com

Frood A. J. M., Beeby S. P., Tudor M. J. and White N. M. (2007), 'Photoresist patterned thick-film piezoelectric elements on silicon', *J Electroceram*, 19, 327–331.

Fu S. L., Chung J. K. and Cheng S. Y. (1985), 'Properties and Applications of Screen-printed Piezoelectric Films', *Japanese Journal of Applied Physics*, 24, Supplement 24-2, 416–418.

Gebhardt S., Partsch U. and Schönecker A. (2004), 'PZT thick-films for MEMS', *Proceedings of 17th IEEE International Symposium on the Applications of Ferroelectrics*, ISAF 2008; Santa Fe, NM, USA, February 23–28, 2008, Article number 4693830.

Gebhardt S., Seffner L., Schlenkrich F. and Schönecker A. (2007), 'PZT thick-films for sensor and actuator applications', *Journal of the European Ceramic Society*, 27, 4177–4180.

Glynne-Jones P., Beeby S. P., Dargie P., Papakostas T. and White N. M. (2000), 'An investigation into the effect of modified firing profiles on the piezoelectric properties of thick-film PZT layers on silicon', *Measurement Science and Technology*, 11, 526–531.

Gwirc S. N. and Negreira C. A. (2006), 'Evaluation of the effect of porosity and substrate on the piezoelectric behavior of thick-film PZT elements', *Journal of Physics D: Applied Physics*, 39, 4215–4221.

Haertling G. H. (1999), 'Ferroelectric ceramics: history and technology', *Journal of the American Ceramic Society*, 82, 797–818.

Hauptmann P. (1991), 'Resonant sensors and applications', *Sensors and Actuators A*, 25–27, 371–377.

Heywang W., Lubitz K. and Wersing W. (2008), *Piezoelectricity Evolution and Future of a Technology*, Springer-Verlag, Berlin, Heidelberg.

Hindrichsen C. C., Lou-Møller R., Hansen K. and Thomsen E. V. (2010a), 'Advantages of PZT thick-film for MEMS sensors', *Sensors and Actuators A*, 163, 9–14.

Hindrichsen C. C., Almind N. S., Brodersen S. H., Lou-Møller R., Hansen K. *et al.* (2010b), 'Triaxial MEMS accelerometer with screen-printed PZT thick-film', *Joutrnal of Electroceramics*, 25, 108–115.

Hirsch S., Doerner S., Salazar Velez D. J., Lucklum R., Schmidt B. *et al.* (2005), 'Thick-film PZT transducers for silicon micro machined sensor arrays', *Proceedings of IEEE Sensors 2005 Conference*, pp. 444–447.

© Woodhead Publishing Limited, 2012

Hrovat M., Holc J., Drnovšek S., Belavič D., Bernard J. *et al.* (2003), 'Characterization of PZT thick-films fired on LTCC substrates', *Journal of Materials Science Letters*, 22, 1193–1195.

Ikeda T. (1989), *Fundamentals of Piezoelectricity*, Oxford University Press, Oxford.

InSensor, *TF2100 PZT thick-film based on Ferroperm Pz26*, 1234182533.pdf. Available from: http://www.insensor.com

Kim H. U., Lee W. H., Rasika Dias H. V. and Priya S. (2009), 'Piezoelectric microgenerators – current status and challenges', *IEEE Transaction on Ultrasonics, Ferroelectrics, and Frequency Control*, 56, 1555–1568.

Kwon T. Y., Kim Y. B., Eom K., Yoon D. S., Lee H. L. *et al.* (2007), Fabrication of stabilized piezoelectric thick-film for silicon-based MEMS device', *Applied Physics A*, 88, 627–632.

Lang S. B. (2005), 'Pyroelectricity: from ancient curiosity to modern imaging tool', *Physics Today*, August, 31–36.

Lefki K. and Dormans G. J. M. (1994), 'Measurement of piezoelectric coefficients of ferroelectric thin films', *Journal of Applied Physics*, 76, 1764–1767.

Leppävuori S., Lozinski A. H. and Ussimäki A. (1995), 'A thick-film pyroelectric PLZT ceramic sensor', *Sensors and Actuators A*, 46–47, 391–394.

Liu S. T. and Long D. (1978), 'Pyroelectric detectors and materials', *Proceedings of IEEE*, 66, 14–26.

Lou-Moeller R., Hindrichsen C. C., Thamdrup L. H., Bove T., Ringgaard E. *et al.* (2007), 'Screen-printed piezoceramic thick-films for miniaturised devices', *J Electroceram*, 19, 333–338.

Lozinski A., Wang F., Ussimäki A. and Leppävuori S. (1997), 'PLZT thick-films for pyroelectric sensors', *Measurement Science and Technology*, 8, 33–37.

Lozinski A., Wang F., Ussimäki A. and Leppävuori S. (1998), 'Thick-film pyroelectric linear array', *Sensors and Actuators A*, 68, 290–293.

Lucat C., Menil F. and Von Der Mühll R. (1997), 'Thick-film densification for pyroelectric sensors', *Measurement Science and Technology*, 8, 38–41.

Mason W. P. (1948), *Electromechanical Transducers and Wave Filters*, Van Nostrand Company, New York.

Microflex, Micro Fabrication Production Technology for MEMS on New Emerging Smart Textiles/Flexibles, EU-FP7 project. Available from: http://microflex.ecs.soton.ac.uk

Morten B., De Cicco G. and Prudenziati M. (1989), 'Piezoelectric properties of PZT-thick-films', *Proceedings of 7th Europ Hybrid Microel Conference*, Hamburg, FRG, paper 8.4.

Morten B., De Cicco G. and Prudenziati M. (1992), 'Resonant pressure sensor based on piezoelectric properties of ferroelectric thick-films', *Sensors and Actuators A*, 31, 153–158.

Morten B., De Cicco G. and Prudenziati M. (1993), 'A thick-film resonant sensor for humidity measurements', *Sensors and Actuators A*, 37–38, 337–342.

Morten B., Prudenziati M., De Cicco G. and Alberigi Quaranta A. (1990), 'Piezoelectric thick-film accelerometer for automotive applications', *Proceedings of the 3rd Prometheus Workshop*, Vol. 4, Turin, Italy, pp. 312–320.

Muralt P. (2001), 'Micromachined infrared detectors based on pyroelectric thin films', *Reports on Progress in Physics*, 64, 1339–1388.

Muralt P. (2008a), 'Piezoelectric films for innovations in the field of MEMS and biosensors', in Heywang W., Lubitz K. and Wersing W. (2008), *Piezoelectricity Evolution and Future of a Technology*, Springer-Verlag, Berlin, Heidelberg, pp. 351–376.

© Woodhead Publishing Limited, 2012

Muralt P. (2008b), 'Recent progress in materials issues for piezoelectric MEMS', *Journal of the American Ceramic Society*, 91, 1385–1396.

Newnham R. E. (2005), *Properties of Materials*, Oxford University Press, New York.

Panda P. K. (2009), 'Review: environmental friendly lead-free piezoelectric materials', *Journal of Materials Science*, 44, 5049–5062.

Park J. H. and Park H. H., (2011), 'In situ method of densification for powder-based piezoelectric thick-films for microelectromechanical system applications', *Micro & Nano Letters*, 6 (9), 749–754.

Park J. H., Kim H., Yoon D. S., Kwang S. Y., Lee J. *et al.* (2010), 'Effects of the material properties on piezoelectric PZT thick-film micro cantilevers as sensors and self actuators', *Journal of Electroceramics*, 25, 1–10.

Park J. H., Kwon T. Y., Kim H. J., Kim S. R., Yoon D. S. *et al.* (2006), 'Resonance properties and mass sensitivity of monolithic microcantilever sensors actuated by piezoelectric PZT thick-film', *Journal of Electroceramics*, 17, 565–572.

Partsch U., Arndt D., Keitel U. and Otschik P. (2003), 'Piezoelectric pressure sensors in LTCC-Technology', *Proceedings of European Microelectronic and Packaging Conference*, Friderichshafen, Germany, pp. 331–335.

Payo I. and Hale J. M. (2010), 'Dynamic characterization of piezoelectric paint sensors under biaxial strain', *Sensors and Actuators A*, 163, 150–158.

Priya S., Ryu J., Park C. S., Oliver J., Choi J. J. *et al.* (2009), 'Piezoelectric and magnetoelectric thick-films for fabricating power sources in wireless sensor nodes', *Sensors*, 9, 6362–6384.

Rödel J., Jo W., Seifert K. T. P., Anton E. M., Granzow T. *et al.* (2009), 'Perspective on the development of lead-free piezoceramics', *Journal of the American Ceramic Society*, 92, 6, 1153–1177.

Samoilov V. B. and Yoon Y. S. (1998), 'Frequency response of multilayer pyroelectric sensors', *IEEE Trans on Ultrasonics, Ferroelectrics, and Frequency Control*, 45, 1246–1254.

Setter N. (2005), *Electroceramic-based MEMS: Fabrication-Technology and Applications*, Springer-Verlag, Berlin, Heidelberg.

Setter N. (2008), 'Trends in ferroelectric/piezoelectric ceramics', *in* Heywang W., Lubitz K. and Wersing W. (eds), *Piezoelectricity Evolution and Future of a Technology*, Springer-Verlag, Berlin, Heidelberg, pp. 552–569.

Tadigadapa S. and Mateti K. (2009), 'Piezoelectric MEMS sensors: state-of-the-art and perspectives', *Measurement Science and Technology*, 20, 092001 (30 pp).

Torah R. N., Beeby S. P. and White N. M. (2004), 'Experimental investigation into the effect of substrate clamping on the piezoelectric behaviour of thick-film PZT elements', *Journal of Physics D Applied Physics*, 37, 1–5.

Torah R., Beeby S. P. and White N. M. (2005), 'An improved thick-film piezoelectric material by powder blending and enhanced processing parameters', *IEEE Trans on Ultrasonics, Ferroelectrics, and Frequency Control*, 52, 10–16.

Torah R. N., Beeby S. P., Tudor M. J. and White N. M. (2007), 'Thick-film piezoceramics and devices', *Journal of Electroceramics*, 19, 95–110.

Uršič H., Hrovat M., Belavič D., Cilenšek J., Drnovšek S. *et al.* (2008), 'Microstructural and electrical characterisation of PZT thick-films on LTCC substrates', *Journal of the European Ceramic Society*, 28, 1839–1844.

Waanders J. W. (1991), *Piezoelectric Ceramics*, Eindhoven, Philips Components.

Walter V., Delobelle P., Le Moal P., Joseph E. and Collet M. (2002), 'A piezo-mechanical characterization of PZT thick-films screen-printed on alumina substrate', *Sensors and Actuators A*, 96, 157–166.

© Woodhead Publishing Limited, 2012

Wang X. Y., Lee C. Y., Peng C. J., Chen P. Y. and Chang P. Z. (2008), 'A micrometer scale and low temperature PZT thick-film MEMS process utilizing an aerosol deposition method', *Sensors and Actuators A*, 143, 469–474.

Wang Z., Zhu W., Miao J., Zhu H., Chao C. *et al.* (2006), 'Micromachined thick-film piezoelectric ultrasonic transducer array', *Sensors and Actuators A*, 130–131, 485–490.

Whatmore R. W. (1986), 'Pyroelectric devices and materials', *Reports on Progress in Physics*, 49, 1335–1386.

White N. M. and Ko V. T. K. (1993), 'Thick-film acoustic wave sensor structure', *Electronics Letters*, 29, 1807–1808.

Yao K. and Zhu W. (1998), 'Improved preparation procedure and properties for a multilayer piezoelectric thick-film actuator'. *Sensors and Actuators A*, 71, 139–143.

Zarnik S. M., Belavič D., Maček S. and Hole J. (2009), 'Feasibility study of a thick-film PZT resonant pressure sensor made on a prefired 3D LTCC structure', *International Journal of Applied Ceramic Technology*, 6 (1), 9–17.

© Woodhead Publishing Limited, 2012

10

Printed thick-film mechanical microsystems (MEMS)

S. P. BEEBY, University of Southampton, UK

Abstract: This chapter discusses the use of printed thick-films in mechanical microsystems or MEMS. It considers two types of microsystem, one based on silicon and the other on ceramic materials. Silicon is the most widely used material for MEMS, and there is a wide range of micromachining processes available to fabricate microstructures. Piezoelectric thick-films such as lead zirconate titanate (PZT) have been successfully printed on silicon but there are difficulties with interfacial reactions and compatibilities with some micromachining processes. Nonetheless, several thick-film MEMS have been realised in silicon and these are described in detail. Printing on ceramics is more straightforward but the range of micromachining processes available is much more limited. Alumina and low-temperature co-fired ceramic (LTCC) substrates have been used to realise ceramic MEMS with LTCC offering the potential for quite complex microstructures. Challenges for the technology include improving film properties, printed resolution and compatibility with micromachining processes and fragile microstructures.

Key words: thick-film MEMS, piezoelectric thick-films, accelerometers, micropumps, resonators, ceramic MEMS, LTCC microstructures

10.1 Introduction

The development of mechanical microsystems (also known as MicroElectroMechanical Systems or MEMS) became an established technical subject during the 1980s. It is now a multi-billion dollar industry with numerous successful devices including ink-jet print heads, pressure sensors, accelerometers and projection systems. The industry remains largely dominated by single crystal silicon (Si) and relies on micromachining processes adapted from the semiconductor industry to fabricate microscale mechanical structures and components. The majority of microsystems are transducers, i.e. they perform some form of sensing or actuating function, and numerous techniques have been developed to achieve this functionality. In the case of sensing applications, physical effects can be monitored by, for example, exploiting the piezoresistive properties of silicon, measuring a change in capacitance, monitoring the resonant frequency of a mechanical structure (resonant sensing) or by using piezoelectric materials deposited on the microstructure. Similarly, actuation can be achieved by generating electrostatic forces, thermal expansion effects and again by using deposited piezoelectric materials. The use of piezoelectric materials in MEMS offers a low power approach for sensing and actuating that fundamentally

© Woodhead Publishing Limited, 2012

scales down well with the size of the structures (a property it shares with electrostatics).

Piezoelectric MEMS have been demonstrated in a number of applications and these are most commonly based upon thin-film piezoelectric materials. Examples of such MEMS include high-frequency resonant devices (DeVoe, 2001), energy harvesting (Marzencki *et al.*, 2008), ultrasonic transducers (Yamashita *et al.*, 2002) and microphones (Ko *et al.*, 2003). Non-ferroelectric piezoelectrics such as zinc oxide (ZnO) and aluminium nitride (AlN) are typically sputter-deposited onto the substrate. Process parameters are critical in obtaining correct film orientation, which is necessary for achieving good piezoelectric properties. Ferroelectric thin films, most commonly based upon lead zirconate titanate (PZT) are also used in MEMS, and these benefit from higher piezoelectric coefficients than the non-ferroelectric materials. The deposition process parameters are again critical in determining the level of activity of the material (Trolier-McKinstry and Muralt, 2005).

Piezoelectric MEMS sensors and actuators require sufficient thickness of the active material in order for the device to meet the requirements for sensitivity and force, respectively. Therefore, in some cases, thin piezoelectric films do not provide enough active material and thicker films are required. This chapter describes the development of printed thick-film layers and their use in MEMS. The majority of the material covered relates to printed piezoelectric thick-films but other types of printed active materials, such as magnetostrictives and piezoresistives, have also been used in MEMS. The chapter first considers thick-film MEMS based upon silicon substrates and this includes details of the processing constraints and limitations that must be considered. A comprehensive review of thick-film MEMS based upon silicon is presented. The chapter then focuses on thick-film MEMS based on other substrate materials such as ceramics, where we see a greater variety of devices. Finally, future trends and opportunities are discussed.

10.2 Printed films with silicon MEMS

MEMS by definition require some form of mechanical component in order to achieve the required mechanical functionality. In the case of a microscale pressure sensor, for example, the mechanical component could be a simple diaphragm. Another example would be a resonant sensor which requires a mechanical structure that is excited into resonance and the frequency of which forms the output of the sensor. Resonant structures can become quite complicated in order to achieve the dynamic properties required for such a high performance sensing mechanism. In either case, the printed films must be combined with a micromechanical structure that is both fragile and delicate. This is even more challenging since the printed material must typically be printed directly on the microstructure itself at the locations of maximum strain. Micromachining processes have to be developed that enable the printing process to be applied to micromechanical structures.

© Woodhead Publishing Limited, 2012

Another consideration is the number of materials and layers required for the printed film to function. For example, a thick-film piezoelectric material requires top and bottom electrodes to function, which means two further conductive layers are necessary. The deposition of these additional layers must also be considered in the design of the overall micromachining process. Before this is explored further, the subject of silicon micromachining will be briefly discussed.

10.2.1 Silicon micromachining

The fabrication process whereby microscale mechanical structures are realised on silicon wafers is known as silicon micromachining. It is a broad term that covers a huge range of processes for depositing materials, transferring designs (photolithography), etching materials and bonding wafers together. There are two types of micromachining approaches, surface micromachining and bulk micromachining.

Surface micromachining refers to processes that fabricate the mechanical structure on the surface of the silicon wafer. A basic example process based upon a sacrificial layer is shown in Fig. 10.1. A thin layer of silicon nitride (Si_3N_4) is deposited onto a bare silicon wafer. This acts to protect the wafer and electrically isolate the subsequent layers from the substrate. Next, a layer of silicon dioxide (SiO_2) is deposited onto the nitride layer. The SiO_2 film is the sacrificial layer in this process and its thickness determines the final gap between the structure and the substrate. The SiO_2 layer is patterned using photolithography and etched with a simple liquid chemical etchant (hydrofluoric acid, HF) or by plasma etching.

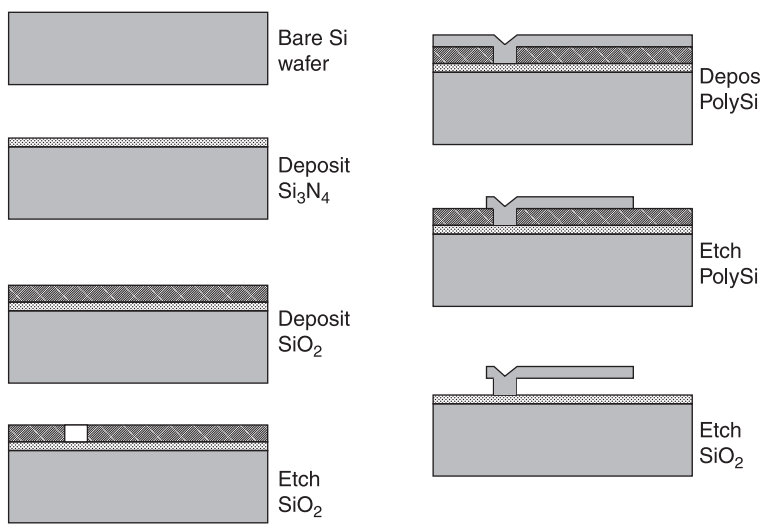

10.1 Sacrificial layer surface micromachining process.

© Woodhead Publishing Limited, 2012

This etching process removes part of the SiO_2 film exposing the nitride layer beneath. These exposed features form the anchor points of the mechanical structure and their location and geometry will depend upon the mechanical deign of the structure. Next, the material that will form the mechanical structure is deposited onto the wafer. This material should have good mechanical properties and polysilicon is a common choice. The thickness of the polysilicon film determines the thickness of the mechanical structure. This mechanical polysilicon layer is patterned by photolithography and selectively removed using a plasma etch. This step transfers the mechanical design to the polysilicon layer. Finally, the silicon dioxide layer is 'sacrificed' by removing it completely with an appropriate etch. This leaves the mechanical structure freestanding on the top surface of the silicon wafer.

Bulk micromachining refers to processes that result in the mechanical structure being fabricated from the single crystal silicon wafer itself, rather than on top of it. This requires etching processes that selectively etch exposed regions of the silicon wafer. An example process is shown in Fig. 10.2. The wafer is protected by films of materials that resist the etch process. For example, in the case of potassium hydroxide (KOH) etch, silicon nitride is used together with a stress-absorbing SiO_2 film. These films are patterned using standard photolithographic techniques and etched to expose the single crystal silicon substrate below. In the case of a wet etch such as KOH, the wafers are simply immersed in the etchant for the required length of time and the exposed silicon is removed at a rate of approximately 0.7 μm/min. KOH is an anisotropic etch, which means the etch rate varies with crystalline direction. The {111} crystal planes are virtually untouched by KOH, which leaves the characteristic sloped side walls shown in Fig. 10.2. The angle of the slope to the

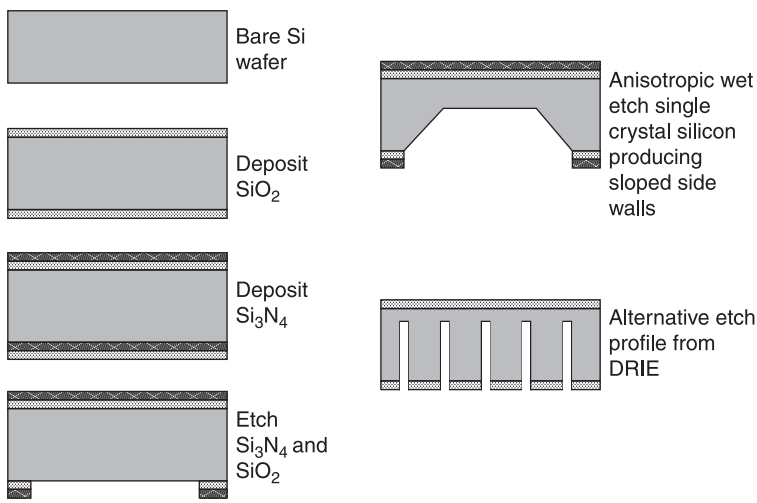

10.2 Bulk micromachining process.

© Woodhead Publishing Limited, 2012

surface of the wafer is 54.7 degrees. More recently, a plasma silicon etch known as deep reactive ion etching (DRIE) has been developed for bulk micromachining. The DRIE process is capable of etching the silicon at rates in excess of 10 μm/min, only requires photoresist as a masking material and etches near vertical sidewalls enabling high aspect ration structures to be formed. An example DRIE etch profile is also shown in Fig. 10.2.

10.2.2 Process considerations for thick-film silicon MEMS

The compatibility of printed thick-films with various micromachining steps is a key issue for identifying a complete process whereby these films can be used with mechanical microsystems (Beeby *et al.*, 1999). One difficulty associated with the thick-film printing process is the pressure applied to the substrate during the printing process. The mechanical structure upon which the PZT is to be printed must be of sufficient strength to withstand this pressure. A second difficulty is the accuracy of registration of the printed layers with respect to micromachined structures and layers patterned using standard photolithographic techniques. The registration accuracy of thick-film layers printed using typical processing equipment is ±50 μm, which is relatively poor compared to photolithography. The effect of both these restrictions can be reduced or overcome if the thick-film printing processes are carried out first, followed by the silicon micromachining. This results in the printing steps being carried out on a partially etched or even completely un-etched silicon wafer. The subsequent micromachining processes could, where applicable, be aligned to the printed layer, thereby improving registration.

This approach requires the printed PZT film to survive the subsequent etching, photolithographic steps and deposition processes. An investigation into the compatibility issues of micromachining silicon wafers with PZT layers printed on the surface has been completed by Beeby *et al.* (1999). This work studied in particular the interaction and adhesion between the printed films and the substrate and the effects of exposure to various micromachining processes.

Interfacial reactions

Printed thick-film PZT layers typically require firing at temperatures in excess of 850 °C, and this causes a problem when the films are printed on silicon due to migration of lead (Pb) atoms from the PZT into the silicon (Beeby *et al.*, 1999, Maas *et al.*, 1997). This migration results in a reaction between the lead and the silicon forming lead silicate compounds at the silicon/film interface. This reaction can cause delamination of the bottom thin film electrode and printed film, and increased conductivity of SiO_2 passivation layers. This increased conductivity can cause short circuits between electrodes and care has to be taken to ensure these are sufficiently physically separated. An example reaction is shown in Fig. 10.3. This

© Woodhead Publishing Limited, 2012

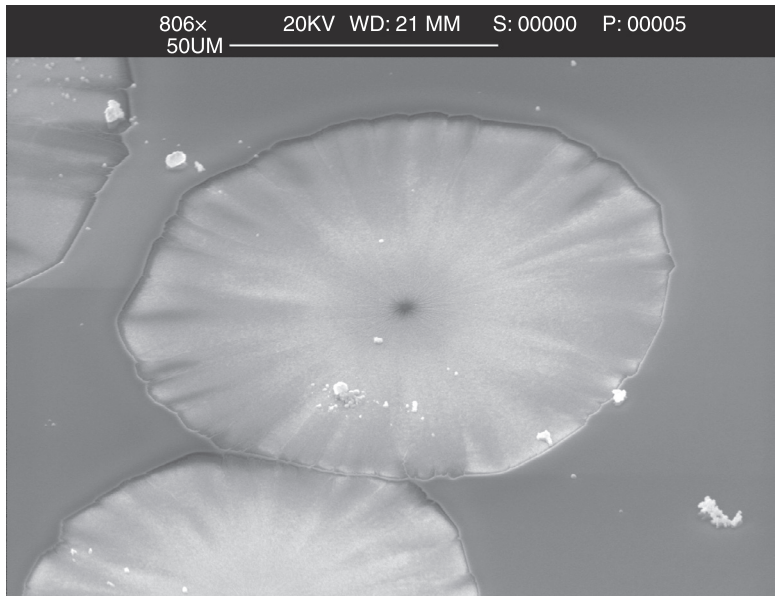

10.3 Example reaction between lead from the PZT and silicon substrate after firing at 900 °C for 1 hour.

migration is unaffected by standard passivation layers such as SiO_2 and Si_3N_4, with the Pb diffusing easily through these layers.

One method of avoiding this is to deposit a diffusion barrier between the printed PZT and the substrate. The diffusion barrier should prevent the Pb atoms reaching the Si substrate whilst being as thin as possible and have sufficient adhesion to both the substrate and the subsequently deposited/printed films (Dorey and Whatmore, 2005). Example diffusion barriers include thin-film (70 nm thick) yttria-stabilised zirconia (YSZ) plus 30 nm titanium dioxide (TiO_2), 120–150 nm zirconium oxide (ZrO_2), 350 nm TiO_2, or thick-film layers of YSZ (1 μm), 1 μm SiO_2/50 nm TiO_2/0.5 μm platinum (Pt) (Dorey and Whatmore, 2005).

Compatibility with micromachining processes

Micromachining processes are required either to selectively etch the substrate, thereby forming the micromechanical structure or to pattern the printed film itself. Given the overall fabrication process described above, it is clearly necessary to etch the silicon substrate or the various deposited films using a process that does not affect the printed film or electrode layers. It is not possible to protect printed thick-films using a photolithographic process because the topology of a printed wafer prevents spin coating resist layers with even thicknesses. Standard wet (liquid) and dry (plasma) etches were evaluated by Beeby *et al.* (1999) in

© Woodhead Publishing Limited, 2012

order to identify suitable methods. Wet etches were found not to be suitable. For example, a common wet anisotropic KOH etch was found to reduce the adhesion of the electrode and PZT films causing the printed areas to float away. Similarly, a wet-buffered hydrofluoric acid (BHF) (a SiO_2 etch) also reduced the adhesion of the printed film. Plasma-based etches, however, were found to have little affect on the printed films or bottom electrode. For example, a sulphur hexafluoride (SF_6) reactive ion etch (RIE), which is a semi-anisotropic Si etch, was found to remove the Si at up to 1 μm a minute depending upon the area of exposed silicon. Depending upon the presence of any reaction material, a short SiO_2 plasma etch based upon CHF_3 may be required beforehand to remove the lead silicate.

10.2.3 Example silicon/thick-film MEMS

A number of different mechanical sensors have been fabricated in silicon and the final fabrication processes developed for these devices highlight the details discussed above.

The first of these is a micromachined silicon micropump fabricated with a thick-film PZT actuator (Koch *et al.*, 1998). The pump, shown in Fig. 10.4, consists of a thin silicon membrane with a thick-film PZT actuator printed on the top surface. This structure is bonded to two other wafers, which form the cantilever valves that control the direction of the fluid flow through the pump. The PZT actuator is activated in one direction causing the membrane to move upwards increasing the volume in the pump chamber and drawing fluid in through the inlet. The actuator is then connected with the opposite polarity, causing the membrane to move down, reducing the chamber volume and forcing the fluid out through the outlet. The device was fabricated by first micromachining the membranes and then printing the PZT and electrode films. This approach highlighted the difficulty of printing onto fragile structures. In this case, the 8 mm × 4 mm diaphragm of the

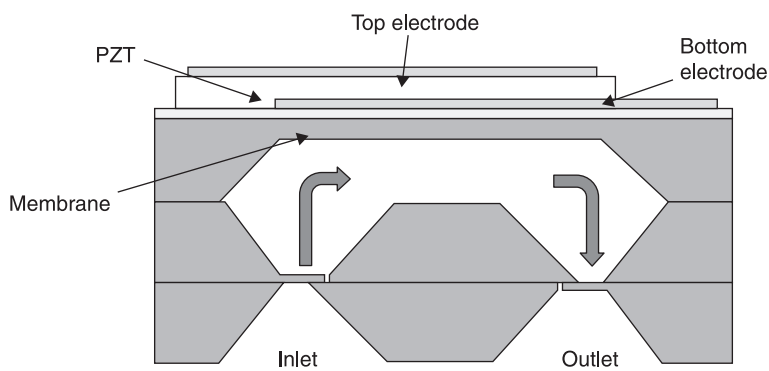

10.4 Silicon micropump with printed thick-film piezoelectric actuation (piezoelectric layer 100 μm thick).

© Woodhead Publishing Limited, 2012

micropump was found to fracture during printing if its thickness was less than 60 μm. The pump proved successful in achieving rates of up to 120 μl min^{-1} but did require a 600 V_{pp} driving voltage.

The next device is a bulk micromachined silicon accelerometer with thick-film PZT elements for sensing the deflections of the inertial mass (Beeby and White, 2001). The device structure is shown in Fig. 10.5 and it demonstrates a fabrication process that overcomes the fragility of the microstructure. It consists of a square inertial mass supported at each corner by a thin silicon beam with the printed thick-film PZT located on the top surface of each beam. As the inertial mass vibrates in and out of the plane of the wafer, the supporting beams deflect and the PZT becomes strained hence generating a charge output. The final device shown in Fig. 10.5 is clearly very fragile and would not survive the physical nature of the screen-printing process. The following process, shown in Fig. 10.6, describes the approach taken to overcome this.

Double-polished, 525 μm thick, type <100> silicon wafers were first patterned using a standard double-sided photolithography process to enable processes carried out on both sides of the wafer to be aligned. The double-sided alignment pattern on the top side also included the chip frame and 1 mm^2 alignment aids for the thick-film printing steps. Next, KOH masking layers (600 nm SiO_2 and 160 nm Si_3N_4) were grown/deposited on both sides of the wafers. These layers were then patterned on the back wafer surface to define the inertial mass using a double-sided alignment process to locate the inertial mass at the centre of the chip.

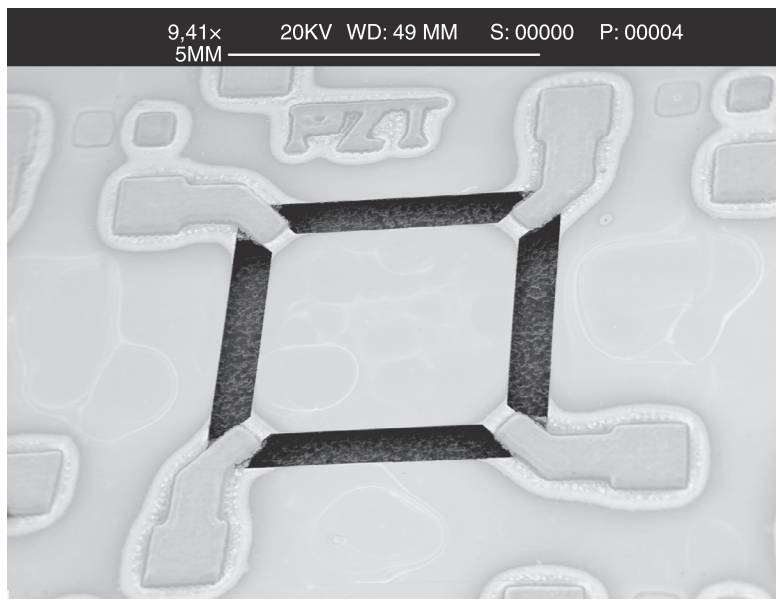

10.5 Micromachined silicon/thick-film PZT accelerometer.

© Woodhead Publishing Limited, 2012

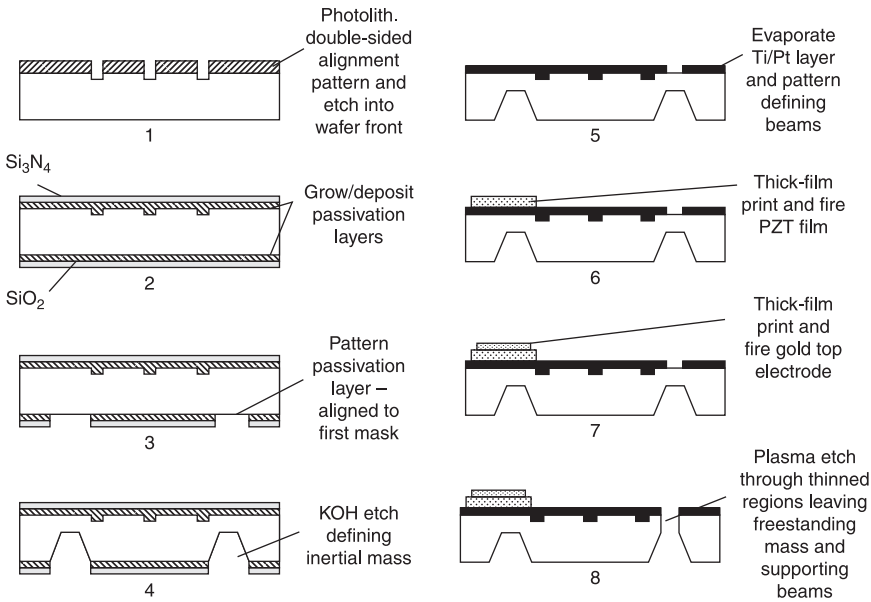

10.6 Complete micromachining process for the silicon/thick-film PZT accelerometer.

The passivation layers were etched using a resist mask and a CHF_3+Ar plasma, after which the resist was removed. The wafers were then immersed in agitated KOH at 70 °C for 13 hours, sufficient to etch down to a depth of 480 μm. This etched a trench around the square inertial mass leaving a thin membrane 40 μm thick and 660 μm wide. The KOH etch has to be performed before printing since the PZT and electrodes cannot withstand this etch. The SiO_2 and Si_3N_4 passivation layers were stripped and the bottom electrode (500 nm Pt + 50 nm Ti) was deposited using an e-beam evaporator. This electrode combination was previously found to be unaffected by an SF_6 plasma etch (Beeby *et al.*, 1999), and could therefore be used as the masking layer for the final etch that defines the beams and releases the inertial mass. The bottom electrode was patterned with a 1.7 mm thick hardbaked layer of resist sufficient to withstand a 12-minute ion beam mill. The layer of resist was then stripped and the substrates prepared for the thick-film printing process. Since the inertial mass was at this stage only supported by a 40 μm thick membrane, additional support was required. This was achieved by bonding the substrate to a host wafer using a thin layer of resist. The host wafer supports the inertial mass during the printing process and protects the etched substrate against the vacuum chuck used by the thick-film printer. Once supported in this manner, the membranes were found to comfortably withstand the pressure exerted during the printing process. The PZT paste was printed through a stainless steel screen with the screen aligned to the 1 mm^2 features defined in the top

© Woodhead Publishing Limited, 2012

surface during step 1. This positioned the PZT elements on the bottom electrodes that define the supporting beams. Two print strokes yielded a thickness of approximately 60 μm after drying and firing at 890 °C for 1 hour, which has been found to sinter the particles adequately without resulting in too much lead loss or reaction. A gold cermet ink, ESL 8836, was printed on the top of the PZT and fired at 890 °C, leaving an approximate thickness of 10 μm. Due to the reaction increasing the conductivity of the oxide, the top electrode was located entirely on the top surface of the PZT and accurate alignment between printed layers was essential to prevent short circuits between the top and bottom electrodes.

The final process involves plasma etching from the front of the wafer through the silicon membrane, with the bottom electrode being used as the masking layer to define the final structure. Given the presence of the reaction material, a CHF_3+ Ar etch for 1 hour was first performed, which cleaned the surface prior the silicon etch. An SF_6 silicon etch for 80 minutes was sufficient to etch through the membranes across the entire wafer, leaving the inertial mass supported by the four beams with the PZT sensing structure already in place on the top surface of each beam. The wafers were once more resist bonded to a host wafer to support the device during dicing. Once sawn, the individual chips were freed from the host wafer by soaking in acetone before being packaged for testing. The yield of this process was excellent, with 97% of devices in the first batch of this kind being successfully fabricated and diced.

Despite being designed primarily to demonstrate the feasibility of the fabrication process, the accelerometer functioned correctly with a flat frequency response up to its first resonant peak at 7.5 kHz. The accelerometer was also used to demonstrate a self-test procedure, where three of the piezoelectric elements were used to excite the inertial mass allowing the operation of the fourth element in the sensing mode to be confirmed (Beeby *et al.*, 2001).

This fabrication process was also used by Beeby and White (2001) to demonstrate the use of screen-printed piezoelectric elements to drive and detect the vibrations of a resonant silicon MEMS beam. Whilst the resonator was not implemented as a sensor, the piezoelectric elements worked well successfully driving the beam into resonance at 56.5 kHz. This work led to the incorporation of printed piezoelectric films on a stainless steel triple beam tuning fork (TBTF) resonator that was employed as a strain gauge (Yan *et al.*, 2004). This device is designed to be used as an alternative to a traditional resistive strain gauge and was therefore quite large (45 mm long, 7 mm wide).

Screen-printed piezoelectric films for silicon MEMS have also been studied by a collaboration between Ferroperm Piezoeceramics A/S (now part of the Meggitt Group) and the Technical University of Denmark. They have developed a commercially available screen-printable piezoelectric material called INSENSOR TF2100, which is based upon Ferroperm Pz26 material, and have combined this with silicon to make a variety of accelerometers. One design is very similar to the device shown in Fig. 10.5 but with a different electrode arrangement and fabricated

© Woodhead Publishing Limited, 2012

using an advanced silicon etch process which is a fast etch that gives high aspect ratio structures with vertical sidewalls (Lou-Moeller *et al.*, 2007). Another version developed by the same team places the supporting beams midway along the length of the inertial mass rather than at the corners, and the volume occupied by the mass is maximised to improve sensitivity (Hindrichsen *et al.*, 2006). In this case, the micromachining process is completed before printing and the device was found to withstand the printing process, provided that the beams were not thinner than 20 μm. This device demonstrated a sensitivity of 4.15 mV/g.

This team has continued to work on accelerometers and has demonstrated a circular device with the advantage that features are not etched completely through the wafer (Hindrichsen *et al.*, 2009). A cross-section is shown in Fig. 10.7 and this design simplifies printing and mechanically reduces off-axis cross sensitivity. The top electrodes are arranged as rings about the periphery of the annular membrane. This is the location of the maximum stresses, which will be of opposite sign during operation. Therefore the inner and outer rings are polarised in opposite directions to compensate for the opposite stresses. The PZT is printed across the device apart from openings that allow access to the SiO_2/Ti/Pt barrier layer and bottom electrode. The PZT film is 24 μm thick and is sintered at 850 °C. The top electrode is a 400 nm thick platinum (Pt) film patterned using a lift off process. The device works well as a uniaxial accelerometer and has a wide operating bandwidth due to the high resonant frequency of 23.5 kHz.

The most recent work by this team has demonstrated a triaxial MEMS accelerometer (Hindrichsen *et al.*, 2010). The device is similar to the previous design with a square inertial mass supported by beams located at the mid point of the sides of the mass. By analysing the output of each bean independently, accelerations in three axes can be detected. The accelerometers are fabricated using silicon on insulator (SOI) wafers with the depth of the buried oxide determining the thickness of the beams. The disparity between the resolution of the MEMS process and the printing step is overcome by first etching through the wafer to define the beams. The printed pattern is designed to overlap the edges of the beams, but since the substrate has been removed the material remains on the

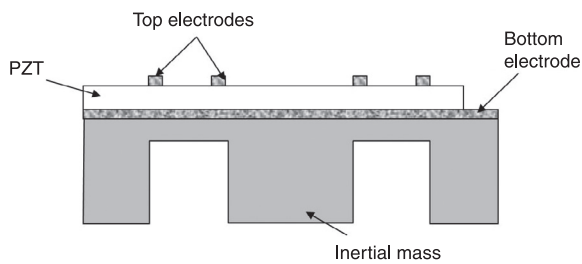

10.7 Circular silicon/thick-film PZT accelerometer.

© Woodhead Publishing Limited, 2012

screen and the resolution effectively becomes the same as for the etch process. However, this approach does not work perfectly since some PZT overhangs of differing dimensions were left and these affected the performance of the device.

Other work on screen-printed piezoelectric layers have avoided the difficulties of the high firing temperatures on silicon by using a laser transfer method (Xu *et al.*, 2005). The thick-film PZT was printed onto a sapphire substrate, dried at 80 °C for 10 minutes and then fired at 1200 °C for 2 hours in a Pb-rich atmosphere. The PZT elements were polished and a thin-film Chrome/Gold (200 Å Cr/5000 Å Au) electrode was evaporated onto the top of the PZT. The PZT elements were bonded to a Pt-coated silicon wafer using conductive silver epoxy. The PZT elements were then exposed to an XeCl excimer laser with 308 nm wavelength and 700 mJ/cm^2 fluence, which releases them from the sapphire substrate. Another Cr/Au film was deposited onto the PZT using a shadow mask to define the pattern. This approach leaves a very dense film with higher dielectric constants than standard thick-films and improved piezoelectric properties. The challenge with this approach would be in aligning the two substrates prior to bonding and achieving a good quality epoxy bond across the entire PZT surface.

10.3 Printed films with ceramic MEMS

Compared with silicon, ceramic substrates offer the advantage of less aggressive interactions with thick-film materials and particularly with PZT films fired at high temperatures. The most common ceramic substrate material is aluminium oxide (Al_2O_3), better known as alumina, which is very limited in terms of bulk micromachining options compared with silicon and can only be cut by laser machining. Due to this limitation, alumina is typically used as a substrate for surface-micromachined structures. Low-temperature co-fired ceramics (LTCCs) are designed to be fired simultaneously with printed passive components, such as resistors, inductors and capacitors, at temperatures below 1000 °C. LTCC substrates are typically stacked on top of each other, laminated under pressure and co-fired to give a multilayer substrate for use with hybrid circuits and multi-chip modules. LTCC is formed from alumina and glass powders and in its green state (unfired) it is much softer than alumina and can be cut and drilled by conventional machining, laser micromachined or even embossed using micromachined nickel tools (Andrijasevic *et al.*, 2007). The ability to stack and bond layers of machined LTCC offers the capability to realise mechanical microstructures suitable for use with thick-film materials for both sensing and actuating applications. A comparison between alumina and LTCC is given in Table 10.1.

10.3.1 Surface-micromachined ceramic MEMS

In this class of devices, the alumina is used simply as a supporting substrate for free-standing micromechanical structures fabricated onto the top surface.

© Woodhead Publishing Limited, 2012

Table 10.1 Comparison between alumina and LTCC

	LTCC	Alumina
Thermal coefficient of expansion (10^{-6}K)	5.8–7	7.6–8.3
Density (g/cm^3)	2.5–3.2	3.7–3.9
Flexural strength (MPa)	170–320	300
Young's modulus (GPa)	90–110	215–415
Thermal conductivity (W/mK)	2–4.5	20–26
Relative dielectric constant	7.5–8	9.2–9.8

Source: Hrovat *et al.*, 2008.

A variety of processes for different applications have been developed, but they are all based upon the sacrificial process illustrated in Fig. 10.1. The following devices are all examples that highlight the capabilities of this approach and the range of applications that have been demonstrated.

The first is a ceramic capacitive pressure sensor designed for high-temperature applications (Sippola and Ahn, 2006). Screen printing has been used to deposit the top and bottom electrodes, the ceramic structural layers and the thick-film sacrificial layer. These layers have been printed onto an alumina substrate that has vias pre-laser drilled through the thickness that allow access for the chemical etchant that removes the sacrificial layer, as illustrated in Fig. 10.8. The gold bottom electrode was screen-printed first and this is patterned to avoid the vias. Next, a standard thick-film dielectric was printed to protect the electrode layer. The third printed layer is a gold film that acts as the sacrificial layer, and the dielectric and top electrode layers are than printed on top of this. The gold sacrificial film is removed by a liquid gold etch leaving a 4.8 mm × 2.8 mm, 32 μm thick diaphragm with a 22 μm thick gap between the electrodes. Finally, a dielectric layer is printed on the back of the alumina to seal the vias. The paper claims that the mechanical properties of the printed dielectric structure are superior to LTCC, and highlights the flexibility offered by the process that enables the gap height to be defined by the thickness of the sacrificial layer. The sensor

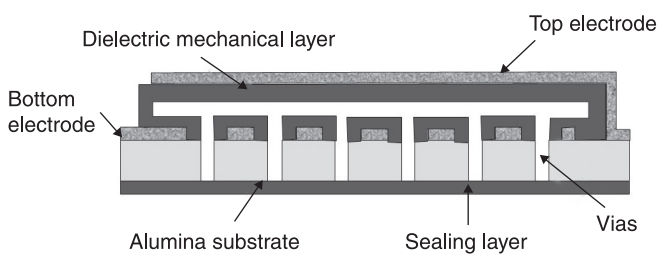

10.8 Ceramic capacitive pressure sensor by Sippola and Ahn, 2006.

© Woodhead Publishing Limited, 2012

proved to be hermetic after firing and demonstrated sensitivities up to 21.9 fF/psi at room temperature and 10 fF/psi at 300 °C.

One disadvantage of the previous device is the cost associated with a gold sacrificial layer. An alternative approach is to use strontium carbonate ($SrCO_3$) powder in an epoxy matrix (Lucat *et al.*, 2008). The epoxy will have decomposed by 450 °C but the $SrCO_3$ can withstand temperatures up to 900 °C and this is simply removed by a weak phosphoric acid aqueous solution. This process has been used to demonstrate a range of printed devices and structures including cantilever force sensors (Lakhmi *et al.*, 2010), micro-channels and an electrothermal actuator (Ginet *et al.*, 2007).

A much more complex surface micromachining approach was developed by Suzuki *et al.* (2009) in the fabrication of a micro accelerometer. This used a screen-printed barium titanate ($BaTiO_3$) film on a platinised alumina substrate. Amorphous silicon, used as the sacrificial layer, was then vapour deposited on top, patterned and etched. This was followed by the deposition and patterning of Parylene, aluminium and a second Parylene layer. The exposed amorphous silicon was then removed by a plasma etch to leave the free-standing inertial mass. It is clear that most of this process is based upon conventional silicon micromachining steps and only the $BaTiO_3$ is actually screen-printed.

The final example of a free-standing microstructure printed on an alumina substrate is a piezoelectric cantilever designed for vibration energy harvesting (Kok *et al.*, 2009). In this work, the sacrificial layer is a printed carbon film that burns out at temperatures above 800 °C. A variety of combinations of electrodes and PZT films were screen-printed over the top of the carbon layer, after which the films were co-fired thereby sintering the films and removing the sacrificial layer. A maximum power output of 40 μW was measured when the harvester was shaken at the cantilever's resonant frequency of 400 Hz and an acceleration level of 0.5 g (1 g = 9.81 m/s^2). Energy harvesting is a topic receiving a great deal of interest at the moment. For a device to be successful it should operate at a target frequency specified by the application and the mass should be maximised to increase the power output. The device should also be robust and operate unchanged for many years. It is not clear if these attributes are achievable with this process or mechanical structure.

10.3.2 Low temperature co-fired ceramic MEMS

The use of LTCC to fabricate microstructures is an established process, with the first devices being demonstrated in the late 1990s. Whilst it offers many advantages in terms of the geometries that can be achieved, restrictions include the limitations on some dimensions (i.e. thicknesses and gaps) by dried tape thickness, which is prescribed by the manufacturer. Also, the mechanical properties are limited to those of the fired film, which are certainly inferior to silicon.

An early example is a capacitive pressure sensor designed to operate wirelessly in high-temperature applications (Fig 10.9) (Fonseca *et al.*, 2002). The sensor is

© Woodhead Publishing Limited, 2012

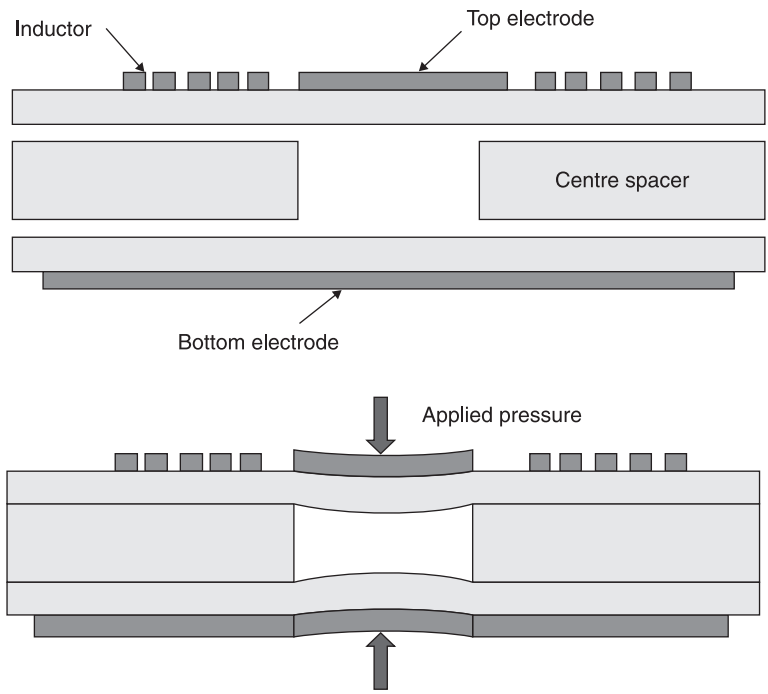

10.9 LTCC capacitive pressure sensor (after Fonseca *et al.*, 2002).

made from three layers of LTCC, with the outer layers being 0.1 mm thick. The centre spacer layer has a circular hole cut in it with a radius of 4.2 mm. The silver top electrode is printed inside a coil inductor and a silver bottom electrode is printed on the bottom layer. The three layers are laminated together in a hot vacuum press and subjected to 3000 psi at 70 °C and then diced up to leave the individual sensors. These are fired in air for 30 minutes at 500 °C and then 20 minutes at 850 °C, which hardens the LTCC and fires the ink. The capacitor and inductor form a resonant LC circuit, the frequency of which depends upon the capacitance, which in turn depends upon the applied pressure. The sensor can be interrogated remotely and was found to operate up to 400 °C and over a pressure range of 7 Bar.

Other sensing mechanisms have also been evaluated on LTCC by the research team at the Jozef Stefan Institute in Slovenia. They compared thick-film resistors, which act as a strain gauge producing a change in resistance when strained, on alumina, pre-fired and co-fired LTCC (Belavic *et al.*, 2007). The resistivity and thermal coefficient of resistance were found to vary between the substrates, but the amount of variation depends upon the resistive ink used. The gauge factor remains largely unaffected, with the LTCC resistors being marginally less sensitive than the alumina case. They also compared PZT thick-films on the same range of substrates and found that the level of piezoelectric activity on LTCC was around

© Woodhead Publishing Limited, 2012

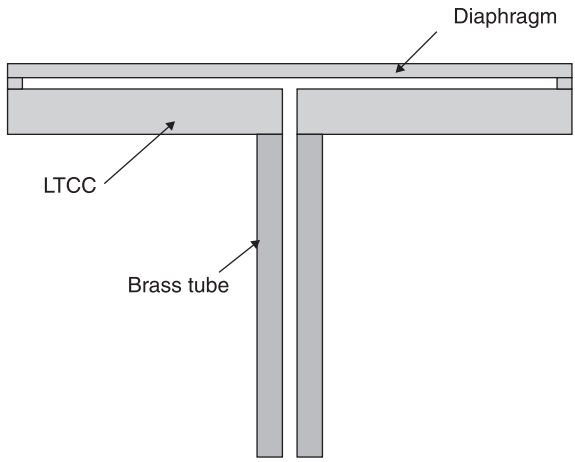

10.10 Piezoresistive LTCC pressure sensor.

50% that of the value found on alumina. This was thought to be due to reactions between the silica in the LTCC and the lead in the PZT.

The same group have also demonstrated an LTCC piezoresistive pressure sensor illustrated in Fig. 10.10. The diaphragm had a diameter of 26 mm and a thickness of 0.2 mm, with four piezoresistors printed in the standard layout for diaphragm pressure sensors with two in the centre and two on the edge. The holes where first cut by laser machining and the assembly laminated at 875 °C. The sensors functioned well in the intended low pressure regime but the offset voltage did exhibit a large temperature dependence of 30–80 μV/K.

The most impressive demonstration of the capability of the LTCC assembly process for microstructures is demonstrated by a solid propellant-based micro thruster (Thakur *et al.*, 2010). Features were laser machined and then up to eight patterned layers were laminated together to form the final structure. The laminated assembly forms a 420 mm thick cavity with an exhaust nozzle located at the side of the chamber. The thick-film aspect of this device is routine, with a screen-printed resistor being located in the chamber for ignition purposes. The conductive tracks and wire bond pads were printed using DuPont 6146 Ag/Pd paste, whilst the resistors were formed from DP 5092D or DP CF011 compositions. After filling with suitable propellant, this was ignited by the thick-film heater, producing an average thrust of 19.5 mN for 150 ms.

10.4 Conclusion and future trends

Thick-film materials will continue to be a niche process within MEMS that does offer some useful advantages but also suffers some drawbacks. Thick-films often offer improved material properties compared to their thin-film counterparts and

© Woodhead Publishing Limited, 2012

also benefit from a very simple low-cost printing deposition process. The drawbacks include the reactions that can occur when printing on silicon, the relatively poor resolution achievable compared to photolithography and the physical nature of the printing process. The properties of some printed materials, such as piezoelectrics, are also inferior to their bulk counterpart, which will reduce the performance of the MEMS device.

These challenges are being addressed and further improvements can be expected with time. Printed piezoelectric film properties, for example, are being improved by increasing the densification and reducing the porosity of the films. The use of nano-size particles to reduce firing temperatures is also an avenue of research, with attention being paid to grain growth during sintering. Alternative printing processes are another area where significant improvements could be obtained that radically increase the use of printed films in MEMS. Digital printing techniques such as ink-jet printing are attractive because they are non contact and do not require a screen. The challenge with ink-jet printing is achieving inks loaded with enough active material to demonstrate useful film properties whilst maintaining the rheology required for the ink-jet process. The viscosity requirements for ink-jet inks are much lower than for screen printing and therefore the inks cannot contain the same concentration of active particles possible in an ink developed for screen printing. Ink-jet printing is also not well suited to achieving thick-printed films: numerous prints are required to build up film thicknesses.

One printing technique that offers the benefits of digital printing without the rheological constraints on the inks is dispenser printing. This involves the use of a pneumatically driven syringe and a computer-controlled x, y, z stage to deposit inks in the pattern required. It is non-contact, does not require a screen and can print existing thick-film inks without modification. Another significant advantage is the potential increase in resolution. Syringe nozzles are available with 1 μm diameter orifices offering the potential for a pattern resolution comparable with most MEMS microstructures.

10.5 References

Andrijasevic D., Smetana W., Zehetner J., Zoppel S. and Brenner W. (2007), 'Aspects of micro structuring low temperature co-fired ceramic (LTCC) for realisation complex 3D objects by embossing', *Microelectronic Engineering*, 84, 5–8, *Proceedings of the 32nd International Conference on Micro- and Nano-Engineering*, May–August 2007, pp. 1198–1201.

Beeby S. P. and White N. M. (2001). 'Silicon micromechanical resonator with thick-film printed vibration excitation and detection mechanisms', *Sensors and Actuators A: Physical*, 88, 189–197.

Beeby S. P., Blackburn A. and White N. M. (1999), 'Processing of PZT piezoelectric thick-films on silicon for microelectromechanical systems', *Journal of Micromechanics and Microengineering*, 9, 3, 218–229.

© Woodhead Publishing Limited, 2012

Beeby S. P., Grabham N. J. and White N. M. (2001), 'Microprocessor implemented self validation of thick-film PZT/Silicon accelerometer', *Sensors and Actuators A: Physical*, 92, 168–174.

Belavic D., Hrovat M., Holc J., Zarnik M. S., Kosec M. *et al.* (2007), 'The application of thick-film technology in C-MEMS' *Journal of Electroceramics*, 19, 4, 363–368.

DeVoe D. L. (2001), 'Piezoelectric thin film micromechanical beam resonators', *Sensors and Actuators A: Physical*, 88, 3, 263–272.

Dorey R. A. and Whatmore R. W. (2005), 'Ceramic thick-films for MEMS', *in* Setter N. (ed.), *Electroceramic-based MEMS*, Springer, New York, pp. 177–197.

Fonseca, M. A., English J. M., von Arx M. and Allen M. G. (2002), 'Wireless micromachined ceramic pressure sensor for high-temperature applications,' *Journal of Microelectromechanical Systems*, 11, 4, 337–343.

Ginet P., Lucat C., Ménil F. and Battaglia J.-L. (2007), 'Modelling and characterizing a screen-printed metallic electrothermal microactuator', *International Journal of Applied Ceramic Technology*, 4, 423–427.

Hindrichsen C. C., Almind N. S., Brodersen S. H., Lou-Moeller R., Hansen K. *et al*. (2010), 'Triaxial MEMS accelerometer with screen-printed PZT thick-film', *Journal of Electroceramics*, 25, 108–115.

Hindrichsen C. C., Larsen J., Thomsen E. V., Lou-Moeller R. and Hansen K. (2009), 'Circular piezoelectric accelerometer for high band width application', *Proceedings of IEEE Sensors Conference*, Christchurch, NZ, October 25–28, pp. 475–478.

Hindrichsen C. C., Thomsen E. V., Lou-Moeller R. and Bove T. (2006), 'MEMS accelerometer with screen-printed piezoelectric thick-film', *Proceedings of IEEE Sensors Conference*, Korea, October 22–25, pp. 1477–1480.

Hrovat M., Belavic D., Ursic H., Kita J., Holc J. *et al*. (2008) 'An investigation of thick-film materials for temperature and pressure sensors on self-constrained LTCC substrates', *Electronics System-Integration Technology Conference (ESTC)*, pp. 339–346.

Ko S. C., Kim Y. C., Lee S. S., Choi S. H. and Kim S. R. (2003), 'Micromachined piezoelectric membrane acoustic device, *Sensors and Actuators A: Physical*, 103, 1–2, 130–134.

Koch M., Harris N., Evans A. G. R., White N. M. and Brunnschweiler A. (1998), 'A novel micromachined pump based on thick-film piezoelectric actuation', *Sensors and Actuators A: Physical*, 70, 98–103.

Kok S.-L., White N. M. and Harris N. R. (2009), 'Fabrication and characterisation of free-standing thick-film piezoelectric cantilevers for energy harvesting', *Measurement Science and Technology*, 20, 124010.

Lakhmi R., Debeda H., Dufour I. and Lucat C. (2010), 'Force sensors based on screen-printed cantilevers', *IEEE Sensors Journal*, 10, 6, 1133–1137.

Lou-Moeller R., Hindrichsen C. C., Thamdrup L. H., Bove T., Ringgaard E. *et al*. (2007), 'Screen-printed piezoceramic thick-films for miniturised devices', *Journal of Electroceramics*, 19, 333–338.

Lucat C., Ginet P., Castille C., Debeda H. and Menil F. (2008), 'Microsystems elements based on free-standing thick-films made with a new sacrificial layer process', *Microelectronics Reliability*, 48, 6, *Thermal, Mechanical and Multi-physics Simulation and Experiments in Micro-electronics and Micro-systems (EuroSimE 2007)*, June, pp. 872–875.

Maas R., Koch M., Harris N., Evans A. and White N. (1997), 'Thick-film printing of PZT onto silicon', *Materials Letters*, 31, 109–112.

Marzencki M., Ammar Y. and Basrour S. (2008), 'Integrated power harvesting system including a MEMS generator and a power management circuit', *Sensors and Actuators A: Physical*, 145–146, 363–370.

© Woodhead Publishing Limited, 2012

Sippola C. B. and Ahn C. H. (2006), 'A thick-film screen-printed ceramic capacitive pressure microsensor for high temperature applications', *Journal of Micromechanics and Microengineering*, 16, 1086–1091.

Suzuki M., Kobayashi Y., Aoyagi S., Tajiri H. and Nagahata T. (2009), 'Micro accelerometer using screen-printed $BaTiO_3$ film on ceramic substrate', *Proceedings of 15th International Conference on Solid-State Sensors, Actuators and Microsystems*, Transducers 2009, Denver, CO, USA, pp. 1174–1177.

Thakur J., Pratap R., Fournier Y., Maeder T. and Ryser P. (June 2010), 'Realization of a solid-propellant based microthruster using low temperature co-fired ceramics', *Sensors and Transducers Journal*, 117, 6, 29–40.

Trolier-McKinstry S. and Muralt P. (2005), 'Thin film piezoelectrics for MEMS', *in* Setter N. (ed.), *Electroceramic-based MEMS*, Springer, New York, pp. 199–215.

Xu B., White D., Zesch J., Rodkin A., Buhler S. *et al*. (2005), 'Characterisitics of lead zirconate titanate ferroelectric thick-films from a screen-printing laser transfer method', *Applied Physics Letters*, 87, 192902.

Yamashita K., Katata H., Okuyama M., Miyoshi H., Kato G. *et al*. (2002), 'Arrayed ultrasonic microsensors with high directivity for in-air use using PZT thin film on silicon diaphragms, *Sensors and Actuators A: Physical*, 97–98, 302–307.

Yan T., Jones B. E., Rakowski R. T., Tudor M. J., Beeby S. P. *et al.* (2004), 'Development of metallic digital strain gauges', *Measurement and Control*, 37, 7, 214–216.*10.6* Complete micromachining process for the silicon/thick-film PZT accelerometer.

© Woodhead Publishing Limited, 2012

11

Printed semiconducting gas sensors

V. GUIDI, C. MALAGÙ, M. C. CAROTTA and B. VENDEMIATI, University of Ferrara, Italy

Abstract: Most common metal-oxide semiconductors featuring chemo-resistive effect, such as SnO_2, TiO_2, WO_3 and ZnO, have been examined as functional materials for gas sensors via thick-film technology. Analysis of the mainly accepted electrical transport models through polycrystalline semiconductors has been carried out and compared to experimental evidence. A theoretical conduction model able to determine the characteristic length below which a material can be properly considered as nanostructured has been considered under thermionic and field-assisted electron emissions. The main methods of material synthesis have been extensively described with special attention to wet chemical routes for powder preparation. The typical parameters for screen-printable pastes obtained from the powders have been considered for deposition of the sensing layers. Electrical, structural and morphological characterizations have been explored in order to highlight the main features of the materials as pure compounds or in a mixture with other oxides. Finally, some concrete implementations carried out at our laboratory have been shown for the possible usage in environmental or industrial frameworks.

Key words: thick-film gas sensors, nanomaterials, semiconductor oxides, chemo-resistive gas sensors.

Dedication: In memory of Professor Giuliano Martinelli – a wonderful person and an eminent scientist.

11.1 Introduction

Semiconductor gas sensors using metal oxides are a popular choice for detecting a wide range of gases. There is a variety of structures, materials and working principles used for semiconductor gas sensors. This chapter will review the most important types of semiconductor gas sensor and it will look at the printing technology for fabricating these sensors. In solid-state metal oxides, the difference in electro-negativity of a metal atom from oxygen changes the polarity of the electron distribution of bond orbitals, thus modulating the physical properties of the solid, including conductivity. In fact, metal oxides are an immensely wide class of materials whose electrical properties span over the full range of conductivity, from insulators to superconductors with semiconductors and metals in between. The high electro-negativity of oxygen renders this atom as negatively polarized, although there is a class of oxides where the metal-to-oxygen bond is weak enough to allow a reversible chemical redox reaction at the surface with a

© Woodhead Publishing Limited, 2012

gaseous species. This condition is met for the metals with amphoteric behaviour, i.e. for which the difference in electro-negativity with oxygen is moderately low.

From the solid-state standpoint, this last occurrence forms a series of energy levels within the energy band-gap at the surface, which are filled up by electrons up to the Fermi level, depleting the volume of the solid neighbouring the surface of electrons. This process builds up a Schottky junction at the surface, which determines charge transport within the semiconductors (see section 11.2). Unlike Λ-probes, for which their elevated working temperature (about 1000 °C) forces diffusion of oxygen deep into the bulk of the material, within 200–600 °C, the interaction of gases with the sensing material occurs mainly at the surface. Thus, polycrystalline materials are recommended to magnify the extension of the surface exposed for reaction. It means that electrical conduction is governed by grain-to-grain percolation, which is in turn established by the height of the inter-grain barrier. Redox reaction of the anions and more rarely of the cations in the metal oxide with a gas causes charge exchange with the solid, leading to lowering or increasing of the energy barrier. In summary, current conduction in a metal oxide is established by the concentration of a gas in the surrounding atmosphere and this is normally referred to as a chemo-resistive effect, i.e. the transduction mechanism of solid-state semiconducting gas sensors (Madou and Morrison, 1989).

The first evidence of the dependence of electrical conductance on the concentration of gases in the environment dates back more than 50 years to a seminal work by Brattain and Bardeen (1953). However, the first generation of commercial devices was introduced in the 1960s by Taguchi, who established Figaro Engineering, Inc. The company's target was the commercialization of small sensing units in the monitoring of explosive gases for Japanese urban agglomerates, which were characterized by wooden houses and widespread gas furnaces. The base material for the devices was SnO_2 deposited via thick-film technology. Regarding the far-sightedness of this choice, we simply claim that Figaro Inc. is nowadays the largest manufacturer of gas sensors, SnO_2 is commonly acknowledged as the 'king material' for gas-sensing and thick-film deposition is still the most widely used technique for the commercial production of sensors.

Since the pioneering scientific and commercial experiences, a big effort has been made to develop higher-performance sensing units over the years, fostered by the need for modern societies to monitor gaseous pollutants, malodours, volatile flammable substances, dangerous leaks and more. In this regard, chemo-resistive sensors grabbed the attention of researchers and investors in preference to other techniques because these sensors can be fabricated cheaply, are very compact and consume little power. In spite of these positive features, there are still drawbacks as highlighted in the following. In some senses, the so-called '3S-rule', i.e. sensitivity, selectivity, stability, is a mandatory direction toward which research must be addressed.

Regarding sensitivity, a large contribution was made by the significant development that nanotechnology underwent in the 1990s, and it significantly impacted the field of gas sensing. The possibility of scaling down the grain size in

© Woodhead Publishing Limited, 2012

the film proportionally enlarged the specific surface involved in gas sensing. In a seminal work, Yamazoe (1991) experimentally showed that a huge improvement in gas response was correlated to a decrease in grain size. Since then, nanophased semiconducting metal oxides have been pre-eminent candidates for gas sensing using the chemo-resistive effect. The level of sensitivity that is currently reached is quite satisfactory and makes any search for still higher sensitivity unnecessary at the present time.

The question of selectivity has not undergone the same boost as that of sensitivity. Chemical reaction at the surface of a given material normally proceeds for a variety of gaseous molecules, i.e. the sensor suffers a lack of selectivity. Indeed, operating with a gas admixture composed of different molecules that a semiconductor may interact with is certainly not unusual; ultimately, sensing in a humid environment is quite normal for working in on-field conditions, and water is unfortunately not an inert molecule for reaction. A first remedy is the use of catalysts in the form of nanoclusters (typically noble metals) spread over the surface of each grain. Except for some specific cases, heterogeneous catalysis ensures only partial solution of the problem, because the molecular species of interest very often lead to similar reactions. In the 1990s and early 2000s, a big effort was dedicated to the study of new materials (such as TiO_2, In_2O_3, WO_3, Fe_2O_3, ZnO, $LaFeO_3$ and others) to investigate their sensing properties. In order to widen the choice of available materials, responding in a diverse way to a given analyte, strong doping, ternary oxides with two metals, in the form of either a mechanical mixture or a solid solution, were intensively investigated. The hope was that an array of films with partly overlapping sensing characteristics would aid the determination of single-species concentrations. Unfortunately the problem is not trivial because sensors respond non-linearly vs. a gas concentration, sometimes with strong cross-sensitivity between chemical species. Software architectures proved helpful in the problem of response deconvolution, in particular the approach relying on neural networks, and more generally in all the techniques of artificial olfactive systems that were adapted to gas sensing. To date, great progress has been made and, under some conditions, the problem of partial selectivity can be coped with, although in most general cases, it is still a problem for chemo-resistive gas sensing.

The last ‘S’ has been probably the toughest problem to solve. As previously mentioned, the rise in sensitivity called forward the use of nanophased materials, which are often in a metastable condition because of the large amount of energy deposited at the surface. This circumstance, combined with the need for keeping a sensor at operational temperature for reversible reaction with gases, often leads to grain coalescence, shrinkage of the specific surface, phase transition, phase segregations and other effects that spoil the response within a time shorter than the duration for which the sensor is designed. Several remedies have been proposed that lead to performance improvement, such as the dispersion of coalescence inhibitors and phase stabilizers for the nanograins, operation at room

© Woodhead Publishing Limited, 2012

temperature via assistance from luminous excitation (to play the role that temperature normally does) and development of novel topologies in the nanomaterials. Regarding the latter, special attention must be paid to the advent of stable single-crystal quasi-one-dimensional semiconductors, normally referred to in the literature as quasi nanotubes, nanorods and nanoribbons, which are promising approaches whose real potential is still to be established (Comini *et al.*, 2002).

The techniques for film preparation can be grouped into two categories depending either on the method used for material preparation, i.e. whether physical or chemical, or on the fashion used for film deposition, that is, thick-film or thin-film technology.

Thick-film deposition normally relies on screen-printing, which is one of the oldest forms of graphic art reproduction known to mankind. A typical thick-film screen consists of a finely woven mesh of stainless steel, polyester or nylon, mounted under tension on a metal loom. The finished screen has apertures for patterning and is held at suitable distance from the substrate. The thick-film paste is transferred onto the top surface of the stencil and a squeegee traverses the screen under pressure. This brings the screen closer to the substrate and forces the paste to flow through the apertures. Normally the pastes contain organic solvents that are needed to achieve the correct viscosity for screen-printing and after deposition they must be evaporated by drying at about 150–200 °C. After drying, adhesion of the film to the substrate is enhanced. Then further annealing is needed, called firing, during which the glass melts, the powders sinter and the film becomes a solid composite material. The function of glass is for binding the film to the substrate and to keep the particles together. Firing is performed in a furnace at a temperature ranging typically between 500 and 900 °C through proper ramping of the temperature, after which the film becomes firmly attached to the substrate. In the case of films for gas sensing, the firing serves also to stabilize the sensing material and to determine grain size and other film properties.

As far as our experience is concerned, one of the main advantages of screen-printing technology for the production of sensing layers is the inherent decoupling between material preparation and film deposition. Here such steps can be optimized separately. This is not the case for some techniques relying on thin-film preparation, for which preparation and deposition are accomplished all at once (e.g. Sberveglieri *et al.*, 1990; Ferroni *et al.*, 2003). For screen-printing deposition, nanometric powder preparation is made mainly via chemical wet methods, e.g. sol-gel synthesis, where catalysts, grain coalescence inhibitors can be added up to the precursors. As an alternative to sol-gel, laser-assisted (Musci *et al.*, 1992) or flame-spray pyrolysis can also be used (Mädler *et al.*, 2002). Then, proper thermal treatment (drying and firing) to stabilize the nanophase to the desired level can be pursued. Eventually, film deposition occurs with the right rheological parameters at the proper temperature. Optimizing this second step results in optimal film porosity and highly reproducible morphological and electrical properties. Porosity

© Woodhead Publishing Limited, 2012

is a key parameter to be controlled: on the one hand, a highly densified aggregation of nanograins would ensure easy current percolation within the film with no critical bottle-neck pathways; on the other hand, too compact a film would result in scarce penetration of the gas-analyte and thereby in incomplete sensing by the volume of the film far from the surface.

The capability of thick-films to sense gases for a variety of applications has been proven over the years. Table 11.1 summarizes some of these gases though it is far from comprehensive and constitutes just an overview of the capability of the method. The table also contains a number of sensing materials used for the purpose.

Thick-film technology is sometimes regarded as a 'conservative approach' to gas sensing via the chemo-resistive effect. Most modern proposals encompass sensing using novel schemes often based on methods borrowed from the technology of fully integrated circuits (e.g. suspended-gate field effect transistors). Screen-printing involves a hybrid technology and this is unlikely to be fully compatible with most futuristic schemes. However, sometimes this is not necessarily a limitation because problems can often be circumvented, as shown by the following example. A potential difficulty that could have risen with screen-printing technology was the implementation of film onto miniaturized micro-hotplates fabricated by silicon micro-fabrication. In some cases, low consumption is a desirable feature, e.g. for portable devices. The need to keep the sensing units at working temperature leads to thermal dissipation, mainly by thermal conductivity through the substrate. The use of thin micrometric insulating SiO_2 membranes onto which a sensing film is deposited ensures operation at a nominal

Table 11.1 Examples of films achieved through thick-film technology

Gas or vapour	Material	Reference
CO	SnO_2	Williams *et al.*, 1994
CO, NO_2, CH_4	SnO_2	Guidi *et al.*, 2002
CO_2	$BaTiO_3$	Hauesler and Meyer, 1996
Ethanol	Fe_2O_3	Tan *et al.*, 2004
H_2	SnO_2	Ansari *et al.*, 1996
H_2S, CH_3SH, $(CH_3)_2S$	$LaFeO_3$	Chu and Siciliano, 2003
HC and VOC	SnO_2	Pijolat *et al.*, 2003
Humidity	$MnWO_4$	Qu and Meyer, 1997
NH_3	ZnO	Rao G. S.T. and Rao D.T., 1999
NO_2	SnO_2	Sahm *et al.*, 2004
NO_2	Cr:TiO_2	Ruiz *et al.*, 2003
NO_2	WO_3	Choi *et al.*, 2003
NO_2	WO_3	Chung *et al.*, 1999
Oxygen	ZrO_2	Izu *et al.*, 2004
Reducing gases	Ga_2O_3	Frank *et al.*, 1996
VOC, benzene, toluene, xylene	In:ZnO	Zhu *et al.*, 2003

© Woodhead Publishing Limited, 2012

temperature with a power more than one order of magnitude lower than for the canonical case with a bulky substrate. The question of whether or not such a thin membrane was capable of tolerating the deposition of a screen-printed film that was ten times thicker was solved using a specifically designed chamfered stencil (Vincenzi *et al.*, 2000).

In summary, we do believe that gas sensing through thick-film technology is, to date, one of the best ways to prepare sensing films for gas detection, its major features being good sensitivity and long-term stability, as witnessed by the use of such technology for producing the overwhelming majority of commercially available gas sensors.

11.2 Principles of operation and modeling

A classical view of the Schottky barrier formation at the surface through drift diffusion theory will be provided, which will be followed by the semi-classical approach to thermionic and field emission in nanostructures. This model for charge-carrier percolation holds for polycrystalline materials, no matter what technique is used for preparation. Both *n*- and *p*-type semiconductors can be used as gas sensors via the chemo-resistive effect, the former category being the most widely used. Therefore, for the sake of simplicity, we will focus our attention on this kind of doping. Other theoretical models for approaching the same systems can be found in the literature (see e.g. Bârsan and Weimar, 2003; Yamazoe, 1991; Lantto *et al.*, 1988).

The density of electrons, n, in the conduction band of *n*-type metal oxide semiconductors can be derived by integrating the Fermi–Dirac distribution over the first Brillouin zone, including second-order expansion of the conduction band near its minimum in k-space, E_c, in terms of the effective mass m_n:

$$n = \frac{2}{\left(2\pi\right)^3} \int\int\int_{1st\,Zone} \left(1 + e^{\frac{E_c - E_F + \frac{\hbar^2 k^2}{2m_n}}{k_B T}} \right)^{-1} d^3k, \qquad [11.1]$$

where k_B is the Boltzmann constant, h is the Plank constant and T the absolute temperature.

By solving Eq. [11.1] in the case of non-degenerate semiconductors, where $E_F << E_c - k_B T$, one obtains:

$$n = N_c e^{\frac{E_F - E_c}{k_B T}}. \qquad [11.2]$$

E_F is the Fermi level and N_c the effective density of states in the conduction band:

$$N_c = 2\left(\frac{m_n k_B T}{2\pi\hbar^2} \right)^{\frac{3}{2}}, \qquad [11.3]$$

© Woodhead Publishing Limited, 2012

which depends only on $T^{3/2}$ and $m_n^{3/2}$.

The Fermi level is in the band gap, therefore it does not coincide with the Fermi energy (because the Fermi surface does not exist in this case), and must be identified with the electrochemical potential of the electrons.

The built-in potential, V_s (see Fig. 11.1(a)), in the case of nanostructured polycrystalline films with grains larger than 10 nm, was measured to be of the order of 1 V (Maffeis *et al.*, 2004) over a depletion region of about 10 nm; the

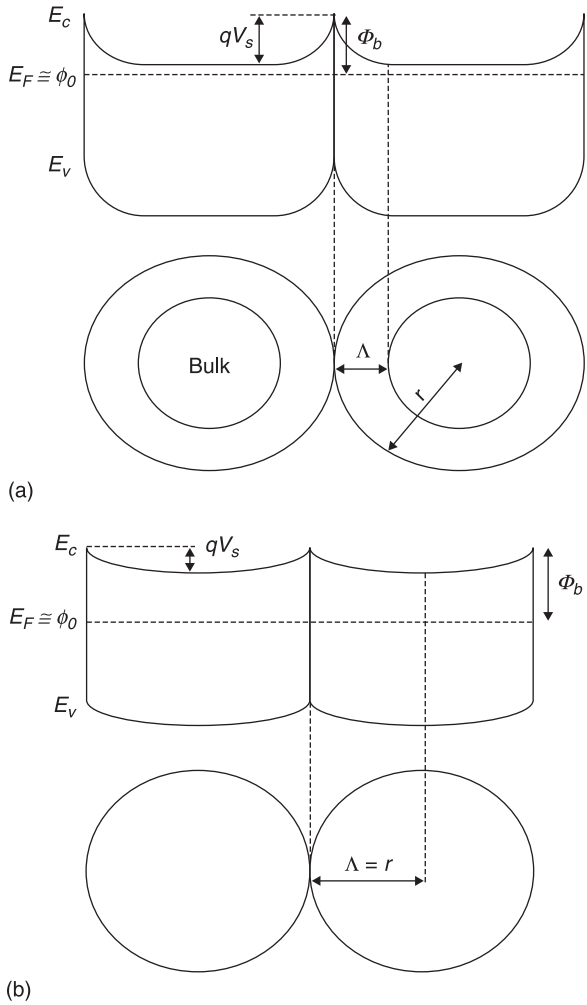

11.1 Grain boundary barrier formation in gas environment. (a) Grain radius is larger than depletion width: the bulk is reached in the core of the grain. (b) Grain radius is equal to depletion width: the grain is fully depleted and band bending starts to flatten.

© Woodhead Publishing Limited, 2012

resulting field is at least two orders of magnitude smaller than the atomic field, which is responsible for the band structure. Therefore, the band structure can be considered unmodified by the electrical field, and the band gap and the effective mass value can still be assumed as constant.

Even more importantly, one is allowed to consider the semi-classical dependence of the conduction band bottom, E_c, on space coordinate x: $E_c = E_c(x)$, thus the built-in field in the depletion region turns out to be:

$$F(x) = \frac{1}{q}\frac{dE_c(x)}{dx}. \qquad [11.4]$$

The zero of energy is set in E_c in the bulk (see Madou and Morrison, 1989; Shur, 1990, pp. 140–199), i.e. far from the surface (interface between two grains, as shown in Fig. 11.1(a)). The donor states constituting the doping level, N_d, are almost all ionized at working temperatures (300–400 °C), therefore, in the bulk, $n = N_d$ with very good approximation. Thanks to this assumption we rewrite Eq. [11.2] for the bulk of the material. Since $E_c(bulk)$ is zero, it follows:

$$N_c e^{\frac{E_F}{k_B T}} = N_d. \qquad [11.5]$$

Eq. [11.5] is an equality between constants and can be applied to Eq. [11.2] to work out the density of electrons in the conduction band as a function of x:

$$n(x) = N_d e^{\frac{-E_c(x)}{k_B T}}. \qquad [11.6]$$

With this choice of zero reference, the conduction band value at the surface coincides with q (positive value of electron charge) times V_s:

$$n(surface) = N_d e^{\frac{-qV_s}{k_B T}}. \qquad [11.7]$$

The current density in a non-degenerate semiconductor is, by applying Einstein's relationship for diffusion and the definition of the quasi-Fermi level, E_{Fn}, to one-dimensional case:

$$J_n = \mu_n n \frac{dE_{F_n}}{dx}, \qquad [11.8]$$

where μ_n is the mobility of the majority carriers (electrons).

Therefore, the current only depends on the electrons capable of reaching the surface conduction band, i.e. those described by Eq. [11.7], and we have, by noticing that the slope of the quasi-Fermi level is proportional to the field due to the external bias along the device, F_{ext}:

$$J_n = q\mu_n N_d e^{\frac{-qV_s}{k_B T}} F_{ext}. \qquad [11.9]$$

The conductivity due to the presented mechanism is then:

$$\sigma = \sigma_0 e^{\frac{-qV_s}{k_B T}}, \qquad [11.10]$$

© Woodhead Publishing Limited, 2012

where $\sigma_0 = q\mu_n N_d$ represents the bulk conductivity. Eq. [11.10], obtained through the drift-diffusion approach, is most widely used to describe the gas sensor electrical response.

In the following, we will analyze deeply the built-in potential and the Schottky barrier formation at the intergrain interface through the mechanism of pinning of Fermi level (Malagù *et al.*, 2004a). The case is sketched in Fig. 11.1(a),(b): a level ϕ_o is defined in the gap, above which the surface states are acceptor-like (neutral when empty) and below which are donor-like (neutral when full) (Bardeen, 1947). The approximation for which gap states above E_F are empty and states below are full holds, so that when E_F coincides with ϕ_o the surface is neutral (all donors are full and all acceptors empty). In the case of *n*-type semiconductors, when oxygen is being adsorbed in the form of O_2^- or O^-, electrons of the conduction band become trapped in the surface acceptors and the conduction band bends, increasing its distance from the Fermi level (Malagù *et al.*, 2004b). Thus, the built-in potential V_s increases and a depletion region develops whose amplitude is Λ, the depletion region width, where the electron density is very low (Fig. 11.1(a)). The position of ϕ_o with respect to the $E_c(surf)$ is constant for a given case, independent of the band bending:

$$L_o = E_c(surf) - \phi_o. \qquad [11.11]$$

The independence of band structure on band bending is assured by the observation on the field magnitude expressed above (Tersoff, 1984). At equilibrium, the surface states below E_F and above ϕ_o are full and acceptors, thus they constitute the negative net surface charge that compensates for the positive space charge, the density of which is N_d [m^{-3}]. The surface density of negatively charged states, N_s [m^{-2}], is given by the product of the energy density of surface states multiplied by the interval of energies where the charged surface states are present:

$$N_s = D_{ss} \times (E_F - \phi_o). \qquad [11.12]$$

When the energy density of surface states D_{ss} is very large, E_F tends to ϕ_o and the Schottky barrier height ϕ_b ($E_c(surf)$-E_F) becomes equal to L_o, as defined in Eq. [11.11]. This is the so-called pinning of the Fermi level, which means that the Schottky barrier is determined only by the position of the neutral level in the gap and is independent of V_s (as can be seen by comparing Fig. 11.1(a) and 11.1(b)).

For the sake of simplicity, we consider that the main adsorbed charged oxygen species is O^-, so the only relevant reaction is reduced to (Sahm *et al.*, 2006):

$$O_2(g) + 2S + 2e^- \Leftrightarrow 2O^-(a), \qquad [11.13]$$

where *S* corresponds to adsorption sites at the surface, (*g*) refers to the gas phase, (*a*) to an adsorbed species and e^- is an electron. Eq. [11.13] states that more oxygen in the ambient implies a larger amount of chemisorbed oxygen and thus higher intergranular barriers and lower film conductivity, as Eq. [11.10] indicates. The mechanism of Eq. [11.13] is responsible for V_s formation (band bending) as described above.

© Woodhead Publishing Limited, 2012

It is well established that tin oxide is a wide band-gap (3.6 eV) semiconductor in which oxygen vacancies are the dominant defects and they behave as donor impurities (Samson and Fonstad, 1973). The oxygen exchange equilibrium is regularly written as

$$O_O \Leftrightarrow V_O^{\bullet\bullet} + 2e^- + \frac{1}{2}O_2, \qquad [11.14]$$

where $V_o^{\bullet\bullet}$ is an empty ionized oxygen vacancy (Kamp *et al.*, 2001). The corresponding mass-action law is:

$$K = \left[V_O^{\bullet\bullet}\right]\left[e^-\right]^2 p\left(O_2\right)^{\frac{1}{2}}. \qquad [11.15]$$

Square brackets denote concentrations, K is the mass action constant, and $p(O_2)$ is oxygen partial pressure.

We are interested here in the basic mechanisms related to the dependence of surface barriers on the pressure of oxygen under equilibrium. Oxygen interstitials must be the diffusing species that alter the vacancy density in the grains of the sensing film and the mechanisms involved in the whole sensing process.

When an *n*-type sensor is exposed to oxygen there is a rapid increase of resistivity, indicating that equilibrium at the surface has rapidly been reached (Eqs. [11.13] and [11.10]). Then, slow resistance increase is observed, which cannot be understood without invoking another mechanism besides surface adsorption. We have explained these results as being a consequence of a decrease of vacancy density with time (Ponce *et al.*, 2008).

For a change in donor concentration, defects constituting donors must vary, i.e. the density of oxygen vacancies must be altered. Two possible mechanisms can be proposed: first, the migration of oxygen vacancies; and second, the generation or annihilation of vacancies. At first sight, both alternatives seem to be equivalent. However, such mechanisms alter the electrical properties very differently.

In the first mechanism, charged oxygen vacancies would be mobile. Since we are dealing with charged species, oxygen vacancies could move through the solid due to a concentration gradient (diffusion) or due to an electrical field (drift). Within the depletion region there is a strong electrical field created by the ionized donors, being the oxygen vacancies themselves. Due to this electrical field, directed from the bulk to the surface, ionized oxygen vacancies would drift towards the surface irreversibly. This is not the best way to justify the experimental evidences shown here for their reversible characteristics, thus it will not be considered in this book, however the non constant doping profile along the space charge region is presently under study. Moreover, the electrical field at the depletion region is very strong to the point of sweeping the vacancies toward the grain surface, which would lead to the collapse of the intergranular barriers. It could be argued that a concentration gradient would be created and then diffusion in the opposite direction would appear. However, as discussed in detail by Romppainen and Lantto (1988), the density of oxygen vacancies under equilibrium would be orders of magnitude larger than it can physically be, close to the grain

© Woodhead Publishing Limited, 2012

surfaces, for the normally acknowledged barrier heights, but it is consistent for lower barriers.

The second possible mechanism is the atomic oxygen diffusion in and out of the grains. Oxygen interstitials would alter the concentration of oxygen vacancies and then the intergranular barriers. Since oxygen interstitials are neutral, the electrical field at depletion regions does not affect their distributions and thus this mechanism is consistent with the reversibility observed in experiments (see section 11.4). If one used Eqs. [11.14] and [11.15] without further analysis, they would imply that the density of vacancies is inversely related to the number of electrons. If this were the case, the density of oxygen vacancies would collapse because of the electron density change across depletion regions. It has been shown that this is not the case and that, in equilibrium, the doping concentration along the grains is constant (Romppainen and Lantto, 1988).

This implies that in equilibrium the density of vacancies is independent of the *n*- or *p*-type character of the sample.

The presented findings allow us to describe the sensing mechanism in tin oxide as follows. It is assumed that temperature is such that species at grains of the sensing film can be considered in equilibrium and that the relevant bulk imperfections are anion interstitials and vacancies. The system also includes the environment where the sensor operates. If the oxygen pressure increases, the amount of adsorbed oxygen increases and the Schottky barrier height increases as well. More oxygen at the surface produces the diffusion of oxygen into the bulk as interstitials establish a new equilibrium between the surface and the bulk in which the amount of vacancies within grains is lower (Eq. [11.14]). Interstitials are mobile and neutral and vacancies are charged but once created they cannot be dragged by the field at the depletion region. (Also, as shown, the numbers of vacancies and interstitials do not depend on the number of electrons present.). When the oxygen pressure is decreased, the lack of equilibrium between the bulk and the surface provokes oxygen diffusion to the grain surface. Simultaneously, new vacancies are created and the system recovers. If the sensor does not recover, we have to consider that at least one of the processes involved is not fast enough for the system to reach equilibrium, or that the system was not originally in equilibrium. By comparing Fig. 11.1(a) and 11.1(b) one can understand that the effect of oxygen in-diffusion in a grain makes Λ increase until it reaches the value of r, the grain radius, then the bottom of the conduction band starts to be lifted and V_s decreases, but the Schottky barrier is pinned to a constant value. From the classical interpretation of thermionic conduction, explained above, conductivity would not change dramatically, since the distance of E_c(surf) from the E_F stays the same. Instead, the tunneling probability of barrier crossing is shown to decrease much more. It was recently demonstrated that an interpretation relying only on thermionic effect of conductivity, normally acknowledged in the field of semiconductor gas sensing, is inaccurate as it neglects tunneling (Malagù *et al.*, 2008).

The tunneling and thermionic contributions to the current density, normalized with respect to the flat band case, were calculated following the classical work of

© Woodhead Publishing Limited, 2012

Crowell and Rideout (1969) for a single parabolic barrier. The whole calculation, for the double Schottky barrier at the interface (as that shown in our model; see Fig. 11.1(a), 11.1(b)), resulted in a factor of 2 in the exponent of the tunneling part of Eq. 13 in Crowell's cited paper. Thus, the tunneling contribution, here called I_1, and the thermionic one, here called I_2, turned out to be:

$$I_1 = \frac{qV_s}{k_B T}\int_0^1 E \exp\left\{-\frac{qV_s}{k_B T}\left[\alpha + \frac{2k_B T_y(\alpha)}{E_{00}}\right]\right\} d\alpha$$
$$I_2 = Exp\left(-\frac{qV_s}{k_B T}\right), \qquad [11.16]$$

where:

$$y(\alpha) = (1-\alpha)^{0.5} - \alpha \ln\left[\frac{1+(1-\alpha)^{0.5}}{\alpha^{0.5}}\right]$$
$$\alpha = \frac{E}{qV_s} \qquad [11.17]$$
$$E_{00} = \frac{qh}{4\pi}\left(\frac{N_d}{m\varepsilon_n}\right)^{0.5},$$

E being the energy of an electron in the conduction band and ε the permittivity; I_2 is the thermionic term, representing the same behavior described in Eq. [11.10], normalized; whereas I_1 depends on the shape of the barrier and not only on its height.

This model allows us to interpr*et all* resistance variations shown in the other sections of this chapter.

11.3 Functional materials

The major requirement in developing semiconducting metal oxides for chemical sensors, and in particular thick-film gas sensing devices, is related to the control of the parameters that can affect the electrical measurements, as specified below (see e.g. Lutic *et al.*, 2007). Besides the electronic driving of the device, the key issue is the synthesis of engineered oxide nanopowders, the functional materials. The main parameters to be controlled are the sensitivity, the lack of specificity toward the target gas and, as a consequence, the cross sensitivity, meaning that the magnitude of the response to the target gas is affected by the contemporary presence of other gases.

The sensing performance is mainly related to the surface properties (chemical, structural and morphological) of the metal oxide, and the chemistry plays a central role in tailoring its 'receptor' function. The chemistry is also the turning point in

© Woodhead Publishing Limited, 2012

powder-processing to obtain sensing layers with reproducible morphology (porosity, surface geometry, size of the necks . . .) that take part in the gas response and transduction phenomena (Bhattacharyya and Basu, 2010).

Special attention will be devoted to the development of nanopowders with tailored characteristics via synthetic liquid–solid transformations performed under mild conditions, also called wet methods. As for any investigation concerning nanopowder synthesis, an accurate morphological, compositional and structural characterization of achieved products plays a very important role. Such studies assist the synthesis with feedback information towards the realization of a material with optimal features for gas sensing. Several specific works have dealt with this topic in the literature (see e.g. MRS Spring Meeting, 2006 and MRS Spring Meeting, 2010). Therefore, such aspects will not be treated in this chapter.

A detailed list of the parameters controlling the performance of both powders and films is shown in Table 11.2.

Chemical methods yield nanopowders with higher performing properties than the conventionally processed powders. The conventional method both for pure and multi-component powders is a solid state reaction reaching processing temperatures typically above 1000 °C. The method is not considered suitable for the synthesis of nanopowders for gas sensing because of a few disadvantages

Table 11.2 Chemistry-controlled properties of nanopowders influencing gas sensing in the powder and processing-controlled properties of film influencing gas sensing

In the powder	Enhancing
Crystalline structure	Not available
Particle size distribution	Narrow around the average
Particle morphology	Homogeneous
Porosity	Mesoporous (20–200 Å)
Purity	Pure, negligible presence of by-products
Specific surface area	As high as allowed by the route and kind of material
Stoichiometry	Oxygen vacancies Chemical homogeneity on molecular scale
In the film	**Enhancing**
Active surface area	As high as allowed by kind of powder and powder processing
Densification after firing	Low
Grain size	Twice the depletion width
Grain size distribution	Narrow around the average
Porosity	Mesoporous (20–200 Å)
Stoichiometry	Oxygen vacancies Chemical homogeneity on molecular scale
Texture of the film	Homogeneous, ex: absence of *hill-valley* effect
Thickness of the film	Depends on the functional material and film processing

© Woodhead Publishing Limited, 2012

Table 11.3 Disadvantages of conventional solid-state synthesis route for powders

Formation of undesirable crystalline phases	
Large grain size	At best about 0.1 μm
Inhomogeneity in grain size	Reducing the grain size by milling can introduce chemical impurities
Poor chemical homogeneity	Critical when doping is required such as grain growth inhibitor or electronic properties promoter

(see Table 11.3). Nanomaterials can also be produced by gas–solid processes, such as in D'Souza and Richards (2007) or in Segal (1997).

Hereafter, we provide a selection of the most well used wet methods, such as co-precipitation, and the sol-gel, hydro-thermal route, which will be described with reference to practical cases of interest.

11.3.1 Co-precipitation

Co-precipitation is used to prepare multicomponent and/or doped oxides via precursor formation, a pure or a variously complex multicomponent intermediate precipitate. The process depends on the ions in the starting materials, usually inorganic salts, precipitated by the addition of stoichiometric amounts of bases or acids. The reaction medium is usually water. The precursor is irreversibly converted into the oxide by calcination, typically performed between 400 and 900 °C. The time and temperature of the calcination belong to the chemical nature of the precursor itself and are evaluated via thermal analysis. The morphology and the specific surface area of the final oxide result as a trade-off between those two parameters. Co-precipitation allows an intimate mixing of all the desired ions in the oxide, maintaining chemical homogeneity on the molecular scale (Segal, 1997). Doping is a chance to enhance or inhibit the chemical and/or physical behavior of nanopowders whether the behavior is intentional or not. In the reaction, close attention to experimental conditions (pH, temperature, concentration) is required. Chemical homogeneity can be enhanced by sonochemical treatment with the application of ultrasound waves, ranging between 20 kHz and 10 MHz, on the reacting mixture. The resulting precursor is a function of the frequency imparted (Buzby *et al.*, 2007). Moreover, SEM analysis assisted by Energy Dispersive Spectrometry (EDS) can be useful to control the elemental composition of small areas of certain samples.

A crucial point of co-precipitation is the kinetically driven control of the particle size and its distribution. In fact, very often the precipitation runs uncontrolled due to the difficulty in matching the suitable experimental conditions. After calcination, the nanopowder undergoes morphological and structural characterization, usually through transmission or scanning electron microscopy (TEM, SEM), specific

© Woodhead Publishing Limited, 2012

surface area measurement by BET (Brauner, Emmett, Teller) method and finally by x-ray diffraction (XRD) analysis.

Synthesis of $LaFeO_3$ powders

$LaFeO_3$ is a highly nonstoichiometric ABO_3 p-type semiconducting perovskite. Its catalytic properties are useful in toxic and noxious gas monitoring, such as NO_2 and CO. For sensing applications, both controlled porous structure and tailored grain size are essential (see, for instance: Toan *et al.*, 2003; Traversa *et al.*, 1995, 1998). $LaFeO_3$, synthesized via co-precipitation, results in nanoporous crystals with high chemical homogeneity. Figure 11.2 shows the general scheme of co-precipitation route for $LaFeO_3$.

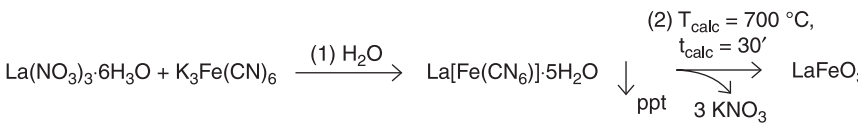

11.2 General scheme of co-precipitation route for $LaFeO_3$: (1) dissolution of the salts in the proper amount of solvent; (2) the cyano-complex (the precursor) is submitted to calcination to gain the $LaFeO_3$ oxide.

Synthesis of WO_3 powders

WO_3 powders for NO_2 detection have been synthesized via precipitation. Two different routes have been compared: the choice of solvent medium is the key point for tuning both the particle size and its distribution (Guidi *et al.*, 2004). Although each reaction starts from WCl_6, the solvent exerts a restraining influence over the precursor precipitate, which leads, in turn, to different morphology of nano-oxide (see Table 11.4).

As highlighted in Traversa *et al.* (1995), for WO_3 there is a wealth of nearly iso-energetic phases (Magneli phases), so that on annealing phase change occurs very easily.

Table 11.4 Synthesis of WO_3 via precipitation routes

Reacting medium	Aqueous/surfactant	Ethanolic/dichetone
Starting material	WCl_6	WCl_6
Precursor	$WO_3 \bullet 2H_2O$	Paramagnetic W(V) complex
Calcination	850 °C maintained for 1 h	850 °C maintained for 1 h
Grain size distribution	Bimodal	Unimodal
Gas sensing	NO_2	NO_2

© Woodhead Publishing Limited, 2012

11.3.2 Sol-gel synthesis method

The sol-gel route consists in the preparation of pure or multicomponent metal oxides by the hydrolysis of inorganic salts in aqueous media or metal-organic compounds in non-aqueous solutions (see for example: Segal, 1997; Buzby *et al.*, 2007; Brinker and Scherer, 1990). A sol-gel reactive solution is a colloidal suspension (the 'sol'), which leads to a solid and wet 3D-skeleton (the wet gel) via sol-gel transition (gelation, the 'gel'). When the solvent is removed under atmospheric pressure, the precursor of the final oxide (the xerogel) is yielded, which is typically an hydroxide, irreversibly converted into the final oxide by calcination at temperatures between 400 and 900 °C.

During the 'sol' formation, the starting material undergoes hydrolysis and then condensation, or cross-condensation in the case of a route for multi-component materials. The essence of sol-gel chemistry is quite simple (Brinker and Scherer, 1990; Gopalakrishnan and Mani, 2009), but considerable efforts are still required in tuning the experimental conditions for tailoring the properties of the powders. The precise choice of both pH and concentration of the reacting mixture play a key role in driving the rate of hydrolysis and, in turn, the morphology, the specific surface area and the presence of by-products. Figure 11.3(a) shows the general scheme of the sol-gel route via inorganic salts.

For the synthesis of multi-component oxides, the route proceeds essentially by the same steps, just considering the co-presence of different cations $M_1 \neq M_2$ starting from step (1).

(1) Dissolution: $(M^{x+} + nH_2O) \rightarrow [M(OH_2)_n]^{x+}$,
x = oxidation number of M
n = coordination number of M^{x+}

(2) Hydrolysis: $[M(OH_2)_n]^{x+} \leftrightarrow [m(OH)_m(H_2O)_{n-m}]^{(x-m)+} + mH^+$
m = number of protons removed from M^{x+}

(3) Self-condensation: $M{-}OY + M{-}OX \rightarrow \underbrace{M{-}(OY){-}M + OX \text{ or } M{-}(OY){-}M{-}OX}$
growing chains, 3D-inorganic skeletons precursor

for simplicity $[M(OH)_m(H_2O)_{n-m}]^{(x-m)+}$ = M–OY or M–OX depending on pH

(3') Cross-condensation: $M_1{-}OY + M_2{-}OX \rightarrow M_1{-}(OY){-}M_2 + OX \text{ or } M_1{-}(OY){-}M_2{-}OX$
$M_1 \neq M_2$

(a)

11.3 (a) General scheme of sol-gel route via inorganic salt (e.g. see Brinker and Scherer, 1990): (1) dissolution of the salt in the reacting media, the metal cations Mx+ are solvated by water; (2) hydrolysis, pH-dependent process; (3) self-condensation, where for graphic simplicity $[M(OH)_m(H_2O)_{n-m}]^{(x-m)+}$ = M–OY or M–OX depending on pH; (3') cross-condensation in the case of the synthesis of a binary oxide where M1 ≠ M2 starting from step (1).

© Woodhead Publishing Limited, 2012

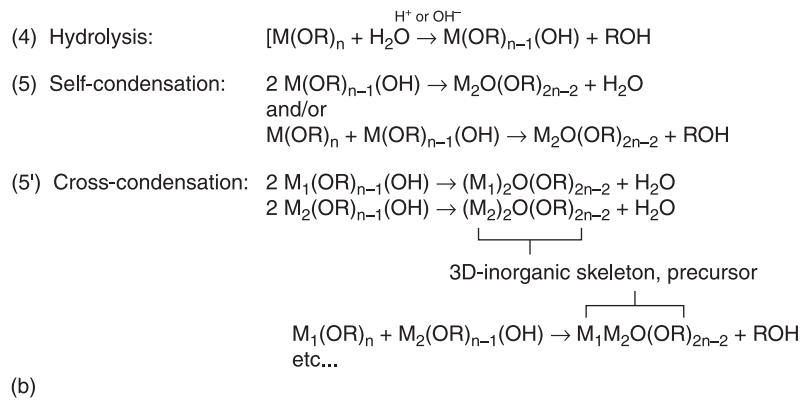

11.3 Continued (b) General scheme of sol-gel route via metalorganic compound (e.g. see Brinker and Scherer, 1990): (4) hydrolysis, acid- or base-catalyzed; (5) self-condensation; (5′) cross-condensation occurs when different alkoxides with M1 ≠ M2 are dissolved in the reaction medium. Step (5′) shows the simplest case i.e. of a binary metal oxide. There are many and complex reactions proceeding in the solution, some of which have been described in the figure. For more information see Segal, 1997, or Brinker and Scherer, 1990.

Metal-organics, hereinafter labeled as $M(OR)_n$ consist of a metal or a metalloid, M, directly linked with the oxygen, and R is usually an alkyl group. Sol-gel processing using metal-organics results in a better-controlled hydrolysis than processing using inorganic salts. Metal-organics are susceptible to atmospheric moisture: the M-O bonds readily react with nucleophiles so they have to be handled under inert conditions and, to avoid by-products, they could be purified before their use. Although a wide set of metal-organics is commercially available, their delicate reactivity and high cost suggest the use of an inorganic salt as starting material, or to synthesize the molecule *in-situ* and use it in a one-pot reaction. Figure 11.3(b) shows the general scheme of sol-gel route via metal-organic compounds.

Synthesis of SnO_2 and MoO_x-SnO_2 powders

SnO_2 is one of the most gas-sensitive semiconductors for environmental monitoring, despite its poor selectivity. This property can be enhanced provided that regular morphology and narrow grain size are accomplished, or by doping. The sol-gel route via Sn-alkoxide reported in Chiorino *et al.* (1999) shows a good chance of achieving suitable powders for the selective detection of NO_2 (see Table 11.5).

© Woodhead Publishing Limited, 2012

Table 11.5 Sol-gel synthesis of SnO_2 via Sn(II)-alkoxide for NO_2 monitoring

Starting material	Sn(II) 2-ethylexanoate
Reacting medium	n-Butanol, water, HNO_3
Calcination	550 °C maintained for 2 h
Average grain size	20 nm
Grain size distribution	Unimodal
Specific surface area (BET method)	31 m^2/g
Total pore volume	$9.8 \bullet 10^{-2}$ cm^3/g
Average pore size	104 Å (mesopores)
Gas sensing	NO_2 (selective)

Synthesis of (Ti, Sn)O_2 solid solutions

Extensive literature reviews the search for better sensing performance with mixed metal oxides and solid solutions when compared to single oxides, because they both have proper physical and chemical properties in respect of the pure counterparts (Radecka *et al.*, 1998; Zakrzewska *et al.*, 2005).

Tin dioxide and titanium dioxide are both wide-gap semiconductors, showing several similarities in structural as well as electronic properties. However, they also exhibit some peculiar differences, such as electrical conductivity and gas sensing behavior. For both materials, the n-type behavior is due to stoichiometric defects, generally oxygen vacancies acting as electronic donor levels, their energetic positions being much deeper inside the band gap for TiO_2.

With respect to the synthesis procedure, in Carotta *et al.* (2009a) it is reported that the sol-gel route via cross-condensation is suitable for yielding a binary solid solution over the whole compositional range.

In particular focusing on the XRD characterization performed on $Ti_xSn_{1-x}O_2$ (x = 0.1, 0.2, 0.3, 0.5, 0.7, 0.9) nano-powders, the Bragg's reflection of the (211) planes linearly shifts with titanium content between the two single oxides.

As highlighted in Carotta *et al.* (2009b), the proportion x = 0.2 is the boundary between tin dioxide and titanium dioxide-like behaviors in structural, electrical and spectroscopic properties.

Synthesis of ZnO powders

In Carotta *et al.* (2009c), zinc oxide with a unimodal grain size distribution of around 30 nm average was prepared via the sol-gel route; see Table 11.6. The films showed a good response toward O_3.

11.3.3 Hydrothermal synthesis

The hydrothermal (HY) processing is 'any heterogeneous chemical reaction in the presence of a solvent, whether aqueous or non-aqueous, above room temperature

© Woodhead Publishing Limited, 2012

Table 11.6 ZnO gas sensors via sol-gel route

Starting material	$Zn(NO_3)_2 \bullet 4H_2O$
Medium	Doubly distilled water
Catalysis	NH_3, pH = 7.5
Calcination	450 °C maintained for 2 h
Average crystallite size	30 nm
Grain size distribution	Unimodal
Gas sensing	O_3

and at pressure greater than 1 atm in a closed system' (Byrappa and Yoshimura, 2001a). The use of different solvents, or a mixture of them, helps to push down the operating pressure and favors both the solubility of the starting materials and the dispersion of the growing particles within the solvent. The reagents used in the HY processing are both inorganic and metal-organic. The precursor of the desired oxide can be synthesized via wet chemistry or via a HY route and then submitted to HY conversion into the oxide.

The equipment used for the processing is an autoclave or a 'bomb' (Byrappa and Yoshimura, 2001b). The technique is being extensively employed to prepare both pure single crystals and polycrystalline materials (Somiya and Roy, 2000). An important application is the synthesis of zeolites, crystalline alumino-silicates used in combination with chemical sensors to enhance their selectivity (Hugon *et al.*, 2000; Sasaki *et al.*, 2002). The powders prepared via HY hinder particle agglomeration yielding fine grain size down to the nanometric domain, and a narrower grain size distribution in comparison with those obtained via wet chemistry routes.

Together with SnO_2, ZnO is one of the first nanomaterials studied for thick-film gas sensing devices. Because of its poor selectivity and high working temperature (400–500 °C), over the years it has become gradually less popular, favoring the study of more promising materials. With emerging powders processing applied in the field of nanoceramics, such as the HY technique, ZnO has been reconsidered with the aim of improving its performances by tailoring, for example, its morphology (Baruwati *et al.*, 2006; Asamoto and Yahiro, 2009).

Hydrothermal synthesis of ZnO

In Baruwati *et al.* (2006), ZnO nanoparticles are synthesized in double distilled water, at 120 °C using an autoclave, showing that HY treatment hinders the ZnO grain growth when compared with ZnO synthesized via the sol-gel route starting from the same reacting conditions (Carotta *et al.*, 2009c), see Table 11.7 and Fig 11.4.

Hydrothermal synthesis of monodispersed perovskite powders

Perovskite-type nanopowders are performing materials for gas sensing devices considering their catalytic behavior (Asamoto and Yahiro, 2009). In Ding *et al.*

© Woodhead Publishing Limited, 2012

Table 11.7 Comparison between the sol-gel (SG) and the hydrothermal (HY) synthesis of ZnO

Process	SG (3.14)	HY (3.20)
Starting material	$Zn(NO_3)_2 \bullet 4H_2O$	$Zn(NO_3)_2 \bullet 4H_2O$
Medium	Doubly distilled water	Doubly distilled water
Catalysis	NH_3, pH = 7.5	NH_3, pH = 7.5
Precursor	$Zn(OH)_2$	$Zn(OH)_2$
Processing conditions	Calcination 450 °C for 2 h	HY 120 °C for 6 ÷ 24 h
Crystal structure	Wurtzite	Wurtzite
Average crystallite size	30 nm	17 nm
Gas sensing	Oxidizing gases (O_3)	Reducing gases (LPG, EtOH)

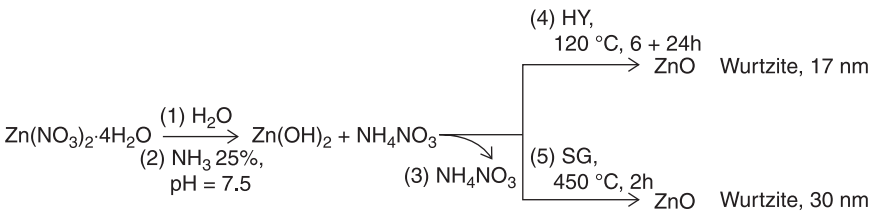

11.4 Chemical equations comparing HY and SG routes for ZnO nanopowders starting from the same reacting conditions. In both reactions $Zn(OH)_2$ is the precursor of the oxide and NH_4NO_3 is the by-product.

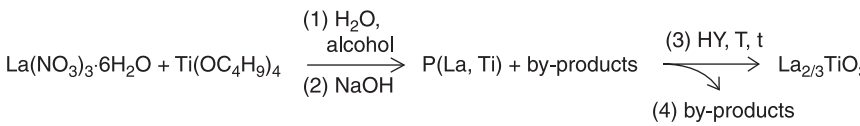

11.5 Chemical equation representing the HY synthetic route for lanthanum titanate nanopowders. The label P(La,Ti) corresponds to the precursor of the final powder whose stoichiometry has been not reported in the literature. The by-products (alcohols, unreacted starting materials and undesired oxides) have been separated from $La_{2/3}TiO_3$ after HY treatment.

(2001), the morphology and structure of perovskites are tailored with HY processing obtaining optimal chemical homogeneity. Details of the synthesis are reported in the Fig. 11.5

Comparison between titania thick-films obtained through sol-gel and hydrothermal synthetic processes

TiO_2 nanopowders are used in thick-film gas sensors for reducing gases. Material calcined above 600 °C undergoes phase transition from anatase into rutile leading

© Woodhead Publishing Limited, 2012

Table 11.8 Comparison between the sol-gel (SG) and the hydrothermal (HY) synthesis of TiO_2

Process	SG	HY
Precursor preparation	SG via hydro-alcoholic solution	SG via hydro-alcoholic solution
Precursor transformation	Calcination, 450 °C for 2 h	HY, 200 °C for 1 or 2 h
TiO_2 grain size	11 nm	7 nm
TiO_2 grain size and crystalline phase after additional thermal treatment		
650 °C	34 nm, 94.5% anatase	10 nm, 100% anatase
750 °C	37 nm, 70% anatase	19 nm, 100% anatase
850 °C	62 nm, 4% anatase	41 nm, 100% anatase

to grain growth and coalescence, reducing its sensitivity toward the environmental changes. In sol-gel processing the morphology of titania is driven by calcination performed on the precursor.

In Carotta *et al.* (2007a), anatase is maintained also after a thermal treatment performed at 850 °C when the precursor has been previously submitted to a HY treatment. A comparison between the results gained in both experiments is reported in Table 11.8.

11.3.4 Rheology, pastes and screen-printing technology

The study of compressing and deforming strengths on a system is the base of rheology, which is crucial to selecting the methodology and the equipment for mass processing the powder. Thick-films are fabricated from printable pastes of functional materials in the form of powder, inorganic additives and organic binders. The structure of a paste easily changes with time, temperature and shear stress. Its physical characteristics depend on all components added to the paste and their interactions (Reed, 1995a). Moreover, the pastes for screen-printing must be thixotropic: during the printing processing, the viscosity of the paste must decrease under an applied shear stress and increase when the stress is removed (Reed, 1995b).

The viscosity of the paste depends on the loading in powder, resins and solvents percentage. Resins dissolved in the solvents yield the organic vehicle, whose viscosity affects that of the paste. The most common formulation for screen-printable paste is listed in Table 11.9; specific paste compositions are highly proprietary.

In screen-printing technology a patterned woven mesh screen defines the pattern to be printed onto a substrate by a squeegee, a polymeric blade whose stiffness is chosen according to the process to be carried out. The screen is a set of

© Woodhead Publishing Limited, 2012

Table 11.9 Typical components in screen-printable paste for gas sensing devices

	Action	Component
Organic vehicle	Functional material (nanopowder)	• Metal • Metal oxide (pure, loaded) • Solid solution or mixed oxide
	Powder sintering aid	• Glass frit (e.g. lead borosilicate)
	Organic wetting agent with low volatility	• Terpineol • Butyl Carbitol or other glycol ethers
	Binder with high molecular weight (resin)	• Ethylcellulose • Acrylic resins • Polyvinylpyrrolidone
	Surfactant	• Lauric acid or other saturated fatty acids
	Catalyst	• Noble metals (e.g. Pt, Pd, Au, Ag)
Rheology of the paste		
	Parameter	Range
	Share rate (s^{-1})	100–1000
	Viscosity (mPa)	70 000–15 000

regularly spaced woven mesh anchored on a rigid frame, under calibrated-tension conditions.

The caliber and type of the cables depend on the detail required for the pattern, the rheology of the paste, shape and roughness of the substrate and the thickness of the final layer. To print a layer with a specific pattern, the paste must flow only through the empty areas of the screen; each printed block will merge into a compact film.

The variables influencing the printing processes are listed in Table 11.10. For both the best pattern resolution and the best printing quality, a trade-off between all the tabulated parameters is a must.

After printing, drying allows the removal of the volatile components from the paste (100–200 °C) (Reed, 1995c).

Shrinkage occurs when the liquid between the solid particles is removed and inter-particle separation decreases; this effect can be reduced when the grain size distribution of the powder is spread over a wide dimensional range. Drying is the step prior to firing, the thermal process that imparts and consolidates the shape of the printed layer, and also develops its microstructure and properties. Unfired ceramics are weak and can sustain only weak stresses without deformation or local fracture. Firing is performed in furnaces under ambient atmosphere between 600 and 1000 °C. The oxygen partial pressure drives the content of metals or metalloids with the proper oxidation state, in the functional material; rarely, some layers need to be treated in a different atmosphere to tailor the stoichiometry of the material itself.

© Woodhead Publishing Limited, 2012

Table 11.10 Parameters influencing the printing processing

	Characteristics and materials	
Substrate	• Mechanical:	Resistant to the pressure applied Resistant to the thermal shocks Low coefficient of thermal expansion
	• Morphological:	Negligible surface defects Negligible bowing
	• Chemical:	Inert toward all components of the paste Inert toward the squeegee's polymer Inert toward the emulsion of the screen
Screen cables	• Polyesters:	Flexible and resilient, for rough surfaces and pastes owing to high viscosity For high squeegee pressure Low resolution of detailed pattern
	• Nylon:	Highly deforming during printing step Poor pattern resolution The best cables for rough substrates and for smoothing the hill-valley effect (irregular covering) For pastes with low viscosity
	• Stainless steel:	Cable's caliber significantly less than those of plastics Only for flat surfaces Excellent for small-area pattern definition, the best for thick-film gas sensors
Squeegee	Hardness: 40–90 Shore's scale	
	• Hard	Flat substrates Better pattern definition
	• Soft	Thick deposition
	Pressure: 1–5 Kg	
	• High	Pastes with high viscosity Poor printing quality
	Velocity: 10–25 mm/sec	
	• Low	Thick deposition Better pattern resolution Pastes with high viscosity

Source: Prudenziati, 1994.

Firing proceeds in three steps: (1) organics burnout and gaseous by-products elimination; (2) sintering; and (3) cooling (Reed, 1995d).

The glass frit, in the paste formulation, is essential to improve the adhesion of the printed film onto the substrate. During sintering it achieves its softening point, turning from a solid to a viscous glassy matrix wetting the grains uniformly. The

© Woodhead Publishing Limited, 2012

matrix draws the particles together enabling their sliding and rearrangement into a denser configuration. Rarely more than 1% w/w of glass frit, with respect to the weight of the powder, is required to coat entirely the grains at the softening point. When the frit is inhomogeneously distributed within the paste, different rates of densification and grain growth may cause inhomogeneous microstructure and a low average density of the resulting film. In Fig. 11.6 the flow chart of the total process is shown.

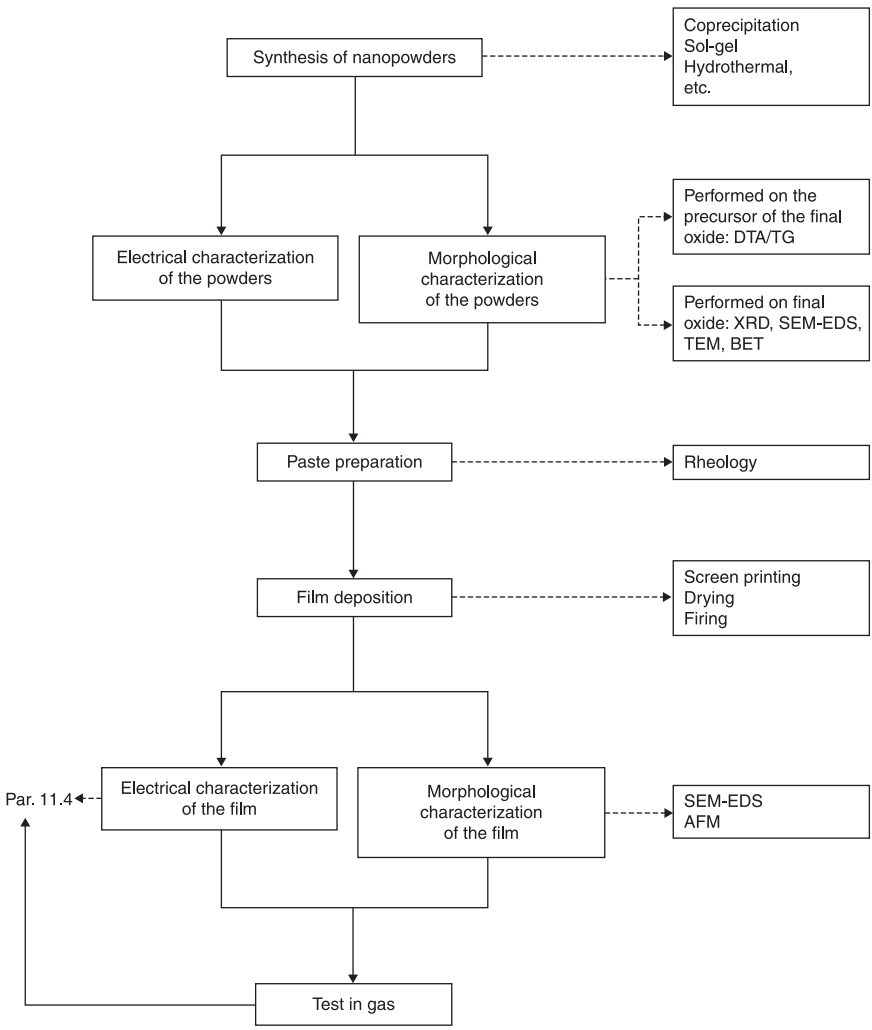

11.6 Flow chart of the process yielding thick-film for gas sensing devices starting from engineered nanopowders.

© Woodhead Publishing Limited, 2012

11.4 Morphological, structural and electrical properties

As highlighted in the previous section, among the most interesting materials for gas sensing, SnO_2, TiO_2, WO_3, ZnO, pure or modified with ion-addition or catalysts are certainly very common.

This section aims to analyze the electrical properties of thick-film gas sensors prepared through the above functional materials, focusing on the peculiar characteristics of each of them.

The interest in wide-gap semiconductor oxides began in the 1960s, when Seiyama *et al.* (1962) discovered their peculiarity of modifying surface properties when interacting with reducing or oxidizing gases. Over the years, a lot of studies have been addressed to improve the sensitivity and selectivity properties of chemo-resistive gas sensors, while probably neglecting the study of factors affecting the repeatability. However, of the various types of metal oxide gas sensors, thick-film gas sensors are surely the most reliable. Indeed, as shown in Fig. 11.7, in which the carbon monoxide concentration was alternately changed between 5 and 40 ppm, the sensor response was quite repeatable.

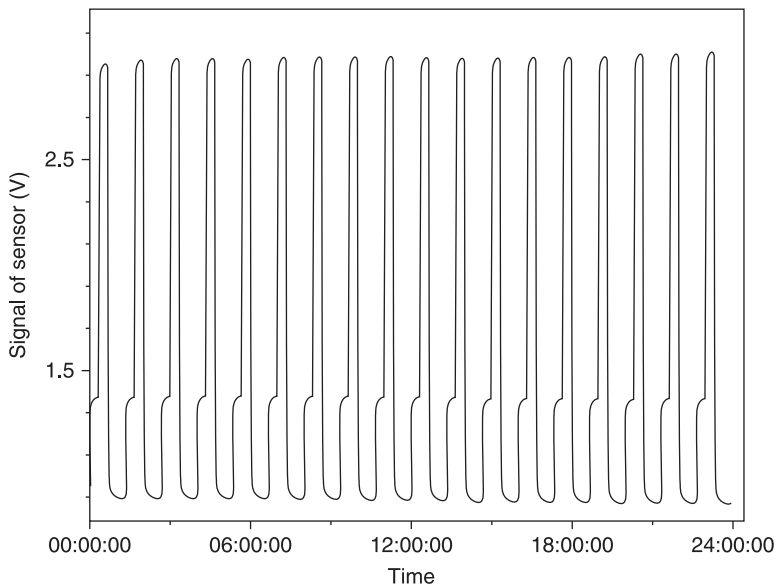

11.7 Alternate response of a SnO_2-based thick-film sensor to 5 and 40 ppm CO. The duration of a whole response is 1 h, the duty cycle is 50%.

© Woodhead Publishing Limited, 2012

11.4.1 SnO_2-based materials

Among the above-mentioned materials, a case in point is tin dioxide, the most widely used material for gas sensing, by which in 1970 Figaro Engineering Inc. fabricated and commercialized the first metal oxide gas sensor device (Taguchi, 1970). SnO_2 exhibits n-type semiconductor behavior due to lattice defects, in particular oxygen vacancies acting as electronic donor levels. Indeed, Samson and Fonstad (1973) experimentally determined the presence of two donor levels, $Ed_1 = 0.034$ and $Ed_2 = 0.145$ eV below the bottom of the conduction band.

Figure 11.8 shows the Arrhenius plot obtained by changing the temperature between 360 and 800 K at the heating rate of 3 K/min (A) and the height of the surface barrier potential versus temperature (B) of a SnO_2 thick-film. To determine the energy barrier (the difference in energy between the conduction band bottom at the surface and that in the bulk) temperature-stimulated conductance measurements were performed with a procedure described elsewhere (Lantto *et al.*, 1988; Carotta *et al.*, 1991).

Different conductivity regions were observed, demonstrating the occurrence of different surface adsorption phenomena, in particular the $O_2^- - O^-$ transformation, as experimentally proven by Chang through the correlation between electrical conductivity and EPR measurements (Chang, 1980). The typical behaviour of the SnO_2 energy barrier versus temperature exhibits a minimum and a maximum corresponding to the increase of the depletion layer depth with temperature attributed to a negative surface charge accumulation, typically O^- ions. The ability of tin dioxide to sense either reducing agents at high temperature or oxidizing ones, like NO_2, at low temperature could be explained according to these characteristics. The interaction between the analyte and the surface of the semiconductor causes changes to the potential barrier height at the inter-granular contact and therefore to electrical conductance variations.

All the electrical measurements here shown have been obtained in a sealed test chamber using the flow-through technique maintaining a constant flow of 0.5 l/min in dry or wet air or in mixtures of air and test gases.

As the first material extensively investigated in gas sensing, many studies have been performed to improve the sensing and selectivity properties of SnO_2, above all by adding small amounts of noble metals on the surface (Yamazoe *et al.*, 1983; Schierbaum *et al.*, 1991; Yamazoe, 1991; Fliegel *et al.*, 1994; Xu *et al.*, 1996; Cabot *et al.*, 2000, 2002). On this subject, in Batzill and Diebold (2005) the role of additives in gas-sensing materials has been thoroughly reviewed. In Chiorino *et al.* (1997), the role of Pd has been examined on two materials, a commercial SnO_2 powder from CERAC and a SnO_2 powder prepared in the laboratory by a precipitation route, differing in grain size and the shape of grains. It turned out that the role of the nanostructure associated with a high dispersion of small additive particles resulted in a higher gas response and reduction of the operating temperature. Figure 11.9(a) shows a result of TEM investigations performed on powders calcined at 550°C and on films loaded with 0.4 at.% of Pd and heated up

© Woodhead Publishing Limited, 2012

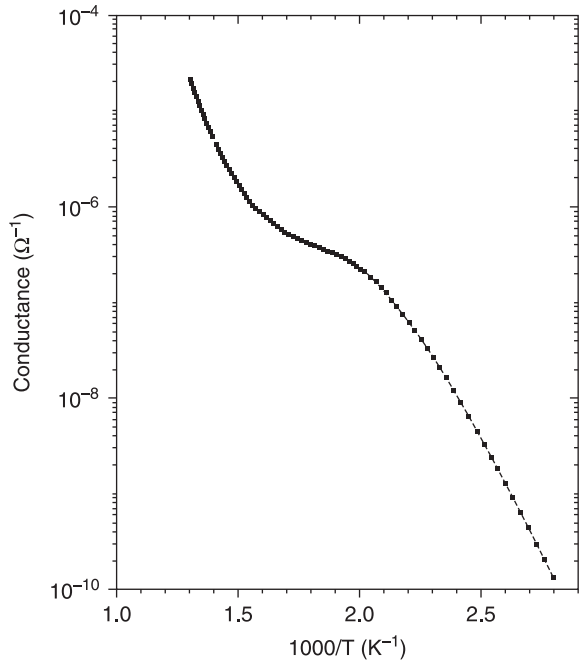

(a)

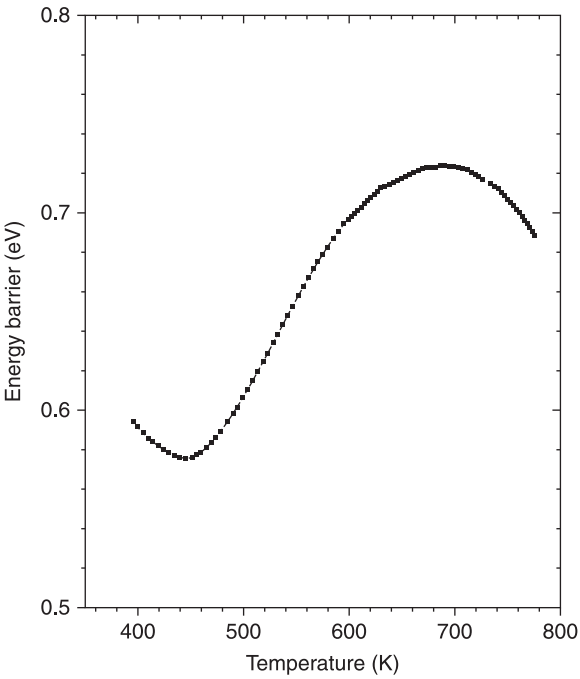

(b)

11.8 Arrhenius plot for (a) conductance and (b) energy barrier vs. temperature, for pure tin oxide films.

© Woodhead Publishing Limited, 2012

to 850 °C (Fig. 11.9(b)). The round-shaped particles exhibit an average diameter of 20 nm, a little wider (<30 nm) in the films.

Moreover, in Fig. 11.10, the SEM micrographs performed on Pd-loaded films show the crack-free film surface (Fig. 11.10(a)) and the optimum degree of particle sintering control (Fig. 11.10(b)).

From the electrical point of view, Fig. 11.11 illustrates the different sensing effect of Pd or Au (0.4 at.%) addition on the detection of carbon monoxide and methane.

Fourier-transform-infrared-spectroscopy (FT-IR) measurements enabled us to clarify the role of the oxygen vacancies for the laboratory-prepared material. Indeed, in the presence of reducing gases, a growth of a very intense and broad absorption peak due to electronic transitions involving oxygen vacancies appeared, which is not present in the commercial powder. On the contrary, for the latter material, only an increase of the scattering of the radiation by free electrons could be found, thus highlighting the difference between a nanostructured material and a coarser one and the importance of a high stoichiometric defectiveness of the sensing material associated with the nanostructure.

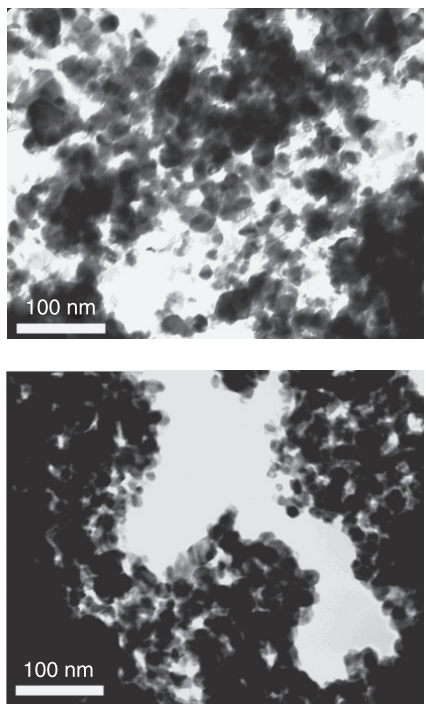

11.9 (a) TEM micrographs on to SnO_2 powder calcined at 550 °C and (b) onto Pd/SnO_2 film fired at 850 °C.

© Woodhead Publishing Limited, 2012

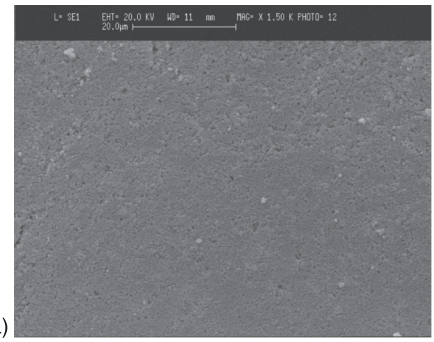

(a)

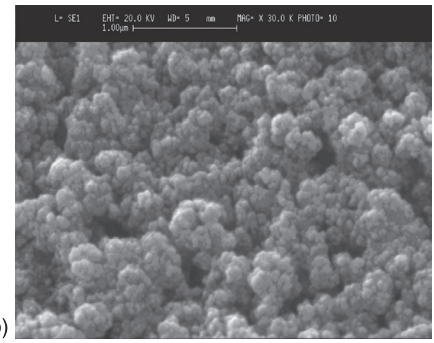

(b)

11.10 SEM micrographs of a Pd/SnO_2 film at (a) low and (b) high magnification.

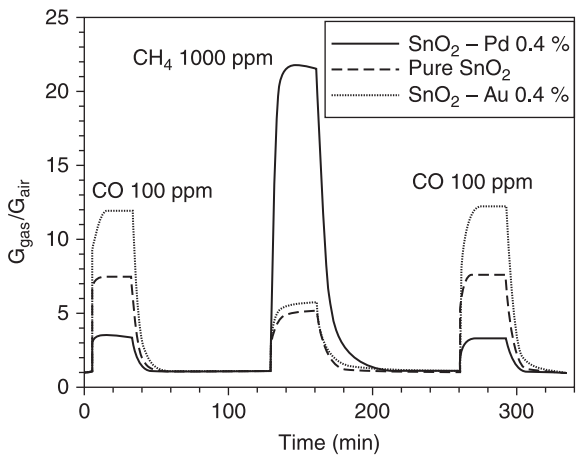

11.11 Responses to CO and CH_4 for pure SnO_2 films and for SnO_2 films loaded with Pd or Au.

© Woodhead Publishing Limited, 2012

Other selectivity properties can be obtained by adding different ions to SnO_2 crystal lattice, such as Mo, W, V, La, etc. The addition of Mo and W generally resulted in a decrease of the response to reducing gases, like CO, and in an increase versus oxidizing gases, such as NO_2, while for V and La addition, a good sensitivity to SO_2 and CO_2, respectively, is reported (Chiorino *et al.*, 1999, 2001; Das *et al.*, 2008; Marsal *et al.*, 2003).

As stated above, the synthesis method involves different electronic properties, while the decrease in grain dimension down to the depletion width provides an enhanced gas response (Malagù *et al.*, 2004a, 2004b; Xu *et al.*, 1991; Vuong *et al.*, 2005; Zhang and Liu, 2000). Actually, in tin oxide thick-film sensors it is unusual to observe the grain size dependence of the response. Indeed, the firing at high temperature causes a grain coalescence of up to 20–30 nm. Because the depletion layer depth in tin oxide is less than 20 nm, in order to observe this phenomenon the sensing layers must be deposited starting from very small powders (<10 nm) and heated at a moderate temperature (≤650 °C) (Malagù *et al.*, 2004c). Under these conditions, we have experimentally verified that the response to carbon monoxide doubles when the grain size is about 10 nm with respect to that of a grain size of about 30 nm.

In spite of the many improvements obtained through material modifications (such as the synthesis of nanostructured powders and the addition of ions or catalysts), a significant cross-sensitivity caused by the presence of a small amount of water vapor greatly hindered the exploitation of tin oxide-based gas sensor devices. Several authors visited the subject following different approaches: first of all by studying the mechanism of interaction between the semiconductor surface, detecting gas and water vapor and afterwards trying to solve the drawback through material modification, filters or processing the sensor signal by mathematical algorithms. Some papers on this subject are listed: Yamazoe *et al.*, 1979; McAleer *et al.*, 1988; Gercher and Cox, 1995; Ghiotti *et al.*, 1997; Bârsan and Weimar, 2003; Harbeck *et al.*, 2003; Marsal *et al.*, 2003; Ankara *et al.*, 2004; Ivanov *et al.*, 2004; Hossein-Babaei and Ghafarinia, 2010. In particular, in Carotta *et al.* (2007b), a compensation algorithm has been obtained through experimental tests and positively applied to the monitoring of atmospheric pollutants. The resulting equation, which represents a surface, contains three terms: two of them represent the response to a single gas and the third one is an interaction term between the water vapor and the testing gas.

11.4.2 TiO_2-based materials

Among the large variety of TiO_2 applications, the photo-assisted degradation of organic molecules is certainly the most exploited. So, the major knowledge of titania as a functional material comes from catalysis and photocatalysis (Fujishima and Honda, 1972; Matsuda and Kato, 1983; Linsebigler *et al.*, 1995; Paz, 2010; Diebold, 2003). In the gas sensing field, titania was first investigated for its application in automotive exhaust sensors, i.e. in the measurement of the oxygen

© Woodhead Publishing Limited, 2012

partial pressure in the exhaust gas, and hence for the control of the air/fuel ratio (Tien *et al.*, 1975; Takami, 1988; Zhu *et al.*, 1996; Sharma *et al.*, 1996). Since the 1990s, titania has been studied to detect atmospheric pollutants at moderate temperature (300–600 °C) (Tang *et al.*, 1995). Actually, titania is suitable for sensing polluting gases in air, allowing good and stable responses only if the grain dimension of the poly-crystalline material is kept at nanometric level. Indeed, in contrast to SnO_2, titanium dioxide, when heated, undergoes a phase transition from anatase into rutile, simultaneously resulting in very large grain coalescence (Hague and Mayo, 1993; Guidi *et al.*, 2003). The anatase phase can be stabilized through the addition of ions with valence 5^+ (Guidi *et al.*, 2003; Akhtar *et al.*, 1992; Martinelli *et al.*, 1999; Carotta *et al.*, 1999; Traversa *et al.*, 2001; Ruiz *et al.*, 2004a; Sacerdoti *et al.*, 2004). In particular, Ta (10 at. %) allowed to hinder the transition to rutile up to 950 °C (Traversa *et al.*, 2001). A different method of stabilizing titania in the anatase phase consists of synthesizing the oxide by using the sol-gel route (SG) followed by an appropriate treatment HY (Ruiz *et al.*, 2004b; Carotta *et al.*, 2007a). In contrast to the traditional SG synthesis, the HY process allows for the maintenance of the anatase phase up to 850 °C without any introduction of foreign elements (Carotta *et al.*, 2007a). In Fig. 11.12, a SEM image of a HY–titania thick-film fired at 850 °C shows nanosized particles with an anatase structure as confirmed by XRD analysis.

In spite of the excellent results in terms of anatase phase stabilization with the consequent maintenance of the grain dimension at nanometric size, the TiO_2-based gas sensors differ in gas-sensing behavior from SnO_2-based ones, the latter being much more reactive versus reducing gases. A theoretical model has been developed to justify this behavior. The idea was to generalize the Schottky relation (Morrison, 1982) to the case of spherical symmetry and to the cases where

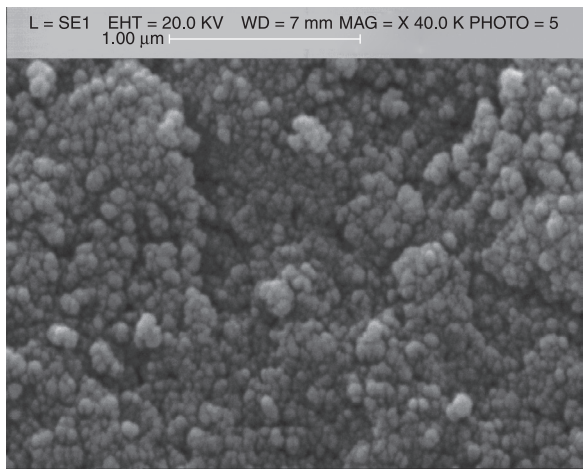

11.12 SEM micrograph of a HY-titania thick-film fired at 850 °C.

© Woodhead Publishing Limited, 2012

the depletion approximation fails. The result is a strong grain-size dependence of the TiO_2 gas-sensing properties caused by the variation of the charged surface states, N_s, with grain radius. SnO_2, instead, exhibits a modest dependence of the gas response on the particle size (as confirmed by experimental evidence) due to an almost constancy of N_s (see section 11.2).

TiO_2 strongly differs from SnO_2 in that it has a much smaller electrical conductivity and the shape of the Arrhenius plot is different (see Fig. 11.13(a)). Indeed, the sigma shape caused in SnO_2 by the occurrence of surface reactions (in particular the O_2^-–O^- transformation in the 200–400 °C range) is not visible in TiO_2 because in this temperature range the bulk donor states are not yet ionized. In fact, the n-type behavior, in TiO_2, as with SnO_2, depends on donor-like stoichiometric defects, generally ascribed to oxygen vacancies, but with energetic positions in TiO_2 that are much deeper inside the band gap with respect to SnO_2 (Samson and Fonstad, 1973; Munnix and Schmeits, 1985). Actually some authors assign donor levels 0.8 eV deep, at Ti^{3+} ions rather than at oxygen vacancies (Diebold, 2003; Göpel *et al.*, 1988). Moreover, titania films feature heights of energy barriers versus temperature that are much higher than SnO_2, where almost three activation energies are exhibited, differently from TiO_2, in which only two regions of barrier are present (see Fig. 11.13(b)).

With respect to the structural properties, SnO_2 and TiO_2 exhibit the same rutile crystalline structure, the space group $P4_2/mnm$ easily giving rise to a solid solution with chemico-physical properties varying with the Ti–Sn molar ratio. In fact, the SnO_2-TiO_2 system has been widely investigated; in some of the papers mentioned here, the characteristics of the immiscibility gap can be found (Park *et al.*, 1975; Yuan and Virkar, 1988; Radecka *et al.*, 1998; Dusastre and Williams, 1999; Radecka *et al.*, 2001). Actually, the SnO_2-TiO_2 mixed oxide is a very interesting material for thick-film gas sensors and its synthesis and investigation (as $Ti_xSn_{1-x}O_2$, $0 < x < 1$ with $x = 0, 0.1, 0.2, 0.3, 0.5, 0.7, 0.9, 1$) allowed us to discover a completely different phenomenon occurring during the sensing process in SnO_2-like materials compared with what happens in TiO_2-like ones. Indeed, through FT-IR analysis under a CO atmosphere, for the materials with $x \leq 0.2$, as already observed in pure SnO_2 (Chiorino *et al.*, 1997), a very broad absorption in the medium IR (MIR) region, related to the photoionization of mono-ionized oxygen vacancies $VO^{\cdot}$, occurred, while samples with $0.3 \leq x \leq 1$ exhibited a completely different phenomenon consisting in an erosion of the absorption edge related to the skeletal M–O vibration modes (Carotta *et al.*, 2009b). This difference of behavior can contribute, together with the definition of the phenomenon of the unpinning of the Fermi level (Malagù *et al.*, 2004b; Carotta *et al.*, 2007a) to understanding the electrical differences between SnO_2 and TiO_2.

In summary, with regard to the electrical properties of the various solid solutions obtained by varying the Ti molar ratio, all examined samples with $0.1 \leq x \leq 0.9$ exhibit good sensing performance, even if they exhibit a crystalline rutile structure. However, it must be noted that these materials do not undergo a phase transformation, exhibiting a rutile phase as synthesized. For this reason, the

© Woodhead Publishing Limited, 2012

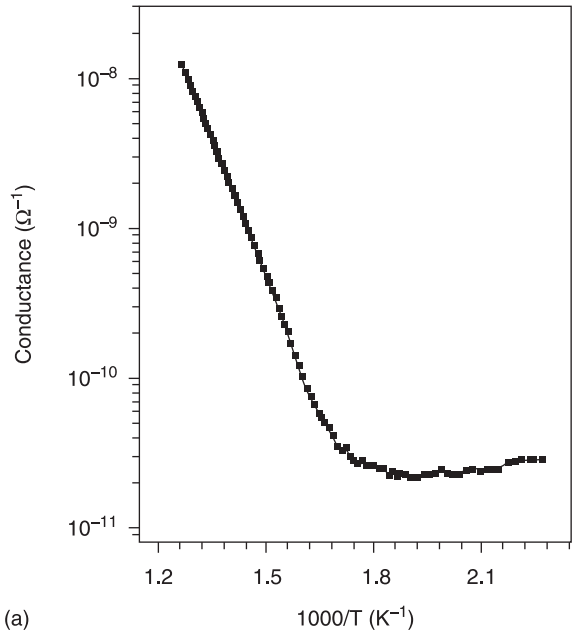

(a)

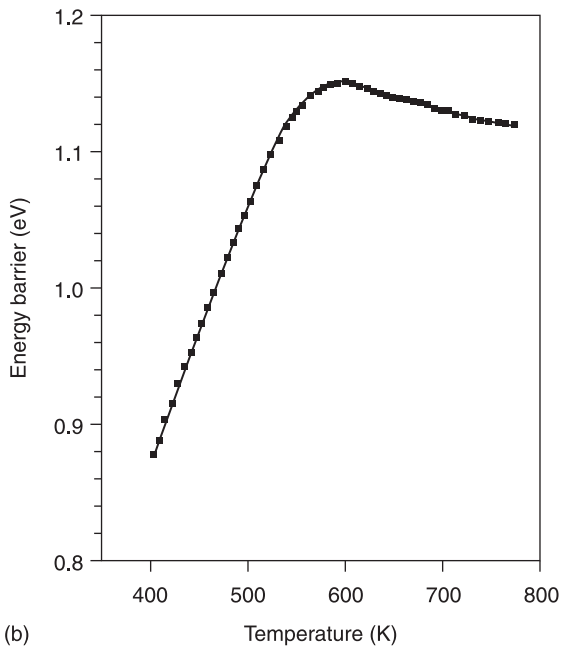

(b)

11.13 Arrhenius plot for (a) conductance and (b) energy barrier vs. temperature for pure titania films.

© Woodhead Publishing Limited, 2012

grains undergo coalescence only moderately when heated at high temperature. In Fig. 11.14(a), the crystallite dimension of the powders calcined at 650 °C, estimated through XRD analysis using Scherrer's equation, is reported, whereas that of pure titania is not reported because at 650 °C the crystalline phase is anatase instead of rutile. In Fig. 11.14(b), the response to 50 ppm of carbon monoxide (working temperature: 550 °C) of the thick-films fired at 650 °C, as a function of the crystallite size of the films, is shown. We note that the crystallite size is strongly dependent on composition, exhibiting the lowest size for $0.3 \leq x \leq 0.5$, while the gas response increases with decreasing grain size rather than with the Ti molar ratio, as might have been supposed (Carotta *et al.*, 2008, 2009a, 2009b).

From the electrical point of view, the materials with $x \leq 0.2$ exhibit conductivity much higher than the compositions with $x > 0.2$; the two classes of materials also show different shapes of conductance curve versus temperature (Carotta *et al.*, 2009b). Concerning surface barrier height trend versus temperature, the sample with $x = 0.1$ behaves similarly to SnO_2 with an increased barrier height corresponding to the decreased conductivity. The samples with $0.3 \leq x \leq 0.9$ behave like titania (temperature dependence), but the height of the energy barrier was determined by the size of the nanoparticles. Indeed, the grain radius of the samples with $x = 0.3$ and $x = 0.5$ are smaller than Λ (the depletion layer width) and the band bending cannot be fully developed (Carotta *et al.*, 2009a, 2009b). In summary, among the various synthesized $Ti_xSn_{1-x}O_2$ solid solutions, the stoichiometry with $x = 0.2$ exhibits a borderline behavior between that SnO_2-like and TiO_2-like oxides, for all examined properties (see Figs. 11.15(a), 11.15(b)).

11.4.3 WO_3-based materials

Tungsten trioxide has been investigated mainly because of its wide number of crystalline forms, in contrast to its simple stoichiometry (Boulova and Lucazeau, 2002; Vogt *et al.*, 1999; Howard *et al.*, 2002). Since then it has been appreciated in many applications and mainly in electrochromic devices (Jiao *et al.*, 2010; Kharade *et al.*, 2010), photo-catalysis under UV and visible light (Bamwenda and Arakawa, 2001; Kim *et al.*, 2010) and, especially from the 1990s, in gas sensing (Akiyama *et al.*, 1991; Tamaki *et al.*, 1994; Tomchenko *et al.*, 1999; Lee *et al.*, 1999; Solis *et al.*, 2001; Guidi *et al.*, 2004; Kanda and Maekawa, 2005; Reyes *et al.*, 2006; Meng *et al.*, 2009; Szilágyi *et al.*, 2010; Senguttuvana *et al.*, 2010). Regarding this application, WO_3 appears mainly investigated in NO and NO_2 sensing. Also H_2S and ammonia have been considered, but very few papers assess the capacity of WO_3 to detect reducing gases, like VOC or hydrocarbons. According to the majority of the authors, the WO_3 thick-films prepared by our group exhibit a strong attitude to oxidizing gases (Guidi *et al.*, 2004; Blo *et al.*, 2004).

Like SnO_2, WO_3 behaves as a n-type semiconductor because of latttice defects, in particular, oxygen vacancies acting as electronic donor levels. However, it shows a band gap ranging from 2.5 to 2.8 eV (Erbs *et al.*, 1984) and

© Woodhead Publishing Limited, 2012

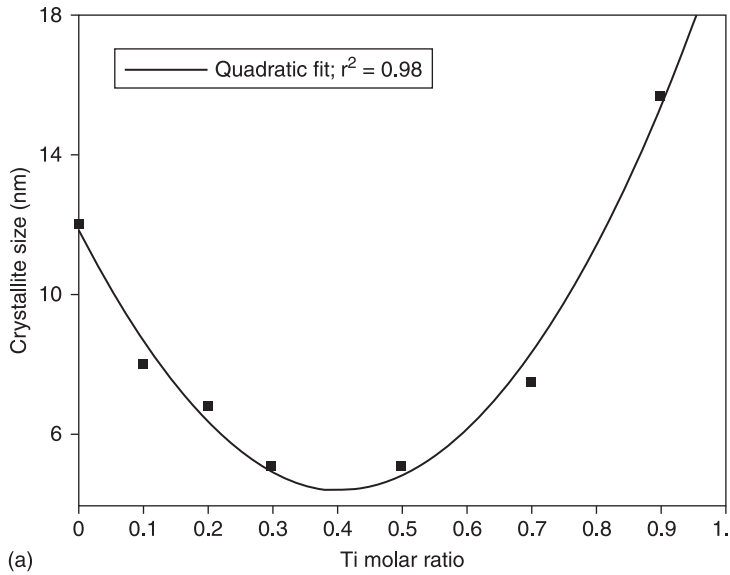

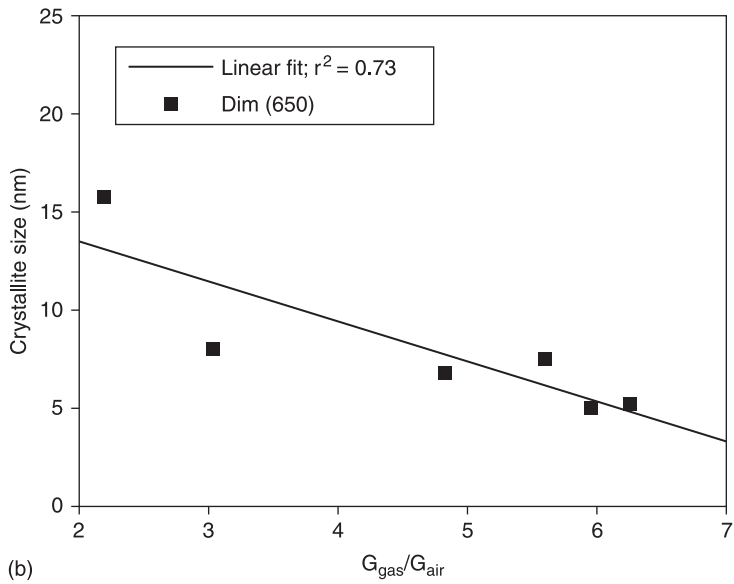

11.14 Crystallite size of (Sn,Ti)-solid solution powders vs. (a) Ti molar ratio and (b) magnitude of the response for (Sn,Ti)-mixed oxide films fired at 650 °C as a function of crystallite size.

© Woodhead Publishing Limited, 2012

© Woodhead Publishing Limited, 2012

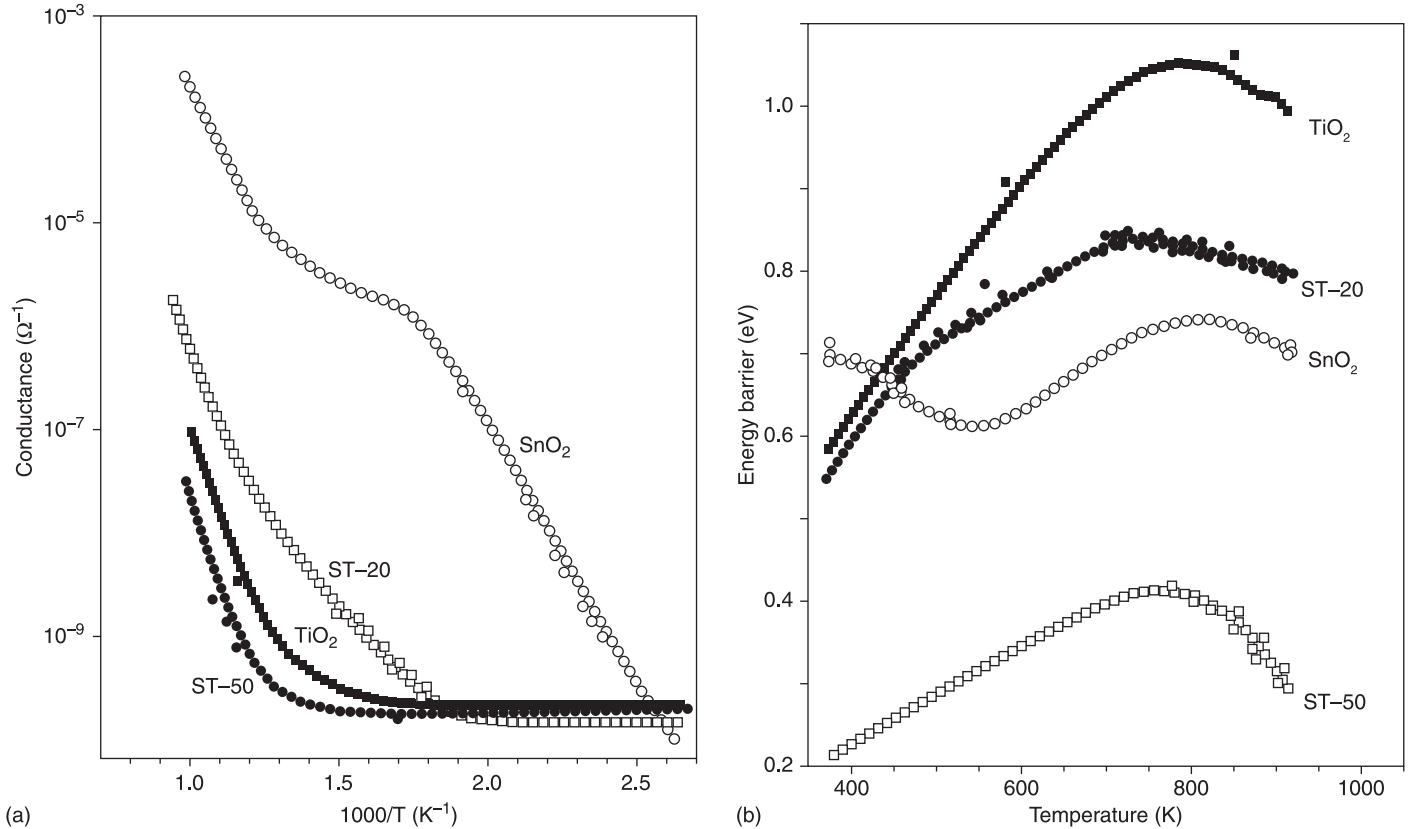

11.15 Arrhenius plot for (a) conductance and (b) energy barrier vs. temperature for pure titania and pure tin oxide films compared with ST-20 and ST-50 films.

contemporaneously a conductance value, at low temperature, almost three orders of magnitude higher than SnO_2 (Fig. 11.16(a)). Both materials exhibit three regions of conductance and therefore the same trend versus temperature of the surface energy barrier, but with a very low value in the case of WO_3 (Fig. 11.16(b)). This fact could explain the ability of WO_3 to detect only oxidizing gases.

Also the preparation of mixed oxides of tungsten and tin tends to exhibit the same behaviour in relation to oxidizing gases. Indeed, as shown in Chiorino *et al.* (2001), adding 1 or 5% of W in SnO_2 progressively modifies the sensing properties of the sensors from the detection of reducing to the detection of oxidizing gases. Furthermore, the solid solution of $(Sn,W)O_3$ (Sn: 10 at.%) did not increase the ability of the mixed oxide with respect to pure WO_3 to detect oxidizing gases (Fig. 11.17).

Under thermal treatment, WO_3 suffers from exaggerated grain coalescence assisted by phase transition as highlighted in Guidi *et al.* (2004) and shown in Fig. 11.18, in which a pure WO_3 film (a) is compared with a film of $(Sn,W)O_3$ (Sn: 10 at.%) (b), both fired at 750 °C. Moreover, it has been proved that NO_2 response depends on particle size (Guidi *et al.*, 2004; Meng *et al.*, 2009), but the phenomenon becomes significant only if the grain size is very small (<30 nm) as reported in Tamaki *et al.* (1994). Unfortunately, to obtain a good electrical stability of the sensors, it is essential to operate them at a sufficiently high temperature. For this reason, specifically for WO_3, particles smaller than 30 nm are not consistent with the manufacturing process. On the other hand, responses to other oxidizing gases, like ozone, are quite independent of particle size, therefore, for WO_3, it does not appear clear if the gas response might even depend on gas molecule size and gas diffusion effect.

11.4.4 ZnO-based materials

ZnO has been a pioneering material in gas sensing (Seiyama *et al.*, 1962). Later it was abandoned, but in the past two decades it has again met the interest of researchers as witnessed by an exponential growth of publications. Zinc oxide is a direct wide band-gap (3.37 eV) semiconductor and exhibits high exciton binding energy (60 meV), which causes an efficient UV emission (~380 nm), making it suitable for UV- and blue-optoelectronic applications. Furthermore, a wide range of other technological applications such as photocatalysis, piezoelectricity, optoelectronics, photovoltaic conversion and gas sensing make ZnO a very attractive material (Özgür *et al.*, 2005; Klingshirn, 2007; Ruske *et al.*, 2007; Dodd *et al.*, 2009; Martins *et al.*, 2004). With the advent of modern nanotechnologies, a lot of metal oxide semiconductors have been synthesized in a large variety of nanostructures such as nanoparticles, nanowires, nanobelts, nanorods or nanotetrapods. Among the various oxides, ZnO is particularly suitable to be synthesized in such nano-forms (Schmidt-Mende *et al.*, 2007; Wang, 2004). In this context, recent works in gas sensing claim the superior performance of two-dimensional nano-morphologies with respect to traditional round-shaped three-dimensional nanoparticles (Schmidt-Mende *et al.*,

© Woodhead Publishing Limited, 2012

© Woodhead Publishing Limited, 2012

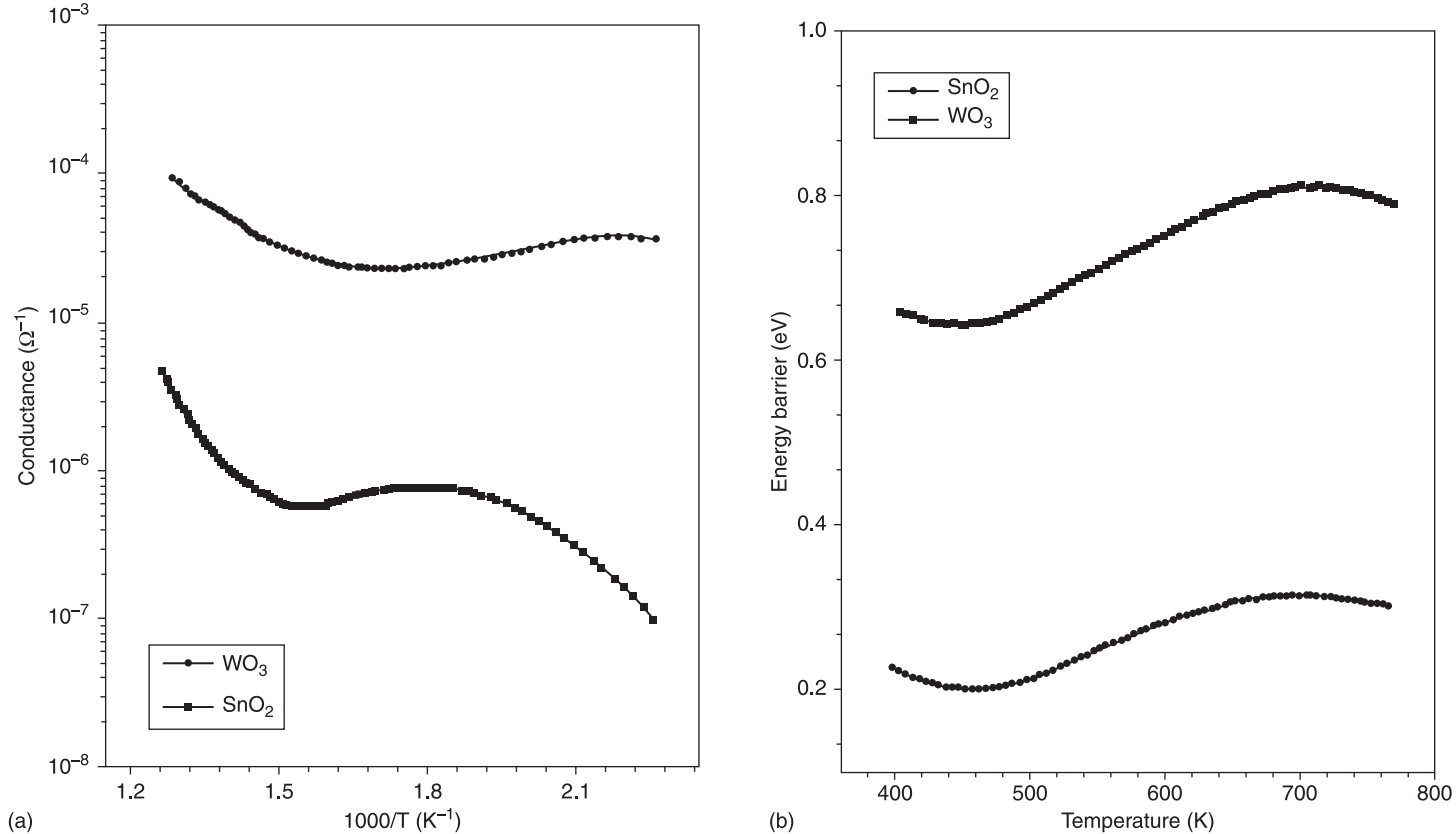

11.16 Arrhenius plot for (a) conductance and (b) energy barrier vs. temperature for WO_3 films

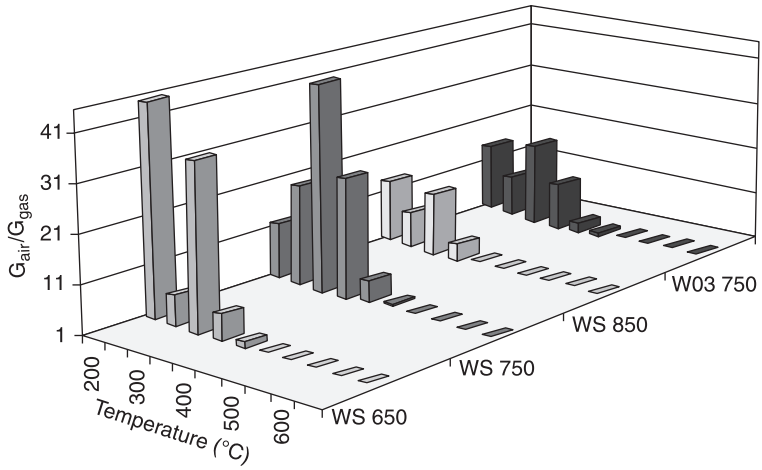

11.17 Magnitude of the response to 100 ppb of NO_2 for pure WO_3 sensor fired at 750 °C compared with those offered by $(Sn,W)O_3$ (Sn: 10 at.%) films fired at 650, 750 or 850 °C.

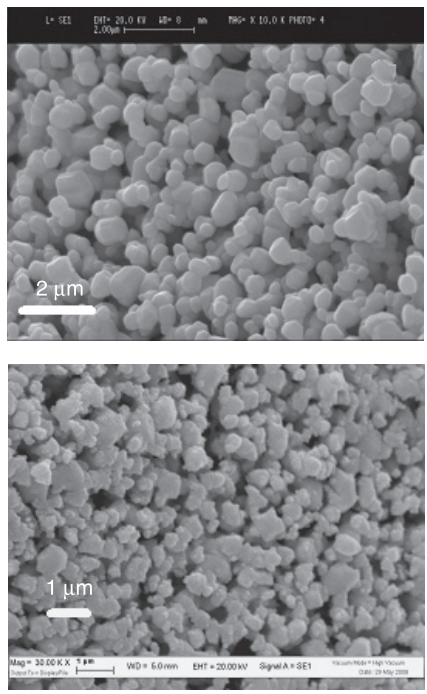

(a)

(b)

11.18 SEM micrographs of (a) WO_3 and (b) $(Sn,W)O_3$ (Sn: 10 at.%) films both fired at 750 °C. Notice the control of the grain growth determined by the addition of Sn in the WO_3 lattice.

© Woodhead Publishing Limited, 2012

2007; Wang, 2004; Lu *et al.*, 2006). In Carotta *et al.* (2009c), a comparison between round-shaped and two-dimensional nanoparticles in the form of tetrapods (TP) has been performed. It turned out that, despite the enormous difference in morphology, both types of sensors behaved similarly with all tested gases, mainly exhibiting very good responses towards oxidizing gases, in particular with ozone. TP films best responded to ozone with faster response time, while sol-gel thick-films best responded to NO_2 with a different temperature of maximum response compared to ozone.

ZnO has been successfully employed also to detect other gases, such as H_2, O_2, H_2S, LPG, HCHO and NH_3 (Patil *et al.*, 2010; Baruwati *et al.*, 2006; Trivikrama Rao and Tarakarama Rao, 1999; Sarala *et al.*, 2006; Xiangfeng *et al.*, 2005). In addition to thermally activated gas sensors, ZnO is particularly suitable to be assisted by UV irradiation. In this operational mode, the sensors work at room temperature overcoming the main technical limitation of the high operating temperature, essential in chemo-resistive gas sensors. Actually, the photoactivation has been investigated for other metal oxide semiconductors, such as, for example, SnO_2 or TiO_2 (Prades *et al.*, 2009; Yan *et al.*, 2010; Yang *et al.*, 2003). However, ZnO is the most investigated material with UV light instead of thermal energy as the excitation source (de Lacy Costello *et al.*, 2008; Gui *et al.*, 2008). Our group successfully applied the gas detection assisted by an UV light-emitting diode (LED) to ZnO sensors for ozone detection (Carotta *et al.*, 2011); for this application (see also the next section), the most appropriate morphology has been obtained by firing the sensing film at 650 °C (see Fig. 11.19).

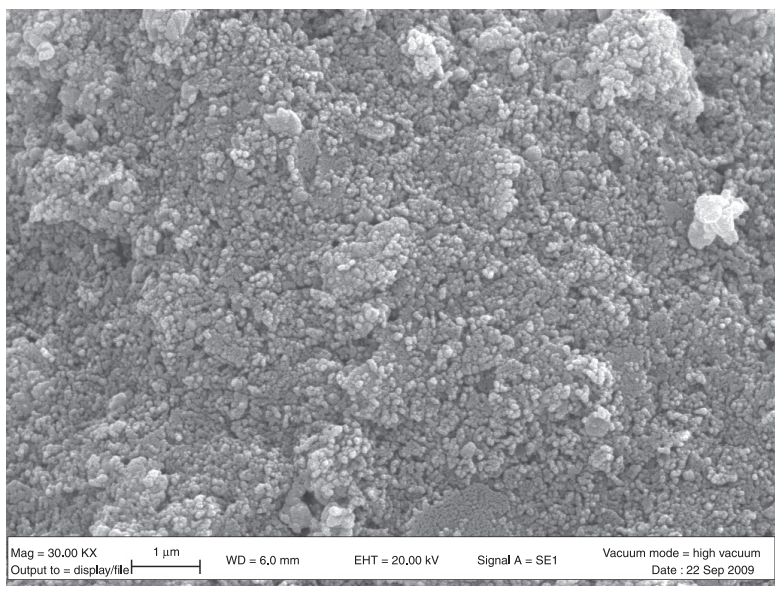

11.19 SEM micrograph of ZnO thick-film fired at 650 °C.

© Woodhead Publishing Limited, 2012

11.5 Applications

Over the years, the wide variety of technological applications, such as heterogeneous catalysis, gas sensing, photocatalysis, piezoelectricity, optoelectronics, photovoltaic conversion, etc. has been driven by extensive investigations on semiconductor metal oxides (MOX). To use them in real applications, many efforts have been addressed to improving their selectivity and repeatability properties, which still represent the main drawback for a single sensor employment. However, the crucial point is to prioritize the identification of the specific application, in order to reduce as much as possible the number of parameters that can influence the measurement. In the following, we will describe the applications to which we have devoted major attention in order to minimize the above expressed problems or to solve them either by using on array of sensors or with dedicated analytical methods.

11.5.1 Environmental monitoring

The worldwide emission of pollutant gases and fine particulate matter caused by vehicular traffic, industrial activities, domestic heating and biomass burning is steadily increasing. In particular, emerging industrial activity in developing countries will further add to the global pollution during the next decades. Increasing concerns for the proven impact of atmospheric pollution on the health of citizens strengthens the necessity of emission control and mitigation, which have to be verified through steady public and private air quality monitoring activities.

Recent developments in the European legislation have enabled proposals for the use of more flexible devices, such as reliable solid-state gas sensors, in addition to cumbersome analytical devices (Commission Directive 2008/50/EC). Indeed, real-time in-situ air quality data acquisition is necessary for assessing pollution, but also as an input for pollutant diffusion models and for the validation and correlation with remote sensing measurements. Nowadays, monitoring is usually performed in few fixed stations in urban areas, and with mobile stations (where the conventional equipment is installed on vehicles) for temporary measurement campaigns or occasional environmental impact estimations. The equipment used in these stations is often complex, expensive and difficult to deploy, requiring controlled environmental conditions and frequent maintenance and calibration. These analyzers are mainly rack-mounted devices with several requirements like external gas cylinders, consumables and periodic fetching and processing of the acquired data by trained personnel.

In this frame, the technology of thick-film gas sensors is an optimal candidate to be implemented in portable devices with low requirements in terms of power, consumables, maintenance and installation costs. Besides an evident cost reduction, this implementation will enable on-board correlation and processing of the acquired data, which can be autonomously distributed in a user-friendly format via the integrated wireless network interfaces and/or radio-modems (Qi and Shimamoto, 2012).

© Woodhead Publishing Limited, 2012

The advanced thick-film gas sensors are prepared as described in section 11.3 with optimal levels of reliability, stability, reproducibility and response speed for the different target gases, such as CO, NOx and O_3. These sensors are used to monitor the air quality with sensitivity, selectivity and reliability comparable to that of conventional analytical devices. In Fig. 11.20 both the sensor components of the system and the assembled monitoring unit are reported.

(a)

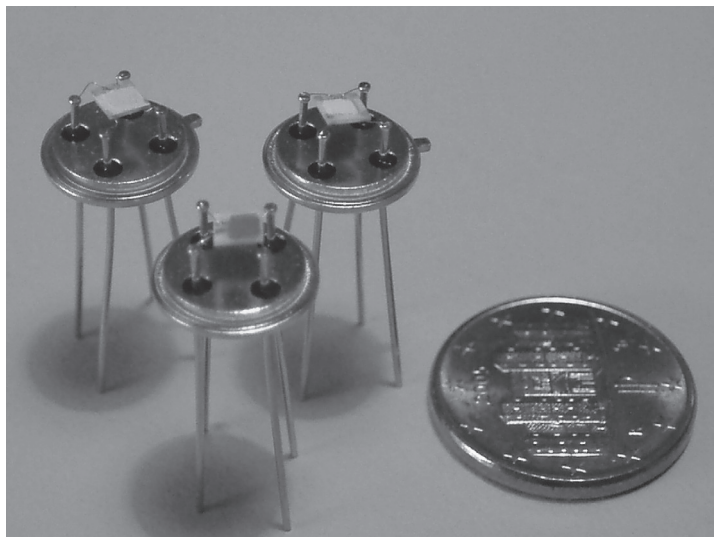

(b)

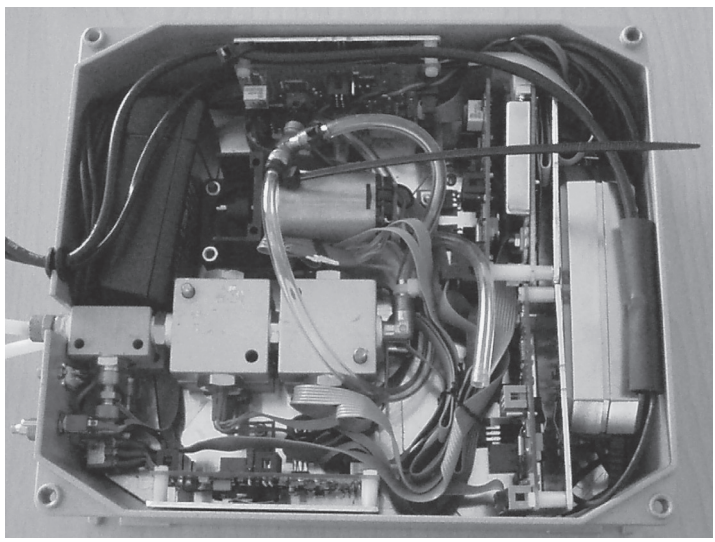

11.20 (a) Photograph of the single sensors of Fig. 11.20(b); (b) prototypal monitoring unit endowed with two sensor test chambers, flow and electronic control systems.

© Woodhead Publishing Limited, 2012

Figure 11.21 shows a comparison between dynamic measurements of (a) CO, (b) NOx and (c) O_3 performed through the described system with those of conventional spectrophotometers, while in Fig. 11.22 the correlation between the results of the two instrumentation is reported for the case of ozone.

The sensors shown in Fig. 11.20 can also be employed inside a gas chromatograph or in an array controlled by suitable electronics; therefore, they fit perfectly a scenario

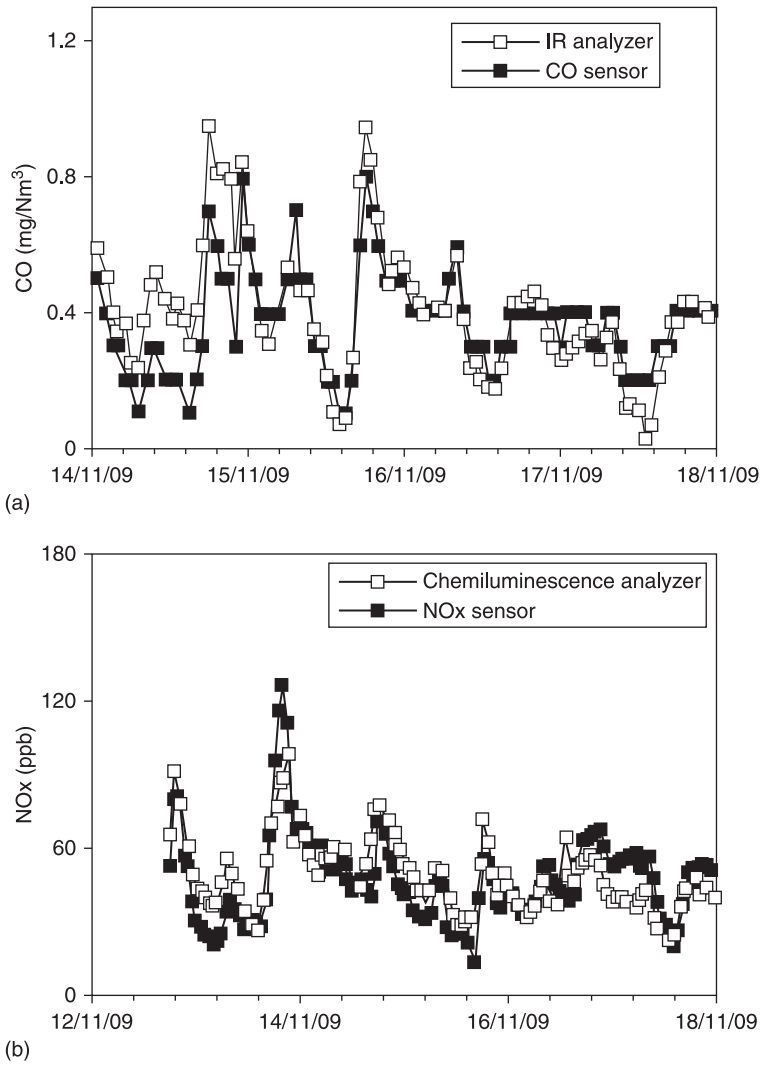

11.21 Dynamic measurements of different gases compared with conventional analyzers (a) CO and (b) NOx.

© Woodhead Publishing Limited, 2012

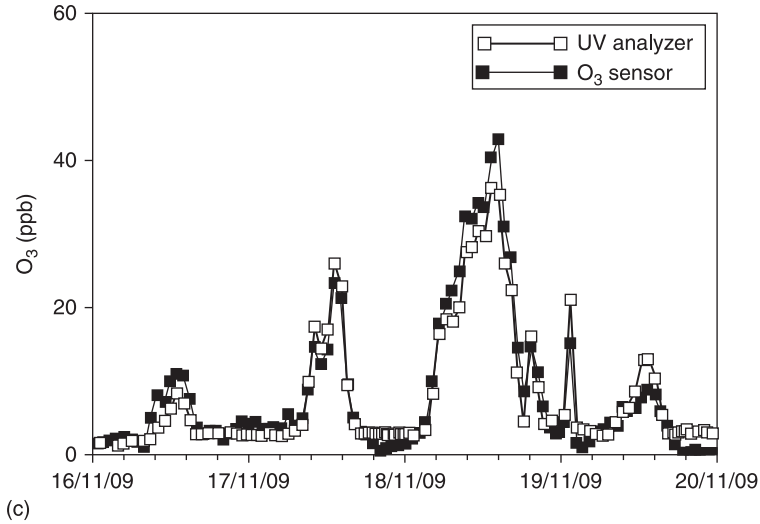

(c)

11.21 Continued (c) O_3.

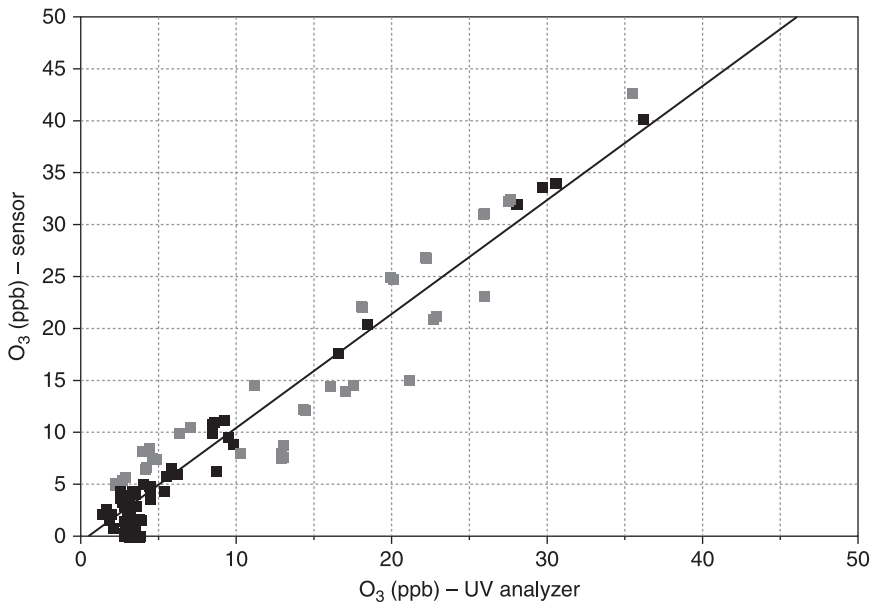

11.22 Correlation between the results of UV analyzers and ozone sensor ($r^2 = 0.94$).

© Woodhead Publishing Limited, 2012

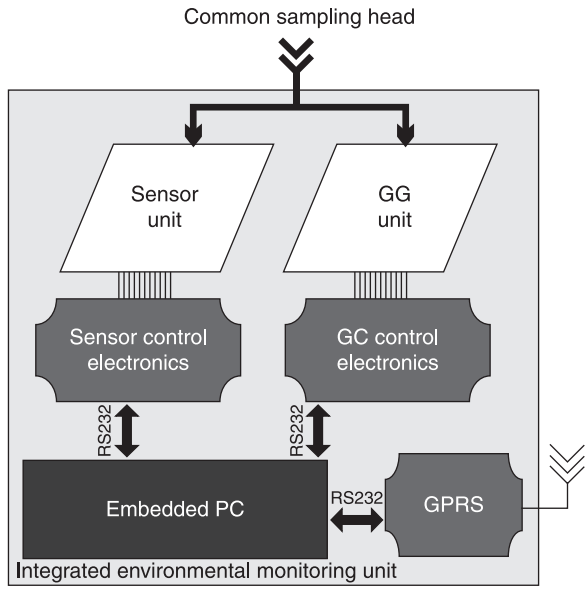

11.23 Diagram of the integrated monitoring station.

in which integrating measurements of outdoor pollutants are performed, from both fixed and mobile web-enabled stations. In this context, an integrated system realized in collaboration with CNR-IMM is sketched in Fig. 11.23.

The integrated innovative system performs detection and quantification of atmospheric pollutants, in particular carbon monoxide, nitrogen oxides, ozone and aromatic volatiles. Details about monitoring gaseous pollutants in the atmosphere using semiconductor sensors as detectors can be found, e.g. in Viricelle *et al.*, 2006; Zampolli *et al.*, 2009; Carotta *et al.*, 2006. The employment of this system on city buses together with geostatistic modelling results in the reconstruction of spatial distribution of pollutants in the area of interest. The system was tested in the year 2010 in the frame of GEOBUS, an Emilia Romagna PRRIITT Programme, a result of which was a picture of the distribution map of the carbon monoxide in a certain area of Bologna.

11.5.2 Photoactivation and photocatalysis

The wide-ranging features of MOX sensors also promoted research into photonic applications, such as light- emitting or laser diodes, transparent conducting oxides (TCO), hybrid solar cells, and material photo-activation and photocatalysis. Moreover, the recent emphasis given to the research on nanostructures and the advent of modern nanotechnologies has opened the way to further improvement in this direction.

© Woodhead Publishing Limited, 2012

In particular, in the case of nanostructured metal oxides used as gas sensors, many studies on exposure to light have been performed (Rao and Rao, 1999; Izu *et al.*, 2004). The basic idea arises from the fact that some metal oxides, known for their good sensing capabilities, also show photocatalytic properties, the photo-generated carriers promoting chemical reactions with the adsorbed species on the semiconductor surface.

The mechanism mainly involved in the described application, is the following: given that the absorption of a photon with enough energy promotes an electron in the conduction band and it generates a hole in the valence band, two specific mechanisms can contribute to the phenomenon: (1) the photo-generated holes recombine with electrons trapped on the surface causing desorption of the adsorbed oxygen ions. This results in a conductivity increase, due to the increased free electron density; (2) since the sensing layer is nanocrystalline, it is reasonable that many of the electron–hole pairs are generated within the depletion region causing a decrease in the energy barrier height.

An experimental result in this frame consisted in the observation that, under UV irradiation, the conductivity of ZnO increased by two orders of magnitude in ZnO. An important application, as reported in Chapter 4, is a ZnO ozone sensor exhibiting excellent performance in sensitivity, in response and recovery times also at room temperature (see Fig. 11.24). This result finds its application both in particularly harsh environments, e.g. in factories and plants

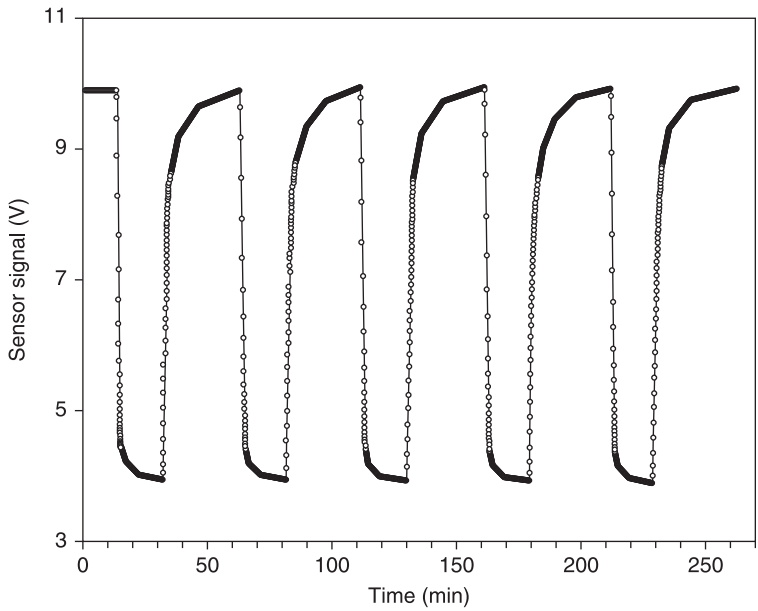

11.24 Dynamical responses to 70 ppb of ozone for RT-UV-assisted ZnO sensor.

© Woodhead Publishing Limited, 2012

where explosives may be present, and in situations where a very low power supply is required.

In the same context, a novel employment of nanostructured metal oxides has been tested by our group consisting in monitoring the photoactivity of functionalized tiles for atmospheric pollution abatement, as can be observed in Fig. 11.25, in which a test of abatement of 2 ppm of NO is monitored through two sensors, one based on ZnO and the second one based on $(Sn,W)O_3$ (Sn: 10 at.%). The opposite response of the two sensors is caused by the contemporaneous presence of NO and NO_2 in the atmosphere induced by operating functionalized tiles.

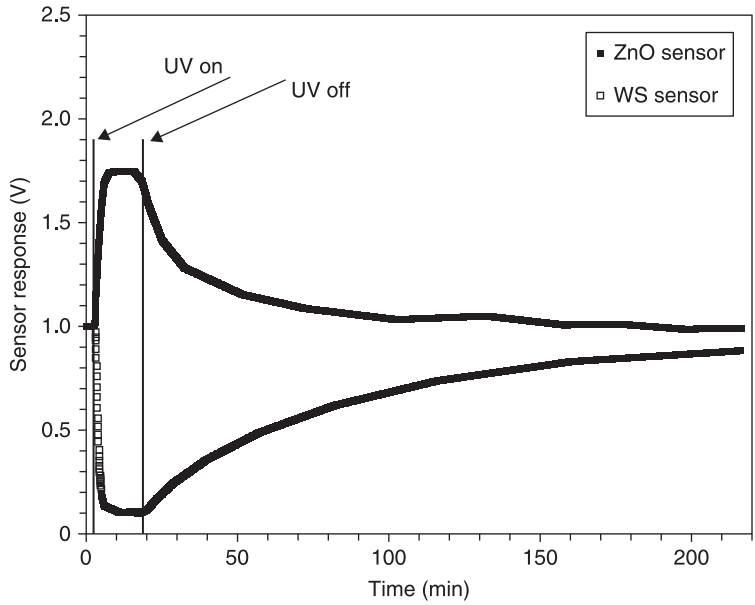

11.25 Responses of the sensors based on ZnO and $(Sn,W)O_3$ (Sn: 10 at.%) at the atmosphere variation caused by the functionalized tile during NO abatement process.

11.6 Future trends

The encouraging results achieved with previous applications foster further improvement for the industrialization of innovative instrumentation to access the market. Indeed, at present, it is only possible to acquire expensive instrumentation, generally cumbersome and of a laboratory type, which makes its widespread diffusion very difficult.

In the case of environmental monitoring, the proposed instrumentation, due to its portability and low cost, can instead offer the possibility of enhancing

© Woodhead Publishing Limited, 2012

the capacity to protect the population from air pollution and assess health risks. It can also enable on-board correlation and processing of the acquired data to be autonomously distributed via the integrated wired and wireless network interfaces.

Sensor-based monitoring is highly portable and user-friendly so as to grab the attention or solve the problems of specific fringes of society (such as children, the elderly, people exposed to work hazards), because it allows the user to check real-time data about air quality, such as ozone concentration in urban parks during the summer season or benzene concentration in petrol stations, and so on.

In the case of the other applications described in section 11.5, the enhanced performance features such as portability and the other described characteristics can result in sustainable development, from both the technical and the economic points of view, with subsequent potential social impact.

11.7 Acknowledgments

We are very grateful to Professor Giuliano Martinelli, head of our laboratory from 1995 to 2010, for passing on his love of and enthusiasm for research to us.

The results reviewed in this paper have been obtained with the help of members of our group (in particular, Michele Benetti, Sandro Gherardi, Alessio Giberti, Marco Nagliati, Daniela Palmeri) and eminent scientists of other institutions: Gian Carlo Cardinali, Stefano Zampolli, Giovanna Ghiotti, Sara Morandi, Pasquale Maddalena, Stefano Lettieri, Michele Sacerdoti, Giorgio Sberveglieri, Elisabetta Comini, Matteo Ferroni, Enrico Traversa, Celso M. Aldao, Miguel A. Ponce, to whom we are indebted.

11.8 References

Akhtar M. K., Pratsinis S. E. and Mastrangelo S. V. R. (1992), Dopants in vaporphase synthesis of titania powders, *J Am Ceram Soc*, 75, 3408–3416.

Akiyama M., Tamaki J., Miura N. and Yamazoe N. (1991), Tungsten oxide-based semiconductor sensor highly sensitive to NO and NO_2, *Chem Lett*, 20, 1611–1614.

Ankara Z., Kammerer T., Gramm A. and Schütze A. (2004), Low power virtual sensor array based on a micromachined gas sensor for fast discrimination between H_2, CO and relative humidity, *Sensors and Actuators B*, 100, 240–245.

Ansari S. G., Boroojerdian P., Kulkarni S., Sinkar S. R., Karekar R. N. *et al.* (1996), Effect of thickness on H_2 gas sensitivity of SnO_2 nanoparticle-based thick-film resistors, *J Mater Sci Mater Electron*, 7, 267–270.

Asamoto M. and Yahiro H. (2009), Catalytic properties of perovskite-type oxide prepared by thermal decomposition of heteronuclear complex, *Catal Surv Asia*, 13, 221–228.

Bamwenda G. R. and Arakawa H. (2001), The visible light induced photocatalytic activity of tungsten trioxide powders, *Applied Catalysis A: General*, 210, 181–191.

Bardeen J. (1947), Surface states and rectification at a metal semi-conductor contact, *Phys Rev*, 71, 717–727.

© Woodhead Publishing Limited, 2012

Bârsan N. and Weimar U. (2003), Understanding the fundamental principles of metal oxide based gas sensors; the example of CO sensing with SnO_2 sensors in the presence of humidity, *J Phys: Condens Matter*, 15, R813–R839.

Baruwati B., Kumar D. K. and Manorama S. V. (2006), Hydrothermal synthesis of highly crystalline ZnO nanoparticles: a competitive sensor for LPG and EtOH, *Sensors and Actuators B*, 119, 676–682.

Batzill M. and Diebold U. (2005), The surface and materials science of tin oxide, *Progress in Surface Science*, 79, 47–154.

Bhattacharyya P. and Basu S. (2010), Nanostructured ceramic materials for chemical sensors: present status and future prospects, *Trans Ind Ceram Soc*, 69, 1–23.

Blo M., Carotta M. C., Galliera S., Gherardi S., Giberti A. *et al.* (2004), Synthesis of pure and loaded powders of WO_3 for NO_2 detection through thick-film technology, *Sensors and Actuators B*, 103, 213–218.

Boulova M. and Lucazeau G. (2002), Crystallite nanosize effect on the structural transitions of WO_3 studied by Raman spectroscopy, *Journal of Solid State Chemistry*, 167, 425–434.

Brattain W. H. and Bardeen J. (1953), Surface properties of germanium, *Bell Syst Tech J*, 32, 1–41.

Brinker J. C. and Scherer G. (1990), *Sol-Gel Science*, Academic, San Diego.

Buzby S., Franklin S. and Ismat Shah S. (2007), Synthesis of metal-oxide nanoparticles: gas–solid transformations, *in* Rodríguez J. A. and Fernandez García M. (eds), *Synthesis, Properties and Applications of Oxide Nanomaterials*, Wiley, New York, pp. 119–134.

Byrappa K. and Yoshimura M. (2001a), *Handbook of Hydrothermal Technology*, Noyes Publications/William Andrew Publishing, LLC, Norwich, pp. 1–43.

Byrappa K. and Yoshimura M. (2001b), *Handbook of Hydrothermal Technology*, Noyes Publications/William Andrew Publishing, LLC, Norwich, pp. 82–151.

Cabot A., Arbiol J., Morante J. R., Weimar U., Bârsan N. *et al.* (2000), Analysis of the noble metal catalytic additives introduced by impregnation of as obtained SnO_2 sol–gel nanocrystals for gas sensors, *Sensors and Actuators B*, 70, 87–100.

Cabot A., Vilà A. and Morante J. R. (2002), Analysis of the catalytic activity and electrical characteristics of different modified SnO_2 layers for gas sensors, *Sensors and Actuators B*, 84, 12–20.

Carotta M. C., Dallara C., Martinelli G., Passari L. and Camanzi A. (1991), CH_4 thick-film gas sensors: characterization method and theoretical explanation, *Sensors and Actuators B*, 3, 191–196.

Carotta M. C., Ferroni M., Gnani D., Guidi V., Merli M. *et al.* (1999), Nanostructured pure and Nb-doped TiO_2 as thick-film gas sensors for environmental monitoring, *Sensors and Actuators B*, 58, 310–317.

Carotta M. C., Ferrari E., Giberti A., Malagù C., Nagliati M. *et al.* (2006), Semiconductor gas sensors for environmental monitoring, *Advances in Science and Technology*, 45, 1818–1827.

Carotta M. C., Gherardi S., Malagù C., Nagliati M., Vendemiati B. *et al.* (2007a), Comparison between titania thick-films obtained through sol–gel and hydrothermal synthetic processes, *Thin Solid Films*, 515, 8339–8344.

Carotta M. C., Benetti M., Ferrari E., Giberti A., Malagù C. *et al.* (2007b), Basic interpretation of thick-film gas sensors for atmospheric application, *Sensors and Actuators B*, 126, 672–677.

Carotta M. C., Cervi A., Giberti A., Guidi V., Malagù C. *et al.* (2008), Metal-oxide solid solutions for light alkane sensing, *Sensors and Actuators B*, 133, 516–520.

© Woodhead Publishing Limited, 2012

Carotta M. C., Cervi A., Gherardi S., Guidi V., Malagù C. *et al.* (2009a), (Ti, Sn)O_2 solid solutions for gas sensing: a systematic approach by different techniques for different calcination temperature and molar composition, *Sensors and Actuators B*, 139, 329–339.

Carotta M. C., Gherardi S., Guidi V., Malagù C., Martinelli G. *et al.* (2009b), Electrical and spectroscopic properties of $Ti_{0.2}Sn_{0.8}O_2$ solid solution for gas sensing, *Thin Solid Films*, 517, 6176–6183.

Carotta M. C., Cervi A., Di Natale V., Gherardi S., Giberti A. *et al.* (2009c), ZnO gas sensors: a comparison between nanoparticles and nanotetrapods-based thick-films, *Sensors and Actuators B*, 137, 164–169.

Carotta M. C., Cervi A., Fioravanti A., Gherardi S., Giberti A. *et al.* (2011), A novel ozone detection at room temperature through UV-led-assisted ZnO thick-film sensors, *Thin Solid Films*.

Chang S. C. (1980), Oxygen chemisorption on tin oxide: correlation between electrical conductivity and EPR measurements, *J Vac Sci Technol*, 17, 366–369.

Chiorino A., Ghiotti G., Prinetto F., Carotta M. C., Martinelli G. *et al.* (1997), Characterization of SnO_2-based gas sensors. A spectroscopic and electrical study of thick-films from commercial and laboratory-prepared samples, *Sensors and Actuators B*, 44, 474–482.

Chiorino A., Ghiotti G., Prinetto F., Carotta M. C., Gnani D. *et al.* (1999), Preparation and characterization of SnO_2 and MoO_x-SnO_2 nanosized powders for thick-film gas sensors, *Sensors and Actuators B*, 58, 338–349.

Chiorino A., Ghiotti G., Prinetto F., Carotta M. C., Malagù C. *et al.* (2001), Preparation and characterization of SnO_2 and WO_x-SnO_2 nano-sized powders and thick-films for gas sensing, *Sensors and Actuators B*, 78, 89–97.

Choi Y. G., Sakai G., Shimanoe K., Miura N. and Yamazoe N. (2003), Wet process-prepared thick-films of WO_3 for NO_2 sensing, *Sensors and Actuators B*, 95, 258–265.

Chu X. F. and Siciliano P. (2003), CH_3SH-sensing characteristics of $LaFeO_3$ thick-film prepared by co-precipitation method, *Sensors and Actuators B*, 94, 197–200.

Chung Y. K., Kim M. H., Hum W. S., Lee H. S., Song J. K. *et al.* (1999), Gas sensing properties of WO_3 thick-film for NO_2 gas dependent on process condition, *Sensors and Actuators B*, 60, 267–269.

Comini E., Faglia G., Sberveglieri G., Pan Z. W. and Wang Z. L. (2002), Stable and highly sensitive gas sensors based on semiconducting oxide nanobelts, *Appl Phys Lett*, 81, 1869–1871.

Commission Directive 2008/50/EC of 21 May 2008 on ambient air quality and cleaner air for Europe.

Crowell C. R. and Rideout V. L. (1969), Normalized thermionic-field (T-F) emission in metal-semiconductor (Schottky) Barriers, *Solid-State Electron*, 12, 89–105.

Das S., Chakraborty S., Parkash O., Kumar D., Bandyopadhyay S. *et al.* (2008), Vanadium doped tin dioxide as a novel sulfur dioxide sensor, *Talanta*, 75, 385–389.

de Lacy Costello B. P. J., Ewen R. J., Ratcliffe N. M. and Richards M. (2008), Highly sensitive room temperature sensors based on the UV-LED activation of zinc oxide nanoparticles, *Sensors and Actuators B*, 134, 945–952.

Diebold U. (2003), The surface science of titanium dioxide, *Surface Science Reports*, 48, 53–229.

Ding Z., Zhang M. and Han J. (2001), Hydrothermal synthesis of monodispersed lanthanum titanate particles, *Mater Phys Mech*, 4, 107–110.

© Woodhead Publishing Limited, 2012

Dodd A., McKinley A., Tsuzuki T. and Saunders M. (2009), Tailoring the photocatalytic activity of nanoparticulate zinc oxide by transition metal oxide doping, *Mater Chem Phys*, 114, 382–386.

D'Souza L. and Richards R. (2007), Synthesis of metal-oxide nanoparticles: liquid–solid transformations, *in* Rodríguez J. A. and Fernandez García M. (eds), *Synthesis, Properties and Applications of Oxide Nanomaterials*, Wiley, New York, pp. 81–117.

Dusastre V. and Williams D. E. (1999), Gas-sensitive resistor properties of the solid solution series $Ti_x(Sn_{1-y}Sb_y)_{1-x}O_2$ ($0 < x < 1$, $y = 0$, 0.01, 0.05), *J Mater Chem*, 9, 445–450.

Erbs W., Desilvestro J., Borgarello E. and Gratzel M. (1984), Visible-light-induced O_2 generation from aqueous dispersions of WO, *J Phys Chem*, 88, 4001–4006.

Ferroni M., Guidi V., Martinelli G., Comini E., Sberveglieri G. *et al.* (2003), Selective sublimation processing of a molybdenum-tungsten mixed oxide thin film, *J Vac Sci Technol B*, 21, 1442–1448.

Fliegel W., Behr G., Werner J. and Krabbes G. (1994), Preparation, development of microstructure, electrical and gas-sensitive properties of pure and doped SnO_2 powders, *Sensors and Actuators B*, 18–19, 474–477.

Frank J., Fleischer M. and Meixner H. (1996), Electrical doping of gas sensitive, semiconducting Ga_2O_3 thin films, *Sensors and Actuators B*, 34, 373–377.

Fujishima A. and Honda K. (1972), Electrochemical photolysis of water at a semiconductor electrode, *Nature*, 238, 37–38.

Gercher V. A. and Cox D. F. (1995), Water adsorption on stoichiometric and defective $Sn0_2$ (110) surfaces, *Surface Science*, 322, 177–184.

Ghiotti G., Chiorino A., Martinelli G. and Carotta M. C. (1997), Moisture effects on pure and Pd-doped SnO_2 thick-films analysed by FTIR spectroscopy and conductance measurements, *Sensors and Actuators B*, 44, 474–482.

Gopalakrishnan J. and Mani R. (2009), Quest for new materials: inorganic chemistry plays a crucial role, *J Chem Sci*, 121, 235–256.

Göpel W., Kirner U. and Wiemhofer H. D. (1988), Surface and bulk properties of TiO_2 in relation to sensor applications, *Solid State Ionics*, 28–30, 1423–1430.

Gui Y., Li S., Xu J. and Li C. (2008), Study on TiO_2-doped ZnO thick-film gas sensors enhanced by UV light at room temperature, *Microelectronics Journal*, 39, 1120–1125.

Guidi V., Butturi M. A., Carotta M. C., Cavicchi B., Ferroni M. *et al.* (2002), Gas sensing through thick-film technology, *Sensors and Actuators B*, 84, 72–77.

Guidi V., Carotta M. C., Ferroni M., Martinelli G. and Sacerdoti M. (2003), Effect of dopants on grain coalescence and oxygen mobility in nanostructured titania anatase and rutile, *J Phys Chem B*, 107, 120–124.

Guidi V., Blo M., Butturi M. A., Carotta M. C., Galliera S. *et al.* (2004), Aqueous and alcoholic syntheses of tungsten trioxide powders for NO_2 detection, *Sensors and Actuators B*, 100, 277–282.

Hague D. C. and Mayo M. J. (1993), The effect of crystallization and a phase transformation on the grain growth of nanocrystalline titania, *Nanostructured Materials*, 3, 61–67.

Harbeck S., Szatvanyi A., Bârsan N., Weimar U. and Hoffmann V. (2003), DRIFT studies of thick-film un-doped and Pd-doped SnO_2 sensors: temperature changes effect and CO detection mechanism in the presence of water vapour, *Thin Solid Films*, 436, 76–83.

Hauesler A. and Meyer J. U. (1996), A novel thick-film conductive type CO_2 sensor, *Sensors and Actuators B*, 34, 388–395.

© Woodhead Publishing Limited, 2012

Hossein-Babaei F. and Ghafarinia V. (2010), Compensation for the drift-like terms caused by environmental fluctuations in the responses of chemoresistive gas sensors, *Sensors and Actuators B*, 143, 641–648.

Howard C. J., Luca V. and Knight K. S. (2002), High-temperature phase transitions in tungsten trioxide – the last word? *J Phys: Condens Matter*, 14, 377–387.

Hugon O., Sauvan M., Benech P., Pijolat C. and Lefebvre F. (2000), Gas separation with zeolite filter, application to the selectivity enhancement of chemical sensors, *Sensors and Actuators B*, 67, 235–243.

Ivanov P., Hubalek J., Malysz K., Prášek J., Vilanova X. *et al.* (2004), A route toward more selective and less humidity sensitive screen-printed SnO_2 and WO_3 gas sensitive layers, *Sensors and Actuators B*, 100, 221–227.

Izu N., Shin W., Matsubara I. and Murayama N. (2004), Development of resistive oxygen sensors based on cerium oxide thick-film, *J Electroceram*, 13, 703–706.

Jiao Z. H., Sun X. W., Wang J. M., Ke L. and Demir H. V. (2010), Hydrothermally grown nanostructured WO_3 films and their electrochromic characteristics, *J Phys D: Appl Phys*, 43, 285501.

Kamp B., Merkle R. and Maier J. (2001), Chemical diffusion of oxygen in tin oxide, *Sensors and Actuators B*, 77, 534–542.

Kanda K. and Maekawa T. (2005), Development of a WO_3 thick-film-based sensor for the detection of VOC, *Sensors and Actuators B*, 108, 97–101.

Kharade R. R., Mane S. R., Mane R. M., Patil P. S. and Bhosale P. N. (2010), Synthesis and characterization of chemically grown electrochromic tungsten oxide, *J Sol-Gel Sci Technol*, 56, 177–183.

Kim J., Lee C. and Choi W. (2010), Platinized WO_3 as an environmental photocatalyst that generates OH radicals under visible light, *Environ Sci Technol*, 44, 6849–6854.

Klingshirn C. (2007), ZnO: from basics towards applications, *Phys Stat Sol B*, 244 (9), 3027–3073.

Lantto V., Romppainen P. and Leppävuori S. (1988), A study of the temperature dependence of the barrier energy in porous tin dioxide, *Sensors and Actuators*, 14, 149–163.

Lee D. S., Han S. D., Huh J. S. and Lee D. D. (1999), Nitrogen oxides-sensing characteristics of WO_3-based nanocrystalline thick-film gas sensor, *Sensors and Actuators B*, 60, 57–63.

Linsebigler A. L., Lu G. and Yates J. T. Jr (1995), Photocatalysis on TiO_2 surfaces: principles, mechanisms, and selected results, *Chemical Reviews*, 95, 735–758.

Lu J. G., Chang P. and Fan Z. (2006), Quasi-one-dimensional metal oxide materials—synthesis, properties and applications, *Mater Sci Eng R*, 52, 49–91.

Lutic D., Sanati M. and Lloyd Spetz A. (2007), Gas sensors, *in* Rodríguez J. A. and Fernandez García M. (eds), *Synthesis, Properties and Applications of Oxide Nanomaterials*, Wiley, New York, pp. 411–450.

Mädler L., Kammler H. K., Müller R. and Pratsinis S. E. (2002), Controlled synthesis of nanostructured particles by flame spray pyrolysis, *J Aerosol Sci*, 33, 369–389.

Madou M. J. and Morrison S. R. (1989), *Chemical Sensing with Solid State Devices*, Academic, New York.

Maffeıs T. G. G., Owen G. T., Malagù C., Martinelli G., Kennedy M. K. *et al.* (2004), Direct evidence of the dependence of surface state density on the size of SnO_2 nanoparticles observed by scanning tunnelling spectroscopy, *Surface Science*, 550, 21–25.

Malagù C., Carotta M. C., Fissan H., Guidi V., Kennedy M. K. *et al.* (2004a), Surface state density decrease in nanostructured polycrystalline SnO_2: modelling and experimental evidence, *Sensors and Actuators B*, 100, 283–286.

© Woodhead Publishing Limited, 2012

Malagù C., Guidi V., Carotta M. C. and Martinelli G. (2004b), Unpinning of Fermi level in nanocrystalline semiconductors, *Appl Phys Lett*, 84, 4158–4160.

Malagù C., Carotta M. C., Galliera S., Guidi V., Maffeıs T. G. G. *et al.* (2004c), Evidence of bandbending flattening in 10 nm polycrystalline SnO_2, *Sensors and Actuators B*, 103/1–2, 50–54.

Malagù C., Martinelli G., Ponce M. A. and Aldao C. M. (2008), Unpinning of the Fermi level and tunneling in metal oxide semiconductors, *Appl Phys Lett*, 92, 162104.

Marsal A., Cornet A. and Morante J. R. (2003), Study of the CO and humidity interference in La doped tin oxide CO_2 gas sensor, *Sensors and Actuators B*, 94, 324–329.

Martinelli G., Carotta M. C., Ghiotti G. and Traversa, E. (1999), Thick-film gas sensors based on nano-sized semiconducting oxides powders, *MRS Bulletin*, 24(6), 30–36.

Martins R., Fortunato E., Nunes P., Ferreira I., Marques A. *et al.* (2004), Zinc oxide as an ozone sensor, *J Appl Phys*, 96 (3), 1398–1408.

Matsuda S. and Kato A. (1983), Titanium oxide based catalysts – a review, *Applied Catalysis*, 8, 149–165.

McAleer J. F., Moseley P. T., Norris J. O. W., Williams D. E. and Tofield B. C. (1988), Tin oxide gas sensors, Parts 1 and 2, *J Chem Soc Faraday Trans 1*, 84 (2), 441–457.

Meng D., Yamazaki T., Shen Y., Liu Z. and Kikuta T. (2009), Preparation of WO_3 nanoparticles and application to NO_2 sensor, *Applied Surface Science*, 256, 1050–1053.

Morrison S. R. (1982), Semiconductor gas sensors, *Sensors and Actuators*, 2, 329–341.

MRS Spring Meeting (2006), *Symposium R – Nanostructured Materials and Hybrid Composites for Gas Sensors and Biomedical Applications*, Cambridge University Press, Cambridge.

MRS Spring Meeting (2010), *Symposium K – Functional Materials and Nanostructures for Chemical and Biochemical Sensing*, Cambridge University Press, Cambridge.

Munnix S. and Schmeits M. (1985), Origin of defect states on the surface of TiO_2, *Physical Review B*, 31, 3369–3371.

Musci M., Notaro M., Curcio F., Casale M. C. and De Michele G. (1992), Laser synthesis of vanadium-titanium oxide catalysts, *J Mater Res*, 7, 2846–2852.

Özgür Ü., Alivov Y. I., Liu C., Teke A., Reshchikov M. A. *et al.* (2005), A comprehensive review of ZnO materials and devices, *J Appl Phys*, 98, 041301.

Park M., Mitchell T. E. and Heuer H. (1975), Subsolidus equilibria in the SnO_2–TiO_2 system, *J Am Ceram Soc*, 58 (1), 43–47.

Patil A. V., Dighavkar C. G., Sonawane S. K., Patil S. J. and Borse R. Y. (2010), Formulation and characterization of Cu doped ZnO thick-films as LPG gas sensor, *Sensors and Transducers Journal*, 9, 11–20.

Paz Y. (2010), Application of TiO_2 photocatalysis for air treatment: patents' overview, *Applied Catalysis B: Environmental*, 99, 448–460.

Pijolat C., Riviere B., Kamionka M., Viricielle J. P. and Breuil P. (2003), Tin dioxide gas sensors as a tool for atmospheric pollution monitoring: problems and possibilities for improvements, *J Mater Sci*, 38, 4333–4346.

Ponce M. A., Malagù C., Carotta M. C., Martinelli G. and Aldao C. M. (2008), Gas in-diffusion contribution to impedance in tin oxide thick-films, *J Appl Phys*, 104, 054907.

Prades J. D., Jimenez-Diaz R., Hernandez-Ramirez F., Barth S., Cirera A. *et al.* (2009), Equivalence between thermal and room temperature UV light-modulated responses of gas sensors based on individual SnO_2 nanowires, *Sensors and Actuators B*, 140, 337–341.

Prudenziati M. (1994), *Handbook of Sensors and Actuators: Thick-film Sensors*, Elsevier, Amsterdam.

© Woodhead Publishing Limited, 2012

Qi J. and Shimamoto S. (2012), A cognitive mobile sensor network for environment observation, *Telematics and Informatics*, 29, 26–32.

Qu W. and Meyer J. U. (1997), Thick-film humidity sensor based on porous $MnWO_4$ material, *Meas Sci Technol*, 8, 593–600.

Radecka M., Zakrzewska K. and Rekas M. (1998), SnO_2-TiO_2 solid solutions for gas sensors, *Sensors and Actuators B*, 47, 194–204.

Radecka M., Przewoźnik J. and Zakrzewska K. (2001), Microstructure and gas-sensing properties of $(Sn,Ti)O_2$ thin films deposited by RGTO technique, *Thin Solid Films*, 391, 247–254.

Rao G. S. T. and Rao D. T. (1999), Gas sensitivity of ZnO based gas sensor to NH_3 at room temperature, *Sensors and Actuators B*, 55, 166–169.

Reed J. S. (1995a), *Principles of Ceramic Processing*, 2nd edn, Wiley & Sons, New York, Chapter 16.

Reed J. S. (1995b), *Principles of Ceramic Processing*, 2nd edn, Wiley & Sons, New York, Chapter 28.

Reed J. S. (1995c), *Principles of Ceramic Processing*, 2nd edn, Wiley & Sons, New York, Chapter 27.

Reed J. S. (1995d), *Principles of Ceramic Processing*, 2nd edn, Wiley & Sons, New York, Chapter 29.

Reyes L. F., Hoel A., Saukko S., Heszler P., Lantto V. *et al.* (2006), Gas sensor response of pure and activated WO_3 nanoparticle films made by advanced reactive gas deposition, *Sensors and Actuators B*, 117, 128–134.

Romppainen P. and Lantto V. (1988), The effect of microstructure on the height of potential energy barriers in porous tin dioxide gas sensors, *J Appl Phys*, 63, 5159–5165.

Ruiz A., Calleja A., Espiell F., Cornet A. and Morante J. R. (2003), Nanosized Nb-TiO_2 gas sensors derived from alkoxides hydrolization, *IEEE Sens J*, 3, 189–194.

Ruiz A. M., Dezanneau G., Arbiol J., Cornet A. and Morante J. R. (2004a), Insights into the structural and chemical modifications of Nb additive on TiO_2 nanoparticles, *Chem Mater*, 16, 862–871.

Ruiz A. M., Sakai G., Cornet A., Shimanoe K., Morante J. R. *et al.* (2004b), Microstructure control of thermally stable TiO_2 obtained by hydrothermal process for gas sensors, *Sensors and Actuators B*, 103, 312–317.

Ruske F., Jacobs C., Sittinger V., Szyszka B. and Werner W. (2007), Large area ZnO: Al films with tailored light scattering properties for photovoltaic applications, *Thin Solid Films*, 515, 8695–8698.

Sacerdoti M., Dalconi M. C., Carotta M. C., Cavicchi B., Ferroni M. *et al.* (2004), XAS investigation of tantalum and niobium in nanostructured TiO_2 anatase, *J Solid State Chem*, 177, 1781–1788.

Sahm T., Mädler L., Gurlo A., Bârsan N., Pratsinis S. E. *et al.* (2004), Flame spray synthesis on tin dioxide nanoparticles for gas sensing, *Sensors and Actuators B*, 98, 148–153.

Sahm T., Gurlo A., Bârsan N. and Weimar U. (2006), Basics of oxygen and SnO_2 interaction; work function change and conductivity measurements, *Sensors and Actuators B*, 118, 78–83.

Samson S. and Fonstad C. G. (1973), Defect structure and electronic donor levels in stannic oxide crystals, *J Appl Phys*, 44, 4618–4621.

Sarala Devi G., Bala Subrahmanyam V., Gadkari S. C. and Gupta S. K. (2006), NH_3 gas sensing properties of nanocrystalline ZnO based thick-films, *Analytica Chimica Acta*, 568, 41–46.

© Woodhead Publishing Limited, 2012

Sasaki I., Tsuchiya H., Nishioka M., Sadakata M. and Okubo T. (2002), Gas sensing with zeolite-coated quartz crystal microbalances-principal component analysis approach, *Sensors and Actuators B*, 86, 26–33.

Sberveglieri G., Faglia G., Groppelli S., Nelli P. and Camanzi A. (1990), A new technique for growing large surface area SnO_2 thin film (RGTO technique), *Semi Sci Tech*, 5, 1231–1233.

Schierbaum K. D., Kirner U. K., Geiger J. F. and Göpel W. (1991), Schottky-barrier and conductivity gas sensors based upon Pd/SnO_2 and Pt/SnO_2, *Sensors and Actuators B*, 4, 87–94.

Schmidt-Mende L. and MacManus-Driscoll J. L. (2007), ZnO – nanostructures, defects, and devices, *Mater Today*, 10 (5), 40–48.

Segal D. (1997), Chemical synthesis of ceramic materials, *J Mater Chem*, 7(8), 1297–1305.

Seiyama T., Kato A., Fulishi K. and Nagatani M. (1962), A new detector for gaseous components using semiconductive thin films, *Anal Chem*, 34, 1502–1503.

Senguttuvana T. D., Srivastava V., Tawal J. S., Mishra M., Srivastava S. *et al.* (2010), Gas sensing properties of nanocrystalline tungsten oxide synthesized by acid precipitation method, *Sensors and Actuators B*, 150, 384–388.

Sharma R. K., Bhatnagar M. C. and Sharma G. L. (1996), Effect of Nb metal TiO_2 oxygen gas sensor, *Applied Surface Science*, 92, 647–650.

Shur M. (1990), *Physics of Semiconductor Devices*, Prentice-Hall, New York.

Solis J. L., Saukko S., Kish L. B., Granqvist C. G. and Lantto V. (2001), Nanocrystalline tungsten oxide thick-films with high sensitivity to H_2S at room temperature, *Sensors and Actuators B*, 77, 316–321.

Somiya S. and Roy R. (2000), Hydrothermal synthesis of fine oxide particles, *Bull Mater Sci*, 23, 453–460.

Szilágyi I. M., Saukko S., Mizsei J., Tóth A. L., Madarász J. *et al.* (2010), Gas sensing selectivity of hexagonal and monoclinic WO_3 to H_2S, *Solid State Sciences*, 12, 1857–1860.

Taguchi N. (1970), UK Patent, 1280809.

Takami A. (1988), Development of titania heated exhaust-gas oxygen sensor, *Ceram Bull*, 67 (12), 1956–1960.

Tamaki J., Zhang Z., Fujimori K., Akiyama M., Harada T. *et al.* (1994), Grain-size effects in tungsten oxide-based sensor for nitrogen oxides, *J Electrochem Soc*, 141, 2207–2210.

Tan O. K., Cao W., Hu Y. and Zhu W. (2004), Nanostructured oxides by high energy ball milling technique: application as gas sensing materials, *Solid State Ionics*, 172, 309–316.

Tang H., Prasad K., Sanjinés R. and Lévy F. (1995), TiO_2 anatase thin films as gas sensors, *Sensors and Actuators B*, 26–27, 71–75.

Tersoff J. (1984), Schottky barrier heights and the continuum of gap states, *Phys Rev Lett*, 52, 465–468.

Tien T. Y., Stagler H. L., Gibbons E. F. and Zacmanidis P. J. (1975), TiO_2 as an air-to-fuel ratio sensor for automobile exhausts, *Am Ceram Soc Bull*, 54, 280–282.

Toan N. N., Saukko S. and Lantto V. (2003), Gas sensing with semiconducting perovskite oxide $LaFeO_3$, *Physica B*, 327, 279–282.

Tomchenko A. A., Emelianov I. L. and Khatko V. V. (1999), Tungsten trioxide-based thick-film NO sensor: design and investigation, *Sensors and Actuators B*, 57, 166–170.

© Woodhead Publishing Limited, 2012

Traversa E., Matsushima S., Okada G., Sadaoka Y., Sakai S. *et al.* (1995), NO_2 sensitive $LaFeO_3$, thin films prepared by R.F. sputtering, *Sensors and Actuators B*, 24–25, 661–664.

Traversa E., Nunziante P., Sakamoto M., Sadaoka Y., Carotta M. C. *et al.* (1998), Thermal evolution of the microstructure of nanosized $LaFeO_3$ powders from the thermal decomposition of a heteronuclear complex, $La[Fe(CN)_6]$ $5H_2O$, *J Mater Res*, 13, 1335–1344.

Traversa E., Di Vona M. L., Licoccia S., Sacerdoti M., Carotta M. C. *et al.* (2001), Sol–gel processed TiO_2-based nano-sized powders for use in thick-film gas sensors for atmospheric pollutant monitoring, *J. Sol–Gel Sci Technol*, 22, 167–179.

Trivikrama Rao G. S. and Tarakarama Rao D. (1999), Gas sensitivity of ZnO based thick-film sensor to NH_3 at room temperature, *Sensors and Actuators B*, 55, 166–169.

Vincenzi D., Butturi M. A., Guidi V., Carotta M. C., Martinelli G. *et al.* (2000), Gas-sensing device implemented on a micromachined membrane: a combination of thick-film and very large scale integrated technologies, *J Vac Sci Technol B*, 18, 2441–2445.

Viricelle J. P., Pauly A., Mazet L., Brunet J., Bouvet M. *et al.* (2006), Selectivity improvement of semi-conducting gas sensors by selective filter for atmospheric pollutants detection, *Mater Sci Eng C*, 26, 186–195.

Vogt T., Woodward P. M. and Hunter B. A. (1999), The high-temperature phases of WO_3, *Journal of Solid State Chemistry*, 144, 209–215.

Vuong D. D., Sakai G., Shimanoe K. and Yamazoe N. (2005), Hydrogen sulfide gas sensing properties of thin films derived from SnO_2 sols different in grain size, *Sensors and Actuators B*, 105, 437–442.

Wang Z. L. (2004), Zinc oxide nanostructures: growth, properties and applications, *J Phys: Condens Matter*, 16, R829–R858.

Williams E. W., Lawor C. M., Keeling A. G. and Gould R. D. (1994), Novel room-temperature carbon-monoxide sensor utilizing rate of change of resistance in thick-films of tin oxide, *Int J Electron*, 76, 815–820.

Xiangfeng C., Dongli J., Djuršić A. B. and Leung Y. H. (2005), Gas-sensing properties of thick-film based on ZnO nano-tetrapods, *Chem Phys Lett*, 401, 4–6, 426–429.

Xu C., Tamaki J., Miura N. and Yamazoe N. (1991), Grain size effects on gas sensitivity of porous SnO_2-based elements, *Sensors and Actuators B*, 3, 147–155.

Xu C.-N., Tamaki J., Miura N. and Yamazoe N. (1996), Nature of sensitivity promotion in Pd-loaded SnO_2 gas sensor, *J Electrochem Soc*, 143, L148–L150.

Yamazoe N. (1991), New approaches for improving semiconductor gas sensors, *Sensors and Actuators B*, 5, 7–19.

Yamazoe N., Fuchigami J., Nishikawa M. and Sejama T. (1979), Tin oxide surface and O_2, H_2O and H_2, *Surface Science*, 86, 334–344.

Yamazoe N., Kurokawa Y. and Seiyama T. (1983), Effects of additives on semiconductor gas sensors, *Sensors and Actuators*, 4, 283–289.

Yan A., Xie C., Zeng D., Cai S. and Li H. (2010), Synthesis, formation mechanism and illuminated sensing properties of 3D WO_3 nanowall, *Journal of Alloys and Compounds*, 495, 88–92.

Yang T. Y., Lin H. M., Wei B. Y., Wu C. Y. and Lin C. K. (2003), UV enhancement of the gas sensing properties of nano-TiO_2, *Rev Adv Mater Sci*, 4, 48–54.

Yuan T. C. and Virkar A. V. (1988), Kinetics of spinodal decomposition in the TiO_2–SnO_2 system: the effect of aliovalent dopants, *J Am Ceram Soc*, 71 (1), 12–21.

© Woodhead Publishing Limited, 2012

Zakrzewska K., Radecka M., Przewoźnik J., Kowalski K. and Czuba P. (2005), Microstructure and photoelectrochemical characterization of the TiO_2–SnO_2 system, *Thin Solid Films*, 490, 101–107.

Zampolli S., Elmi I., Mancarella F., Betti P., Dalcanale E. *et al.* (2009), Real-time monitoring of sub-ppb concentrations of aromatic volatiles with a MEMS-enabled miniaturized gas-chromatograph, *Sensors and Actuators B*, 141, 322–328.

Zhang G. and Liu M. (2000), Effect of particle size and dopant on properties of SnO_2-based gas sensors, *Sensors and Actuators B*, 69, 144–152.

Zhu B. L., Zeng D. W., Wu J., Song W. L. and Xie C. S. (2003), Synthesis and gas sensitivity of In-doped ZnO nanoparticles, *J Mater Sci Mater Electron*, 14, 521–526.

Zhu J., Ren C., Chen G., Yu C., Wu J. *et al.* (1996), New automotive air/fuel sensor based on TiO_2-doped Nb_2O_5 thin film by ion-beam-enhanced deposition, *Sensors and Actuators B*, 32, 209–213.

© Woodhead Publishing Limited, 2012

12

Printed gas sensors based on electrolytes

C. LUCAT, F. MENIL and H. DEBEDA,
University of Bordeaux, France

Abstract: In this chapter we present significant examples of solid electrolyte sensors. Lambda probes constitute one of the rare commercial success stories of gas sensors. The more recently developed proportional probes could still compete with them commercially with the development of lean-burn and diesel engines. Planar thick-film technology appears the most promising manufacturing process. It is cheaper and more versatile than traditional ceramic processes, with lower manufacturing costs and fewer ageing problems than planar thin film technologies. Although the measurement of oxygen partial pressure constitutes the leading application of solid electrolyte sensors, this chapter shows many possibilities for detecting other gases. Sensing such gases probably constitutes the most promising application to date. Some of these sensors are currently proposed commercially. They generally imply coupling catalytic with thermodynamic processes. Many studies must still be undertaken in order to address outstanding problems.

Key words: gas sensors, solid electrolytes, screen-printing, potentiometric sensors, amperometric sensors.

12.1 Introduction

Solid electrolytes play a special part in the field of gas sensors, for at least two reasons:

1. Studies on this type of sensor were among the earliest in the gas sensor field and a large amount of R&D has been devoted to solid electrolyte sensors since the early 1960s.
2. The λ-sensor based on zirconia for oxygen sensing in automotive exhausts is certainly the most successful story of a commercial sensor, with several hundreds of millions of units manufactured.

Section 12.2 will initially recall some basic notions on solid electrolytes. Since solid electrolytes are ion conductors, transport properties in such materials are primarily ensured by ions and not by electrons or holes, as in semiconductors. Solid electrolytes can be applied to the field of gas sensing in at least two types of devices: potentiometric and amperometric. The former can be based on O^{2-}, F^{-}, H^{+}, Li^{+}, Na^{+}, Ag^{+} . . . ion conductors, whereas the latter is practically restricted to O^{2-} ion conductors, namely zirconia.

Potentiometric sensors, dealt with in section 12.3, are classified by whether they are working at thermodynamic equilibrium or not. In case of thermodynamic

© Woodhead Publishing Limited, 2012

equilibrium, potentiometric sensors are further classified according to the relationship between the gaseous species' capability to sense and the mobile ion in the solid electrolyte. Potentiometric sensors can be assimilated to batteries that deliver at zero current, an electromotive force function of the partial pressure of the gas that is to be sensed (target gas).

Amperometric sensors, dealt with in section 12.4, are based on oxygen pumping by the application of a voltage across zirconia. Without a diffusion barrier at the cathode, the device does not operate as a sensor but as a simple ionic pump. Gaseous oxygen O_2 or oxygen contained in oxygenated gases such as CO_2, NO_x, H_2O, etc. is reduced to the cathode in O^{2-} ions. These ions are attracted towards the anode by the applied voltage and re-oxidized in gaseous oxygen O_2 when they reach the anode. The presence of a diffusion barrier above the cathode limits this ionic current and ensures the proportionality between the latter (so-called limiting current) and the partial pressure of the target gas. More sophisticated devices are considered in section 12.5, associating several of the previous principles: oxygen pumps, potentiometric sensors and amperometric sensors. The best-known applications are detailed in corresponding sections, both on a theoretical basis and also from the point of view of the manufacturing technologies used. It will be demonstrated that printing technologies are of primary interest for the fabrication of many solid electrolyte sensors. Some possible future trends will be briefly mentioned in the conclusion.

12.2 Solid electrolytes

A solid electrolyte is, as its name indicates, a solid in which the transport of the electric charges is ensured by ions, as in liquids. However, whereas in a liquid, all the positive and negative charges are mobile under the action of an electric field, in a solid electrolyte generally only one species of ion can move within the crystal structure. To allow the movement of an ion, the crystal structure must necessarily comprise vacant sites, which will transitorily accommodate the mobile ions. Classically, there are two types of sites by which the ions can advance: vacancies characterized by the absence of ions in normal position in the crystal structure (Schottky defects) and interstitial sites, which are normally unoccupied (Frenkel defects). These defects can have two origins:

- A thermodynamic system at a temperature different from absolute zero always tends to evolve to a maximum entropy to minimize its Gibbs energy (G = H-TS). Consequently, any material in its purest state will always present pairs of defects (one negative and one positive defect per pair to respect electric neutrality). The higher the temperature is, the larger their number will be. These defects are known as *intrinsic*.
- The introduction of elements into the crystal structure with a valence different from that of the normal elements, will necessarily involve the presence of defects. For example, in the case of zirconia (ZrO_2) doped with yttrium, which

© Woodhead Publishing Limited, 2012

is the most well-known solid electrolyte (yttrium-stabilized zirconia, YSZ for), the substitution of tetravalent zirconium by trivalent yttrium must be compensated by an equivalent reduction of the negative charge, which leads to the presence of oxygen vacancies. The defects resulting from such a doping are known as *extrinsic*.

Experimentally, the ionic conductivity is thermally activated according to an Arrhenius relation:

$$\sigma_i = \sigma_0 \exp(-E_A/kT). \quad [12.1]$$

At moderated temperatures, i.e. in the range where the extrinsic defects are prevalent, the activation energy E_A reflects the energy required for an ion to jump from a vacant site to a nearby vacant site. At high temperatures, where the intrinsic defects dominate, the activation energy will include, in addition to the preceding term, a term relating to the energy formation of the intrinsic defects. The terms intrinsic and extrinsic, just as the various modes of conductivity, remind us of semiconductors. However, it is important to note that for the ionic conductivity, defined by the relation:

$$\sigma_i = c_i z_i q u_i. \quad [12.2]$$

the mobility u_i of the ions is generally 100 to 1000 times lower than that of the electrons in semiconductors (c_i represents the voluminal concentration in mobile ions i and z_i the charge number of these ions). To allow ionic conductivity to dominate the transport properties in a material, the concentration in electrons will have to be lower than the concentration in mobile ions by a factor of the same order of magnitude.

This is a first explanation for the relatively limited number of solid electrolytes. A second explanation arises from the nature of the mobile ions. To be able to move easily in the crystal structure, a mobile ion must conform to two conditions that one conceives rather well intuitively: firstly it must have a low valence as a high charge would indeed attract them too strongly towards the fixed ions of opposite charge of the crystal lattice; secondly it must be of small size. These two conditions produce the situation that the mobile cations are made up of almost only monovalent ions (H^+, Li^+, Na^+, K^+, Rb^+, Ag^+, Tl^+) and the mobile anions of ions fluorine F^- and oxygen O^{2-}, oxygen preceding very largely the other ions. The first true studies on solid electrolyte sensors were carried out for the proportioning of oxygen with zirconia (Peters and Mobius, 1961; Wagner, 1957; Weissbart and Ruka, 1961). The other principal coupled solid electrolyte/mobile ions studied are:

- alkaline carbonates and sulphates (Li^+, Na^+, K^+)/Li^+, Na^+, K^+,
- silver halides/Ag^+,
- LiSICON and NaSICON (for Super Ionic CONductor)/Li^+, Na^+,
- β-alumina /H^+, Na^+, Ag^+,

© Woodhead Publishing Limited, 2012

- HUP (hydrogen uranyl phosphatetetrahydrate: HUO_2PO_4, $4H_2O/H^+$,
- lanthanum fluoride LaF_3/F^-,
- lead fluoride PbF_2/F^-,
- doped ceria CeO_2/O^{2-}.

The only criterion common to the various solid electrolytes for a use as a functional sensor material is to have an electronic conductivity that is as low as possible and a notable ionic conductivity in the temperature range concerned with detection. The parameter of ionic conductivity increasing exponentially with temperature (Eq. [12.1]) is eminently critical in sensor operation. For example, stabilized zirconia is almost insulating at room temperature and sensors using this electrolyte cannot function properly below 500–600 °C. β-alumina and NaSICON can function at high temperatures, but also at temperatures hardly higher than the ambient one. Sulphates, on the other hand, break up beyond a few hundreds of degrees Celsius, and HUP can be generally used only at room temperature. More extensive lists of solid electrolytes with a potential use as sensor functional material are reported in Kleitz *et al.* (1991); Pasierb and Rekas (2009).

12.3 Potentiometric sensors

Potentiometric gas sensors may involve several mechanisms being used at the same time, and for this reason, an easy classification is not obvious. For our first step, we have tried to separate devices only controlled by thermodynamics from those controlled by both thermodynamics and kinetics.

12.4 Thermodynamically controlled sensors

A classification for this type of sensors was first given by Weppner (1987). For type I sensors, the target gas coincides with the mobile ion of the solid electrolyte (e.g. O_2 with O^{2-} in zirconia, H_2 with H^+ in HUP). In type II, the target gas coincides with the non-mobile ion of a binary compound (e.g. I_2 with I^- in AgI, which is an Ag^+ ion conductor). As for type III, the target gas does not match with any element of the ion conductor. One or several so-called auxiliary phases are required to achieve thermodynamic equilibrium between the gas phase, the electrode, the auxiliary phase(s) and the solid electrolyte.

What these various types of sensors all have in common is the ability to operate at thermodynamic equilibrium and to be able to deliver an e.m.f. depending on the partial pressure of the target gas. For this reason, the simplest theoretical approach to the operating principle of these sensors makes abundant use of electrochemical potentials. Electrochemical potential is of primary interest since it includes both chemical potential, which will take into account the partial pressure of the target gases, and electrical potential, which will determine the e.m.f. Before entering into more detail regarding the operating principles of the various sensor types, the

© Woodhead Publishing Limited, 2012

following sub-section will briefly recall the definitions, properties and useful relationships in chemical and electrochemical potentials, especially in thermodynamic equilibriums.

12.4.1 Electrochemical potential properties at thermodynamic equilibrium

A simple approach consists in extending the well-known results obtained at thermodynamic equilibrium with chemical systems, containing only neutral species, to electrochemical systems containing at least one type of charged species (Menil, 2008).

Chemical systems without any charged species

In a chemical system without any charged species, only the caloric and mechanical energies are taken into account. The chemical potential μ_i of species i is defined as:

$$\mu_i = \left(\frac{\delta G}{dn_i}\right)_{T,P,n_j},$$

where G is the Gibbs energy of the system, $i, j \ldots$ the various types of species in the system, $n_i, n_j \ldots$ the corresponding number of moles, T and P the temperature and total pressure of the system. For a gaseous system, the previous definition of the chemical potential leads to:

$$\mu_i = \mu_i^{0,P=1} + RT \ln(p_i) = \mu_i^0 + RT \ln(x_i), \quad [12.3]$$

where R is the perfect gas molar constant, μ_i^0 the Gibbs energy of one mole of gas i, taken in its pure state (not in a mixture), x_i the molar fraction of gas i in the mixture and p_i its partial pressure, defined by:

$$p_i = (n_i/\Sigma_i n_i)P = x_i P. \quad [12.4]$$

If the system contains non-gaseous species, the chemical potential of such species has the same formulation, but the molar fraction should in principle be replaced by the activity.

Considering now a chemical system in equilibrium between two thermodynamic states (I) and (II):

$$I \leftrightarrow II \Rightarrow \Sigma_i^I \alpha_i i \leftrightarrow \Sigma_i^{II} \alpha_i i,$$

where the $\alpha_i, \alpha_j \ldots$ are the stoichiometric coefficients of species i,j . . . in each member of the equilibrium, the Gibbs energy is the same for both states:

$$\Delta G_{I \to II} = 0$$

Hence:

$$\Sigma_i^I \alpha_i \mu_i = \Sigma_i^{II} \alpha_i \mu_i. \quad [12.5]$$

© Woodhead Publishing Limited, 2012

The development of this relationship leads to the mass action law. Another major consequence is that, if the same species is present in both states, its chemical potential is the same in both states:

$$\mu_i^{I} = \mu_i^{II}. \qquad [12.6]$$

One may take the example of water molecules in a system consisting of an aqueous liquid phase in equilibrium with its vapour. The chemical potential of water molecules has the same value in both states (which in the present case coincide with both liquid and gaseous phases). Because the chemical potential of water molecules is constant throughout the whole system, as well as that of all other species, no diffusion between liquid and gas phases occurs (on a macroscopic level), in agreement with the absence of spontaneous evolution of a system at thermodynamic equilibrium ($\Delta G_{I\rightarrow II} = 0$).

Electrochemical systems with at least one type of species charged

For an electrochemical system in which at least one type of species is charged, not only the calorific and mechanical energies have to be taken into account, but also the electrical energy. One possible approach to dealing with such a system is to define electrochemical functions, which will play a part similar to the previous chemical functions, but which will include electrical energy. To distinguish an electrochemical function from a chemical one, a tilde is added above the symbol of the chemical function. The chemical Gibbs energy – G – thus becomes the electrochemical Gibbs energy – $\tilde{G}$, and the chemical potential – μ – becomes the electrochemical potential $\tilde{\mu}$. Transferring the results of the previous sub-section leads to:

$$\tilde{\mu}_i = \left(\frac{\delta \tilde{G}}{\delta n_i} \right)_{T, P, n_j}.$$

The relationship for an electrochemical equilibrium becomes:

$$\Delta \tilde{G}_{I\rightarrow II} = \tilde{G}_{II} - \tilde{G}_{I} = 0 \qquad [12.7]$$

Combining [12.7] with the well-known relationship $\Delta G_{I\rightarrow II} = -zFE$ (as for example in batteries where E is the e.m.f., F the Faraday constant and z the number of charges implied in the equilibrium) leads to:

$$\Delta \tilde{G}_{I\rightarrow II} = \Delta G_{I\rightarrow II} + zFE. \qquad [12.8]$$

Intuitively, Eq. [12.8] suggests that the electrochemical potential of species i will have the form:

$$\tilde{\mu}_i = \mu_i + z_i F\Phi, \qquad [12.9]$$

where z_i and Φ are respectively the algebraic value of the charge and the electrical potential of species i.

Combining Eqs. [12.3] and [12.9] leads to:

© Woodhead Publishing Limited, 2012

$$\tilde{\mu}_i = \mu_i^0 + RT\ln(x_i) + z_i F\Phi. \quad [12.10]$$

Note that for uncharged species, the electrochemical potential identifies the chemical potential.

Considering now an electrochemical system in equilibrium between two thermodynamic states (I) and (II):

$$I \leftrightarrow II \Rightarrow \Sigma_i^I \alpha_i\, i \leftrightarrow \Sigma_i^{II} \alpha_i\, i,$$

the electrochemical Gibbs energy is the same for both states ($\tilde{G}_{I\rightarrow II} = 0$), which leads to:

$$\Sigma_i^I \alpha_i \tilde{\mu}_i = \Sigma_i^{II} \alpha_i \tilde{\mu}_i. \quad [12.11]$$

The development of this relationship usually yields the Nernst law. As another consequence, when the same species is present in both states, its electrochemical potential has the same value in both states:

$$\tilde{\mu}_i^I = \tilde{\mu}_i^{II}. \quad [12.12]$$

In other words, the electrochemical potential of a given species is constant in the whole system. Note that for conduction electrons, in metals and semiconductors, the electrochemical potential identifies to the Fermi level.

12.4.2 Type I sensors

Principle

The best representative sensor of this type is of course the oxygen zirconia gauge. Figure 12.1 shows the principle of such a cell, based on dense oxygen ion-conducting YSZ.

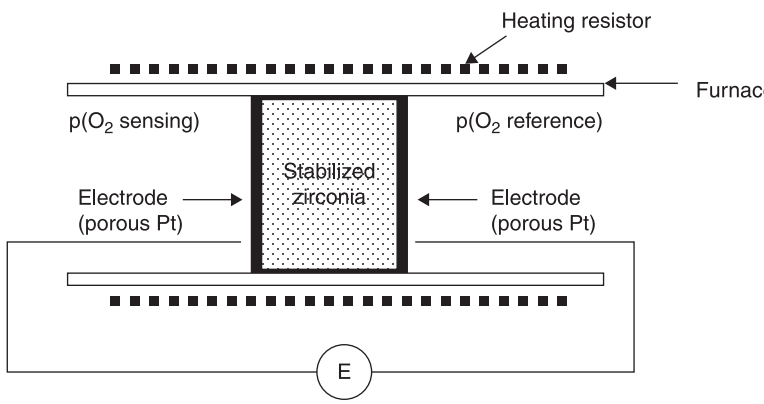

12.1 Principle of the potentiometric zirconia-based oxygen sensor.

© Woodhead Publishing Limited, 2012

This solid electrolyte covered with two identical porous electrodes made of platinum, for example, separates the sensing compartment from the reference one, in which the oxygen partial pressure is known. At sufficiently high temperatures (typically 800 °C), the gaseous oxygen, the mobile oxygen ions in zirconia and the conduction electrons of platinum electrodes in the electrodes are in thermodynamic equilibrium.

Let us take the following as given:

- $\tilde{\mu}(e_{se})$ and $\tilde{\mu}(e_{re})$ the electrochemical potential of electrons in the sensing (se) and reference (re) electrodes, respectively,
- $\mu(e_{se})$ and $\mu(e_{re})$ the chemical potential of electrons in the sensing and reference electrodes,
- $\tilde{\mu}(O^{2-}_{se})$ and $\tilde{\mu}(O^{2-}_{re})$ the electrochemical potential of O^{2-} ions in zirconia at the interface with the sensing and reference electrodes,
- $\mu(O_{2,\,se})$ and $\mu(O_{2,\,re})$ the chemical potential of gaseous oxygen in the sensing and reference compartments,
- Φ_{se} and Φ_{re} the electrical potentials of sensing and reference electrodes.

At each electrode, the following equilibrium occurs:

$$O_2 + 4e^- \leftrightarrow 2\,O^{2-}. \qquad [12.13]$$

Applying Eq. [12.11] to this equilibrium at each interface leads to:

$$\mu(O_{2,\,se}) + 4\tilde{\mu}(e_{se}) = 2\,\tilde{\mu}(O^{2-}_{se}), \qquad [12.14]$$

$$\mu(O_{2,\,re}) + 4\tilde{\mu}(e_{re}) = 2\,\tilde{\mu}(O^{2-}_{re}). \qquad [12.15]$$

Moreover, since the system is in thermodynamic equilibrium, the electrochemical potential of O^{2-} ions is constant throughout the whole zirconia, and especially at the interfaces:

$$\tilde{\mu}(O^{2-}_{se}) = \tilde{\mu}(O^{2-}_{re}). \qquad [12.16]$$

Combining Eqs. [12.14], [12.15] and [12.16] and applying the definition of chemical potential to gaseous oxygen and that of electrochemical potential to platinum electrons allows us to deduce:

$$\begin{aligned}\mu^\circ(O_2) + RT\ln[p(O_{2,\,se})] + 4\mu^\circ(e_{Pt}) - 4F\Phi_{se} = \mu^\circ(O_2)\\ + RT\ln[p(O_{2,\,re})] + 4\mu^\circ(e_{Pt}) - 4F\Phi_{re}.\end{aligned} \qquad [12.17]$$

The Nernst Law results from Eq. [12.17]:

$$E = \Phi_{se} - \Phi_{re} = (RT/4F)\ln\{[p(O_{2,\,se})]/[p(O_{2,\,re})]\}. \qquad [12.18]$$

The knowledge of $p(O_{2,\,re})$ in the reference compartment and the measurement of the e.m.f. enable the determination of the unknown oxygen partial pressure $p(O_{2,\,se})$ in the sensing compartment. This principle, already used in the 1960s for determining the oxygen content in molten metals, was transposed ten years later

© Woodhead Publishing Limited, 2012

to the air/fuel ratio monitoring in internal combustion engines with so-called λ-sensors.

λ-sensors

The emission of large amounts of polluting gases by the old petrol engines without catalytic converters was the origin of serious pollution problems in California at the beginning of the 1960s. Research programs were launched for the reduction of these emissions and a regulation was initially defined in the USA in 1968, then in Europe in 1971. Since 1993, all vehicles using gasoline that are produced in Europe are equipped with catalytic converters, which eliminate the three principal pollutants from exhaust gases: NO_x, HC and CO, by transforming them into nitrogen, oxygen, water and carbon dioxide. The catalysis is ensured inside the converter by a so-called three-way catalyst containing platinum, palladium and rhodium.

The correct operation of the catalytic converter supposes, however, that the admission gas mixture is regulated precisely by stoichiometry, i.e. the volume ratio of air to fuel (A/F) is equal to 14.6. This condition is fulfilled using a YSZ-based potentiometric sensor placed in the exhaust gas. Indeed, for A/F where the values are very slightly below the stoichiometric ratio of 14.6 (admission mixtures known as 'rich' in fuel), the composition of the exhaust gas (known as 'rich-burn') is excessively rich, with very low oxygen partial pressures. As soon as the A/F ratio of the admission mixture crosses the stoichiometric point (mixtures known as 'lean' in fuel), the oxygen partial pressure in the exhaust gas (known as 'lean-burn') increases by several orders of magnitude to possibly reach the afore-mentioned percentage. The logarithmic dependence of the sensor electromotive force with the oxygen partial pressure (Eq. [12.18]) makes it possible to measure this variation easily and to address a feedback signal to bring back the admission mixture to stoichiometry (Duecker *et al.*, 1975; Eddy, 1971; Engh and Wallman, 1977; Fleming *et al.*, 1973; Friese *et al.*, 1973).

The left part of Fig. 12.2 represents a schematic cross view of a lambda probe like the type of those installed at the engine exit. The solid electrolyte, based on stabilized zirconia ceramic sintered at a high temperature, appears as a thimble of approximately 25 mm in length, 5 mm in internal diameter and 2 mm in thickness. Two porous platinum electrodes are deposited on the internal and external walls of the thimble, in the form of layers of a few microns in thickness. The internal electrode is linked by the sheath of the connexion lead, to the surrounding 'clean' air, which is used as a reference. In the internal cavity of the thimble, a cylindrical ceramic of approximately 3 mm in external diameter, equipped with a heating resistance deposited in a thick layer, ensures a minimal temperature of 700 °C for the operating of zirconia. The external electrode, covered with a protective coating of $MgAl_2O_4$ spinel is in direct contact with the exhaust gas through a metal envelope, which is used as mechanical sleeve for the unit. The latter electrode works as a sensing electrode. The right part of Fig. 12.2 shows the abrupt variation of the sensor f.e.m. when the admission mixture crosses the stoichiometric point.

© Woodhead Publishing Limited, 2012

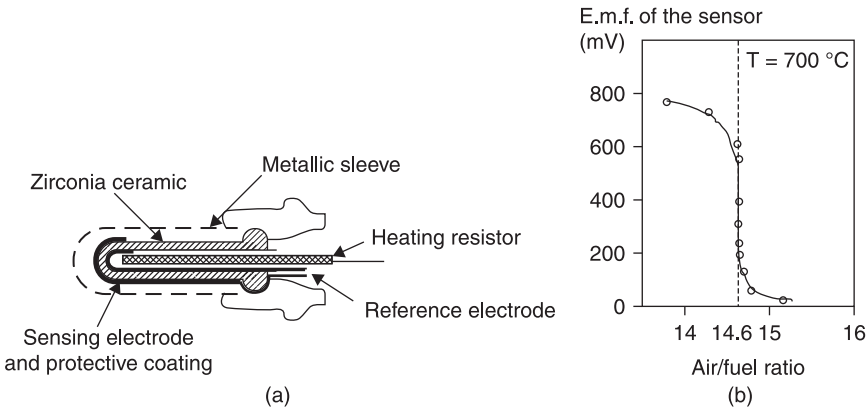

12.2 (a) Schematic view of λ-sensor and (b) typical response after Logothetis *et al.* (1992).

Various designs of planar lambda probes have been proposed. Figure 12.3 presents a sensor based on co-fired multilayer ceramics technology, which consists in assembling, before pressing and co-firing, raw ceramic sheets on which leads, electrodes and heating resistance (Ogasawara and Kurachi, 1988) are deposited by screen-printing. A cavity is arranged in one ceramic sheet so as to communicate with the surrounding air and to ensure the reference compartment for the sensor.

Planar lambda probes, containing multi-layer ceramics, are now proposed by car equipment suppliers (Riegel *et al.*, 2002).

Up to now, only dense ceramics have been considered in manufacturing the zirconia electrolyte used in type I oxygen sensors. In porous ceramics, diffusion of gaseous oxygen occurs between the sensing and reference compartments. This is the main reason why the use of printed zirconia paste as solid electrolyte in type I sensors is not straightforward. Sputtered thin films are comparatively denser. Figure 12.4 shows an oxygen sensor made of sputtered YSZ on a sapphire

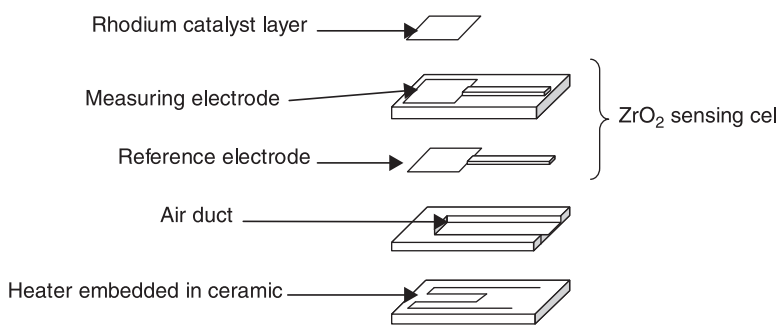

12.3 Perspective of a planar λ-sensor made with the co-fired multi-layer technology, after Ogasawara and Kurachi (1988).

© Woodhead Publishing Limited, 2012

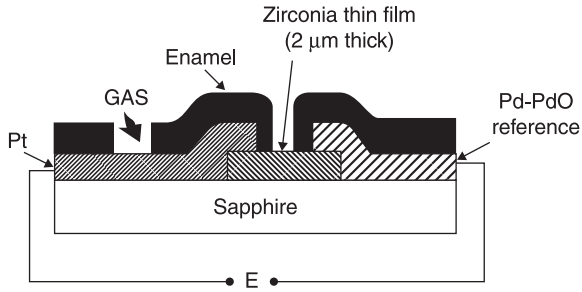

12.4 Schematic diagram of a thin film λ-sensor, after Velasco *et al.* (1982).

substrate (Velasco *et al.*, 1982). Conversely to previous cases, for which ambient air fixes the oxygen concentration in the reference compartment, the reference oxygen concentration in the thin film device of Fig. 12.4 is fixed thanks to a so-called 'oxygen buffer' or solid-state internal reference made of Pd/PdO.

Hydrogen sensors

The use of a protonic conducting solid electrolyte for the detection of hydrogen gas, via the equilibrium:

$$H_2 \leftrightarrow 2\,H^+ + 2e^- \qquad [12.19]$$

constitutes another example of a type I sensor. Various studies were carried out on this topic in the 1980s with protonic conductors such as β-alumina, some zeolites but especially HUP (HUO_2PO_4, $4H_2O$) (Kumar and Fray, 1988; Lundsgaard *et al.*, 1982; Schoonman *et al.*, 1982, 1986; Velasco *et al.*, 1982). Figure 12.5 represents two sensors of this type in the form of sintered pellet and thin layers for the

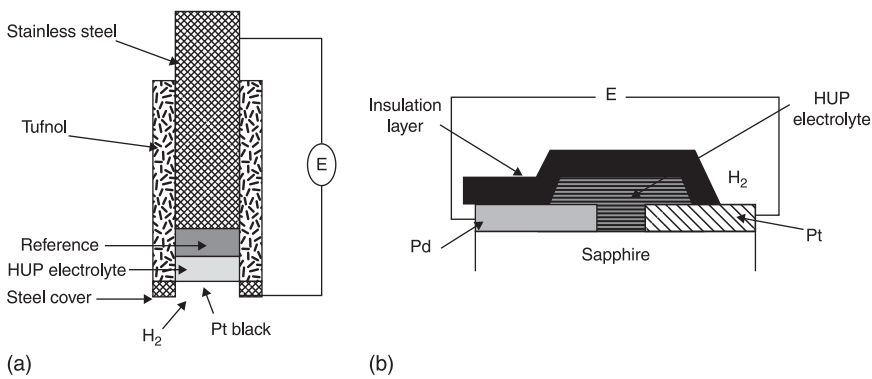

12.5 Hydrogen sensors based on HUP, in the form of (a) sintered ceramic (Kumar and Fray, 1988) and (b) thin film (Velasco *et al.*, 1982).

© Woodhead Publishing Limited, 2012

measurement of the hydrogen partial pressure. One of the references likely to be used to fix the chemical potential of hydrogen is of course palladium, for its capacity to absorb this gas. The exchange of hydrogen with the HUP makes it possible to form at the interface the Pd/PdHx system, which is used then as an internal reference.

12.4.3 Type II sensors

Type II sensors have not yet found any application and they mostly spark pedagogical interest. For example, an electrochemical cell, analogous to that of Fig. 12.1, in which O^{2-}-ion conducting YSZ is replaced by Ag^{+}-ion conducting AgI, could be considered from a theoretical point of view for iodine vapour sensing. Conversely to type I sensors, the target gas (I_2) does not correspond to the mobile ion (Ag^{+}) of the binary solid electrolyte AgI, but to the other element. A theoretical treatment similar to that applied to zirconia again leads to Nernst's Law, assuming at each interface the following equilibrium: $AgI \leftrightarrow Ag^{+} + I$.

In the case of symmetrical sensors (type I or type II), the only difference between the reference and sensing compartments is the partial pressure or the target gas. The e.m.f. does not depend on anything other than the logarithm of the ratio of the partial pressures. When the reference side consists of an internal solid reference, the e.m.f. still depends on the logarithm of the partial pressure of the target gas on the sensing side, but is shifted by a constant term corresponding to the standard Gibbs energy of formation of the internal reference. For example, let us consider a type II sensor based on the following galvanic cell:

> I_2/Pt (sensing electrode), // AgI (solid electrolyte) // Ag (reference electrode).

The application of a formalism analogous to that of section 12.4.2 (see subheading *Principle*) to the following equilibriums:

- at the interface Pt/AgI:

$$\tfrac{1}{2}\, I_2 + e^{-}_{se} \leftrightarrow I^{-}_{se}$$

$$I^{-}_{se} + Ag^{+}_{se} \leftrightarrow AgI;$$

- at the interface AgI/Ag:

$$Ag^{+}_{re} + e^{-}_{re} \leftrightarrow Ag$$

leads to the following expression for the e.m.f.:

$$E = (RT/2F)\ln[p(I_2)] - (1/F)\,\Delta G^{\circ}_{f(AgI)} \qquad [12.20]$$

(neglecting the difference between the chemical potentials of electrons in platinum (e^{-}_{se}) and silver (e^{-}_{re}), which corresponds to the junction potential between both metals).

© Woodhead Publishing Limited, 2012

The previous theoretical treatment is in principle only valid for binary solid electrolytes. When the solid electrolyte consists of more than two elements, as in KAg_4I_5, which to our knowledge, has been used for the sole practical study of iodine vapour detection (Rolland, 1974), variations of the iodine partial pressure induce variations of the chemical potential not only of the mobile ion Ag^+, but also of the K^+ ion. No well-defined relationship between the chemical potentials of I^- and Ag^+ exists any longer. The treatment, however, remains valid with some modifications, when the element corresponding to the non-mobile ion is replaced by a molecular group, such as SO_3, SO_4, CO_3, etc.

12.4.4 Type III sensors

As seen in section 12.2, mobile ions are mostly limited to F^-, O^{2-}, H^+, Li^+, Na^+, K^+, Ag^+, Tl^+, which considerably restricts the possibilities of sensing chemical species with type I or type II sensors. In type III sensors, the addition of one or several auxiliary phases between the target gas and the solid electrolyte on the sensing electrode side enables us to circumvent the previous restrictions. Yamazoe and his co-workers have further subdivided the classification of Weppner for these type III sensors into a, b, c . . ., according to the relationship between the auxiliary phase with the target gas and the solid electrolyte (Miura *et al.*, 1993a).

Type IIIa sensors

In this configuration, the auxiliary phase contains both the mobile ion of the solid electrolyte and element(s) of the target gas. Various devices associating sodium ion conductors such as NaSICON or β-alumina with auxiliary phases such as sodium carbonate, sodium sulfate, sodium nitrate or sodium nitrite have successfully been tried for CO_2, SO_2, NO_2 and NO sensing respectively. Figure 12.6 represents such a device with a tubular shape, for NO or NO_2 sensing. If the oxygen partial pressure is the same on both the reference and sensing sides, the e.m.f. is again found to follow Nernst's Law, with the partial pressure of nitrogen oxide independent of the oxygen partial pressure (Miura *et al.*, 1993b; Yao *et al.*, 1992a). NOx concentrations down to the ppm have been measured with such devices.

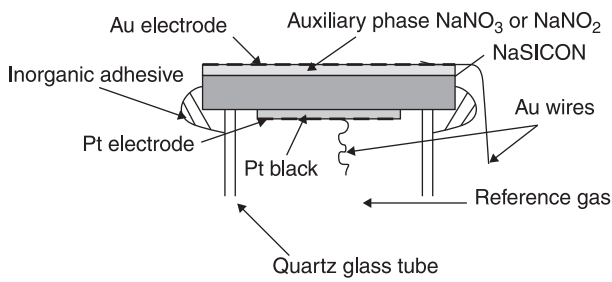

12.6 Structure of a tubular NO_x-type IIIa sensor, according to Yao *et al.* (1992a).

© Woodhead Publishing Limited, 2012

Carbon dioxide sensors

CO_2 sensors are the potentiometric sensors most studied after the oxygen sensors. The most obvious applications are ventilation control in houses, residences, schools, cinemas, tunnels, etc. and leak detection around the future sites of carbon dioxide storage. Review papers on these sensors were reported by various authors recently (Baliteau, 2005; Möbius, 2004; Pasierb and Rekas, 2009). NaSICON is the more used electrolyte.

In addition to good characteristics for detecting carbon dioxide, commercial development of a carbon dioxide sensor requires a low manufacturing cost, small overall dimensions and simplicity of use. If a device similar to that in Fig. 12.6, with a carbonate as an auxiliary phase, can attract interest at the research level for detecting CO_2, it is clear that the use of a fixed and known gaseous reference, other than the ambient air, which generally constitutes the medium to be analysed, does not prove easy to utilize.

Planar devices represent an unquestionable projection towards the objectives of simplicity, miniaturization and low cost. These objectives obviously go hand in hand with the use of an 'open' reference, where both reference and sensing electrodes are exposed to the same analysed atmosphere (Holzinger *et al*, 1996). From a thermodynamic point of view, the best solution consists in using:

- a sensing electrode in equilibrium on one hand with the carbon dioxide and the oxygen of the target gas, and on the other with the auxiliary phase containing sodium carbonate, the latter being itself in equilibrium with the Na^+ ions of NaSICON;
- a metal or metallic oxide electrode with solid reference, in equilibrium with the sole oxygen of the gaseous phase (thus not with carbon dioxide) and with the Na^+ ions of NaSICON.

An assembly of this type was recently reported, with the electrodes, the auxiliary phase and the solid reference screen-printed on both sides of a sintered pellet of NaSICON (Baliteau 2005; Baliteau *et al.*, 2005). Barium carbonate is added to the sodium carbonate for better resistance to moisture of the auxiliary phase. The reference electrode consists of mixed lanthanum strontium oxide (LSM) and the solid reference of a mixture of titanium oxides $Na_2Ti_3O_7$-$Na_2Ti_6O_{13}$. The electrochemical chain is then the following one:

$$CO_2, O_2/Au, Na_2CO_3\text{-}BaCO_3//NaSICON // Na_2Ti_3O_7\text{-}Na_2Ti_6O_{13}, LSM/O_2\ (CO_2)$$

The agreement between the experimental results and the thermodynamic Nernstian model is excellent, in particular for the 2 $Na_2Ti_3O_7$/1 $Na_2Ti_6O_{13}$ composition corresponding to the stoichiometric coefficients of the thermodynamic equilibrium between both compounds. Unfortunately, no solid reference studied until now seems to entirely give satisfaction with the level of long-term stability of the sensor.

© Woodhead Publishing Limited, 2012

Implementing NaSICON thick layers deposited with the electrodes, the auxiliary phase and, if necessary, the solid reference on the same side of a substrate (of alumina, for example), brings important advantages in comparison to the sintered pellets. Screen-printing technology makes it possible moreover to easily integrate a heating resistance, necessary for the operation of the sensor, by simply depositing it either on the same side, or on the back of the substrate. Initial work on this type of entirely screen-printed sensor was completed by Chu *et al.* (1991). Modifications of the initial device have since been made by various authors. Figure 12.7 represents a sensor of this type, studied by the authors of the present chapter, with major modifications compared to the initial sensor of Chu *et al.*:

- the replacement of platinum by gold as the electrode metal, the former not being inert with respect to alkaline carbonates,
- the replacement of NaSiCON by the homologous Li^+ conductor, LiSICON, being more resistant to moisture,
- the substitution of lithium carbonate with sodium carbonate, which is more resistant to moisture,
- the addition of alkaline-earth carbonate (Ca, Ba) to lithium carbonate, so as to minimize the influence of moisture on the sensor response,
- the realization of a composite sensing electrode by mixing carbonate and gold screen-printing inks.

The galvanic cell corresponding to Fig. 12.7 is:

$$O_2(CO_2)/\,Au\ //\ LiSICON\ \left(Li^+\ conductor\right)\ //\ Li_2CO_3,\ Au\ /\ O_2,\ CO_2.$$

Reference electrode — Sensing electrode

On the sensing electrode side:

$$2Li^+_{se} + CO_2 + \tfrac{1}{2}\,O_2 + 2e^-_{se} \leftrightarrow Li_2CO_3. \qquad [12.21]$$

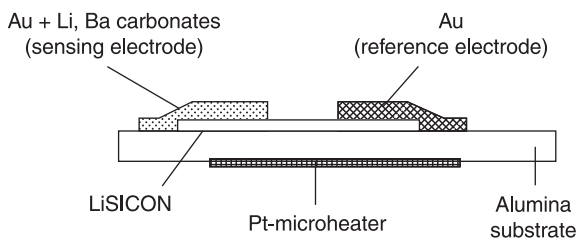

12.7 Screen-printed CO_2 sensor based on LiSICON, after Menil *et al.* (2005).

© Woodhead Publishing Limited, 2012

Hence, by applying [12.11] to [12.21]:

$$2\tilde{\mu}(Li^+_{se}) + \mu(CO_2) + \tfrac{1}{2}\mu(O_2) + 2\tilde{\mu}(e^-_{se}) = \mu(Li_2CO_3). \quad [12.22]$$

On the reference electrode side, the lithium ions of LiSICON are supposed to react only with oxygen and not with carbon dioxide, which implies the presence of the Li_2O phase (which is supposed to form *in situ*):

$$2Li^+_{re} + \tfrac{1}{2}O_2 + 2e^-_{re} \leftrightarrow Li_2O. \quad [12.23]$$

Hence:

$$2\tilde{\mu}(Li^+_{re}) + \tfrac{1}{2}\mu(O_2) + 2\tilde{\mu}(e^-_{re}) = \mu(Li_2O). \quad [12.24]$$

Because the system is in thermodynamic equilibrium, the electrochemical potential of the Li^+ ions is constant throughout the whole electrolyte:

$$\tilde{\mu}(Li^+_{re}) = \tilde{\mu}(Li^+_{se}). \quad [12.25]$$

Combining [12.22], [12.24] and [12.25]:

$$2\tilde{\mu}(e^-_{re}) - 2\tilde{\mu}(e^-_{se}) = \mu(Li_2O) - \mu(Li_2CO_3) + \mu(CO_2), \quad [12.26]$$

with:

$$\mu(Li_2CO_3) = \mu^0(Li_2CO_3)$$

$$\mu(Li_2O) = \mu^0(Li_2O) + RT\ln(a_{Li_2O}) \qquad (a_{Li_2O} \text{ is the lithium oxide activity in LiSICON})$$

$$\mu(CO_2) = \mu^0(CO_2) + RT\ln[p(CO_2)]$$

$$\tilde{\mu}(e^-_{re}) = \mu(e^-_{re}) - F\Phi_{re}$$

$$\tilde{\mu}(e^-_{se}) = \mu(e^-_{se}) - F\Phi_{se}.$$

Since the metal is the same on both the reference and sensing sides ($\mu(e^-_{re}) = \mu(e^-_{se})$):

$$E = \Phi_{se} - \Phi_{re} = \Delta G^\circ_{f(Li_2CO_3)}/2F + (RT/2F)\ln(a_{Li_2O}) + (RT/2F)\ln[p(CO_2)]. \quad [12.27]$$

$\Delta G^\circ_{f(Li_2CO_3)}$ is the Gibbs standard energy for the formation of lithium carbonate from Li_2O and CO_2. Assuming that the Li_2O activity in LiSICON constant leads to:

$$E = \Phi_{se} - \Phi_{re} = C^{nt} + (RT/2F)\ln[p(CO_2)]. \quad [12.28]$$

The sensor of Fig. 12.7 follows Nernst's Law above 100 ppm CO_2 in air. The sensor is barely sensitive to humidity and has a satisfying long-term stability. The critical point concerns the reality of Li_2O, which is supposed to form *in situ* in a very small quantity, but which is known to be normally unstable.

© Woodhead Publishing Limited, 2012

Type IIIb

In the case of type IIIb sensors, the mobile ion in the solid electrolyte differs from the mobile ion in the auxiliary phase, but is of the same sign. For example, one can quote the CO_2 sensors with NaSICON as the conductor of Na^+ ions and lithium carbonate as the auxiliary phase (Yao *et al.*, 1992b). The continuity of the electrochemical chain requires the presence of a junction phase at the interface ionic conductor/auxiliary phase, in which both mobile ions Li^+ and Na^+ coexist.

Type IIIc

In this type of sensor, the mobile ions of the solid electrolyte and of the auxiliary phase differ not only in kind as in the preceding case, but also in sign. A typical example is the CO_2 sensor with stabilized zirconia as solid electrolyte (O^{2-} ions conductor) and lithium carbonate as auxiliary phase (Li^+ ions conductor) (Miura *et al.*, 1995). Again, the presence of a junction phase at the interface ionic conductor/auxiliary phase, in which the Li^+ and O^{2-} ions coexist, proves to be necessary.

With zirconia, one can always also quote work on a NO sensor with barium nitrate $Ba(NO_3)_2$ doped with calcium carbonate, as an auxiliary phase (Kuroswawa *et al.*, 1995). Figure 12.8 represents a studied planar configuration.

The corresponding galvanic cell is as follows:

$$O_2\ (NO)/Pt\ //\ MgSZ\ (O^{2-})\ //\ Ba(NO_3)_2 - CaCO_3\ //\ Au/O_2,\ NO.$$

The experimental results and the theoretical treatment, which imply *in situ* formation of a second auxiliary phase $BaZrO_3$ between zirconia and nitrate, show that the e.m.f. depends not only on the NO partial pressure, but also on the oxygen partial pressure, following the relation:

$$E = E_0 + (RT/F)\ \ln[(p(NO)] + (3RT/4F)\ \ln[(p(O_2).$$

This device, which functions at 450 °C, is also sensitive to NO_2.

Another example of the type IIIc sensor relates to the association of lanthanum fluoride (F^- ion conductor) as a solid electrolyte with a carbonate (alkali-ion conductor) as an auxiliary phase, for carbon dioxide detection (Miura *et al.*, 1993a).

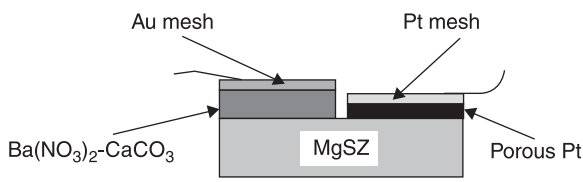

12.8 Structure of a planar NO_x-type IIIc sensor, according to Kuroswawa *et al.* (1995).

© Woodhead Publishing Limited, 2012

12.5 Sensors controlled by both thermodynamics and kinetics

We therefore come back to the type I zirconia oxygen sensor. The Nernst's law [12.18] is obtained by considering the sole equilibrium [12.13], i.e. the lattice oxygen ions at the three phase boundaries (zirconia, platinum, gas) are in equilibrium only with gaseous oxygen. This approximation is not valid under any circumstances. The literature reports many examples of a zirconia oxygen sensor that does not obey Nernst's law in the presence of other gases, especially those resulting from engine combustion processes. Various mechanisms have been proposed to explain these interferences. We now present an experimental mechanism, based on proposals and results collected in the above-mentioned literature (Menil *et al.*, 2000).

Schematically, the relevant reactions likely to occur at the electrode level in an engine exhaust gas can be divided into three sets:

$$O_2 + 4e^- \Leftrightarrow 2O^{2-}, \qquad [12.29]$$

$$CO + 1/2O_2 \Leftrightarrow CO_2, \qquad [12.30a]$$

$$H_xC_y + (\frac{x}{4} + y)O_2 \Rightarrow \frac{x}{2}H_2O + yCO_2, \qquad [12.30b]$$

$$2NO \Rightarrow N_2 + O_2, \qquad [12.30c]$$

$$NO + \frac{1}{2}O_2 \Leftrightarrow NO_2, \qquad [12.30d]$$

$$CO + O^{2-} \Leftrightarrow CO_2 + 2e^-, \qquad [12.31a]$$

$$H_xC_y + (\frac{x}{2} + 2y)O^{2-} \Rightarrow \frac{x}{2}H_2O + yCO_2 + (x + 4y)e^-, \qquad [12.31b]$$

$$2NO + 4e^- \Rightarrow N_2 + 2O^{2-}, \qquad [12.31c]$$

$$NO + O^{2-} \Leftrightarrow NO_2 + 2e^-. \qquad [12.31d]$$

The sense of equilibrium will depend on temperature and oxygen partial pressure. Moreover, it is important to note that reactions [12.30a–d] cannot take part directly in the electrochemical process, since no electron exchange is involved.

12.5.1 Oxygen electrode

This is the situation sought afterwards to measure the oxygen partial pressure in the exhaust gas. At relatively high temperatures, typically above 600 °C, the kinetics of reactions [12.31a–d] are low compared to that of reaction [12.29]. If, moreover, the electrode metal has a negligible catalytic activity with regard to

© Woodhead Publishing Limited, 2012

reactions [12.30a–d], we practically come back to the ideal case of a type I sensor, which follows the Nernst's law as a function of the sole oxygen partial pressure. Among metals exhibiting this property, silver, gold, and some alloys between platinum and bismuth may be quoted.

12.5.2 Equilibrium electrode

Conversely, but always in the same range of temperatures for which the kinetics of reactions [12.31] remain low compared to that of reaction [12.29], metals such as rhodium, palladium and sometimes platinum strongly catalyze reactions [12.30a–d]. Electrodes made of such metals are called equilibrium electrodes since they will promote the thermodynamic equilibrium of the exhaust gas.

At the electrode level, reactions [12.30a–d] induce a net production or consumption of oxygen. This quantity will either add or subtract to the oxygen already present in the exhaust gas. Nernst's law will be ruled by this global oxygen partial pressure. The e.m.f. will no longer represent the free oxygen partial pressure in the exhaust gas, but the oxygen partial pressure that the exhaust gas would have if it were in thermodynamic equilibrium. This *a priori* drawback for oxygen sensing may, however, be useful for sensing other species.

12.5.3 Mixed potential electrode

At temperatures below 500–600 °C, the kinetics of reactions [12.31a–d] may become comparable to that of reaction [12.29]. Moreover, if the electrode has a weak catalytic activity regarding reactions [12.30a–d], reactions [12.31a–d] directly compete with reaction [12.29]. Thus, the chemical potential of the O^{2-} ions at the three phase boundaries on the sensing electrode side will not be fixed only by the partial pressure of oxygen at the electrode level, but also by that of other gases. This direct involvement of gases (such as CO, H_xC_y, and NO) in the electrochemical process, in the same way as oxygen, leads to the notion of mixed (Arias de Velasco *et al.*, 1993; Baier *et al.*, 1992; Okamoto *et al.*, 1981) or non-Nernstian potential (Baier *et al.*, 1993; Vogel *et al.*, 1993).

This mechanism is especially attractive for sensing gases other than oxygen. The basic operating design of such sensors consists in using differential configurations. Two electrodes are exposed to the same gas to be detected, but only one, of the mixed potential type, exhibits a catalytic activity with regard to one of the reactions [12.31]. The other is either an oxygen or an equilibrium electrode. Over the past 20 years, various configurations based on this concept have been proposed (Menil *et al.*, 2000; Pasierb and Rekas, 2009; Zhuiykov and Miura, 2007), even though the precise theoretical treatment of such sensors remains unknown.

Silver, gold, bismuth and lead, as well as alloys of these metals with platinum, are quoted as having a low catalytic activity with regard to reactions [12.30a–d].

© Woodhead Publishing Limited, 2012

Electrodes made with these metals or alloys, when operated at a low temperature, are quoted as mixed potential electrodes (Baier *et al.*, 1993; Friese *et al.*, 1995; Hamburg *et al.*, 1993; Hoetzel *et al.*, 1995; Lukacs *et al.*, 1994; Vogel *et al.*, 1993). Instead of using a metal or an alloy as a mixed potential electrode, it is also possible to use an inorganic oxide with metallic conductivity, such as perovskites $La_{1-x}Sr_xMO_3$ (M = Cr, Mn, Fe, Co) (Brueser *et al.*, 1994; Moebius *et al.*, 1992). Asymmetry may also be introduced by coating or undercoating one electrode of a symmetrical sensor (sensor with two Pt electrodes, for example) with a catalyst. The catalyst may also simply be added by mixing it with the paste of the metallic electrode, before sintering.

CO sensing

Several papers deal with CO sensors based on zirconia. Both electrodes of a unique sensor immersed in the gas to sense (the exhaust of engines or of boilers) are dissymmetrical with regard to their catalytic activity. Working temperatures do not exceed 600 °C. In a similar device (Lalauze *et al.*, 1993), the solid electrolyte is made of β-alumina, the mixed potential electrode of gold and the equilibrium electrode of platinum. The operating temperature is 500 °C.

Two regular platinum electrodes may also be used, but one of them is coated with a catalyst such as Pt-doped alumina (Okamoto *et al.*, 1980) or CuO/ZnO (Li *et al.*, 1993). Figure 12.9 represents the scheme of the latter device and the response to carbon monoxide. In both cases, the sensitivity vanishes above 500 °C. Because of the low operating temperature, the uncoated platinum electrode works as a mixed potential electrode (platinum at higher temperatures normally works as oxygen or equilibrium electrode). CO is oxidized in the catalyst, thus coating the other electrode, i.e. thermodynamic equilibrium is achieved upstream of the coated electrode, which then operates as an equilibrium electrode.

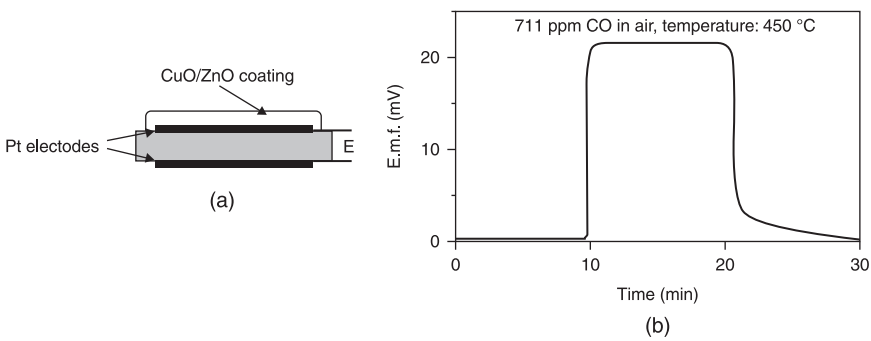

12.9 (a) Planar structure and (b) response curve of a catalytic CO sensor, according to Li *et al.* (1993).

© Woodhead Publishing Limited, 2012

NO_x sensing

In order to decrease both fuel consumption and carbon dioxide production, and thus contribute to reducing the greenhouse effect, new engines with an excess of air versus stoichiometry have been developed. Such engines, operated above the A/F stochiometric value of 14.6 (see *λ-sensors*, section 12.4.2) are said to be 'lean' in fuel and the corresponding engines are called 'lean-burn' engines, in contrast to engines operated at stoichiometry. Diesel engines are also operated in the 'lean-burn' region. As mentioned above, the three-way catalyst does not operate properly when the admission mixture departs from stoichiometry. For this reason, NO_x emissions, mostly eliminated with the three-way catalyst in stoichiometric engines, have again become a problem with lean-burn engines. NO_x sensors have thus been mostly developed for this type of engine.

The principle for NO sensing is the same as for CO sensing: use a zirconia planar substrate with two (usually screen-printed) electrodes with a different catalytic activity. In Brueser *et al.* (1994), the equilibrium electrode is made of platinum and the mixed potential electrode of perovskite: $La_{1-x}Sr_xMO_3$ (M = Cr,Mn,Fe,Co). Various oxides such as WO_3, Cr_2O_3, spinels, ZnO, NiO, etc. have been added to one platinum electrode to create the asymmetry (see Table 2 in Zhuiykov and Miura, 2007).

One of the problems in applying the previous simple design to NO_x sensing in automotive exhaust is that NO_x comprises both NO and NO_2, which often induce e.m.f. variations in opposite directions. Fig. 12.10 presents a more sophisticated device, taking into account the whole NO_X (Ono *et al.*, 2004).

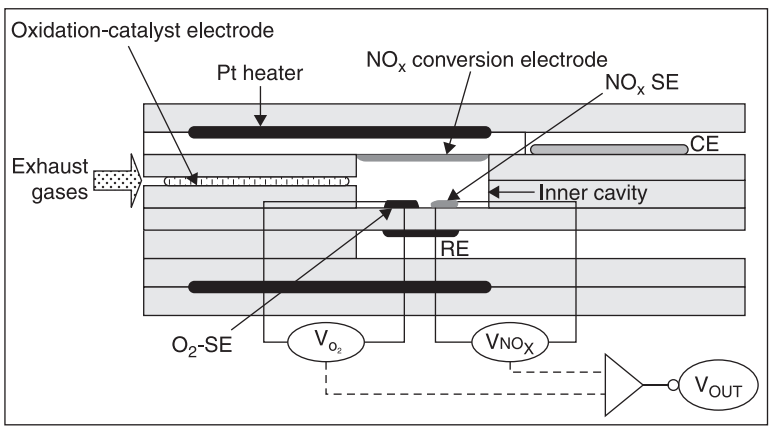

12.10 Cross-sectional view of the laminated-type total-NO_x sensor attached with oxidation-catalyst (reprinted from Ono *et al.*, 2004, with permission from Elsevier Science).

© Woodhead Publishing Limited, 2012

The sensor is manufactured by pressing and sintering YSZ green sheets on which electrodes and a platinum heater are screen-printed. Thanks to the oxidation-catalyst, located upstream away from the inner cavity, and to the NO_x conversion electrode located in the inner cavity, the gas composition in the inner cavity is likely to consist mostly of oxygen, nitrogen, carbon dioxide, water vapor and NO_2, all reducing gases such as CO, NO and HC which have been oxidized. The oxygen sensing electrode and the reference electrode are made of platinum only. Thus, the electrode pair O_2-SE + RE operates as a regular type I oxygen sensor. The NO_x sensing electrode (actually NO_2 sensing electrode since NO is supposed to have been completely converted), based on Cr_2O_3, is also sensitive to oxygen. Since both O_2 and NO_x sensing electrodes are mounted in differential with the same reference electrode, the NO_x response yields the total $NO + NO_2$ concentration, independently from the amount of the oxygen.

12.6 Amperometric sensors

12.6.1 Oxygen sensors

Another concept for sensing oxygen was introduced in 1982 (Dietz, 1982). The corresponding structure, schematized in Fig. 12.11(a), consists of a zirconia cell having one electrode confined in a restricted volume, which communicates with the gas to sense by a small aperture or diffusion hole.

When the electrode inside the restricted volume is negatively biased, gaseous oxygen O_2 is reduced to anions O^{2-} at this cathode, according to Eq. [12.13]. These anions are attracted inside zirconium towards the anode by the bias and re-oxidized to gaseous oxygen when they reach the anode. The current given by Faraday's Law removes gaseous oxygen from the restricted volume through the solid electrolyte at a rate equal to I/4 F. Inside the restricted

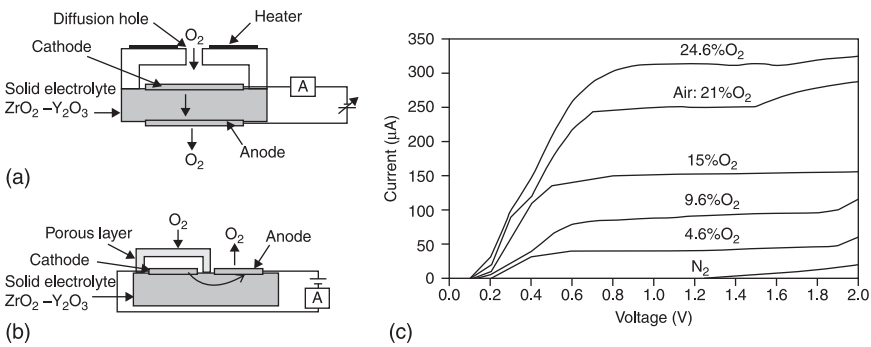

12.11 (a) Amperometric oxygen sensors with a diffusion hole and (b) with a porous layer, and (c) response curves at 600 °C of the latter, according to Ishibashi *et al.* (1993).

© Woodhead Publishing Limited, 2012

volume, the oxygen pumping will cause a decrease of the oxygen partial pressure from its initial value $p(O_2)$ to $p_{rv}(O_2)$. Simultaneously, an oxygen flux will leak through the aperture, according to Fick's first diffusion law: $D(O_2)[p(O_2)-p_{rv}(O_2)]$, with $D(O_2)$ Signifying the leak conductance with respect to oxygen. At the steady state, the sum of both pumping and leaking fluxes cancels out, so that:

$$I/4F = D(O_2)[p(O_2) - p_{rv}(O_2)].$$

If the applied voltage is high enough (typically between 0.3 and 1.5 V), the oxygen partial pressure inside the restricted volume will decrease to nearly zero, because the diffusion hole limits the oxygen entry. With this limiting condition, the pumping current only depends on the oxygen diffusion rate through the hole. The corresponding so-called limiting current is given by:

$$I_{lim} = 4FD(O_2)p(O_2). \qquad [12.32]$$

An equivalent planar configuration is shown in Fig. 12.11(b). Both cathode and anode are on the same side of the solid electrolyte, and a porous layer coating the cathode acts as diffusion barrier (Ishibashi *et al.*, 1993). Figure 12.11(c) represents the corresponding I(V) characteristics. The limiting currents, determined by the plateaus, are proportional to the oxygen concentration.

Proportional exhaust oxygen sensor

The relationship between the current and the oxygen partial pressure is linear in an amperometric sensor and not logarithmic, as in the potentiometric mode (Nernst's Law). This is the reason why, in the field of exhaust sensors, this type of sensor is also called a proportional oxygen sensor, in order to distinguish it from the logarithmic λ-sensor.

The use of a λ-sensor is only satisfactory for stoichiometric engines, because the crossing of the stoichiometric admission ratio (A/F = 14.6 for gasoline) induces a change in the exhaust oxygen partial pressure of several orders of magnitude, resulting in a variation of the e.m.f. of several hundred mV. For 'lean-burn' engines (see *NO_x sensing*, section 12.5.3) operated above stoichiometry, as well as for diesel engines, the curve in Fig. 12.2 shows that the e.m.f. variation of the λ-sensor becomes rather small, for example around A/F = 15, because the oxygen concentration does not vary much in this region. For such engines, the use of an amperometric sensor, which provides a response proportional to the oxygen concentration and no longer to the logarithm of the concentration, is highly preferable. Proportional exhaust oxygen sensors are now proposed by car equipment suppliers. Fig. 12.12 represents a planar proportional oxygen sensor, manufactured by the Robert Bosch Company. The structure again consists of pressed and sintered green sheets of YSZ.

© Woodhead Publishing Limited, 2012

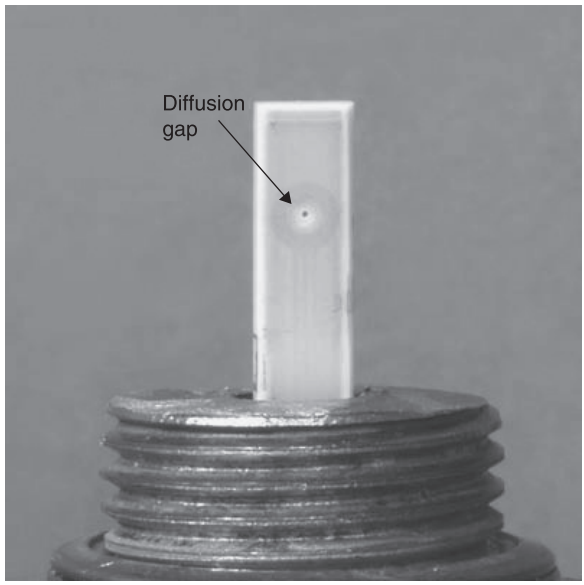

12.12 A planar proportional exhaust oxygen sensor (Robert Bosch LSU sensor element).

12.6.2 Combustible sensors

Sensing combustibles (H_xC_y, CO, H_2) with an amperometric cell *a priori* requires the presence of oxygen. The principle proposed by Logothetis *et al.* (1992) relies on the determination of the remaining oxygen in the restricted volume, after the combustion of the reducing gases on the platinum electrode at temperatures above 700 °C, according to reactions [12.30a], [12.30b]. The limiting current is shown to depend linearly on the concentration of the combustible.

At temperatures below 550 °C, another mechanism has been proposed for CO sensing (Zhang *et al.*, 1995). It involves the direct participation of CO in the electrochemical process (reaction [12.31a]), which causes the current to decrease. The occurrence of this mechanism has been demonstrated in a paper where the oxidation of combustibles such as CO, CH_4, C_3H_8 (Somov and Guth, 1998) at relatively low temperatures is proved to be only of electrochemical nature. The device shown in Fig. 12.13 is built with two amperometric cells mounted in series in the restricted volume, downstream of the diffusion hole. The first electrode, made of gold, works as cathode and carries out if necessary the nearly complete pumping of oxygen, without catalytic oxidation of the combustibles. The platinum electrode of the second cell works as an anode and ensures the electrocatalytic oxidation of the combustibles. Since the response of this double cells sensor to a few percent of methane is nearly the same, whether the nitrogen carrier gas contains oxygen or not (Fig. 12.14), the mechanism can only be explained on the

© Woodhead Publishing Limited, 2012

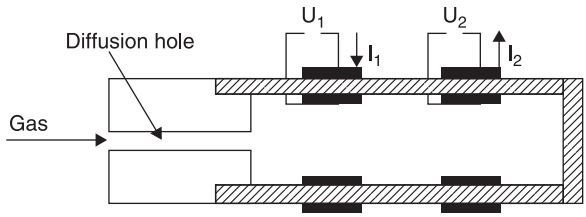

12.13 Amperometric combustible sensor with double cells in series, according to Somov and Guth (1998).

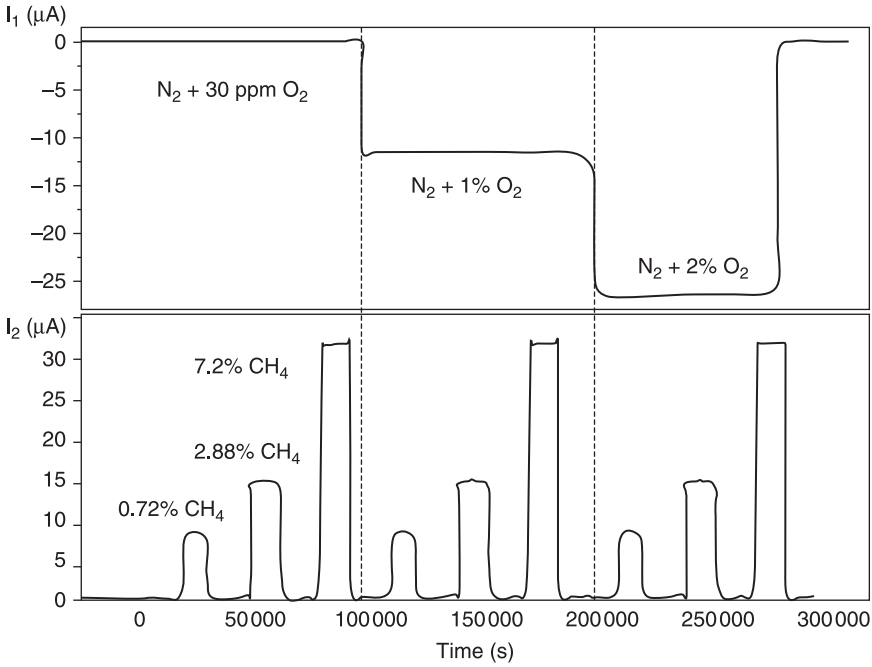

12.14 Simultaneous oxygen and methane responses of the sensor represented in Fig. 12.13, according to Somov and Guth (1998).

basis of the electrochemical oxidation of methane, according to reaction [12.31b], excluding any chemical oxidation (reaction [12.30b]).

12.6.3 NO differential sensor

Rhodium was used for the chemical dissociation of NO by NGK Insulators, Ltd. as early as 1988 (Noda *et al.*, 1988). A unique zirconia substrate is used with two amperometric cells mounted in differential mode (Fig. 12.15). The diffusion barrier is a porous layer. All electrodes are made of platinum, but on the side of the diffusion

© Woodhead Publishing Limited, 2012

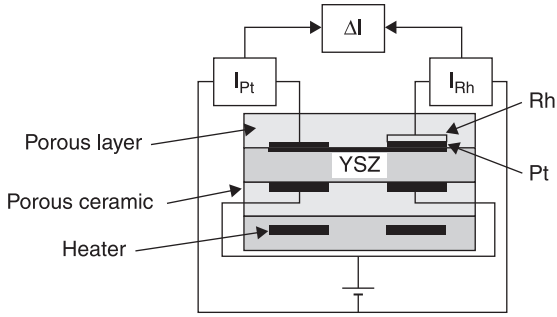

12.15 Differential potentiometric and amperometric sensor with a diffusion hole for NO sensing, according to Noda *et al.*, 1988.

barrier, one cathode is covered with a rhodium layer. The plot of the differential limiting current $\Delta I = I_{Rh} - I_{Pt}$ versus the NO_x partial pressure is linear with a slope of about 10 µA/5000 ppm, for a fixed oxygen partial pressure (20% in N_2). The proposed mechanism is the appearance of a larger oxygen partial pressure at the rhodium-covered electrode, resulting from the NO chemical rather than electrochemical decomposition (i.e. reaction [12.30c] rather than [12.31c], from left to right).

12.7 NO_x sensing device, associating upstream oxygen pumping with potentiometric and amperometric operating principles

An extension of the concept presented in Fig. 12.15 has been proposed by NGK Insulators Ltd. (Kato and Nakagaki, 1996). The sensor consists of six superimposed zirconia layers (Fig. 12.16), using the same co-firing process. The operation principle is schematized in Fig. 12.17.

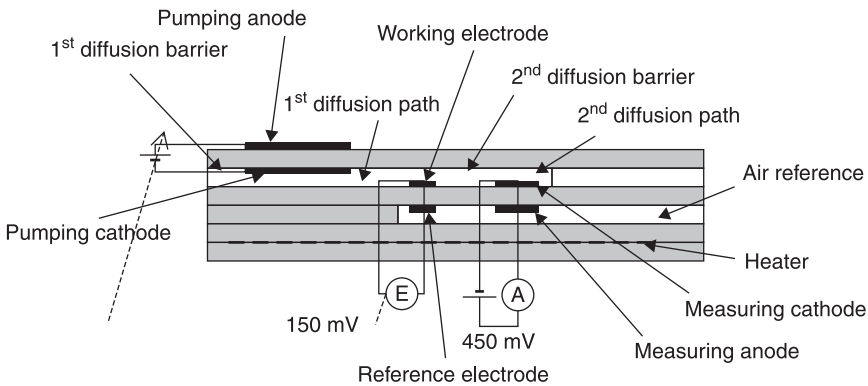

12.16 Cross view of a NO sensor with upstream oxygen pumping down to 1000 ppm, according to Kato and Nakagaki (1996).

© Woodhead Publishing Limited, 2012

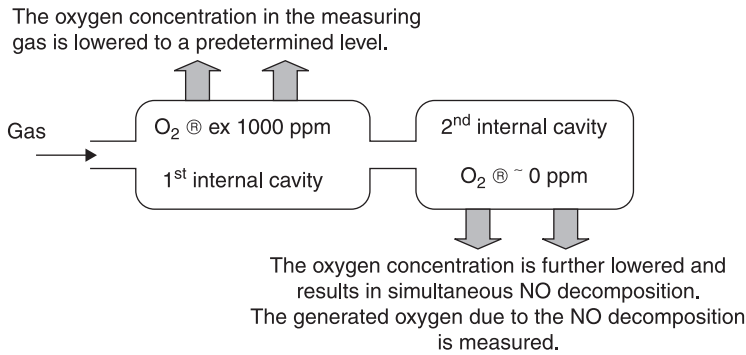

12.17 Principle of the NO sensor according to Kato and Nakagaki (1996).

The device consists of three cells:

- A first, pumping amperometric cell with its diffusion barrier and its restricted volume, from which oxygen is removed.
- A potentiometric cell, which measures the oxygen level in this first restricted volume and monitors the first pump so that the oxygen level is kept constant at 1000 ppm. This level has been chosen as a compromise for removing the maximum amount of oxygen without reducing NO.
- Downstream of the first restricted volume is a second diffusion barrier followed by a second restricted volume. The remaining 1000 ppm oxygen is totally removed by this second amperometric cell. Because of the total oxygen consumption in this second restricted volume, the NO dissociation reaction [12.30c] is completely shifted to the right, especially in presence of rhodium catalyst at the electrode. Consequently, the current of the second amperometric cell is proportional to the sum of the oxygen partial pressure issued from the first restricted volume (equal to the 1000 ppm pre-selected level) and of the oxygen partial pressure resulting from the complete NO dissociation.

The operating temperature is 700 °C. The current slope of the second amperometric cell as a function of NO concentration is about 0.6 µA/100 ppm NO.

12.8 Conclusion and possible future trends

In this chapter we tried to present the most significant examples of solid electrolyte sensors. The lambda probes constitute one of the rare success stories of gas sensors at a commercial level, with today one probe manufactured for each car using gasoline. The more recently developed proportional probes could nevertheless catch up with the former at the commercial level with the development of lean-burn and diesel engines.

© Woodhead Publishing Limited, 2012

Although the measurement of oxygen partial pressure certainly constitutes the leading application of solid electrolyte sensors, whether they work on a potentiometric or an amperometric principle, it was shown throughout this chapter that many possibilities exist for detecting other gases. The sensing of nitrogen oxides, carbon monoxide and unburnt hydrocarbons, in particular in exhaust gases, carbon dioxide in various mediums (house automation, storage, environment), probably constitute the most promising applications to date. Some of these sensors are currently proposed commercially (CO_2, NO_x). Nevertheless, the physical phenomena are not as simple as for oxygen. They generally imply the coupling of catalytic processes with thermodynamic processes. Many studies will have still to be undertaken from an empirical point of view as well as from a fundamental point of view, before being able to apprehend the problems not correctly solved to date. One of the major problems is certainly related to the lack of long-term reliability of most of these devices. Moreover, what about the influence, which is very seldom studied but undeniable, of the relative surfaces of the sensing and reference electrodes on the e.m.f. for some type III sensors with open reference, against all classically allowed theories to date (Guillet *et al.*, 2002; Menil *et al.*, 2005)?

As for manufacturing processes, the planar thick-film technology certainly appears as the most promising one. It is cheaper and more versatile than traditional ceramic processes, used for example to manufacture the thimble-shape λ-sensor. Manufacturing costs are also lower than for planar thin film technologies. Moreover, ageing problems linked to diffusion phenomena at high temperatures are comparatively worse with thin films.

For planar thick-film sensors requiring gas-tight electrolytes, green sheets will certainly remain favored. This is especially the case for zirconia sheets, which serve both as electrolyte and as substrate to screen-printed electrodes, auxiliary phases, catalyst, etc. When tightness to gas is not required, for example for sensors with both electrodes exposed to the same gas to sense (open reference), the electrolyte substrate may be replaced by an ion-conducting screen-printing paste deposited on an insulating substrate such as alumina.

12.9 References

Arias de Velasco A. A., Moseley P. T., Peat R. and Peleaz J. G. (1993), Atmosphere-dependent potentials at oxide interfaces, *Sensors and Actuators*, B15 (1–3), 55–62.

Baier G., Vogel A. and Schuele V. (1992), Zirconia mixed potential sensors for control of combustion processes, VDI-Ber, 939 (Sensoren), 439–444.

Baier G., Schuele V., and Vogel A. (1993), Non-nernstian zirconia sensors for combustion control, *Appl Phys A*, A57 (1), 51–56.

Baliteau S. (2005), Thesis, University of Grenoble.

Baliteau S., Sauvet A.-L., Lopez C. and Fabry P. (2005), Characterization of a NaSICON-based CO_2 sensor, *J Eur Ceram Soc*, 25, 2965–2968.

Brueser V., Lawrenz U., Jacob S., Moebius H. H. and Schoenauer U. (1994), NO_x determination with galvanic zirconia solid electrolyte cells, *Diffus Defect Data, Pt B*, 39–40 (System with fast ionic transport – IV), 269–272.

© Woodhead Publishing Limited, 2012

Chu W. F., Leonhard V., Erdmann H. and Ilgenstein M. (1991), Thick-film chemical sensors, *Sensors and Actuators*, B4, 321–324.

Dietz H. (1982), Gas diffusion controlled solid electrolyte oxygen sensors, *Solid State Ionics*, 6 (2), 175–183.

Duecker H., Friese K. H. and Haecker W. D. (1975), Ceramic aspects of the Bosch Lambda-sensor, *SAE [Tech Pap]*, 750223, Robert Bosch GmbH, 18 pp.

Eddy D. S. (1971), Electrochemical apparatus for monitoring exhaust gas, US 3616274, 26 October 1971, General Motors Corp., 6 pp.

Engh G. T. and Wallman S. (1977), Development of the Volvo Lambda-sond system, *SAE [Tech Pap]*, 770295, AB Volvo, 16 pp.

Fleming W. J., Howarth D. S. and Eddy D. S. (1973), Sensor for on-vehicle detection of engine exhaust gas composition, *SAE [Tech Pap]*, 730575, General Motors Corp., 16 pp.

Friese K. H., Geier H., Pollner R. and Schallert H. (1973), Electrochemical sensor for determination of oxygen in exhaust gases, *Ger Offen DE*, 2211585, 13 September, Robert Bosch, GmbH, 12 pp.

Friese K. H., Wiedenmann H. M. and Stanglmeier F. (1995), Electrochemical sensor with non catalytic measuring electrode for determining the oxygen concentration in rich exhaust gases, *German patent DE*, 4408361 A1 950928, 6 pp.

Guillet N., Lalauze R., Viricelle J.-P. and Pijolat C. (2002), The influence of the electrode size on the electrical response of a potentiometric gas sensor to the action of oxygen, *IEEE Sensors J*, 2, 349–353.

Hamburg D. R., Logothetis E. M., Visser J. H. and Soltis R. E. (1993), Oxygen sensor for exhaust gases, *PCT Int Appl*, WO 9303357 A1, 40 pp.

Hoetzel G., Neumann H., Riegel J. and Stanglmeier F. (1995), Exhaust gas sensors with catalytic electrodes, *German patent DE*, 4408504 A1 950921, 8 pp.

Holzinger M., Maier J. and Sitte W. (1996), Fast CO_2-selective potentiometric sensor with open reference electrode, *Solid State Ionics* 86–88, 1055–1062.

Ishibashi K., Kashima T. and Asada A. (1993), Planar type of limiting current oxygen sensor, *Sensors and Actuators*, B13 (1–3), 41–4.

Kato N. and Nakagaki K. (1996), Thick-film ZrO_2 sensor, *SAE*, 960334.

Kleitz M., Siebert E., Fabry P. and Fouletier J. (1991), Solid-state electrochemical sensors, *in* Gopel W., Hesse J., Zemel J. N. (eds), *Sensors: A Comprehensive Survey. Chemical and Biochemical Sensors*, Vol. 2, V.C.H. Weinheim, chapter 8, p. 341.

Kumar R. V. and Fray D. J. (1988), Development of solid-state hydrogen sensors, *Sensors and Actuators*, 15, 185–191.

Kuroswawa H., Yan Y., Miura N. and Yamazoe N. (1995), Stabilized zirconia-based NO_x sensor operative at high temperature, *Solid State Ionics*, 79, 338–343.

Lalauze R., Visconte E., Montanaro L. and Pijolat C. (1993), A new type of mixed potential sensor using a thick-film of β-alumina, *Sensors and Actuators*, B13 (1–3), 241–243.

Li N., Tan T. C. and Zeng H. C. (1993), High temperature carbon monoxide potentiometric sensor, *J Electrochem Soc*, 140 (4), 1068–1073.

Logothetis E. M., Visser J. H., Soltis R. E. and Rimai L. (1992), Chemical and physical sensors based on oxygen pumping with solid state electrochemical cells, *Sensors and Actuators*, B9 (3), 183–189.

Lundsgaard J. S., Malling J. and Birchall M. L. S. (1982), *Solid State Ionics*, 7, 53–56.

Lukacs Z., Sinz M., Staikov G., Lorenz W. J., Baier G. *et al*. (1994), Electrochemical investigations of a carbon monoxide – oxygen sensor, *Solid State Ionics*, 68, 93–98.

Menil F., Coillard V. and Lucat C. (2000), Critical review of nitrogen monoxyde sensors for exhaust gases of lean burn engines, *Sensors and Actuators*, B67, 1–23.

© Woodhead Publishing Limited, 2012

Menil F., Ould Daddah B., Tardy P., Debéda H. and Lucat C. (2005), Planar LiSICON-based potentiometric CO_2 sensors: influence of the working and reference electrodes' relative size on the sensing properties, *Sensors and Actuators*, B107, 695–707.

Menil F. (2008), Chemical sensors and electronic components: a common approach (in French), Chapter 2, *in* F. Menil (ed.) *Microcapteurs de gaz*, Lavoisier.

Miura N., Yao S., Sato M., Shimizu Y., Kuwata S. *et al.* (1993a), Carbon dioxide sensor using combination of fluoride ion conductor and metal carbonate, *Chem Lett*, 1993, 1973–1976.

Miura N., Yao S., Shimizu Y. and Yamazoe N. (1993b), Development of high-performance solid-electrolyte sensors for NO and NO_2, *Sensors and Actuators*, B13 (1–3), 387–390.

Miura N., Yan Y., Nonaka S. and Yamazoe N. (1995), Sensing propreties and mechanism of a planar carbon dioxide sensor using magnesia-stabilized zirconia and lithium carbonate auxiliary phase, *J Mater Chem*, 5(9), 1391–1394.

Moebius H., Sandow H., Hartung R., Jakobs S., Guth U. *et al.* (1992), Development of new sensor systems with galvanic high-temperature solid-state electrolyte cells, *DECHEMA Monogr, 126 (Elektrochem Sens: Neues Forsch Anwend)*, 329–344.

Möbius H.-H. (2004), Galvanic solid electrolyte cells for the measurement of CO_2 concentrations, *J Solid Electrochem*, 8, 94–109.

Noda M., Kato N. and Kurachi H. (1988), Electrochemical nitrogen oxide (NO_x) sensor, *Eur Pat Appl EP* 257842 A2, 17 pp.

Ogasawara T. and Kurachi H. (1988), Multi-layered zirconia oxygen sensor with modified rhodium catalyst electrode, *SAE*, 880557, 89–95.

Okamoto H., Obayashi H. and Kudo T. (1980), Carbon monoxide gas sensor made of stabilized zirconia, *Solid State Ionics*, 1, 319–326.

Okamoto H., Obayashi H. and Kudo T. (1981), Non-ideal emf behavior of zirconia oxygen sensors, *Solid State Ionics*, 3–4, 453–456.

Ono T., Hasei M., Kunimoto A. and Miura N. (2004), Improving of sensing performance of zirconia-based total NO*x* sensor by attachment of oxidation-catalyst electrode, *Solid State Ionics*, 175, 503–506.

Pasierb P. and Rekas M. (2009), Solid-state potentiometric gas sensors – current status and future trends, *J Solid State Electrochem*, 13, 3–25.

Peters H. and Mobius H. H. (1961), Ger (East) Pat 21673.

Riegel J., Neumann H. and Wiedenmann H. M. (2002), Exhaust gas sensors for automotive emission control, *Solid State Ionics*, (152–153), 783–800.

Rolland P. (1974), Thesis, University of Paris.

Schoonman J., Franceschetti D. R. and Hannken J. W. (1982), Electrochemical determination of local hydrogen concentration in a metal, *Ber Bunsenges Phys Chim*, 86, 701–703.

Schoonman J., de Roo J. L., de Kreuk C. W. and Mackor A. (1986), Electrochemical hydrogen sensor, *in* Aucouturier J. L. *et al.* (eds), *Proceedings of International Meeting on Chemical Sensors*, Bordeaux, pp. 319–322.

Somov S. I. and Guth U. (1998), A parallel analysis of oxygen and combustibles in solid electrolyte amperometric cells, *Sensors and Actuators*, B47, 131–138.

Velasco G., Schnell J. P. and Croset M. (1982), Thin solid state electrochemical gas sensors, *Sensors and Actuators*, 2, 371–384.

Vogel A., Baier G. and Schuele V., (1993), Non-Nernstian potentiometric sensors: screening of potential working electrode materials, *Sensors and Actuators*, B15 (1–3), 147–150.

Wagner C. (1957), *Proceedings of International Committee Electochemical Thermodynamics and Kinetics (CITCE)*, Butterworth Scientific Publisher, London, pp. 361–377.

© Woodhead Publishing Limited, 2012

Weissbart J. and Ruka R. (1961), Oxygen gage, *Rev Sci Instrum*, 32, 593–595.
Weppner W. (1987), Solid-state electrochemical gas sensor, *Sensors and Actuators*, B12 (2), 107–119.
Yao S., Shimizu Y., Miura N. and Yamazoe N. (1992a), Use of sodium nitrite auxiliary electrode for solid electrolyte sensor to detect nitrogen oxides, *Chem Lett*, 4, 587–590.
Yao S., Shimizu Y., Miura N. and Yamazoe N. (1992b), Solid electrolyte carbon dioxide sensor using sodium ion conductor and Li_2CO_3-$BaCO_3$ electrode, *Jpn J Appl Phys* 31, L197–L199.
Zhang Yi Can, Narita H., Mizusaki J. and Tagawa H. (1995), Detection of carbon monoxide by using zirconia oxygen sensor, *Solid State Ionics*, 79, 344–348.
Zhuiykov S. and Miura N. (2007), Development of zirconia-based potentiometric NO*x* sensors for automotive and energy industries in the early 21st century: what are the prospects for sensors? *Sensors and Actuators*, B121, 639

© Woodhead Publishing Limited, 2012

13

Printed thick-film biosensors

K. C. HONEYCHURCH,
University of the West of England, UK

Abstract: The present review focuses on the thick-film electrochemical biosensors fabricated using screen-printing technology over the Past four years. Biosensors are composed of a biological recognition element acting as a receptor and a transducer, which converts the resulting biological activity into a measurable signal. A number of different transducers have been employed, but one of the most popular and successful is that manufactured by thick-film technologies such as screen-printing. These offer a number of advantages, such as economy, bio-compatibility and the possibility of miniaturisation, therefore allowing for the production of disposable one-shot devices. The review is divided by application area and specific emphasis is placed on sensor fabrication methods, operating details and performance characteristics for selected applications.

Key words: screen-printed electrodes, biosensor, environmental, medical, enzyme, nanoparticles, quantum dots.

13.1 Introduction

13.1.1 Thick-film biosensors

Screen-printing is a proven technology used for the manufacture of devices in a wide range of industries, such as electronics and solar cells, through to the graphic arts. The technique of screen-printing is capable of producing electrodes in the range of a few μm to 100 μm in thickness; the sensors can hence be defined as thick-film electrodes. Various geometries can be easily made by simple alteration of the screen design, and other features, such as reference, counter electrodes and dielectric layers can be readily added in further printing steps. Carbon is a low-cost material and when coupled with screen-printing manufacturing can produce sensors very economically in large numbers, allowing these to be viewed as disposable, 'one shot' devices. This offers the possibility of decentralised testing, particularly in medical applications, exemplified by their application in the blood glucose monitoring market. Screen-printed electrodes (SPEs) offer comparable electrochemical behaviour to more expensive electrode materials, such glassy carbon, but can be used once and discarded, hence removing the need for regeneration or pre-treatment between each measurement. This also allows for their use by relatively untrained personnel, as no knowledge of the more in-depth aspects of electrochemistry and preparation is needed.

© Woodhead Publishing Limited, 2012

Reagents such as enzymes, antibodies, mediators, catalysts and chelating agents can be readily immobilised to the surface of the carbon or mixed with the ink itself. Because of this, and the economic manner in which SPEs can be manufactured, they offer an attractive approach for the construction of many different types of biosensors. These advantages have led to a large, active interest, both in research into and for the commercial application of these devices. A number of reviews have recently reported on the application of these sensors (Domínguez-Renedo *et al.*, 2007; Hart *et al.*, 2004, 2007; Kalcher *et al.*, 2009; Mahbubur Rahman *et al.*, 2010; Pohanka and Skládal, 2008; Privett *et al.*, 2010; Reyes Plata *et al.*, 2010).

Figure 13.1 shows a representation of a screen-printed sensor, illustrating the general components that can be readily laid down by this technique. As can be seen, all the components required for the biosensor can be readily realised by screen-printing. Arrays of sensors can also be made, such as the 'comb' or array of screen-printed carbon electrodes (SPCEs), which have recently been developed for the determination of a number of organophosphate pesticides (OPs) at nM concentrations by Crew *et al.* (2011).

The following section gives a short overview of the underlying electrochemistry of these sensors and a brief history of the development of these devices. This is then followed by a review of the current applications of thick-film biosensors reported in the past four years. Emphasis is placed on sensor fabrication methods, operating details and performance characteristics for selected applications.

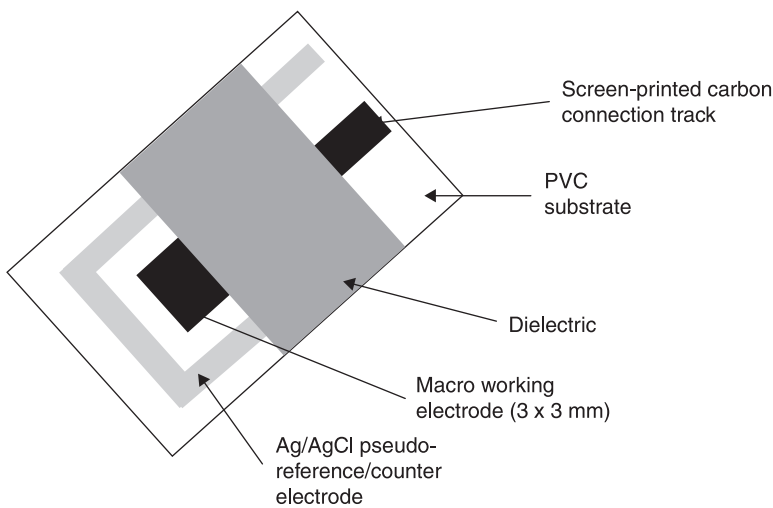

13.1 Illustration of a typical SPE.

© Woodhead Publishing Limited, 2012

13.1.2 Definition of a biosensor

Biosensors can be defined in a number of ways (Ronkainen *et al.*, 2010). Figure 13.2 shows a generalised scheme for the components of a thick-film or screen-printed electrode.

For the purposes of this review, biosensors have been defined using a version of the definition given by Théavenot *et al.* (1999). Hence, they are analytical devices that incorporate some form of biological material, such as tissue, microorganisms, organelles, cell receptors, enzymes, antibodies, nucleic acids, etc. These biological components are intimately associated with or integrated within a physicochemical transducer or transducing microsystem. Such devices usually produce a digital electronic signal that is proportional to the concentration of a specific analyte or group of analytes.

13.1.3 Practical experimental considerations

Reference electrodes

More detailed explanations regarding the underlying chemistry of commonly used reference electrodes (Bott, 1995; Compton and Banks, 2011) and their screen-printed counterparts have been already given (Shinwari *et al.*, 2010). Reference electrodes are necessary to provide a stable, drift-free, accurate value of potential as a reference voltage. This can be used to monitor accurately the applied potential 'sensed' at the working electrode, so that, if necessary, adjustments can be made. Standard electrode potentials are written as reductions with respect to the standard hydrogen electrode (HE). The HE consists of a platinised platinum electrode immersed in a solution of HCl over which hydrogen gas bubbles at one atmosphere. It is extremely accurate, but is not convenient to use on a day-to-day basis. Alternative reference electrodes have been based upon metals that are in intimate contact with sparingly soluble salt of the corresponding

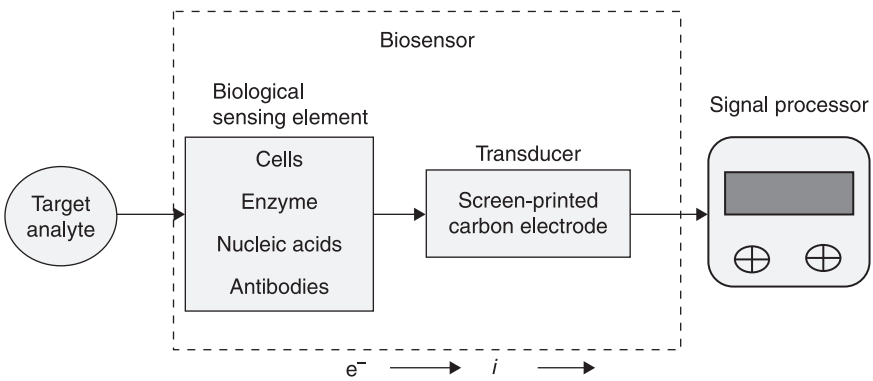

13.2 Generalised scheme for an electrochemical thick-film biosensor.

© Woodhead Publishing Limited, 2012

cation, such as the Ag/AgCl (Eq. [13.1]) and calomel (Hg/Hg_2Cl_2) (Eq. [13.2]) reference electrodes.

$$AgCl + e^- \leftrightharpoons Ag + Cl^-, \quad [13.1]$$

$$Hg_2Cl_2 + 2e^- \leftrightharpoons 2Hg + 2Cl^-. \quad [13.2]$$

It is important that the potential of the reference electrode be stable and not susceptible to change. To ensure this, the reference electrode is generally isolated from direct contact with the sample solution via a salt bridge.

Commonly, thick-film sensors employ reference electrodes screen-printed from various proprietary Ag/AgCl ink formulations. The choice of these materials is governed by their low solubility and toxicity. Strictly speaking, these thick-film reference electrodes should be referred to as quasi- or pseudo-reference electrodes, as they are not isolated from the sample and can be influenced by changes in chloride ion concentration or other sample components. However, generally this is not an issue, as a large proportion of thick-film sensors are designed as single-shot devices for samples with well-defined parameters.

The counter or auxiliary electrode

The counter or auxiliary electrode provides a means of applying input potential to the working electrode. The purpose of these electrodes is to complete the circuit and allow charge to flow. Consequently, they need to be manufactured from inert material such as carbon or platinum, and their size should be much larger than the working electrode to ensure no current limitations arise. The term 'counter electrode' is best used in connection with two-electrode experiments and auxiliary electrode is reversed for three-electrode experiments (Kissinger and Heineman, 1984).

Working electrodes

The working electrode can be defined as the electrode where the electrochemical reactions of interest occur. Ideally it should have a good signal-to-noise ratio, reproducible response, no interfering reactions over the potential of interest, high electrical stability, low cost, availability, low toxicity and long-term stability. Due to these factors, the working electrode has been made from noble metals such as Au, Ag, Pt, or Hg and C in the form of carbon paste or graphite.

Ink formulations for the production of these electrodes are generally commercially sensitive and hence not generally available for discussion or dissemination. However, these generally contain a number of components such as pH modifiers, humectants, resins, antifoaming agents, wetting agents, thickeners and preservatives (Wring *et al.*, 1992). Nevertheless, generally, conductive inks used for screen-printing are comprised of three basic constituents (Gonzalez-Macia *et al.*, 2010):

© Woodhead Publishing Limited, 2012

- *A conductor.* Powdered gold, platinum, silver or carbon.
- *A binding agent.* Glass powder, resins or cellulose acetate
- *A solvent.* Such as terpineol, 2-ethoxyethanol, cyclohexanone, ethylene glycol.

The solvent is necessary to provide suitable viscosity during the printing process and volatility for thermal curing. The binding agent is required to give sufficient mechanical strength and adhesion on the substrate. Once printed, the deposited ink is then cured by either UV irradiation or heating. Other sensor components, such as a dielectric insulator, can be printed using the same approach. The formulation of the ink and its subsequent printing can have a great effect on the performance and electrochemical properties of the biosensor (Kadara *et al.*, 2009).

13.1.4 Electrochemical techniques

Common methods employed in the development of thick-film biosensors and their applications are amperometry, chronoamperometry, potentiometry, conductimetry and impedance spectroscopy. More recently, techniques such as stripping voltammetry have also been employed in conjugation with nanoparticle-based immunoassays, the application of which is described later. More detailed discussions dealing with the underlying mechanisms and parameters that can be probed and calculated by these techniques have been given (Adams, 1969; Compton and Banks, 2011; Galus, 1976; Grieshaber *et al.*, 2008; Kissinger and Heineman, 1983, 1984; Mabbott, 1983; Pletcher, 1991; J. Wang, 2006). The following scheme gives a summary of the basic relationships:

- *Chronoamperometry*: current with voltage change.
- *Amperometry*: current at constant voltage.
- *Potentiometry*: potential difference at zero current.
- *Conductimetry*: inverse of solution resistance
- *Voltammetry*: current with voltage change.
- *Impedance*: AC voltage, reactance, resistance measured.

Cyclic voltammetry

A very commonly employed electrochemical technique, however, generally employed for the development of biosensors, rather than in the actual application and determination of target analytes. The technique consists of cycling the applied potential from an initial starting potential to a switching potential where the potential is then reversed back to the starting potential using the triangular-shaped waveform shown in Fig. 13.3(a). This can be applied once or several times, depending on the information being sought. This is carried out as a function of time (change in applied potential/second) at the working electrode in a quiescent solution and then measuring the resulting current. This represents a very powerful technique for probing the redox behaviour of species present both in solution and

© Woodhead Publishing Limited, 2012

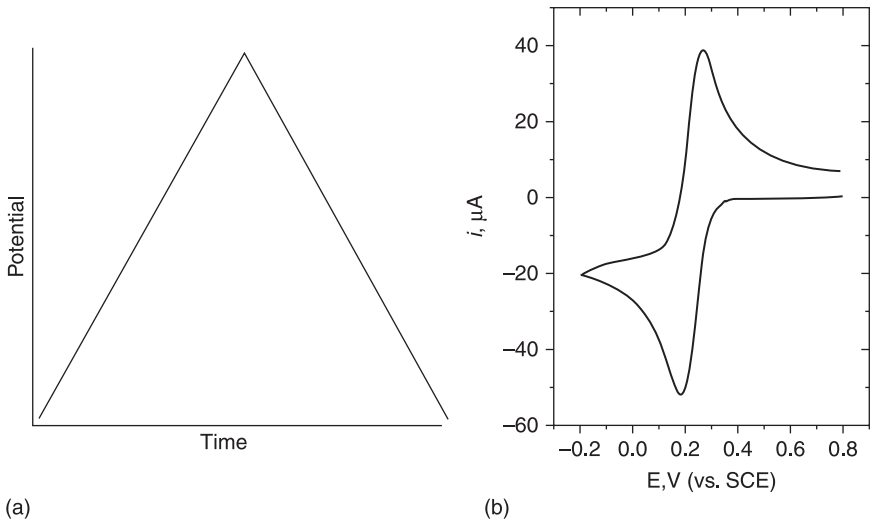

13.3 Typical input waveforms (a) and output (b) for cyclic voltammetry.

sorbed to the electrode. A simple cyclic voltammogram representative of the resulting output for a quasi-reversible diffusion-controlled species is shown in Fig. 13.3(b). Cyclic voltammetry is a complicated time-dependent function of a large number of chemical and physical parameters. More detailed discussion and explanations of the underlying mechanisms and parameters that can be probed and calculated by this technique have been given (Compton and Banks, 2011; Galus, 1976; Kissinger and Heineman, 1983, 1984; Mabbott, 1983; Pletcher, 1991; J. Wang, 2006).

For a diffusion-controlled system, the peak currents (i_p) can be explained by the Randles–Sevcik equation:

$$i_p = (2.69 \times 10^5) n^{3/2} A D^{1/2} v^{1/2} C^*, \qquad [13.3]$$

at 25 °C, where i_p is the peak current, n is the number of electrons transferred, A is the electrode area (cm^2), D is the diffusion coefficient of the species (cm^2/s), v is the scan rate (V/s) and C^* is the concentration of the species in the bulk solution (mol/cm^3). For a diffusion-controlled system, i_p will be directly proportional to the concentration of the bulk solution (C^*) and to the square root of scan rate ($v^{1/2}$).

Chronoamperometry

Due to its relative simplicity, chronoamperometry is one of the most commonly employed techniques utilised with blood glucose sensors. The waveform used in chronoamperometry is shown in Fig. 13.4(a). As with cyclic voltammetry, this

© Woodhead Publishing Limited, 2012

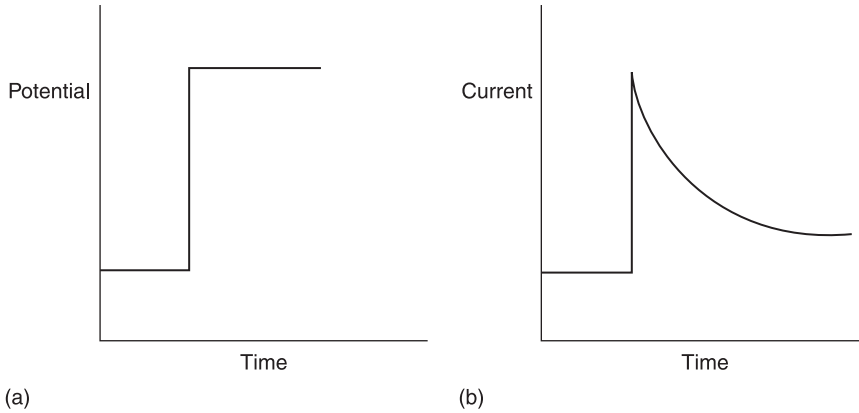

13.4 Typical input waveforms (a) and output (b) for chronoamperometry.

technique is undertaken with a stationary electrode in quiescent solution, initially at open circuit or at a potential, where the target analyte does not undergo any electrochemical reactions. The potential is then stepped to a point beyond that required for the target analyte to be electrochemically oxidised or reduced. Here its surface concentration becomes effectively zero. The resulting current–time dependence is monitored and a typical profile is shown in Fig. 13.4(b).

The shape of this can be explained by the changes in concentration distance profiles of the target analyte in a similar manner as described for cyclic voltammetry. The characteristic shape of the resulting chronoamperogram can be represented by the Cottrell equation (Eq. [13.4]):

$$i_t = \frac{nFAC^* D^{1/2}}{\pi^{1/2} t^{1/2}}, \qquad [13.4]$$

where n is the moles of electrons involved in the reaction, F is the Faraday constant, A is the area of the electrode (cm^2), C^* the concentration of the analyte in the bulk solution ($mol./dm^3$), D is the diffusion coefficient (cm^2/s) and t is time (s). Consequently, i will be proportional to $t^{-1/2}$.

Amperometry

This is one of the simpler electrochemical approaches requiring only the application of a fixed potential (Fig. 13.5(a)) and the reading of the subsequent current generated as a function of time (Fig. 13.5(b)). The general approach for this technique uses a constant potential applied in a solution under forced convection. The initial short-lived charging current is allowed to die before measurement is undertaken.

© Woodhead Publishing Limited, 2012

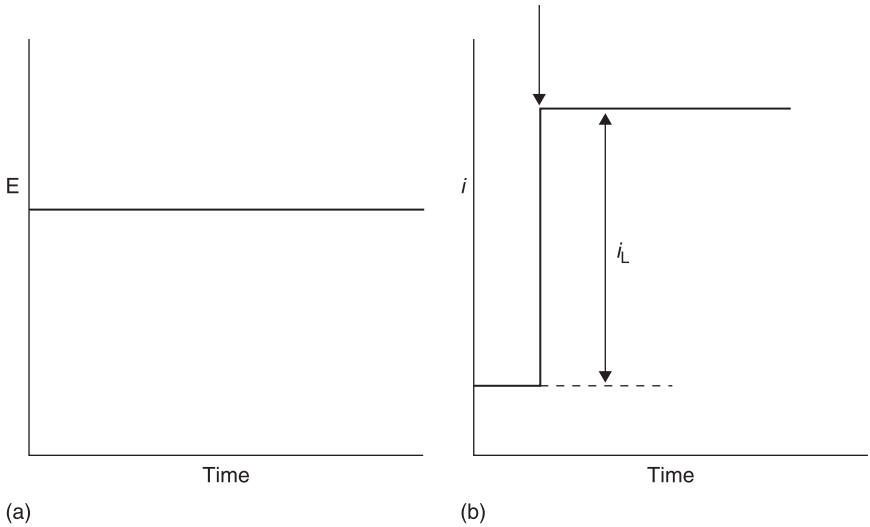

13.5 Typical (a) input and (b) resulting amperogram. Arrow indicates analyte addition.

The resulting current (i_L) can be described by the following equation [13.5]:

$$i_L = \frac{nFADC^*}{\delta}, \qquad [13.5]$$

where *FAD* and *C** are described and δ is the Nernst diffusion layer thickness.

Stripping voltammetry

Stripping voltammetry (Compton and Banks, 2011; J. Wang, 1985, 2006; Vydra *et al.*, 1976) has been demonstrated to be a very sensitive and rapid electroanalytical technique. It has been successfully applied to the detection and quantitative determination of about 30 elements for some time (Vydra *et al.*, 1976). Flameless atomic adsorption and inductively coupled spectroscopy are the only two common techniques that match it in terms of sensitivity. Stripping analysis is essentially a two-step technique. The first, deposition step or plating step, involves the electrolytic deposition of small portions of the target analyte ions in solution onto the electrode surface. This deposition step results in an effective pre-concentration step without the inherent problems of phase exchange or physical transfer of the sample. This is followed by the stripping step (measurement step), which involves the dissolution (stripping) of the deposit from the electrode. The deposited analyte is stripped from the electrode by a linear potential scan back into solution. The resulting current is proportional to the concentration of analyte deposited on the electrode and hence to the concentration in the original bulk sample solution.

© Woodhead Publishing Limited, 2012

More detailed reviews on the application of SPEs have been given previously (Arduini *et al.*, 2010a, 2010b; Honeychurch and Hart, 2003; Kokkinos and Economou, 2008; Stozhko *et al.*, 2008; Svancara *et al.*, 2010).

Potentiometry

Potentiometric sensors measure the accumulation of a charge potential at the working electrode compared to the reference electrode in an electrochemical cell with zero current flowing between them. The most commonly encountered example of this is the glass pH electrode and the ion-selective electrodes commonly utilised for the determination of ions such as Ca^{2+}, Cl^{-}, K^{+} and NH_4^{+}. The relationship between the concentration and the potential is given from a variation of the Nernst equation (Eq. [13.6]):

$$E = E_0 \pm \left(\frac{RT}{nF}\right) lna_1, \qquad [13.6]$$

where E_0 is the standard potential for $a_1 = 1\,\text{M}$, R the universal gas constant, T the absolute temperature in degrees Kelvin, n the total number of charges on the ion, F the Faraday constant and a_1 is analyte activity. More detailed discussions have previously been given (Evans, 1987; J. Wang, 2006). Biosensors can be readily made using this approach by modifying an ion-selective electrode with a suitable biological component, such as an enzyme, which produces a species that can then be detected at the ion-selective electrode potentiometrically (Mascini and Guilbault, 1986).

Conductometry

These generally consist of two noble-metal electrodes immersed in the sample solution where the conductance is measured. Some enzymatic reactions convert neutral substrates into charged products, which can be measured through the change arising in the conductance. Although this approach is relatively non-specific, the technique has been shown to be highly sensitive and rapid when used with whole cell-based biosensors (Lei *et al.*, 2006).

Electrochemical impedance spectroscopy

Impedance spectroscopy measures the resistance and capacitance properties of a material via application of a sinusoidal AC excitation signal of *c.* 2–10 mV. An impedance spectrum is obtained by varying frequency over a defined range. The capacitance and resistance of the system can be then calculated by measurement of the in-phase and out-of-phase current responses. Impedance spectroscopy can be can be used to detect immunological binding events such as antibody binding occurring on the electrode surface. The technique has recently been applied to cell

© Woodhead Publishing Limited, 2012

toxicology studies, monitoring changes in the cell motion and morphology (Z. Wang *et al.*, 2009). Reportedly (Ronkainen *et al.*, 2010), impedance can offer some advantages over amperometric-based biosensors, being able to directly monitor binding events that occur at the electrode overcoming issues with interference such as ascorbate and urate, which can interfere with amperometric-based biosensors, and there is no requirement for a mediator.

13.1.5 History of thick-film biosensors

Several very good reviews of the history and development of biosensor technology have already been given (D'Orazio, 2003; Newman and Turner, 2005; Vaddiraju *et al.*, 2010; J. Wang, 2001, 2008). The first reported biosensor was made by Clark and Lyons in 1962 based on a modification of the laboratory-based oxygen electrode (Clark and Lyons, 1962). Their innovative idea was to modify working electrodes with glucose oxidase and measure the oxygen consumed by the enzyme as an indirect measurement of the glucose present in the sample. Utilising this approach, it was found possible to analyse a range of other biomedically important compounds by employing other oxidase enzymes (Chistiansen and Jakobsen, 1995; Guilbault, 1968; Mascini and Guilbault, 1986). In 1975, Yellow Springs Instrument Company put this concept on the market, making the first commercially available dedicated blood glucose sensor. However, these first-generation biosensors were found to suffer from variations in oxygen tension and stoichiometric limitations that can occur in the sample.

In the mid-1970s, non-physiological electron acceptors were introduced to overcome these issues (Schlapfer *et al.*, 1974). Examples of such mediators include quinones and conductive organic salts, such as ferricyanide and ferrocene derivatives. A large volume of work occurred on these second-generation biosensors in the 1980s (Cass *et al.*, 1984; Frew and Hill, 1987). This decade also saw the introduction of the first modified disposable thick-film screen-printed glucose biosensors (Hilditch and Green, 1991; Matthews *et al.*, 1987), an important advance allowing for the decentralised testing and development of cheap single-shot devices, such as that used in the commercial ExacTech blood glucose meter (Cardosi and Turner, 1991), launched by Medisense Inc. in 1987. The introduction of this device led to a sea change in biosensors technology with the introduction of pen-sized (Cardosi and Turner, 1991) and mobile phone (Heller and Feldman, 2010) amperometric-based devices. The current operation of most commercial glucose biosensors does not differ significantly from the ExacTech meter.

A number of drawbacks have been highlighted with these second-generation biosensors. The potential toxicity of the mediator and its possible leaching from the electrode means that the possibility of *in vivo* usage is problematic. It is also possible that even when utilising a mediator the presence of oxygen can still result in the oxidation of the reduced enzyme, leading to errors in quantification. In the

© Woodhead Publishing Limited, 2012

1990s, a number of investigations into co-immobilising the enzyme and the mediator at the electrode surface were made to address some of these issues. This can be achieved by immobilising the mediator and enzyme in a conductive redox polymer on the electrode surface (Gregg and Heller, 1990; Ohara *et al.*, 1993). This offers other advantages; surrounding the enzyme in this way helps to transport electrons from the redox centre of the enzyme to the electrode in an array of rapid electron relays, so giving faster responses and higher current densities. More recently, further advances have been obtained by the introduction of nanotechnology. Due to the similar size of these materials and the enzyme, it is possible to 'wire' the redox centre of the enzyme directly to the electrode (Gilardi and Fantuzzi, 2001). Reportedly, this can overcome problems associated with oxygen dependence. In these third-generation biosensors, the enzyme redox centre is bound to the electrode surface. This allows for electrons to flow to and from the electrode, directly monitoring the enzyme's redox behaviour and its interaction with the substrate.

Commercially, the biosensor market is still dominated by glucose biosensors, accounting for approximately 85% of the world biosensors market in 2004, which was then estimated to be US$5 billion. According to one recent report, this will reach US$11.5 billion by 2012 (Yoo and Lee, 2010), and grow to an estimated US$14.42 billion by 2016 (Anon, 2010). Predictions show that security and bio-defence have exhibited the largest increase in annual revenue growth rates.

Nevertheless, market penetration can be difficult (Luong *et al.*, 2008). Recent reviews highlight the problems and issues that commercialisation faces (Luong *et al.*, 2008; Siontorou and Batzias, 2010). The reported cost of introducing the FreeStyle glucose biosensor to the commercial biosensor market was US$100 million, a sum beyond the means of most small companies (Heller and Feldman, 2010). At present, there are 18 companies in the USA producing 56 different glucose biosensors; however, only four major companies, Abbott, Bayer, LifeScan, and Roche, account for over 90% of the USA market (Yoo and Lee, 2010).

Future developments will properly focus on the further application of nanotechnology and techniques such as plastic electronics (Sokolov *et al.*, 2009) and synthetic biology (Keasling, 2008). Other new markets will be identified, such as coronary heart disease, which at present represents the main cause of death throughout the world (World Health Organisation, 2008) and consequently presents an opportunity for the development of biosensors capable of its early diagnosis.

13.2 Pharmaceutical and medical applications of thick-film biosensors

13.2.1 Screen-printed glucose biosensors

Usiu and Ozkan (2007) have reviewed the application of SPEs and carbon electrodes for the determination of a number of pharmaceuticals. Arguably, the

© Woodhead Publishing Limited, 2012

most successful both in terms of commercial successes and related research activity is the glucose biosensor (Hu, 2009; Lee, 2008; J. Wang, 2001, 2008). As can be seen from Table 13.1, the majority of these utilise glucose oxidise, EC 1.1.3.4 (GOx) with a suitable mediator for the measurement of the enzymatically generated hydrogen peroxide. GOx offers several advantages as it is a stable enzyme, allowing for the manufacture of sensors that are durable and reproducible. In the presence of oxygen, GOx catalyses via its redox centre flavin adenine dinucleotide (FAD) the formation of gluconolactone and hydrogen peroxide (Eq. [13.7]). Consequently, glucose concentrations can be determined by the consumption of oxygen or by the concentration of hydrogen peroxide produced, as described earlier. The former approach suffers from a number of problems, as the ambient level of oxygen must be controlled and needs to be constant, a situation that is not readily obtainable in real blood samples. Oxygen also exhibits a fairly high reduction potential in which other sample components may interfere, and its redox reaction is not readily reversible.

$$\text{Glucose} + O_2 \xrightarrow{\text{Glucose oxidase}} \text{gluconolactone} + H_2O_2 \qquad [13.7]$$

The latter approach, of monitoring the hydrogen peroxide generated, offers advantages over the measurement, allowing for simpler and more selective amperometric measurements to be utilised. The direct electrochemical determination of hydrogen peroxide requires high applied potentials, leaving the approach open to interference from a number of common blood components, such as uric acid and ascorbic acid. However, it is possible to employ some form of mediator or catalyst to lower the applied potentials required. This also has the added advantage of lowering the background currents and lessens the extent of interference of other sample components.

Screen-printed biosensors based on the cobalt phthalocyanine-mediated determination of hydrogen peroxide

As depicted in Fig. 13.6, one such approach to determining the enzymatically generated hydrogen peroxide is the use of the electrocatalyst, cobalt phthalocyanine (CoPC), a compound that has been used for the determination of number compounds (Zagal *et al.*, 2010).

The hydrogen peroxide generated by the enzymatic oxidation of glucose can be oxidised electrocatalytically via its interaction with the central Co^{2+} ion of the CoPC mediator, followed by electrochemical re-oxidation of Co^{+} at low overpotential giving the analytical signal. Cobalt phthalocyanine offers a number of other advantages for the development of screen-printed sensors, as it can be readily homogenised with the ink and used for printing. It is also insoluble in water and biological fluids, and hence will not leach from the printed electrode.

© Woodhead Publishing Limited, 2012

Table 13.1 Summary of some recent reported screen-printed glucose sensors

Enzyme	Entrapment method	Mediator	Linear range	Applied potential	Sample	Reference
Glucose oxidase	Multiwalled carbon nanotubes	Ferrocene	3–15 mM	+0.5V	Reverse iontophoresis	Sun *et al.* (2010)
Glucose oxidase	Dried to surface with mediator	Potassium ferrocyanide	8–461 mg/dl	+0.5V	Blood in 200 nl sample well	Kitamura *et al.* (2006)
Glucose oxidase	Drop-coated	MBRS	0–10 mM	+0.3V	Strawberries	Bordonaba and Terry (2009)
Three approaches: glucose oxidase; oxygen with a hydrogen peroxide catalyst; and glucose dehydrogenase	Calcium alginate(2-hydroxyethyl methacrylate), and polyurethane foam	Potassium ferrocyanide, Prussian blue, potassium ferricyanide	0–1000 μM		Tears	Bishop *et al.* (2010a,b)
Glucose oxidase	Mixed with bulk ink before printing	Cobalt phthalocyanine	0.45 mM–9.0 mM	+0.4V	Cell culture media	Pemberton *et al.* (2009b)
Glucose oxidase	Mixed with bulk ink before printing coated with nafion	Rhodium dioxide	1–250 mg/l	0.2V	Instant tea, honey	Kotzian *et al.* (2006)
Glucose oxidase	Au nano-particle	Ferricyanide	–	+0.35V	–	Iwamoto *et al.* (2009)

© Woodhead Publishing Limited, 2012

Glucose oxidase	Silver nanoparticles-doped silica sol-gel and polyvinyl alcohol hybrid film	Prussian blue	1.25×10^5 M – 2.56×10^3 M	0.05V	Rabbit serum	Zuo *et al.* (2008)
Glucose oxidase	Chitosan oligomers	Ferricyanide	1.38 mM – 33.3 mM	+0.3V	–	Lee *et al.* (2006)
Glucose oxidase	Polycarbonate membranes	Gold nanowires	1.0×10^4 M – 3.1×10^2 M	+0.55 to +0.65V	–	Vastarella *et al.* (2007)
Glucose oxidase	None, immobilised directly to SPCE surface	Pre-anodised SPCE	0–0.9 mM	0.5V	–	Yang *et al.* (2008)
Glucose oxidase	Crosslinking with BSA and GA	Horseradish peroxidase	4.9–49.0 μM	0.1V	Grape juice	Gonzalo-Ruiz *et al.* (2007)
Glucose oxidase	Photo resist coated filter paper	Ferrocene	0.2–22.2 mM	+0.5V	–	Nie *et al.* (2010)
Glucose oxidase	Drop-coated onto filter paper	Prussian Blue	0–100 mM	0 V	Human serum	Dungchai *et al.* (2009)
Glucose oxidase	Mixed with ink before printing step	Cobalt phthalocyanine	10–30 mM	+0.4V	HepG2 monolayer cell cultures	Pemberton *et al.* (2011)

© Woodhead Publishing Limited, 2012

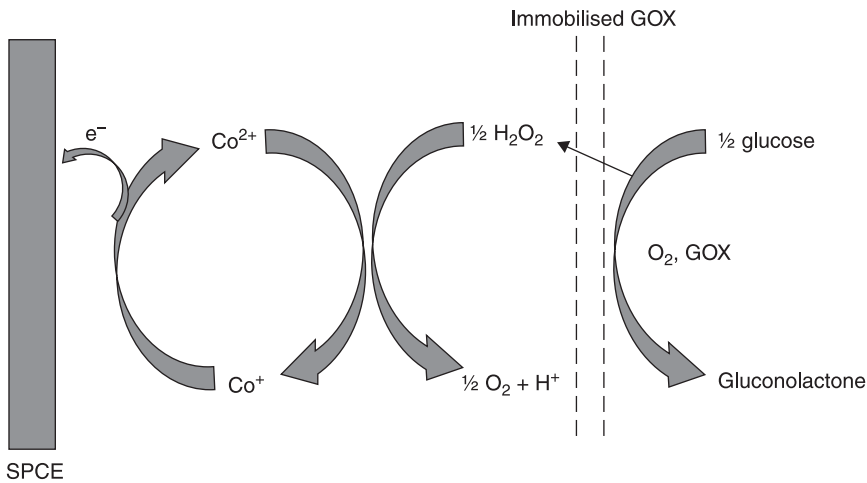

13.6 Sequence of reactions giving rise to analytical signal in the GOx-based glucose biosensor.

Recently, Pemberton *et al.* (2009a) have utilised such an approach with a screen-printed microband electrode for the determination of glucose in bovine serum. The use of such screen-printed working electrodes with dimensions in the μm range exhibit a number of advantages, including high mass transport, low ohmic drop and enhanced signal to noise ratios (Xie *et al.*, 2005). Recent studies have shown the possibility of producing devices with features in the region of 100 μm × 85 μm by screen-printing coupled with a technique known as 'print-n-shrink' (Sollier *et al.*, 2009). This approach utilised printing designs onto the child's toy known as 'Shrinky-Dinks' (Chen *et al.*, 2008; Grimes *et al.*, 2008; Mandon *et al.*, 2010). The material for this toy is formed from pre-stressed transparent polystyrene, which upon heating (3–5 min, 160 °C), shrinks isotropically in plane by approximately 63%, hence reducing the size of the printed sensor printed upon it. However, generally, the reproducible direct screen-printing of electrodes with dimensions in the μm is difficult. Nevertheless, microband electrodes could be readily fabricated by a simple procedure from the conventional-sized screen-printed glucose biosensors (Pemberton *et al.*, 2009a). By cutting through the substrate, screen-printed track and dielectric, the thin 20 μm layer of screen-printed carbon track is exposed, hence in this case giving a 20 μm × 3 mm screen-printed carbon microband working electrode. Cyclic voltammetric investigations demonstrated sigmoidal-shaped voltammograms, indicative of microelectrode behaviour, and were found to be indicative of radial diffusion over the range of 1 to 50 mV/s; however, signals were not found to be completely independent of the scan rate, demonstrating mixed-mechanism mass transport involving both radial diffusion and planar diffusion. Further amperometric investigations in stirred and non-stirred solutions demonstrated no significant changes in maximum currents, confirming that the predominant mechanism was radial

© Woodhead Publishing Limited, 2012

diffusion. In this study, a water-based screen-printing ink was utilised for the production of the working electrodes; this offers several advantages compared to conventional solvent-based SPCEs in terms of environmental considerations, and health and safety in production. However, most notably, utilising a biologically benign ink facilitates the direct incorporation of biological compounds, such GOx. This allows for a simpler manufacturing process, as the enzyme and ink can be printed in one step.

13.2.2 Glucose dehydrogenase-based screen-printed biosensors

Compared to GOx-based systems, glucose dehydrogenase (GDH) enzymes can offer certain advantages, such as oxygen independence, allowing for their use in low oxygen conditions such as fermentation. However, problems have been reported with the utilisation of the pyrroloquindine quinone (PQQ)-dependent form of GDH as this has a high relative activity in the presence of maltose, presenting a serious problem in the determination of blood glucose levels and consequent misdiagnoses. Again, as with H_2O_2, the direct determination of nicotinamide adenine dinucleotide (NADH) requires high applied potentials for its determination. However, it is possible to monitor this with the use of a suitable mediator.

Figure 13.7 illustrates that the underlying mechanism utilised for one such mediated approach is that made by Piano *et al.* (2010a) as part of a flow injection system for the determination of glucose in serum. The SPCE was modified with the electrochemical mediator Meldola's Blue–Reinecke Salt (MBRS), coated with GDH (from *Bacillus* sp.), and NAD^+. A cellulose acetate layer was deposited on top of the device to act as a perm-selective membrane. The developed prototype biosensors were found to be stable for at least 240 days at a temperature of 37 °C. Using an applied potential of +50 mV, the response was found to be linear over the range of 0.075–30 mM glucose, with the former representing the detection limit.

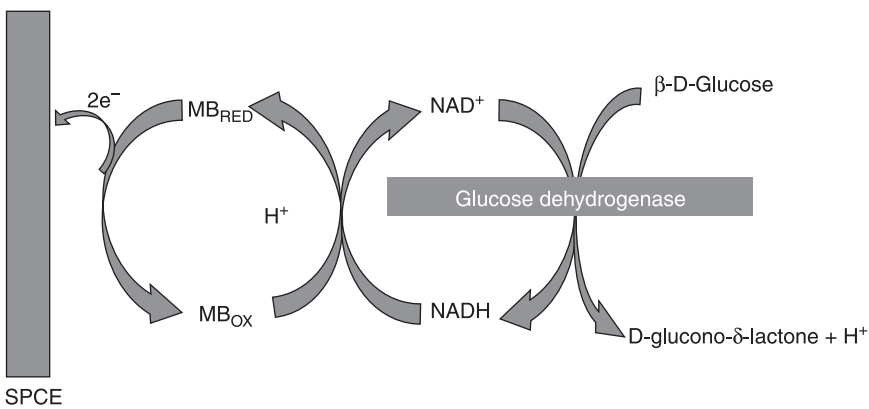

13.7 Sequence of reactions involved in the operation of the GDH-based glucose biosensor (adapted from Piano *et al.*, 2010a).

© Woodhead Publishing Limited, 2012

Screen-printing technology has focused on the production of two-dimensional sensors, planar sensors, which can be then integrated with devices produced by other production techniques, such as plastic injection moulding, if further functionality is required. Nevertheless, alternative approaches have been recently investigated, such as that reported recently by Santiago *et al.* (2010). They have utilised screen-printing to fabricate three-dimensional carbon micro-devices. These screen-printed microsystems consisted of a microchannel structure formed by two electrodes printed in parallel on a polyester film substrate; the sides of these act as the walls of the microchannel electrochemical cell. The working electrode was a graphite ink, and the reference/counter electrode was Ag/AgCl. The screen-printed carbon-exposed edge area was reported to be *c.* 0.1 cm^2 with a final volume of the microchannel being in the region of 20 µl. The developed sensor was applied to the ultrasensitive electrochemical detection of alkaline phosphatase, obtaining a detection limit of below 10^{-12} M for GOx-and of 10^{-15} M for GDH-modified systems using a 15 minutes of incubation time. A potential pulse polypyrrole electropolymerised generated film was used to entrap either GOx or GDH to the working carbon electrode. This is reported to be superior to common methods of entrapment, as it is more reproducible and more stable.

13.2.3 Lactate

The monitoring of lactate is important for disciplines such as sport science, as it is produced in increasing amounts during physical exercise. Its major use is in the food and beverage industries, where it is used in cider and wine manufacture, and as an acidulant and for the manufacture of bread additives. It is also used as a chemical intermediate in textile finishing and in leather tanning. Recently, its determination has been utilised for monitoring toxic events in cell culture media at a screen-printed biosensor (Rawson *et al.*, 2009).

Principally, two enzymes are used for the production of lactate biosensors; lactate oxidase (LOX) and lactate dehydrogenase (LDH). The combination of these with SPCEs has been shown to be a highly effective method and has been recently been reviewed (Hart *et al.*, 2004, 2007; Kalcher *et al.*, 2009; Nikolaus and Strehlitz, 2008; Privett *et al.*, 2010; Zhou *et al.*, 2009). A number of these devices are summarised in Table 13.2. LOX is one of the most commonly reported for biosensor construction; in the presence of oxygen it catalyses the production of pyruvate and hydrogen peroxide (EQ. [13.8]):

$$\text{Lactate} + O_2 \xleftarrow{\text{Lactate Oxidase}} \text{Pyruvate} + H_2O_2. \qquad [13.8]$$

As with GDH, described in the previous section, alternatively LDH can be utilised (Eq. [13.9]). The enzyme does not require the presence of oxygen for the detection of lactate and so can be used in anaerobic conditions.

© Woodhead Publishing Limited, 2012

Table 13.2 Recent biosensors employed for the detection of lactate using either LOX or LDH as the biological agent incorporated into SPCEs

	Entrapment method	Type of assay	Mediator	Assay time (s)	Lower linear range	Upper linear range	Applied potential, mV	Reference
LDH	Entrapped and dropped coated with Nafion	Amperometric	Variamine blue	–	5	450	+200	Raodi *et al.* (2008)
LOX	Methocel membrane	Electrochemiluminescent	Luminol	150	8	0.2	+500	Martínez-Olmos *et al.* (2009)
LOX LDH	Enzymes in solution	Amperometric	Prussian blue	95	10	10.0	0.0	Ricci *et al.* (2007b)
LDH	Entrapped within a sol-gel ink	Amperometric	NAD^+ and poly (MBRS)	30	125	2.48	+100	Prieto-Simón *et al.* (2007)
LDH	Entrapment by phase invasion (polysulfone solidifies in solution entrapping LDH)	Amperometric	Epoxy-graphite composite	30	1	0.125	+100	Ricci *et al.* (2007b)
LOX	Methocel membrane	Electrochemiluminescent	Luminol	–	10	0.5	+500	Ballesta-Claver *et al.* (2009)
LOX	Bulk ink entrapment	Chronoamperometric	Potassium ferricyanide	300	1000	50	+400	Sato and Okuma (2006)

© Woodhead Publishing Limited, 2012

$$\text{L} - \text{Lactate} + \text{NAD}^{+} \xleftrightarrow{\text{Lactate Dehydrogenase}} \text{Pyruvate} + \text{NADH} + \text{H}^{+}. \quad [13.9]$$

Piano *et al.* (2010b) have recently reported on the use of SPCEs modified with MBRS complex for the flow injection analysis of lactate with LDH. This was found to be an advantage over the previously reported MBRS-mediated electrodes, as the Reinecke salt was found to be insoluble and not leached from the SPCE, allowing for flow injection analysis to be successfully performed. The screen-printed biosensors were stable for at least 17 days when stored at 4° C.

13.2.4 Ethanol biosensors

Previous investigations on screen-printed alcohol biosensors have been reviewed (Hart *et al.*, 2004; Kalcher *et al.*, 2009). More recently, alcohol screen-print-based sensors have been developed for use in the field of forensic science investigations. Luo *et al.* (2008) have utilised such an approach for the forensic determination of blood alcohol utilising alcohol dehydrogenase (ADH) (Luo *et al.*, 2008). This was fabricated by cross-linking ADH with glutaraldehyde and NAD^{+} on a screen-printed electrode previously modified with nafion. The electrode was modified with MBRS via repeated voltammetric scanning of a 1 mM solution in 0.1 M phosphate pH 8 buffer. The developed biosensor was able to determine serum alcohol concentrations over the range 1 to 5 mM. This could be used to determine alcohol concentrations in intoxicated drivers. However, post-mortem analysis of blood alcohol appears impossible, since the biosensor cannot differentiate between common alcohols and aldehydes found in these samples.

Mediator-free screen-printed alcohol and acetaldehyde biosensors have recently been reported for their determination in breath (Gessei *et al.*, 2009). These 'bio-sniffers' were formed by screen-printing a carbon working electrode on one side of a filter paper substrate and on the reverse side, the Ag/AgCl electrode. The working electrodes were modified by either immobilizing alcohol oxidase (AOx) or aldehyde dehydrogenase (ALDH). AOx oxidises ethanol to acetaldehyde and hydrogen peroxide. The latter was detected directly by monitoring the amperometric oxidation peak as observed at +0.9 V. In the presence of NAD^{+}, acetaldehyde is oxidised to acetic acid, NADH and proton by ALDH. Hence by monitoring amperometric oxidation of NADH at +0.65 V, the concentrations of acetaldehyde could be determined. Good responses to ethanol and acetaldehyde vapour were recorded over the ranges 1.0 to 100 ppm and 0.2 to 4.0 ppm, respectively, covering the ranges expected to be seen in human breath after consumption of alcoholic beverages.

13.2.5 Cholesterol

The term 'total cholesterol' refers to the total concentration of the two forms of cholesterol present in blood: the free form and the esterified form. To measure

© Woodhead Publishing Limited, 2012

total cholesterol, two enzymatic reactions have been utilised. Cholesterol esterase (ChE) is employed to convert ester to cholesterol, which together with the original cholesterol can then be measured using cholesterol oxidase (ChOx), which in the presence of oxygen converts cholesterol to cholest-4-en-3-one and hydrogen peroxide. A number of previous applications of SPCEs for the determination of cholesterol have been reviewed by Hart *et al.* (2004, 2007).

Using a similar approach to that described for glucose and lactate above, the hydrogen peroxide generated can be monitored as an indirect way to quantify the concentration of cholesterol present in the sample. Shih *et al.* (2009) have used a similar approach to this, however, in utilising the catalytic reduction of hydrogen peroxide at a SPCE modified with Fe_3O_4, ChOx and ChE. Using a 10 µl sample volume, the screen-printed sensor was able to gain a detection limit of 19.4 mg/dl with a linear range from 100 to 400 mg/dl for total cholesterol.

Utilising electrodes fabricated from metals such as Au or Pt, it is possible to measure hydrogen peroxide at relatively low applied potentials. Shen and Lui (2007) have used an Au electrode with a self-assembled ChOx monolayer for the determination of cholesterol. The Au working was part of a screen-printed three-electrode cell, consisting of a screen-printed Ag/AgCl reference and Au counter electrode. Gold was found to be superior to Pt as a working electrode, giving better sensitivity.

Alternatives to ChOx have been also investigated at SPEs, such as a cholesterol biosensor based on cytochrome P450scc (Carrara *et al.*, 2008). P450scc is highly specific towards cholesterol and its metabolites, catalysing the side-chain cleavage of C27 cholesterol to C21 pregnenolone in the presence of molecular oxygen and NADPH-ferri hemoprotein reductase. This approach has been investigated at a rhodium–graphite SPE modified with multi-walled carbon nanotubes (MWCNT) and cytochrome P450scc as catalytic enzyme. Recently its activity has also been shown to be enhanced at SPEs modified with gold nanoparticles (AuNP; Shumyantseva *et al.*, 2005).

13.2.6 Miscellaneous proteins, peptides and amino acids

The amylases group of enzymes break down starches and glycogen to maltose and are widely distributed in both animal and plant tissues. The main biological function of salivary alpha-amylase (sAA) is the enzymatic digestion of carbohydrates, converting these to maltose and maltotriose. Consequently, during periods of energy expenditure and stress, elevated concentrations are seen and can be utilised as a method of evaluating and identifying such periods. Mahosenaho *et al.* (2010) have utilised a three-enzyme SPCE biosensor for its determination of sAA activity, but enzymatic products of this reaction are not readily determinable. However, utilising α-glucosidase, maltose, which can be hydrolysed to α-glucose, once generated, this can be covered by mutarotase into β-D-glucose, the substrate of GOx. The generated β-D-glucose is then hydrolysed to gluconic

© Woodhead Publishing Limited, 2012

acid and hydrogen peroxide by GOx. The resulting hydrogen peroxide generated can then be measured via chronoamperometry utilising its Prussian blue-mediated reduction.

13.2.7 Nucleic acids and purines

SPCEs have recently been utilised for the monitoring of genotoxicity (Rawson *et al.*, 2010). Investigations were made using differential pulse voltammetry (DPV) to identify the oxidation products generated from the interaction of Cr^{6+} with double-stranded DNA. Using such an approach, the reaction products could be readily screened in a single voltammetric scan. In a separate study, Ferancová *et al.* (2007) have investigated the effects of Sn^{2+} and As^{3+} at a DNA multi-walled nanotube modified SPCE using $[Co(phen)_3]^{3+}$ as an electrochemical DNA cleavage marker. Here, by utilising DPV, it was found possible to readily identify the DNA damage.

A number of drugs are known to interact with DNA and recently these interactions have been monitored voltammetrically at a SPCE. Ravera *et al.* (2007) has demonstrated that it possible to monitor covalent binding at N7 of guanine, electrostatic interactions, and intercalation resulting from interactions of antitumoral Pt-, Ru-, and Ti-based metallodrugs at DNA immobilised on screen-printed electrodes.

13.2.8 Food pathogens

Staphylococcus

The detection of micro-organisms capable of causing food poisoning is a highly important area. Escamilla-Gomez *et al.* (2008) have reported on the development of a biosensor for *Staphylococcus aureus*, one of the predominant food-borne pathogens. The amperometric immunosensor was formed by covalent immobilisation of antibodies at Au SPEs via hetero-bifunctional cross-linkers (3,3-dithiodipropionic acid di(*N*-succinimidyl ester), DTSP). The biosensor utilised tetrathiafulvalene as a redox mediator entrapped at the electrode surface. A limit of detection of 3.7×10^2 cells/mL was obtained with a dynamic range from 1.3×10^3 to 7.6×10^4 cells/mL.

Salmonella

Salmonella serotypes are one of the most common bacteria responsible for food-borne gastroenteritis and can be utilised as a potential micro-organism for bioterrorism. Salam and Tothill (2009) have recently reported a chronoamperometric screen-printed immunosensor capable of the rapid detection of *Salmonella typhimurium*. This was based on a screen-printed Au working electrode with co-printed carbon counter and Ag/AgCl pseudo-reference electrodes. Both physical

© Woodhead Publishing Limited, 2012

and covalent immobilizations via amines were used to couple the *S. typhimurium* antibody to carboxymethyldextran on the surface of the gold working electrode. A direct sandwich enzyme-linked immunosorbent assay format was utilised using polyclonal anti-Salmonella antibodies conjugated to horseradish peroxidase (HRP) as the enzyme label and 3,3′,5,5′-tetramethylbenzidine dihydrochloride (TMB)/H_2O_2 was utilised as the enzyme mediator/substrate the system. The determination of *S. typhimurium* concentrations of 5×10^3 cells/mL to 20 cells/mL was achieved by physical and covalent antibody immobilization, respectively.

Escherichia coli

Bacteriophages are small viruses that have recently been postulated as promising recognition elements for the production of bacterial biosensors. Shabani *et al.* (2008) have recently shown the possibility of immobilising phage onto SPCEs in a similar manner to antibodies or DNA probes. In this approach, SPCEs were modified with 1-(3-dimethylaminopropyl)ethylcarbodiimide hydrochloride (EDC) by chronoamperometry using a potential of +2.2 V to oxidise the carbon surface. The carboxyl groups generated react with EDC to produce an ester intermediate that can react with amines, resulting in their covalent attachment at the surface. Using this approach, the amino acids present on the outer membrane of a phage can bind to the SPCE-activated carboxylic groups, resulting in the attachment of phage to the surface. This approach was used in this work to covalently attach T4 bacteriophage (wild type). The SPCEs were rinsed with deionised water and then immersed and shaken in a solution of T4 bacteriophage (10^8 pfu/mL in SM buffer solution, pH 7.5). After washing, the modified SPCEs were dipped in a solution of borine serum albumin solution and rinsed with SM buffer. The biosensors were then exposed to a solution containing *Escherichia coli* K12 (10^8 cfu/mL) suspension in SM buffer pH 7.5 for 20 minutes. After rinsing with buffer, the SPCEs were covered with SM buffer to perform impedance measurements, allowing for a rapid, direct and label-free means of detecting specific bacteria. A detection limit of 10^4 cfu/mL for 50 µl samples was obtainable.

13.2.9 Viruses

Screen-printed biosensors have been developed for the detection of a number of important viruses and recently been reviewed (Yadav *et al.*, 2010). Mahmoud and Luong (2010) have reported the development of a screen-printed gold electrode (SPGE) surface modified with either AuNPs or thiolated single-walled carbon nanotubes/gold nanoparticles (SWCNT/AuNPs) for the determination of human immunodeficiency virus 1 (HIV-1) in sera. DPV investigations showed a linear relationship between shifts in peak potential and increasing numbers of HIV-1 viruses over the range 6.8×10^2 to 1.11×10^6 copies/mL in HIV-infected serum samples.

© Woodhead Publishing Limited, 2012

13.3 Environmental applications of screen-printed electrodes

As a result of the possibility for decentralised testing that the use of screen-printed biosensors allows, a great deal of research has focused on this area (Badihi-Mossberg *et al.*, 2007; Tudorache and Bala, 2007). The following section deals with this in greater detail.

13.3.1 Phosphate

The determination of inorganic phosphate (Pi) is important both environmentally and medicinally. It is an important parameter for both environmental and potable water quality. In the presence of inorganic phosphate, oxygen and cofactors, pyruvate can be decarboxylated by pyruvate oxidase to give H_2O_2, acetyl phosphate and CO_2. It is possible to utilise the enzymatically generated H_2O_2 to quantify the corresponding concentration of Pi. Gilbert *et al.* (2009, 2010) have utilised this approach for the determination of Pi in human urine and water samples at a CoPC-modified SPCE. Utilising the CoPC-mediated electrocatalytic oxidation of the generated peroxide, a linear response for Pi was gained over the range 2.27×10^{-5} to 1.81×10^{-4} M, with a corresponding limit of detection of 4.27×10^{-6} M. The principles underlying the mechanism of this biosensor are shown in Fig. 13.8.

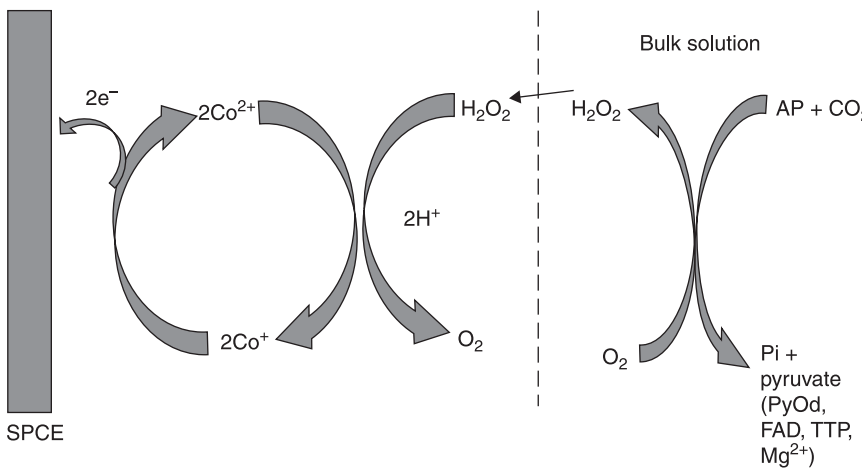

13.8 Schematic representation of the electrocatalytic oxidation of H_2O_2 at the cellulose acetate–CoPC–SPCE. The dashed line represents the 1.5% cellulose acetate membrane (adapted from Gilbert *et al.*, 2009, 2010).

© Woodhead Publishing Limited, 2012

13.3.2 Nitrates and nitrites

Nitrates are of both commercial and environmental importance, widely used in both explosives and fertilisers. One particular area of concern is pollution of the environment from agricultural run-off of nitrates to rivers, lakes and potentially to drinking water. Consequently, there is increasing interest in the development of sensors capable of determining nitrate levels in the environment and water-courses. Recently, Albanese *et al.* (2010) have utilised SPCEs modified with nitrate reductase obtained for *Escherichia coli.* The two mediators, Azure A or methyl viologen, were investigated. However, Azure A was found to be less effective, open to problems such as leaching into the sample solution. Using the optimised methyl viologen-based sensor as part of a flow injection system, detection limits of 0.1 mM with a linear to 10 mM nitrate were obtained.

Quan *et al.* (2005) have immobilised nitrate reductase derived from yeast using a polymer (poly(vinyl alcohol))-entrapment method to both a glassy carbon electrode and a SPCE. Utilising the electron-transfer mediator, methyl viologen, at an applied potential of −0.90 V (vs. Ag/AgCl), a linear range of 15–250 μM and a detection limit of 5.5 μM was reported. The utility of the proposed sensor system was demonstrated by determining nitrate in Han River water samples, before and after treatment. Good agreement was obtained between the results gained by both ion chromatography and spectroscopic determination and the SPCE biosensor. The activity of nitrate reductase was affected by the presence of oxygen; however, this effect was readily overcome by the addition of a sulphite to the sample as an oxygen scavenger.

13.3.3 Pesticides and chemical warfare agents

A number of SPCE-based applications for the determination of OPs and chemical warfare agents have previously been reviewed (Amine *et al.*, 2006; Andreescu and Marty, 2006; Arduini *et al.*, 2010a; Hart *et al.*, 2004, 2007; Kalcher *et al.*, 2009; Miao *et al.*, 2010; Wanekaya *et al.*, 2008) and Table 13.3 summarises some recent developments made in this area. OPs and warfare agents act by inhibiting the enzyme acetylcholinesterase (AChE) required for normal nervous function, catalysing the hydrolysis of the neurotransmitter acetylcholine into acetate and choline. The inhibition of AChE results in the build-up of acetylcholine, which interferes with muscular responses, leading to a number of symptoms and eventually death due to respiratory failure (Miao *et al.*, 2010).

Amperometric measurement of enzyme inhibition can be made in a number of ways, such as by the measurement of thiocholine produced by the action of AChE on acetylthiocholine, or via the production of hydrogen peroxide formed by the oxidation of choline by choline oxidase (Wu *et al.*, 2009). Similarly, *p*-aminophenol formed from the hydrolysis of *p*-aminophenyl acetate by AChE can also be readily

© Woodhead Publishing Limited, 2012

Table 13.3 Summaries of some recent developments in the application of screen-printed biosensors for the determination of OPs

Enzyme		Entrapment method	Applied potential	Linear range	Detection limit	Analytes	Samples	References
Acetylcholinesterase	Carbon nanotube, Flow injection	Cellulose membrane	Amperometric, +0.3 V			Paraoxon	Saliva	Du *et al.* (2009)
Acetylcholinesterase	Zirconia nanoparticle and quantum dots (ZnS@CdS)		Stripping analysis of its metallic component, Cd after an acid-dissolution step	10 pM–4 nM	80 pM	Paraoxon	Human plasma	Liu *et al.* (2008)
Acetylcholinesterase	Magnetic particles, ZnS@ CdS quantum dots		Square wave voltammetry	0.3–300 ng/mL	0.15 ng/mL	Paraoxon	Plasma	Wang *et al.* (2008a)
Acetylcholinesterase	Carbon nanotubes		Micro-flow injection	5 pM–0.5 nM	2 pM	Paraoxon	Rat saliva	Wang *et al.* (2008b)
Choline oxidase	Nafion		Amperometry, 50 mV mediated by Prussian blue	0.1 μM–1.0 μM	0.1 μM	Paraoxon	–	Sajjadi *et al.* (2009)
Acetylcholinesterase	Coated Fe_3O_4/Au magnetic nanoparticulate, Zirconia nanoparticles		Differential pulse voltammetry	1.0×10^3–10 ng/mL	5.6×10^4 ng/mL	Dimethoate	Chinese cabbage	Gan *et al.* (2010)
Acetylcholinesterase				Up to 10 ng/mL	5 ng/mL	Fenitrothion, methidathion, parathion methyl, chlorpyrifos	Orange juice	Roepcke *et al.* (2010)

© Woodhead Publishing Limited, 2012

Acetylcholinesterase	Polyvinyl alcohol photopolymer	7,7,8,8-tetracyano quinodimethane			2 ng/mL	Carbaryl, chlorpyrifos, chlorfenvinphos	Waste water	Hildebrandt *et al.* (2008)
Acetylcholinesterase (*Nippostrongylus brasilienis*) and monooxygenase P450BM-3	Sol–gel				1 ng/mL paraoxon and 10 ng/mL for parathion	Paraoxon, parathion	–	Waibel *et al.* (2006)
Cholinesterase			Mediated by either CoPC +0.1 V, or Prussian blue +0.2 V	CoPC 1×10^6 -7×10^5 M, Prussian blue 5×10^6–5×10^4 M	Aldicarb 12 ng/mL, carbaryl 25 ng/mL, paraoxon 2 ng/mL, chlorpyrifos-methyl oxon 0.5 ng/mL	Aldicarb, carbaryl, Paraoxon, Chlorpyrifos-methyl oxon	Waste and river water	Arduini *et al.* (2006)
Acetylcholinesterase	Gold disposable electrochemical printed (DEP) chips		Differential pulse voltammetry		10 ng/mL for Paraoxon and 8 ng/mL for carbofuran	Paraoxon, carbofuran	Milk and water	Dounin *et al.* (2010)
Acetylcholinesterase		Cross-linking with glutaraldehyde, Nafion, and bovine serum albumin	50 mV mediated by Prussian blue	8–1000 ng/mL	8 ng/mL in buffer, 33 ng/mL for sample extract	Coumaphos	Honey	Carlo *et al.* (2010)

© Woodhead Publishing Limited, 2012

determined. However, AChE activity can be inhibited by neurotoxins other than Ops, such as carbamates and heavy metals, and hence selectivity can suffer.

Organophosphate hydrolase (OPH) has also been utilised in such sensors (Joshi *et al.*, 2006) exhibiting broad substrate specificity hydrolysing a number of OPs and chemical warfare agents such as sarin (O-isopropy lmethylphosphonofluoridate) and soman to *p*-nitrophenol, which can be detected electrochemically. Reportedly, this approach, utilising OPH, offers advantages for the biosensing of OPs as they act as the substrates for the enzyme rather than an inhibitor.

Arduini *et al.* (2007) have utilised a SPCE modified with an *in-situ* generated layer of Prussian blue formed from the addition of potassium ferricyanide in 10 mM HCl and 0.1 M ferric chloride in 10 mM HCl directly on the surface of the working electrode. Butyrylthiocholine (BChE) or AChE was then immobilised on the SPCE surface with glutaraldehyde and a nafion/BSA membrane was added across the surface. Sarin gas measurements were made by the addition of a 5 µl of a pH 7.4 phosphate buffer, the resulting depletion in enzyme activity was found to be dependent on sarin gas exposure and, for a 30 s incubation time, inhibitions of 43% and 34%, were obtained for 0.1 and 0.5 mg m^{-3}, respectively.

13.3.4 Whole cell photosynthetic pesticide biosensors

A contrasting approach is the application of whole cell photosynthetic-based biosensors for the determination of pesticides (Tibuzzi *et al.*, 2008), recently reviewed by Scognamiglio *et al.* (2010). Several herbicides have been investigated in this manner utilising a screen-printed carbon transducer. Interestingly, screen-printing of actual algal cells has also been shown possible (Shitanda *et al.*, 2009). The algal ink was prepared by mixing unicellular microalga *Chlorella vulgaris* cells, carbon nanotubes and a sodium alginate solution. The modified ink was screen-printed directly onto the surface of a SPCE. Photosynthetically generated oxygen was monitored amperometically as part of a flow injection system and exposures to atrazine (12 µM) and Duiron (DCMU) (1 µM) resulted in a 50% depletion in oxygen production.

13.3.5 Polychlorinated biphenyls

An important part of many assays is the isolation and separation of the target analyte from the sample and a wide number of procedures have been developed to achieve this goal. Recently, attention has focused on the development and application of magnetic separation techniques, which employ small magnetic particles (Šafařik *et al.*, 1999, 2004; Saiyed *et al.*, 2003). These consist mainly of nano-sized iron oxide particles (Fe_3O_4 or γ-Fe_2O_3), which are suspended in a carrier liquid. Frequently referred to as magnetic, the majority of the particles presently used are in fact superparamagnetic, consequently requiring an external

© Woodhead Publishing Limited, 2012

magnetic field to be magnetic, and once this is removed they redisperse. This allows for a simple method for concentrating and isolating the particles from the sample matrix. It is possible to modify these particles with different ligands (streptavidin, Protein A, etc.) and chemically derivatised particles with specific recognition groups such as monoclonal and polyclonal antibodies. This allows for the possibility of using these modified particles to isolate analytes to the magnetic bead, which can then be easily isolated by the application of a magnetic field.

Magnetic bead-based screen-printed biosensors have been reported assays for the determination of several polychlorinated biphenyls (PCBs) (Centi *et al.*, 2007). These are a group of highly stable and persistent industrial pollutants. They have been shown to undergo bioaccumulation and as a result are responsible for a number of environmental issues and poisonings.

Centi *et al.* (2006) have utilised magnetic beads modified with protein G for subsequent coating with the PCB antibodies, immunoglobalin G (IgG) anti-PCB28 or IgG anti-PCB77. A 50 mL suspension of these antibody-coated beads was then mixed with 940 mL of sample and 10 mL of alkaline phosphatase-labelled antibodies. After incubation for 20 minutes, the beads were magnetically separated down onto the SPCE surface and the supernatant removed.

Then the enzymatic substrate (α-naphthyl phosphate) in buffer was deposited on the SPCE to close the electric circuit. After five minutes, the enzymatic product was determined by DPV. Detection limits were found to be between 0.3 and 0.8 µg/l. The developed immunosensors were successfully applied for detection of PCBs in marine sediment extracts. Lin *et al.* (2008a) have utilised a similar approach with antibody-labelled magnetic beads. However, this approach utilised a HRP-labelled PCB (HRP–PCB) and an alkali phosphate-labelled PCB to compete with the native sample PCB. Once the competitive assay was complete, the beads were magnetically isolated and the enzyme substrate added for determination by square wave voltammetry at the SPCE.

13.3.6 Polyaromatic hydrocarbons

Polyaromatic hydrocarbons (PAHs) are known to interact with DNA producing a number of differing products, some of which result in strand cross-linking and eventual mutations. However, it is possible to utilise there phenomena as a means to determine their presence and concentration. Del Carlo *et al.* (2008) have used DNA electrochemical biosensors based on four different types of DNA (calf thymus ssDNA, calf thymus dsDNA, salmon testis ssDNA and salmon testis dsDNA). Using benzo(a)anthracene and phenanthrene as model compounds, they showed that variation in the guanine signal revealed the interaction of PAHs with the immobilised DNA. The salmon ssDNA modified device was found to be the most successful and was further evaluated for benzo(a)anthracene, fluorene, indeno(1,2,3-cd)pyrene, anthracene and phenanthrene in 5–40 ng/mL

© Woodhead Publishing Limited, 2012

solutions, and for benzo(a)pyrene (5–50 ng/mL). A concentration-dependent variation of the DNA guanine oxidation peak was observed for all compounds. Using the salmon ssDNA-modified device, the PAH concentrations present in samples of contaminated mussels (*Mytilus galloprovincialis*) were successfully investigated.

13.3.7 Biosensors for metal ion detection

A large volume of research has focused the determination of metal ions utilising stripping voltammetry at either at SPEs modified with Bi or Hg or at plain unmodified SPEs. These are not classed as biosensors and are consequently outside the scope of this review. However, a number of extensive reviews on these sensors have been recently reported (Arduini *et al.*, 2010a; Honeychurch and Hart, 2003; Kokkinos and Economou, 2008; Stozhko *et al.*, 2008; Svancara *et al.*, 2010). Nevertheless, as mentioned earlier in the pesticide section above, other toxins, such as heavy metals, can also readily inhibit enzyme activity (Andreescu and Marty, 2006), an effect that can be harnessed to develop biosensors for their determination (Amine and Mohammadi, 2007). One such recent example utilises the inhibition effect that Hg^{2+} ions exhibit on the enzymatic activity of urease, which can be monitored at AuNP-modified SPCEs. (Domínguez-Renedo *et al.*, 2009). Urease was immobilised to the SPCE surface by cross-linking with bovine serum albumin and glutaraldehyde. Metallic AuNPs were found to enhance the sensitivity of the sensor. These were electrochemically deposited on the modified carbon working electrode surface, using a 0.1 mM solution of $HAuCl_4$ in 0.5 M H_2SO_4. Mercury measurements were undertaken once a steady-state current was obtained after the addition of urea. Additions of Hg^{2+} resulted in a current decrease proportional to the amount of Hg^{2+} added. Using this approach, a detection limit for Hg^{2+} of 4.2 μM was obtained. The sensor was found capable of successfully determining human plasma samples fortified with 1.0 μM Hg^{2+}.

A similar approach has been utilised by Sanllorente-Méndez *et al.* (2010) for determining arsenite (AsO_3^{3-}) as, in this case, an AchE-modified SPCE. Arsenite concentrations were measured utilising the inhibitory effect this species has on the activity of AChE on the conversion of acetylthiocholine iodide to thiocholine iodide and acetic acid. As thiocholine is electrochemically active, the product of this reaction can be readily monitored amperometically utilising the optimised applied potential of +0.6 V. As additions of As^{3+} inhibit the enzymatic reaction, a corresponding drop in the amperometric signal is gained with increasing As^{3+} concentration. Using such an approach, a detection limit of 1.1×10^{-8} M with a corresponding linear range up to 1×10^{-7} M As^{3+} was obtained. The developed sensor was capable of determining 1.0 μM As^{3+} in tap water. Further investigation on a certified As^{5+} water sample was possible on adding sodium thiosulphate to facilitate the reduction of the AChE inert As^{5+} to As^{3+}.

© Woodhead Publishing Limited, 2012

The interaction of arsenate with L-cysteine has been successfully utilised as the basis of a biosensor for the determination of As in a number of environmental water samples (Sarkar *et al.*, 2010). L-cysteine reduces arsenate to arsenite and is in the process oxidized to L-cystine. The reaction involves electron transfer at the working electrode and thus the response can be monitored amperometically. By immobilising L-cysteine to the surface of the SPCE, it was found possible to gain a limit of detection of between 1.2 and 4.6 ng/mL. Interferences for oxidising agents such as nitrate were investigated, and no effects were found from nitrate concentrations commonly present in drinking water.

SPCE biosensors based on the well understood glucose oxidase enzyme system have also been described for the determination of a number of metal ions, including; Hg^{2+}, Ag^{+}, Cu^{2+}, Cd^{2+}, Co^{2+} and Ni^{2+} (Guascito *et al.*, 2009). As part of a flow injection system the sensor was able to obtain detection limits in the low ppm with Ag^{+} detection limits in the ppb region.

Shewanella sp. is known for its role in biogeochemistry, as a metal-reducing bacterium involved in the cycling of iron, manganese, trace elements and phosphates. Prasad *et al.* (2009) have demonstrated the use of these bacteria as the electron transfer material for electrochemical sensors in the determination of arsenite, hydrogen peroxide and nitrite. *Shewanella* sp. CC-GIMA-1 bacterial suspension (prepared in 0.1 M, pH 7.4 phosphate-buffered saline solution) was drop-coated on the electrode surface and allowed to settle under room temperature for 1 hour. This simple approach was found better than growing bacterial biofilm on electrode material, which was laborious and time consuming. Cyclic voltammetric investigations showed the bacteria exhibit electron exchange with the SPE surface, behaving similarly to a bacterial biofilm. It is well known that graphite electrodes, containing a carbon–oxygen functional group similar to humates, provide a natural habitat for the bacteria. The bacteria films were found to be able to sustain themselves by using carbon–oxygen functionalities of SPCE as electron acceptors for respiration. The effects of arsenite (50–500 µM) hydrogen peroxide (50 µM–2.5 mM), and nitrite (100–500 µM) were studied by cyclic voltammetry and the reduction peak current of the *Shewanella* sp. modified electrode was found to increase in the case of As from *c.* 6 µA–10 µA for an addition of 500 µM arsenite. Additions of Fe^{3+} were also found to exhibit similar voltammetric behaviour.

13.3.8 Immunoassay based on stripping voltammetry of metal nanoparticle labels

Nanoparticles, owing to their similarity in sizes to a number of important biomolecules such as antibodies or DNA strands, make good candidates for labels in immunoassays. This is practically true if Au or other heavy metal nanoparticles are utilised, allowing for sensitive electrochemical techniques such as stripping voltammetry to be utilised. This approach has recently been reviewed

© Woodhead Publishing Limited, 2012

by Escosura-Muniz and Merkoci (2010). One of the first reports using such an approach was made by Dequaire *et al.* (2000), who used AuNPs as labels for the determination of IgG. Quantification of the AuNPs was achieved by anodic stripping voltammetry (ASV) at a screen-printed electrode, gaining a detection limit of *c.* 450 pg/mL (3 pM). Similarly low detection limits (20 pg/mL) were reported using Cd nanoparticles labels for the determination of prostate-specific antigen (PSA) by Liu *et al.* (2007, 2008) and Lin *et al*. (2008b), again utilising ASV as the measurement step at a SPCE, a detection limit of 0.02 ng/mL being reported. Brainina *et al.* (2010) have utilised Fe nanoparticles for the determination of *Salmonella typhimurium* (strain SL 7207) utilising a magnetic-based separation, followed by digestion of the Fe nanoparticles in a mixture of 0.36 M H_2SO_4 and 0.28 M HNO_3. The concentration of Fe^{3+} liberated was quantified by the cathodic adsorptive stripping voltammetry of its catechol complex in 0.1 M sodium acetate.

Silver nanoparticles have been used in a similar manner by Chikae *et al.* (2010). These have been utilised as part of a sandwich-type immunoassay for human chorionic gonadotropin (hCG). The biosensor comprises a primary antibody immobilised on the surface of a SPCE and an Ag nanoparticle-labelled secondary antibody. After the immunoreaction, the concentration of Ag captured on the SPCE surface was measured by ASV. To achieve this, the immobilised Ag metal nanoparticle was first electrochemically oxidised to form Ag^+ ions by applying by a potential of +1.6 V. The concentration of these Ag^+ was then determined by a differential pulse voltammeter. Utilising this approach, a detection limit of 7.2 pg/mL hCG was obtained with a linear range from 10 to 1000 pg/mL.

13.3.9 Food

The application of SPCEs and biosensors for the determination of a wide range of analytes in food has recently been reviewed (Cock *et al.*, 2009; Ricci *et al.*, 2007a; Tudorache and Bala, 2007; Viswanathan *et al.*, 2009). Romanazzo *et al.* (2009, 2010) have used an electrochemical competitive enzyme-linked immunomagnetic assay based on the use of magnetic beads as solid support for the immunochemical chain at a SPCE as a sensing platform. Their developed sensor was able to determine the total amount of the mycotoxins, HT-2 and T-2. The magnetic beads were first coated by immobilizing a HT2-KLH conjugate toxin, and after a blocking step to avoid non-specific absorption, a monoclonal antibody was then added allowing for competition between the immobilised HT-2 and free HT-2 or T-2 present in the sample. Hence at the end of the competition step, the amount of the monoclonal antibody linked to the immobilised HT-2 at the magnetic beads is inversely proportional to the amount of toxin that was present in the sample solution. A secondary antibody labelled with alkaline phosphatase is then added to bind with the immobilised HT-2. The final measurement step was performed by

© Woodhead Publishing Limited, 2012

dropping an aliquot of magnetic bead suspension onto the surface of a screen-printed working electrode. The magnetic beads are immobilised and concentrated by means of a magnet placed precisely under the SPE. After two minutes of incubation between magnetic beads and a substrate for alkaline phosphatase, the enzymatic product is detected by DPV, giving a voltammetric signal proportional to the original mycotoxins' sample concentration.

Recently, the inhibition of alkaline phosphatase by caffeine has been utilised for its determination in tea, coffee and cola at the Au SPE biosensor (Akyilmaz and Turemis, 2010). By measuring the decrease in conversion of the substrate, *p*-nitrophenol phosphate by alkaline phosphatase, a linear relationship with caffeine concentration was found from 0.1 µM to 10 µM, with a corresponding limit of detection of 8 nM.

Acetaldehyde is commonly found in alcoholic beverages, resulting from oxidation of ethanol by ADHs and from the fermentation of pyruvate by pyruvate decarboxylase. It is usually present in wine at concentrations between 60 µM and 300 µM. Its determination is important in such beverages as it interferes with the antioxidant and antiseptic function of sulphur dioxide. Noguer *et al.* (2004) have utilised a MBRS-modified SPE, modified with a sol-gel matrix containing AILDH and NAD^+ for the determination of acetaldehyde in wine as part of a flow injection system. Acetaldehyde can be determined in beverages using enzymatic oxidation by an NAD^+-dependant ALDH according to the reaction shown in equation (Eq. [13.10]).

$$\text{Acetaldehyde} + NAD^+ + H_2O \xleftrightarrow{\text{ALDH}} \text{acetic acid} + NADH + H^+ \quad [13.10]$$

The NADH formed is stoichiometric with the amount of acetaldehyde present and can be readily amperometically determined via its interaction with MBRS as described in the section describing glucose determination with GDH using an applied potential of −150 mV.

The ability to monitor the fertility of animals is an important parameter in animal husbandry. Recently, Pemberton and Hart (2007) have developed a biosensor for the determination of progesterone in bovine milk. Oestrus onset is indicated by a rapid fall in the concentration of milk progesterone to below 2–5 ng/mL. The biosensor was based on competitive immunoassay either in batch mode (chronoamperometric measurement) or in stop–flow mode in a continuous flow system (amperometric). Utilising the chronoamperometric batch mode, a detection limit of around 5 ng/mL was obtained suitable for monitoring the onset of oestrus, giving a result within 40 minutes. However, this approach requires the use of a blank measurement step to cater for any variations due to electroactive interferents or surface-adsorbed species present in the milk sample. This problem can be overcome by utilising DPV instead of chronoamperometry. The stop–flow amperometric approach has the advantage of requiring no blank subtraction, but requires 60 minutes to complete and lends itself more to off-site rather than on-site analysis.

© Woodhead Publishing Limited, 2012

13.3.10 Aflatoxins

Aflatoxins produced by moulds *Aspergillus flavus* and *Aspergillus parasiticus* are carcinogenic to humans. Aflatoxin has an inhibitory effect on AchE, allowing for its measurement using a choline oxidase amperometric biosensor. Ben Rejeb *et al.* (2009) have utilised a choline oxidase enzyme-modified SPE for the determination of aflatoxin. The residual activity of the enzyme was calculated after application of the sample, hence giving an indirect detection of the aflatoxin that may be present. The AChE activity is highly pH-dependent with best results obtained at pH 7.4. The amperometric method allowed for the detection of low aflatoxin concentrations that cannot be detected by the classical spectrophotometry assay because of the omission of the dilution step commonly used for this latter approach.

13.3.11 Antibiotics

Sulphonamide antibiotics such as sulfamethoxazole (SMX) and sulfapyridine (SP) are widely used and have been employed for the control of diseases such as American foulbrood (*Bacillus larvae*) and European foulbrood (*Streptococcus pluton*) seen in the honey-bee. Consequently, it is necessary to monitor their residues in the honey produced. Centi *et al.* (2010) have utilised a screen-printed eight-electrode array for their determination. Each working electrode was printed with its own screen-printed silver pseudo-reference electrode and graphite counter electrode. An eight-hole methacrylate box was fixed onto the strip, so giving an eight-cell electrochemical array. Each array was then placed in a holding block with eight magnet bars. The assay was based on a competitive scheme, in which sulphonamides (competitors) compete with a fixed concentration of 2-(4-aminobenzensulfonylamino)ethanoic acid–alkaline phosphatase labelled (SA1-(CH2)5-AP), against antibodies immobilised on magnetic beads. Once the affinity reaction occurred, the electrochemical measurement was carried out by DPV to evaluate the extent of the immunochemical reaction. It was found necessary to utilise a sample clean-up step using solid phase extraction, as one of the sulphonamides was found to react with the reducing sugars in honey.

Tsekenis *et al.* (2008) have utilised a labelless immunosensor for the antibiotic ciprofloxacin in milk using AC impedance. Polyaniline was electrodeposited onto the SPE to immobilise a biotinylated antibody for ciprofloxacin using classical avidin–biotin interactions. The antibody-modified electrodes were exposed to solutions of antigen in milk and interrogated using AC impedance. The faradaic component of the impedance of the electrodes was found to increase with the growing concentration of antigen. Control sensors were fabricated using antibodies specific to species not found in milk. Calibration curves were obtained by subtraction of the responses for specific and control antibody-based sensors, so eliminating the effects of non-specific adsorption of antigen. Sensors exposed to ciprofloxacin in milk gave increases in impedance, whereas ciprofloxacin in

© Woodhead Publishing Limited, 2012

phosphate buffer led to decreases, indicating the possibility of developing sensors that can both detect and differentiate between free and chelated antigen. A linear dependence of impedance current with $\log_{10}$ of concentration was obtained between 0.1 and 100 ng/mL ciprofloxacin.

13.4 Conclusions

The screen-printing of electrodes based on thick-film micro-fabrication allows for large-scale mass production of reproducible low-cost electrochemical biosensors. The number of applications utilising SPEs has increased greatly over the past four years. It would now seem that thick-film SPEs are now one of the common electrodes presently used. The biocompatible nature of carbon has been shown to permit easy modification, allowing for the production of a wide range of different biosensors. Whole cells, enzymes, DNA and antibodies have all been reported and successfully employed for the determination of a wide range of samples and analytes. However, glucose is still an important analyte, with a number of reports focused on both new research and new commercial developments for thick-film glucose biosensors.

Techniques such as genetic engineering techniques, such as protein engineering (Campàs *et al.*, 2009) and synthetic biology will become more important in the future, providing improvements in the selectivity, sensitivity and range of the biological recognition element.

Miniaturisation of electrodes and use of nanomaterials and nanotechnology are becoming increasingly more important. There are an increasing number of reports utilising the highly sensitive method of stripping voltammetry for determining the metal nanoparticle labels utilised in immunoassay.

Recently there have been more reports made using more environmentally friendly and biocompatible inks and substrates, such as paper. As SPEs are principally seen as disposable and 'one-shot' devices, it is possible that more interest will develop in these areas.

The majority of the biosensors identified in this review are yet to be commercialised. Several reports have highlighted problems facing the introduction of new biosensors to the market, such as those recently identified by Siontorou and Batzias (2010). Issues such as limited stability of the biosensor biological component have been cited as a concern in their commercial adoption. However, recent reports (Choi, 2005; Piano *et al.*, 2010a) have shown that shelf lives of up to year at 4 °C are obtainable.

13.5 Sources of further information

Brett C. M. A. and Brett A. M. O. (1998) *Electroanalysis*, no. 64, Oxford Chemistry Primers.
Compton R. G. and Banks C. E. (2011) *Understanding Voltammetry*, 2nd edn, Imperial College Press.

© Woodhead Publishing Limited, 2012

Cooper J. and Cass A. E. G. (eds) (2004), *Biosensors. A Practical Approach*, 2nd edn, The Practical Approach Series, Oxford University Press.
Eggins B. R. (2007), *Chemical Sensors and Biosensors* (Analytical Techniques in the Sciences), John Wiley & Sons.
Fisher A. C. (1998), *Electrode Dynamics*, no. 34, Oxford Chemistry Primers.
Hart J. P. (1990) *Electroanalysis of Biologically Important Compounds*, Ellis Horwood, London.
Hobby A. (1997), *Screen Printing for the Industrial User*, DEK Printing Machines Ltd. March, available from Gwent Electronic Material Ltd. (http://www.gwent.org/Gem/index.html). A good guide to the practice and technical aspects of screen-printing.
Kissinger P. T. and Heineman W. R. (1996), *Laboratory Techniques in Electroanalytical Chemistry*, 2nd edn, Marcel Dekker, Inc.
Pletcher D. (1991), *A First Course in Electrode Processes*, The Electrochemical Consultancy.
Wang J. (2006) *Analytical Electrochemistry*, 3rd edn, Wiley-VCH.

13.6 Acknowledgements

I would like to thank all the researchers whose work has been described in this review.

13.7 References

Adams R. N. (1969), *Electrochemistry at Solid Electrodes*, Chapter 5, Dekker, New York.
Akyilmaz E. and Turemis M. (2010), An inhibition type alkaline phosphatase biosensor for amperometric determination of caffeine, *Electrochim Acta*, 55, 5195–5199.
Albanese D., Di Matteo M. and Alessio C. (2010), Screen-printed biosensors for detection of nitrates in drinking water, *in* Piercucci S. and Buzzi G. (eds), *20th European Symposium on Computer Aided Chemical Engineering*, Vol. 28, pp. 283–288.
Amine A. and Mohammadi H. (2007), *Electrochemical Biosensors for Heavy Metal Based on Enzyme Inhibition*, *in* Alegret S. and Merkoçi, A. (eds), *Electrochemical Sensor Analysis*, Vol. 49, Elsevier, Amsterdam, The Netherlands, pp. 299–310.
Amine A., Mohammadi H., Bourais I. and Palleschi G. (2006), Enzyme inhibition-based biosensors for food safety and environmental monitoring, *Biosens Bioelectron*, 21, 1405–1423.
Andreescu S. and Marty J.-L. (2006), Twenty years research in cholinesterase biosensors: from basic research to practical applications, *Biomol Eng*, 23, 1–15.
Anon (2010), *Analytical Review of World Biosensors Market*, June, Frost & Sullivan.
Arduini F., Amine A., Moscone D. and Palleschi G. (2010a), Biosensors based on cholinesterase inhibition for insecticides, nerve agents and aflatoxin B1 detection (review), *Microchim Acta*, 170, 193–214.
Arduini F., Calvo J. Q., Amine A., Palleschi G. and Moscone D. (2010b), Bismuth-modified electrodes for lead detection, *TrAC*, 29, 1295–1304.
Arduini F., Amine A., Moscone D., Ricci F. and Palleschi G. (2007), Fast, sensitive and cost-effective detection of nerve agents in the gas phase using a portable instrument and an electrochemical biosensor, *Anal Bioanal Chem*, 388, 1049–1057.
Arduini F., Ricci F., Tuta C. S., Mosconea D., Amine A. *et al.* (2006), Detection of carbamic and organophosphorous pesticides in water samples using a cholinesterase biosensor based on Prussian Blue-modified screen-printed electrode, *Anal Chim Acta*, 580, 155–162.

© Woodhead Publishing Limited, 2012

Badihi-Mossberg M., Buchner V. and Rishpon J. (2007), Electrochemical Biosensors for Pollutants in the Environment, *Electroanalysis*, 19, 2015–2028.

Ballesta-Claver J., Valencia Mirón M. C. and Capitán-Vallvey L. F. (2009), Disposable electrochemiluminescent biosensor for lactate determination in saliva, *Analyst*, 134, 1423–1432.

Ben Rejeb I., Arduini F., Arvinte A., Amine A., Gargouri M. *et al.* (2009), Development of a bio-electrochemical assay for AFB1 detection in olive oil, *Biosens Bioelectron*, 24, 1962–1968.

Bishop D. K., La Belle J. T., Vossler S. R., Patel D. R. and Cook C. B. (2010a), A Disposable Tear Glucose Biosensor – and concept testing, Part 1: design, *J Diabetes Sci Technol*, 4, 299–306.

Bishop D. K., La Belle J. T., Vossler S. R., Patel D. R. and Cook C. B. (2010b), A disposable tear glucose biosensor – Part 2: system integration and model validation, *J Diabetes Sci Technol*, 4, 307–311.

Bordonaba J. G. and Terry L. A. (2009), Development of a glucose biosensor for rapid assessment of strawberry quality: relationship between biosensor response and fruit composition, *J Agric Food Chem*, 57, 8220–8226.

Bott A. W. (1995), Practical problems in voltammetry 3: reference electrodes for voltammetry, *Curr Separations*, 14, 64–68.

Brainina K. Z., Kozitsina A. N. and Glazyrina Y. A. (2010), Hybrid electrochemical/magnetic assay for *Salmonella typhimurium* detection, *IEEE Sens J*, 10, 1699–1704.

Campàs M., Prieto-Simón B. and Marty J.-L. (2009), A review of the use of genetically engineered enzymes in electrochemical biosensors, *Semin Cell Dev Biol*, 20, 3–9.

Cardosi M. F. and Turner A. P. F. (1991), Mediated electrochemistry. A practical approach to biosensing, *Advances in Biosensors*, 1, 125–169.

Carlo M. D., Pepe A., Sergi M., Mascini M., Tarentini A. *et al.* (2010), Detection of coumaphos in honey using a screening method based on an electrochemical acetylcholinesterase bioassay, *Talanta*, 81, 76–81.

Carrara S., Shumyantseva V. V., Archakov A. I. and Samorí B. (2008), Screen-printed electrodes based on carbon nanotubes and cytochrome P450scc for highly sensitive cholesterol biosensors, *Biosens. Bioelectron*, 24, 148–150.

Cass A. E. G., Davis G., Francis G. D., Hill H. A. O., Aston W. J. *et al.* (1984), Ferrocene-mediated enzyme electrode for amperometric determination of glucose, *Anal Chem*, 56, 667–671.

Centi S., Marrazza G. and Mascini M. (2007), Coupling of Screen-printed Electrodes and Magnetic Beads for Rapid and Sensitive Immunodetection: polychlorinated Biphenyls analysis in environmental samples, *in* Alegret S. and Merkoçi, A. (eds), *Electrochemical Sensor Analysis*, Vol. 49, Elsevier, Amsterdam, The Netherlands pp. 585–602.

Centi S., Rozum B., Laschi S., Palchetti I. and Mascini M. (2006), Disposable electrochemical magnetic beads-based immunosensors for monitoring polychlorinated biphenyl (PCBs) pollutants, *Chem Anal (Warsaw)*, 51, 963–975.

Centi S., Stoica A. I., Laschi S. and Mascini M. (2010), Development of an electrochemical immunoassay based on the use of an eight-electrodes screen-printed array coupled with magnetic beads for the detection of antimicrobial sulfonamides in honey, *Electroanalysis*, 22, 1881–1888.

Chen C.-S., Breslauer D. N., Luna J. I., Grimes A., Chin W.-C. *et al.* (2008), Shrinky-dink microfluidics: 3D polystyrene chips, *Lab Chip*, 8, 622–624.

Chikae M., Idegami K., Nagatani N., Tamiya E. and Takamura Y. (2010), Highly sensitive method for electrochemical detection of silver nanoparticles labels

© Woodhead Publishing Limited, 2012

in metalloimmunoassay with peroxidation/reduction signal enhancement, *Electrochemistry*, 78, 748–753.

Chistiansen T. F. and Jakobsen K. M. (1995), The slow penetration of enzyme-based biosensors into clinical chemistry analysis, *Acta Anaesthesiol Scand*, 39, Sup 104, 31–35.

Choi M. M. F. (2005), Application of a long shelf-life biosensor for the analysis of L-lactate in dairy products and serum samples, *Food Chem*, 92, 575–581.

Clark L. C. and Lyons C. (1962), Electrode systems for continuous monitoring in cardiovascular surgery, *Ann NY Acad Sci*, 102, 29–45.

Cock L. S., Arenas A. M. Z. and Aponte A. A. (2009), Use of enzymatic biosensors as quality indices: a synopsis of present and future trends in the food industry, *Chil J Agr Res*, 69, 270–280.

Compton R. G. and Banks C. E. (2011), *Understanding Voltammetry*, 2nd ed. Imperial College Press, London.

Crew A., Lonsdale D., Byrd N., Pittson R. and Hart J. P. (2011), A screen-printed, amperometric biosensor array incorporated into a novel automated system for the simultaneous determination of organophosphate pesticides, *Biosens Bioelectron*, 26, 2847–2851.

D'Orazio P. (2003), Biosensors for clinical chemistry, *Clin Chim Acta*, 334, 41–69.

Del Carlo M., Di Marcello M., Perugini M., Ponzielli V. and Sergi M. (2008), Electrochemical DNA biosensor for polycyclic aromatic hydrocarbon detection, *Microchim Acta*, 163, 163–169.

Dequaire M., Degrand C. and Limoges B. (2000), An electrochemical metalloimmunoassay based on a colloidal gold label. *Anal Chem*, 72, 5521–5528.

Domínguez-Renedo O., Alonso-Lomillo M. A. and Arcos Martınez M. J. (2007) Recent developments in the field of screen-printed electrodes and their related applications, *Talanta*, 73, 202–219.

Domínguez-Renedo O., Alonso-Lomillo M. A., Ferreira-Goncalves L. and Arcos-Martínez M. J. (2009), Development of urease based amperometric biosensors for the inhibitive determination of Hg (II), *Talanta*, 79, 1306–1310.

Dounin V., Veloso A. J., Schulze H., Bachmann T. T. and Kerman K. (2010), Disposable electrochemical printed gold chips for the analysis of acetylcholinesterase inhibition, *Anal Chim Acta*, 669, 63–67.

Du D., Wang J., Smith J. N., Timchalk C. and Lin Y. (2009), Biomonitoring of organophosphorus agent exposure by reactivation of cholinesterase enzyme based on carbon nanotube-enhanced flow-injection amperometric detection, *Anal Chem*, 81, 9314–9320.

Dungchai W., Chailapakul O. and Henry C. S. (2009), Electrochemical detection for paper-based microfluidics, *Anal Chem*, 81, 5821–5826.

Escamilla-Gomez V., Campuzano S., Pedrero, M. and Pingarron, J. M. (2008), Electrochemical immunosensor designs for the determination of *Staphylococcus aureus* using 3,3-dithiodipropionic acid di(*N*-succinimidyl ester)-modified gold electrodes, *Talanta*, 77, 876–881.

Escosura-Muniz A. D. L. and Merkoci A. (2010), Electrochemical detection of proteins using nanoparticles: applications to diagnostics, *Expert Opin Med Diagn*, 4, 21–37.

Evans A. (1987), *Potentiometry and Ion Selective Electrodes*, Analytical Chemistry by Open Learning, John Wiley & Sons, Chichester.

Ferancová A., Adamovski M., Gründler P., Zima J., Barek J. *et al.* (2007), Interaction of tin(II) and arsenic(III) with DNA at the nanostructure film modified electrodes, *Bioelectrochemistry*, 71, 33–37.

© Woodhead Publishing Limited, 2012

Frew J. E. and Hill H. A. O. (1987), Electrochemical biosensors, *Anal Chem*, 59, 933A–944A.

Galus Z. (1976), *Fundamentals of Electrochemical Analysis*, John Wiley & Sons, NY.

Gan N., Yang X., Xie D., Wu Y. and Wen W. (2010), A disposable organophosphorus pesticides enzyme biosensor based on magnetic composite nano-particles modified screen-printed carbon electrode, *Sensors*, 10, 625–638.

Gessei T., Sato H., Kazawa E., Kudo H., Saito H. *et al*. (2009), Bio-sniffers for ethanol and acetaldehyde using carbon and Ag/AgCl coated electrodes, *Microchim Acta*, 165, 179–186.

Gilardi G. and Fantuzzi A. (2001), Manipulating redox systems: application to nanotechnology, *Trends Biotechnol*, 19, 468–476.

Gilbert L., Jenkins A. T. A., Browning S. and Hart J. P. (2009), Development of an amperometric assay for phosphate ions in urine based on a chemically modified screen-printed carbon electrode, *Anal Biochem*, 393, 242–247.

Gilbert L., Browning S., Jenkins A. T. A. and Hart J. P. (2010), Studies towards an amperometric phosphate ion biosensor for urine and water analysis, *Microchim Acta*, 170, 331–336.

Gonzalez-Macia L., Morrin A., Smyth M. and Killard A. (2010), Advanced printing and deposition methodologies for the fabrication of biosensors and biodevices, *Analyst*, 135, 845–867.

Gonzalo-Ruiz J., Alonso-Lomillo M. A. and Munoz F. J. (2007), Screen-printed biosensors for glucose determination in grape juice, *Biosens Bioelectron*, 22, 1517–1521.

Gregg B. A. and Heller A. (1990), Cross-linked redox gels containing glucose oxidase for amperometric biosensor applications, *Anal Chem*, 62, 258–263.

Grieshaber D., MacKenzie R., Vörös J. and Reimhult E. (2008), Electrochemical biosensors – sensor principles and architectures, *Sensors*, 8, 1400–1458.

Grimes A., Breslauer D. N., Long M., Pegan J., Lee L. P. *et al.* (2008), Shrinky-dink microfluidics: rapid generation of deep and rounded patterns, *Lab Chip*, 8, 170–172.

Guascito M. R., Malitesta C., Mazzotta E. and Turco A. (2009), Screen-printed glucose oxidase-based biosensor for inhibitive detection of heavy metal ions in a flow injection system, *Sens Lett*, 7, 153–159.

Guilbault G. G. (1968), Use of enzymes in analytical chemistry, *Anal Chem*, 40, 459R–471R.

Hart J. P., Crew A., Crouch E., Honeychurch K. C. and Pemberton R. M. (2004), Some recent designs and developments of screen-printed carbon electrochemical sensors/biosensors for biomedical, environmental, and industrial analyses, *Anal Lett*, 37, 789–830.

Hart J. P., Crew A., Crouch E., Honeychurch K. C. and Pemberton R. M. (2007), Screen-printed electrochemical (bio)sensors in biomedical, environmental and industrial applications, *in* Alegret S. and Merkoçi, A. (eds), *Electrochemical Sensor Analysis*, vol. 49, Elsevier, Amsterdam, The Netherlands, pp. 497–557.

Heller A. and Feldman B. (2010), Electrochemistry in Diabetes Management, *Acc Chem Res*, 43, 963–973.

Hildebrandt A., Ribas J., Bragos R., Marty J.-L., Tresanchez M. *et al*. (2008), Development of a portable biosensor for screening neurotoxic agents in water samples, *Talanta*, 75, 1208–1213.

Hilditch P. M. and Green M. (1991), Disposable electrochemical biosensors, *Analyst*, 116, 1217–1220.

Honeychurch K. C. and Hart J. P. (2003), Screen-printed electrochemical sensors for monitoring metal pollutants, *TrAC*, 22, 456–469.

© Woodhead Publishing Limited, 2012

Hu J. (2009), The evolution of commercialized glucose sensors in China, *Biosens Bioelectron*, 24, 1083–1089.

Iwamoto M., Tokonami S., Shiigi H. and Nagaoka T. (2009), Activity enhancement of a screen-printed carbon electrode by modification with gold nanoparticles for glucose determination, *Res Chem Intermed*, 35, 919–930.

Joshi K. A., Prouza M., Kum M., Wang J., Tang J. *et al.* (2006), V-type nerve agent detection using a carbon nanotube-based amperometric enzyme electrode, *Anal Chem*, 78, 331–336.

Kadara R. O., Jenkinson N. and Banks C. E. (2009), Characterisation of commercially available electrochemical sensing platforms, *Sensor Actuat B-Chem*, 138, 556–562.

Kalcher K., Svancara I., Buzuk M., Vytras K. and Walcarius A. (2009), Electrochemical sensors and biosensors based on heterogeneous carbon materials, *Monatsh Chem*, 140, 861–889.

Keasling J. D. (2008), Synthetic biology for synthetic chemistry, *ACS Chem Biol*, 3, 64–76.

Kissinger P. T. and Heineman W. R. (1983), Cyclic voltammetry, *J Chem Edu*, 60, 702–706.

Kissinger P. T. and Heineman W. R. (1984), *Techniques in Electroanalytical Chemistry*, Dekker, New York.

Kitamura T., Kaimori S., Harada A., Ishikawa T., Fujimura T. *et al.* (2006), Development of blood glucose monitoring sensor strip that uses small blood sample, *SEI Technical Review*, 63, 19–22.

Kokkinos C. and Economou A. (2008), Stripping at bismuth-based electrodes, *Curr Anal Chem*, 4, 183–190.

Kotzian P., Brazdilová P., Rezková S., Kalcher K. and Vytras K. (2006), Amperometric glucose biosensor based on rhodium dioxide-modified carbon ink, *Electroanalysis*, 18, 1499–1504.

Lee S.-H., Fang H.-Y. and Chen W.-C. (2006), Amperometric glucose biosensor based on screen-printed carbon electrodes mediated with hexacyanoferrate–chitosan oligomers mixture, *Sensor Actuat B-Chem*, 117, 236–243.

Lee T. M.-H. (2008), Over-the-counter biosensors: past, present, and future, *Sensors*, 8, 5535–5559.

Lei Y., Chen W. and Mulchandani A. (2006), Microbial biosensors, *Anal Chim Acta*, 568, 200–210.

Lin Y.-Y., Liu G., Wai C. M. and Lin Y. (2008a), Bioelectrochemical immunoassay of polychlorinated biphenyl, *Anal Chim Acta*, 612, 23–28.

Lin Y.-Y., Wang J., Liu G., Wu H., Wai C. M. and Lin Y. (2008b), A nanoparticle label/immunochromatographic electrochemical biosensor for rapid and sensitive detection of prostate-specific antigen. *Biosens Bioelectron*, 23, 1659–1665.

Liu G., Lin Y.-Y., Wang J., Wu H., Wai C. M. *et al.* (2007), Disposable electrochemical immunosensor diagnosis device based on nanoparticle probe and immunochromatographic strip, *Anal Chem*, 79, 7644–7653.

Liu G., Wang J., Barry R., Petersen C., Timchalk C. *et al.* (2008), Nanoparticle-based electrochemical immunosensor for the detection of phosphorylated acetylcholinesterase: an exposure biomarker of organophosphate pesticides and nerve agents, *Chem Eur J*, 14, 9951–9959.

Luo P., Liu Y., Xie G., Xiong X., Deng S. *et al.* (2008), Determination of serum alcohol using a disposable biosensor, *Forensic Sci Inter*, 179, 192–198.

© Woodhead Publishing Limited, 2012

Luong J. H. T., Male K. B. and Glennon J. D. (2008), Biosensor technology: technology push versus market pull, *Biotechnol Adv*, 26, 492–500.

Mabbott G. A. (1983), An introduction to cyclic voltammetry, *J Chem Edu*, 60, 697–701.

Mahbubur Rahman M., Saleh Ahammad A. J., Jin J.-H., Ahn S. J. and Lee J.-J. (2010), A comprehensive review of glucose biosensors based on metal-oxides, *Sensors*, 10, 4855–4886.

Mahmoud K. A. and Luong J. H. T. (2010), A sensitive electrochemical assay for early detection of HIV-1 protease using ferrocene-peptide conjugate/Au nanoparticle/single walled carbon nanotube modified electrode, *Anal Lett*, 43, 1680–1687.

Mahosenaho M., Caprio F., Micheli L., Sesay A. M., Palleschi G. *et al.* (2010), A disposable biosensor for the determination of alpha-amylase in human saliva, *Microchim Acta*, 170, 243–249.

Mandon C. A., Heyries K. A., Blum L. J. and Marquette C. A. (2010), Polyshrink™ based microfluidic chips and protein microarrays, *Biosens Bioelectron*, 26, 1218–1224.

Martínez-Olmos A., Ballesta-Claver J., Palma A. J., Valencia-Mirón M. del C. and Capitán-Vallvey L. F. (2009), A portable luminometer with a disposable electrochemiluminescent biosensor for lactate determination, *Sensors*, 9, 7694–7710.

Mascini M. and Guilbault G. G. (1986), Clinical uses of enzyme electrode probes, *Biosensors*, 2, 147–172.

Matthews D., Holman R., Bown E., Streemson J., Watson A. *et al.* (1987), Pen sized digital 30-second blood glucose meter, *Lancet*, 2, 778.

Miao Y., He N. and Zhu J.-J. (2010), History and new developments of assays for cholinesterase activity and inhibition, *Chem Rev*, 110, 5216–5234.

Newman J. D. and Turner A. P. F. (2005), Home blood glucose biosensors: a commercial perspective, *Biosens Bioelectron*, 20, 2435–2453.

Nie Z., Nijhuis C. A., Gong J., Chen X., Kumachev A. *et al.* (2010), Electrochemical sensing in paper-based microfluidic devices, *Lab Chip*, 10, 477–483.

Nikolaus N. and Strehlitz B. (2008), Amperometric lactate biosensors and their application in (sports) medicine, for life quality and wellbeing, *Microchim Acta*, 160, 15–55.

Noguer T., Szydlowska D., Marty J.-L. and Trojanowicz M. (2004), Sol-gel immobilization of aldehyde dehydrogenase and NAD^+ on screen-printed electrodes for designing of amperometric acetaldehyde biosensor, *Polish J Chem*, 78, 1679–1689.

Ohara T. J., Rajagopalan R. and Heller A. (1993), Glucose electrodes based on cross-linked bis(2,2′-bipyridine)chloroosmium(+/2+) complexed poly(1-vinylimidazole) films, *Anal Chem*, 65, 3512.

Pemberton R. M. and Hart J. P. (2007), Preparation of electrochemical screen-printed immunosensors for progesterone and their application in milk analysis, *in* Alegret S. and Merkoçi A. (eds), *Electrochemical Sensor Analysis*, vol. 49, Procedure 35, Elsevier, Amsterdam, The Netherlands, pp. 1207–1212.

Pemberton R. M., Pittson R., Biddle N. and Hart J. P. (2009a), Fabrication of microband glucose biosensors using a screen-printing water-based carbon ink and their application in serum analysis, *Biosens Bioelectron*, 24, 1246–1252.

Pemberton R. M., Xu J., Pittson R., Biddle N., Drago G. A. *et al.* (2009b), Application of screen-printed microband biosensors to end-point measurements of glucose and cell numbers in HepG2 cell culture, *Anal Biochem*, 385, 334–341.

Pemberton R. M., Xu J., Pittson R., Drago G. A., Griffiths J. *et al.* (2011), A screen-printed microband glucose biosensor system for real-time monitoring of toxicity in cell culture, *Biosens Bioelectron*, 26, 2448–2453.

© Woodhead Publishing Limited, 2012

Piano M., Serban S., Biddle N., Pittson R., Drago G. A. *et al.* (2010a), A flow injection system, comprising a biosensor based on a screen-printed carbon electrode containing Meldola's Blue-Reinecke salt coated with glucose dehydrogenase, for the measurement of glucose, *Anal Biochem*, 396, 269–274.

Piano M., Serban S., Pittson R., Drago G. A. and Hart J. P. (2010b), Amperometric lactate biosensor for flow injection analysis based on a screen-printed carbon electrode containing Meldola's Blue-Reinecke salt, coated with lactate dehydrogenase and NAD^+, *Talanta*, 82, 34–37.

Pletcher D. (1991), *A First Course in Electrode Processes*, The Electrochemical Consultancy, Royal Society of Chemistry, London.

Pohanka M. and Skládal P. (2008), Electrochemical biosensors–principles and applications, *J Appl Biomed*, 6, 57–64.

Prasad K. S., Arun A. B., Rekha P. D., Young C. C., Chang J. L. *et al.* (2009), Microbial sensor based on direct electron transfer at *Shewanella* Sp. Drop-coated screen-printed carbon electrodes, *Electroanalysis*, 21, 1646–1650.

Prieto-Simón B., Fàbregas E. and Hart A. (2007), Evaluation of different strategies for the development of amperometric biosensors for L-Lactate, *Biosens Bioelectron*, 22, 2663–2668.

Privett B. J., Shin J. H. and Schoenfisch M. H. (2010), Electrochemical sensors, *Anal Chem*, 82, 4723–4741.

Quan D., Shim J. H., Kim J. D., Park H. S., Cha G. S. *et al.* (2005), Electrochemical determination of nitrate with nitrate reductase-immobilized electrodes under ambient air, *Anal Chem*, 77, 4467–4473.

Raodi A., Compagnone D., Valcarcel M. A., Placidi P. and Materazzi S. (2008), Detection of NADH via electrocatalytic oxidation at single-walled carbon nanotubes modified with Variamine blue, *Electrochim Acta*, 53, 2161–2169.

Ravera M., Bagni G., Mascini M. and Osella D. (2007), DNA-metallodrugs interactions signaled by electrochemical biosensors: an overview, *Bioinorg Chem Appl*, 2007, Article ID 91078.

Rawson F. J., Jackson S. K. and Hart J. P. (2010), Voltammetric behaviour of DNA and its derivatives using screen-printed carbon electrodes and its possible application in genotoxicity screening, *Anal Lett*, 43, 1790–1800.

Rawson F. J., Purcell W. M., Xu J., Pemberton R. M., Fielden P. R. *et al.* (2009), A microband lactate biosensor fabricated using a water-based screen-printed carbon ink, *Talanta*, 77, 1149–1154.

Reyes Plata M., Contento A. M. and Ríos A. (2010), State-of-the-art of (bio)chemical sensor developments in analytical Spanish groups, *Sensors*, 10, 2511–2576.

Ricci F., Volpe G., Micheli L. and Palleschi G. (2007a), A review on novel developments and applications of immunosensors in food analysis, *Anal Chim Acta*, 605, 111–129.

Ricci F., Amine A., Moscone D. and Palleschi G. (2007b), A probe for NADH and H_2O_2 at low applied potential for oxidase and dehydrogenase based biosensor application, *Biosens Bioelectron*, 22, 854–862.

Roepcke C. B. S., Muench S. B., Schulze H., Bachmann T., Schmid R. D. *et al.* (2010), Analysis of phosphorothionate pesticides using a chloroperoxidase pretreatment and acetylcholinesterase biosensor detection, *J Agric Food Chem*, 58, 8748–8756.

Romanazzo D., Ricci F., Vesco S., Piermarini S., Volpe G. *et al.* (2009), ELIME (enzyme linked immuno magnetic electrochemical) method for mycotoxin detection, *J Vis Exp*, 32, e1588, doi: 10.3791/1588.

© Woodhead Publishing Limited, 2012

Romanazzo D., Ricci F., Volpe G., Elliott C. T., Vesco S. *et al.* (2010), Development of a recombinant Fab-fragment based electrochemical immunosensor for deoxynivalenol detection in food samples, *Biosens Bioelectron*, 25, 2615–2621.

Ronkainen N. J., Halsall H. B. and Heineman W. R. (2010), Electrochemical biosensors, *Chem Soc Rev*, 39, 1747–1763.

Šafařık I. and Šafařková M. (1999), Use of magnetic techniques for the isolation of cells, *J Chromatograph B*, 722, 33–53.

Šafařık I. and Šafařková M. (2004), Magnetic techniques for the isolation and purification of proteins and peptides, *BioMagn Res Technol*, 2, 7.

Saiyed Z. M., Telang S. D. and Ramchand C. N. (2003), Application of magnetic techniques in the field of drug discovery and biomedicine, *BioMagn Res Technol*, 1(1), 2.

Sajjadi S., Ghourchiana H. and Tavakoli H. (2009), Choline oxidase as a selective recognition element for determination of paraoxon, *Biosens Bioelectron*, 24, 2509–2514.

Salam F. and Tothill I. E. (2009), Detection of *Salmonella typhimurium* using an electrochemical immunosensor, *Biosens Bioelectron*, 24, 2630–2636.

Sanllorente-Méndez S., Domínguez-Renedo O. and Arcos-Martínez M. J. (2010), Immobilization of acetylcholinesterase on screen-printed electrodes. Application to the determination of arsenic(III), *Sensors*, 10, 2119–2128.

Santiago L. M., Bejarano-Nosas D., Lozano-Sanchez P. and Katakis I. (2010), Screen-printed microsystems for the ultrasensitive electrochemical detection of alkaline phosphatase, *Analyst*, 135, 1276–1281.

Sarkar P., Banerjee S., Bhattacharyay D. and Turner A. P. F. (2010), Electrochemical sensing systems for arsenate estimation by oxidation of L-cysteine, *Ecotox Environ Safe*, 73, 1495–1501.

Sato N. and Okuma H. (2006), Amperometric simultaneous sensing system for D-Glucose and L-Lactate based on enzyme-modified bilayer electrodes, *Anal Chim Acta*, 565, 250–254.

Schlapfer P., Mindt W. and Racine P. (1974), Electrochemical measurement of glucose using various electron acceptors, *Clin Chim Acta*, 57, 283–289.

Scognamiglio V., Pezzotti G., Pezzotti I., Cano J., Buonasera K. *et al.* (2010), Biosensors for effective environmental and agrifood protection and commercialization: from research to market, *Microchim Acta*, 170, 215–225.

Shabani A., Zourob M., Allain B., Marquette C. A., Lawrence M. F. *et al.* (2008), Bacteriophage-modified microarrays for the direct impedimetric detection of bacteria, *Anal Chem*, 80, 9475–9482.

Shen J. and Liu C.-C. (2007), Development of a screen-printed cholesterol biosensor: comparing the performance of gold and platinum as the working electrode material and fabrication using a self-assembly approach, *Sensor Actuat B-Chem*, 120, 417–425.

Shih W.-C., Yang M.-C. and Lin M. S. (2009), Development of disposable lipid biosensor for the determination of total cholesterol, *Biosens Bioelectron*, 24, 1679–1684.

Shinwari M. W., Zhitomirsky D., Deen I. A., Selvaganapathy P. R., Deen M. J. *et al.* (2010), Microfabricated reference electrodes and their biosensing applications, *Sensors*, 10, 1679–1715.

Shitanda I., Takamatsu S., Watanabe K. and Itagaki M. (2009), Amperometric screen-printed algal biosensor with flow injection analysis system for detection of environmental toxic compounds, *Electrochim Acta*, 54, 4933–4936.

Shumyantseva V. V., Carrara S., Bavastrello V., Riley J. D., Bulko T. V. *et al.* (2005), Direct electron transfer between cytochrome P450scc and gold nanoparticles on screen-printed rhodium–graphite electrodes, *Biosens Bioelectron*, 21, 217–222.

© Woodhead Publishing Limited, 2012

Siontorou C. G. and Batzias F. A. (2010), Innovation in biotechnology: moving from academic research to product development – the case of biosensors, *Crit Rev Biotechnol*, 30, 79–98.

Sokolov A. N., Roberts M. E. and Bao Z. (2009), Fabrication of low-cost electronic biosensors, *Mater Today*, 12, 12–20.

Sollier K., Mandon C. A., Heyries K. A., Blum L. J. and Marquette C. A. (2009), 'Print-n-Shrink' technology for the rapid production of microfluidic chips and protein microarrays, *Lab Chip*, 9, 3489–3494.

Stozhko N. Y., Malakhova N. A., Fyodorov M. V. and Brainina K. Z. (2008), Modified carbon-containing electrodes in stripping voltammetry of metals. Part II. Composite and microelectrodes, *J Solid State Electrochem*, 12, 1219–1230.

Sun T.-P., Shieh H.-L., Ching C. T.-S., Yao Y.-D., Huang S.-H. *et al.* (2010), Carbon nanotube composites for glucose biosensor incorporated with reverse iontophoresis function for noninvasive glucose monitoring, *Int J Nanomed*, 5, 343–349.

Svancara I., Prior C., Hocevar S. B. and Wang J. (2010), A decade with bismuth-based electrodes in electroanalysis, *Electroanalysis*, 22, 1405–1420.

Théavenot D. R., Toth K., Durst R. A. and Wilson G. S. (1999), Electrochemical biosensors: recommended definitions and classification, *Pure Appl Chem*, 71, 2333–2348.

Tibuzzi A., Pezzotti G., Lavecchia T., Rea G. and Giardi M. T. (2008), A portable light-excitation bio-amperometric for electrogenic biomaterials to support the technical development of most biosensors, *Sensors and Transducers Journal*, 88, 9–20.

Tsekenis G., Garifallou G.-Z., Davis F., Millner P. A., Pinacho D. G. *et al.* (2008), Detection of fluoroquinolone antibiotics in milk via a labeless immunoassay based upon an alternating current impedance protocol, *Anal Chem*, 80, 9233–9239.

Tudorache M. and Bala C. (2007), Biosensors based on screen-printing technology, and their applications in environmental and food analysis, *Anal Bioanal Chem*, 388, 565–578.

Usiu B. and Ozkan S. A. (2007), Electroanalytical application of carbon based electrodes to the pharmaceuticals, *Anal Lett*, 40, 817–853.

Vaddiraju S., Tomazos I., Burgess D. J., Jain F. C. and Papadimitrakopoulos F. (2010), Emerging synergy between nanotechnology and implantable biosensors: a review, *Biosens Bioelectron*, 25, 1553–1565.

Vastarella W., Della Seta L., Masci A., Maly J., De Leo M. *et al.* (2007), Biosensors based on gold nanoelectrode ensembles and screen-printed electrodes, *Intern J Environ Anal Chem*, 87, 701–714.

Viswanathan S., Radecka H. and Radecki J. (2009), Electrochemical biosensors for food analysis, *Monatsh Chem*, 140, 891–899.

Vydra F., Stulik K. and Julakova E. (1976), *Electrochemical Stripping Analysis*, Ellis Horwood, Chichester.

Waibel M., Schulze H., Huber N. and Bachmann T. T. (2006), Screen-printed bienzymatic sensor based on sol–gel immobilized *Nippostrongylus brasiliensis* acetylcholinesterase and a cytochrome P450 BM-3 (CYP102-A1) mutant, *Biosens Bioelectron*, 21, 1132–1140.

Wanekaya A. K., Chen W. and Mulchandani A. (2008), Recent biosensing developments in environmental security, *J Environ Monit*, 10, 703–712.

Wang J. (1985), *Stripping Analysis: Principles, Instrumentation and Applications*, VCH, Weinheim.

Wang J. (2001), Glucose biosensors: 40 years of advances and challenges, *Electroanalysis*, 13, 983–988.

Wang J. (2006), *Analytical Electrochemistry*, 3rd edn, Wiley-VCH, Hoboken, NJ.

© Woodhead Publishing Limited, 2012

Wang J. (2008), Electrochemical glucose biosensors, *Chem Rev*, 108, 814–825.
Wang H., Wang J., Timchalk C. and Lin Y. (2008a), Magnetic electrochemical immunoassays with quantum dot labels for detection of phosphorylated acetylcholinesterase in plasma, *Anal Chem*, 80, 8477–8484.
Wang J., Timchalk C. and Lin Y. (2008b), Carbon nanotube-based electrochemical sensor for assay of salivary cholinesterase enzyme activity: an exposure biomarker of organophosphate pesticides and nerve agents, *Environ Sci Technol*, 42, 2688–2693.
Wang Z., Zhu Q., Kiely J. and Luxton R., (2009), Hilbert Huang transform impedance measurement data for cellular toxicity monitoring, *Proceedings of the 2009 IEEE International Conference on Networking, Sensing and Control*, Okayama, Japan, March 26–29, pp. 767–772.
World Health Organisation (2008), The top ten causes of death, Fact sheet No 310, November 2008, World Health Organisation.
Wring S. A., Hart J. P. and Birch B. J. (1992), Development of an amperometric assay for the determination of reduced glutathione, using glutathione peroxidase and screen-printed carbon electrodes chemically modified with cobalt phthalocyanine, *Electroanalysis*, 4, 299–309.
Wu H.-Z., Lee Y.-C., Lin T.-K., Shih H.-C., Chang F.-L. *et al.* (2009), Development of an amperometric micro-biodetector for pesticide monitoring and detection, *J Taiwan Inst Chem E*, 40, 113–122.
Xie X., Stueben D. and Berner Z. (2005), The application of microelectrodes for the determination of trace metal in water, *Anal Lett*, 38, 2281–2300.
Yadav R., Dwivedi S., Kumar S. and Chaudhury A. (2010), Trends and perspectives of biosensors for food and environmental virology, *Food Environ Virol*, 2, 53–63.
Yang T.-H., Hung C.-L., Ke J.-H. and Zen J.-M. (2008), An electrochemically preanodized screen-printed carbon electrode for achieving direct electron transfer to glucose oxidase, *Electrochem Comm*, 10, 1094–1097.
Yoo E.-H. and Lee S.-Y. (2010), Glucose biosensors: an overview of use in clinical practice, *Sensors*, 10, 4558–4576.
Zagal J. H., Griveau S., Silva J. F., Nyokong T. and Bedioui F. (2010), Metallophthalocyanine-based molecular materials as catalysts for electrochemical reactions, *Coord Chem Rev*, 254, 2755–2791.
Zhou J.-L., Nie P.-P., Zheng H.-T. and Zhang J.-M. (2009), Progress of electrochemical biosensors based on nicotinamide adenine dinucleotide (phosphate)-dependent, *Chin J Anal Chem*, 37, 617–623.
Zuo S., Teng Y., Yuan H. and Lan M. (2008), Development of novel silver nanoparticles-enhanced screen-printed amperometric glucose biosensor, *Anal Lett*, 41, 1158–1172.

© Woodhead Publishing Limited, 2012

14

Printed actuators

R. A. DOREY and G. J. T. LEIGHTON,
Cranfield University, UK

Abstract: An actuator can be defined as a mechanical device that creates a physical movement within a system. While this definition can encompass many different devices, the focus of this chapter is on printed films that are able to impart an actuation action by virtue of being composed of an active material (piezoelectric, magnetostrictive and shape memory alloy) that deforms mechanically when subjected to an external stimulus. For film-based actuators, actuation is most commonly achieved by coupling the active material with an inactive support structure that induces a bending moment when the active material is made to contract or expand parallel to the film plane. The approaches used to integrate thick active films with a variety of substrates are examined, along with the limitations and microstructural effects that arise as a consequence of co-processing materials.

Key words: piezoelectric, magnetostrictive, shape memory alloy, co-processing, thick-film, patterning, microstructure.

14.1 Introduction

An actuator can be defined as a mechanical device that creates a physical movement within a system. This definition can encompass many different devices, including hydraulic, pneumatic, magnetic, electrostatic actuators, as well as electric motors, each making use of different operating principles. The focus of this chapter, and indeed this book, is on printed films that are able to impart an actuation action by virtue of being composed of an active material that deforms mechanically when subjected to an external impulse. Examples of active materials that have been used in actuator systems include piezoelectric, magnetostrictive (MS) and shape memory alloy (SMA) materials.

14.2 Films as actuators

When the simplified case of a freestanding volume of active material is considered, it is possible to envision three fundamental modes of actuation (Fig. 14.1). The first two are simple cases of changes in thickness and width (or length) of the material. Due to the Poisson's ratio effect associated with materials, these two modes actually occur simultaneously. i.e. as the material gets thicker it also gets narrower. The third mode of operation involves the relative movement of one face with respect to the other in a shearing type of action. When a film is considered, the thickness is considerably reduced (by definition) resulting in a large reduction in the magnitude of the thickness and shear deformations.

© Woodhead Publishing Limited, 2012

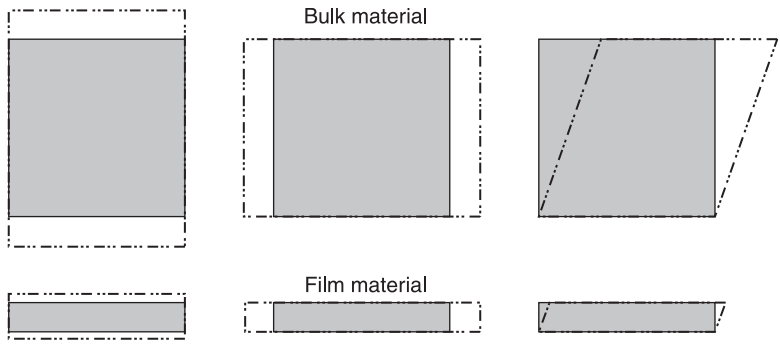

14.1 Examples of actuation mechanisms of bulk and film active materials.

Now also consider the fact that a film, due to the limitations in mechanical strength, will not exist in isolation – it will be attached to a substrate, which will itself have an effect on the way in which the film responds to stimuli. In many cases there may be more than one other material system present. For instance, electrically activated systems will require support materials as well as electrode materials to be combined with the active film. When a film is combined with another material (i.e. a substrate), two effects take place due to the constraining effects of the non-active material. Firstly, the substrate will restrict the ability of the film to deform in the directions parallel to the substrate surface and, because the thickness and width deformations are related through the Poisson's ratio of the film, the movement in the direction perpendicular to the substrate surface will also be reduced. Secondly, the presence of the non-deforming substrate will induce a bending moment in the film/substrate structure causing it to deform out-of-plane. This bending concept is the basis of a great many film actuators and can be found in cantilever, bridge and diaphragm actuators. The precise optimum ratio of the film and substrate dimensions will depend strongly on the material properties of the film and substrate materials, as well as the type of actuator. As a rough guide, the support material should be between one and two times as thick as the active film. Much less substrate material, and some of the active film, will be on the opposite side of the neutral axis and actively oppose motion. Conversely, too much substrate material and the substrate will resist deformation of the beam.

These thickness and bending modes are the basis of a multitude of microscale actuator devices. Bending mode devices are represented by low-frequency (kHz–MHz) ultrasound, actuators based on cantilevers, bridges and diaphragms, and electrical transformers. Thickness mode devices are represented by high frequency (MHz) ultrasound and surface acoustic wave type devices. In both cases, the operation of these devices is greatly influenced by the microstructure of the films. The microstructure of the films is, in turn, influenced by the processing conditions which, in turn, are dictated by the limitations of the materials used within the actuator.

© Woodhead Publishing Limited, 2012

14.3 Actuation mechanisms

14.3.1 Piezoelectricity

Piezoelectric materials are capable of exhibiting all three of the actuation mechanisms (longitudinal, transverse and shear) outlined at the start of this chapter. The parameters that describe these properties are related to the poling direction (direction 3) and the notation of the axis (British Standards Institution, 2002). For longitudinal and transverse actuation, the material is poled in the same direction as the applied electric field used to drive the actuator. For shear actuation, the poling direction is at 90° to the applied field. Longitudinal actuation is described by the parameter d_{33}, which indicates that the applied field, represented by the first subscript, is applied in the direction of poling (3) and that the measured displacement, represented by the second subscript, is in the same direction (3), as depicted in Fig. 14.2. Transverse actuation is described by the parameter d_{31} which indicates the field is applied in the direction of poling (3) but the resultant displacement is at 90° to the applied field (1). Shear actuation in piezoelectric films is rare due to the difficulties of poling the film and applying electrodes at 90° to the poling direction. Shear is described by the parameter d_{15}: the first subscript indicates that the applied field is at 90° to the poling direction (3), and the direction of motion, indicated by the second subscript, resulting from the relative shear motion of the two electroded surfaces is around the (2) direction. For piezoelectric ceramics, the three parameters shown are the only constants that are independent due to crystal symmetry. For further explanation of crystal symmetry, the authors recommend the book by Nye (1957).

Piezoelectric materials are an excellent choice for micro-sized actuators due to their excellent operating properties, which scale very well (Chang and Cohen, 1999), and the simplicity of design and use of the materials. One of the benefits of piezoelectric materials is that they generate high levels of force, making them ideal for actuation purposes. The disadvantage is that this high level of force is produced with a small strain, typically limited to 0.1%. In order to make use of this small strain to generate practical displacements, a mechanical amplifier needs

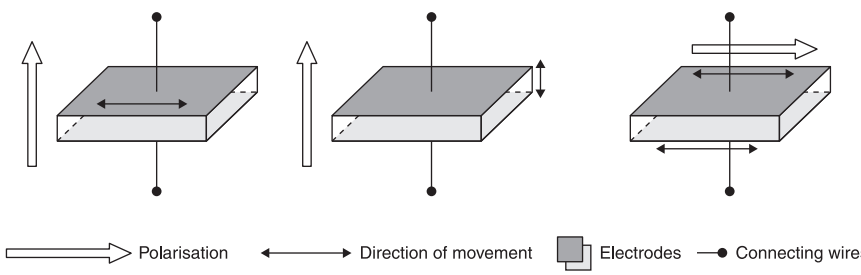

14.2 Schematic representation of transverse, longitudinal and shear actuation of piezoelectric materials.

© Woodhead Publishing Limited, 2012

to be used. The most straightforward mechanical amplifier is a simple cantilever but other innovative physical designs of actuator structure can also be used. At the heart of a mechanical amplifier is the principle that a high force/small strain can be converted to a low force/high strain. A classic bimetallic strip is a common example of this phenomenon, where the small differences in the thermal expansion of two different metals in intimate contact result in a significant strain as the strip bends. Individually, each material would exhibit microstrain but when placed in intimate contact along their length – constraining the touching faces to have the same length – the resultant beam will bend significantly when subjected to temperature changes. Any two materials connected in such a way will exhibit this effect, and it can be used to create printed film actuators that are controlled by changes in temperature.

In creating a piezoelectric bending mode actuator there are two design possibilities to stimulate such bending motion. The piezoelectric material can either be deposited onto an inactive material to create a unimorph structure (Fig. 14.3(a)) or two piezoelectric elements can be combined to create a bimorph structure (Fig. 14.3(b)). The unimorph structure is the most commonly utilised design in film actuators owing to the relative simplicity of fabrication (it is significantly easier to print a film on a substrate than it is to create a free-standing structure consisting of two printed films) and because the inactive material provides the necessary mechanical strength and toughness to prevent the device from failing. A bimorph can also be created by printing on both sides of an electrically conducting material that then acts as the central electrode, although this is not without difficulty in ensuring accurate registration of the two printed films.

In the unimorph design the film is constrained by its connection to the passive layer. On actuation, the strain developed by the piezoelectric film is opposed by the passive material, resulting in the generation of internal stresses in the system, which causes the structure as a whole to bend. Common materials for the passive layer are silicon, thin film oxides such as SiO_2 and SiN_x, metals and ceramics such as alumina. Much work has been undertaken examining the first two groups due

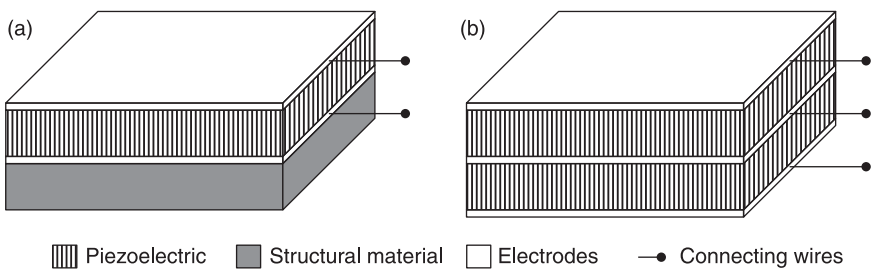

14.3 (a) Schematic representation of a unimorph actuator and (b) a bimorph actuator.

© Woodhead Publishing Limited, 2012

to the maturity of traditional silicon processing techniques used in the processing of micro electromechanical system (MEMS) devices (Madou, 2002). The alumina substrate cantilever is often favoured in screen-printing applications due to the ability to withstand higher processing temperatures and relative inertness of alumina with respect to other materials. A bimorph design can operate with no extraneous structural layers as it consists of two layers of the piezoelectric material sandwiched between conductive electrodes to define the structure. The layers can be operated in series or parallel (determined by the direction of poling in the constituent films and the connections to the electrodes). To generate a bending moment in such a structure, the layers that make up the device are operated in opposition to each other such that one layer expands while the other contracts. In the case of the serial-connected bimorph shown in Fig. 14.4(a), the poling directions within each of the films are in opposition when a voltage is applied across the structure as shown; one layer will expand while the other layer will contract, causing a bending displacement. If the poling in the films were in the same direction when a voltage was applied, a d_{31} expansion of both layers would be seen but no out-of-plane motion would be achieved. In a bimorph beam with a parallel connection, the poling direction of the constituent layers is the same, but the electric field is applied in opposite directions via a common connection to the two outer electrodes and a connection to the centre electrode (Fig. 14.4(b)). This ensures that the opposite strain effect is generated in each layer despite the poling directions being the same.

It should be noted that the terms 'unimorph' and 'bimorph' relate to the active material within the structure and not the overall structure. Both approaches consist of two main layers of material. However, it is common in the literature that the term 'bimorph' is used for both forms of device.

The cantilever, bridge and diaphragm type designs all make use of the lateral strain caused by the application of an electric field in the film thickness direction,

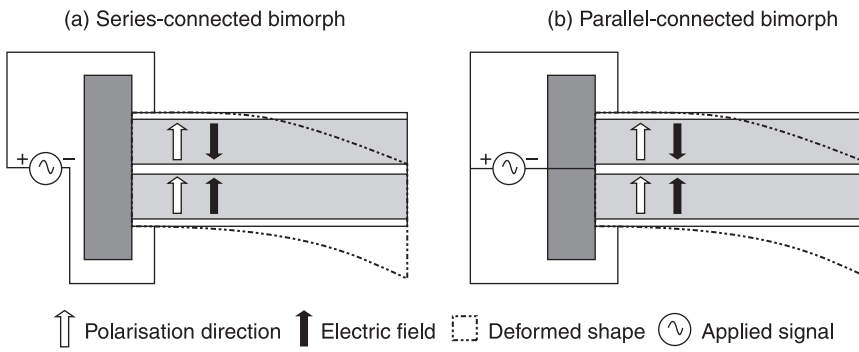

14.4 Schematic representation of (a) parallel and (b) series bimorph actuators.

© Woodhead Publishing Limited, 2012

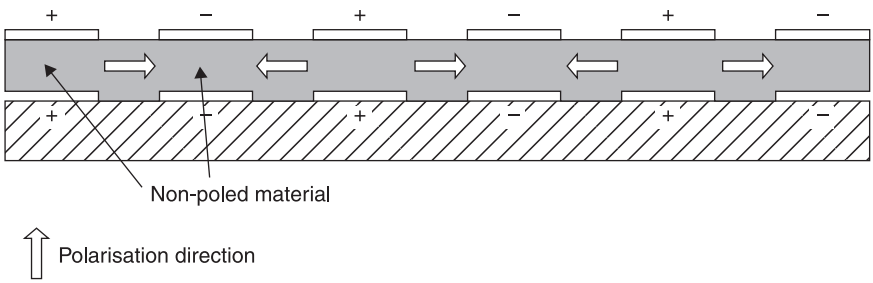

14.5 Schematic of d_{33} mode activated cantilever using an interdigitated electrode (IDE) structure.

e.g. d_{31} mode. Bridges and diaphragms are extensions of the cantilever concept with both ends fixed or the whole circumference fixed, respectively.

It is also possible to create such devices that make use of the d_{33} mode of actuation by employing interdigitated electrodes (IDE). In such devices, the piezoelectric film is still deposited as before, but the arrangement of the electrodes is markedly changed such that the applied electric field is in the lateral (in-plane) direction (Fig. 14.5). The rationale for this approach is that d_{33} is much larger than d_{31}, so it should be possible to achieve a greater displacement. In practice, the performance of the two systems is comparable largely due to the inactive material under each electrode. For this reason, and the much simpler processing and better reliability, the d_{31} mode of actuation is still favoured.

The need to create small, reliable actuators is a driving force for development, pushing researchers to develop new piezoelectric materials and device designs, which exhibit greater strains and generate higher forces with shorter response times (Muralt, 2000). In conjunction with research on new materials for enhanced performance, another important aspect of research is environmentally friendly solutions for non-toxic piezoelectric materials, specifically lead-free ones. A key part of this work is addressing the issues associated with materials that contain volatile elements (e.g. Pb, Na, K). Such elements become volatised during processing, leading to depletion at the surface. For bulk materials, this is not generally a specific issue as the degraded material represents a small fraction of the total (or it can be removed easily), but for films, the presence of an inactive surface layer can significantly reduce the performance of the device as it represents a much larger fraction of the active material as a whole. For this reason there are often restrictions in the thermal processing temperature, which impacts the microstructure and performance (see section 14.6).

For film-based piezoelectric actuators, the most prolific materials are the ferroelectric perovskite ceramics such as lead zirconate titanate (PZT) and barium titanate ($BaTiO_3$).

© Woodhead Publishing Limited, 2012

14.3.2 Magnetostriction

Magnetostrictive (MS) materials undergo a dimensional change through the application of a magnetic field. Such materials tend to be ferromagnetic in nature and it is the reorientation of anisotropic magnetic domains in the structure that gives rise to a macroscopic strain in a similar way to the ferroelectric domain reorientation giving rise to piezoelectric response.

Amorphous materials such as TbFe and SmFe alloys have high MS coefficients, but with low permeability require high external magnetic field to achieve significant actuation. Amorphous FeSiB and TbDyFe alloys exhibit higher permeability and thus enhanced responses. Exhibiting one of the highest MS behaviours, Terfinol-D is one of the most commonly employed MS materials and has a composition of around $Tb_{0.3}Dy_{0.7}Fe_{1.9}$. Galfenol ($Fe_{81.6}Ga_{18.4}$) is MS material that exhibits greater ductility and machinablity with respect to Terfinol-D (Ueno *et al.*, 2008) and is favoured when shaping of the MS material is required.

The advantage of MS actuators is that there is no requirement for complex electrical interconnects as the actuating (magnetic) field is applied externally. This means that a MS actuator can consist of just two materials – the MS material and the support material – making them extremely robust and reliable.

14.3.3 Shape memory alloy

Shape memory alloys (SMAs) form a group of metals that have the ability, when trained, to recover their shape under the application of heat due to a solid state phase transformation from martensite to austenite. At room temperature, the material has a highly twinned martensitic phase that can be easily plastically deformed through the action of stress. This easy deformation occurs due to the propagation of the twin boundaries, which gives rise to a macroscopic plastic deformation. On heating above the transition temperature, the material undergoes a phase change from the deformed twinned martensite phase to the austenitic phase. At a macroscopic level, this is seen as the material returning to its original trained shape. On cooling, the austenite phase retransforms to martensite, but in the highly twinned state, with no macroscopic dimensional changes. Up to 8% strain can be observed in these materials on strain recovery. In operation, the SME is first trained to a certain shape by annealing at elevated temperatures. The system is then deformed through the application of stress (e.g. springs or thermal expansion differences on cooling). On activation through the application of heat, the SMA will then attempt to return to its 'trained' shape, resulting in the actuation action.

In common with MS systems, SMAs do not require electrical drive circuits to be incorporated and can instead be actuated through a change in the ambient temperature. It is also possible to use resistive heating (either via current passage through the SMA itself or via separate heater elements located at strategic points in the device), which provides the ability to control temperatures locally and

© Woodhead Publishing Limited, 2012

create faster response times as the volume of material being heated/cooled is much reduced. When the system cools, if the mechanical stress is still present (i.e. if there is a spring in the system), it will cause the actuator to return to the 'stand-by' state.

The most common of these SMA materials is the alloy of Ni-Ti with typical operating ranges of −100 to +100 °C. The Cu-Ta alloy system also exhibits SMA behaviour and has a larger operating temperature range but shows a lower strain behaviour coupled with poor ageing characteristics where the martensite phase is stabilized over time and corrosion of the alloy occurs.

14.3.4 Viability of printing active materials

Piezoelectric materials can readily be formed into films using a variety of printing techniques combined with high temperature processing to bring about densification of the green body films. Unlike piezoelectric materials, the majority of MS and SMA materials are metallic in nature and do not lend themselves to printing-based processes, which typically require high processing temperatures in oxidative environments.

While MS- and SMA-based actuators can readily be fabricated using RF sputtering (Ishiyama and Yokota, 2008; Lee and Cho, 2008), it is more pertinent to this chapter to consider the cases where such actuators have been fabricated by screen printing or other powder-based printing methods. Thick-film MS actuators have been produced by screen printing where the active material (Terfinol-D) was mixed with a glass frit and an organic carrier (Grabham *et al.*, 2002) to create a printable ink that was deposited onto alumina substrates and sintered at temperatures ranging from 400 to 890 °C for between one and two hours. The sintering of SMA materials is much more challenging due to the rapid oxidation of Ti in the presence of oxygen (Zhang *et al.*, 1992). Today the vast majority of SMA actuators employ SMA wire or sheet materials (Lan and Fan, 2010; Nespoli *et al.*, 2010; Williams *et al.*, 2010) instead of printed films.

For the printed MS actuators, the properties obtained were lower than that of pure Terfinol-D partially due to the presence of the glass frit but also due to residual porosity in the system. This dependence on microstructure is similar to piezoelectric systems (see section 14.6) where porosity and second phases reduce the performance of the active films.

Due to the processing limitations of the SMA and MS materials, the remainder of the chapter will focus on the application of piezoelectric materials for actuator applications.

14.4 Piezoelectric actuators

The most common structure for a piezoelectric film device is a simple rectangular beam, which has a plethora of practical uses. The cantilever uses the transverse

© Woodhead Publishing Limited, 2012

d_{31} actuation mode where the expansion in-plane results in an out-of-plane motion due to the differential strain developed at the PZT–substrate interface.

Such devices have been used to align optical fibres where perfect alignment is essential to avoid unnecessary signal attenuation. The simple cantilever beam used $Pb_{0.97}Nd_{0.02}(Zr_{0.55}Ti_{0.45})O_3$ as the piezoelectric material integrated with a low temperature co-fired ceramic (LTCC) system (Tuominen *et al.*, 2006). In use, an optical fibre was bonded to the surface of the cantilever and the cantilever was then actuated until the fibre was positioned to give maximum signal to the collection system. Similar structures have been achieved using screen-printed PZT on LTCC (Hrovat *et al.*, 2006) for cantilever actuators. The composite sol-gel approach has also been used to deposit PZT on Si- (Dauchy and Dorey, 2007; Zhu *et al.*, 2008), Ni- (Rocks *et al.*, 2009) and Ni-based alloys (Inconel 750 – using a $La_{0.8}Sr_{0.2}MnO_3$ barrier) (Es-Souni *et al.*, 2007) to create actuator structures operating using the bending and thickness modes.

Where the previous cantilever actuator made use of a single pair of electrodes to create an out-of-plane motion (i.e. up and down), a combination of multiple actuator areas on a single structure can give rise to far more complex motions. Combining two actuator circuits, along either side of an actuator beam, can enable a cantilever to be driven in-plane (i.e. side to side) with a simulated plate shear effect. The cantilever beam is effectively composed of two piezoelectric unimorph actuators each positioned along each edge of the beam, but connected along their entire length, as shown in Fig. 14.6. By operating these unimorph actuators out-of-phase

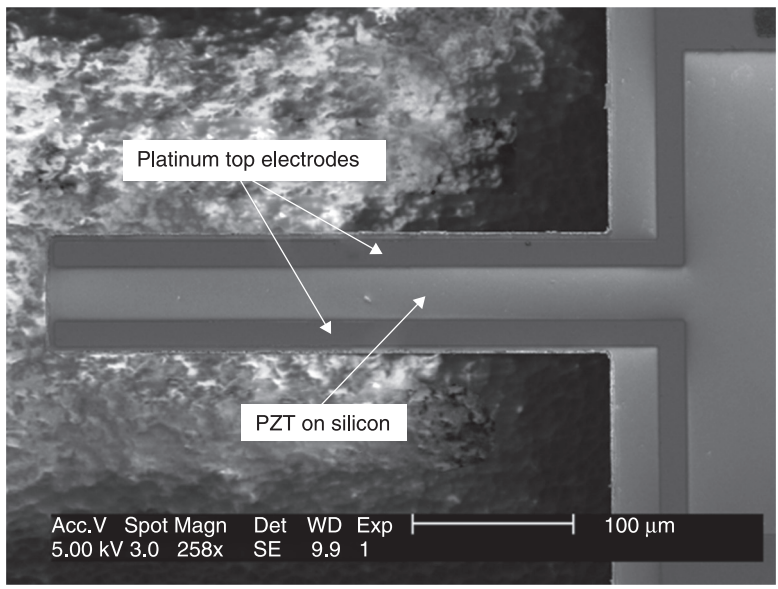

14.6 Cantilever beam using two piezoelectric stacks to simulate in-plane shear actuation.

© Woodhead Publishing Limited, 2012

to each other, one expands while the other contracts, generating an in-plane motion (Leighton *et al.*, 2007). Unlike out-of-plane cantilevers, these in-plane actuators are symmetrical through their thickness (i.e. both top and bottom electrodes are identical and no substrate is present) so that no out-of-plane bending is generated.

Combining multiple actuators together can create mechanical amplifier systems able to develop more complex motion paths. For example, multiple piezoelectric cantilevers can be combined within a single structure to generate motion such as the moving plate. This type of structure can be used as a scanning mirror for barcode readers or with the inclusion of a second conductive plate in close proximity a variable capacitor structure can be realised such as that demonstrated with four actuators by Park *et al.* (2001). Tani *et al.* (2007) have used piezoelectric beams incorporated into a silicon meander structure to create a complex scanning mirror that has X and Y scanning capability. When the films on adjacent beams are actuated in opposition to each other, a large deflection is generated; this translates in a static angle of 8.6°, which has applications in fibre optic switching, image display systems and adaptive lighting for vehicles. A still more complex structure consisting of three double-ended cantilevers has been used to create a microscale probe that is capable of describing motion in X, Y and Z directions (Claverley and Leach, 2010). Each actuator arm is composed of two independent actuators able to create more than just simple curvatures in the beam. Combining three of these actuators in a three-legged structure produces a device able to actuate in many different directions. Due to the small size of the features required for this device, a subtractive processing route was employed (Dorey *et al.*, 2007), where the PZT was first printed and then the final shaping realised using wet etching.

14.5 Piezoelectric actuator fabrication

There are many ways to create film-based actuator structures using a printing approach. Broadly these can be classified as subtractive, where continuous films are printed and then material selectively removed to reveal the structure, and additive, where material is selectively deposited to create the structure directly (e.g. screen printing and ink-jet printing). Techniques such as screen printing have the advantage of only depositing the material that is required. The disadvantages are that less resolution and larger feature size are achievable (10s of μm) than with the subtractive techniques (Dorey *et al.*, 2008). With subtractive techniques, once the desired functional film has been deposited, the next stage of processing is to remove the excess material that is not required for the functional device. This can be done chemically (e.g. acids), physically (e.g. powder blasting) or with the use of high-energy species (e.g. reactive ions) (Dorey, 2009). In all cases, it is first necessary to deposit a masking material that will protect the material that is to remain in place. The material is then exposed to the etching media until all of the unwanted material has been removed. Using this approach, much finer features (μm level) can be obtained.

© Woodhead Publishing Limited, 2012

Irrespective of which approach is adopted, the deposition and integration of the piezoelectric materials are at the heart of the process. In all cases, the key to the creation of thick-films is the reduction of the processing temperature so that the surrounding materials are not degraded. This can be achieved by using a low melting temperature sintering aid such as PbO (Yao *et al.*, 2005), Pb_5GeO_{11} (Duval *et al.*, 2003), or Cu_2O:4PbO (Dorey and Whatmore, 2002), which can reduce processing temperatures to between 700 and 950 °C allowing materials such as silicon, stainless steel, titanium and LTCC to be used instead of refractory materials such as alumina. The sintering aids enhance particle reorientation during the early stages of sintering and dissolution, atomic diffusion and repreciptitation during the latter sintering stages. While increasing density, they also introduce a second non-piezoelectric phase that can degrade functional properties, resulting in a need to balance the enhancing effect of increased density and the degrading effects of a second phase. Typically between 1 and 10 vol % of sintering aid is added to achieve optimum results. The exact level of sintering required will depend on the materials involved, the size of the particles in the ink and the processing temperatures used.

Alternatively, printed PZT ceramics can be infiltrated with a ceramic, producing sol (a metal organic precursor solution) to increase the density of the films (Lee, 2007). While the infiltration can be conducted after sintering, if it is done before sintering the maximum processing temperature can also be reduced (Dorey *et al.*, 2003; Kwon *et al.*, 2006). Higher numbers of infiltrations result in an increase in remnant polarisation, coercive field and relative permittivity. However, the piezoelectric coefficient can decrease due to increased clamping of the substrate and internal stresses (Dorey and Whatmore, 2002) caused by shrinkage of the sol during processing.

A logical extension of this approach is to create a printable ink composed of sol and powder (Kindl *et al.*, 1991; Wu *et al.*, 1993). By creating an ink where the conventional inert carrier fluid and binder are replaced by a ceramic producing sol, it is possible to produce a system where the sol serves the dual role of carrier fluid and binder. By compositionally matching the sol to the powder it is possible to produce high-density piezoelectric films at low temperatures with little presence of second phase.

14.6 Processing–properties–microstructure interrelationship

The desirable characteristics of an actuator include good reproducibility, low actuation drive requirements, fast response time, high strain and high force. Piezoelectric devices have an intrinsic fast response time. The strain and force response of the actuator will be a function of the piezoelectric coefficient, although it should be remembered that in general high strain/low force response is still obtained with cantilever devices, while low strain/high force response is obtained

© Woodhead Publishing Limited, 2012

from thickness mode devices. High piezoelectric properties will simply enhance the response of a given type of actuator. Low actuation drive is reliant on high piezoelectric coefficients, as well as device designs that keep electrode separation as small as possible. This is best achieved where the film is actuated across its thickness or where small-spaced IDEs/multilayer electrodes are used. Reproducibility is maintained through a stable piezoelectric response. It can be seen that at the heart of all of these requirements is the need for a high and stable piezoelectric response.

While microstructural features affect the performance of all materials, the performance of thick-films is particularly sensitive to the microstructure of the film because it also affects the interaction with the substrate and the response of the device. In particular, the degree of actuation is affected not only by the piezoelectric properties of the material, but also by its elastic properties. For example, high piezoelectric properties coupled with low elastic properties may result in low degrees of actuation where the piezoelectric material is unable to deform the surrounding structure.

Examples of microstructural features (figure 14.7) that will affect the performance of thick-films include the following.

14.6.1 Second (inactive) phases

Such features are predominantly introduced in thick-films when sintering aids are used to enhance densification at low processing temperatures. They represent an inactive component that decreases the piezoelectric response of the film (Dorey *et al.*, 2008). Interfacial reaction layers are another form of second phase that can arise when the piezoelectric materials react with the substrate, electrode or environment during processing.

14.6.2 Porosity

Pores mainly arise as a result of poor sintering caused by the need to use low processing temperatures. In an analogous way to second phases, the presence of porosity will decrease piezoelectric properties, but will also decrease the mechanical properties including stiffness and strength.

14.6.3 Defects and damage

Crystallographic defects may be present in thick-film materials due to the use of lower processing temperatures that do not allow the inherent defects in piezoelectric powders (caused by mechanical damage, limited crystallisation and residual unreacted phases) to be effectively annealed out. This will affect the ability of domains to move within the material and adversely affect the ability to pole the material and the piezoelectric properties. At the other extreme, processing

© Woodhead Publishing Limited, 2012

damage (i.e. as a result of etching or cutting) will degrade a greater proportion of the material leading to more obvious degradation.

14.6.4 Grain size

The size of the grains is known to affect the piezoelectric properties of materials. With the use of lower sintering temperatures and reduced sintering, the size of grains in thick-films is often smaller than that found in bulk materials and below the optimum size for high piezoelectric properties to be obtained.

The main discrepancy between bulk and thick-film properties originates from the difference in microstructure caused by the need to use lower processing temperatures and constrained sintering when dealing with thick-films. As all the above microstructural features are affected by processing it is difficult to separate the effects. In general, thick-films have lower densities, more second phase, smaller grains and higher levels of internal defects, stress and constraint.

Where films exhibit a high density (<5 vol% porosity), their elastic properties are approximately linearly dependant on porosity, but as the level of porosity increases the degradation in properties is much larger (Walter *et al.*, 2002). The same behaviour is observed in d_{33} but not with trends in d_{31},where the piezoelectric properties are degraded significantly by relatively small levels of porosity. This has obvious implications for bending mode actuator devices that rely on high piezoelectric properties to achieve high deflection levels. Hence for bending mode devices the creation of high density films is of paramount importance. For some applications, such as resonant sensing devices, the magnitude of the piezoelectric coefficient does not affect the effectiveness of the device. Here, films with second phases and up to 30 vol% porosity achieved mass sensitivities as high as 30 pg/Hz (Park *et al.*, 2006). The ability to use printed films to reduce the size of the

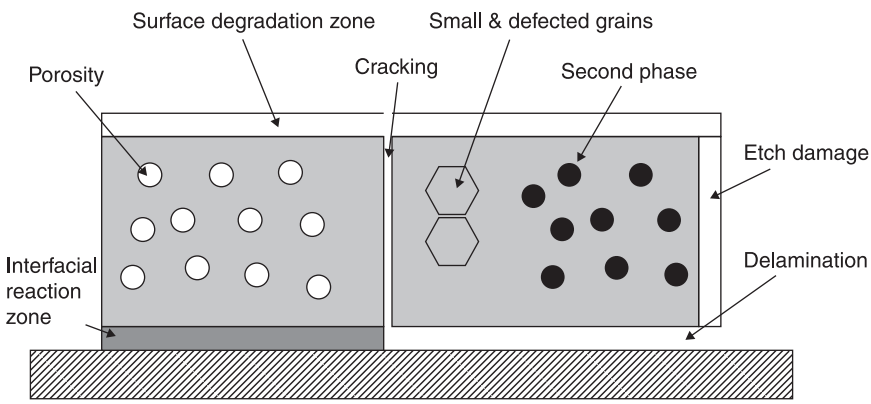

14.7 Schematic of microstructural features that can cause degradation of actuator response.

© Woodhead Publishing Limited, 2012

resonating devices was the main reason for achieving such high sensitivities (Yi *et al*, 2003). Conversely, thickness mode actuation devices may be able to accommodate a certain degree of porosity, particularly if the substrate restraint is reduced by the presence of porosity as this can actually enhance the d_{33} response because the material is more able to deform in the thickness direction.

It is often observed that small-scale actuators do not perform as predicted by the models, which can give rise to a degree of disappointment. Such reduced performance can arise due to processing challenges in maintaining accurate dimensions and the effects of interfacial layers not included in models, as well as the reduced properties of the materials themselves.

As the size of the features decreases, the tolerances of the different manufacturing techniques begin to have a greater impact on the behaviour and reproducibility of the device as a whole. For example, a batch of 10 mm × 2 mm cantilevers produced with a tolerance of ±10 μm would likely see a slight deviation from the predicted behaviour and a small variation in performance from one device to another. However, as the size of the device is reduced, the same variation in processing will have a much larger effect. So a batch of 1 mm × 0.2 mm cantilevers produced with the same tolerance of ±10 μm would exhibit a significant variation across the batch and could also behave very differently from model predictions. This need to control the processing variance can often drive the choice of processing technology, with subtractive routes favoured for small devices and additive routes favoured for larger devices.

Another cause for deviation between model and device is the assumed properties of the materials. It is relatively straightforward to compensate for variances in mechanical properties caused by different microstructures (e.g. grain size, porosity, etc.) by adjusting the material data used in the models and redesigning the device based on updated figures. However, it becomes more complex to account for the variations in functional properties as these vary depending on the nature and relative size of the surrounding materials. This is particularly pertinent with piezoelectric materials as their piezoelectric properties are affected not only by the microstructure of the material but also by the chemical homogeneity and the surrounding stress states during processing and use.

As piezoelectric film actuators are generally used in a structure containing more than one layer, piezoelectric film behaves very differently from its bulk counterpart and this has a significant impact on the piezoelectric properties of the film. This change in behaviour results from the reduction in domain wall motion due to substrate clamping in the case of d_{ij} and the influence of substrate bending in the case of e_{ij} properties. Equations that compensate for these effects are shown below. Note that the d_{ij} and e_{ij} properties are denoted as film properties with the suffix *f* (Southin *et al.*, 2001):

$$d_{33,f} = d_{33} - 2s_{13}\mathrm{E}s_{11}\mathrm{E} + s_{12}\mathrm{E}d_{31} \quad [14.1]$$

$$e_{31,f} = d_{31}s_{11}\mathrm{E} + s_{12}\mathrm{E} \quad [14.2]$$

© Woodhead Publishing Limited, 2012

In general, all of the d_{ij} properties of piezoelectric thin films are reduced in comparison to their bulk counterparts with the same composition, while the e_{ij} properties of the piezoelectric thin films are in practice higher due to substrate bending-induced stresses in the film, which adds further charge contributions from deformation in other orientations. What is particularly challenging about using such predictions is that both the unconstrained mechanical and piezoelectric material properties depend on the microstructure of the material. In addition, these equations account for full clamping, but at an intermediate level of constraint deviations from these values will occur. These two points make it very difficult to predict accurately the behaviour of actuators from modelling alone. At this point it is worth noting that even comparing quoted material properties can be complicated by the fact that the properties quoted for films are often the film versions of the properties – i.e. $d_{33,f}$.

Further compounding the issue is the assumption that the materials are fully poled. When printed films are produced they are invariably under a degree of tensile stress resulting from the shrinkage induced during processing. When films are poled through their thickness, this tensile stress opposes the poling field and can retard the degree of poling. This is seen clearly in measurements of ferroelectric hysteresis loops, which typically exhibit lower remnant polarisations and higher coercive fields, indicative of degraded domain reorientation (Dorey and Whatmore, 2002).

Finally, the very act of processing the materials during the manufacture of the device can lead to differences between the device's performance and the model. Such discrepancies occur due to interfacial reactions that result in regions of material with different properties to that modelled. Size again is critical here, as the interfacial regions are likely to remain unchanged as the device is reduced in scale. So a 100 μm thick piezoelectric actuator with a 1 μm thick inactive interfacial or surface zone will not exhibit a significant variation from the predicted performance. Conversely, a 10 μm thick piezoelectric film with the same 1 μm inactive layer will exhibit at least a 10% reduction in performance. The interfacial layer remains approximately constant as it is controlled by the reaction kinetics, and for a given processing profile the reaction kinetics remain constant. Diffusion barrier layers can be used to prevent reactions between materials, but their very presence may in itself affect the performance of the device. This is seen in ultrasound devices where barrier layers above a certain size can start to interact with the acoustic waves. In cantilever devices, the incorporation of very thick, or highly stressed layers, can result in unexpected deformation of the device.

14.7 Conclusion and future trends

14.7.1 Polymer and composite active materials

While this chapter has focussed on the inorganic functional materials, there are a number of polymeric materials that also exhibit functional behaviour including

© Woodhead Publishing Limited, 2012

piezoelectricity and SMA behaviour. With advances in plastic electronics and related printing technologies there is potential for this group of materials to be employed as actuators to a greater degree. Such materials can easily be printed using the same techniques used to print ceramic and metallic films but without the issues associated with controlling particle size, clogging and sintering. There are, however, other issues including lower properties and the need to mechanically treat polymeric films that need to be addressed before widespread uptake.

Individual carbon nanotubes (CNTs) are able to deform on the application of electrical signals and have been used as nano scale actuators (Li *et al.*, 2008). While printed films of CNTs have not been used as the active material on their own in actuators, they have been used as part of actuators. Due to their conductive nature they can be applied as a monolayer and used as a transparent electrode, as shown by Yu *et al.* (2006), and even incorporated into electroactive polymers to enhance their performance. When embedded and aligned in a polymer matrix, CNTs have been shown to partially realign when an external electric field is applied. The resulting twisting motion of the CNTs within the polymeric matrix results in a macroscopic deformation of the composite. Printed films could feasibly be created using this approach.

14.7.2 Multiferroic active materials

Combining piezoelectric and magnetic behaviour, multiferroic (MF) materials offer increased flexibility with actuators that can be activated both electrically and magnetically. Historically, MF materials have exhibited relatively poor performance and MF activity has been achieved by combining ferromagnetic and piezoelectric materials to create a composite system. Recent developments in studies on $BiFeO_3$ have shown that true MF materials with good properties exist and could be used in actuators. Dye-modified BFO ($Bi_{0.7}Dy_{0.3}FeO_3$)-based cantilevers have been fabricated using pulsed laser deposition to create unimorph cantilever actuators 100–300 μm in length with Si as the substrate (Prashanthi *et al.*, 2011). This shows great promise as MF materials can be handled and processed in the same way as ceramic piezoelectric materials for which there exists a great deal of processing knowhow.

14.7.3 Direct-write technologies

Along with advancements in new active materials and actuators designs, there is also significant interest in developing new and more flexible processing routes to directly print actuator materials. Where at one time screen printing and high-temperature firing were seen as the way to produce printed films (particularly with inorganic active materials), new technologies employing more flexible and precise fabrication capabilities are evolving. Of particular interest are techniques such as

© Woodhead Publishing Limited, 2012

transfer printing, embossing/moulding (Wang *et al.*, 2009), laser sintering and ink-jet (and related) droplet deposition techniques.

14.8 Further information and advice

Actuator design is constantly evolving and the role that printed films have to play in this evolution is growing. The vast majority of current commercially available actuator technologies are not based on printed film technology. In addition to the references in this chapter there are a number of generic texts on actuators and related devices including: review of non-film-based piezoelectric actuators by Watson *et al.* (2009) and review of microscale sensors and actuators by Wilson *et al.* (2007).

14.9 References

British Standards Institution (2002), *BS EN 50324-1:2002 Piezoelectric properties of ceramic materials and components. Part 1: Terms and definitions*. Brussels: Cenelec.

Chang, L., and Cohen, Y. B. (1999), Scaling laws of microactuators and potential applications of electroactive polymers in MEMS, *Proceedings of the SPIE's 6th Annual International Symposium on Smart Structures and Materials*, SPIE, Newport Beach, California.

Claverley, J. D. and Leach, K. L. (2010), A vibrating micro-scale CMM probe for measuring high aspect ratio structures, *Microsystems Technology*, 16, 1507–1512.

Dauchy, F. and Dorey, R. A. (2007), Thickness mode high frequency MEMS piezoelectric micro ultrasound transducers, *J Electroceram*, 19, 383–386.

Dorey, R. A. (2009), Challenges in integration of piezoelectric ceramics in micro electromechanical systems, *Materials Science Forum*, 606, 43–50.

Dorey, R. A. and Whatmore, R. W. (2002), Apparent reduction in the value of the d_{33} piezoelectric coefficient in PZT thick-films, *Integrated Ferroelectrics*, 50, 111–119.

Dorey, R. A., Whatmore, R. W., Beeby, S. P., Torah, R. N. and White, N. M. (2003), Screen-printed PZT thick-films using composite film technology, *Integrated Ferroelectrics*, 54, 651–658.

Dorey, R. A., Dauchy, F., Wang, D. and Berriet, R. (2007), Fabrication and characterisation of annular thickness mode piezoelectric micro ultrasonic transducers, *IEEE Transactions on Ultrasounics, Ferroelectrics, and Frequency Control*, 54, 2462–2468.

Dorey, R. A., Rocks, S. A., Dauchy, F., Wang, D., Bortolani, F. *et al.* (2008), Integrating functional ceramics into microsystems, *Journal of the European Ceramic Society*, 28, 1397–1403.

Duval, F. F. C., Dorey, R. A., Zhang, Q. and Whatmore, R. W. (2003), Lead germanium oxide sinter assisted PZT composite thick-film, *Journal of the European Ceramic Society*, 23, 1935–1941.

Es-Souni, M., Maximov, S., Piorra, A., Krause, J. and Solterbeck, C.-H. (2007), Hybrid powder-sol–gel PZT thick-films on metallic membranes for piezoelectric applications, *Journal of the European Ceramic Society*, 27, 4139–4142.

Grabham, N. J., Beeby, S. P. and White, N. M. (2002), The formulation and processing of a thick-films magnetostrictive material, *Meas Sci Technol*, 13, 59–64.

© Woodhead Publishing Limited, 2012

Hrovat, M., Holc, J., Drnovsek, S., Belavic, D., Cilenšek, J. *et al.* (2006), PZT thick-films on LTCC substrates with an interposed alumina barrier layer, *Journal of the European Ceramic Society*, 26, 897–900.

Ishiyama, K. and Yokota, C. (2008) Cantilevered actuator using magnetostrictive thin film, *Journal of Magnetism and Magnetic Materials*, 320, 2481–2484.

Kindl, B, Carlsson, D. J., Deslandes, Y. and Hoddenbagh, J. M. A. (1991), Preparation of a-alumina ceramics: the use of boehmite sols as dispersing agents, *Ceramics International*, 17, 347–350.

Kwon, T. Y., Park, J. H., Kim, Y. B., Yoon, D. S., Cheon, C. I. *et al.* (2006), Preparation of piezoelectric $0.1Pb(Zn_{0.5}W_{0.5})O_3$-$0.9Pb(Zr_{0.5}Ti_{0.5})O_3$ solid solution and thick-films for low temperature firing on Si-substrate, *J Cryst Growth*, 295, 172–178.

Lan, C.-C. and Fan, C.-H. (2010) An accurate self-sensing method for the control of shape memory alloy actuation flexures, *Sensors and Actuators A*, 163, 323–332.

Lee, S.-G. (2007), Effects of sol infiltration on the screen-printed lead zirconate titanate thick-films, *Materials Letters*, 61, 1982–1985.

Lee, H.-S. and Cho, C. (2008), Study on advanced multilayered magnetostrictive thin film coating techniques for MEMS applications, *Journal of Materials Processing Technology*, 201, 678–682.

Leighton, G. J. T., Kirby, P. B. and Fox, C. H. J. (2007), In-plane excitation of thin silicon cantilevers using piezoelectric thin films, *Applied Physics Letters*, 91, 183510.

Li, C., Thostenson, E. T. and Chou, T.-W. (2008), Sensors and actuators based on carbon nanotubes and their composites, *Composites Science and Technology*, 68, 1227–1249.

Madou, M. J. (2002), *Fundamentals of Microfabrication: The Science of Miniaturization*, 2nd edition, CRC Press, Boca Raton.

Muralt, P. (2000), Ferroelectric thin films for micro-sensors and actuators: a review, *Journal of Micromechanics and Microengineering*, 10, 136–146.

Nespoli, A., Besseghini, S., Pittaccio, S., Villa, E. and Viscuso S. (2010), The high potential of shape memory alloys in developing miniature mechanical devices: a review on shape memory alloy mini-actuators, *Sensors and Actuators A*, 158, 149–160.

Nye, J. F. (1957), *Physical Properties of Crystals: Their representation by Tensors and Matrixes*, Oxford University Press, Oxford.

Park, J. Y., Yee, Y. J., Nam, H. J. and Bu, J. U. (2001), Micromachined RF MEMS tuneable capacitors using piezoelectric actuators, *International Microwave Symposium Digest,* 3, 2111–2114.

Park, J. H., Kwon, T. Y., Kim, H. J., Kim, S. R., Yoon, D. S. *et al.* (2006), Resonance properties and mass sensitivity of monolithic microcantilever sensors actuated by piezoelectric PZT thick-film, *J Electroceram*, 17, 565–572.

Prashanthi, K., Mandal, M., Duttagupta, S. P., Pinto, R. and Palkar, V. R. (2011), Fabrication and characterisation of a novel magnetoelectric multiferroic MEMS cantilever on Si, *Sensors and Actuators A*, 166, 83–87.

Rocks, S. A., Tredez, Q., Almond, H. J., Shaw, C. P. and Dorey, R. A. (2009), Bottom up fabrication of a nickel-lead zirconate titanate piezoelectric microcantilevers, *Materials Letters*, 63, 88–90.

Southin, J. E. A., Wilson, S. A., Schmitt, D. and Whatmore, R. W. (2001), $e_{31,f}$ determination for PZT films using a conventional 'd_{33}' meter, *Journal of physics D: Applied physics*, 34, 1456–1460.

Tani, M., Akamatsu, M., Yasuda, Y. and Toshiyoshi, H. (2007), A two-axis piezoelectric tilting micromirror with a newly developed PZT-meandering actuator, *20th International Conference on Micro Electro Mechanical Systems*, Hyogo, Japan, pp. 699–702.

© Woodhead Publishing Limited, 2012

Tuominen, J., Lappalainen, J., Hiltunen, J., Ollilia, J. and Lantto, V. (2006), Piezoelectric thin film unimorph actuator for optical fibre alignment applications, *Journal of Optics A: Pure Applied Optics*, 8, 5398–5404.

Ueno, T., Summers, E., Wun-Fogle, M. and Higuchi, T. (2008), Micro-magentostrictive vibrator using iron-gallium alloy, *Sensors and Actuators A*, 148, 280–284.

Walter, V., Delobelle, P., Le Moal, P., Joseph, E. and Collet, M. (2002), A piezo-mechanical characterization of PZT thick-films screen-printed on alumina substrate, *Sensors and Actuators A*, 96, 157–166.

Wang, D, Rocks, S. A. and Dorey, R. A. (2009), Micromoulding of PZT film structures using electrohydrodynamic atomization mould filling, *Journal of the European Ceramic Society*, 29, 1147–1155.

Watson, B., Friend, J. and Yeo, L. (2009), Piezoelectric ultrasonic micro/milli-scale actuators, *Sensors and Actuators A*, 152, 219–233.

Williams, E. A., Shaw, G. and Elahinia, M. (2010), Control of an automated shape memory alloy mirror actuator, *Mechatronics*, 20, 527–534.

Wilson, S. A., Jourdain, P. J., Zhang, Q., Doregy, R. A., Bowen, C. R. *et al.* (2007), New materials for micro-scale sensors and actuators. An engineering review, *Materials Science and Engineering R*, 56, 1–129.

Wu, J., Chen, M., Jones, F. R. and James, P. F. (1993), Mullite and alumina–silica matrices for composites by modified sol-gel processing, *J Non-Cryst Solids*, 162, 197–200.

Yao, K., He, X., Xu, Y. and Chen, M. (2005), Screen-printed piezoelectric ceramic thick-films with sintering additives introduced through a liquid-phase approach, *Sensors and Actuators A*, 118, 342–348.

Yi, J. W., Shih, W. Y., Mutharasan, R. and Shih, W.-H. (2003), In situ cell detection using piezoelectric lead zirconate titanate–stainless steel cantilevers, *J App Phys*, 93, 619–625.

Yu, X., Rajamani, R., Stelson, K. A. and Cui, T. (2006), Carbon nanotube-based transparent thin film acoustic actuators and sensors, *Sensors and Actuators A*, 132, 626–631.

Zhang, N., Khosrovabadi, P. B., Lindenhovius, J. H. and Kolster, B. H. (1992), TiNi shape memory alloys prepared by normal sintering, *Materials Science and Engineering*, A150, 263–270.

Zhu, B. P., Wu, D. W., Zhou, Q. F., Shi, J. and Shung, K. K. (2008), Lead zirconate titanate thick-film with enhanced electrical properties for high frequency transducer applications, *Applied Physics Letters*, 93, 012905.

© Woodhead Publishing Limited, 2012

15

Printed heater elements

G. RADOSAVLJEVIC and W. SMETANA,
Vienna University of Technology, Austria

Abstract: Thick-film technology has been proved for a long time as a well established technology for the fabrication of microelectronic circuits of high reliability meeting also stringent operation requirements. Beside this conventional application, the production of heater elements by screen printing has been developed as an important alternative area of application for thick-film technology. This chapter deals with the summary and characterization of thick-film materials available for heater construction, the design procedure of heater elements, which is exemplarily demonstrated, and the fabrication and characterization of heater elements provided for different application areas. Also highlighted are specific problems that have to be considered during the process of developing and fabricating heater elements.

Key words: thick-film heaters; thick-film sensors; thick-film actuators; temperature distribution analysis.

15.1 Introduction

Heaters fabricated in thick-film technology have drawn attention for a long time for commercial and industrial applications because they provide a number of advantages in comparison with conventional metal-sheathed resistance elements. In general, thick-film heaters show a low profile, improved temperature uniformity over large surfaces, a fast thermal response due to the low thermal mass, and a higher operating efficiency. Another advantage of thick-film heaters deals with quality issues. Due to the heating element structures traditional failures related to moisture adsorption and electrical leakage are avoided. Heaters are made on flat substrates as well as on tubes in varying types of heater pattern arrangements. Multiple heating elements and varying power outputs can be incorporated across a single substrate in order to achieve requested temperature distribution. Spiral patterns may be considered as a speciality for tube applications. Depending on the heat transfer conditions, the watt densities on the hot track can be increased up to 100 W/cm^2.

Heaters are printed directly on glass, ceramic, polymer or metal-based substrates using metal/alloy-loaded thick-film pastes. The development and realization of heaters are often crucial procedures since they must be considered as a part of a system thus comprising also its environment. During the design phase of a heater, a range of boundary conditions related to the thermal performance, the power consumption, geometrical proportions, and finally also cost aspects have to be considered.

© Woodhead Publishing Limited, 2012

A combination of the substrate material with specific thermal charcteristics and the adequate paste systems has to be selected to form a heater with the requested thermal performance. For many thick-film applications the substrate acts only as a robust and reliable base for electronic circuits. By contrast, for the heater fabrication the substrate acts as a significant functional part that enables the adjustment of the device's final performance. A wide range of substrate materials with different thermal characteristics have to be considered during the design phase of the heater. Additionally, appropriate paste systems also have to be selected that are compatible with the potential substrate candidate. It is not an easy procedure since, for certain material combinations, there is no prior experience to refer to, and only limited references and recommendations are available from paste suppliers.

Applications of thick-film heaters are very wide. They can be used in tea kettles, for waffle irons, clothes dryers, stove-top burners, humidifiers, water heaters, boilers, thermal print heads, glue guns, ceiling heating panes, fridge defrosting, deicing or demisting devices, warming trays, car reversing mirrors, evaporators and plate heat exchangers, etc.

Beside such conventional applications, thick-film heaters are also used as functional parts of a sensor or actuator systems.

15.2 Materials for heater fabrication

15.2.1 Substrates

Thick-film heaters on ceramic substrates provide for low thermal expansion, high temperature stability, low dielectric constant and rigidity. Additionally they show chemical compatibility/inertness and they are used for critical processing applications where ultra pure materials are required, as in the semiconductor industry. Due to direct surface contact, these thick-film heaters ensure greater heat transfer through the thermally stable ceramic substrates than other types of heaters. Alumina and AlN have been used for a long time as the standard substrate materials for fabricating electronic circuits in thick-film technology. Beside this conventional application, these ceramics have been proved as excellent substrate materials for thick-film heater employments. The maximum attainable power density of such a ceramic heater plate is about 6 to 10 W/cm^2. When the power per unit area is higher (up to a maximum of 30 W/cm^2), the heating element must be connected to a compensating material such as an aluminium, copper or brass plate.

A comparison between the heating characteristics of heaters fabricated on AlN and conventional alumina substrates (Kumagai *et al.*, 1993) is shown in Fig. 15.1.

The heater applied on an alumina substrate develops thermal stress fractures from a 60 W load, whereas the AlN-heater substrate will not be destroyed up to 120 W. It can be seen that the heaters on AlN-substrates are faster than the heaters fabricated on alumina substrates. Figure 15.2 shows the surface temperature

© Woodhead Publishing Limited, 2012

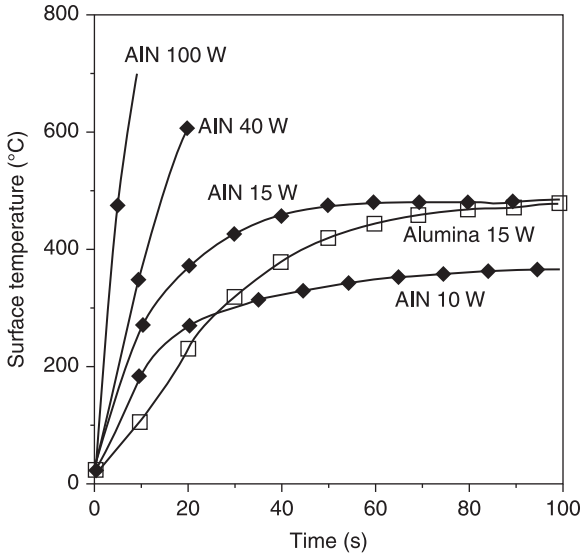

15.1 Substrate surface temperature in dependence on applied power (lateral heater dimensions: 20 mm × 10 mm).

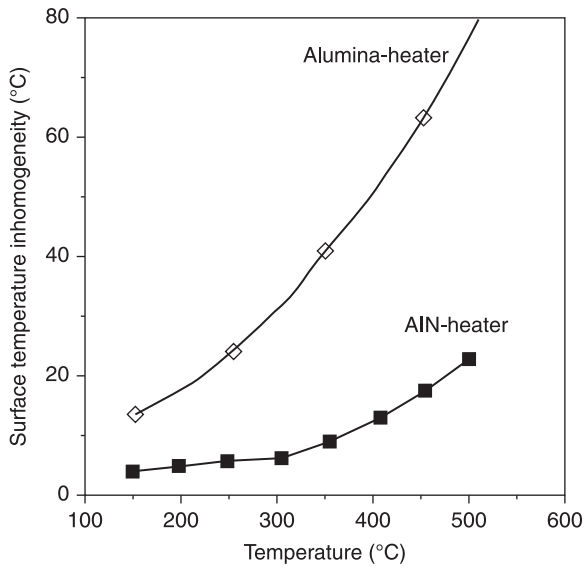

15.2 Temperature inhomogeneity along different ceramic heater plates (lateral heater dimensions: 20 mm × 10 mm).

© Woodhead Publishing Limited, 2012

variation of heaters operating at various temperatures. The maximum temperature difference across the surface for the AlN-substrate at 500 °C is 25 °C, whereas for the alumina heater substrate it is much higher, at 83 °C.

The features of the AlN-heater can be summarized as follows: rapid heating and cooling are possible because of its high thermal shock resistance. Preheating of the heater substrate is unnecessary, because rapid heating is possible. A compact size and light-weight heater performance can be realized because high electric power density can be applied to the AlN-heater. The implementation of a heat-equalizing plate is not required because the AlN-ceramic itself acts already as a heat equalizer.

Alumina serves as a reference material for characterization and calibration of most thick films. Disadvantages associated with alumina are the risk of cracking due to thermal and mechanical shock. Hence, rapid temperature change necessary in some heater applications may induce substrate cracking. Thick-film heaters on silica glass are ideal for use in numerous applications where visibility and/or corrosion resistance are required.

Physical data for ceramic heater substrate candidates are summarized in Table 15.1 (Buchanan, 2004; Imanaka, 2004; Datasheet Heraeus Quarzglas, 2009). The value for the thermal shock resistance is of interest when a heater with a fast heat-up and cool-down rate has to be designed. Substrates characterized by low shock resistance values show an increased risk of crack formation when they are exposed to fast heating cycles. Beside AlN, the fired low-temperature co-fired ceramic (LTCC) tapes show excellent shock resistance. This enables the application of LTCC-substrates for heater elements in sensor and actuator systems where a fast response and heating rate are required.

If a greater substrate thickness is required in order to attain an improved mechanical strength for the heater element, the cost of substrate and consequently that of the heater will increase. Substrate costs may be a restricting factor for the selection of thick-film heaters for many consumer applications such as houshold appliances. Thick-film manifold heaters are manufactured alternatively using

Table 15.1 Material property data of ceramic substrates

	Al_2O_3	AlN	LTCC	Quartz
Dielectric constant ε_r (1)	8.2–10.2	8–9.2	6–9	3.8
Dielectric strength (kV/mm)	14–24	14–27	15	8
Young's modulus E (GPa)	397	320	93	72.5
Thermal expansion coefficient α (10^{-6}/K)	7.2	4.1	4.1	0.5
Poisson's ratio υ (1)	0.24	0.25	0.17	0.17
Fracture strength s_F (MPa)	350–400	350–400	150	50
Thermal conductivity λ (W/mK)	25	200	2.5	1.38
Thermal shock resistance R (K)	96	210	326	1.122

© Woodhead Publishing Limited, 2012

thick-film technology on stainless steel plates. Insulated steel is an alternative substrate with a number of advantages. It has high mechanical strength, enabling its use as part of the construction of a domestic appliance. It also has a high thermal conductivity similar to that of alumina, which provides uniform heating over large areas. But nevertheless one must be aware that the glass ceramic insulation layer acts as a heat barrier. The insulation layer may be enamel, applied either by dipping or an electrostatic technique, or a glass ceramic deposited by screen printing.

Porcelain enamelled steel (PES) has been used as a thick-film substrate for many years (Baumbach *et al.*, 1990). The porcelain is acting as an electrical insulation layer. PES was developed using low-carbon steel (« 0.003% C), which is chemically cleaned and etched to remove surface oxides. After nickel plating, a glass powder is applied to the surface by either dipping or electrostatic spraying techniques followed by firing to produce a glassy surface. Conventional porcelain enamels for low-carbon steel substrates are, in general, based on alkali borosilicate glasses. These glasses fire at a typical peak temperature of 780–850 °C (about 5 minutes above 700 °C) in a continuous fast-belt furnace with a cycle time of about 20 minutes. Insulation resistance (IR) is dependent on coating thickness but composition is found to be more critical for maintaining high IR at an elevated temperature. The enamel layer of a heater separates the base (Iow-carbon steel) metal substrate and the heater tracks. Therefore, the required electrical performance of low leakage current and high breakdown voltage is governed by the electrical properties of the enamel layer. The IR of enamels often decreases with rising temperature, especially in the temperature range of 200–300 °C, due to an excessive alkali ion content. PES is strong, not brittle, it may be formed into three-dimensional shapes and it is relatively cheap to produce. The disadvantage of PES for many applications is that the coating will not withstand subsequent processing procedures at temperatures over 600 °C. This requirement precludes the use of conventional thick-film resistive pastes, which are usually processed at 850 °C.

Glass ceramic coating systems for steel substrates are now available that are fully compatible with the conventional thick-film process (Tait *et al.*, 1994). The base material of metal-core heating elements consists of insulated chrome steel. Ferritic as well as austenitic steels are used to manufacture heating elements. Ferritic steels are plain chromium steels with varying Cr content between 11% and 28%, but with low carbon content. They have moderate-to-good corrosion resistance, but below a content of 12% Cr, steels are generally not stainless. Austenitic stainless steels typically contain between 16 and 26% chromium (Cr) and 8–22% nickel (Ni). Additional elements are often added such as molybdenum, titanium or copper to modify or improve their properties, making them suitable for many critical applications. In contrast to the ferritic steels, they have an excellent corrosion resistance, but they are a more expensive substrate material. Steel substrates are suitable for a power load density up to 50 W/cm^2. Thick-film

© Woodhead Publishing Limited, 2012

heaters on stainless steel are ideal for use in applications where fast response and temperature uniformity are essential issues. Thick-film on stainless steel provides to generate a low profile heater of any two-dimensional shape since the heater plate can be laser cut or machined to fit any shape requirements. This technology ensures greater heat transfer through thermally stable substrates. Different glass–ceramic compositions matched to the thermal coefficient of expansion (TCE) for the ferritic (TCE ~ 12 ppm/°C) and austenitic (TCE ~ 18 ppm/°C) stainless steel substrates have been introduced. They can be screen-printed onto selected grades of pre-oxidized stainless steel and fired in the range of 850 to 950 °C to provide an insulation layer upon which a variety of regular thick-films can be processed. While changes in the dielectric composition can give significant improvements in the results, properties like breakdown voltage still necessitate the use of coatings of sufficient thickness. Tape processing provides a method of obtaining the required coating thickness without resorting to the multiple printing/firing steps associated with conventional thick-film processing. The composition of tapes – denominated as transfer tapes – corresponds in general to that of the glass–ceramic paste provided for insulating the steel substrates (Stein *et al.*, 1995). The tapes are available in different thicknesses. They enable the application of dielectric layers in a desired and uniform thickness in one processing step ('transfer process'), which may be considered as an approach to increase production efficiency. The risk of pinhole inclusions that adversely affect the dielectric strength can be avoided. Flexible sheets of green LTCC-tape of the desired thickness in the range of 125 to 175 μm are laminated to the adequately prepared metal bases using pressures of 250 to 500 psi at 75 °C. After tape lamination, the parts are fired in a standard thick-film belt furnace at a peak temperature of 850 °C. The resulting thickness of fired tape layer is typically in the range of 90 to 160 μm. Tests conducted with the glass ceramic-coated substrates have proved the high thermal shock resistance of this compound. The glass ceramic dielectric-coated steel substrate is finally covered with specifically designed resistor tracks forming the heater element and a dielectric overglaze acting as protection against hazards. A maximum substrate temperature of 550 °C is usually attained with glass ceramic-coated thick-film steel heaters.

Introducing insulated aluminium substrates that are actually used as heat sinks of high efficiency may also be considered as an interesting approach for the fabrication of thick-film heaters, providing a high temperature uniformity over the total substrate area (Eisermann *et al.*, 2009).

15.2.2 Heater tracks

Different resistor/conductor paste formulations offer a wide range of electrical resistances and temperature coefficients of resistance (TCR), enabling several options in terms of heater design and product performance. Cermet pastes for the fabrication of heater elements are usually based on Ag compositions doped

© Woodhead Publishing Limited, 2012

with Pt- or Pd-additives to control sheet resistance and TCR. In order to reduce costs, attempts have been made to replace the noble metal dopants by a glass phase.

An intrinsic temperature control can be achieved by using resistor materials with a high positive temperature coefficient of resistance (PTC). These materials are characterized by a significant increase in resistance when they are heated up. This performance results in a decrease in the current flow, hence power consumption, under constant voltage supply. The described effect is illustrated in Fig. 15.3(a) and 15.3(b), where the performance of water heaters of the same design, constructed with a regular thick-film resistor and a PTC resistor, are compared (Tait *et al.*, 1994).

In both examples, the water reaches an equilibrium temperature of 85 °C before complete evaporation starts, but the course of the temperature and the current are quite different for both heater elements. The current in the resistor heater element with a low TCR remains constant throughout the heating phase, which finally results in an increase of element temperature to a very high level when the stabilizing effect of the water is removed. By contrast, the PTC element heats more rapidly to the equilibrium state. At the evaporation of the water, a stable state is reached at a much lower temperature than the heater element with a low TCR. This demonstrates the suitability of using thick-film PTC resistors in the construction of efficient temperature-controlled water heaters such as hotplates in domestic appliances. Additionally, PTC pastes can also be used to implement discrete temperature-sensing elements in heater configurations fabricated with resistive pastes of rather low TCR.

Depending on the selected substrate material, different values for sheet resistance and TCR of heater elements are attained (Hrovat *et al.*, 2001; Vanek *et al.*, 2009). This effect is especially pronounced if resistor materials matched to alumina substrates are applied onto glass ceramic-coated steel substrates, as demonstrated in Table 15.2 for PTC pastes (Stein *et al.*, 1995). Resistance values on the tape-coated stainless steel (austenitic steel substrate) are twice as large as on Al_2O_3, while TCR values retain their desired high positive values.

Resinate thick-film pastes are interesting metallization systems for the fabrication of heater elements designated for sensor and actuator applications where especially fast heating rates and low power consumption are required. Heater elements fabricated with resinate pastes show only a low thermal mass in comparison with a corresponding thick-film resistor or conductor elements acting as a heater device, since the layer thickness of resinate components is <1 μm. But nevertheless, the heating rate of miniaturized heater elements depends strongly on the applied substrate. In Fig. 15.4, the heating charcateristics of a small thick-film resistor and an equivalent Au-resinate resistor with the same lateral dimensions for a bare as well as for a glass ceramic-coated alumina substrate are shown.

© Woodhead Publishing Limited, 2012

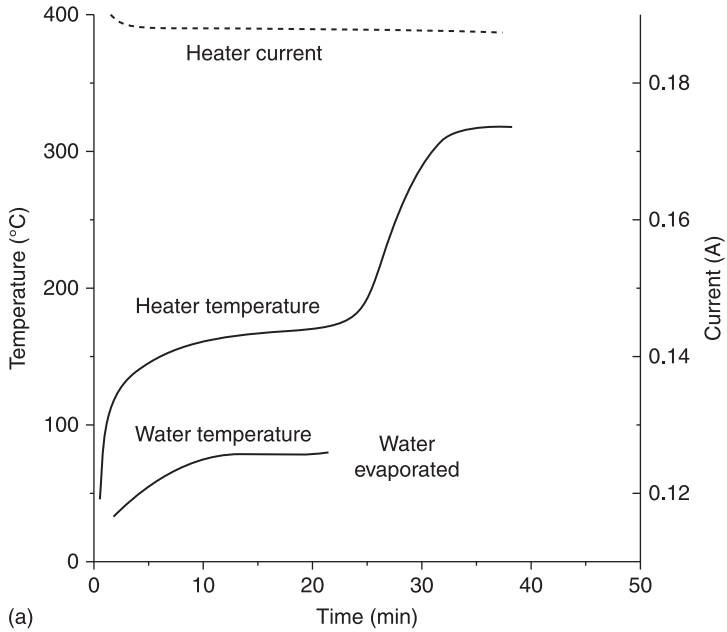

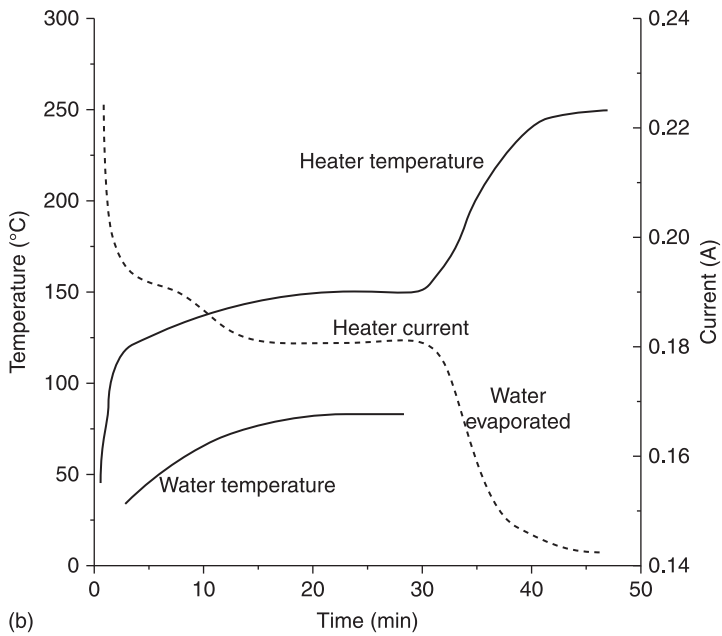

15.3 (a) Temperature regulation for heater-element with low TCR; (b) temperature regulation for PTC.

© Woodhead Publishing Limited, 2012

Table 15.2 Influence of substrate on characteristic data of PTC-resistors

Material	Sheet resistance (Ω/□)		TCR (ppm/°C)	
	Al_2O_3 substrate	On insulated steel	Al_2O_3 substrate	On insulated steel
PTC-2650-1	5.0	10.8	3006	3165
PTC-2611	11.0	20.6	2703	2735
PTC-2612	95.0	280	2320	1900

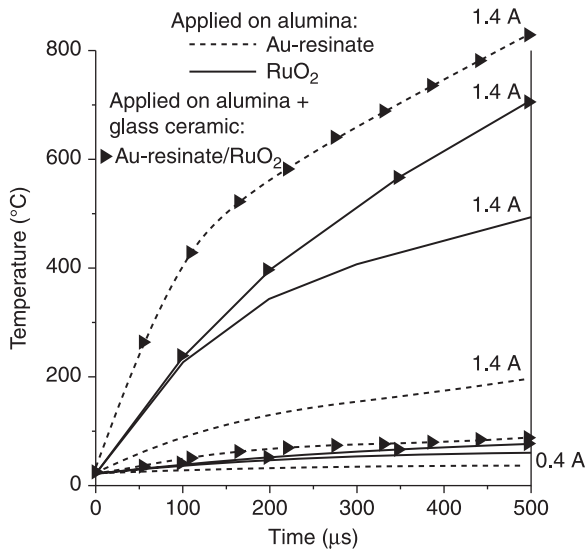

15.4 Influence of substrate on heating rate of different resistor elements.

The thickness of the glass ceramic coating, which acts as thermal barrier, as well as that of the resinate resistor, govern the heating rate as well as the attained peak temperature of the heating element. If heater structures are fabricated using resinate pastes, aspects of substrate compatibility with regard to their mechanical integrity have especially to be considered. Additionally, the electrical characteristics of Pt-resistor elements fabricated with resinate pastes vary with the employed substrate material. Pt-resinate pastes of two different suppliers applied on an alumina substrate show rather similar electrical performance but different characteristics are attained using a LTCC-substrate (Fig. 15.5).

Besides the ceramic-based pastes, polymer systems can also be applied to the fabrication of heater elements, providing a high flexibility with regard to the

© Woodhead Publishing Limited, 2012

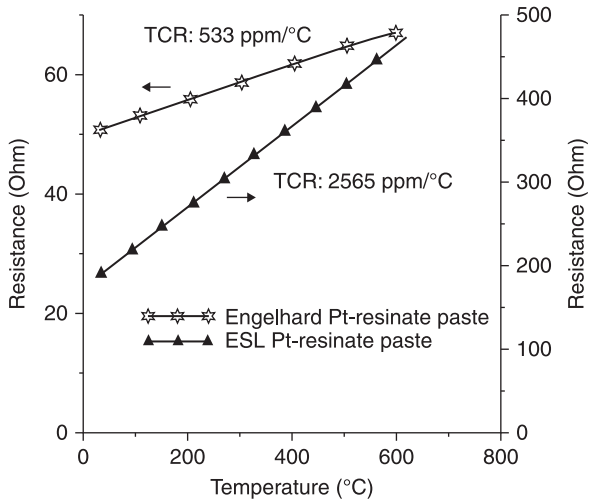

15.5 Influence of substrate on performance characteristic of Pt-resinate resistor elements (meander structure).

substrate selection. Refractory as well as polymer materials can be used as substrate materials. For the fabrication of polymer heater elements, silver- or carbon-filled polymer thick-film (PTF) pastes are used (Gilleo, 1996). With polymer paste it is also possible to design heating tracks showing a pronounced PTC characteristic.

15.3 Heater designs

15.3.1 Polymer thick-film heaters

Printed polymer heaters are based on low-resistance printed silver- or carbon-filled polymer lines acting as heater tracks. The heating elements are built by screen printing of a number of PTF electric circuits onto a wide range of substrates, including metals, ceramics, glass, mica, plastics, polyimide and polyester foils, textile materials, etc. (Table 15.3).

The size and shape of the rigid boards and foils can be customized to match almost any 2D/3D heating configuration. There are also heater constructions with PTC-characteristics available. At first, silver is printed on the polyester film, then a carbon layer is printed on top of it. As the temperature of the heater increases, the carbon layer causes the silver layer's resistance to increase. This means that the elements serve as their own sensor – at lower temperatures, they increase the wattage, and decrease the wattage at increasing temperature. This increase in

© Woodhead Publishing Limited, 2012

Table 15.3 Characteristic data of PTF heaters

	Characteristics
Sheet resistance (Ω/□)	1000–90 000
TCR (ppm/°C)	5000–300 000
Heat-up rate (°C/s) (depending on substrate thermal mass, power density and heat transfer conditions)	Up to 100
Attainable power density (W/cm^2) (depending on substrate and heat transfer conditions)	<1.0 in still air <2.0 in forced air <4.0 for water heating
Maximal operating temperature (°C) (depending on substrate and PTF)	100 (polypropylene, polyethylene) 130 (polyester (Mylar)) 180 (polyimide (Kapton), Nylon, PTFE, PPS, Epoxy/glass, mica, glass, ceramics, metals)

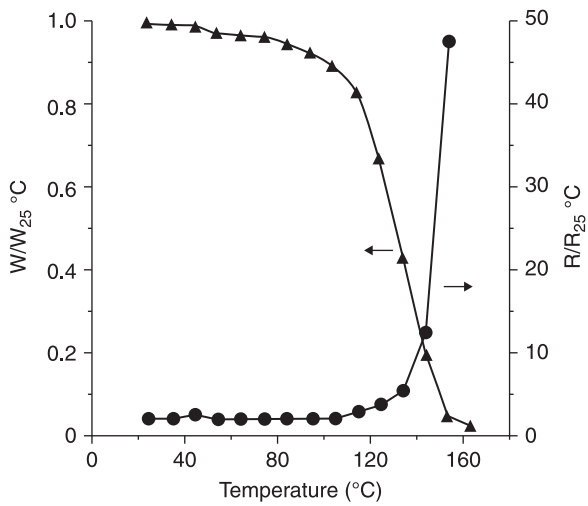

15.6 Characteristic of a PTC resistor in PTF technology.

electrical resistance corresponds to the decrease in wattage (Fig. 15.6) (Zoppas Industries, 2003).

The PTC effect makes the heater self limiting and hence hot and cold spots are avoided as the power is generated where it is required, which yields a more efficient heating system. This characteristic acts for keeping the heater at the designed steady thermal conditions by modulating the power at any change of the heat transfer conditions. The same mechanism stops the current absorption if

© Woodhead Publishing Limited, 2012

any abnormally poor heat transfer condition should occur, preventing any accidental overheating of the device. The flexibility of screen printing and the wide range of available PTF resistance formulations allow for the design of multiple heater circuit patterns matching any requirement for power load distribution and surface temperature control. Parallel circuit designs are preferred since they offer the advantage of heater output self-regulation according to the local heat transfer conditions optimizing power dissipation, and allowing the heater to continue operation even in the event of local damage to the circuit.

Polymer heaters are corrosion-resistant compared to the metal heater versions.

15.3.2 Heaters on glass substrates

Ag-conductor tracks are usually used as demister heating elements on the rear windows of automobiles. Such a demister consists of a parallel line array of conductive tracks between two bus bars. A study has been conducted using Ag as well as various base metal compositions that have been printed on soda–lime glass (Stein *et al.*, 1981). The heater test configuration covers 100 square elements forming the heating track. The resistance of the different conductors is shown in Table 15.4 at firing temperatures of 625 and 700 °C.

In Fig. 15.7, the voltage vs. temperature characteristics for different heater elements fired at 700 °C are presented. The values for glass failure by cracking are indicated. It appears that heaters on glass using Al or Cu conductive tracks might be able to withstand hot spot temperatures of 250 °C or more. The same glass plates using Ag heaters seem to be limited to a maximum temperature of approximately 150 °C. This problem might be related to the wattage or power density and thermal gradients achieved in each case. The base metal conductors show promise, acting as demister elements for automotive windows and other applications on many different substrates. Some rearrangement of the heater geometry would be required to balance the different resistivities and the low available voltages.

Table 15.4 Resistance of demister (array of parallel conductor lines)

	Resistance (Ω)	
Firing temperature/material	625 °C	700 °C
590-C Ag	0.073	0.045
2554 Ni	1.060	0.477
2590 Al	4.600	0.152
2560 Cr	26.000	14.800
2321 Cu	–	0.312

© Woodhead Publishing Limited, 2012

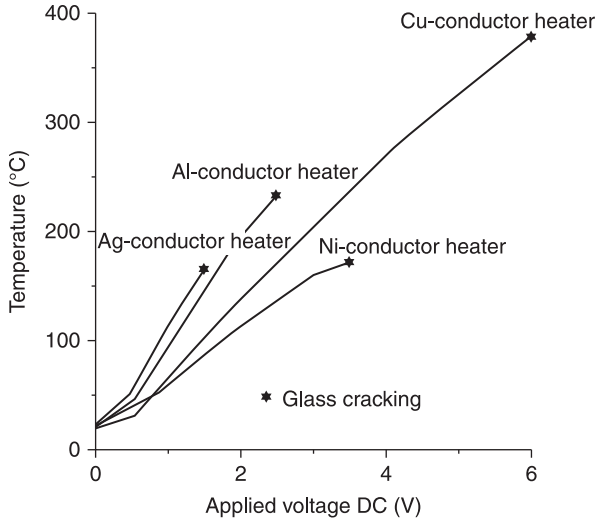

15.7 Demister temperature–voltage characteristics for different heater metallization systems.

15.3.3 Ceramic heater

Figure 15.8 illustrates a heater set-up for a biological application. A fluidic channel is formed by a rectangular groove machined in a plastic body that is clamped to an alumina substrate carrying a thick-film heater element on the opposite side of the substrate. A temperature of 37 °C has to be maintained in the water-filled channel by the heater element. A constant temperature with a tolerance of ±0.25 °C along and within the channel is required. The final temperature distribution should be achieved within 15 s after the cold start of the device with an already water-filled channel or after an intermediate sample liquid change.

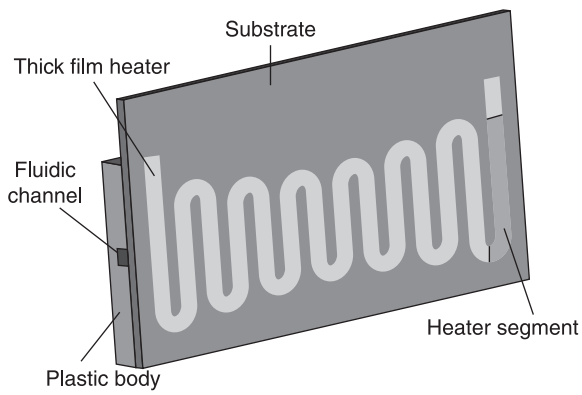

15.8 Schematic of ceramic heater set-up.

© Woodhead Publishing Limited, 2012

The design of the heater is based on a feasibility study applying finite element analysis (FEA), where different heater structures and material combinations have been evaluated. Starting rather intuitively with a heater model, the final optimized structure has been modeled in a range of iterative simulation steps providing the required uniform temperature distribution along the channel. Temperature distribution along the cross-section of the water-filled channel is demonstrated in Fig. 15.9.

In an additional simulation procedure, the settling time for the stabilization of temperature and the system response in the case of an abrupt change of sample liquid has been determined. Applying a PI-controller, it is possible to warm up the already water-filled channel within 11 s free from overshoot (Fig. 15.10). After an an operation time of 20 s, the liquid has been changed by applying a pressure of 0.2 bar for a period of 3 s. The resulting flow velocity of the liquid in the center of the channel amounts to 55 mm/s. After the exchange of the fluid, the temperature in the channel has been stabilized again within 14 s.

The heater is realized by a single heater track using a conventional Ag-based heater paste, while on the opposite side of the substrate, at specific channel positions, three PTC-resistor elements are placed acting as temperature sensors required for the temperature control unit. Figure 15.11 shows the thermal image

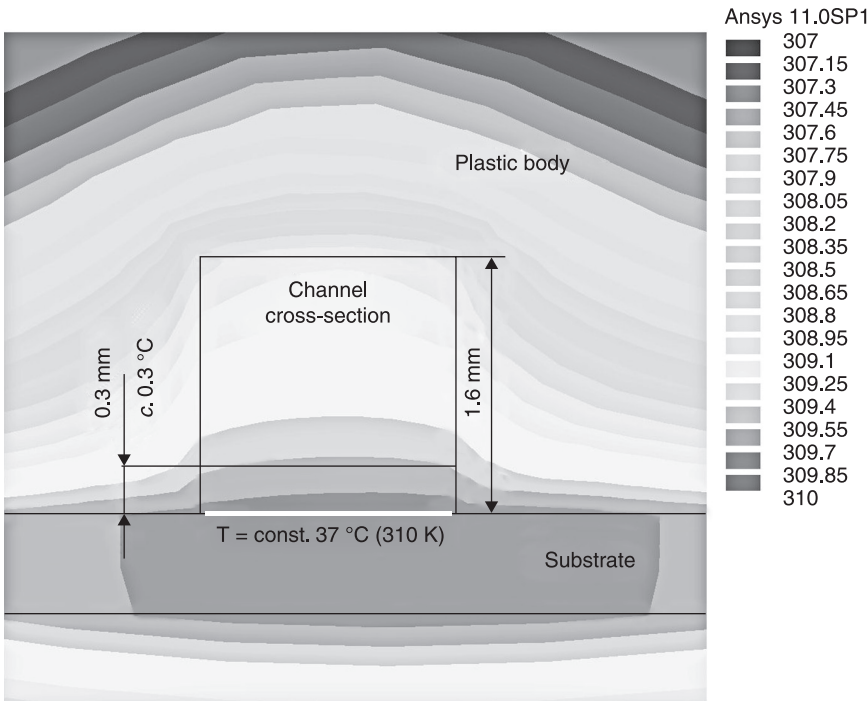

15.9 Temperature distribution along the cross-section of the water-filled channel (numerical simulation: temperature data in K).

© Woodhead Publishing Limited, 2012

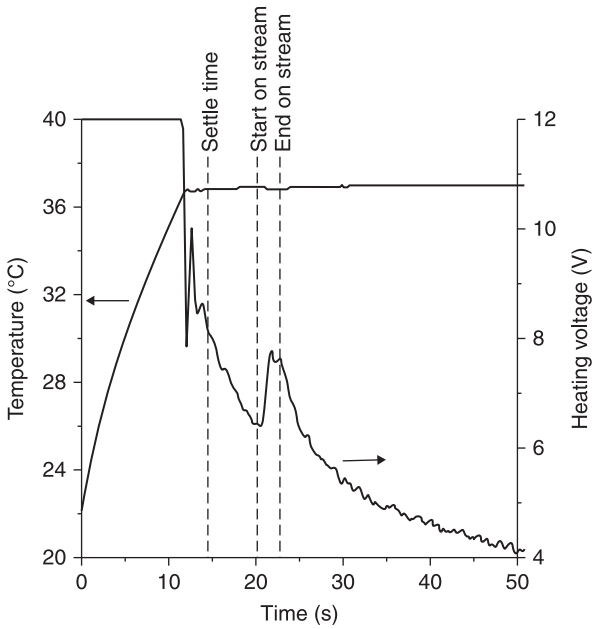

15.10 Temperature control of water at different operation conditions (numerical simulation).

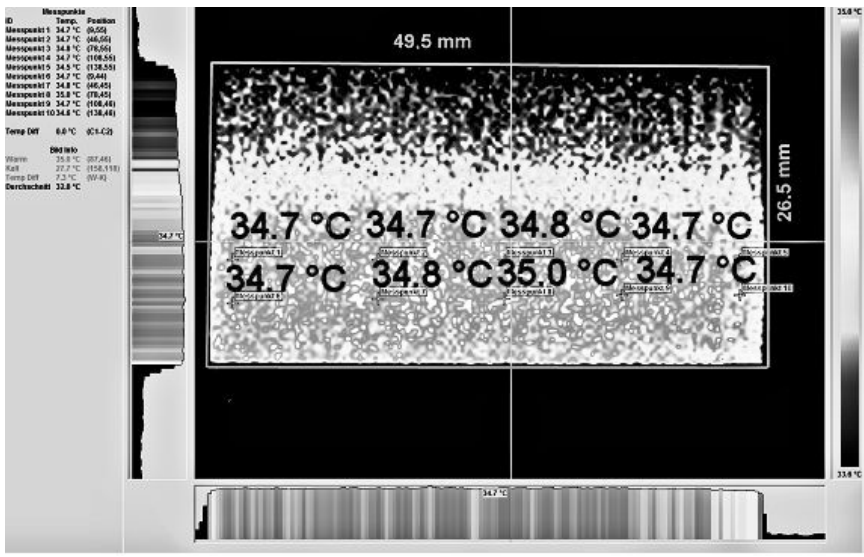

15.11 Thermal image of substrate (opposite side of heater element arrangement).

© Woodhead Publishing Limited, 2012

of the substrate recorded with an infrared-camera for checking the attained temperature uniformity on the substrate.

15.3.4 Stainless steel heater

Flat heater

Steel, unlike alumina, is electrically conductive. Any thick-film heater system printed on insulated steel is subjected to very comprehensive regulations. To withstand the insulation breakdown specified in the relevant standards (DIN 57700/1and EN 0700/1), a coating material for stainless steel must have a high dielectric strength. In order to save cost this must be attained without excess print thickness.

Dielectric coatings have been developed with a wide range of dielectric constants and compatibility with a number of different substrates. High chromium content ferritic stainless steels are frequently chosen for the metal base. These materials provide good corrosion resistance, adherent oxide films, high temperature firing capability and low TCE values (as compared to the austenitic types). For the austentic and ferritic types of steel, different dielectric pastes are available to build up an electrical insulating layer with a sufficiently high breakdown voltage and IR. Paste suppliers often recommend a pretreatment of the steel to improve the adhesion and bonding of the dielectric on the steel. Metal preparation starts with the removal of any dirt, oil or grease. The surface is roughened and oxidized to promote dielectric wetting and adherence. Sandblasting is used to achieve the desired roughness, while the oxidation is done in belt furnaces at peak temperatures between 850 and 930 °C in 45-minute cycles. Sandblasting especially is a very critical processing step and because of that it must be ensured that both sides of the substrate are uniformly sandblasted otherwise extreme substrate bowing can result, which impairs the subsequent screen-printing steps. Depending on the application of the heater, the dielectric has to withstand a defined breakdown voltage.

Thick-film dielectric insulation pastes have been designed to provide better thermal expansion matching to the low carbon steel to reduce warpage, which becomes significant as the dielectric layer thickness increases. Breakdown voltage values even greater than 2500 V can be attained with both tape and thick-film-coated substrates having sufficient dielectric thickness. The performance of the dielectric coating at increased temperatures determines the useable upper operating temperature of the resulting film-heated metal base. The breakdown voltage specified for Class 1 Domestic appliances, i.e. those in which the exposed metal parts are grounded, is 1250 V AC. Thick-film dielectrics have a very low leakage, up to 400–450 °C, and breakdown occurs only at temperatures greater than 550 °C during high break down voltage testing at 1 250 V AC for 60 s (Steinbrück *et al.*, 2005). If a specific grade of steel has to be applied to certain applications it is often mandatory to evaluate the performance of the selected dielectric insulation layer applied to the considered substrate sample.

© Woodhead Publishing Limited, 2012

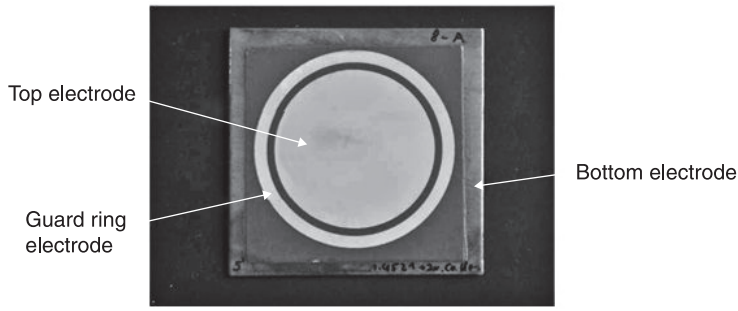

15.12 Test configuration for IR and dielectric strength measurement.

With regard to paste consumption, processing steps and thermal resistance, the insulation thickness should be as thin as possible. To assess the characteristics of the insulating dielectrics, a test configuration presented in Fig. 15.12 can be used. This test set-up can be used to measure IR as well as dielectric strength. The top electrode is connected to an AC/DC source, the guard ring electrode and the steel substrate being connected to ground, and the voltage required to cause breakdown of the dielectric is assessed.

The graph in Fig. 15.13 shows the influence of holding time at peak temperature on the resulting IR of a layered dielectric applied on an austenitic metal base in

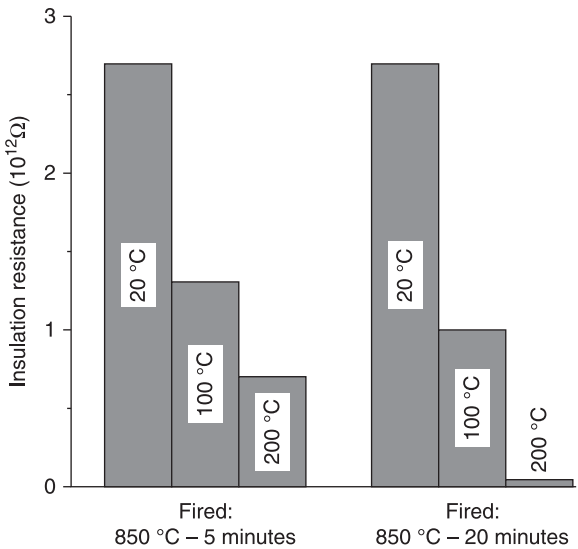

15.13 Change in IR of a dielectric insulation layer in dependence on temperature.

© Woodhead Publishing Limited, 2012

dependence on operating temperature. The dielectric coating is built up with one layer of ESL-4916 paste directly applied on an austenitic steel substrate and two additional layers of the ESL-4924 dielectric. The ESL-4924 layers have a balancing function in this configuration. A glass–ceramic composition ESL-4924 is usually designated for coating ferritic steel but it shows also good compatibility with resistive thick-film materials, which are matched to alumina like the PTC-resistors, as well as with the insulation composition provided for coating the austenitic steel. The total insulation layer thickness amounts to 70 μm. Evidently the IR of the dielectric layer drops with increasing temperature. If the dielectric is exposed to a temperature of 100 °C, its IR decreases to a half of that at room temperature and at 200 °C the resistance drops to already a quarter of its original value at ambient. The samples processed with a holding time of 20 minutes show a more drastic decrease in IR than the samples fired at a holding time of only 5 minutes (Fig. 15.13). No difference in the breakdown voltage performance can be observed for samples fired with different holding time at peak temperature. In Fig. 15.14, the values for the breakdown voltage (AC and DC) for the different processed samples are summarized. Depending on the test conditions a great difference in the value for the breakdown voltage occurs for the samples tested under DC or AC conditions.

The electrical performance of the dielectric may be affected by flaws occurring in the insulation layers due to thermal stress induced by thermal mismatch, as well as processing conditions. Material incompatibility may result in poor adhesion strength between substrate and dielectric. For evaluating the adhesion quality of

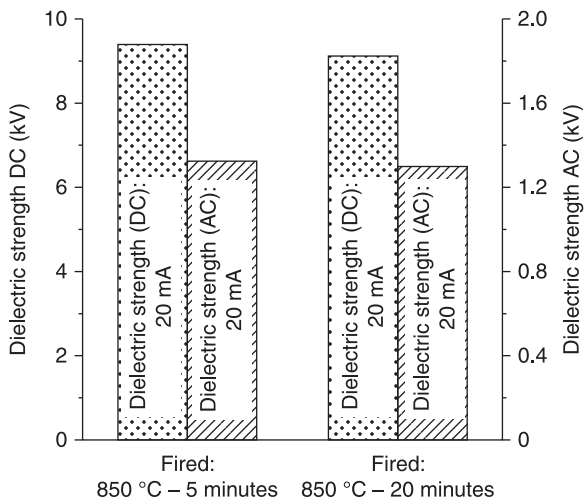

15.14 Breakdown voltage of insulation layer for different testing conditions (AC and DC).

© Woodhead Publishing Limited, 2012

an insulation layer on the steel substrate, there is the so called bend test (Levitsky *et al.*, 1999). The bend test is a 90° bending of the coated steel over a rod with a radius of 20 mm. This verifies the adhesion of the dielectric to the steel. After the 90° bend, the dielectric and the circuit are inspected for any signs of cracking and peeling. This is a pass/fail test. If the dielectric is intact after the bend test, the circuit has passed. If the circuit shows any delamination, cracking or peeling, the part has failed. Further methods of qualifying the adhesion of tape coating layers are the thermal shock test and the drop tests (Stein *et al.*, 1995). Thermal shock testing is done by immersing samples that have been furnace-heated at 700 °C in water. This water shock test is repeated five times and then the parts are examined for cracking. The drop test is done by dropping the coated substrates on a concrete floor from 2 m ten times and examining them for cracks. Dye-testing shows if cracking of the dielectric in the respecting tests has occurred.

Layout and geometry are important design aspects that have to be considered when making the heater devices. For customized configurations, often highly uniform temperature distributions have to be attained. In Fig. 15.15, a photograph of a heater sample is shown. It is recommended that the layout of the element should concentrate the density of heating tracks more toward the edges of the substrate, and to cover a large area to spread the heat as much as possible. In addition to the film heater element, a thick-film heat sensor, in the form of a high positive TCR resistor, may also be implemented. The resistor must have high temperature sensitivity and be very stable in its thermal characteristics so that the

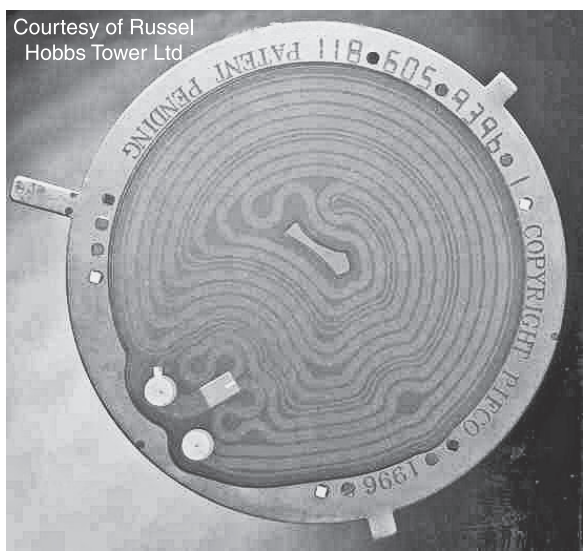

15.15 Heater element insulated stainless steel substrate (reproduced with permission of ESL Europe).

© Woodhead Publishing Limited, 2012

changes produced by temperature variation can be used to control the current flow in the heater element accurately.

As already indicated, it is also possible to use thick-film resistor materials with a high PTC, which enable the fabrication of heater tracks that have self-regulating properties, eliminating the need for external control in some applications (Fig. 15.3b).

An alternative method to apply the dielectric onto a steel substrate by means of screen printing is the transfer tape technology which has been described in section 15.2.1.

Tubular heater

Instant water flow heater

Figure 15.16(a) shows a conventionally manufactured 2.1 kW instant flow heater for washing water. It shows a rather complex assembly that can be replaced by an identical version using thick-film on tube technology shown in Fig. 15.16(b). It is characterized by a rather smart set-up in comparison with the conventionally manufactured element. The design and fabrication aspects of this instant heater in thick-film on tube technology will be described in more detail in the following.

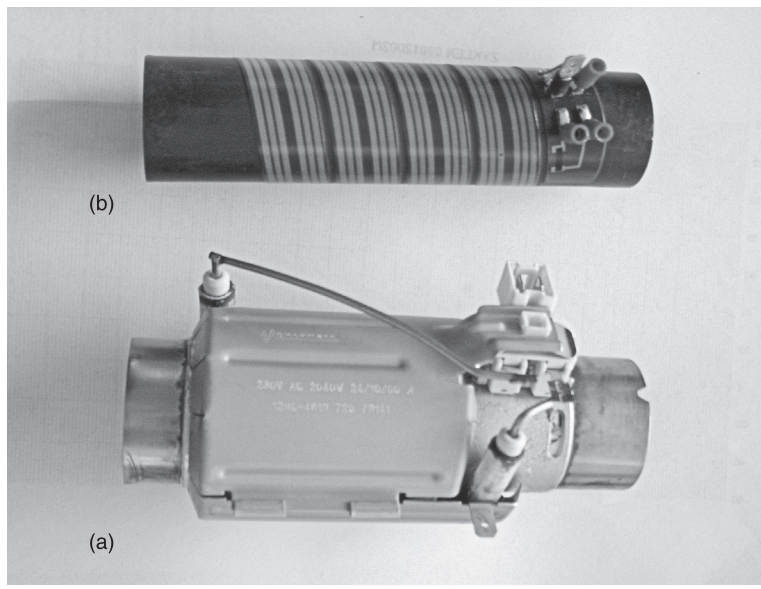

15.16 Photograph of the instant water flow heater (operating power: 2.1 kW) fabricated in (a) conventional and (b) thick-film on tube technology.

© Woodhead Publishing Limited, 2012

The design and arrangement of heater elements on the steel tube and the selection of heater material rely on the results of FEA taking into account a range of boundary conditions. The boundary conditions concern the geometry of the tube and certain limitations referring to the heat flux density at the inner surface of the tube. The respective continuous water heater should be fabricated using a steel tube with a length of 140 mm, a diameter of 40 mm and a wall thickness of 0.8 mm. This tube should be coated over a length of 100 mm with an electrically insulating glass ceramic layer. A maximal heat flux density on the inner surface of the tube must not exceed 16 W/cm^2 in order to avoid proteins in washing water may flocculating and adhering to the tube wall, which ultimately increases thermal resistance between heater and washing medium, resulting in lower heater efficiency.

By means of FEA, the temperature distribution of the tubular heater at different operating conditions can be described by varying the geometrical and electrical parameters of the heater element. For carrying out the numerical simulation, both the characteristic material data and the different heat transfer coefficients responsible for the heat transmission between the tube and the surrounds, as well as the inner wall of the tube and the flowing water, are required. Additionally, the heat transfer coefficient at the inner wall of the tube for an accidental operating condition is requested, referring to the heating up of the tube without any water inside. These thermophysical data have to be derived by application of the relevant relations for the Reynolds-, Prandtl- and mean Nusselt- and Grashof-numbers and using the corresponding material data for water and air (Verein Deutscher Ingenieure, 1994).

Table 15.5 shows the material characteristics of the tube and that of the glass ceramic coating. In Table 15.6 and Table 15.8, material characteristics of water and air are presented. Calculated heat transfer coefficients for the relevant fluid and values for the coefficient of natural convection are summarized in Tables 15.7 and 15.9.

Based on the calculations of the different heat transfer coefficients (Tables 15.7 and 15.9), a mean value of 6400 $W \cdot m^{-2} \cdot K^{-1}$ has been selected for the heat transfer coefficient between the inner wall of the tube and the flowing water and 4.5 $W \cdot m^{-2} \cdot K^{-1}$ for an empty tube. A value of 8.0 $W \cdot m^{-2} \cdot K^{-1}$ has been derived for the heat transfer coefficient for a horizontally aligned tube exposed to free convection.

Table 15.5 Material property data

	Austenitic steel (1.4301)	Glass ceramic
Density ($kg \cdot m^{-3}$)	7900	2230
Thermal conductivity ($W \cdot m^{-1} \cdot K^{-1}$)	16	1.02
Specific thermal capacity ($J \cdot kg^{-1} \cdot K^{-1}$)	500	837
Function	Heating tube (wall thickness: 800 μm)	Insulating layer (thickness: 70 μm)

© Woodhead Publishing Limited, 2012

Table 15.6 Thermophysical data of water

Water	At 20 °C	At 85 °C
Density ($kg \cdot m^{-3}$)	998	968
Thermal conductivity ($W \cdot m^{-1} \cdot K^{-1}$)	0.5984	6.728
Kinematic viscosity ($m^2 \cdot s^{-1}$)	1.004×10^{-6}	0.344×10^{-6}
Flow rate ($m \cdot s^{-1}$)	0.797	0.822
Reynolds-number	31 753	95 581
Prandtl-number	7.001	2.082

Note: For a mass flow rate of water: 1 kg/s.

Table 15.7 Heat transfer coefficient: Tube-water

Heat transfer coefficient (calculated): Tube-water ($W \cdot m^{-2} \cdot K^{-1}$)		
At 20 °C	At 55 °C	At 85 °C
4608	6782	8511

Table 15.8 Thermophysical data of air

Air	At 200 °C	At 420 °C
Thermal conductivity ($W \cdot m^{-1} \cdot K^{-1}$)	36.68×10^{-3}	49.96×10^{-3}
Kinematic viscosity ($m^2 \cdot s^{-1}$)	329.3×10^{-7}	645.1×10^{-7}
Grashof-number	230 111	89 675
Nusselt-number	8.8	6.9

Table 15.9 Heat transfer coefficient: Tube-natural convection

Heat transfer coefficient (calculated): Tube-natural convection ($W \cdot m^{-2} \cdot K^{-1}$)	
At 200 °C	At 420 °C
8.1	8.6

It has been proved that a helically shaped arrangement of heater tracks on the tube yields a more uniform temperature distribution than a serpentine pattern since at the point of the reversing track loop a hot spot may easily develop due to an increased current density, which may finally result in a device failure. A remedy is to overprint this area with a highly conductive paste to avoid hot spot generation. A heating conductor in a helical arrangement has been modeled with 10 turns and a heater track width of 5 mm, whereby between the individual turns a distance of

© Woodhead Publishing Limited, 2012

likewise 5 mm has been provided. If this heater is operated with 2.1 kW, a power density of 32 W.cm^{-2} is attained at the inner tube wall, which exceeds the admissible value of 16 W.cm^{-2}. By means of splitting the heater track in separate small lines that are connected in parallel, the uniformity of the temperature distribution along the tube and the critical heat flux density at the inner tube wall can be improved. As a consequence, the number of turns has to be increased. The influence of the conductor line width and the corresponding split-line configurations on the resulting heat flux density are presented in Fig. 15.17. The spacing between the split tracks is 1 mm and the distance between each turn is 2 mm. The triple split track with the line width dimensions 2.2 mm, 2.0 mm, 2.2 mm, meets very well the requested boundary conditions.

For a caloric heater output in the range of 2.1 kW (230 V AC), a thick-film heater track with an electrical resistance of 25.2 Ω +/− 10% is required. A heater track with a length of 1500 mm and an effective line width of 6.4 mm has to be realized by using a heater conductor paste with a sheet resistance of 100 mΩ/□ to attain the requested caloric output wattage providing a maximal power density of 0.25 W mm^{-2}. The heater line must be arrangend in 12 turns along the tube. Figure 15.18 shows the heating-up performance of the thick-film heater passing through a water flow of 1 l s^{-1}.

Within 30 s, a steady-state temperature situation is attained with a surface temperature of 120 °C at the outer tube wall and an inner wall temperature of approximately 60 °C. Analyzing the temperature distribution along the cross-section

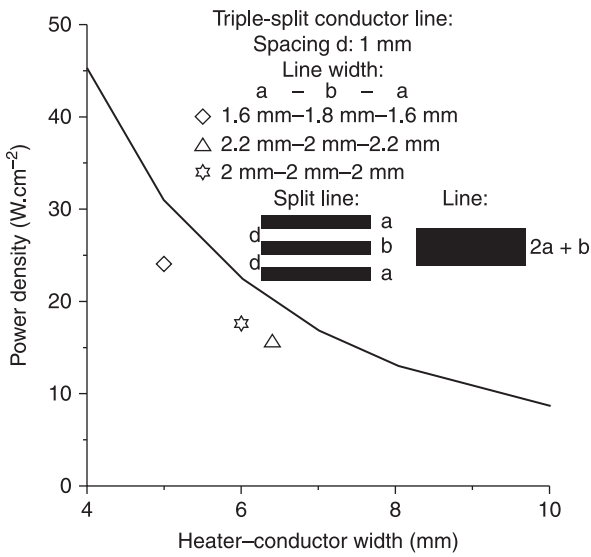

15.17 Dependence of power density on the inside of the tube on the width of applied heater conductor line.

© Woodhead Publishing Limited, 2012

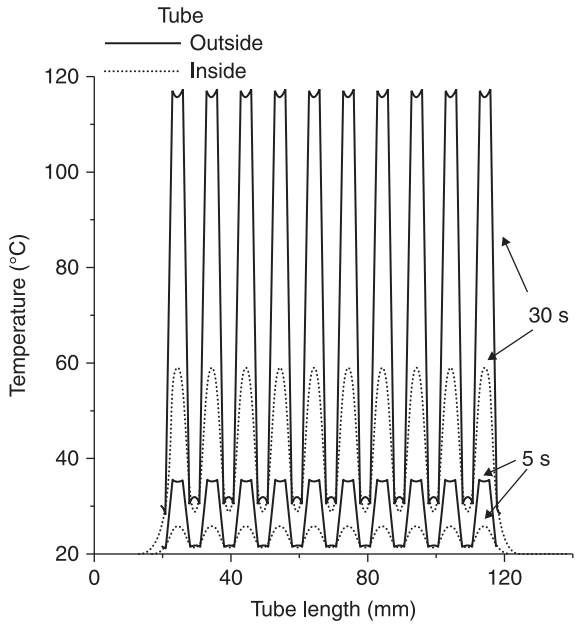

15.18 Heating up of a tube by continuous water flow.

of the tube wall demonstrates the rather high thermal resistance of the glass ceramic insulation. The region of highest temperature is restricted only to the surface of the insulation layer adjacent to the heater. In the catastrophic event that an empty tube is heated up, a tube temperature of 800 °C is also attained within 30 s (Fig. 15.19).

The inner and outer sides of the tube have attained nearly the same high temperature. It becomes evident that for such a catastrophic operating condition the heater has to be equipped, in addition to a temperature sensor, with an appropriate reliable fuse element to avoid potential fire hazards. It must be guaranteed in such a case that the heater is disconnected definitely from the line by means of an appropriate fusible. Such a thermal release can be built into thick-film technology as described in Dennis (1996).

Figure 15.16b shows the heater element completely finished in thick-film technology, using an appropriate tube printing machine. Special attention has to be paid to the uniformity of heating element thickness. Any deviation may affect the temperature distribution uniformity leading also to hot spot formation.

Hot air gun

Another example of a heater fabricated in thick-film on tube technology is a miniaturized hot air gun for joining microparts by adhesive preforms that are

© Woodhead Publishing Limited, 2012

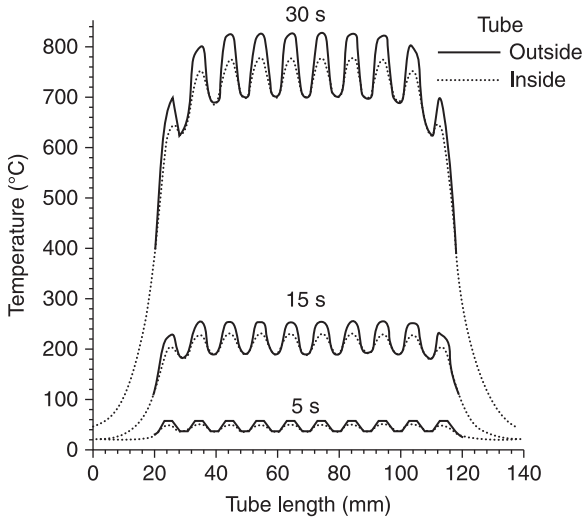

15.19 Heating up of an empty tube.

softened by a hot gas stream (Andrijasevic *et al.*, 2006). The design of this heater is based on the results of FEA.

The set-up consists of a gas tank (technically clean air), a heating tube, a nozzle, a flow meter and connecting pipes. In order to attain a compact set-up, the heating element is realized on a steel tube (inner diameter of 2 mm, outer diameter of 4 mm and length of 120 mm). The heating element is formed helically on the tube as follows: dielectric glass ceramic paste (ESL D-4916) is first applied on the metal tube to provide an electrical insulation function. Then, low resistance (ESL 29115; sheet resistance: 100 mΩ/□) resistor paste is applied in a spiral shape acting as heater track that is covered by an additional glass ceramic layer (ESL D-4916) providing a shock-proof protection. Finally, on the ends of the heater track, a conductive paste (ESL 9695) forms the contact pads. Metal nozzles (CrNiMo), with an inner diameter between 150 µm and 300 µm, are used to focus the gas stream at the targeted point (Fig. 15.20). A peak temperature of 600 °C can be attained on the heating tube applying a heating power of 28.1 W.

The experimentally and numerically derived heating-up characteristic of the temperature on the substrate's surface versus the air-flow and temperature on the heating element is shown in Fig. 15.21 (nozzle diameter 300 µm; distance from nozzle outlet to substrate: 3 mm). At a nozzle–substrate distance of 3.5 mm, the temperature of the air stream drops already significantly because of spreading of the stream and the increasing influence of the environmental factors.

Beside these examples there are other potential applications for heaters on tube. Thick-film heaters on tube may also be used for fabrication of sensors e.g. a calorimetric flow sensor (Güleryüz *et al.*, 2005).

© Woodhead Publishing Limited, 2012

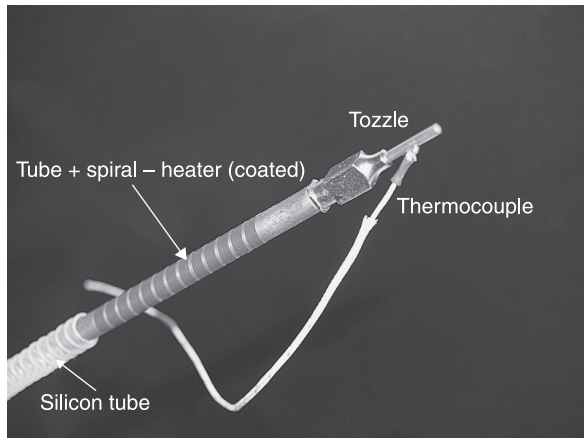

15.20 Photograph of a micro-hot gas gun (partially assembled).

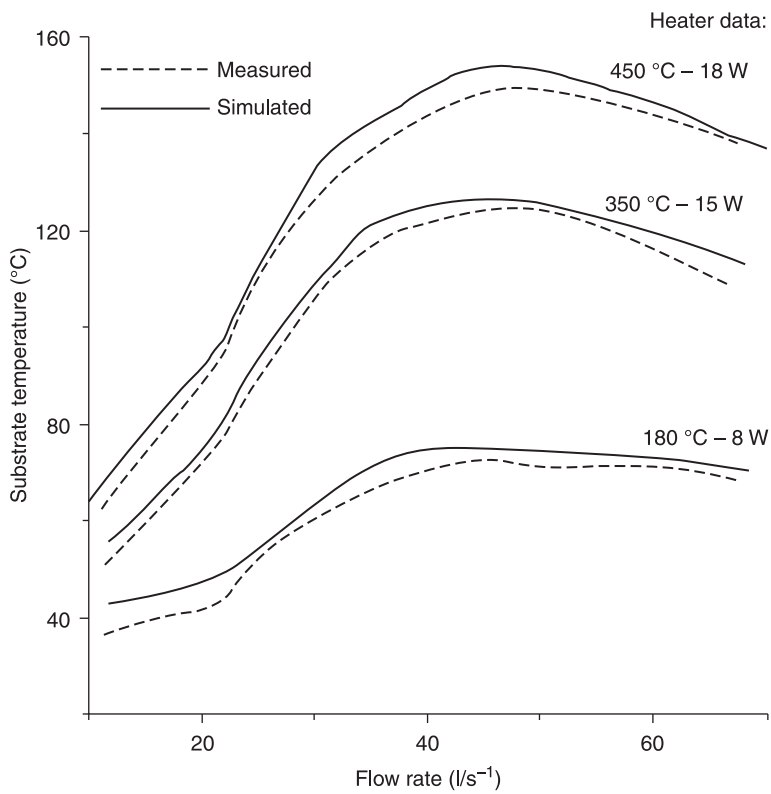

15.21 Substrate surface temperature characteristic vs. air flow rate at varying operating power.

© Woodhead Publishing Limited, 2012

15.4 Heaters for sensor and actuator applications

Micro heaters represent an essential functional part of chemoresistive gas sensors, which are usually fabricated in silicon technology (Afridi *et al.*, 2002; Briand *et al.*, 2000; Kunt *et al.*, 1998; Sberveglieri *et al.*, 1997; Suehle *et al.*, 1993). The heating element must produce an accurate and uniform heating output onto the sensor surface. Silicon hotplates for gas sensors have been known from the beginning of the 1990s. Substrates for gas sensors are made by combining silicon micromachining and thin-film technology. Two types of such sensors exist. Membrane types (or closed membrane type) consist of a silicon frame that carries a thin membrane. In spider-type (or suspended membrane) devices, the hotplate is suspended on four beams. The latter type is more often used due to its easier fabrication process. Metal electrodes are deposited on the top of the membrane. Silicon hotplate gas sensors are characterized by a very low power consumption (0.06–0.25 W), an excellent thermal constant (<200 ms, in extreme cases down to 10 ms) and small dimensions.

These properties suggest that ceramic thick-film gas sensors are not advantageous. Unfortunately, the possibilities for structuring typical alumina substrates are limited. An alternative, realizing thick-film heater elements of small thermal mass on alumina substrates suitable for gas sensor applications, is shown in Lucat *et al.* (2008). It demonstrates the fabrication of free-standing thick-film structures using $SrCO_3$-based-epoxy sacrificial pads, which are overprinted with thick-film paste. After firing, the thick-film structures are released from the alumina substrate by dissolution of the sacrificial pads in an H_3PO_4 aqueous solution. In contrast, ceramic tape materials can be easily structured in the green state. It is well known that, with LTCC technology, small compact sensors can be constructed. Compared with standard devices on alumina, such sensors consume less power due to their lower thermal conductivity (Table 15.3). However, simple replacement of substrate is not sufficient. LTCC offers the possibility to structure unfired tapes easily. Therefore, the sensor substrate may have almost any desired shape. In contrast to standard configuration of thick-film gas sensors on alumina or even on LTCC, the hotplate principle allows a significant reduction in power consumption. The sensors are made by laser structuring of printed and unfired LTCC tapes. It is possible to minimize the power consumption by decreasing the size of hotplate and by reducing the cross-sectional area of the beams.

A hotplate gas sensor is presented by Kita *et al.* (2005), where the small hotplate (3.24 mm^2) is suspended on four beams. Heater contacts and electrodes are deposited on the frame by standard screen printing. The LTCC tapes are laser structured after screen printing. The heaters are made from conventional thick-film Pt-paste (LPA 88-11, Heraeus).

Thickness of the green tape from different suppliers varies between 70 and 300 μm. Structured tapes are stacked, laminated and fired as recommended by the manufacturers. Generally tapes shrink during firing. Due to the shrinkage, the

© Woodhead Publishing Limited, 2012

beam width after firing is between 290 and 310 µm (instead of 400 µm). In the case of zero shrinkage tape, a beam width of about 370 µm is obtained. A deformation of beams is observed after firing. This phenomen goes along with the shrinkage process and the mechanical stress that occurs. But nevertheless there are also tapes available that do not show any deformation after firing.

Although laser cutting enables beams of a width of 200 µm (fired) to be obtained, the comparison of benefits (lower power consumption) and disadvantages (poor mechanicaI stability) indicates that maximal reduction of beam cross-sections is not recommended (Table 15.10).

A further reduction in power consumption may be attained by reducing the hotplate dimensions. A reduction of about 14% in one dimension gives a decrease in power consumption of approximately 25%. Heater elements made up with Pt-pastes have a resistance vs. temperature characteristic that is very close to the platinum characteristics described in the DIN IEC 751 standard. The long-term stability of heater and substrate is as important as the stability of the gas-sensitive layer. An unstable heater can cause an undesired temperature distribution on the hotplate that might lead to decreasing sensitivity and/or selectivity of the gas sensor. The long-term stability testing is performed under typical operating conditions of the structure. The heaters are actively heated up to 400 °C and kept there for 120 hours. Resulting variations in the resistance of heater elements were below 1% during this period. During the stability test no problems with mechanical stability are observed. Neither do the beams break nor temperature gradients cause fractures in the hotplates. Due to the special design of the sensor, the beams remain cold in comparison to the hotplate area. The shape of the beam reduces thermo-mechanical stresses. Pt-heaters have also been proved as suitable devices acting for temperature control of the considered hotplate gas sensor. The platinum heaters are characterized by a high long-term stability that other considered alternative materials, e.g. AgPt, are missing.

Another micro heater for gas sensor applications, which is also built up on a suspended ceramic membrane, is presented. A slightly different processing procedure is applied for the fabrication of the heater element. It is designed and fabricated by combining laser milling techniques and the filling of trenches by screen printing conductive heater paste (Johander *et al.*, 2006). A commercial femtosecond Ti:sapphire laser system is used to perform the micromachining of

Table 15.10 Influence of beam width on power consumption

Beam width (µm)	Power consumption (Tmax = 400 °C) (mW)
300	598
400	617
500	682

© Woodhead Publishing Limited, 2012

the LTCC tape. The heating element is produced by laser machining a serpentine groove with a depth of 45 μm directly into the LTCC-substrate material of 400 μm thickness, and filling the cavity with AuPtPd paste. The releasing operation is first performed by machining the four bridges around the heater in order to minimise the dissipation of the heat in the substrate. Once the releasing step is completed, the thinning of the back face is conducted providing the thermal isolation of heating and sensing elements from the surrounding substrate. As a result of the thinning process, a total of 175 μm of material thickness is removed, resulting in a final substrate thickness of about 225 μm.

The heater positioned on the released membrane reaches a temperature of about 490 °C in 5 s. Because heat is conducted in all directions away from the unmachined heater elements, a circular temperature distribution around the element is observed compared to the angular temperature distribution observed for the released heater element. The temperature is uniform within the released membrane area.

15.4.1 Humidity sensor

A twin heater sytem of hotplate membrane type has been realized on a thin LTCC substrate acting as a functional part of a humidity sensor (Smetana and Unger, 2008). Figure 15.22 shows the model of the thermal conductivity-based humidity sensor where the cap of the device is partially cut off.

The set-up of the humidity sensor comprises two resistor elements on a substrate acting as temperature-sensing devices as well as heaters: one of them serves as the humidity-detecting element, while the other acts as the reference sensor element. The reference sensor element is sealed from the environment ('dry atmosphere' with thermal conductivity (1)) by attaching a ceramic cap, and the humidity-sensing element is exposed to the environment ('vapor atmosphere' with thermal conductivity (2)) where it is enclosed by a perforated ceramic cap.

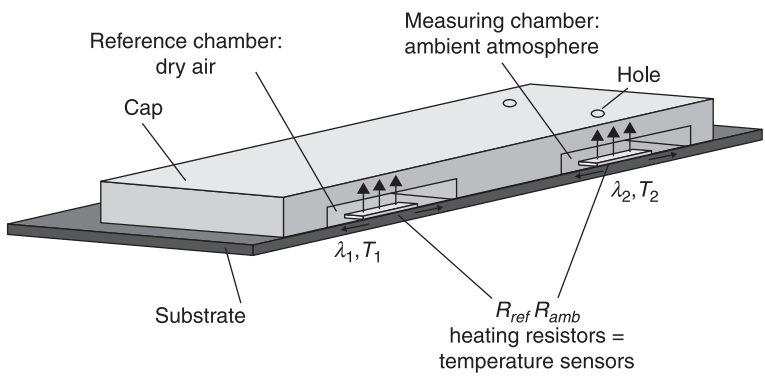

15.22 Schematic of humidity sensor set-up.

© Woodhead Publishing Limited, 2012

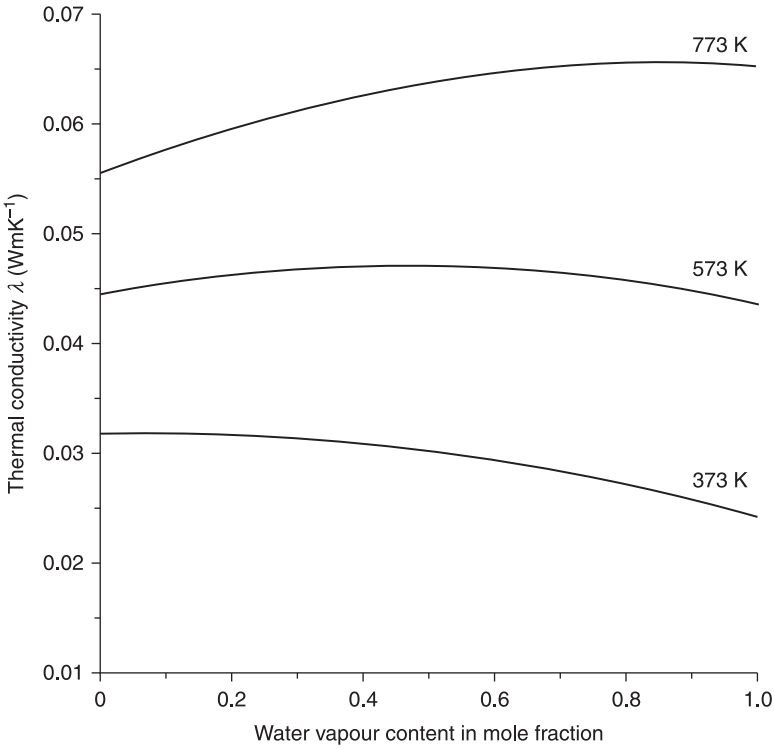

15.23 Thermal conductivity λ_{mix} of air in dependence on water vapour content for different temperatures.

The thermal conductivity of humid air depends strongly on temperature as demonstrated in the graph of Fig. 15.23 (Lindsay and Bromley, 1950). It becomes mandatory to operate the heater-elements of the humidity sensor at a sufficiently high temperature by applying a current pulse in order to achieve a pronounced change of thermal conductivity in dependence on humidity.

Results of numerical simulation have proved that the thickness of the substrate carrying the sensor elements is a crucial parameter with a considerable impact on sensor performance. The temperature difference between both sensor elements increases with decreasing substrate thickness. It contributes to an increase of thermal resistance within the substrate, which consequently impedes a thermal balance between both heater elements. This results in a better signal resolution, lower power consumption and a shorter response time.

In accordance with the results of FEA, a single layer of ESL 41020 tape is used as substrate. After firing in a conventional belt furnace at a peak temperature of 875 °C, the tape shows a lateral shrinkage in the range of 20% where the shrinkage in thickness is negligible. Tape thickness of 114 μm remains nearly constant. The

© Woodhead Publishing Limited, 2012

temperature-sensing elements, which also act as heaters, are fabricated with a commercially available Pt-resinate paste (Heraeus, RP 10003/12.5%) terminated by a silver-rich Pd/Ag-paste (Heraeus, C4140) applied on the fired LTCC-membrane by a conventional thick-film process. The resinate paste is applied by three printing and firing cycles in order to achieve a uniform and sufficient film thickness in the range of 2 μm. The heater elements show a nominal value of 6 Ω ±10% at room temperature. The temperature resistance characteristics of the Pt-sensor elements show a nearly identical linearity and high positive TCR of 0.28%/°C. The heat generated by the resistor elements should be mainly dissipated within the vapor, which bridges the clearance between resistor surface and the coversheet of the cap. The caps of the sensor consist of three laminated layers of ceramic tapes (CeramTec GC). Structuring of tapes (green state) is conducted by laser machining (NdYAG). The frame of the twin cap is established by a single layer of tape, where the enclosure of the caps is formed by two layers of tape. The layers of the sensor cap covering the resistor element R_{ref}, carry two holes providing the permeation of ambient air (Fig. 15.22). With regard to the high operating temperature of the sensor elements and the requirement of gas tightness, the caps are fixed by a reflow glass solder process (ESL 4011C) at a peak soldering temperature of 550 °C onto the substrate.

When current flows through the Pt-resistor elements (R_{ref} and R_{amb} in Fig. 15.22), their temperature T is drastically increased, which results consequently in increased power dissipation. The temperature of the heater element is known by measurement of the resistance change of the Pt-heater material. The heater is warmed up to about 800 K within 200 ms by application of a constant current of 0.55 A; only the gas in the region adjacent to this heater element will quickly be heated up to this temperature and then reach the thermal equilibrium state.

In Fig. 15.24, the courses of temperature differences between the positions of R_{ref} and R_{amb} for different humidity conditions are illustrated. The temperature difference value attained at 300 ms is acting as a measure for the humidity content in atmosphere using a 200 ms duration rectangular current pulse.

Figure 15.25 shows the course of the temperature difference characteristic in dependence on humidity determined by experiment as well as by FE-simulation. The numerically derived characteristic is based on a non-linear FE-simulation model where the temperature dependence of the thermophysical data of vapour, air, Pt and glass ceramic have been considered.

15.4.2 Airbag initiator element

A heater element acting as an airbag initiator element has to meet stringent boundary conditions. In the past few years, the automotive industry has been working on increasing the number of pyrotechnically released safety devices like seat belt pretensioners, side curtain airbags, side bags, inflatable seatbelts, rearseat bags, battery cable cutters, etc. to the point where the energy level required to

© Woodhead Publishing Limited, 2012

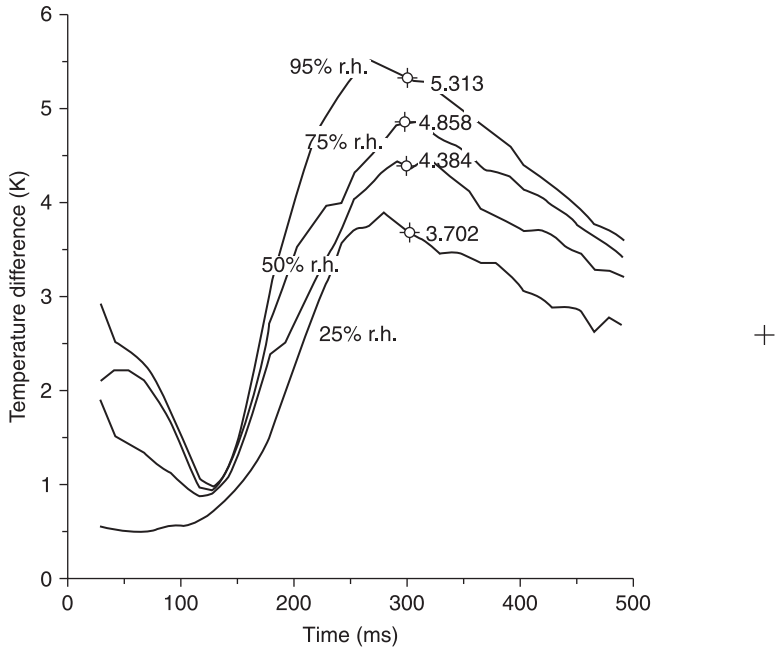

15.24 Course of temperature difference between Pt-heater elements exposed to dry and vapour atmospheres by application of a single current pulse for varying relative humidity (r.h.) levels.

initiate ignition of pyrotechnics has become a very serious cost consideration. Crash sensors in cars induce, in the case of an accident, a current pulse in the resistive initiator element. As the device is heated up to a critical temperature, the explosive detonates and consequently the safety unit of the vehicle will be released.

The realization of reliable low-energy detonators utilizing the traditional bridge wire technology would fail. A wire of a small diameter (<10 μm) would be required. However, due to its small size it can neither be easily handled nor is a sufficient contact area with the pyrotechnic material available to provide efficient heat transfer. Thick-film techniques have already been successfully applied for the realization of miniaturized heating elements for thermal printers (Sato *et al.*, 1993). Similar requirements have to be fulfilled for initiators. Thick-film bridge resistor elements have been proved as a viable alternative that has to be matched to the specific requirements for such pyrotechnical devices (Smetana *et al.*, 2005). Fig. 15.26 shows the thick-film replacement for the bridge wire. In this design, a resistive film bridge element realized onto a glass ceramic-coated alumina substrate is shown. Different resistance values and energy levels are controlled by the pattern etched or laser machined into the metal film. The broad flat surface of the metal film assures maximum contact with the pyrotechnics and the ceramic

© Woodhead Publishing Limited, 2012

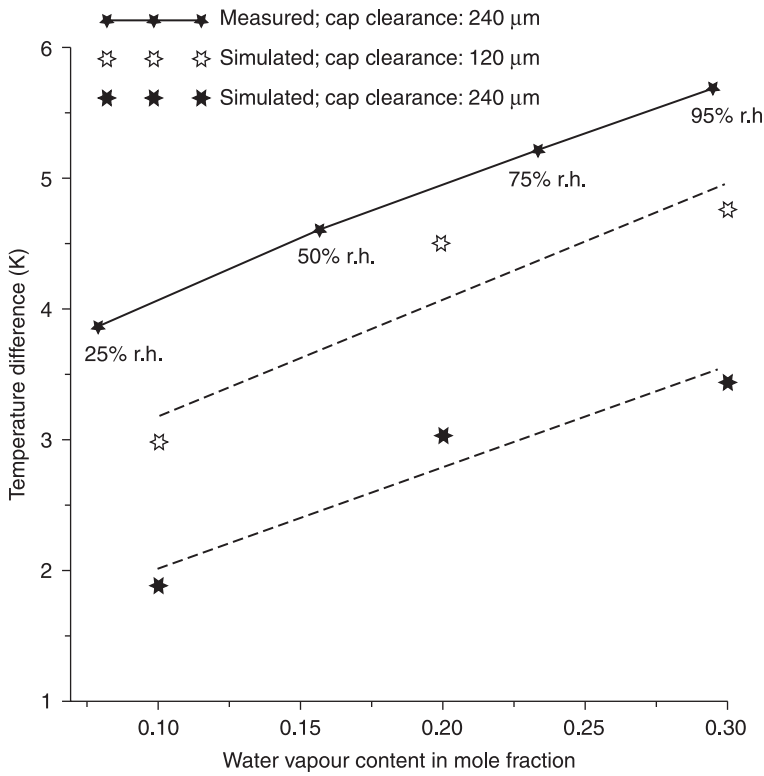

15.25 Characteristic course of temperature difference determined experimentally as well as by numerical simulation at an ambient temperature of 70 °C (343 K). r.h., relative humidity.

substrate provides the mechanical rigidity of the initiator element. The lands of the device are solder or conductive epoxy, bonded with the pins of the package.

The parameters commonly used for describing an electro-explosive device performance are 'no-fire' and 'all-fire' current. To perform a 'no-fire' current test with the bridge element, a constant current is applied for a certain period. The resulting bridge temperature has to remain below the critical temperature of the explosive where ignition occurs. At the 'all-firing' current, the bridge temperature reaches the ignition temperature of the explosive powder. Ignition occurs and the bridge is either destroyed by the reaction or eventually fused (burned open) by the firing current. In Table 15.11, the relevant data for such an initiator element are summarized (Duguet, 1996).

The thermal characteristics of the bridge element have to be adjusted to certain ignition requirements that are also strongly related to the performance of the pyrotechnic material.

© Woodhead Publishing Limited, 2012

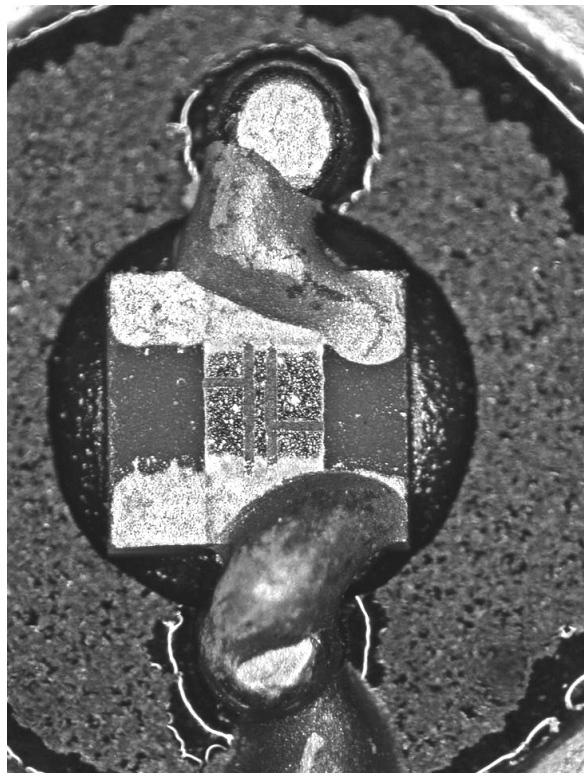

15.26 Photograph of a laser patterned thick-film initiator element.

Table 15.11 Performance data of initiator

Initiator characteristics	
Resistance	2 Ω ± 10%
'No-fire' current/duration	500 mA/10 s
'All-fire' current/response/time	1.2 A/500 μs – 2 ms

Since the miniaturization capability of thick-film resistor dimensions with regard to film thickness is limited, the thermal capacitance of a conventional thick-film resistor element is too high to meet the requested fast response time as well as the required low-power ignition. Basic considerations prove that the conventional type of thick-film resistors is not suitable for this application. But nevertheless, screen-printable resinate pastes are considered to be a viable solution since the attainable film thickness of fired resinate pastes is <1 μm, which enables the realization of devices in the desired performance range. Additionally, a glass

© Woodhead Publishing Limited, 2012

ceramic layer has to be applied onto the alumina substrate acting as heat barrier, which improves the heating up rate of the device significantly.

The performance of such heating elements as a bare (uncoated) element has been analysed by FEA, as well as the final version of the device where the element is coated with the explosive. This additional layer contributes to a significant heat removal from the surface of the element. The applied explosive is a $Sb/KMnO_4$ pyrotechnic powder with an ignition temperature of 233 °C.

Materials' property data to be considered for numerical simulation are summarized in Table 15.12 (Beck and Brown, 1983; Berry *et al.*, 1968; Lide, 1992–1993; Powell and Liley, 1972).

Based on the theoretically derived model, thick-film initiator elements have been realized with a commercially available Au-resinate paste (Heraeus, RP 20003/236) terminated with a silver-rich Pd/Ag-paste (Heraeus, C4140) applied on a glass ceramic (Heraeus, IP 211)-coated conventional 96% Al_2O_3 substrate (CeramTec, RUBALIT 708S), where the coating-layer is acting as a heat barrier. After a drying and firing procedure, a resistive film with a thickness of 0.2 μm has been attained.

A series of tests with initiator samples were carried out including both normal firing and sub-threshold current levels. The hottest areas of bare initiator elements have been determined experimentally by means of increasing the applied current and/or the pulse duration until fusing of resistor material occurred. Unlike the results attained by numerical simulation, fusing starts at either of the termination ends of the experimental resistors (Fig. 15.27), and not in the center of the resistor path. The reason for this effect must be related to diffusion induced by sintering the termination pads that are overlapping resistor path (Abdurakhmanov and Vakhidova, 1995).

These diffusion zones at the termination ends of the resistor element can be determined optically by a distinct colouring different from that of the bulk material (Fig. 15.27). The length d of this zone extending from the termination pads, which are related to diffusion, amounts to 100 μm. A theoretical evaluation has proved

Table 15.12 Materials' property data

	Al_2O_3	Glass ceramic	Au	Ag	$Sb/KMnO_4$
Density ($kg \cdot m^{-3}$)	3780	2230	19300	10500	2070
Thermal conductivity ($W \cdot m^{-1} \cdot K^{-1}$)	16	1.02	317	429	0.3
Specific thermal capacity ($J \cdot kg^{-1} \cdot K^{-1}$)	800	837	129	235	506
Resistivity (Ωm)	1×10^{18}	2×10^{13}	2.5×10^{-8}	1.617×10^{-8}	–
Thickness (μm)	200	40	0.2	15	200
Function	Substrate	Heat barrier	Resistor	Termination	Explosive

© Woodhead Publishing Limited, 2012

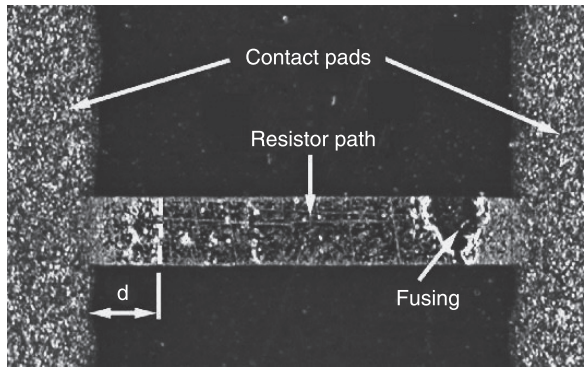

15.27 Photograph of fused initiator element (diffusion zone d: 100 μm).

this assumption: the Ag-concentration profile in the resistor element is calculated applying the second Fick's law. Based on the resultant concentration profile and the resistivity vs. concentration data reported in the literature (Berry *et al.*, 1968, pp. 306–307), it is possible to calculate the resistivity profile of the diffusion zone.

In a very restricted region of the diffusion zone near the termination pad the resistivity peak may induce a hot spot. But this zone is too small to provide a reliable ignition of the explosive. Consequently, it is necessary to generate an area of higher resistance within the resistor element exceeding the peak resistance value of the diffusion zones.

A modified model of the initiator element, comprising a contraction (Fig. 15.28), covered by the $Sb/KMnO_4$ explosive, has been designed for

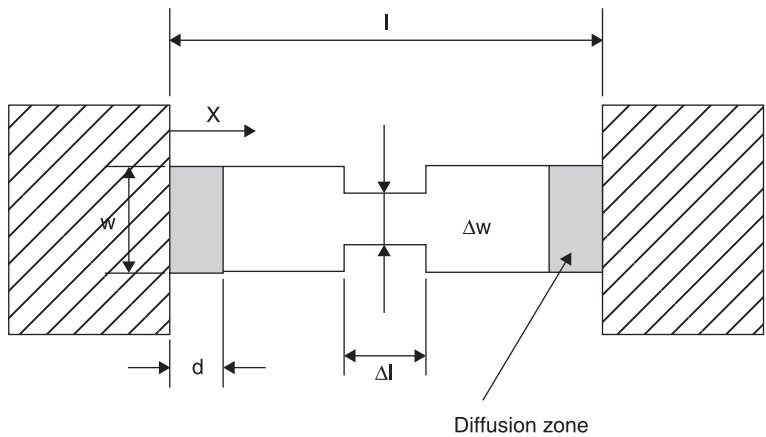

15.28 Adapted model of initiator element (dimensions: l = 900 μm, w = 100 μm, d = 100 μm, Δl = 500 μm, Δw = 60 μm, t = 0.2 μm, resistor value: 2 Ω).

© Woodhead Publishing Limited, 2012

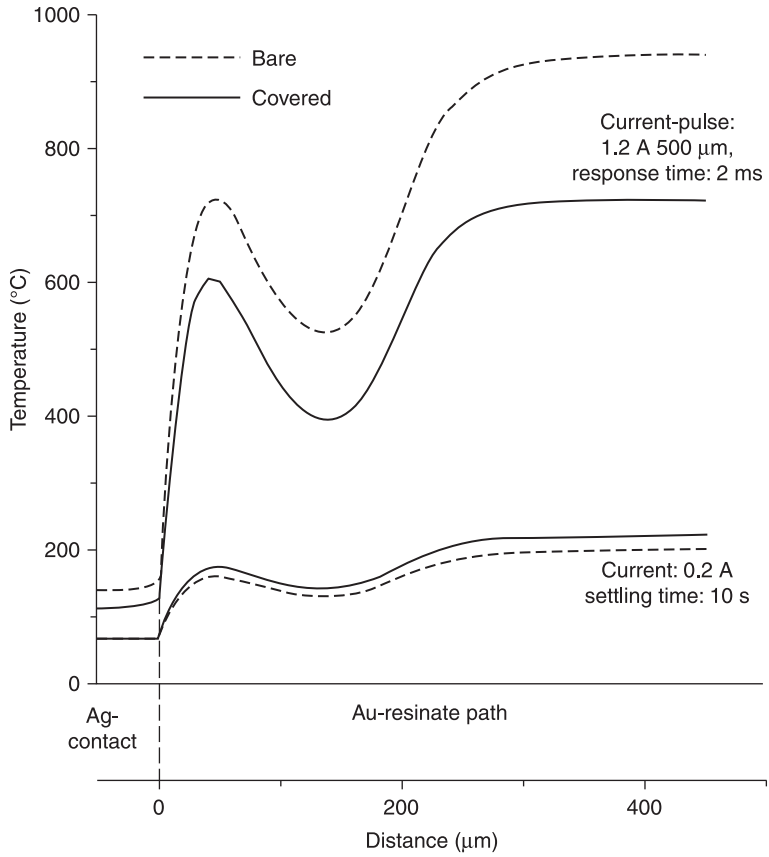

15.29 Temperature distribution of the modified initiator element with contraction zones without explosive as well as covered by explosive, reflecting the two different operation modes.

numerical analysis where the above-mentioned material diffusion effect has been taken into account.

The results of numerical temperature distribution analysis are shown in Fig. 15.29. A nearly uniform temperature level already exceeding the peak temperature of the diffusion zone at a settling time of >50 μs is attained in the area of reduced resistor width. It has been provided that the area of peak temperature is always encountered in the center of the resistor element, exceeding the melting temperature of Au at the moment of fusing within a settling time of 2 ms.

With regard to the small lateral dimensions of the device, the conventional thick-film process must be appropriately adapted to the miniaturization requirements. A rather large Au-path is printed and the final structure with the area of contraction is formed by laser machining (Kripesh *et al.*, 2000), a procedure similar to the trimming

© Woodhead Publishing Limited, 2012

process of conventional thick-film resistors (Fig. 15.26). Actual experiments with the explosive have proved the functionality of the initiator element.

15.5 Conclusion

Examples of different heater elements fabricated by screen printing have been examplarily demonstrated. A combination of different thick-film and substrate materials enables the development and fabrication of new and innovative heater elements that meet specific thermal requirements. Thick-film heaters still show an emerging potential due to the introduction of new materials. LTCC-technology especially offers new areas of application for thick-film heaters. LTCC-technology provides the potential of creating 3D-microsystems where miniaturized thick heater elements may be implemented acting as a functional part of a device for biological and/or chemical analyses, as well as for sensor and actuator systems (Gongora-Rubio *et al.*, 2001; Güleryüz and Smetana, 2005; Malecha *et al.*, 2009).

15.6 References

Abdurakhmanov G. R. and Vakhidova G. S. (1995), 'Diffusion and electrical conductivity of thick-film resistors', *Technical Physics*, 40 (7), 735–737.

Afridi M. Y., Suehle J. S., Zaghloul M. E., Berning D. W., Hefner A. R. *et al.* (2002), 'A monolithic CMOS microhotplate-based gas sensor system', *IEEE Sensors Journal*, 2, 644–655.

Andrijasevic D., Giouroudi I., Smetana W., Boehm S., Zehetner J. *et al.* (2006), 'New approach to micro-joining by hot gas stream', *Microelectronic Engineering*, 83 (4–9), 1445–1448.

Baumbach P., Stein M. A., Tait R. and Whitmarsh J. (1990), 'Materials, substrates and designs for manufacturing heaters using thick-film technology', *Proceedings of the 1990 ISHM Conference*, Chicago, USA, pp. 699–705.

Beck M. W. and Brown M. E. (1983), 'Thermal analysis of antimony/potassium permanganate pyrotechnic compositions', *Thermochimica Acta*, 65 (2–3), 197–212.

Berry R. W., Hall P. H. and Harris M. T. (1968), *Thin Film Technology*, Van Nostrand Reinhold, New York, pp. 306–307.

Briand D., Krauss A., van der Schoot B., Weimar U., Barsan N. *et al.* (2000), 'Design and fabrication of high-temperature micro-hotplates for drop-coated gas sensors', *Sensors and Actuators B*, 68, 223–233.

Buchanan R. C. (2004), *Ceramics Materials for Electronics*, Third Edition, Marcel Dekker Inc., New York, pp. 539–542.

Datasheet Heraeus Quarzglas (2009), 'Base materials'. Available from: www.base-materials.heraeus-quarzglas.com

Dennis G. (1996), 'A thermal fuse', WO Patent 9603761.

Duguet J. R. (1996), 'Electro-pyrotechnical initiator', US Patent, 5, 544–585.

Eisermann E., Höll K., Smetana W., Tusler W., Unger M. *et al.* (2009), 'Comparison of low cost, insulated aluminium substrates used as integrated heat sinks with conventional technology', *Microelectronics International*, 26, 2:3–2:9.

Gilleo K. (1996), *Polymer Thick-film*, Van Nostrand Reinhold, New York, pp. 118–119 and 303.

© Woodhead Publishing Limited, 2012

Gongora-Rubio M. R., Espinoza-Vallejos P., Sola-Laguna L. and Santiago-Aviles J. J. (2001), 'Overview of low temperature cofired ceramics tape technology for meso-system technology (MsST)', *Sensors and Actuators A*, 89, 222–241.

Güleryüz D. and Smetana W. (2005), 'Mass flow sensor realized in LTCC-technology', *Proceedings of 29th International Conference of IMAPS*, Koszalin-Darlowko, Poland, pp. 373–376.

Güleryüz D., Smetana W., Homolka H., Mündlein M. and Unger M. (2005), 'Aspects concerning the optimization of a calorimetric flow sensor built up in thick-film technology', *Proceedings of 28th ISSE*, Wr. Neustadt, Austria, pp. 370–376.

Hrovat M., Belavic D., Smetana W., Homolka H., Reicher R. *et al*. (2001), 'Thick-film resistors on steel substrates', *Proceedings of 37th International Conference on MIDEM*, Bohinj, Slovenia, pp. 249–254.

Imanaka Y. (2004), *Multilayered Low Temperature Cofired Ceramics (LTCC) Technology*, Springer, New York, pp. 105–110.

Johander P., Goenaga I., Gomez D., Moldovan C., Nedelcu O. *et al.* (2006), 'Design and manufacturing of micro heaters for gas sensors', *Proceedings of 4M2006 2nd International Conference on Multi-Material Micro Manufacture*, Grenoble, France, pp. 117–122.

Kita J., Rettig F., Moos R., Drüe K. -H. and Thust H. (2005), 'Hot plate gas sensors – are ceramics better?', *International Journal of Applied Ceramics Technology*, 2 (5), 383–389.

Kripesh V., Gust G., Bhatnagar S. K. and Osterwinter H. (2000), 'Effect of Nd:YAG laser micromachining on gold conductor printed over ceramic substrates', *Materials Letter*, 44, 347–351.

Kumagai M., Maeda E. and Ogasahara K. (1993), 'High thermal conductivity AIN substrate and its metallized products', *Kawasaki Steel Technical Report*, 28, 34–37.

Kunt T. A., McAvoy T. J., Cavicchi R. E. and Semancik S. (1998), 'Optimization of temperature programmed sensing for gas identification using micro-hotplate sensors', *Sensors and Actuators B*, 53, 24–43.

Levitsky M. E., Flick S. and Malanga D. (1999), 'A cofireable dielectric on stainless steel thick-film material system for automotive applications', *Proceedings of the 1999 International Conference of IMAPS*, Chicago, USA, pp. 112–117.

Lide D. R. (1992–1993), *CRC Handbook of Chemistry and Physics*, CRC Press, pp. 12–34, 12–35 and 12–130.

Lindsay A. L. and Bromley L. A. (1950), 'Thermal conductivity of gas mixtures', *Journal of Industrial and Engineering Chemistry*, *42*, 1508–1510.

Lucat C., Ginet P., Castille C., Debéda H. and Ménil F. (2008), 'Microsystems elements based on free-standing thick-films made with a new sacrificial layer process', *Microelectronics Reliability*, 48, 872–875.

Malecha K., Pijanowska D. G., Golonka and Torbiczb W. (2009), 'LTCC microreactor for urea determination in biological fluids', *Sensors and Actuators B*, 141, 301–308.

Powell C. Y. and Liley P. E. (1972), 'Thermal conductivity of the elements', *J Phys Chem Ref Data*, 1(2), 340 and 395.

Sato K., Watanabe M. and Seino T. (1993), 'Development of a thick-film print head for full color video printer', *International Journal of Microcircuits and Electronic Packaging*, 2, 145–160.

Sberveglieri G., Hellmich W. and Muller G. (1997), 'Silicon hotplates for metal oxide gas sensor elements', *Microsystem Technologies*, 3, 183–190.

Smetana W. and Unger M. (2008), 'Design and characterization of a humidity sensor realized in LTCC-technology', *Microsystem Technologies*, 14, 979–987.

© Woodhead Publishing Limited, 2012

Smetana W., Reicher R. and Homolka H. (2005), 'Improving reliability of thick-film initiators for automotive applications based on FE-analyses', *Microelectronics Reliability*, 45, 1194–1201.

Stein S. J., Huang C. and Cang L. (1981), 'Possibilities for air fireable base metal conductors', *Electrocomponent Science and Technology*, 8, 159–165.

Stein S. J., Wahlers R., Heinz M. and Stein M. A. (1995), 'Thick-film heaters made from dielectric tape bonded stainless steel substrates', *Proceedings of 30th International Conference of IMAPS*, Los Angeles, USA.

Steinbrück H., Sridharan S., Svanbom P., Brown O., Ringler S. *et al.* (2005), 'Thick-film heated oven with low energy consumption', *Proceedings of the 20th International Enamellers' Congress*, Istanbul, Turkey, pp. 1–9.

Suehle J. S., Cavicchi R. E., Gaitan M. and Semancik S. (1993), 'Tin oxide gas sensor fabricated using cmos micro-hotplates and in-situ processing', *IEEE Electron Devices Letters*, 14, 118–120.

Tait R. B., Humphries R. and Lorenz J. (1994), 'Thick-film heater elements and temperature sensors in modern domestic appliances', *IEEE Transactions on Industry and Applications*, 30 (3), 573–577.

Vanek J., Smetana W., Weilguni M. and Szendiuch I. (2009), 'Characterization of PTC resistor pastes applied in LTCC technology', *Proceedings of 17th EMPC*, Rimini, Italy, pp. 1–5.

Verein Deutscher Ingenieure (1994), *VDI-Wärmeatlas: Berechnungsblätter für den Wärmeübergang*, VDI-Verlag.

Zoppas Industries (2003), 'R&D Bulletin, Thick-film technology'. Available from: http://portal.zigroup.net/docsites/products/thick_film.pdf

© Woodhead Publishing Limited, 2012

16

Screen-printing for the fabrication of solid oxide fuel cells (SOFC)

C. PIJOLAT, École Nationale Supérieure des Mines, France

Abstract: This chapter is focused on current development efforts in the field of fuel cells (FCs). After an introduction on the principle of FCs, the relevance of screen-printing to solid oxide fuel cells (SOFCs) developments is pointed out. The main part of the chapter is devoted to the use of screen-printing for material elaboration with a large difference between electrolytes and electrodes: it is necessary to obtain thin and dense layers for electrolytes; conversely, for electrodes (anodes and cathodes) the challenge lies in getting thick and porous layers. Special applications are presented in the last part of the chapter with micro SOFCs on silicon membranes, and also the highly challenging concept of single-chamber SOFCs.

Key words: screen-printing, fuel cells, SOFCs, micro SOFCs, single chamber.

16.1 Introduction

Fuel cells (FCs) have long been studied; however, environmental concerns have increased research and development efforts in this field. The first part of this chapter introduces FCs, and discusses the advantages and challenges of solid oxide fuel cells (SOFCs) and the relevance of screen-printing in these developments (the main focus of this chapter). The second part of the chapter concentrates on screen-printing for electrolyte materials, especially yttrium-stabilized zirconia (YSZ) and the difficulties in obtaining good materials with a high degree of densification. Screen-printing is well suited to the realization of SOFC electrodes. The electrodes (anodes and cathodes) are described in the third part of the chapter. The potential of screen-printing will be demonstrated for the large range of thicknesses and porosities that can be obtained. Regarding applications, two types of SOFC device are presented: micro-SOFCs realized by screen-printing on silicon membranes; and single-chamber SOFCs – a highly challenging concept but one well suited to screen-printing fabrication.

16.2 Fuel cells: principle, types and challenges (Hoogers, 2003; Larminie, 2000)

All types of FC are based on the same principle: to use two electrochemical reactions produced at two electrodes (anode and cathode) involving a common ion that is transported from one electrode to the other one by an electrolyte media. This well-known and simple system is the inverse system of the water electrolysis:

© Woodhead Publishing Limited, 2012

$$2H_2 = 4H^+ + 4e^- \text{ (anode)}$$

$$O_2 + 4e^- + 4H^+ = 2H_2O \text{ (cathode)}$$

On the basis of thermodynamic equations, the electrical potential created in this case is:

$$E \text{ equilibrium} = -\Delta G/nF = 1.23 \text{ Volts}$$
(with $\Delta G = -285$ kJ/mole at 25 °C and under 1 Atm).

This generated potential is obtained without current (OCV: open circuit voltage) and decreases rapidly with increasing current. There are many couples of electrochemical reactions that can be used for FCs. The following OCVs depend then on the thermodynamic data of these electrochemical systems. Among the main systems, we can separate the FCs into two groups according to their electrolyte, i.e. liquid or solid. The main FCs with liquid electrolytes are the alkaline fuel cell (AFC), used for example in the past for the Apollo program, the phosphoric acid fuel cell (PAFC) and the molten carbonate fuel cell (MCFC), which are all used for large energy plants (up to MW capacity). For solid electrolytes, there are two well-known types: the proton exchange membrane fuel cell (PEM-FC) and the SOFC. The PEM-FC uses a polymer as the electrolyte to transport protons (H^+) and consequently works up to 100–150 °C. The SOFC uses a ceramic material as the electrolyte to transport oxygen ions (O^{2-}) from the cathode to the anode. Taking into account the electrical conductivity of such electrolyte materials, SOFCs can be exploited at high temperatures, typically near 800 °C. This is a big advantage over PEM-FCs because the totality of the energy can be used (electricity + heat) and consequently the yield of the SOFC can theoretically be maximum (near 100%), in comparison to the yield loss with PEM-FCs due to the necessity of cooling the system in order to avoid the destruction of the polymeric membrane. The following parts of this chapter will be dedicated only to SOFCs (Fergus, 2009; Singhal, 2003).

To understand the challenges for SOFC development, it is important to have in mind the characteristic I–V (current-voltage) of a fuel cell (Fig. 16.1).

When the FC is connected to a load resistance to produce a current, the voltage decreases rapidly from the OCV level with increasing current. This is the result of three main phenomena: activation losses, ohmic losses and transport losses. The activation losses are mainly due to the charge transfer and they are especially present in PEM-FCs (as on Fig. 16.1) at low temperature. This is one of the advantages of SOFCs in comparison to PEM-FCs: the high temperature in SOFCs avoids these activation losses and the curve I-V is practically horizontal (at OCV level) in this range of low current. Charge transfers include several phenomena that are mainly governed by the quality of the electrode, especially the catalytic activity (role of temperature) and the quality of the electrical contacts. The second type of losses is related to the ohmic resistance of

© Woodhead Publishing Limited, 2012

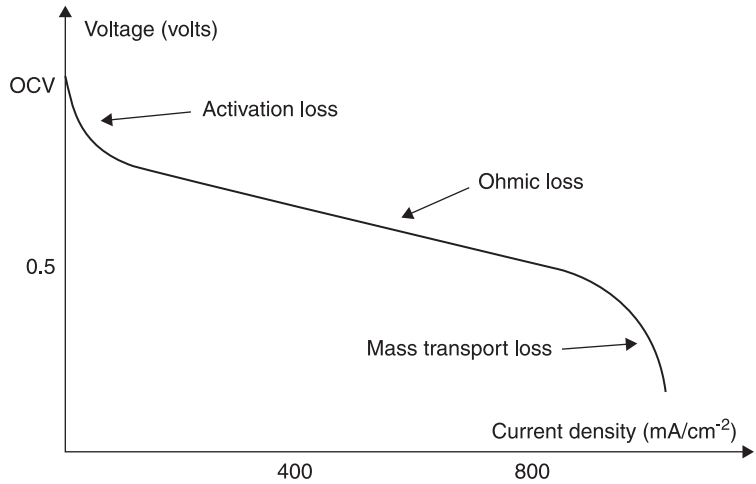

16.1 Typical performance (current–voltage) of a PEM-FC with the main voltage loss.

the electrolyte. These ohmic losses are controlled by the conductivity value and consequently high conductivity is required to reduce the ohmic resistance. In this sense, PEM-FCs are more attractive than SOFCs. This constitutes the second big challenge of SOFCs: to develop oxygen ionic conductors with high conductivity, so to have dense ceramic membranes. The third type of losses is due to the transport of the chemical species (gases) to their reaction point. For the high current, there are difficulties in keeping good concentrations of the reactant species. Because this limitation is due to the diffusion of gases in the electrodes, the third challenge will be to control the good porosity of these electrodes, but also keep good electrical properties (in relation to the charge transfers). To summarize the requirements for SOFCs:

- *Electrolyte*: pure ionic conductor for O^{2-} (no electronic conduction), high conductivity, dense material in order to avoid gas diffusion from one electrode side to the other one, stable material under both oxidizing and reducing atmospheres. Typical material: YSZ.
- *Anode*: mixed conductor (ionic and electronic), porous material with a high number of triple points, high catalytic activity for hydrogen (or hydrocarbon HC) dissociation and reaction with O^{2-} to produce water (H_2O), stable in reducing gases. Typical material: nickel oxide (NiO) (mixture with YSZ).
- *Cathode*: mixed conductor (ionic and electronic), porous material with a high number of triple points, high catalytic activity for oxygen (or air) dissociation and transfer O^2 to electrolyte, stable in oxidizing gases. Typical material: lanthanum strontium manganite (LSM).

© Woodhead Publishing Limited, 2012

16.3 Electrolytes

SOFCs present the advantage of allowing the co-generation of electrical and thermal production. The catalytic reactions are sufficiently exothermic to heat the FC system to high temperatures for all types of FCs. In the case of PEM-FCs, the presence of the polymer membrane means that the system has to be cooled to under 150 °C and then lose a part of the available energy. This is not the case with SOFC and the catalytic reactions at electrodes allow for reaching high temperatures near 850 °C. Nevertheless, this advantage also presents the difficult problem of sealing between the two compartments at the anode and cathode. The sealing is critical in regards to the explosion risk if there are gas leaks from one electrode cell to the other one. They are also many other problems at high temperatures, i.e. the sintering of the electrodes, the thermal expansion coefficients and the chemical diffusions in materials. All of them contribute to a rapid degradation of performance. To solve or reduce these problems, the current challenge is to develop SOFCs that are able to work at lower temperatures, for example near 600 °C or below, and which are called intermediate temperature SOFCs (IT-SOFCs). The new challenge is to keep good electrical conductivities under these lower temperatures. This can be achieved with new ionic electrolytes or with a decrease in the thickness for conventional materials such as YSZ.

The best known ionic conductor for O^{2-} is YSZ (ZrO_2 stabilized with Y). This material has been widely used for oxygen sensors or ceramic membranes for filtration and reactors (Kang, 2007). It is no problem to produce porous thick-films using different methods or dense pellets, but it is more difficult to produce the dense YSZ films that are required for SOFCs. The general trend now is to realize the thick-films on porous electrodes that act as support for the electrolyte deposition. There are many publications dealing with the fabrication and use of porous NiO-YSZ anodes for SOFC substrates (Fukui *et al.*, 2003). An example of supported SOFCs on such porous anodes can be seen in Fig. 16.2(b) (Ge *et al.*, 2006). This publication deals with the fabrication of the YSZ film using the screen-printing technique. As outlined previously, the difficulty is to obtain dense films by screen-printing. The authors reported good performances for sintering at 1400 °C. The quality of the YSZ surface can be observed in Fig. 16.2(a).

The influence of the starting powder for the quality of screen-printed YSZ films for SOFC electrolyte is also reported (Zhang, Y. *et al.*, 2006). In all cases, the performance of the SOFC devices depends on several parameters of the electrolyte films. A typical characteristic of I-V curves is reported in Fig. 16.3 with the influence of the YSZ thickness (Moon *et al.*, 2006).

We can observe a decrease of the powder density ($P = V \times I$) by a factor of 4 when the YSZ thickness changes from 5 to 20 μm. This is a good illustration of the interest in thinner electrolyte films. These results are directly related to the values of electrical conductance of the electrolyte films. We can see that similar

© Woodhead Publishing Limited, 2012

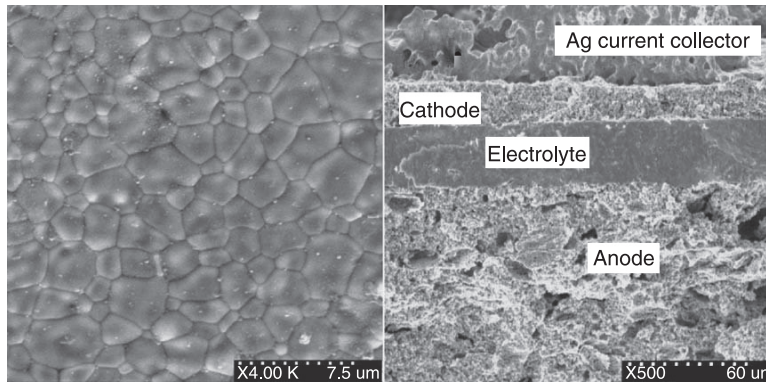

16.2 SOFC obtained by screen-printing – (a) surface of YSZ thick-film; (b) cross-sectional view of the fuel cell LSM (cathode)/YSZ (electrolyte)/Ni-YSZ (anode support) (Ge *et al.*, 2006).

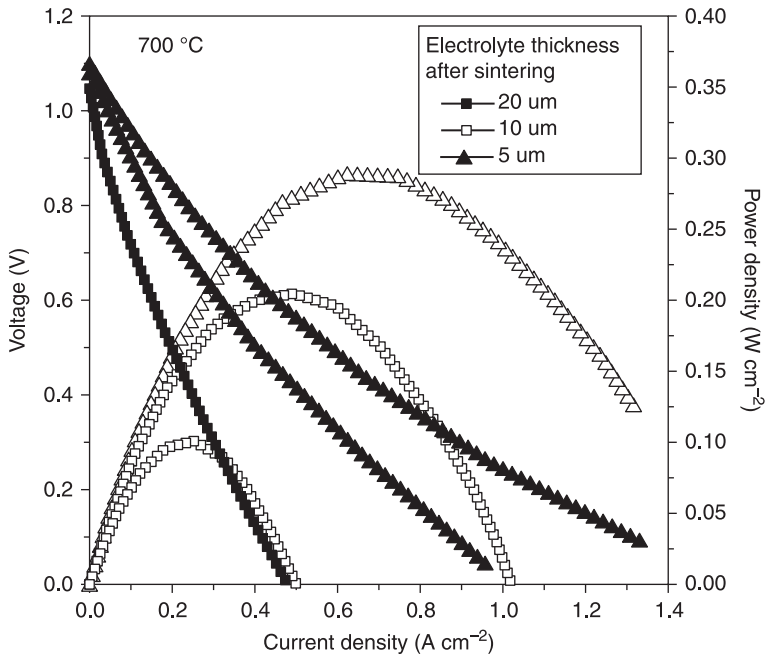

16.3 Influence of electrolyte thickness (5, 10 and 20 μm YSZ) on I-U characteristics with a SOFC fuel cell LSM-YSZ/YSZ/Ni-YSZ realized by tape casting (LSM and YSZ) on anode support (Moon, 2006).

© Woodhead Publishing Limited, 2012

decreases of power density are also obtained with the temperature (factor 5 from 850 to 650 °C). Of course, screen-printing is not the only way to produce electrolyte thick-films. Many other techniques have been reported, such as tape casting, slip-casting, or electrophoretic deposition (EPD), and also for thinner films by chemical vapour deposition (CVD) or PLD. The previous results on Fig. 16.3 have been obtained with YSZ tape-casting films. Very dense materials can be obtained as reported in Fig. 16.4 for slip-cast films (Wanzenberg *et al.*, 2003) or in Fig. 16.5 for EPD (Homosi *et al.*, 2007).

Note that Fig. 16.5 is a very good illustration of the typical structure of a SOFC with a thin (3 μm) and very dense electrolyte and the two electrodes, which are

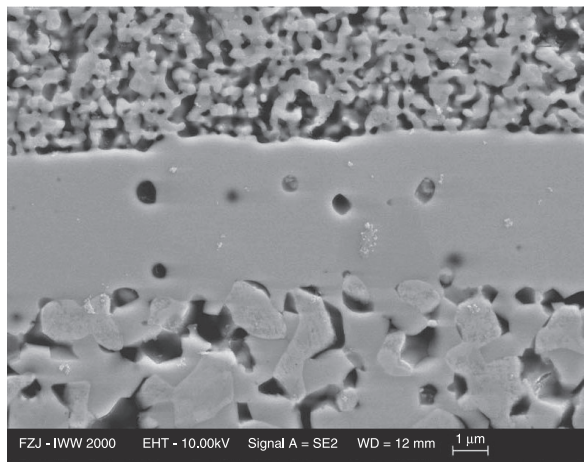

16.4 Example of very dense YSZ electrolyte obtained by slip-casting (Wanzenberg *et al.,* 2003).

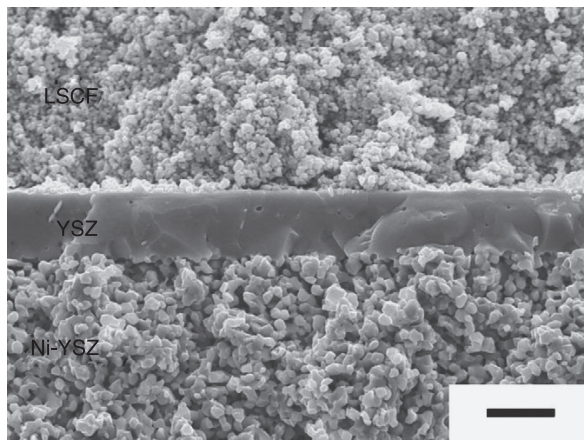

16.5 Example of a dense 5 μm YSZ electrolyte obtained by electrophoretic deposition (Hosomi *et al.,* 2007).

© Woodhead Publishing Limited, 2012

thicker (generally near 100 μm) in order to increase the surface for reaction, and very porous in order to keep good diffusion of gases.

As has been explained previously, for long-term stability and technical developments, the current trend is to reduce the operating temperature of SOFCs. In this sense, CeO_2-based oxides are among the best materials to replace YSZ for IT-SOFCs (Steele, 2000; Xia and Liu, 2001). Electrolytes such as Sm-doped Ceria (SDC) or Gd-doped Ceria (CGO) present better conductivity than YSZ in the range of intermediate temperature. Moreover, these materials have a thermal expansion coefficient that is closer to that of Ni-based substrates (anode supports). This parameter is always very important for the long-term stability of complete SOFC stacks. Nevertheless, these materials are stable in reducing atmosphere only below 600 °C. Above this temperature, these electrolytes lose the characteristic of pure ionic conduction to become mixed conductors with the appearance of electronic conduction. As for YSZ film elaboration, many deposition techniques can be used for Ceria-doped thick-films. Screen-printing is always used with good results, as illustrated in Fig. 16.6 (Zhao *et al.*, 2008). Of course, there are several other materials which are studied as electrolytes. We can report for example, the perovskyte-type materials like LSGM ($La0.9Sr0.1Ga_{0.8}Mg_{0.2}O_{3-d}$) (Pena-Martinez *et al.*, 2006) or composites materials like bi-layers SDC-YSZ prepared by screen-printing (Zhang, X. *et al.*, 2006). Such bilayer electrolytes are also prepared by pulse laser deposition (PLD) in order to reduce the electrolyte thicknesses (Cho *et al.*, 2011).

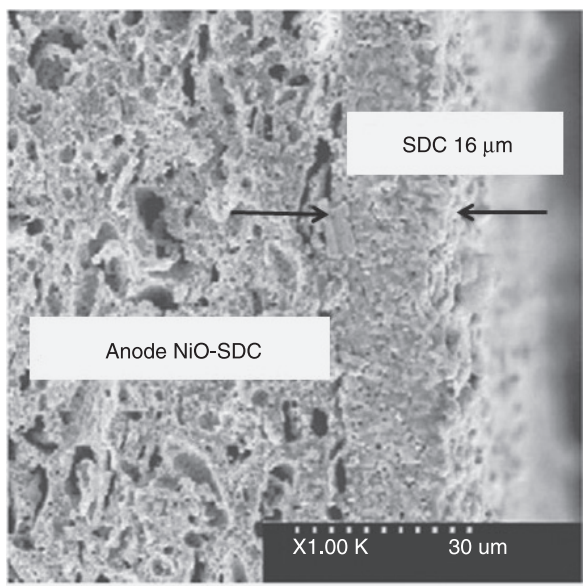

16.6 Cross-sectional view of a SDC electrolyte film obtained by screen-printing (Zhao *et al.*, 2008).

© Woodhead Publishing Limited, 2012

16.4 Electrodes

In contrast to the electrolyte, which must only be an ionic conductor, the electrodes of SOFCs must have several properties in order to catalyse the electrochemical reactions and to transfer the electrical charges. The electrodes must be mixed conductors, ionic for the transfer of O^{2-} ions from electrolyte and electronic for the e-transfer for current exploitation. This can be achieved in two different ways: on one hand using a mixed electrical conductor, as is generally the case with cathodes (LSM), or on the other hand using cermets, which are a mixture of metal and ceramic, as is generally the case with Ni-based anodes. The electrodes must be very porous for gas diffusion and to ensure good current collection. For this last point, the quality of the electrical contacts is of prime importance and consequently their thermal expansion coefficient must be well adapted to the electrolyte and the metal collector. Moreover, the electrodes must be stable in a reducing atmosphere for anodes and an oxidizing atmosphere for cathodes. Finally, their more complex properties are related to their catalytic performances depending on the nature of gases (poisoning by impurities, carbon depiction . . .).

16.4.1 Anodes

Nickel (Ni) is the most widely used material for anodes. It presents a high catalytic activity for several reactions, of course for H_2 dissociation, but also for many HC decompositions, which allows the SOFCs to work directly with a large range of gases, from CH_4 to several mixtures of HC or syngas CO + H_2. Taking into account its thermal coefficient and its pure electronic conductivity, Ni is generally mixed with the electrolyte to form a cermet. The cermet is usually manufactured by starting from NiO powders and then reducing the NiO into Ni during the first step of SOFC exploitation. The best performances are obtained only if the cermet presents a high number of triple points (TPB: three phases boundary) (Fig. 16.7). This is necessary to produce the electrochemical reaction involving the electrons, the gas and the O^{2-} ions. It is important to obtain three percolated networks: electrolytes grains, Ni grains and porosity.

An example of such a cermet anode produced by screen-printing is presented in Fig. 16.8 (Gadacz, 2010).

The paste is prepared with a mixture of commercial powders (60% NiO and 40% CGO), added to a conventional organic binder and a solvent (ESL company). Five deposition steps are necessary to obtain, after sintering at 1200 °C, a 25 µm thick porous film (Fig. 16.8(a)). The reduction of the NiO-CGO film is achieved at 580 °C after 3 hours under H_2 (2% in helium). The specific area and porosity are 2.7 $m^2.g^{-1}$ and 59%–respectively, before reduction and 3.1 $m^2.g^{-1}$ and 69%, respectively, after reduction. The final porosity of the film can be observed in Fig. 16.8(b).

According to the many constraints of SOFC device fabrication, and especially the necessity to get thinner electrolytes, the general trend is to develop the SOFCs

© Woodhead Publishing Limited, 2012

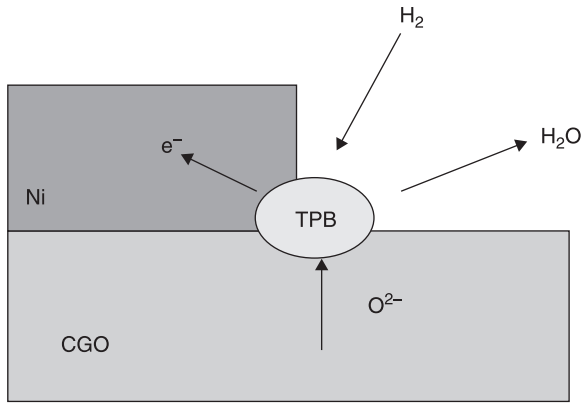

16.7 Scheme of TPB for electrochemical reactions with gas–anode–electrolyte contact.

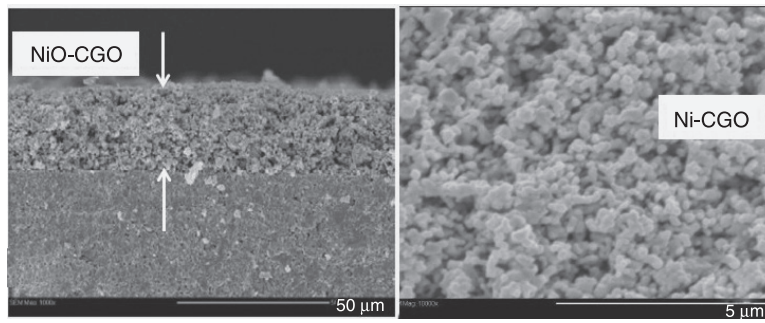

(a) (b)

16.8 Thick-film of a cermet 20 µm NiO-CGO deposited by screen-printing before reduction to obtain the Ni-CGO anode. (a) Cross-section and (b) surface (Gadacz, 2010).

on porous anodes, which serve as deposition substrates. There are now many papers dealing with the fabrication of such cermets (Fukui *et al.*, 2003; Wang *et al.*, 2008). An example is presented in Fig. 16.9 (Song *et al.*, 2008) for conventional materials: LSM as the cathode, YSZ as the electrolyte and Ni-YSZ as the anode. The anode support and the YSZ electrolyte are prepared together by tape casting and co-firing. After delamination, the LSM cathode is deposited by screen-printing. The main advantage of the process is related to the cost reduction.

In conclusion, anodes are generally cermets with Ni associated with the electrolyte of the SOFC, i.e. Ni-YSZ, or Ni-SDC and Ni-CGO for IT-SOFC. There are only some attempts to propose other materials for the anode like LSCM ($La_{0.75}Sr_{0.25}Cr_{0.5}Mn_{0.5}O_{3-\delta}$), which are perovskite-structure (Huang *et al.*, 2007).

© Woodhead Publishing Limited, 2012

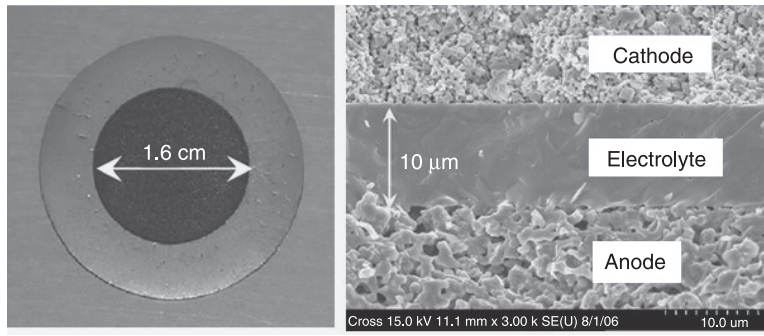

(a) (b)

16.9 LSM/YSZ/Ni-YSZ fuel cell realized by tape casting and co-firing on anode support; (a) cathode LSM (black) and cermet Ni-YSZ (outer circle); (b) cross-section (Song *et al.*, 2008).

16.4.2 Cathodes

The literature on cathodes for SOFCs is very significant. This is certainly due to the impact of cathode performances on SOFCs. Cathodes must have all the general properties of SOFC electrodes: high charge transfer, good stability (in oxidizing atmosphere) and good compatibility with electrolyte in terms of chemical reactivity and of mechanical behaviour (expansion coefficient). Cathodes must also dissociate oxygen to produce the O^{2-} ions and to transfer them into the electrolyte.

Just as nickel is the preferred material for anodes, there is one material that is widely used for cathodes, i.e. strontium-doped lanthanum manganite (called LSM) with the composition $La_{0.8}Sr_{0.2}MnO_3$. This material is interesting for several reasons. Firstly, LSM is well adapted to porous film preparation. An example of a screen-printed film is given in Fig. 16.10 (Caillol *et al.*, 2007). The LSM inks here are obtained from LSM commercial powder (superconductive) added to a conventional organic binder and a solvent from ESL. The films are deposited with a 180-mesh screen using a semi-automatic machine (Aurel C890). Five deposition steps are necessary to obtain a 65 μm thickness. Between each deposition, the layers are dried at 100 °C. The final electrode is then sintered at 1200 °C for two hours. We can observe the high porosity of the LSM film and also a good sintering between the LSM grains (Fig. 16.10(b)).

Nevertheless, LSM cathode materials exhibit poor ionic conductivity. There are many studies dealing with models for ionic transport to the LSM–electrolyte interface in order to improve the electrical performances (high mixed conductivity, increasing of TPB points . . .) (Adler *et al.*, 1996). The solutions here are similar to the cermets for anodes and composite cathodes; LSM-YSZ are also proposed. The cathode layers can always be prepared by screen-printing (Piao *et al.*, 2008)

© Woodhead Publishing Limited, 2012

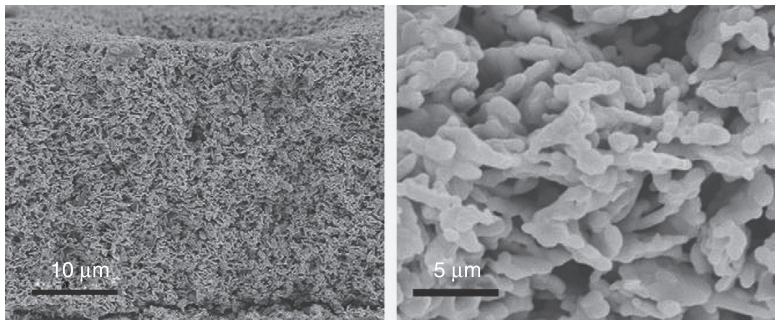

16.10 LSM thick-film obtained by screen-printing and sintered for 2 hours at 1200 °C. (a) Cross-section and (b) detail of porosity (Caillol *et al.*, 2007).

or by electrostatic spray deposition (ESD) (Princivalle and Djurado, 2008). We can appreciate in Fig. 16.11 the differences in porous structures that can be obtained with ESD by varying the ratio of LSM/YSZ (21, 43, 50 and 60 mol.% from left to right on the figure). An example of a SOFC produced using screen-printing with an LSM cathode deposited above a mixed LSM/YSZ layer is shown in Fig. 16.12 (Haanappel *et al.*, 2005).

For IT-SOFC development, LSM exhibits poor performances at low temperatures. Many studies have been performed to obtain new cathode materials for IT-SOFCs, especially those that can exhibit mixed conductivity. The two main materials are cobaltites, so-called SSC, with composition $Sm_{0.5}Sr_{0.5}CoO_3$ (Xia *et al.*, 2002) or ferrites, so-called BSCF, with composition $Ba_{0.5}Sr_{0.5}Co_{0.8}Fe_{0.2}O_3$. One example of an IT-SOFC with SDC electrolyte and with a BSCF cathode or mixed BSCF/SDC cathode is reported in Fig. 16.13 (Zhang *et al.*, 2008).

Among the other materials studied for cathodes, we can also identify screen-printed films of nickelate oxides $Pr_2NiO_{4-\delta}$ (Ferchaud *et al.*, 2011), composite

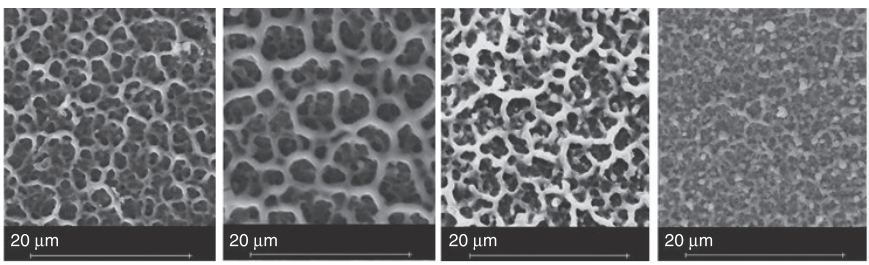

16.11 Microstructures of LSM-YSZ composite cathodes obtained by ESD. Left to right: (a) 21, (b) 43, (c) 50 and (d) 60 mol.% YSZ (Princivalle and Pjurado, 2008).

© Woodhead Publishing Limited, 2012

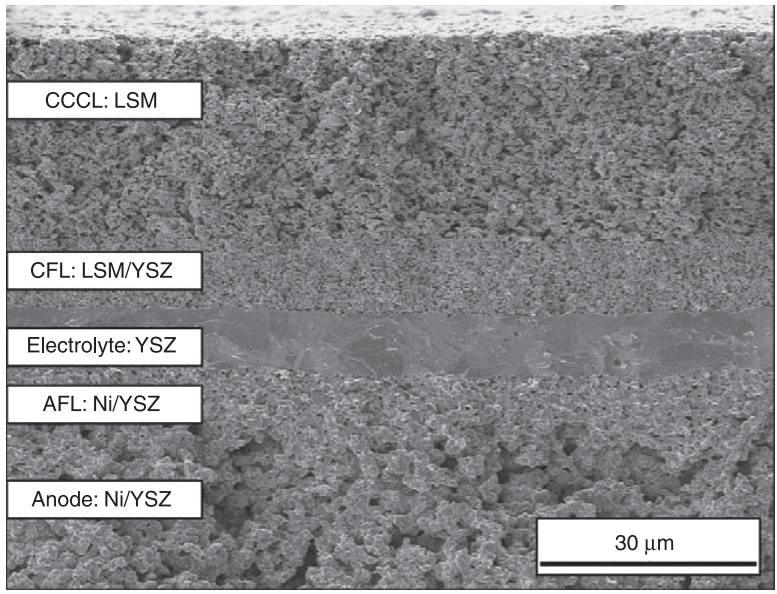

16.12 Cross-section of a SOFC fuel cell with the bi-layer cathode LSM above LSM-YSZ film. Cathode deposited by screen-printing and YSZ by vacuum slip-casting on an anode support (Haanppel *et al.*, 2005).

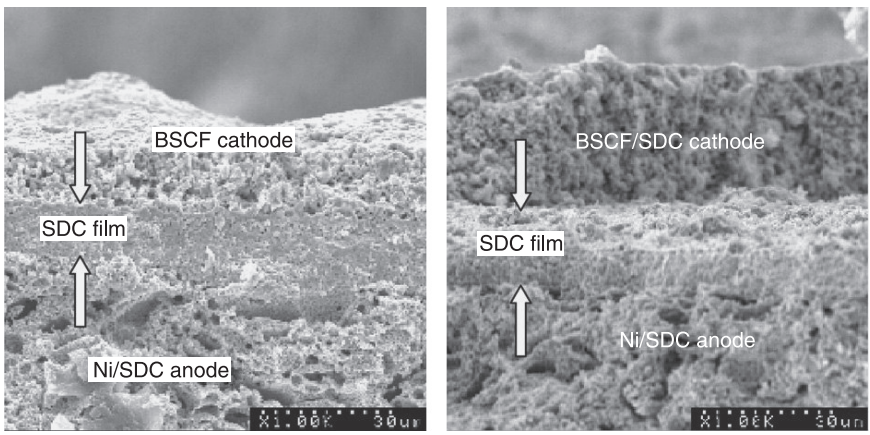

(a) (b)

16.13 BSCF cathode onto SDC film obtained by (a) screen-printing and (b) with an intermediate composite films of BSCF-SDC (Zhang *et al.*, 2008).

© Woodhead Publishing Limited, 2012

cathodes with GDC and $Pr_{0.58}Sr_{0.4}Fe_{0.8}Co_{0.2}O_{3-\delta}$, so-called PSCF (Patro *et al.*, 2010) or composite cathodes with a 50 µm porous LSCF ($La_{0.6}Sr_{0.4}Co_{0.2}Fe_{0.8}O_{3-\delta}$) produced by screen-printing associated with a very thin (200 nm) and dense LSCF layer deposited by PLD (Hildenbrand *et al.*, 2011). All these studies address the same types of research: to find new materials that can offer both ionic and electronic conductivity called MIEC (mixed ionic electronic conductivity), which can be deposited as porous thick-films, without chemical reactivity with the electrolyte, and of course with high electrical performances. All these studies include important experimental parts for the chemical reactivity and electrical properties according to the exact composition of the materials and the elaboration parameters, especially the sintering condition. It is always necessary to control the interface between the electrode and the electrolyte (DRX or SIMS experiments) perfectly. There is always a compromise to make between mechanical properties (good adhesion for the contact) and the absence of a chemical reaction. Electrical impedance measurements are also always performed to determine the type of conductivity, the values of conductivity versus temperatures, or the polarization resistance that is representative for the oxygen transfer. As an example of such experiments, we can see below the results obtained with $Sr_{1.5}La_xMnO_4$ with x = 0.35, 0.40, 0.45 (Li-Ping *et al.*, 2011). $Sr_{1.5}La_{0.35}MnO_4$ cathodes gave the lowest polarization resistance value of 0.25 Ω cm^2 at 750 °C. Impedance spectra for different oxygen partial pressures are reported in Fig. 16.14. These spectra are used to determine the different electrical contributions. The electrode polarisation resistances obtained with three electrode system (symmetric cell) are reported in Fig. 16.15 for the different compositions versus temperature.

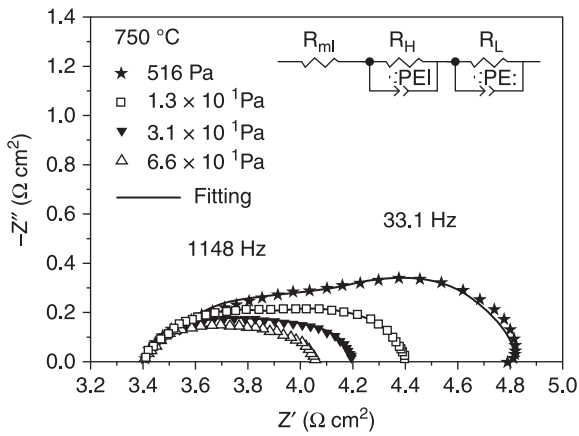

16.14 Influence of oxygen partial pressure on the impedance spectra with LSM cathode on CGO electrolyte (Li-Ping *et al.*, 2011).

© Woodhead Publishing Limited, 2012

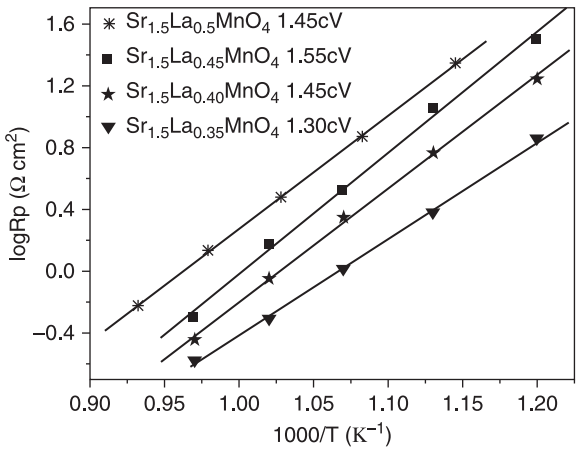

16.15 Arrhenius plot of the polarization resistances of $Sr_{1.5}LaxMnO_4$ with x = 0.35, 0.40, 0.45 and 0.50 (Li-Ping *et al.*, 2011).

16.5 Single-chamber SOFCs

The conventional operating condition for SOFCs is to have a gas-tight separation between the two cells of anode and cathode. A typical bench for laboratory studies of such conventional SOFCs is shown in Fig. 16.16 (Rotureau *et al.*, 2005).

This bench is called a 'two-chambers' bench. Generally it is used to study laboratory prototypes of SOFCs, i.e. a pellet that produces a potential below the OCV (1.23 volts for H_2-O_2 system). The industrial developments of SOFCs need to reach a higher potential, i.e. 24 or 48 volts, and consequently the SOFCs are

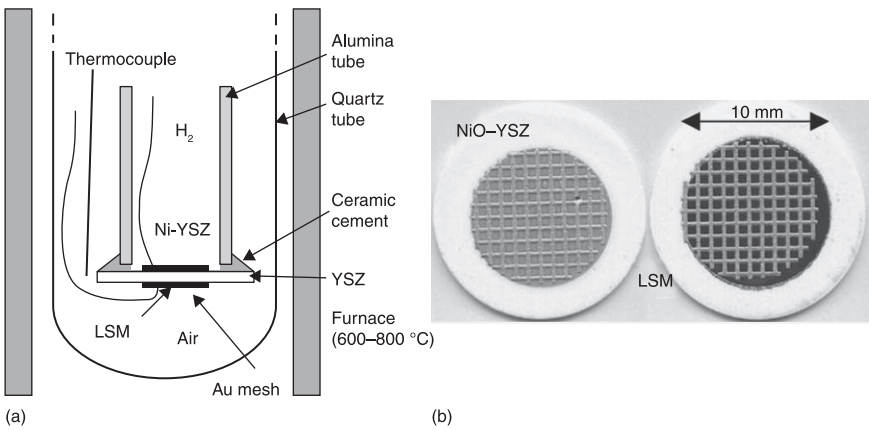

16.16 Experimental set-up (a) to study conventional SOFC fuel cell and (b) view of the two sides of a YSZ pellet with LSM cathode and Ni-YSZ anode (Rotureau *et al.*, 2005).

© Woodhead Publishing Limited, 2012

joined together to form a 'stack' with 12, 24 or 48 single cells. Consequently, the term 'single cell' is sometimes used to highlight the difference with the stacks.

Now, we introduce the term 'single-chamber' SOFC, which is a fairly new concept introduced ten years ago. With conventional two-chamber SOFCs, the tightness is the critical step because you absolutely must avoid gas leaks between the two chambers. The dramatic consequences could be a gas explosion (LIE of H_2 at 4% in air) and loss of electrical performances. If this point is difficult to solve at the laboratory scale, it is even more important at the industrial scale with stacks. It was one of the reasons for trying to develop IT-SOFCs working nearer to 600 °C rather than 800 °C. In our case (Fig. 16.16a), the choice of cement and its associated process was a key point. An example of a conventional SOFC used for these experiments is reported in Fig. 16.16(b). The configuration is LSM/YSZ/Ni-YSZ. The electrodes are deposited on an YSZ pellet. We can see here the importance of electrolyte densification. With electrolyte support (YSZ pellet here), it is necessary to have sufficient thickness for mechanical constraints. Consequently, the electrical performances are not good. This is one of the reasons that has led to the development of the SOFC with electrode supports like anode support. All these technological difficulties have also led to the new concept of a single-chamber SOFC, which is a fuel cell without gas separation between the two electrodes. This concept comes partly from the research community on gas sensors and especially on potentiometric sensors (YSZ sensors for oxygen). The first structured studies were proposed by the group of Hibino (Hibino *et al.*, 1995). Recent reviews on single-chamber SOFCs are available (Kuhn and Napport, 2010; Yano *et al.*, 2007). The principle is demonstrated in Fig. 16.17.

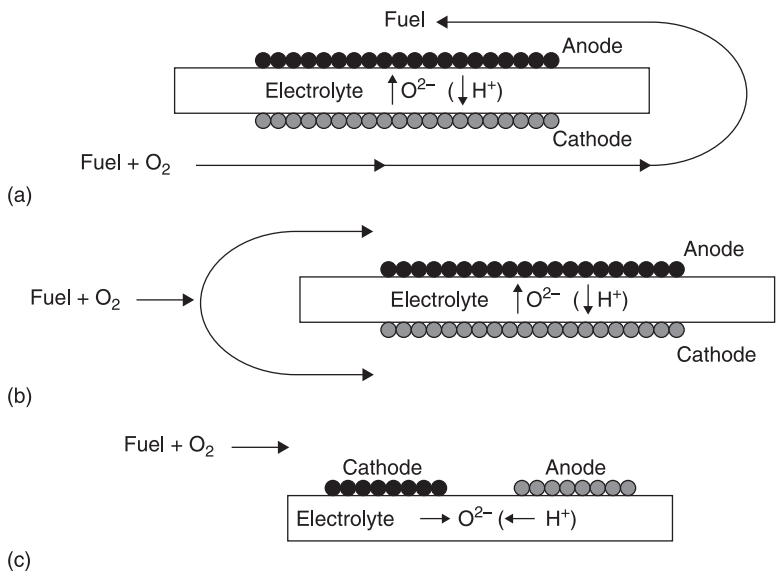

16.17 Three types of geometries for single-chamber SOFCs (Yano *et al.*, 2007).

© Woodhead Publishing Limited, 2012

The mixture of gases (oxygen and HC) is injected in a single cell containing the device, which consists of an electrolyte supporting both electrodes. A potential will be created as the result of the difference of catalytic activity between the two electrodes: the cathode must dissociate oxygen without any activity with HC and the anode must catalyse the dissociation of HC and the reaction with O^{2-} ions. The control of the system is especially dependant on these catalytic activities taking into account the presence of the mixture of gases and the same temperature for the two electrodes. The main problems are related to explosion control, carbon deposition on electrodes (and poisoning effect), the chemical stabilities of material in a mixed atmosphere (oxidizing and reducing) and cell design and model similar to catalytic reactors. The main advantages are the possibility of using direct mixtures of gases and the reduction of production costs due the simplest technology, especially the absence of gas seals and no requirement of high density for the electrolyte. Consequently the use of screen-printing is well adapted for the low-cost fabrication of such single-chamber SOFCs.

Due to our own activity on gas sensors, we have worked on the single-chamber SOFCs. In the field of gas sensors, we have also proposed (Guillet *et al.*, 2004; Pupier *et al.*, 1999) some potentiometric sensors with two different electrodes deposited on the electrolyte without gas separation as with conventional potentiometric sensors (YSZ oxygen sensor with reference air). The model of these sensors is based on the difference of catalytic activity between two different electrodes, for example platinum and gold, deposited on the ionic conductor. These gas sensors were produced completely by screen-printing. In consequence, our first single-chamber SOFC prototypes were very close to gas sensors (Rotureau *et al.*, 2005). These first devices (Fig. 16.18) were produced with conventional materials: a LSM cathode and a Ni-YSZ anode deposited by screen-printing on YSZ pellets.

The current collectors were also Pt and Au screen-printed grids. There is considerable benefit in using such screen-printed grids as opposed to conventional grids, as can be seen in Fig. 16.19 (Gadacz, 2010) which exhibits an improvement of power from 13 to 28 $mW.cm^{-2}$.

From the first single-chamber prototypes proposed in the past, there are now many studies including new materials with better efficiencies in term of catalysis and chemical stabilities. All the special materials presented previously for cathodes and anodes in particular have been studied again in a mixture of gases (oxygen and HC). The problems are now very complex. The oscillations that can be observed during increasing temperature steps with a Ni-CGO/CGO/LSM single-chamber are a good illustration of this complexity (Fig. 16.20) (Viricelle *et al.*, 2010). These experiments are observed under a mixture of air and propane (C_3H_8/O_2 = 0.55). The OCV presents some oscillations in the 550–650 °C range and also a rapid decrease above 700 °C. These results can be partly explained by the Ni-NiO redox cycles (Wang *et al.*, 2006). The problem of the re-oxidation of the cermet Ni-electrolyte is always very complex, even with

© Woodhead Publishing Limited, 2012

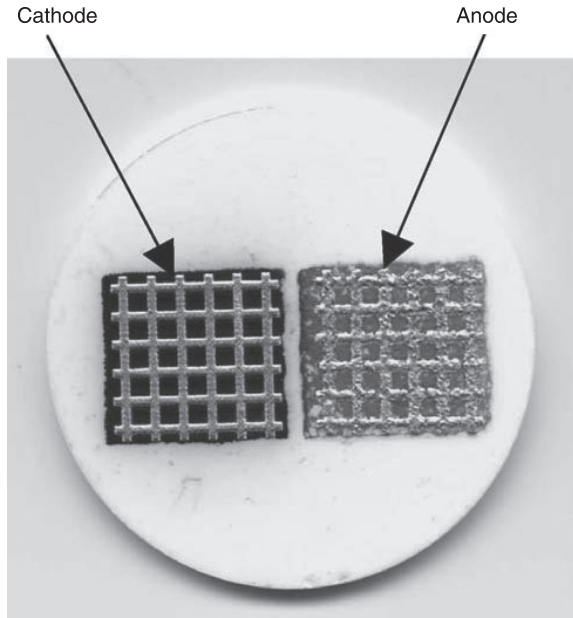

16.18 Laboratory prototype of single-chamber SOFC with LSM cathode, Ni-YSZ anode and gold grids for current collectors deposited by screen-printing on YSZ pellet (Rotureau *et al.*, 2005).

conventional SOFCs, and because we always start from NiO and make a reduction cycle to get the Ni anode.

The catalytic activities of the electrodes are of prime importance. Figure 16.21(b) shows the propane conversion for three cathodes' materials: LSM, SSC and BSCF for the same air–propane mixture (C_3H_8/O_2 = 0.55). We can observe that LSM activity is very high for propane conversion. But for the cathode, the minimum of HC conversion is necessary. BSCF seems to be the best material. Nevertheless, BSCF presents a low conductivity compared to an SSC cathode (Fig. 16.21(a)).

In conclusion, with such a configuration of an SFC device (LSM-GDC-Ni), a maximum power density of 20 mW.cm^{-2} has been obtained. For nickel anodes, in our test conditions, a minimum temperature of 535 °C was required to avoid its re-oxidation. Considering the too high catalytic activity of LSM towards HC conversion, and the low studied temperature of around 600 °C, SSC and BSCF cathode materials should lead to higher performances compared to LSM. However, the working condition in air–HC mixtures must be improved in regards to the stability of SSC and BSCF materials. For these problems of stability, we have decided to work with LSCF as a cathode. With a Ni-SDC/SDC/LSCF-SDC single-chamber SOFC, and under methane (CH_4/O_2 = 1), our current experiments at 700 °C show power densities of 60 mW.cm^{-2} with electrolyte support and more

© Woodhead Publishing Limited, 2012

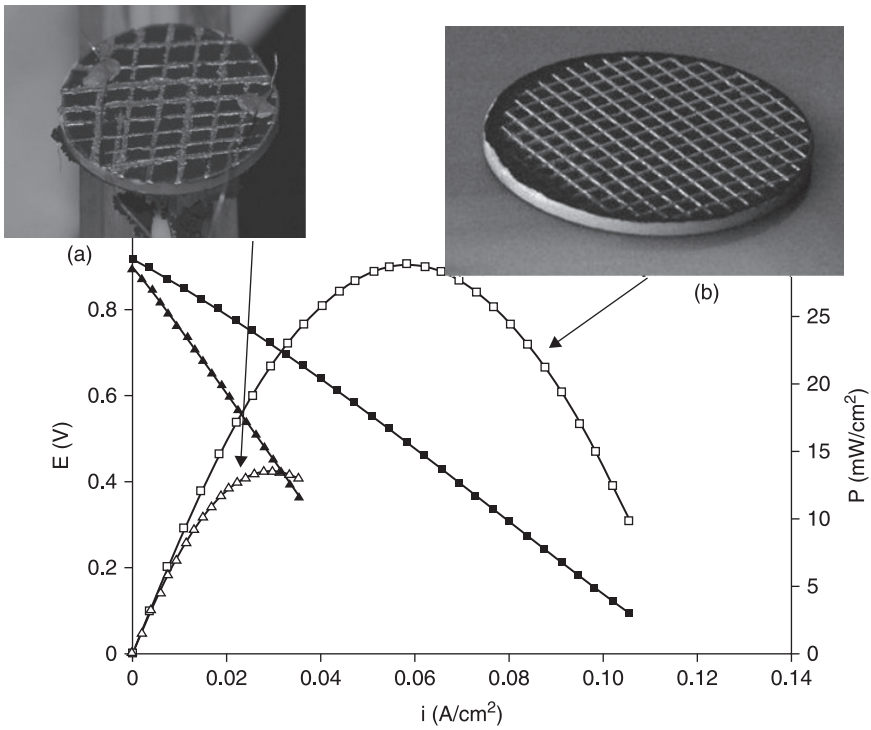

16.19 Improvement of electrical performances of SC-SOFCs using (b) screen-printed gold grid in place of (a) pressed grid (Gadacz, 2010).

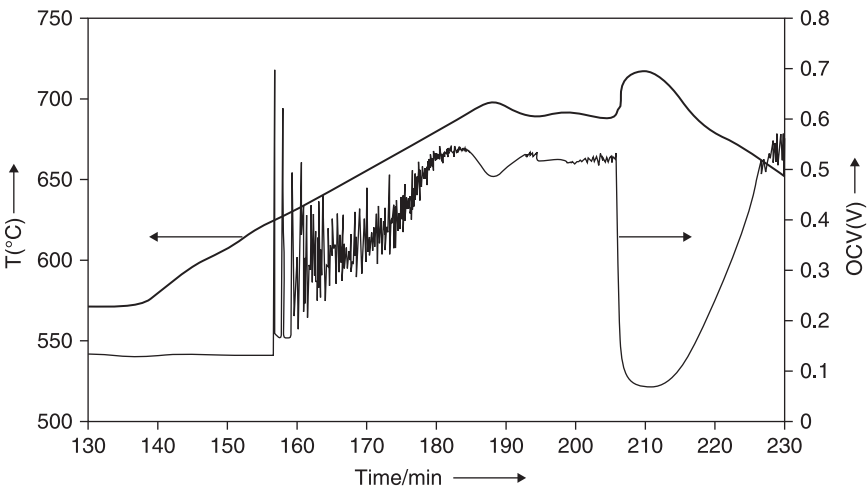

16.20 Detail of oscillations on the OCV time dependence of a single-chamber Ni-CGO/CGO/LSM fuel cell under air–propane mixture (C_3H_8/O_2 = 0.55) (Viricelle *et al.*, 2010).

© Woodhead Publishing Limited, 2012

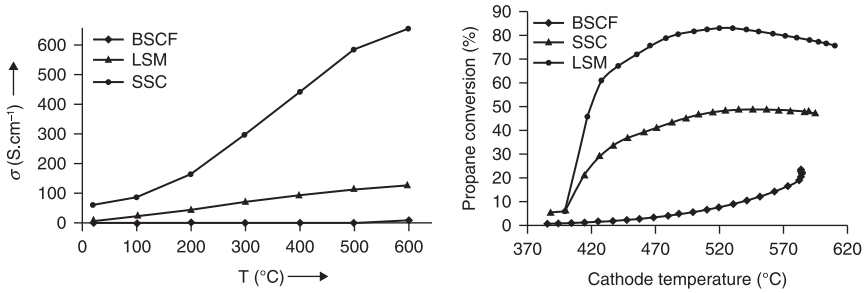

16.21 Influence of cathode material (LSM, BSCF and SSC) on (a) the electrical conductivity and (b) on the catalytic activity for propane conversion (Viricelle *et al.*, 2010).

than 200 mW.cm^{-2} with anode support. A typical cathode of 30 µm LSCF-SDC deposited by screen-printing on electrolyte support (pellet of 1 mm SDC) is shown in Fig. 16.22 (result to be published).

Beside the complexity of controlling single-chamber working conditions, there are more and more publications reporting very good power densities that are close to the power of conventional SOFCs (around 1 W.cm^{-2}). With a single-chamber BSCF-SDC/SDC/Ni-SDC, a power density of 760 mW.cm^{-2} is reported in the literature (Shao *et al.*, 2006). We show only one example in Fig. 16.23 (Hibino *et al.*, 2002) of high performances obtained with a single-chamber Ni-SDC/SDC/SSC under methane. The particularity here is the addition of a Pd catalyst (0.7%) in the anode Ni-SDC. With a 0.15 mm electrolyte (support of SOFCs), and under a ratio CH_4/O_2 = 1, the power density at 550 °C is 600 mW.cm^{-2}. These types of results are really encouraging and exciting for future works.

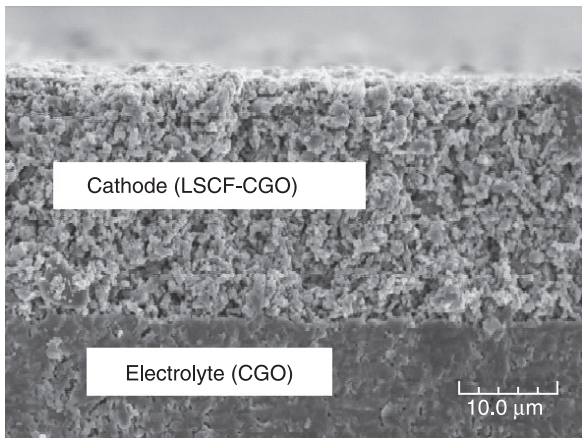

16.22 A 30 mm LSCF-CGO cathode deposited by screen-printing on CGO electrolyte.

© Woodhead Publishing Limited, 2012

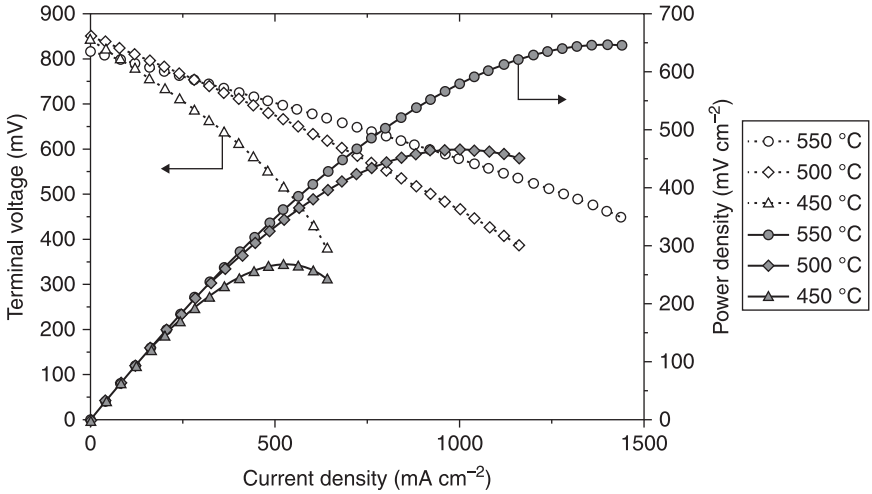

16.23 Influence of operating temperature (450, 500 and 550 °C) on the powder density for a Pd-doped Ni-SDC/SDC/SSC single-chamber and under mixture $CH_4/O_2 = 1$ (Hibino *et al.*, 2002).

16.6 Micro single-chamber SOFCs

Today, there is a high demand for small-scale energy-delivering systems for portable electronic devices such as mobile phones, PDAs and laptops. For this, SOFCs appear to be the best compromise in terms of specific energy (per mass of device) and energy density (per volume of device). Micro-SOFCs present several advantages over other FC systems (PEM or direct methanol FCs) or batteries. The development of such micro-SOFCs has been facilitated by the micro-membrane development in silicon technology. In fact, these silicon membranes were initially developed for pressure sensors. They have more recently been used for micro-FCs' fabrication, especially PEM, which are low-temperature FCs (Kundu *et al.*, 2007). Si technologies allow the creation of miniaturized systems with a large range of shapes and sizes. Thin Si membranes are obtained by dry etching. Moreover, holes can be also etched as can be seen in Fig. 16.24 (Yeom *et al.*, 2005). These types of structures are then used to support micro-FCs. PEM and DMFC have been developed on the basis of such concepts because the three materials (electrolyte, anode and cathode) can be deposited on these membranes by thin film technologies. More recently, these silicon membranes have been similarly used for micro-SOFCs because they are well adapted to high-temperature applications and thin electrolyte deposition (Evans *et al.*, 2009). The possibility of developing micro single-chamber SOFCs was quickly put forward (Buergler *et al*, 2007).

© Woodhead Publishing Limited, 2012

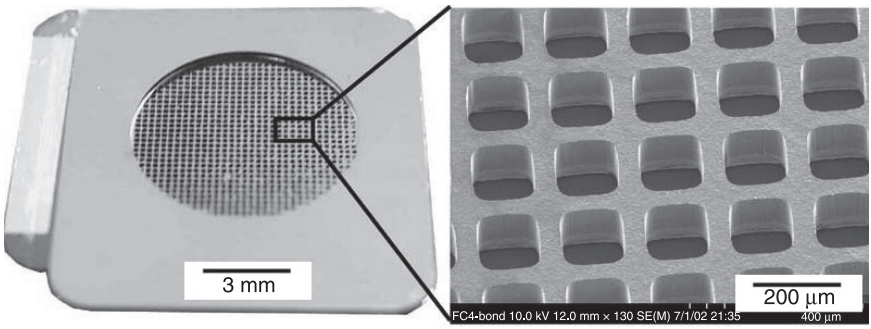

16.24 (a) Silicon grid obtained by dry etching DRIE for micro-fuel cell and (b) details of the 150 µm holes (Yeom *et al.,* 2005).

As has been previously pointed out, screen-printing is often used for SOFC realization, especially for porous electrodes with complicated materials (LSM, BSCF, SSC . . .). The difficult point here is to realize the screen-printing directly on silicon membranes without breaking the membranes. We personally have in our laboratory past experience of gas sensor developments on such micro-membranes. The objective was to deposit, by screen-printing, SnO_2 thick-films on silicon micro-hotplates. These hotplates are silicon membranes equipped with a platinum heater for the 400–500 °C operating temperature of the gas sensors. This silicon development is of interest because of the mass and low-cost production of gas sensors. The objective is to have a high level of miniaturization and to reduce the number of operations. Consequently, it was necessary to realize the screen-printing of the sensing material as the last step in the process, so it was done on thin liberated membranes (after the deep reactive ion etching (DRIE)) and with only low-temperature heating in order to avoid the degradation of the platinum heater. Our solution was then to set-up a new low-temperature process for the screen-printing of SnO_2 films (Riviere *et al.*, 2003). The solution is to prepare SnO_2 pastes with a mixture of SnO_2 powder and SnO_2 gel obtained with a tin precursor (tin-ethylexanoate-alkoxide). This process allows the deposition of SnO_2 thick-films by screen-printing with good electrical performances for gas sensing and sufficiently good mechanical adhesions after only a low-temperature annealing (300 °C) to allow the saw cutting of silicon wafers as the final step. Finally, the process was improved using the direct addition of a tin alkoxide precursor in place of tin gel. The best viscosity leads to better adhesion and microstructure of the thick-films (Fig. 16.25) (Viricelle *et al.*, 2005). The size of the SnO_2 film is 300×500 µm. The film is deposited on an insulated film that covers the platinum heater.

Our gas sensors background described above has been exploited for the micro single-chamber SOFC. We have developed miniaturized single chambers with

© Woodhead Publishing Limited, 2012

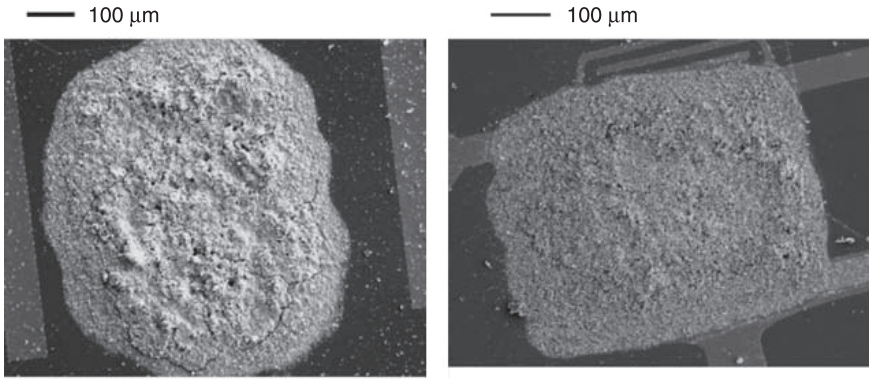

16.25 Screen-printing of SnO_2 films on silicon micro-hotplates: influence of ink composition with addition (a) of tin gel or (b) tin alkoxide precursor (Viricelle *et al.*, 2005).

conventional materials Ni-YSZ/YSZ/LSM onto alumina substrates (Fig. 16.26) (Viricelle *et al.*, 2006). The size of the SOFCs is 4 × 4 mm. The three materials are deposited by screen-printing. The YSZ electrolyte films are not dense films even if they are annealed at 1380 °C over two hours. Nevertheless, one advantage of a single chamber is that it does not require a high density level for the electrolyte. The power density obtained with such laboratory prototypes is only a few mW. cm^{-2}. In order to go to micro single-chamber SOFCs on silicon substrates with the objective of a higher level of miniaturization, similar depositions as for gas sensors have been realized on silicon micro-hotplates. The preliminary results for LSM deposition by screen-printing onto silicon substrates are presented in Fig. 16.27: (a) a detail of one silicon micro-hotplate 2 × 2 mm and (b) LSM spots on a chip of 7 × 7 hotplates. The silicon micro-hotplates are produced by IMT at Neuchatel. Unfortunately the electrical conductivity of these LSM films is low (a

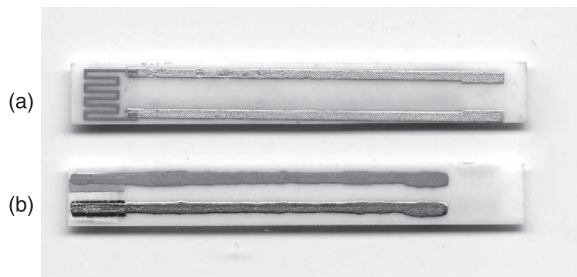

16.26 Miniaturized single-chamber SOFC on alumina substrate: LSM (a)/YSZ/Ni-YSZ (b) with gold and platinum connections and back side with Pt heater (Viricelle *et al.*, 2006).

© Woodhead Publishing Limited, 2012

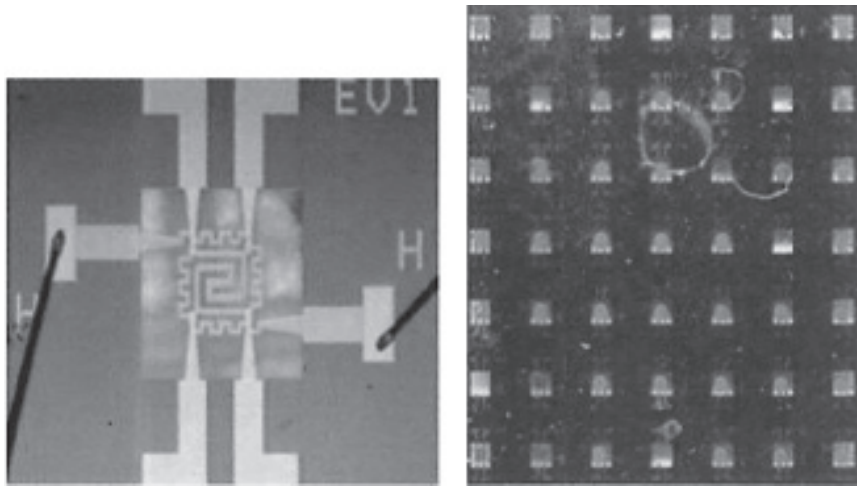

(a) (b)

16.27 (a) Silicon micro-hotplate 2 × 2 mm realized by IMT-Neuchatel and (b) LSM spots (450 × 450 μm) on a 7 × 7 membranes wafer (Viricelle *et al.*, 2006).

few S/cm at 630 °C) compared to normal values (near 100 S/cm). This is certainly the consequence of the low-temperature annealing (600 or 800 °C) of LSM films, which is necessary to avoid the degradation of the silicon micro-hotplates. As for the development of SnO_2 gas sensors, the elaboration of ink including precursors of the desired material (LSM) may be a solution that could be used.

The recent advances in micro technologies today allow for new processes for micro single-chamber SOFCs' realization. One example is reported in Fig. 16.28 (Kim *et al.*, 2010).

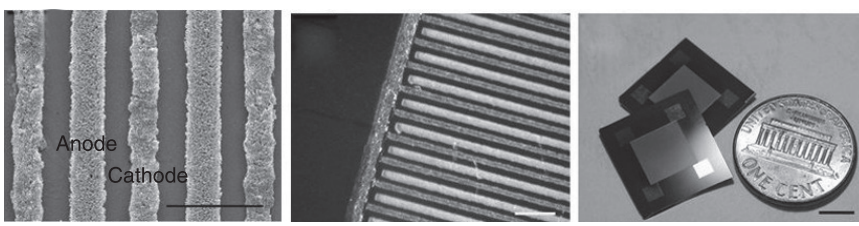

(a) (b) (c)

16.28 Micro single-chamber Ni-CGO/CGO/SSC realized with molds: (a) alternative cathode and anode design, (b) with gold current collector (scale bar: 50 μm) and (c) final form of SC-SOFC (scale bar: 5 mm) (Kim *et al.*, 2010).

© Woodhead Publishing Limited, 2012

A thin electrolyte CGO film has been deposited by e-beam evaporation on silicon substrates. The two electrodes (anode Ni-CGO, cathode SSC) are then deposited here using a multi-step photoresist molding process. The advantage of such planar single-chamber SOFCs is related to the many possible configurations for design, which are offered especially in order to increase the network of alternative electrodes (anode and cathode) to obtain the best power densities. With the device proposed in Fig. 16.28, the authors report a power density near 60 mW cm^{-2}.

16.7 Conclusion and trends

SOFCs present the best potential for FCs to produce energy in relation to the co-generation (electrical and heat) possibilities they offer. This means their development will continue in the coming years. The range of potential applications is very large, from very large stationary units to home systems, from automotive to aeronautic domains (APU under test by Airbus) and portable power sources. The main challenge concerns the reduction of working temperatures from 800 down to 400–500 °C. There is today a large R&D effort to develop such IT-SOFCs. The solutions consist in finding new electrolyte materials with better conductivity, or in reducing the thicknesses of the current electrolytes. This means producing SOFCs using thin-and/or thick-film technologies. In this sense, the use of screen-printing is well adapted for thick-film depositions of complex materials and for low-cost production. In comparison to PEM-FC, SOFCs also have the advantage of being able to work with different gas mixtures (no danger of platinum poisoning, etc.). Nevertheless, it will be of prime importance in the future to find new materials for electrodes with new catalytic properties in order to increase the possibilities of using complex gas mixtures and better electrical performances to improve the efficiencies. The development of micro power sources will also escalate in regards to the high demand for electrical portable devices. In another way, the concept of single-chamber SOFCs appears as a really interesting challenge in regards to the power densities obtained, which are now close to those of conventional SOFCs. The future challenge will be to shift from the laboratory scale to industrial systems. Single-chamber SOFCs present a real possibility for micro-FCs.

16.8 References

Adler S. B., Lane J. A. and Steele B. C. H. (1996), 'Electrode kinetics of porous mixed-conducting oxygen electrodes', *Journal of the Electrochemical Society*, 143, 11, 3554–3564.

Buergler B. E., Ochsner M., Vuillemin S. and Gauckler L. J. (2007), 'From macro to micro single chamber solid oxide fuel cells'. *Journal of Power Sources* 171, 310–320.

Caillol N., Pijolat M. and Siebert E. (2007), 'Investigation of chemisorbed oxygen, surface segregation and effect of post-treatments on powder and screen-printing layers for solid oxide fuel cell cathodes', *Appl Surface Science*, 253, 4641–4648.

© Woodhead Publishing Limited, 2012

Cho S., Kim Y. N., Kim J. H., Manthiram A. and Wang H. (2011), 'High power density thin film SOFCs with YSZ/GDC bilayer electrolyte', *Electrochimica Acta*, 56, 5472–5477.

Evans A., Bieberle-Hutter A., Rupp J. and Gauckler L. J. (2009), 'Review on microfabricated micro-solid oxide fuel cell membranes', *J Power Sources*, 194, 119–129.

Ferchaud C., Grenier J. C., Zhang-Steenwinkel Y. K., Van Tuel M. M. A., Van Berkel F. P. F. *et al.* (2011), 'High performance praseodymium nickelate oxide cathode for low temperature solid oxide fuel cell', *Journal of Power Sources*, 196, 1872–1879.

Fergus J. (2009), *SOFC, Material Properties and Performances*, Baca Rato, CRC Press.

Fukui T., Ohara S., Naito M. and Nogi K. (2003), 'Performance and stability of SOFC anode fabricated from NiO/YSZ composite particles', *Journal of the European Ceramic Society*, 23, 2963–2967.

Gadacz G. (2010), *Développement d'une anode cermet Ni-CGO pour une pile à combustible monochambre fonctionnant sous un mélange* O_2/C_3H_8, PhD thesis, École des Mines St-Etienne.

Ge X., Huang X., Zhang Y., Lu Z., Xu J. *et al.* (2006), 'Screen-printed thin YSZ films used as electrolytes for solid oxide fuel cells', *Journal of Powder Sources*, 159, 1048–1050.

Guillet N., Lalauze R. and Pijolat C. (2004), 'Oxygen and carbon monoxide role on the electrical response of a non-Nernstian gas sensor: proposition of a model', *Sensors and Actuators B*, 98 (2–3), 130–139.

Haanappel V. A. C., Mertens J., Rutenbeck D., Tropartz C. and Herzhof W. (2005), 'Optimization of processing and microstructural parameters of LSM cathodes to improve the electrochemical performance of anode-supported SOFCs', *Journal of Power Sources*, 141, 216–222.

Hibino T., Ushiki H., Sato T. and Kuwahara Y. (1995), 'A novel cell design for simplifying SOFC system', *Solid State Ionics*, 81, 1–3.

Hibino T., Hashimoto A., Yano M., Suzuki M., Yoshida S. *et al.* (2002), 'High performance anodes for SOFCs operating in methane–air mixture at reduced temperatures', *Journal of Electrochemical Society*, 149 (2), A133–A136.

Hildenbrand N., Boukamp B. A., Nammensma P. and Blank D. H. A. (2011), 'Improved cathode/electrolyte interface of SOFC', *Solid State Ionics*, 192, 12–15.

Homosi T., Matsuda M. and Miyake M. (2007), 'Electrophoretic deposition for fabrication of YSZ electrolyte film on non-conducting porous NiO–YSZ composite substrate for intermediate temperature SOFC', *Journal of the European Ceramic Society*, 27, 173–178.

Hoogers G. (2003), *Fuel Cell Technology Handbook*, CRC Press, Boca Raton.

Huang B., Wang S. R., Liu R. Z., Ye X. F., Nie H. W. *et al.* (2007), 'Performances of $La_{0.75}Sr_{0.25}Cr_{0.5}Mn_{0.5}O_{3-\delta}$ pervoskite-structure anode material at Lanthanum gallate electrolyte for IT-SOFC running on ethanol fuel', *Journal of Power Sources*, 167, 39–46.

Kang L. (2007), *Ceramic Membranes for Separation and Reaction*, Wiley, Chichester.

Kim H., Choi S. H., Kim J., Lee H. W., Song H. *et al.* (2010), 'Microfabrication of single chamber SOFC with co-planar electrodes via multi-step photoresist molding with thermosetting polymer', *Journal of Materials Processing Technology*, 210, 1243–1248.

Kuhn M. and Napport T. (2010), 'Single-chamber solid oxid fuel cell technology – from its origins to today's state of the art', *Energies*, 3, 1–80.

Kundu A., Jang J. H., Gil J. H., Jung C. R. and Lee H. R. (2007), 'Micro-fuel cells: current development and applications', *Journal of Power Sources*, 170, 67–78.

Larminie J. (2000), *Fuel Cell Systems Explained*, Wiley, Chichester.

Li-Ping S., Qiang L., Li-Hua H., Hui Z., Guo-Ying Zhang *et al.* (2011), 'Synthesis and performance of $Sr_{1.5}La_xMnO_4$ as cathode materials for intermediate temperature solid oxide fuel cell', *Journal of Power Sources*, 196, 5835–5839.

© Woodhead Publishing Limited, 2012

Moon H., Kim S. D., Hyun S. H. and Kim H. S. (2006), 'Development of IT-SOFC unit cells with anode supported thin electrolytes via tape casting and co-firing', *International Journal of Hydrogen Energy*, 33, 1758–1768.

Patro P. K., Delahaye T. and Bouyer E. (2010), 'Development of $Pr_{0.5}8Sr_{0.4}Fe_{0.8}Co_{0.2}O_{3-\delta}$ – GDC composite cathode for oxide fuel cell (SOFC) application, *Solid State Ionics*, 181, 1378–1386.

Pena-Martinez J., Marrero-Lopez D., Ruiz-Morales J. C., Buergler B. E., Numez P., *et al.* (2006), 'Fuel cell studies of perovskyte-type materials for IT-SOFC', *Journal of Power Sources*, 159, 914–921.

Piao J., Sun K., Zhang N. and Xu S. (2008), 'A study of process parameters of LSM and LSM-YSZ composite cathode films prepared by screen-printing', *Journal of Power Sources*, 175, 288–295.

Princivalle A. and Djurado E. (2008), 'Nanostructured LSM/YSZ composites cathodes for IT-SOFC: a comprehensive microstructural study by electrostatic spray deposition', *Solid State Ionics*, 179, 1921–1928.

Pupier, C., Pijolat, C., Marchand, J. C. and Lalauze, R. (1999), 'Oxygen role in the electrochemical response of a gas sensor using ideally polarizable electrodes', *Journal of the Electrochemical Society*, 146 (6), 2360–2364.

Riviere B., Viricelle J. P. and Pijlat C. (2003), 'Development of tin oxide material by screen-printing technology for micro-machined gas sensors', *Sensors and Actuators B*, 93, 531–537.

Rotureau D., Viricelle J.-P., Pijolat C., Caillol N. and Pijolat M. (2005), 'Development of a planar SOFC device using screen-printing technology', *Journal of the European Ceramic Society*, 25, 2633–2636.

Shao Z., Mederos J., Chueh W. C. and Haile S. M. (2006), 'High power-density single chamber fuel cells operated on methane', *Journal of Power Sources*, 162, 589–596.

Singhal S. (2003), *High Temperature SOFC, Design and Application*, Elsevier, Oxford.

Song J. H., Park S. I., Lee J. H. and Kim H. S. (2008), 'Fabrication characteristics of an anode-supported thin-film electrolyte fabricated by tape casting method for IT-SOFC', *Journal of Materials Processing Technology*, 198, 414–418.

Steele B. C. H. (2000), 'Materials for IT-SOFC stacks – 35 years R&D: the inevitability of gradualness', *Solid State Ionics*, 134, 3–20.

Viricelle J. P., Riviere B. and Pijolat C. (2005), 'Optimization of SnO_2 screen-printing inks for gas sensors applications', *Journal of the European Ceramic Society*, 25, 2137–2140.

Viricelle J. P., Pijolat C., Riviere B., Rotureau D., Briand D. *et al.* (2006), 'Compatibility of screen-printing technology with micro-hotplate for gas sensors and solid oxide fuel cell development', *Sensors and Actuators B*, 118, 263–268.

Viricelle J. P., Udroiu S., Gadacz G., Pijolat M. and Pijolat C. (2010), 'Development of single chamber solid oxide fuel cells (SCFC)', *Fuel Cells*, 10 (4), 683–692.

Wang Z., Lu Z., Wei B., Chen K., Huang X. *et al.* (2006), 'Redox of Ni/NiO anodes and oscillatory behavior in single-chamber SOFC under methane oxidation conditions', *Electrochimica Acta*, 56, 6688–6695.

Wang Z. R., Qian J. Q., Wang S. R., Cao J. D. and Wen T. L. (2008), 'Improvement of anode-supported solid oxide fuel cells', *Solid State Ionics*, 197, 1593–1596.

Wanzenberg E., Tietz F., Kek D., Panjan P. and Stover D. (2003), 'Influence of electrode contacts on conductivity measurements of thin YSZ electrolyte films and the impact on solid oxide fuel cells', *Solid State Ionics*, 164, 121–129.

Xia C. and Liu C. (2001), 'Low-temperature SOFCs based on $Gd_{0.1}Ce_{0.9}O_{1.95}$ fabricated by dry pressing', *Solid State Ionics*, 144, 249–225.

© Woodhead Publishing Limited, 2012

Xia C., Rauch W., Chen F. and Liu M. (2002), '$Sm_{0.5}Sr_{0.5}CoO_3$ cathodes for low-temperature SOFCs', *Solid State Ionics*, 149, 11–19.

Yano M., Tomita A., Sano M. and Hibino T. (2007), 'Recent advances in single–chamber solid oxide fuel cells: a review', *Solid State Ionics*, 177, 3351–3359.

Yeom J., Mozsgai G. Z., Flachsbart B. R., Choban E. R., Asthana A. *et al.* (2005), 'Microfabrication and characterization of a silicon-based millimeter scale PEM fuel cell operating with hydrogen, methanol or formic acid', *Sensors and Actuators B*, 107, 882–891.

Zhang X., Robertson M., Deces-Petit C., Xie Y. and Hui R. (2006), 'NiO-YSZ cermets supported low temperature solid oxide fuel cells', *Journal of Power Sources*, 161, 301–307.

Zhang Y., Huang X., Lu Z., Ge X., Xu J. *et al.* (2006), 'Effect of starting powder on screen-printed YSZ films used as electrolyte in SOFCs', *Solid State Ionics*, 177, 281–287.

Zhang Y., Liu J., Huang X., Lu Z. and Su W. (2008), 'Low temperature solid oxide fuel cell with $Ba_{0.5}Sr_{0.5}Co_{0.8}Fe_{0.2}O_3$ cathode prepared by screen-printing', *Solid State Ionics*, 179, 250–255.

Zhao L., Huang X., Zhu R., Lu Z. and Sun W. (2008), 'Optimisation on technical parameters for fabrication of SDC film by screen-printing used as electrolyte in IT-SOFC', *Journal of Physics and Chemistry of Solids*, 69, 2019–2024.

© Woodhead Publishing Limited, 2012

17

Printed varistors

M. A. DE LA RUBIA, Ceramic and Glass Institute (CSIC)
and ETSI Telecommunication (UPM), Spain

Abstract: Thick-film zinc oxide (ZnO)-based varistors have been prepared by screen-printing and tape-casting techniques. The manufacture of varistor thick-films by screen printing shows two critical problems: the excessive volatilization of Bi_2O_3 during the sintering step due to the exaggerated area–volume ratio of these devices and the lack of density of the green compacts, a problem inherent to screen-printing technology. Tape casting improves compact density and it is possible to include an additional press step before sintering. An electrical and microstructure comparison between thick-films prepared by both technologies has been carried out for a wide range of sintering temperatures. The excessive volatilization of Bi_2O_3 is overcome by sintering the films in a controlled Bi-rich sealed atmosphere, leading to high reliability and reproducibility in their nonlinear response.

Key words: varistor, ZnO, thick-film, screen printing, tape casting, bismuth vaporization, electrical properties.

17.1 Introduction

Zinc oxide-based varistors are multiphase ceramic devices prepared by sintering highly conductive n-type ZnO grains in the presence of a small amount of Bi_2O_3 and other metal oxides. Their nonlinear electrical characteristics, with excellent capability in applications for transient suppressions, were announced by Matsuoka *et al.* in 1969 [1] and further detailed in a topical 1971 paper [2]. General Electric (GE) acquired a licence for the related patents, and the joint development effort of GE and Matsuoka resulted in the market introduction of GE-MOV® varistors in 1972. This development has been one of the great successes of ceramic technologies. Presently, ceramic varistors are mass-produced in several countries, with applications ranging from power switching in electrical transmission lines to surge protection in automobiles and semiconductor electronics.

Recent interest in surface-mounted tape-casted and printed thick-film varistors (TFVs), especially in low-voltage circuits, has stemmed from the potential advantages of better integration, improved thermal exchange through the substrate and control of electrical properties [3,4]. Both tape casting and thick-films are well-developed technologies in microelectronics, benefiting from low cost, the possibility of miniaturization and design versatility among the recognised advantages. Nevertheless, the development of TFVs has so far posed notable problems. Their performance has suffered from the inadequate reproducibility of

© Woodhead Publishing Limited, 2012

the electrical characteristics and a value of the nonlinear coefficient much lower than that of ceramic varistors.

This chapter describes ways in which printing technologies are contributing, and are expected to further contribute, to the realization of 'low profile' ZnO-based varistors.

17.2 The varistor action

ZnO-based ceramic varistors exhibit highly nonlinear current–voltage characteristics [6–13] that find widespread applications for circuit protection against voltage transients and power overload [7], from single electronic devices to power transmission lines.

An examination of varistor behaviour requires the display of current versus voltage on a logarithmic scale. Figure 17.1 gives the current density J versus the applied field F for a typical varistor, measured at a temperature near 300 K. In the standby situation (no spikes across) the varistor exhibits a high resistivity ($\rho > 10^{12}\,\Omega$cm), i.e. it acts like an open circuit; but if the voltage across the terminals exceeds the critical breakdown voltage V_b, the varistor demonstrates a remarkable conductive behaviour ($\rho < 1\,\Omega$cm), so that the varistor is a short circuit for the current. The transition occurs in nanoseconds, is completely reversible, and is without hysteresis.

It is a common practice to divide the I–V curve in three different regions, as shown in Fig. 17.1:

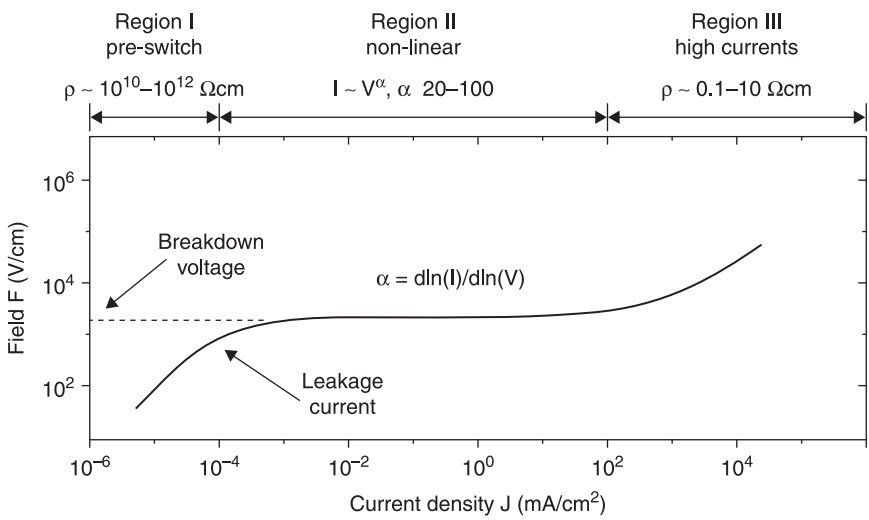

17.1 The current density J versus the applied field F for a typical varistor, measured at a temperature near 300 K.

© Woodhead Publishing Limited, 2012

17.2.1 Region I (pre-switching or pre-breakdown)

In this region, where the varistor resistivity is higher than $10^{10}\,\Omega$cm, the current is denoted as 'leakage current'; it determines the dissipated power by the varistor at standby and it is a notable function of the temperature [6]. High leakage currents imply an increase in temperature, due to the Joule effect, and consequently a degradation of the varistor performance. For practical reasons a reference leakage current is stated at a voltage equal to 85% of the breakdown voltage.

17.2.2 Region II (nonlinear, switching region)

In this region, i.e. starting from an applied voltage V across the terminals larger than the so-called breakdown voltage, there is an enormous variation in current (a factor of 10^3–10^5) despite the moderate change in the applied voltage V. A power law equation is conveniently used to describe this behaviour, that is:

$$I = kV^{\alpha}, \qquad [17.1]$$

where k is a constant that depends on the varistor dimensions. Hence α is derived from the experimental curve as $\alpha = \mathrm{dlog(I)/dlog(V)}$. The higher the exponent α, the more efficient the varistor action is. In a ceramic varistor this is typically in the range 40–50.

17.2.3 Region III (high currents)

In this region, the deviation from the power law and the very high electrical currents can be interpreted as the existence of the ohmic series resistance associated with the oxide grains in the varistors.

Excellent reviews on different aspects of varistor ceramics are found in Clarke (1999) [5], Eda (1989) [14] and Gupta (1990) [15]. These papers point out the considerable technical and scientific efforts made to advance our understanding of the varistor action and improve their performance, because of the complexity of the physico-chemical phenomena involved. Even today there remain several points that require further investigation, e.g. the role played by the intrinsic defects and the 'dopant oxides' in the development of the microstructure and thus on their electrical behaviour.

However, the knowledge gained about ceramic varistors (hereafter also mentioned as bulk or disk varistors) is the natural background for the development of other forms of varistors, such as multilayer varistors (MLVs), surface-mounted tape-casted and printed TFVs [3,4]. Although both tape casting and thick-films are well-developed technologies in microelectronics, benefiting from the possibility of miniaturization, design versatility and low cost, the development of TFVs has posed notable problems so far. Their performance has suffered from inadequate reproducibility of the electrical characteristics and a value of the

© Woodhead Publishing Limited, 2012

nonlinear coefficient $\alpha \sim 20$ [16] that is much lower than in ceramic varistors ($\alpha \geq 40$). The origin of this poor behaviour is the excessive bismuth loss [17,18] during the sintering process, a loss that hampers the formation of a proper double Schottky barrier (DSB) at grain boundaries (GBs) [19–21]. In order to understand the role played by bismuth in the varistor action and thus the relevance of its loss in the varistor performance, it is appropriate to briefly summarise the main features of the varistor action.

Figure 17.2 shows the polished and chemically etched surface of a ZnO-based ceramic varistor: ZnO grains, a few micrometers in size, are adjoined by other crystalline phases, the most easily recognized being bi-reach compounds and the spinel $ZnSb_2O_6$.

The overall microstructure can be described as ZnO grains isolated from each other by a three-dimensional series-parallel network of ZnO intergranular layers, responsible for charged GBs. The essential concept underlying the varistor action is that the J-V characteristics are controlled by potential barriers at these GBs arising from defects and dopants, which introduce electronic states in the energy gap and act as a trap for the charge carriers.

One such a barrier in thermal equilibrium is depicted in Fig. 17.3, where we observe the energy bands bending in two adjacent grains of the n-type semiconductor (ZnO).

Pure ZnO is a non-stoichiometric n-type semiconductor.

A sheet of trapped electrons at the boundary leaves behind a layer of positively charged donor sites on either side of the boundary, and creates an electrostatic field with a barrier at the boundary junction. Assuming an areal density, n_t of trapped electrons and the charge carrier concentration in the grains of N_D, the

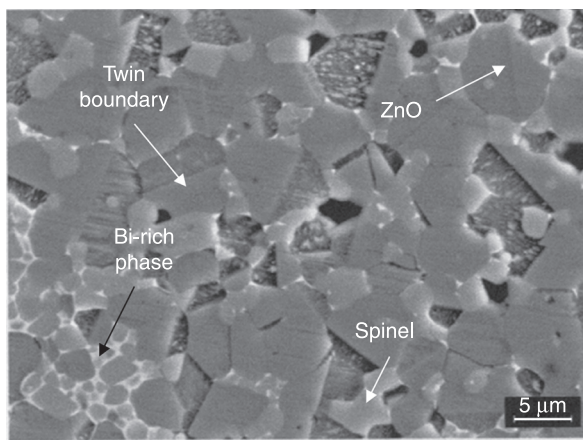

17.2 The polished and chemically etched surface of a ZnO-based ceramic varistor.

© Woodhead Publishing Limited, 2012

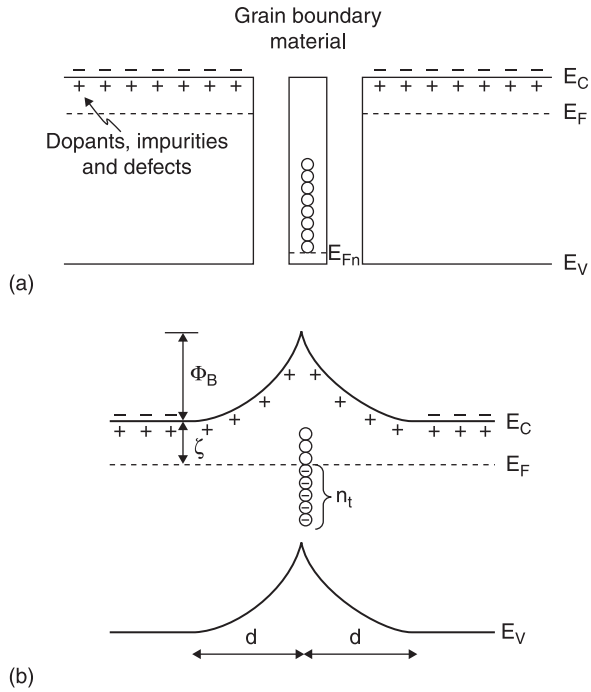

17.3 Energy bands bending in two adjacent grains of the n-type semiconductor (ZnO), (a) join of two semiconductor grains separated by an intermediate layer of grain boundary material and (b) formation of the double Shottky potential barrier.

solution of the Poisson equation will give us the barrier height $\phi_B(V = 0)$ and the depletion layer width ö:

$$\Phi_B\ (\mathrm{V}=0) \equiv \Phi_0 = \frac{q_e N_d}{2\varepsilon_r \varepsilon_0} d^2 = \frac{Q_i^2}{8 q_e \varepsilon_r \varepsilon_0 N_d} \qquad [17.2a]$$

$$\ddot{o} = Q_t/2\ N_D = \qquad [17.2b]$$

In the pre-switching region, the I-V characteristics (their ohmic behaviour and temperature dependence) fit very well a model of thermionic emission of electrons over these GB barriers, according to:

$$J = A^{\circ} T^2 \{exp[-(;+lPB)/kT]\}\{1 - \exp(-\mathrm{eV}/kT)\}, \qquad [17.3]$$

where A° is the Richardson constant, T the absolute temperature and k the Boltzmann constant.

The barrier height is thus dependent on the applied voltage and on the energy distribution of the trapping centers, as shown in Fig. 17.3, 17.4: $V \neq 0$ shifts the local 'quasi' Fermi level and in turn results in a different concentration of trapped charges Q_t.

© Woodhead Publishing Limited, 2012

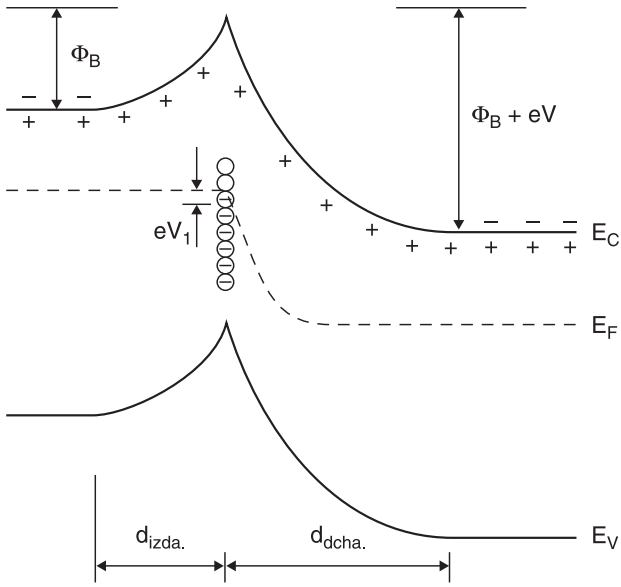

17.4 $V \neq 0$ shifts the local 'quasi' Fermi level and in turn results in a different concentration of trapped charges Q_t.

This DSB model is no longer adequate to describe the J-V curves in the switching region: another phenomenon occurs, namely under very high electric fields, some of the electrons crossing the barrier gain sufficient kinetic energy that they can produce minority carriers by impact ionization of the atoms within the depletion region. The minority carriers – holes – diffuse back to the GB under the influence of the electrostatic field at the boundary and compensate part of the trapped negative charge. In doing so, the potential barrier is lowered, thereby increasing the electron flow across the barrier. This 'feedback' process provides a high degree of nonlinearity in the electron transport in a manner similar (although not identical) to the 'avalanche' effect in Zener diodes [7].

A quantitative analysis of the model in line with these concepts shows that there is a critical doping level for a ZnO-based varistor, at about $N_D > 10^{17}\,cm^{-3}$ to reach an electric field high enough for impact ionization. Analysis of experimental data shows that the typical values for the trap density, donor concentration and barrier height are $Q_i \sim -10^{12}–10^{13}\,cm^2$, $N_D \sim 10^{17}–10^{18}\,cm^{-3}$ and $\phi \sim 0.8\,eV$, respectively. With these values, the depletion width is ~0.1 µm, and the corresponding electric field in the vicinity of the GB is ~1 MV cm^{-1} [1–10]. The corresponding breakdown voltage V_{bo} per barrier is typically in the range 3 to 3.5 V. The breakdown voltage V_b of the varistor body (thickness L) is proportional to the number of barriers between the electrodes and therefore inversely proportional to the average ZnO grain size d, according to:

$$V_b = V_{bo}\, L/d. \qquad [17.4][21]$$

© Woodhead Publishing Limited, 2012

17.3 Composition, preparation and microstructure of ceramic ZnO-based varistors

The varistor action has been observed in ZnO-based varistors containing bismuth, manganese and antimony oxides as minor components, as well as in simpler formulations containing only bismuth and manganese oxides and ZnO with bismuth Bi_2O_3 alone (although in the latter case the non-ohmic behaviour was far from high-performing, i.e. with α never larger than 10 [22, 23]). Yet, the typical formulation of ZnO-based ceramic-type varistors comprises ZnO (>95 mol %) and minor amounts of other metal oxides, such as Bi_2O_3, Sb_2O_3, Cr_2O_3, MnO_2, NiO and CoO among others [24–29]. Current commercial varistors may contain as many as eight metal oxides or more.

The reason for this complex composition is related to the aim of optimizing all the properties requested for applications, such as stability, conduction uniformity, power dissipation, maximum surge current, energy dissipation capability, grain resistivity, and so forth, in addition to the nonlinearity exponent.

If the nonlinearity coefficient were the only important device parameter, with an acceptable low pre-breakdown current value, simpler compositions would be appropriate, e.g. those adding to ZnO, Bi_2O_3 and one or two more oxides of Co and/or Mn. Co and Mn are necessary to increase varistor nonlinearity [6, 30]. These ions, in their divalent state, are known to go into solution in ZnO, but their valence state may change in the vicinity of a GB, especially with local changes in the oxygen potential; oxides of Ni [31] and Cr [32] are valuable for increasing the stability, while Sb_2O_3, which forms the spinel $Zn_7Sb_2O_{12}$ phase segregated at the GBs, restrains the ZnO grain growth [33–34].

Other identified features are: (1) SnO_2 shows a behaviour similar to that of Sb_2O_3 and, in addition, provides donors to ZnO [35]; (2) SiO_2 contributes to stabilize the low temperature polymorphs of Bi_2O_3 [36–38] decreasing the leakage current as well as the grain growth; (3) Al_2O_3 contributes to the grain growth control and reduces the leakage current [39]; TiO_2, BeO or Li_2O [6] are also used to control the grain growth.

The close control of grain growth is vital to 'define' the breakdown voltage, according to Eq. [17.4]. Exaggerated grain growth could be a critical event during the sintering process. Here again, Bi_2O_3 plays a major role as shown below. In fact, Bi_2O_3 melts at 825 °C, but the first liquid phase is just formed at a lower temperature (~740 °C), i.e. at the eutectic point of the ZnO–Bi_2O_3 binary system [40–43]. The presence of the liquid phase favours matter transport and thus the densification of the material but it would also be responsible for exaggerated ZnO grain growth if a secondary phase, insoluble in the liquid, did not impede the GBs' movement.

Usually ZnO varistors are fabricated via conventional ceramic powder processing methods to form a powder compact starting from ZnO and other oxides, which are weighed, mixed, dispersed and milled down to small size

© Woodhead Publishing Limited, 2012

(e.g. 0.2–0.5 μm). The mixture is pressed into arbitrary forms, such as disks that are sintered in an electric furnace at 1150–1250 °C for 1–5 hours in air. The temperature is increased or decreased at low rates (e.g. 50–200 °C/hr). Finally electrodes are prepared on both surfaces.

In a simplified picture of the development of the microstructure and electrical properties from the compacted powders to the sintered solid body, the most critical recognized events are:

- The introduction of one/two liquid phases at relatively low temperatures: i.e. at 735 °C where the ZnO-Bi_2O_3 eutectic point is, and the melting at 525 °C of Sb_2O_5 formed by oxidation of the original Sb_2O_3.
- The formation of the $ZnSb_2O_6$ solid (spinel) phase above 700 °C and secondary solids, including a pyrochlore $2Zn_2Bi_3Sb_3O_{14}$(s) until about 950 °C.
- The further decomposition of the pyrochlore into the spinel and liquid Bi_2O_3 above 950 °C, accompanied by the dissolution of dopants to form Bi-rich liquids.
- In this high-temperature stage, the diffusion of dopants into the ZnO grains to provide a uniform dopant distribution and liquid-phase densification. Concurrently, grain growth occurs. The sintering temperature and time are chosen so as to optimize compositional uniformity, densification and grain size.
- In the following stage, during cooling down to intermediate temperatures, processes occur that include the crystallization of the secondary phases from the bismuth-rich liquid and the retraction of the liquid from two-GBs to the triple junctions. In this stage, potential barriers arise because in retracting from the two-grain junctions, the liquid leaves behind a segregation layer containing bismuth and other large ions. Details of the microstructure (barrier size, distribution of elements, oxidation states, etc.) depend mainly on how the varistor material is processed during cooling to room temperature.
- Also, the close control of the oxygen partial pressure is recognized as a mandatory requirement to obtain high-performance varistors [44,45].

Therefore, not only is the varistor action mostly due to Bi-rich phases at the ZnO GBs [24–29], but Bi is also involved in the main processes that lead to the development of the varistor microstructure.

17.4 Printing process in varistors fabrication

From the advent of surface-mount technology (SMT) it was advisable to design new forms of transient voltage suppression devices capable of meeting the new technological needs. The benefits in comparison with disk-shaped varistors were, among others: increased miniaturization and integration, low profiles, and drastic reduction of leads to minimize the inductive effects and thus reduce even further the overshoot voltage generated by fast-rising transients.

© Woodhead Publishing Limited, 2012

Both surface-mounted monolayer (SMV) and MLVs were introduced as a chip, that is, as discrete devices to be added to a board [3]. The multilayer technology has mostly progressed and devices from many manufacturers (e.g. Panasonic, Littelfuse, Cooper Bussmann, Epcos AG) with a wide range of characteristic parameters are today available. Conversely, pastes and processes for varistors to be directly deposited on the same substrate as a hybrid circuit – or embedded inside a low-temperature co-fired ceramic (LTCC) system – are still under development.

The issues arising in the transition from the ceramic to the thick-film technology come from three differences intrinsic to the latter one:

1. The amount of organic (medium) required to achieve the right rheology, with the accompanying effects, i.e. the change of chemical environment in the sintering (firing) atmospheres at low–medium temperatures, and the reduction in functional material density (intrinsic initial porosity).
2. The high area/volume ratio: surface effects are notably more influential in varistor layers a few tens of micrometers thick (the films) than in mm thick disks.
3. In typical thick-film processes, no pressure is applied to densify the dried paste before annealing. The exception (Ménil *et al.* [53]), mentioned below, remarks the importance of this step of process when related to TFVs.

The overall predominant effect of the listed features is that the loss of Bi via porosities and open spaces in general is enhanced in comparison to ceramic varistors, even though other effects cannot be excluded. In the case of MLVs, the processability of internal contacts with the varistor layers is a further issue.

The state of the art in the development of MLVs and the main steps in the progress of tape-casted and TFVs will be described in the following sections.

17.5 Multilayer varistors

The MLVs are formed by an alternate configuration of electrode layers and ZnO-based ceramic inner layers stacked together into a monolithic block, as depicted schematically in Fig. 17.5. This design greatly increases the available cross-sectional functional area, with the consequence of diverting transient over-voltages more effectively. This compact arrangement allows for higher resistances at lower voltages with faster response times than metal oxide varistors (MOVs), higher energy and heat dissipation. Breakdown voltage values span from a few (5 to 9 volts) to hundreds of volts [46–48]. However it is the low voltage range of applications that currently stimulates the manufacture of reliable MLVs.

The fabrication usually relies on the conventional multilayer ceramic technology. ZnO and other oxides are weighed, mixed, dispersed and milled down

© Woodhead Publishing Limited, 2012

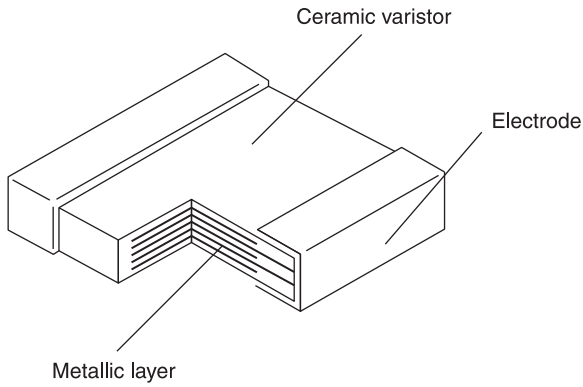

17.5 Schematic showing how the MLVs are formed by an alternate configuration of electrode layers and ZnO-based ceramic inner-layers stacked together into a monolithic block.

to a small size (e.g. 0.2–0.5 μm). Binders and plasticizers are mixed to obtain a slip to cast in green sheets using a doctor blade. A conductive paste is printed onto the green sheet to produce the inner electrodes. Next the printed sheets are stacked, laminated and cut into chips. Finally, free sintering or hot-pressing sintering under uniaxial pressure is conducted to densify these bricks. The outer contacts are then applied and cured.

Entering the field from the development of ceramic technology, a variety of new points have to be considered, including: (1) compatibility of inner electrodes with the varistor material; (2) grain growth conditioned by the space available between the inner electrodes [49]; (3) optimization of dielectric layer thickness and its homogeneity.

Platinum would be the metal of choice for inner electrodes, because it is inert with Bi_2O_3-doped ZnO; however, it is too expensive for mass production. A possible candidate is 70Ag/30Pd alloy, which however is known to interact with bismuth-based electroceramics [50] and to form Bi_2PdO_4 (in the temperature range 350 to 835 °C). This reaction can lead to profound changes in the MLV microstructure, according to the time/temperature sintering schedule. Moreover, the Bi_2PdO_4 decomposition (at $T > 835$ °C) is reportedly responsible for the possible delamination of multilayer stacks. On the other hand, attaining a homogeneous microstructure is necessary to control the electrical properties, since the electrical current tends to pass through the path with the smallest number of grains within inner electrodes; this 'percolation' effect can state the leakage current as well as the nonlinear coefficient α and the breakdown voltage. A successful strategy to accomplish homogeneous MLV microstructure is hot-pressing sintering in place of free sintering [51].

© Woodhead Publishing Limited, 2012

17.6 Screen-printed and fired thick-film varistors

Several authors have prepared low-voltage ZnO-based varistors by screen printing with and without glass in the composition. The glass phase was intended to accomplish denser and well-adhered layers on the substrate; however, the glassy phase is responsible for a marked change in microstructure and intergranular properties in comparison with those of bulk varistors and accordingly for very poor electrical properties, with nonlinear values of 8 and breakdown voltages of 15 V. Chiou and Jih [4] obtained breakdown voltages of 36 V and a nonlinear coefficient α of 16 with 'screen-printed varistors in sandwich configuration'.

Governeur *et al.* [52] and Ménil *et al.* [53] proposed overcoming the drawbacks of porosity and short circuits observed in TFVs without glass by means of isostatic or uniaxial pressure of several Kilobars applied to the so-called wet film, i.e. after the evaporation of solvents and before the firing. This additional step to the standard screen-printing procedure results in a valuable expedient to reduce the porosity and prepare TFVs, sintered at 1150 °C with breakdown voltage of 30 V and $\alpha \sim 15$ with isostatically pressed samples and α in the range 17–19 in uniaxially pressed samples, respectively. Perrot [54] also studied uniaxially pressed screen-printed TFVs; he produced films with a good nonlinear coefficient ($\alpha = 12$) but a breakdown voltage of 675 V, too high for the intended applications. Later, Martin [55] prepared varistors with planar configuration (Fig. 17.6) where the electrodes were screen-printed in parallel on top of the pressed pre-sintered varistor film.

Therefore the measured properties were mostly due to the 'near-surface' section of the varistor rather that to the entire film. This configuration presents several advantages such as: the choice of conductive ink for the electrode is not affected by the sintering temperature of the varistor thick-films since the electrodes are fired after the sintering of the varistor itself. In this configuration, the possible reaction between the electrode ink and the active material is avoided during the sintering. On the other hand, this configuration only shows the electrical response of the surface and is not representative of the electrical response of the bulk material shaped like a thick-film. Such samples show a nonlinear coefficient α of 15 when sintered at 1150 °C/15 min. Hence, despite the certainly relevant Bi_2O_3

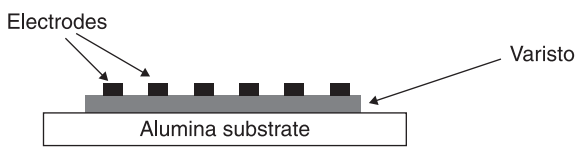

17.6 Prepared varistors with planar configuration where the electrodes were screen-printed in parallel on top of the pressed pre-sintered varistor film.

© Woodhead Publishing Limited, 2012

loss at this temperature [56], high-temperature sintering of pressed films is promising. Unfortunately it is difficult to state how much the configuration of the electrodes affected the measured quantities. In summary, the majority of TFVs studied until recently exhibited nonlinear coefficients α, between 10 and 20. The properties observed by Martin [55] were among the best (comparable with bulk varistors), notwithstanding that some doubt exists on the homogeneity of behaviour of their TFVs.

17.7 Progress in the development of ZnO-based thick-films and tape-casted varistors

The results described in this chapter refer to activities carried out for developing thick-film varistors at the Ceramic and Glass Institute (CSIC) from 2004 to 2006.

Samples discussed hereafter were prepared from powders of nominal composition: 95.5 mol% ZnO, 1.5 mol% Sb_2O_3, 1.0 mol%, Bi_2O_3, 0.5 mol% Co_3O_4, 0.4 mol% Cr_2O_3, 0.5 mol% Mn_2O_3 and 0.3 mol% NiO, Table 17.1.

Three different pastes were prepared and designed:

1. *Batch SCM*: Prepared by the traditional mixed-oxide route including ball milling for 2 h in ethanol, calcination treatment at 950 °C–1 h and milling.
2. *Batch SP:* Traditional mixed-oxide route but replacing the Sb_2O_3 by the equivalent amount of a previously synthesized $Zn_7Sb_2O_{12}$, an orthorhombic spinel phase.
3. *Batch SP plus sillenite:* As above, but replacing the Sb_2O_3 with the equivalent amount of $Zn_7Sb_2O_{12}$ (orthorhombic spinel phase) and the Bi_2O_3 with $Bi_{38}ZnO_{58}$ (sillenite) phase, previously synthesized.

The average grain size of the starting powders was between 1 and 1.5 μm. The weighted oxides or compounds were mixed, dispersed and homogenized in a three-roller mill or in a planetary milling, with an appropriate vehicle. In order to achieve proper thixotropic properties (see Chapters 2–3) of the paste for the screen-printing process, the vehicle consists in α-terpineol, ethlyl-cellulose and [2-(2-butoxy-ethoxy-ethyl) acetate. Ethanol, ethylmethyl-ketone, polyvinylbuthyral,

Table 17.1 Three batches of powder

Nomenclature	Ceramic powder processing
Powder 1	Mixed oxides fired at 950 °C/1 h.
Powder 2	Mixed oxides with the spinel phase $Zn_7Sb_2O_{12}$ previously synthesized
Powder 3	Mixed oxides with the spinel $Zn_7Sb_2O_{12}$ and the sillenite $Bi_{38}ZnO_{58}$ phase previously synthesized.

© Woodhead Publishing Limited, 2012

polyethylenglycol and benzylbuthylphtalate were used for the tape casting process. The amounts of mineral and organic phases were adjusted to match the rheological properties of the paste. Reference samples were prepared with the same compositions but the standard method of the ceramic technology, in order to compare and contrast microstructure and electrical behaviour.

17.7.1 Tape casting

In the tape-casting process, the paste is extended and levelled by knives on the substrate (doctor blade technique). The casting speed and the opening of the knives determine the thickness of the tape. Tape casting of the varistor ink was carried out on a commercial polymeric substrate (Mylar®) with 0.4 mm opening, producing tapes 70–90 µm thick after drying (30 °C). The dried films are cut according to the electroded substrate (2.5 × 5 cm) and both were pressed (0.6 Bar) together for 5–10 min at a temperature in the range 60 to 80 °C, i.e. close to the softening temperature of the substrate. Several tapes can be pressed in a single step. The firing cycles were carried out at 500 °C/2 h with heating and cooling rates of 0.2 and 1 °C/min [57]. Mylar is removed when the thick-film is dried at room temperature prior to the pressing process.

17.7.2 Screen-printed films

Dense alumina (96% Al_2O_3) was used for substrates because of its suitable properties, being a refractory, dielectric material with sufficiently high thermal conductivity. The pastes were screen-printed with a DEK 65 manual screen printer.

A Pt-based paste (Engelhard 6082) was printed on alumina and fired (850 °C/30 min) first. This film acts as the lower electrode for the varistor (screen-printed varistors in sandwich configuration) as well as a barrier to interaction between the alumina and the varistor element.

The ZnO-based paste was then printed, dried and sintered, varying the processing strategies with the intention to densify the varistors, avoid excessive Bi_2O_3 volatilization and control the ZnO grain growth. A single printed and fired varistor film is typically 10 µm thick. To accomplish thicker samples, 60–70 µm thick, free from cracks and electrical shorts and reproducible in electrical behaviour, up to six films were printed in sequence carrying out a drying step at 150 °C/15 min between each printing process. Next, thick-films are fired at 425 °C/0 h (i.e. without permanence at the peak temperature) with a heating rate of 0.5 °C and they dwell at 195, 270 and 385 °C for 30 min. Each thick-film is dried at 150 °C/15 min before screen printing the following thick-film, but the firing step to remove the organic additives from all of the films is carried out simultaneously before the sintering process. Figure 17.7 shows the surface of these fired samples.

© Woodhead Publishing Limited, 2012

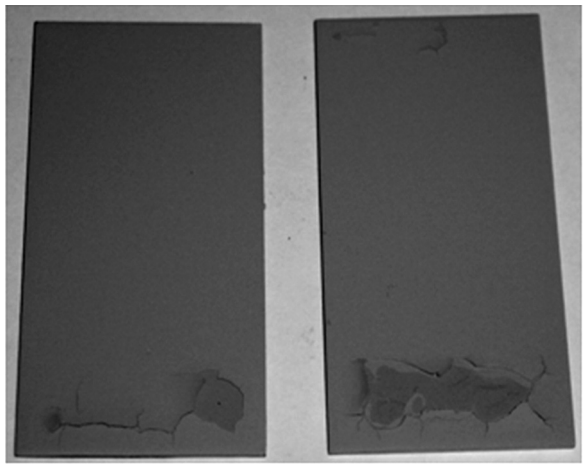

17.7 The surfaces of thick-films that have been fired to remove organic additives.

It is obvious that the thermal processes to sinter and achieve the varistor action in printed or casted films cannot simply replicate those applied to bulk varistors, the main reasons being:

- The first step required is to burn out the organic vehicle. It has to proceed at a very low rate (0.1–0.5 °C) for complete elimination without cracks and sample distortions.
- A sintering process at high temperature over a long time, which should promote densification, also creates excessive Bi_2O_3 volatilization because of the unfavourable surface/volume ratio. Metz *et al.* [56] found that ZnO-based bulk varistors sintered at 1250 °C on alumina substrate had only 5% in weight remaining of the initial concentration of Bi_2O_3 and Peiteado *et al.* [58] measured losses of 60% in weight of initial Bi_2O_3 in high-voltage devices (bulk varistors). It is very important to take into account the fact that the area–volume ratio in thick-films is two orders higher than in bulk varistors and Bi_2O_3 volatilization is very much favoured and therefore it is easy to think that conventional sintering carried out in bulk varistors produces a complete loss of Bi_2O_3 in the thick-films. Therefore it is not easy obtaining ZnO-based varistors shaped as thick-films. These studies have confirmed that the Bi_2O_3 volatilization takes place from a Bi_2O_3-rich liquid phase formed from the decomposition of the pyrochlore according to:

$$2Zn_2Sb_3Bi_3O_{14} + 17ZnO$$
$$900–1050\,°C$$
$$3Zn_7Sb_2O_{12} + 3Bi_2O_3\ (\text{liquid}) \qquad [17.5]$$

© Woodhead Publishing Limited, 2012

17.7.3 Characterization of ZnO-based varistors

The electrical properties referred to in the following section were measured on printed and casted varistors with sizes of 1*2.5 cm, and thickness between 30 and 40 μm. Also data are shown consisting of three laminated layers of tape-casted samples of about 100 μm thick to increase the thickness of the film and have several grains between the electrodes. With three layers, the electrical response is more reproducible because there are more ZnO grains between the electrodes and therefore more GBs, which are responsible for the nonlinear behaviour. A series of sputtered Au dots uniformly distributed on the varistor was used to collect J-V curves in various regions of the sample and thus verify the homogeneity of its behaviour (Fig. 17.8).

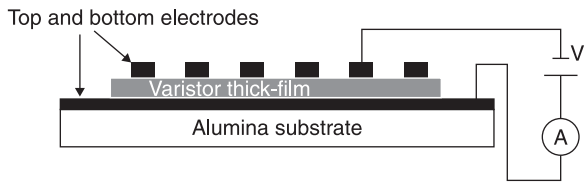

17.8 Measuring the electrical properties of ZnO-based varistors.

The characteristic electrical parameters reported hereafter are: the breakdown voltage (Vc) measured at 0.3 mA/cm^2, the leakage current (J) measured at V = 0.85 Vc and the nonlinear coefficient α measured between 1 and 10 mA/cm^2. For comparative purposes, measurements were carried out on ceramic varistors prepared with powder SCM. These samples exhibited a nonlinear coefficient α of 50 when sintered in the temperature range from 1140–1180 °C for 2 h.

17.8 Microstructural and electrical characterization of ZnO-based varistors prepared by screen printing and tape casting

Tables 17.2, 17.3 and 17.4 show the nonlinear coefficient α measured on samples prepared with the three types of powders, fired at different peak temperatures (Tables 17.2 and 17.4) and at different dwell times (Table 17.3). Powder 3 shows an electrical behaviour similar to powder 2 although slightly poorer and therefore the following studies were carried out only with powders 1 and 2.

These results suggest that 900–950 °C is the most favourable peak temperature range for our samples, to avoid short circuits and attain reasonably high nonlinearity. The microstructure of the films fired in this temperature range is illustrated in Fig. 17.9 and 17.10.

© Woodhead Publishing Limited, 2012

Table 17.2 The nonlinear coefficient α measured on samples prepared with the three types of powders, fired at different peak temperatures

Sintering temperature (°C)	Powder 1	Powder 2	Powder 3
850	Short-circuited	Short-circuited	Short-circuited
900	Short-circuited	20	18
950	2	15	12
1000	7	10	8
1050	14	9	7
1100	12	7	6
1150	9	5	5

Table 17.3 The nonlinear coefficient α measured on samples prepared with the three types of powders, fired at different dwell times

Sintering time (h)	α
1	20
4	6
8	5

Table 17.4 The nonlinear coefficient α measured on samples prepared with powders 1 and 2, fired at different peak temperatures

Sintering temperature (°C)	P1	P2
900	Short-circuited	16
950	Short-circuited	18
1000	14	18
1050	11	11
1100	7	6
1150	5	4

Figure 17.9 shows SEM micrographs of TFVs (top surfaces, not polished nor thermally or chemically etched) prepared from powders 1, 2 and 3 and sintered at 900 °C/1 h. Figure 17.10 is the SEM micrograph of a tape-casted layer sintered at 950 °C/1 h. In both cases (screen-printing and casting processes), grains in the size range of 2 to 4 micrometers are observed, showing that at these relatively low firing temperatures (900–950 °C), a limited grain growth occurred; the densification is likewise modest and accompanied by pores. On the other hand, Bi_2O_3 volatilization is not notable.

We can argue that the only contribution to the moderate grain growth was to a solid-state reaction or the low (about 750 °C) temperature when a first Bi-rich liquid phase was formed. At temperatures over 900–950 °C, the decline of α value is to be reasonably associated with increased Bi_2O_3 volatilization.

© Woodhead Publishing Limited, 2012

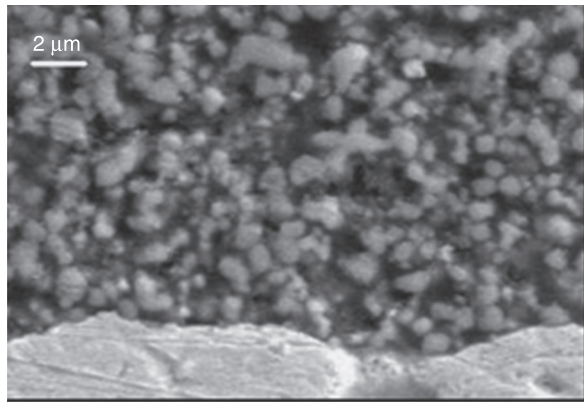

(a)

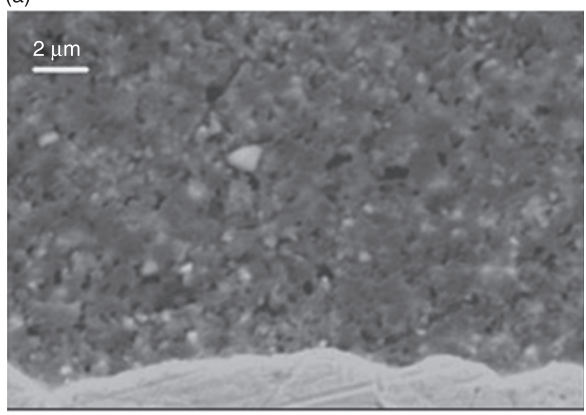

(b)

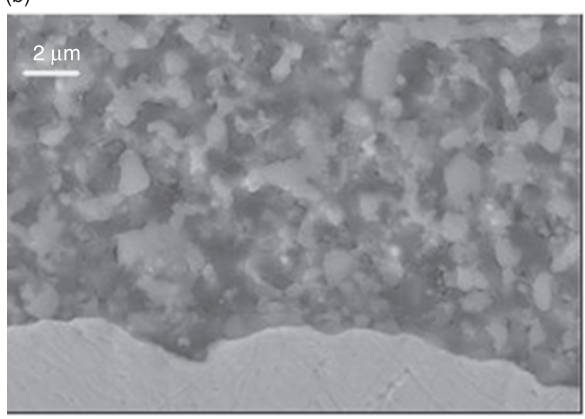

(c)

17.9 SEM micrographs of TFVs (top surfaces, not polished nor thermally or chemically etched) prepared from powders (a), (b) and (c) and sintered at 900 °C/1 h.

© Woodhead Publishing Limited, 2012

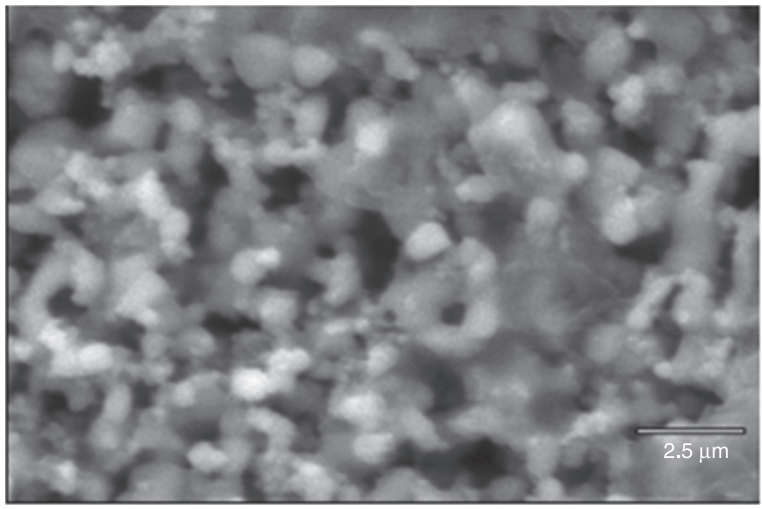

17.10 A SEM micrograph of a tape-casted layer sintered at 950 °C/1 h.

Figure 17.11 compares the microstructures of a screen-printed TFV and a bulk varistor, both sintered at 1000 °C. The difference in microstructure elucidates the difference in electrical response, α = 10 for thick-films and about 35 for bulk varistors. The thick-film still shows a Bi-rich liquid phase and the grain size essentially does not change in relation to the powders in the paste. On the contrary, the bulk varistor exhibits the characteristic microstructure with a homogeneous phase distribution of ~4 μm large ZnO grains, the spinel phase grains are distributed between the ZnO grains and in the triple points. It is important to point out that, at the same temperature, the microstructures of thick-films and bulk varistors are very different, and a consequence of this is their differing electrical response. The microstructural evolution is very different and this indicates that it

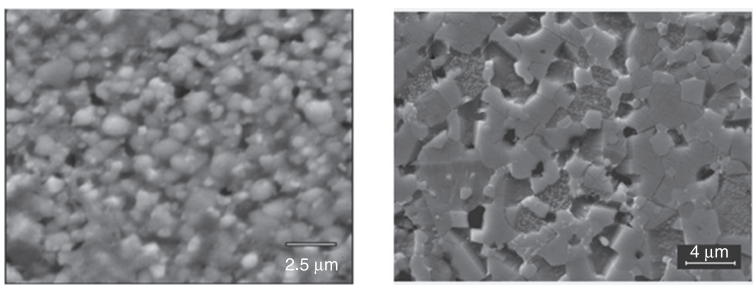

(a) (b)

17.11 Comparison of the microstructures of a screen-printed TFV and a bulk varistor, both sintered at 1000 °C.

© Woodhead Publishing Limited, 2012

is not as easy to achieve varistor thick-films with very good varistor properties using a starting powder that gives rise to very good nonlinear varistor properties when the material is shaped as a bulk varistor.

Figure 17.12 compares the microstructures of two types of our ZnO-based varistors. The one that was sintered in air with a conventional process exhibits the best electrical properties for its own class, i.e. the screen-printed film sintered at 900 °C/1 h (α = 20, E = 15 kV/cm, J = 1.2 mA/cm^2 and the ceramic varistor sintered at 1180 °C/2 h (α = 48, E = 2.8 kV/cm, J = 0.035 mA/cm^2). Both were prepared from the same powder, but show notable differences in grain size (less than 4 μm in the thick-film, and 7–8 μm for the disk), homogeneity (poor in the film) and appearance of the spinel phase (clear grey grains) located in the GBs in the ceramic sample, but not easily identified in the film. In addition to the microstructural differences, there are meaningful differences relating to the defects equilibrium in the interface or GB. The defects equilibrium reached at lower temperatures does not allow shaping of high potential barriers and, as a consequence, the nonlinear response is lower. High sintering temperatures are required since these temperatures favour the formation of the electronic defects needed for a suitable defects equilibrium (electronic states in the interface, cationic and anionic vacants, dopants, impurities, oxygen diffusion . . .) where the electrons are trapped, giving place to the Schottky barrier responsible for the nonlinear behaviour.

A similar comparison is presented in Fig. 17.13 between a tape-casted layer and a bulk varistor, again taking the samples sintered in the conditions that offer the best characteristics in their own group. The tape is similar to the screen-printed film, having small grains, many pores attributed to Bi_2O_3 volatilization and poor densification.

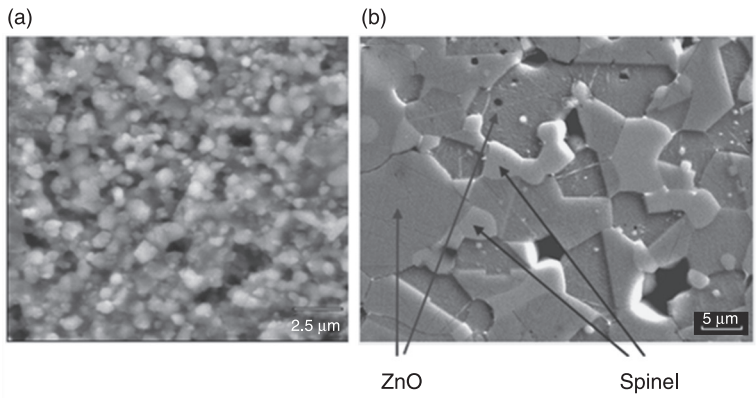

17.12 Comparation of the microstructures of two types of our ZnO-based varistors: (a) the screen-printed film that was sintered in air by a conventional process and exhibits the best electrical properties for its own class and (b) a bulk varistor.

© Woodhead Publishing Limited, 2012

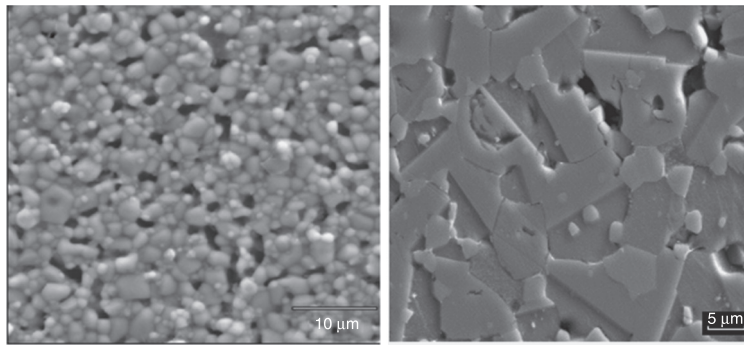

17.13 Comparation of the microstructures of (a) a tape-casted layer and (b) a bulk varistor.

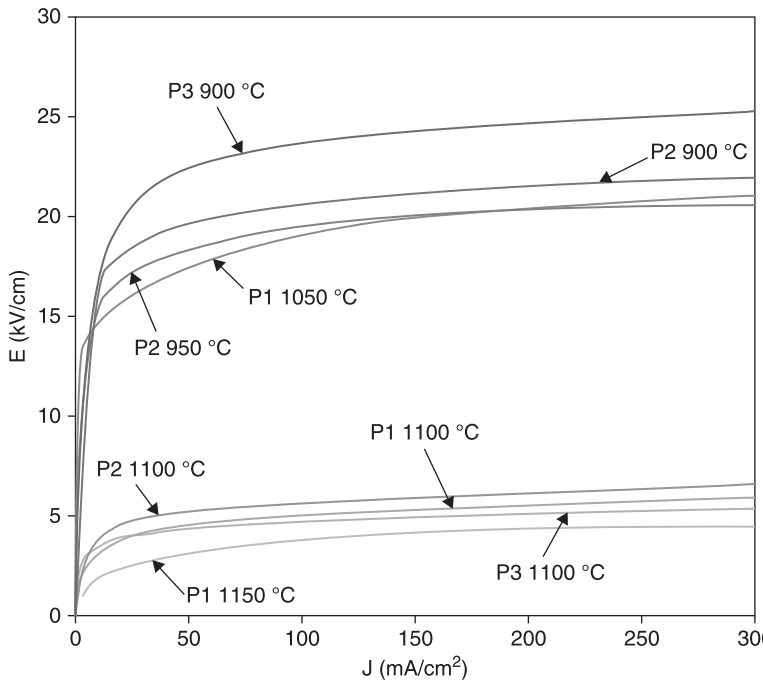

17.14 The J-V characteristics measured in screen-printed varistors prepared with the various batches of powder described in Table 17.1.

Figures 17.14 and 17.15 show the J-V characteristics measured in screen-printed and tape-casted varistors, respectively, prepared with the various batches of powder described in Table 17.1. The results indicate that, in both cases (screen-printing and tape casting), powders 1 and 2 resulted in very similar behaviour. The best nonlinear coefficient value is never higher than 20 (Table 17.2).

© Woodhead Publishing Limited, 2012

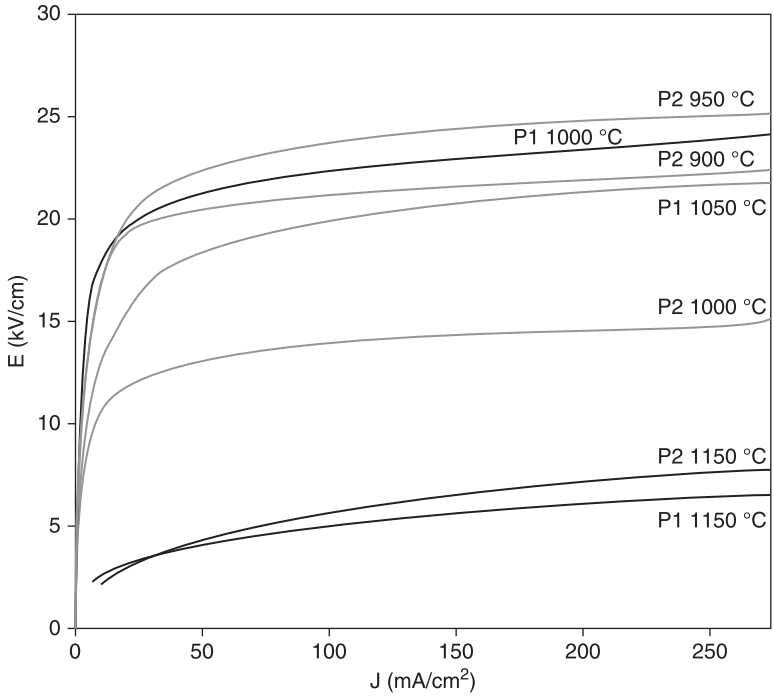

17.15 The J-V characteristics measured in tape-casted varistors prepared with the various batches of powder described in Table 17.1.

The only notable difference between the printed and cast samples concerns the fact that the latter exhibit electrical responses that are much less affected by the sintering temperature. The experiments always confirm that:

- Tape casting results in films with higher similarity in their electrical behaviour, despite variations in their sintering temperatures, associated with a higher similarity in microstructure.
- As expected, the higher the compact materials are, the higher the sintering temperature that is permitted before excessive loss of Bi_2O_3.

The varistor behaviour of the powders of the different batches, is reproducible always such as pressed samples of these batches (bulk). If the different processing steps are carried out in the same way, taking account of the following requirements of the raw materials, the obtained electrical response will be reproducible. However, it is necessary to use raw materials with high purity and small, homogeneous particle size of the ZnO and dopants raw materials. In the following ceramic processing steps (mixing oxide routes), it is necessary to carry out the processing in the same way without any variations. TFVs fabricated by screen printing show a reproducibility in electrical characterization of about 50% in the

© Woodhead Publishing Limited, 2012

spots measured, due to the inherent porosity associated with this technique, and as a consequence of it, thick-films deposited by screen printing are less dense than the ones produced by tape casting. The reproducibility in the electrical behaviour of thick-films produced by tape casting reaches values around 90%. Almost all the electrical measurements carried out between the bottom electrode and different electrodes homogeneously distributed on the top surface of the thick-films show the same nonlinear behaviour. This result indicates that the microstructure is very homogeneous.

In short, all the attempts to improve the performance of our samples in terms of nonlinear coefficient and adequate microstructure were not successful when firing/sintering in standard ambient and standard conditions. Only when we started from powders of different batches were minor differences noted, and varistor action was only possible with peak temperatures below about 950 °C [58]. Therefore it was decided to approach the problem with various strategies aimed at limiting the bismuth loss from the samples, or at replacing the lost bismuth with new bismuth after the high-temperature process.

Four strategies were tested:

1. A Bi_2O_3 paste was screen-printed over the varistor thick-films previously printed (not sintered) on Pt/Alumina. The idea was to establish a quasi liquid-vapour equilibrium for Bi during the co-firing at high temperature (1150 °C) to prevent Bi_2O_3 vaporization from inside the film (Fig. 17.16). Regardless of the powder composition (P1–P3) and dwell times, no significant progress was obtained for the α-value (best results $\alpha = 19$); on the contrary, the excess of liquid phase resulted in abnormal grain growth, a decrease in breakdown voltage and an increase in leakage current. The nonlinear behaviour improves if it is compared with thick-films sintered at high temperature without changes in the shaping of the films but the α value obtained is rather lower than in bulk varistors. α values of around 20 are obtained in thick-films without changes in the sintering process at low temperature (900 °C), but the final objective is to try to reach nonlinear coefficient values similar to those in bulk varistors ($\alpha \sim 40$).

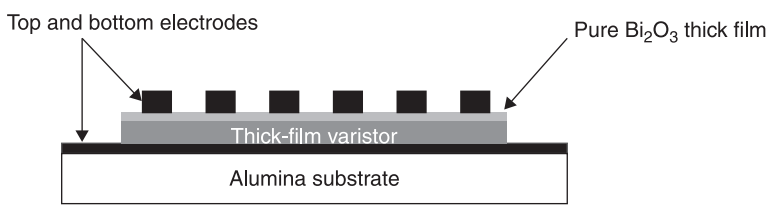

17.16 A quasi liquid-vapour equilibrium for Bi during the co-firing at high temperature (1150 °C) used to prevent Bi_2O_3 vaporization from inside the film.

© Woodhead Publishing Limited, 2012

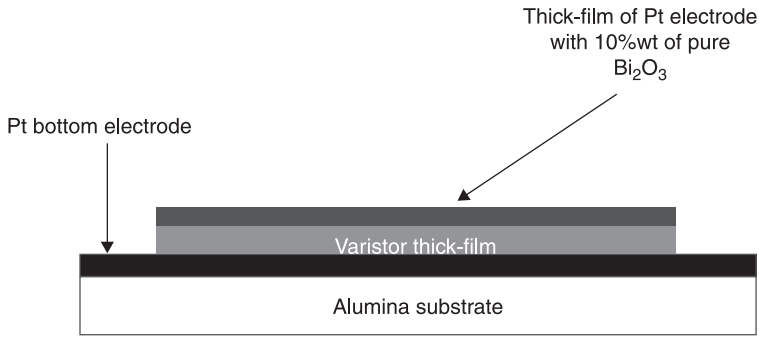

17.17 A platinum-based ink with 10%wt of Bi_2O_3 printed on sintered varistor layers.

2. Firing the upper electrode, consisting of a paste of Pt enriched with Bi_2O_3, printed on top of the varistor layer. A platinum-based ink with 10%wt of Bi_2O_3 was printed on sintered varistor layers (Fig. 17.17). The film was then fired at 850 °C/30 min. The idea was to compensate, with the Bi_2O_3 in the conductive film, for the Bi_2O_3 lost during the sintering at high temperature. Yet, no significant progress in achieving high nonlinear coefficients was observed, regardless of the applied samples and sintering process.

   According to Martin [55], this strategy resulted in ZnO-based TFVs with nonlinear coefficients α between 35 and 40, but they carried out the measurements of I-V between electrodes both located on top of the varistors. We can therefore guess that compensation for the Bi_2O_3 lost occurred near the varistor/electrode interface, whereas the Bi_2O_3 diffusion length in the already sintered varistor was too small to be efficient at larger distances.
3. Samples fired in a 'closed' space with Bi_2O_3 powder (Fig. 17.18).

   The idea is to 'maintain a Bi-rich atmosphere' around the sample. The spinel powder around the alumina 'cover' reacts with the Bi_2O_3 that is diffusing out (after this latter melts at 825 °C) to form a pyrochlore phase at temperatures between 700–900 °C. This compound 'seals' the alumina cover to the alumina crucible.

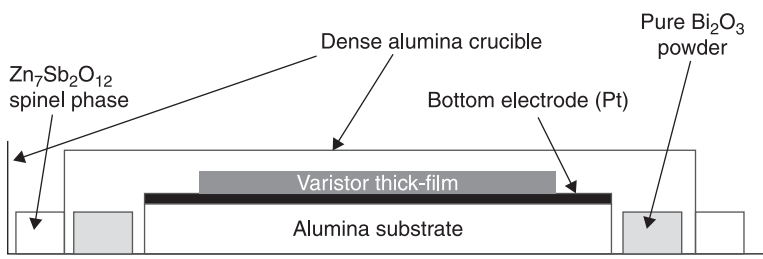

17.18 Samples fired in a 'closed' space with Bi_2O_3 powder.

© Woodhead Publishing Limited, 2012

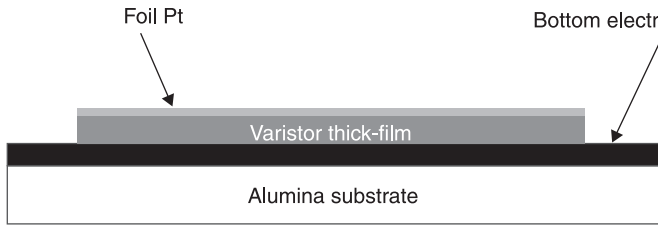

17.19 An experimental design intended to to maintain in equilibrium the Bi_2O_3 in the vapour phase and in the liquid phase in the film.

4. As in case (3), a closed space is created around the varistor, but with a Pt foil. The scope is to maintain in equilibrium the Bi_2O_3 in the vapour phase and in the liquid phase in the film (Fig. 17.19). Note that this experimental design would be unacceptable in industrial manufacturing processes due to the high price of Pt foils.

Data in Table 17.5 and Fig. 17.20 demonstrate the high effectiveness of strategies (3) and (4) above. Table 17.5 compares the electrical parameters of varistor tapes prepared with powder 1 and sintered in air or Bi-rich atmospheres. Figure 17.20 shows the corresponding J-V curves: the significant increase in the nonlinear coefficient is accompanied by a sharp transition from the pre-breakdown to the breakdown region, and by low leakage currents. Table 17.5 data correspond to three thick-films pressed and produced by tape casting and Table 17.2 data refer to one thick-film deposited by screen printing. The properties displayed by the tapes sintered in the Bi-rich atmosphere are close to those measured for a ceramic varistor sintered at a peak temperature of 1180 °C/2 h ($\alpha = 43$, $J_{eff} = 0.003$, $E = 4.1$).

In Fig. 17.21, the nonlinear behaviour (I-V response) obtained for a ZnO bulk varistor and the ZnO thick-films is compared, with conventional sintering such as the films sintered with the changes carried out in the thermal treatment.

Figure 17.22 shows SEM micrographs of a bulk varistor sintered at 1180 °C/2 h in air with tape-cast layers sintered at 1150 °C/1 h under the conditions described above. Tapes are observed without polish or chemical attacks whereas the ceramic

Table 17.5 Comparison of the electrical parameters of varistor tapes prepared with powder 1 and sintered in air or Bi-rich atmospheres

Sintering	α	E_{eff} (kV/cm)	J_{eff}(mA/cm^2)
Conventional	20	4	2.3
Sealing in a Bi_2O_3 atmosphere	43	4.1	0.003
Pt sealing	36	4.3	0.005

© Woodhead Publishing Limited, 2012

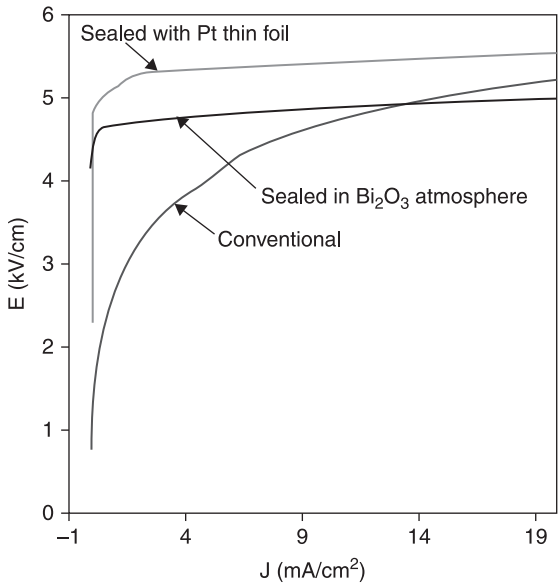

17.20 J-V curves corresponding to Table 17.5.

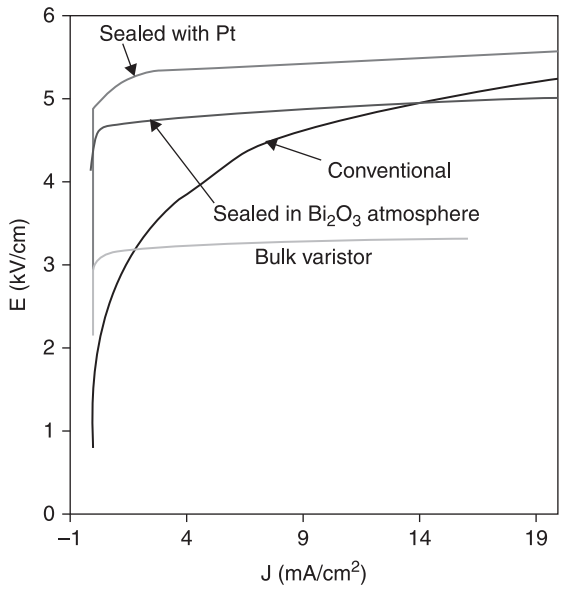

17.21 Comparison of the nonlinear behaviour (I-V response) obtained for a ZnO bulk varistor and the ZnO thick-films, with conventional sintering such as the films sintered with the changes carried out in the thermal treatment.

© Woodhead Publishing Limited, 2012

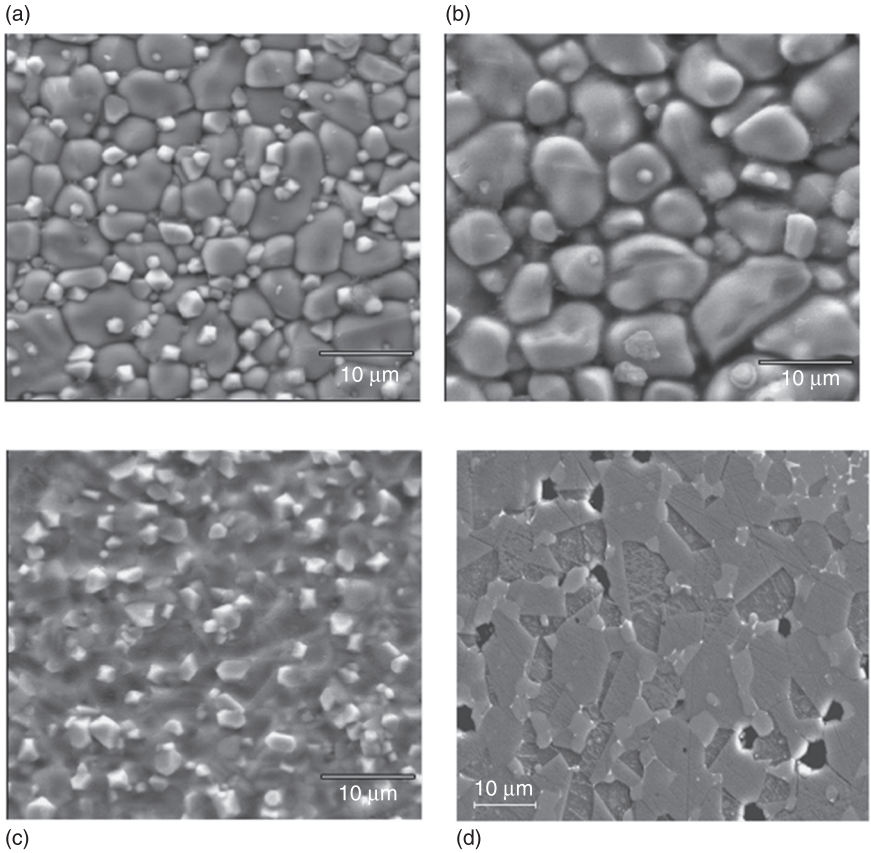

17.22 Comparison of the microstructures of tape-casted layers sintered at 1150 °C/1 h under different conditions and bulk ZnO-based varistors sintered at 1180 °C/2 h. (a) Layer sealed in a platinum foil. (b) Sintered in a Bi_2O_3-rich atmosphere. (c) Sintered in air (conventional). (d) Bulk varistor sintered in air. Layers are observed without polish or chemical attacks whereas the bulk ceramic sample is polished and chemically attacked.

sample is polished and chemically attacked. The effect of sintering in a Bi_2O_3-rich atmosphere in terms of a limited loss of volatilized Bi_2O_3, and consequently in terms of grain growth, densification and homogeneous distribution of phases (including the spinel phase, brighter than the ZnO in Fig. 17.22) is quite evident. The grain size in sealed samples is comparable to that of a bulk varistor.

17.9 Conclusion

Although much work is yet to be carried out to demonstrate the full potential of thick-film and tape-casting technologies in the development of film varistors,

© Woodhead Publishing Limited, 2012

important steps in this direction have been accomplished. It has been shown that nonlinear coefficients $\alpha > 40$ are accessible by ZnO-based film varistors sintered in a Bi_2O_3-rich atmosphere. Also, the other electrical characteristics tested approach those of ceramic ZnO-based varistors.

Further improvements might be reached by combining the approach of sintering in the presence of Bi_2O_3 powder in a near-closed space, with other expedients, such as pressures applied on wet films or layers, or a Bi-rich sol added to the oxide powders in the pastes.

Finally, we should not disregard approaches such as direct-write (ink-jet) deposition of new specially designed varistor inks, as this technology looks promising for varistor fabrication in the future [59].

17.10 Acknowledgements

Acknowledgements are to Dr. M. Peitedado, Dr. A. C. Caballero and Professor J. F. Fernandez of the Electroceramic Department of the Ceramic and Glass Institute (CSIC, Spain), Professor J. de Frutos of the ETSI Telecomunicación (UPM, Spain) and Professor M. Kosec of the Jozef Stefan Institute (Slovenia).

17.11 References

1. Matsuoka M., Masuyama T. and Iida Y., 'Voltage nonlinearity of zinc oxide ceramics doped with alkali-earth metal oxide', *Jpn J Appl Phys*, 8, 1275–1276 (1969).
2. Matsuoka M., 'Nonohmic properties of zinc oxide ceramics', *Jpn J Appl Phys*, 10 (6), 736–746 (1971).
3. Puyané R., 'Applications and product development in varistor technology', *J Mat Proc Tech*, 55 (3–4), 268–277 (1995).
4. Chiou B. -S. and Jih F. W., 'Studies on oxide-doped ZnO varistors with conventional pellet form and thick-film form', *British Ceramic Proceedings*, 36, 129–141 (1985).
5. Clarke D. R., 'Varistor ceramics', *J Am Ceram Soc*, 82 (3), 485–502 (1999).
6. Philipp H. R. and Levinson L. M., 'Degradation phenomena in ZnO varistors: a review', in *Advances in Ceramics*, vol. 7, Additives and interfaces in electronic ceramics, edited by M. F. Yan and A. H. Heder. *Am Ceram Soc*, Colombus, OH, pp. 1–21 (1983).
7. Blatter G. and Greuter F., 'Electrical properties of grain boundaries in polycrystalline compound ceramics', *Semicond Sci Technol*, 5 (1), 111–137 (1990).
8. Mukae K., 'Electrical properties of grain boundaries in ceramic semiconductors', in *Key Engineering Materials*, vol. 125–126, Electrical properties of oxide materials, edited by J. Nowotny and C. C. Sorrell. Trans Tech Publications, Switzerland, pp. 317–330 (1997).
9. Levinson L. M. and Philipp H. R., 'The physics of metal oxide varistors', *J Appl Phys*, 46, 1332–1341 (1975).
10. Eda K., 'Conduction mechanism of nonohmic zinc oxide ceramics', *J Appl Phys*, 49, 2964–2972 (1978).
11. Mahan G. D., Levinson L. M. and Philipp H. R., 'Theory of conduction in ZnO varistors', *J Appl Phys*, 50 (4), 2799–2812 (1979).

© Woodhead Publishing Limited, 2012

12. Morris W. G., 'Physical properties of electrical barriers in varistors', *J Vac Sci Technol*, 13 (4), 926–931 (1976).
13. Levine J. O., 'Theory of varistor electrical properties', *CRC Crit Rev Solid State Sci*, 5, 597–608 (1975).
14. Eda K., Matsushita Electric Industrial Co. Ltd., 'Zinc oxide varistors', *IEEE Electrical Insulation Magazine*, 5 (6), 28 (1989).
15. Gupta T. K., 'Application of zinc oxide varistors', 73 (7), 1817–1840 (1990).
16. Bernasconi J., Strassler S., Knecht B., Klein H. P. and Menth A., 'Zinc oxide-based varistors: a possible mechanism', *Solid State Commun*, 21, 867–870 (1977).
17. Hower P. L. and Gupta T. K., 'A barrier model for ZnO varistors', *J Appl Phys*, 50, 4847–4855 (1979).
18. Eizinger R., 'Grain boundary phenomena in ZnO varistors', in *Grain Boundaries in Semiconductors*, edited by H. J. Leamy, G. E. Pike and C. H. Seager. Elsevier, New York, pp. 343–355 (1982).
19. Pike G. E., 'Semi-conducting polycrystalline ceramics', in *Materials Science and Technology*, Vol. 11, edited by M. V. Swain. VCH, Weinheim, Germany, pp. 731–754 (1994).
20. Fernández Hevia D., de Frutos J., Caballero A. C. and Fernández J. F., 'Mott–Schottky behaviour of strongly pinned barriers and characterization of ceramic varistors', *J Appl Phys*, 92 (5), 2890–2898 (2002).
21. Tuller H. L., 'ZnO grain boundaries: electrical activity and diffusion', *J Electroceram*, 4 (S1), 33–40 (1999).
22. Tanaka S., Akita C., Ohashi N., Hawai J., Haneda H. *et al.* 'Chemical state analysis of grain boundaries in ZnO varistors', *J Solid State Chem*, 105 (1), 36–43 (1993).
23. Matsuoka M., 'Nonohmic properties of zinc oxide ceramics', *Jpn J Appl Phys*, 10 (6), 736–746 (1971).
24. Morris W. G., 'Electrical properties of ZnO-Bi_2O_3 ceramics', *J Am Ceram Soc*, 56 (7), 360–364 (1973).
25. Inada M., 'Formation mechanism of nonohmic zinc oxide ceramics', *Jpn J Appl Phys*, 19 (3), 409–419 (1980).
26. Wong J., 'Sintering and varistor characteristics of ZnO-Bi_2O_3 ceramics', *J Appl Phys*, 51 (8), 4453–4459 (1980).
27. Takemura T., Kobayashi M., Takada Y. and Sato K., 'Effects of bismuth sesquioxide on the characteristics of ZnO varistors', *J Am Ceram Soc*, 69 (5), 430–436 (1986).
28. Olsson E. and Dunlop G. L., 'The effect of Bi_2O_3 content on the microstructure and electrical properties of ZnO varistor materials', *J Appl Phys*, 66 (9), 4317–4324 (1989).
29. Magnusson K. O. and Wiklund S., 'Interface formation of Bi on ceramic ZnO: a simple model varistors grain boundary', *J Appl phys*, 76 (11), 7405–7409 (1994).
30. Yodogawa M. and Yamakazi T. 'The role of CO ions on the appearance of nonlinear I-V characteristics in ZnO based ceramics', *J Electroceram*, 4 (S1), 49–53 (1999).
31. Asokan T., Iyengar G. N. K. and Nagabhushana G. R., 'Influence of additive oxides on the electrical characteristics of ZnO-based composites', *Br Ceram Trans J*, 86, 190–193 (1987).
32. Kim T. H., Kawamura H. and Nawata M., 'The effect of Cr_2O_3 additive on the electrical properties of ZnO varistor', *J Mater Sci*, 32, 1665–1670 (1997).

© Woodhead Publishing Limited, 2012

33. Senda T. and Bradt R. C., 'Grain growth of zinc oxide during the sintering of zinc oxide-antimony oxide ceramics', *J Am Ceram Soc*, 74 (6), 1296–1302 (1991).
34. Wu L., Shen C. Y., Chen Y. C., Wei Y. F., Chen M. H. *et al.* 'The microstructure of ZnO varistor doped with antimony oxide', *Jpn J Appl Phys*, 30, 2850–2856 (1991).
35. Bernik S. and Daneu N., 'Characteristics of SnO_2 -doped ZnO-based varistor ceramics', *J Eur Ceram Soc*, 21, 1879–1882 (2001).
36. Levin E. M. and Roth R. S., 'Polymorphism of bismuth sesquioxide II. Effect of oxide additions on the polymorphism of Bi_2O_3 ', *J Res Natl Bur Stand: A Phys Chem*, 68A (2), 197–206 (1964).
37. Shao H. Q., Gao X. H. and Cao Z. C., 'Effect of annealing on phase structure and degradation of a zinc oxide varistor with Si-additive', *J Eur Ceram Soc*, 17, 55–59 (1997).
38. Kutty T. R. N. and Ezhilvalavan S., 'The role of silica in enhancing the nonlinearity coefficients by modifying the trap states of zinc oxide ceramic varistors', *J Phys D: Appl Phys*, 29, 809–819 (1996).
39. Tanahashi M., Ito M., Murao M. and Iga A., 'Effect of Al-doping on the grain growth of ZnO', *Jpn J Appl Phys*, 36 (Part 2–5A), 573–576 (1997).
40. Kimv J., Kimura T. and Yamaguchi T., 'Effect of bismuth oxide content on the sintering of zinc oxide', *J Am Ceram Soc*, 72 (8), 1541–1544 (1989).
41. Senda T. and Bradt R. C., 'Grain growth in sintered ZnO and ZnO-Bi_2O_3 ceramics', *J Am Ceram Soc*, 73 (1) 106–114 (1990).
42. Dey D. and Bradt R. C., 'Grain growth of ZnO during Bi_2O_3 liquid-phase sintering', *J Am Ceram Soc*, 75 (9) 2529–2534 (1992).
43. Guha J. P., Kunej S. and Suvorov D., 'Phase equilibrium relations in the binary system Bi_2O_3-ZnO', *J Mater Sci*, 39, 911–918 (2004).
44. Stucki F. and Greuter F., 'Key role of oxygen at zinc oxide varistor grain boundaries', *Appl Phys Lett*, 57 (5), 446–448 (1990).
45. Bueno P. R., Leite E. R., Oliveira M. M., Orlandi M. O. and Longo E., 'Role of oxygen at the grain boundary of metal oxide varistors: a potential barrier formation mechanism', *Appl Phys Lett*, 79 (1), 48–50 (2001).
46. 'Varistors: general technical information', Epcos AG Product Catalogue, Munich, Germany (2002).
47. Villegas M. 'Multilayers ceramic materials' in *Introduction to Electroceramics*, edited by J. F. Fernández and J. de Frutos, Fundación Rogelio Segovia para el Desarrollo de las Telecomunicaciones, FUNDETEL, Madrid (2003).
48. Rocak D., Kosec M. and Degen A., 'Ceramic suspension optimization using factorial design of experiments', *J Eur Ceram Soc*, 22, 391–395 (2002).
49. Kuo S.-T., Tuan W.-H., Lao Y.-W., Wen C.-K. and Chen H.-R., 'Inner electrodes for multilayer varistors', *Int J Appl Ceram Technol*, 6 (2), 223–230 (2009).
50. Wang F. and Huebner W., 'Interaction of silver/palladium electrodes with lead- and bismuth-based electroceramics', *J Am Ceram Soc*, 76 (2), 474–480 (1993).
51. Lee W.-H., Chen W.-T., Hu C.-L., Lee Y.-C., Lin S.-P. *et al.* 'Characterization of ZnO-based multilayer varistor sintered by hot-press sintering', *Jpn J Appl Phys*, 45 (4A), 2689–2694 (2006).
52. Gouverneur S., Lucat C., Ménil F. and Aucouturier J. L., 'New densification process of thick-film', *IEEE Trans Compon Hybrids, Manuf Technol*, 16, 505–510 (1993).

© Woodhead Publishing Limited, 2012

53. Ménil F., Debeda H. and Lucat C., 'Screen-printed thick-films: from materials to functional devices', *J Eur Ceram Soc*, 25 (12), 2105–2113 (2005).
54. Perrot F., doctoral thesis 'The effects of multicurrent impulses on the low current bula distribution in varistor materials, under continuous AC operation', Brighton University, UK (1995).
55. Martin M. P., doctoral thesis 'Realisation de varistances sérigraphies à base de ZnO pour des applications en électronique de puissance: influence des électrodes sur les propiétés électriques du composant de protection', University of Bordeaux 1, France (2003).
56. Metz R., Delalu H., Vignalou J. R., Achard N. and Elkhatib E., 'Electrical properties of varistors in relation to their true bismuth composition after sintering', *Mater Chem Phys*, 63, 157–162 (2000).
57. Fernandez J. F., Nieto E., Moure C., Duran P. and Newnham R. E. 'Processing and microstructure of porous and dense PZT thick-films on Al_2O_3', *J Mater Sci*, 30 (21), 5399–5404 (1995).
58. Peiteado M., de la Rubia M. A., Velasco M. J., Valle F. J, and Caballero A. C., 'Bi_2O_3 vaporization from ZnO-based varistors', *J Eur Ceram Soc*, 25 (9), 1675–1680 (2005).
59. Tohver V., Morissette S. L., Lewis J. A., Tuttle B. A., Voigt J. A. *et al.*, 'Direct-write fabrication of zinc oxide varistors', *J Am Ceram Soc*, 85 (1), 123–128 (2002).

© Woodhead Publishing Limited, 2012

18

Laser-printed micro- and meso-scale power generating devices

A. PIQUÉ, Naval Research Laboratory, USA

Abstract: This chapter describes how laser direct-write (LDW) processes can be applied to the rapid prototyping of micro- and meso-scale power sources. The chapter reviews the use of laser-induced forward transfer (LIFT) to deposit patterns of complex suspensions comprising the functional materials required for printing ultracapacitors, primary and secondary batteries and dye-sensitized solar cells (DSSC). The chapter describes the preparation of embedded microbatteries via LDW and concludes with a discussion on the present and future status of these laser-based digital microfabrication techniques.

Key words: laser direct-write (LDW), laser-induced forward transfer (LIFT), laser-printed micro-power sources, embedded microbatteries.

18.1 Introduction

The trend for developing increasingly smaller and more autonomous microelectronic systems has not yet been matched by power sources with correspondingly reduced volumes. These microelectronic systems and devices have created a need for unique types of micro-power sources capable of delivering high energy densities within usually limited form factors. Furthermore, to be effective, the micro-power sources must be comprised of different components such as energy-harvesting elements for power generation, microbatteries for energy storage and electrochemical capacitors for activities requiring high power surges. Depending on the application and performance requirements, various combinations of these components might be required.

This need has gone unfulfilled due to the difficulties of depositing and processing at low temperatures complex materials for power generation and of building the required structures within limited form factors using traditional thin-film deposition techniques. Furthermore, standard lithography techniques involving multiple steps such as material deposition, lithographic masking and etching processes are not well suited for the fabrication of non-planar structures common in most power sources. As an alternative, non-lithographic processes known as direct-write techniques allow the printing of patterns of complex material systems onto virtually any type of surface to generate the required structures in digital fashion.The use of printing techniques such as laser direct-write (LDW) offer unique opportunities towards the development and customization of various types of micro-power sources such as electrochemical ultra-capacitors and die-sensitized solar cells, as well as primary and secondary

© Woodhead Publishing Limited, 2012

embedded batteries. In this chapter, the use of laser-based direct-write techniques for printing intricate patterns of thick-film structures for the development of micro- and meso-power generating devices will be reviewed and the results obtained to date briefly described.

The application of laser printing or LDW techniques has grown steadily since the first reports of patterned copper deposition by laser forward transfer made by Bohandy and coworkers 25 years ago (Bohandy *et al.*, 1986). These general techniques employ a pulsed laser to locally transfer material from a source film onto a substrate in close proximity to or in contact with the film. The source is typically a coated laser-transparent substrate, referred to as the target, donor substrate, or ribbon. Laser pulses propagate through the transparent ribbon until they are absorbed by the film. Above an incident laser energy threshold, material is ejected from the film and transferred toward the acceptor or receiving substrate. Such laser-induced forward transfer techniques, known as LIFT, belong to a class of laser-based direct-write processes capable of generating a high-resolution pattern without the need for lithogaphic processes afterwards. Other examples of LDW techniques include pyrolitic or photolytic decomposition of gas- or liquid-phase precursors, also known as laser chemical vapor deposition (CVD) or laser-assisted deposition (Herman, 1989; Osgood and Deutsch, 1985). However, these non-forward transfer techniques will not be discussed in this chapter because they are not suitable for printing the types of materials required for the fabrication of power sources.

Translation of the ribbon and receiving substrate, and/or scanning and modulating the laser beam enable complex pattern formation. Commercially available, computer-controlled translation stages or galvonometric scanning mirrors enable high-resolution patterns from the individually written 3D pixels or voxels resulting from the laser forward transfer process. Figure 18.1 shows a schematic illustrating the basic elements required for the LDW apparatus. Since the source of energy for the transfers, i.e. the laser, is decoupled from the material to be printed, very high writing speeds, in excess of meters per second, can be achieved. In practice, the printing speeds are limited by the firing rate of the laser and/or how fast the ribbon and the receiving substrate can be translated, although roll-to-roll processes are certainly compatible with LDW.

One may consider the LDW technique to be analogous to ink-jet deposition of functional materials without the constraints of a nozzle, and with the added benefits of laser processing, such as material modifications and micromachining. This added versatility in comparison to other printing methods enables LDW to find opportunities in fields ranging from metals to biological and soft condensed matter, and have been applied successfully to the printing of materials for power generation applications.

This chapter will provide a brief overview of the laser forward transfer and LDW literature, with a particular emphasis towards its application for the fabrication of micropower storage systems such as ultracapacitors and microbatteries, and energy -harvesting systems such as dye-sensitized solar cells

© Woodhead Publishing Limited, 2012

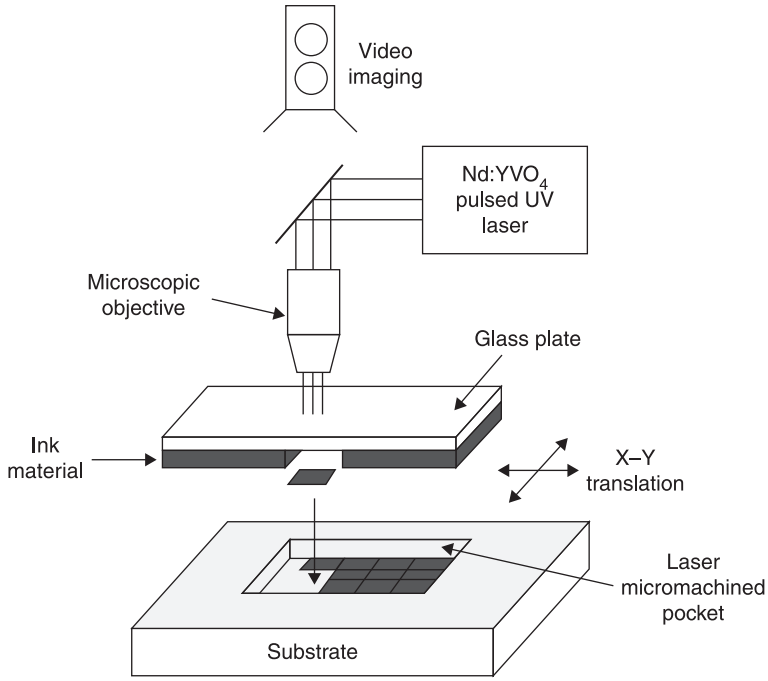

18.1 Schematic illustration of a LDW set-up for printing voxels on a substrate.

(DSSC). The chapter concludes with a discussion of the role that the LDW technique may play in the future of microelectronic manufacturing and provides a glimpse of what the future of printed power sources might look like.

18.2 Background to laser-induced forward transfer (LIFT)

The laser forward transfer process was first used in depositing copper metal patterns inside a vacuum chamber (Bohandy *et al.*, 1986). Excimer laser pulses (= 193 nm, 15 ns) were focused with a cylindrical lens to a 25 mm long by 50 μm wide line on a source substrate containing a thin copper film. The Cu was transferred to Si and fused silica substrates, where further examination revealed resistivities ranging between 3 to 50 times the value for bulk copper with adhesion behavior that passed the 'tape test'. Bohandy's group coined the term laser-induced forward transfer (LIFT) to denote the process and developed a model to describe how it worked. According to this model: (1) the laser pulse heats the interface of the film at the source substrate; (2) a resulting melt front propagates through the film until it reaches the free surface; (3) at about this time, the material at the interface is superheated beyond its boiling point until, (4) the resulting

© Woodhead Publishing Limited, 2012

vapor-induced pressure at the interface propels the molten film forward towards the acceptor substrate (Adrian *et al.*, 1987). The same group then demonstrated that this process can be carried out in air, i.e. under atmospheric conditions, without the need for a vacuum (Bohandy *et al.*, 1988).

The LIFT technique is simple and can be used with a wide variety of film materials, mainly metals such as Cu and Ag (Bohandy *et al.*, 1988), Al (Schultze and Wagner, 1991), W (Tóth *et al.*, 1993; Kántor *et al.*, 1994) and Cr (Zergioti *et al.*, 1998a). Reports of LIFT for other materials such as Al_2O_3 (Greer and Parker, 1988), In_2O_3 (Zergioti, 1998a), and even high-temperature superconductors (Fogarassy *et al.*, 1989) are worth mentioning, although the quality of the transferred ceramics was not as good as those deposited by traditional film growth techniques. The thickness of the transferred film on the acceptor substrate can be adjusted by repetitive transfers from the ribbon. In a similar way, multilayer structures can be deposited. In general, to achieve uniform transfers with good morphology and spatial resolution on the acceptor substrate, the following conditions must be satisfied: (1) the material to be transferred from the ribbon should strongly absorb the laser wavelength in use; (2) the ribbon should be in close proximity (<100 μm) to the acceptor substrate; and (3) the laser energy densities, or fluences, should barely exceed the threshold fluence for removal of the film from the ribbon. This last parameter is very important in order to control the quality of the films, since too high fluences result in excessive explosive vaporization of the film, affecting the morphology and resolution of the transfers, while too low fluences result in incomplete transfers. In fact, it is the ability to precisely control the intensity and nature of the interaction of the laser pulse at the interface between the transparent ribbon substrate and its coating that endows LIFT with its unique properties, as the next sections will show.

18.2.1 Evolution of LIFT

Despite its successful application to the deposition of thin metal layers, the actual uses of the original LIFT technique are limited due to several shortcomings. In traditional LIFT, metal films must be deposited on the ribbon by conventional vapor deposition techniques that require vacuum processes not generally compatible with most of the materials required in the fabrication of power sources, i.e. electrolytes, separators and complex oxide electrodes. Furthermore, the melting and solidification of the transferred material during LIFT leads to the formation of interfaces between adjacent voxels, which can have deleterious effects in the electrical transport properties of the patterned structure being fabricated. In fact, the melting of the transferred material becomes a serious issue when LIFT is performed under atmospheric conditions, because most metals are easily oxidized when melted in air. Moreover, the rapid quenching of the metal voxels can result in high intrinsic stresses between the transferred metal and the substrate, ultimately leading to poor adhesion and delamination of the transferred

© Woodhead Publishing Limited, 2012

layers. Finally, LIFT is not suited for the transfer of ceramics and other inorganic phases given the irreversible phase changes and decomposition that tend to be exhibited by these materials upon melting and solidification.

The above limitations explain why traditional LIFT is not suitable for the laser transfer of complex, sensitive materials such as those found in electronic and power generation devices. In fact, this realization is underscored by the decline in the number of publications reporting on LIFT of metals and other inorganic materials that followed in the late 1990s. Despite these shortcomings, the capability for laser transferring materials in patterned form is extremely important for many commercial, aerospace and military applications.

The first variation of the LIFT process to attempt to overcome these limitations employed multilayered films (Tolbert *et al.*, 1993a). The multilayers are formed by depositing a thin laser-absorbing layer (usually a metal) on the transparent support, followed by a layer of the material to be transferred. During transfer, the laser pulse interacts with the absorbing layer, referred to as the dynamic release layer or DRL, causing it to vaporize in a similar manner as in LIFT. This confined layer forces the material in the second layer to be removed from the film and transferred to the acceptor substrate. The advantage of this approach is that it allows the transfer of materials for which the previously described LIFT process is not effective. For instance, this can include materials with weak absorption of the laser radiation, or materials that can be damaged by their interaction with the laser pulse. This variation on the LIFT process was originally intended for high speed laser color printing applications, and was called laser ablation transfer (Tolbert *et al.*, 1993a). More recently this approach has been used for the LDW of extremely laser sensitive materials such as DNA biomolecules (Fernández-Pradas *et al.*, 2004; Serra *et al.*, 2004).

The work by Tolbert using the dynamic release layer approach to LIFT showed for the first time that the pulse duration has an effect on the transfer process. Their experiments indicated that picosecond laser pulses are more efficient in ablating the multilayered films than nanosecond pulses, with transfer laser fluence thresholds an order of magnitude smaller (Tolbert *et al.*, 1993b). Since then, various reports on the use of femtosecond lasers for laser forward transfer have validated Tolbert's results. Most of the applications of femtosecond LIFT have been related to the laser transfer of metals (Bähnisch *et al.*, 2000; Papakonstantinou *et al.*, 1999; Zergioti *et al.*, 1998b). However, femtosecond LIFT has also been applied to the transfer of biological materials (Karaiskou *et al.*, 2003; Zergioti *et al.*, 2005).

A second variation on the LIFT process employs an organic precursor compound (palladium acetate) rather than a pure metal for transfer (Esrom *et al.*, 1995). This is significant as it demonstrates that the laser forward transfer process can take advantage of the photoinduced decomposition of a precursor at the ribbon/coating interface to propel the remainder of the film forward and create a metal pattern. By irradiating the transferred mixture with additional laser pulses, a very thin (<100 nm) but grainy Pd coating is produced, on which a thicker metal layer can be obtained by electroless plating. In their paper, the authors consider the laser

© Woodhead Publishing Limited, 2012

transfer and subsequent electroless metal plating as a two-step process enabling the selective deposition of metal patterns. However, their key contribution shows that the LIFT process can be used to deposit a precursor of the desired material, which once transferred can be further decomposed or processed into its final form.

A third variation of the LIFT process involves the transfer of various materials in powder form mixed with organic binders. The advantage of this approach resides in the fact that the transfer of thicker films from the ribbon can be achieved at lower laser fluences than with LIFT of homogenous films. Furthermore, the mixture is transferred in its solid phase, thus avoiding the melting and re-condensation steps that take place in traditional LIFT. This modified LIFT approach has been used for the LDW of diamond nanopowders (Pimenov *et al.*, 1995), ferroelectric ($BaTiO_3$ and $SrTiO_3$) and ferrite ($Y_3Fe_5O_{12}$) micron-sized powders (Piqué *et al.*, 1999a, 1999b), and carbon composite polymers for gas sensing elements (Piqué *et al.*, 2000a). A limitation of this approach is that the adhesion of the transferred layers can be poor and the organic binder remains after the transfer, thus high-temperature calcination steps are necessary to achieve dense layers.

Finally, instead of using a solid binder, the use of complex fluid mixtures leading to the direct transfer of rheological systems has also been demonstrated (Auyeung *et al.*, 2000; Piqué *et al.*, 2000b). The realization that pastes, inks, suspensions and sol-gel solutions can be laser transferred without physical or chemical modification represents a totally new form of LIFT and has led to a number of new applications with a wider range of materials and formulations.

18.3 Laser transfer of complex rheological systems

The use of LDW for the deposition of high-quality electronic and power generating materials requires the formation of structures comprising of multiple voxels, adjacent or on top of each other, that readily merge to form a single, continuous pattern. Electrical interconnects provide a perfect example of this requirement as heterogeneous interfaces between voxels can degrade the overall conductivity. By enabling the transferred material to remain fluid, adjacent voxels on the receiving substrate will merge into one continuous segment. Figure 18.2 shows a simple schematic illustrating the basic steps on the LDW of such rheological systems.

In reality, the process represents an important difference from prior LIFT technology as functional materials are deposited without direct vaporization, which under ambient conditions degrades their physical or chemical properties such as electrical conductivity, dielectric properties or electrochemical activity. As shown schematically in Fig. 18.2, for absorbing materials, a small region of the ink interacts with a low fluence ($<100\,mJ/cm^2$) laser pulse, causing a small amount of the ink to evaporate. As the resulting vapor expands, it generates shear forces that result in the ejection of a droplet from the film, which is unaffected by the incident laser. The droplet is then propelled in jet-like fashion towards the receiving substrate, where it is deposited with its original rheological properties intact. The claim that most if not

© Woodhead Publishing Limited, 2012

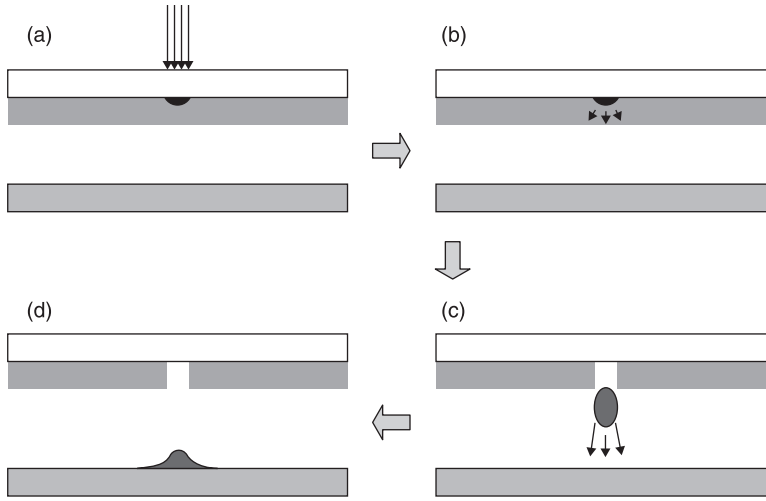

18.2 Schematic representation of the steps involved in the forward transfer of rheological systems during the LDW process. (a) The laser pulse is absorbed in the ink layer adjacent to the transparent glass plate. (b) The absorbed energy causes solvent vaporization to occur and (c) propel a droplet away from the film. (d) Finally, the droplet splashes down on the substrate.

all of the transferred fluid does not interact with the laser pulse has been substantiated by the results obtained with transfers of extremely laser-sensitive systems, such as buffer solutions containing biomaterials, proteins and living cells (Wu *et al.*, 2001), or electrochemically sensitive materials discussed below (Arnold *et al.*, 2004a).

The capability offered by the LDW technique to conformally transfer viscous fluids, pastes or inks has been used with great success for the fabrication of metal interconnects, vias and antenna structures (Piqué *et al.*, 2003; 2005). In fact, the LDW process has been used to deposit metallic screen-printable inks over complex 3-D surfaces, i.e. conformal coatings, which has always been extremely difficult if not impossible using traditional lithographic processes. For example, LDW of thick-film polymer or ceramic pastes has been used to fabricate passive electronic components such as resistors (Modi *et al.*, 2001) and interdigitated capacitors (Young *et al.*, 2001). The use of LDW to fabricate simple electronic circuits comprising several passive components and their interconnects has been demonstrated, as in the case of a simple chemoselective gas sensor circuit (Piqué *et al.*, 2002) and RF filter test structures (Zhang *et al.*, 2003).

18.4 Laser-printed micro-power sources

Recent advances in integration and processing techniques have enabled microelectronic and microelectromechanical devices to shrink in size dramatically.

© Woodhead Publishing Limited, 2012

While these devices have been used as components in larger sensor, actuator and control systems, the lack of commensurately sized power sources has limited their ability to function autonomously. One solution to this challenge is to integrate the micropower sources directly into or adjacent to the microdevice, thus forming a self-sufficient system. The resulting savings in volume and weight would allow the development of truly miniaturized autonomous systems, such as those needed for distributed wireless sensor networks. In these types of applications, the necessary-size scale is on the order of microns to millimeters. Such a vision might become a reality with the use of techniques such as laser printing, laser micromachining and laser processing.

For the purposes of this chapter, we will consider energy-related electrochemical systems, such as ultracapacitors, batteries, or electrochemical solar cells, to be composed of three main internal components: the negative electrode or anode, the positive electrode or cathode, and the electrolyte/separator. Each of these materials typically has a large degree of structural complexity and comprises a wide range of materials, such as nanocomposites, solid-state polymers, liquids and mesoporous mixtures of electrochemically active materials. Micro- and meso-scale power sources employ similar types of materials, but the unique challenge is to maintain their electrochemical activity and structural integrity in a confined space subject to the limitations, such as temperature and pressure, imposed by the microdevices, their substrates and their packaging.

To meet the power demands of a given microdevice, combinations of different types of power source are needed (Koeneman *et al.*, 1997). For instance, an application may require constant low power, supplied by a lithium or alkaline microbattery, or an occasional short burst of energy, supplied by an ultracapacitor, combined with long intervals in 'stand-by' mode, during which recharging takes place by harvesting energy from the environment supplied by a solar cell. The laser-printing techniques described in this chapter are ideally suited to prototype, optimize and fabricate these electrochemical components. Advanced laser techniques can also embed the electrochemical components directly within a substrate, further reducing the packaged size of an entire microdevice, while allowing their geometry to be adapted to fit virtually any form factor.

In constructing electrochemical cells for energy storage and power generation, it is instructive to consider the desired operating geometries. The two main approaches include placing the anode and cathode adjacent to each other in the same plane (planar), or layering the anode and cathode on top of one another (stacked). There are particular advantages and disadvantages to each of these different geometries. In the case of stacked geometries, one can obtain higher area densities and lower resistances owing to the relatively thin separator layer, but this layer must be structurally stable to support the anode, cathode and associated current collectors. This feature rules out highly conductive gel and wet electrolytes. From a fabrication standpoint, planar geometries are easier to process since they can accommodate softer and rougher materials, but they have higher internal

© Woodhead Publishing Limited, 2012

resistances due to the greater distance between the electrodes, and therefore tend to have lower performance at high currents. From a power density standpoint, stacked structures are more efficient but harder to fabricate using printing processes. With LDW, both planar and stacked structures have been demonstrated (Arnold *et al.*, 2007). Using LDW, the printing speeds by which these structures can be deposited depends on the type of material being deposited and the desired feature resolution. For micro-power sources, the typical voxel size that can be printed by LDW with each laser pulse is about 100 micrometers square and about 5 micrometers thick. For a typical translation stage traveling at 1 m/s, a 10 kHz laser pulse rate would be sufficient to print 10 000 of such voxels in one second, covering an area of 1 cm^2 each second with a layer 5 micrometers thick. So it is feasible to laser print the cathode, separator and anode layers required for a simple stacked 1 cm^2 meso-scale battery in a few seconds.

18.4.1 Laser-printed ultracapacitors

Ultracapacitors based on a combination of sulfuric acid and hydrous ruthenium oxide have been successfully fabricated by laser-printing techniques (Arnold, 2004a). These electrochemical systems are conceptually the easiest to understand, as they form a planar structure that is symmetric, namely, the anode and cathode are made from the same materials. Furthermore, hydrous ruthenium oxide exhibits one of the largest specific capacitances of any material (Zheng *et al.*, 1995), which will be exploited in these small-scale systems. Ultracapacitors, also known as supercapacitors or pseudocapacitors, are a class of electrochemical capacitor that exhibits large specific capacity (Conway, 1999). These systems display electronic properties similar to both batteries and capacitors. Like a capacitor, an ultracapacitor has the ability to discharge its energy very rapidly, leading to a high power density. However, like a battery, it has the ability to store a large amount of energy in the charge state of the active materials. In the most basic manner, we can think of an ultracapacitor as a battery with a high discharge rate. These devices are typically used for load leveling and applications where a short burst of power is needed.

The fundamental mechanisms for charge storage in these devices come from two possible sources. The first effect is similar to a typical capacitor in which the electrostatic double-layer at the interface between the electrode and electrolyte stores charge. A high surface area leads to large amounts of charge stored in the system. These effects are common in carbon-based ultracapacitor systems. The second effect stores charge through a Faradaic transfer at the surface of the electrode material. This is similar to the oxidation/reduction reactions that occur in a regular battery, but once again, the high surface area enables a large amount of charge storage and rapid charge transfer through this mechanism. These effects become relevant in metal oxide ultracapacitor systems. In either case, the discharge properties of the device resemble that of a capacitor. Namely, at constant current, the voltage across the device will decrease linearly with time.

© Woodhead Publishing Limited, 2012

Hydrous ruthenium oxide is an ideal electrode material for a micro-ultracapacitor due to its high specific capacitance (capacitance per unit mass). The rapid insertion and release of protons and electrons through the material enables a large pseudocapacitance effect, which, in combination with a high specific surface area, leads to the large amounts of charge stored in the material (Sarangapani *et al.*, 1996; Trasatti and Kurzweil, 1994). This effect is enhanced by the presence of structural water in the lattice that provides nanostructured percolation pathways for proton conduction into the bulk of the material (Dmowski *et al.*, 2002).

In the context of a small-scale ultracapacitor system, the main challenge is to produce electrodes that preserve the desirable electrochemical properties of the active material while maintaining the structure necessary for high surface area, subject to the process temperature/pressure limitations. These stringent requirements have made the growth of hydrous ruthenium oxide films incompatible with standard vacuum techniques such as physical or chemical vapor deposition for thin-film growth. Other thin-film techniques such as sol-gel techniques (Fang *et al.*, 2001) or electrostatic spray deposition (Kim and Kim, 2001) are compatible with the material constraints, but require multiple processing steps, including additional lithography to produce the two-dimensional structures required for making microultracapacitors. Laser printing provides a solution to these challenges.

The laser printing of ultracapacitors starts with the preparation of an ink composed of an active material and a suitable transfer liquid. The ability to premix the electrode material with electrolyte gives LDW a distinct advantage over other direct-write methods such as ink-jet or MicroPen as it enables better control over impurities in the electrodes and has been shown to significantly improve the discharge behavior of these cells (Arnold *et al.*, 2002). In general, any substrate and electrode geometry is possible, provided two electronically isolated current collectors are formed. The printed material is porous, exhibiting a random network of connected grains. This structure is ideally suited for the penetration of liquid or gel electrolyte, which enables a large surface area in contact with the electrolyte for charge transfer. This in turn leads to better utilization of the electrode material and improved transport throughout the electrode. LDW is unique in comparison to other deposition techniques in its ability to create these electrochemically desirable structures on the mesoscale. An encapsulating layer of Nafion® is placed on top of the structure and a droplet of sulfuric acid is added to assure a fully saturated membrane. Characterization of the laser-printed ultracapacitors has shown that these cells can be discharged at currents above 50 mA and can be connected in series and parallel combinations to yield the proper voltage values (Arnold *et al.*, 2003). The overall size and mass of these systems is small at <100 μg, while the power output is above 1 mW. Dual laser techniques, used to remove the electrolyte locally and then micromachine gaps to isolate the electrodes (Arnold *et al.*, 2004c) have also been demonstrated. These dual laser techniques enable a level of process optimization toward the ultimate goal of high-throughput fabrication. Figure 18.3

© Woodhead Publishing Limited, 2012

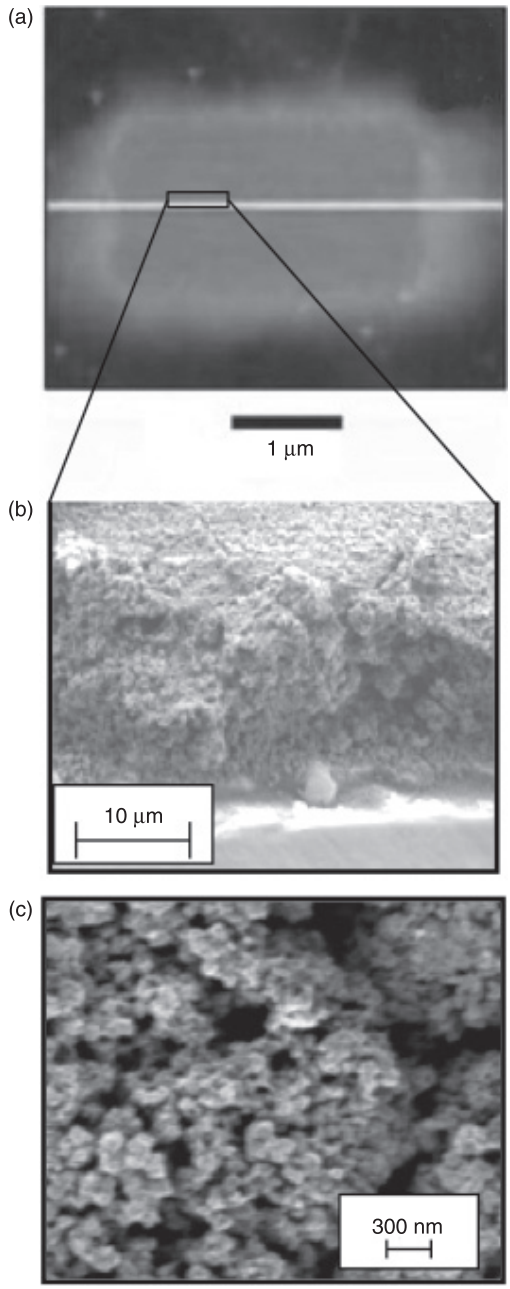

18.3 (a) Micrograph of a laser-printed hydrous ruthenium ultracapacitor. (b) SEM detail of the laser micromachined groove between electrodes. (c) Higher magnification SEM revealing the mesoporous structure and interconnected ruthenium oxide backbone.

© Woodhead Publishing Limited, 2012

shows a micrograph of such a planar ultracapacitor laser-printed on a glass substrate and SEM images illustrating the mesoporous structure of the laser-printed hydrous ruthenium oxide electrode.

18.4.2 Laser-printed microbatteries

With batteries, the stored chemical energy is converted to electrical energy through oxidation and reduction reactions at the electrodes. Electrons generated by oxidation of the anode material generate work in the electrical circuit before recombining to reduce the cathode material. The separator/electrolyte enables the flow of ions between the anode and cathode to complete the circuit. The large number of chemical possibilities are discussed and reviewed in readily available reference books (Linden and Reddy, 2001; Vincent and Scrosati, 1997).

In the case of small-scale microbatteries, the main challenge is to create mesoscale patterns of these active materials while maintaining the necessary physical and chemical properties of a functioning cell. There has been significant effort to develop small microbatteries for various primary and secondary chemistries. Examples include secondary solid-state lithium-ion cells in a stacked configuration (Arnold *et al.*, 2004a; Bates *et al.*, 1995, 2000) and primary alkaline microbatteries in a planar configuration where the anode and cathode are located adjacent to each other on the substrate (Arnold *et al.*, 2004c; Humble *et al.*, 2001; LaFollette *et al.*, 2001).

18.4.3 Primary alkaline batteries made by laser printing

Alkaline batteries are one of the most ubiquitous battery chemistries in use today. Their low cost, relative environmental safety and high discharge rates make them readily available for consumer applications. In comparison to other alkaline chemistries, the zinc/silver oxide (Zn-Ag_2O) system has found extensive use in applications that require maintaining a constant voltage throughout the battery discharge. Primary Zn-Ag_2O alkaline microbatteries have been demonstrated using LDW techniques by laser-printing zinc and monovalent silver oxide (Ag_2O) powders in both planar and stacked geometries on a variety of substrates (Arnold *et al.*, 2004a, 2004b; Piqué *et al.*, 2004b). The typical weight of all laser-printed material is 250 µg, while the thickness of the anode and cathode layers is about 10–20 µm. In order to activate the planar cells, a drop of 25 wt% KOH solution is placed on the electrodes. Figure 18.4 shows micrographs from sample alkaline microbatteries made by laser printing.

Electrochemical evaluation of the cell voltage and discharge behavior of the alkaline microbatteries demonstrated similar behavior to that of larger cells. The open-circuit potential for both planar and stacked microbatteries was 1.55 V, while their discharge at constant currents showed the characteristic flat response of the

© Woodhead Publishing Limited, 2012

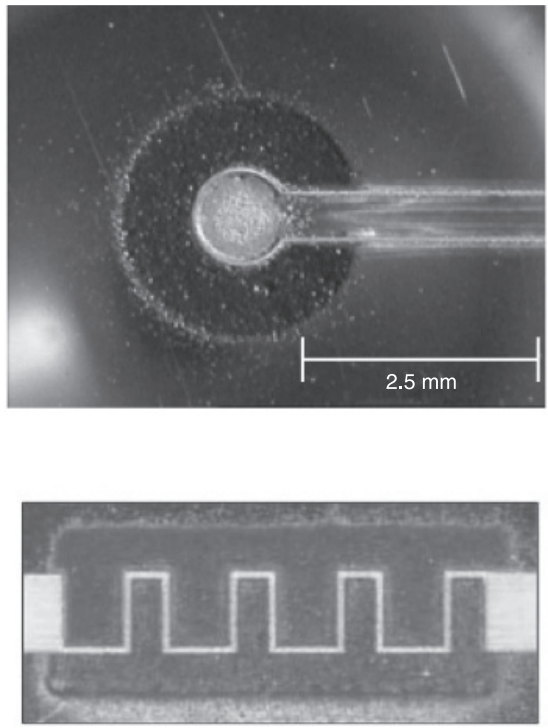

18.4 Optical micrographs of two laser-printed planar alkaline microbatteries' configurations: (a) ring-shaped with a zinc center electrode and an outer silver oxide electrode; (b) interdigitated arrangement with silver oxide top and zinc bottom electrodes.

Zn-Ag_2O alkaline system. High capacity cells are obtained in this manner. For instance, planar cells have been fabricated with capacities greater than 450 mAhr/cm^2. An important challenge remains in how to package these cells for commercial use. Since a liquid consisting of a highly corrosive alkaline solution is used as the electrolyte of the Zn-Ag_2O microbatteries, sealing these tiny structures is not easily achieved without compromising their size and wasting significant mass and footprint on the packaging. A better alternative would be to fabricate 'dry' microbatteries, where issues such as leakage and contamination of the electrolyte are not as critical, or employ embedding strategies as discussed later in the chapter. For example, ionic liquids can be used to create new types of solid state cells that mimic standard alkaline cells, without the need for highly acidic or basic electrolytes. At the US Naval Research Laboratory, ionic liquids are being studied both as the electrolyte/separator in primary solid state batteries, and as a reactive species in the cell's electrochemical makeup (Sutto *et al.*, 2011).

© Woodhead Publishing Limited, 2012

18.4.4 Secondary batteries made by laser printing

Lithium microbatteries offer significantly higher energy densities than other rechargeable battery systems owing to the small size of Li and its high reduction potential. Secondary lithium ion intercalation microbatteries have been fabricated by laser printing $LiCoO_2$ powders for the cathode and graphite powders for the anode in stacked geometries.

Two types of separators have been used to make the lithium cells. In one case, porous polymer membranes were laser cut and placed between the cathode and anode layers (Wartena *et al.*, 2004), while on the other an ionically conductive polymer nanocomposite membrane was laser-printed on top of the cathode layer (Sutto *et al.*, 2006). The $LiCoO_2$ cathodes and carbon anodes were deposited by LDW onto aluminum and copper foils, respectively. Characterization of the charge/discharge cycling performance (C/18 rate) of a packaged Li-ion microbattery demonstrated the expected behavior for the $LiCoO_2$/Li system. Typical laser-printed microbatteries had a charge/discharge efficiency of ~98% and a capacity per unit area of 205 μAhr/cm^2, which compares favorably to the value of 163 μAhr/cm^2 achieved for sputter-deposited Li microbatteries reported by Bates and colleagues (Bates *et al.*, 2000).

LDW techniques can also be used to print thick-film electrodes for microbatteries with a significantly higher discharge capacity, power and energy densities than those made by sputter-deposited thin-film techniques. This increased performance is attributed to the porous structure of the laser-printed electrodes, which allows improved ionic and electronic transport through the thick-film electrodes (~100 μm) without a significant increase in internal resistance (Kim *et al.*, 2007). Figure 18.5 shows the cross-section of a Li-ion microbattery made by LDW as well as SEM images of the cathode and anode laser-printed electrodes. When compared to other types of microbatteries, such as thin-film microbatteries, the laser-printed thick-film microbatteries deliver significantly higher discharge capacities (~2586 μAh/cm^2) at a current density of 100 μA/cm^2 than those reported for sputter-deposited thin-film microbatteries (~160 μAh/cm^2) (Kim *et al.*, 2007).

18.4.5 Laser-printed dye-sensitized photovoltaics

DSSC are a photosensitive electrochemical cell with a more complicated electrode configuration in comparison to the ultracapacitors and microbatteries previously discussed. The anode in this case comprises light-absorbing dye molecules attached to the surface of nanocrystalline-TiO_2 (nc-TiO_2) particles. The electrons generated by oxidation of the dye molecules are injected into the conduction band of the wide band-gap TiO_2 and transported to the external circuit through a transparent conducting oxide layer. On the cathode side, a metal catalyst enables the direct reduction of the electrolyte itself (I^-/I_3^-), which subsequently reduces

© Woodhead Publishing Limited, 2012

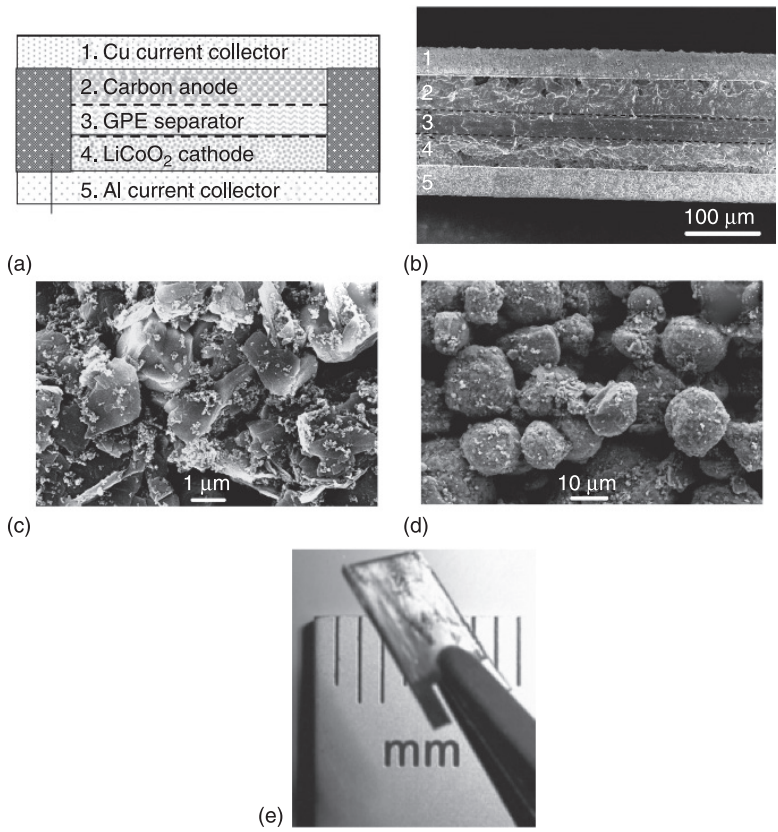

18.5 (a) Cross-sectional schematic diagram (not to scale) of a typical Li- on microbattery. (b) Cross-sectional SEM micrograph of a packaged thick-film Li-ion microbattery. (c) SEM image of a laser-printed $LiCoO_2$ cathode. (d) SEM image of a laser-printed carbon anode. (e) Optical micrograph of a packaged Li microbattery made by LDW.

the oxidized dye molecules to their initial state. The schematic structure of a DSSC is shown in Fig. 18.6.

Over the last decade, DSSCs based on nc-TiO_2 films have been extensively studied as possible alternatives to silicon-based solar cells due to their high power conversion efficiencies (~10%) and expected low materials and manufacturing costs (Barbe *et al.*, 1997; Nakada *et al.*, 2002; Nazeeruddin *et al.*, 1993; O'Regan and Grätzel, 1991). Mesoporous nc-TiO_2 layers with high surface area are essential for achieving high efficiency in the DSSC system because a large amount of dye can be adsorbed on the surface of the nc-TiO_2 particles resulting in an increased solar light absorption and an increased reacting interface per unit area.

The general structure of a LDW DSSC is similar to the stacked geometry described in the previous sections on microbatteries. However, in this case, we use traditional vapor deposition to create the transparent conducting

© Woodhead Publishing Limited, 2012

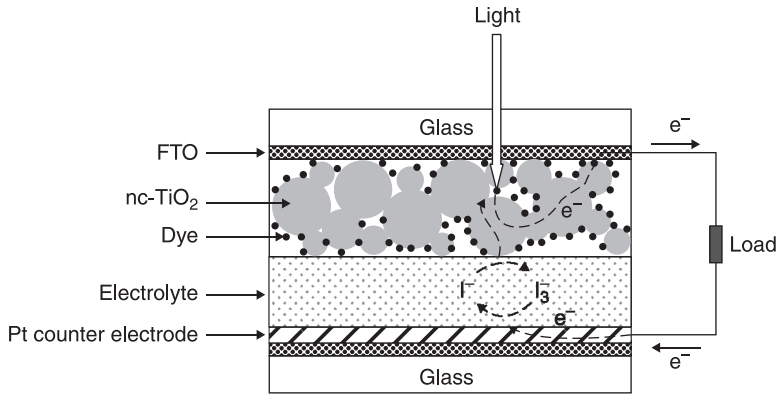

18.6 Schematic of a typical DSSC illustrating its basic structure and operation.

oxide layers and Pt cathode. The inks used are made from water-based colloidal suspensions of nc-TiO_2 powders mixed with organic additives. Mesoporous, nc-TiO_2 films are deposited onto fluorine-doped tin oxide (FTO)-coated glass substrates by laser printing of these inks (Kim *et al.*, 2004, 2005). The transferred films are dried in air and sintered in the oven at 450 °C for 30 minutes. Once the films are sintered, the electrode is soaked in the dye solution in order to coat the TiO_2 surface. Finally, the completed cells are assembled and sealed using a Surlyn gasket to separate the anode and cathode layers and provide a reservoir for the I^-/I_3^- electrolyte. As with the laser-printed microbatteries, the transferred materials maintain a homogeneously distributed network of particles with a high degree of porosity, consistent with a high surface area structure.

Laser-printed dye-sensitized solar cells (DSSCs) made with an optimum thickness of 15 μm exhibited a J_{sc} of 10.1 mA/cm^2, V_{oc} of 0.64 V, a fill factor (*ff*) of 0.65 and a light power conversion efficiency (η) of ~4.3 %. The conversion efficiency is comparable to those reported earlier for analogous cells fabricated with commercial TiO_2 powders (P25) using traditional techniques such as screen printing or stenciling (Hinsch *et al.*, 2001; Nakada *et al.*, 2002; Okuya *et al.*, 2002). Using laser-sintering techniques, it is possible to remove the 450 °C oven curing step from the overall process (Kim *et al.*, 2005). The power conversion efficiency of the devices based on the laser-sintered nc-TiO_2 electrodes is a factor of two greater than non-sintered films, but still less than what can be obtained from high-temperature processes. Nevertheless, use of such laser processing techniques allows the transfer of the TiO_2 colloidal suspensions and *in situ* sinter of the mesoporous nc-TiO_2 electrodes using the same UV laser, thus simplifying the processing steps required for fabricating DSSCs at low-temperatures and making them compatible with low-temperature substrates such as flexible polymers. Further optimization of the laser sintering conditions such as power intensity, laser beam spot size and translation speed leave ample room for refinement.

© Woodhead Publishing Limited, 2012

18.5 Laser-printed embedded micro-power sources

One of the important issues for microbatteries and other small-scale electrochemical systems is the development of an appropriate packaging scheme that protects the device from environmental degradation and preserves its small size. In order to address this issue, one can utilize more advanced surface restructuring and processing than is possible with laser printing techniques.

In many cases where microbatteries are required, one desires to place the cell directly on the substrate of the microdevice to be powered. In these cases, one can take advantage of the existing substrate as a packaging material by placing the battery *within* the substrate rather than on top of the substrate. For instance, in the case of fiberglass or polyimide circuit boards, one can laser-micromachine pockets of desired dimensions and deposit each of the electrode layers inside, as shown in Fig. 18.7. The problem is then reduced to sealing the top of the battery with a metallic current collector to produce a fully embedded solution. With further refinements, one can create a separator layer from the substrate itself by laser micromachining both top and bottom to leave a thin layer of polymer or fiberglass before refilling it from both sides. In the case of solid-state Li-ion microbatteries, it is also possible to LDW all the layers inside a well within the substrate, as shown in Fig. 18.7(b). The ability to completely transfer and assemble

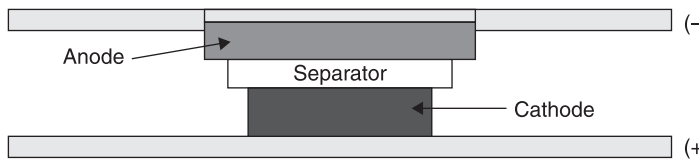

(a)

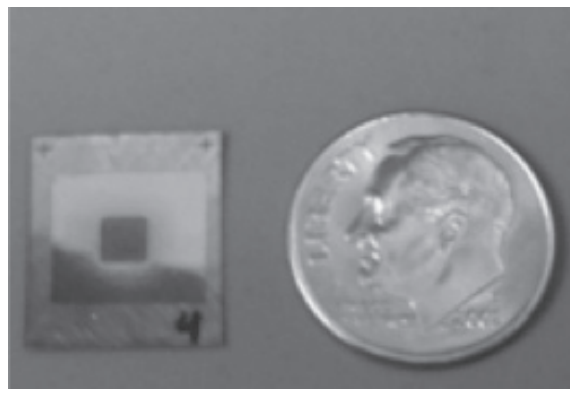

(b)

18.7 (a) Schematic showing an embedded Li-ion microbattery in cross-section view. (b) Optical micrograph of a laser-printed solid-state Li-ion microbattery embedded in a polyimide substrate.

© Woodhead Publishing Limited, 2012

electrochemically and thermally stable micropower sources into bulk materials can be extended to more advanced applications in which the power source is directly incorporated and sealed within the substrates used by the microdevice (Arnold *et al.*, 2004d).

Progress towards printing fully embedded micropower sources requires the implementation of alternative material systems for the electrodes and separator layers. For example, Li-ion batteries use a liquid electrolyte, which causes drawbacks in areas of packaging, cost, safety and size when trying to develop a micro-battery. In order to overcome these limitations, it is important to replace the liquid electrolyte with a solid-state polymer electrolyte. This would allow for easier packaging with less material. Also, these polymer electrolytes can be made much thinner than the currently used permeable membranes. Using a solid-state polymer as an electrolyte also eliminates safety concerns, since the volatility of the liquid electrolyte is no longer an issue. Ionically conductive solid-state electrolyte membranes have been incorporated into fully functional prototype embedded Li-ion microbatteries by LDW techniques (Ollinger *et al.*, 2006).

18.6 Challenges and opportunities

The use of laser printing, laser micromachining and laser sintering techniques for the transfer, removal and processing of electronic and power-generating materials has been reviewed in the previous sections. Numerous examples of the types of components fabricated using these techniques are described, and it is clear that these processes, referred to as LDW, are well suited to transferring or printing inks or fluids containing suspensions or mixtures of the required power-generating materials. The cured inks form conformal patterns that are continuous and well-adhered to the substrate and are used to generate patterns of mesoporous structures with extremely high effective surface areas required in the fabrication of micropower devices such as ultracapacitors, microbatteries and DSSCs. Each of these is an indispensable element in the fabrication of autonomous, self-powered microelectronic systems such as wireless sensor networks. However, in order to reach the full potential of the LDW processes, it is desired that these elements be integrated into fully functional circuits.

Work toward this goal is progressing rapidly. Laser forward transfer and LDW techniques are poised to play an important role in the development of the next generation of electronic systems as work toward the goal of complete device integration steadily progresses. For example, future microelectronic designs will require integration of many different and increasingly smaller components. To achieve this, it is necessary to accurately place small-scale energy storage systems and individual electrical components such as semiconductor bare die and submillimeter discrete passive components on surfaces that may not be compatible with traditional ‘pick-and-place’ equipment. The placement of each of these

© Woodhead Publishing Limited, 2012

components onto virtually any type of surface is enabled by the use of laser transfer methods.

An alternative approach to device integration and miniaturization can be accomplished by incorporating electronic components, energy storage, and their interconnects within the volume of a substrate. Rather than limiting their placement to its surface, it will be possible to integrate electronic circuits within any type of form factor. The development of such 'embedded' electronics is being explored using LDW techniques. Embedded surface-mount devices (SMDs), semiconductor bare die integrated circuits (ICs), interconnects and power source elements, offer the ability to achieve levels of miniaturization beyond the capabilities of current manufacturing techniques. Given an arbitrary circuit design, significant reductions in volume and overall weight can be achieved by using embedded components. Furthermore, embedded circuits exhibit higher device density and improved electrical performance, resulting in enhanced functionality within a given form factor. In the past few years, various demonstrations of the use of LDW techniques for the fabrication of embedded electronic circuits have been published (Piqué *et al.*, 2004a, 2005; Wang *et al.*, 2010).

18.7 Conclusion and future trends

Laser printing processes and other LDW techniques are enabling technologies for the fabrication of various types of micro- and mesoscale power-generating devices such as ultracapacitors, DSSCs and microbatteries, both primary and rechargeable, as the prior sections have shown. Notably, the laser printing process is not chemistry-specific, allowing different types of materials to be deposited using the same tool by simply changing the source ribbon. More advanced techniques, such as deposition of a liquid phase polymer nanocomposite that dries into a solid, ionically conductive micron-thick solid separator, or the removal of material from a surface via laser micromachining for embedded structures, make possible other types of microelectrochemical cells that can be incorporated into a wide variety of microdevices.

LDW techniques encompass many laser-based processes, which allow the subtraction (i.e. laser micromachining), addition (i.e. laser transfer) and modification (i.e. laser annealing) of many types of materials. As this chapter has shown, LDW can be used for the generation of mesoscale patterns of electronic and power-generating materials directly on a substrate without requiring lithographic processing. These patterns can be assembled to form simple structures such as metal lines for establishing the connections between devices in functional circuits, or more complex ones such as the multilayers required for a stacked Li-ion microbattery. The energy storage devices fabricated through these techniques exhibit outstanding performance characteristics. In each case, the ability to transfer complex suspensions from a ribbon to an acceptor substrate under ambient

© Woodhead Publishing Limited, 2012

conditions and without changing their physical or chemical properties is one of the unique attributes of the LDW process. Another key attribute of LDW processes is that they can be used for rapid prototyping applications, allowing the design, fabrication and testing of a given structure to be carried out quickly.

The recent application of LDW techniques for the transfer of preformed devices such as semiconductor bare dies, and for embedding microbatteries and simple electronic circuits, opens the door for the development of a unique laser-based microelectronics fabrication tool. Such a tool would be capable of fabricating and embedding electronic circuits with the required power storage and power-harvesting components within the same substrate. The resulting fully integrated systems could easily be reconfigured to fit within a desired form factor, thus allowing the placement of electronic systems in places that seem inconceivable today. Such a system, although not yet available, would play a very important role in the development of next generation sensor networks and autonomous systems. Given LDW's ability to print not only the power sources but also the associated electronics, the rapid manufacture of fully functional application specific sensor nodes would be as easy as it is today to print a 3D model.

18.8 Acknowledgements

The author would like to thank all the members of the LDW group at the Naval Research Laboratory. Special thanks to Heungsoo Kim, Craig Arnold, Mike Ollinger, Ray Auyeung and Tom Sutto. This work was sponsored by the US Office of Naval Research.

18.9 References

Adrian, F. J., Bohandy, J., Kim, B. F., Jette, A. N. and Thompson, P., 1987, A study of the mechanism of metal deposition by the laser-induced forward transfer process, *Journal of Vacuum Science and Technology*, B5: 1490–1494.

Arnold, C. B., Wartena, R. C., Pratap, B., Swider-Lyons, K. E. and Piqué, A., 2002, Laser direct writing of hydrous ruthenium dioxide micro-pseudocapacitors, in: D. B. Chrisey and S. C. Danforth, eds, *Electroactive polymers and rapid prototyping*, Vol. 689, pp. 275–280, Pittsburgh, PA. Materials Research Society.

Arnold, C. B., Wartena, R. C., Swider-Lyons, K. E. and Piqué, A., 2003, Direct-write planar micro-ultracapacitors by laser engineering, *Journal of Electrochemical Society*, 150: A571–A575.

Arnold, C. B., Kim, H., Sutto, T. E. and Piqué, A., 2004a, Direct write laser processing for miniature electrochemical systems, *Laser Focus World*, 40: 9–12.

Arnold, C. B., Kim, H. and Piqué, A., 2004b, Laser transferred primary alkaline microbatteries, *Applied Physics A*, 79: 417–420.

Arnold, C. B. and Piqué, A., 2004c, 'Self-filling wet electrochemical cells by laser processing', US patent application 20040256359.

Arnold, C. B., Piqué, A., Auyeung, R. C. Y. and Nurnberger, M., 2004d, 'Laser-based technique for producing and embedding electrochemical cells and electronic components directly into circuit board materials', US patent application 2005000613.

© Woodhead Publishing Limited, 2012

Arnold, C. B., Serra, P. and Piqué, A., 2007, Laser direct-write techniques for printing of complex materials, *MRS Bulletin*, 32: 23–31.

Auyeung, R. C. Y., Wu, H. D., Modi, R., Piqué, A., Fitz-Gerald, J. M. *et al.*, 2000, Matrix-assisted laser transfer of electronic materials for direct-write applications, *Proceedings of SPIE*, 4088: 393–396.

Bähnisch, R., Gross, W. and Menschig, A., 2000, Single-shot, high repetition rate metallic pattern transfer, *Microelectronic Engineering*, 50: 541–546.

Barbe, C. J., Arendse, F., Comte, P., Jirousek, M., Lenzmann, F. *et al.*, 1997, Nanocrystalline titanium oxide electrodes for photovoltaic applications, *Journal of American Ceramic Society*, 80: 3157–3171.

Bates, J. D., Dudney, N. J., Lubben, D. C., Gruzalski, G. R., Kwak, B. S. *et al.*, 1995, Thin-film rechargeable lithium batteries, *Journal of Power Sources*, 54: 58–62.

Bates, J. B., Dudney, N. J., Neudecker, B., Ueda, A. and Evans, C. D., 2000, Thin-film lithium and lithium–ion batteries, *Solid State Ionics*, 135: 33–45.

Bohandy, J., Kim, B. F. and Adrian, F. J., 1986, Metal deposition from a supported metal film using an excimer laser, *Journal of Applied Physics*, 60: 1538–1539.

Bohandy, J., Kim, B. F., Adrian, F. J. and Jette, A. N., 1988, Metal deposition at 532 nm using a laser transfer technique, *Journal of Applied Physics*, 63: 1158–1162.

Conway, B. E. 1999, *Electrochemical supercapacitors, scientific fundamentals and technological applications*, Kluwer Academic, New York.

Dmowski, W., Egami, T., Swider-Lyons, K. E., Love, C. T. and Rolison, D. R., 2002, Local atomic structure and conduction mechanism of nanocrystalline hydrous RuO_2 from x-ray scattering, *Journal of Physical Chemistry B*, 106: 12 677–12 683.

Esrom, H., Zhang, J.-Y., Kogelschatz, U. and Pedraza, A. J., 1995, New approach of a laser-induced forward transfer for deposition of patterned thin metal films, *Applied Surface Science*, 86: 202–207.

Fang, Q. L., Evans, D. A., Roberson, S. L. and Zheng, J. P., 2001, Ruthenium oxide film electrodes prepared at low temperatures for electrochemical capacitors, *Journal of Electrochemical Society*, 148: A833–A837.

Fernández-Pradas, J. M., Colina, M., Serra, P., Dominguez, J. and Morenza, J. L., 2004, Laser-induced forward transfer of biomolecules, *Thin Solid Films*, 453–454: 27–30.

Fogarassy, E., Fuchs, C., Kerherve, F., Hauchecorne, G. and Perriere, J., 1989, Laser-induced forward transfer of high-T_cYBaCuO and BiSrCaCuO superconducting thin films, *Journal of Applied Physics*, 66: 457–459.

Greer, J. A. and Parker, T. E., 1988, Laser-induced forward transfer of metal oxides to trim the frequency of surface acoustic wave resonator devices, *Proceedings of SPIE*, 998: 113–125.

Herman, I. P., 1989, Laser-assisted deposition of thin films from gas-phase and surface-adsorbed molecules, *Chemical Reviews*, 89: 1323–1357.

Hinsch, A., Kroon, J. M., Kern, R., Uhlendorf, I., Holzbock, J. *et al.* 2001, Long-term stability of dye-sensitized solar cells, *Journal of Progress in Photovoltaics: Research and Applications*, 9: 425–438.

Humble, P. H., Harb, J. N. and LaFollettte, R., 2001, Microscopic nickel–zinc batteries for use in autonomous microsystems, *Journal of Electrochemical Society*, 18: A1357–A1361.

Kántor, Z., Tóth, Z., Szorenyi, T. and Tóth, A. L., 1994, Deposition of micrometer-sized tungsten patterns by laser transfer technique, *Applied Physics Letters*, 64: 3506–3508.

Karaiskou, A., Zergioti, I., Fotakis, C., Kapsetaki, M. and Kafetzopoulos, D., 2003, Microfabrication of biomaterials by the sub-ps laser-induced forward transfer process, *Applied Surface Science*, 208–209: 245–249.

© Woodhead Publishing Limited, 2012

Kim, H., Kushto, G. P., Arnold, C. B., Kafafi, Z. H. and Piqué, A., 2004, Laser processing of nanocrystalline TiO_2 films for dye-sensitized solar cells, *Applied Physical Letters*, 85: 464–466.

Kim, H., Auyeung, R. C. Y., Ollinger, M., Kushto, G. P., Kafafi, Z. H. and Piqué, A., 2005, Laser-sintered mesoporous TiO_2 electrodes for dye-sensitized solar cells, *Applied Physics A*, 83 (1): 73–76.

Kim, H., Auyeung, R. C. Y. and Piqué, A., 2007, Laser-printed electrodes for solid-state rechargeable Li-ion microbatteries, *Journal of Power Sources*, 165: 413–419.

Kim, I. H. and Kim, K. B., 2001, Ruthenium oxide thin film electrodes for supercapacitors. Electrochem, *Solid-State Letters*, 5: A62–A64.

Koeneman, P. B., Busch-Vishniac, I. J. and Wood, K. L., 1997, Feasibility of micro power supplies for MEMS, *Journal of Microelectromechical Systems*, 6: 355–362.

LaFollettte, R., Harb, J. N. and Humble, P., 2001, in: R. S. L. Das and H. Frank, ed., *Sixteenth Annual Battery Conference: Applications and Advances*, IEEE, Piscatawy, NJ, pp. 349–354.

Linden, D. and Reddy, T. B., 2001, *Handbook of batteries*, 3rd edn, McGraw-Hill, New York.

Modi, R., Wu, H. D., Auyeung, R. C. Y., Gilmore, C. M. and Chrisey, D. B., 2001, Direct writing of polymer thick-film resistors using a novel laser transfer technique, *Journal of Material Research*, 16: 3214–3222.

Nakada, S., Matsuda, M., Kambe, S., Saito, Y., Kitamura, T. *et al.*, 2002, Dependence of TiO_2 nanoparticle preparation methods and annealing temperature on the efficiency of dye-sensitized solar cells, *Journal of Physical Chemistry B*, 106: 10 004–10 010.

Nazeeruddin, M. K., Kay, A., Rodicio, I., Humphry-Baker, R., Muller, E. *et al.*, 1993, Conversion of light to electricity by cis-X_2Bis(2,2′-bipyridyl-4,4′-dicarboxylate) ruthenium(II) charge-transfer sensitizers (X = Cl^-, Br^-, I^-, CN^- and SCN^-) on nanocrystalline TiO_2 electrodes, *Journal of American Chemical Society*, 115: 6382–6390.

Okuya, M., Nakade, K. and Kaneko, S., 2002, Porous TiO_2 thin films synthesized by a spray pyrolysis deposition (SPD) technique and their application to dye-sensitized solar cells, *Solar Energy Materials and Solar Cells*, 70: 425–435.

Ollinger, M., Kim, H., Sutto, T. and Piqué, A., 2006, Laser printing of nanocomposite solid-state membranes for Li micro-batteries, *Applied Surface Science*, 252: 8812–8816.

O'Regan, B. and Grätzel, M., 1991, A low-cost, high-efficiency solar cell based on dye-sensitized colloidal TiO_2 films, *Nature*, 353: 737–740.

Osgood, R. M. and Deutsch, T. F., 1985, Laser-induced chemistry for microelectronics, *Science*, 227: 709–714.

Papakonstantinou, P., Vainos, N. A. and Fotakis, C., 1999, Microfabrication by UV femtosecond laser ablation of Pt, Cr and indium oxide thin films, *Applied Surface Science*, 151: 159–170.

Pimenov, S. M., Shafeev, G. A., Smolin, A. A., Konov, V. I. and Vodolaga, B. K., 1995, Laser-induced forward transfer of ultra-fine diamond particles for selective deposition of diamond films, *Applied Surface Science*, 86: 208–212.

Piqué, A., Chrisey, D. B., Auyeung, R. C. Y., Lakeou, S., Chung, R. *et al.*, 1999a, Laser direct writing of circuit elements and sensors, *Proceedings of SPIE*, 3618: 330–339.

Piqué, A., Chrisey, D. B., Auyeung, R. C. Y., Fitz-Gerald, J., Wu, H. D. *et al.*, 1999b, A novel laser transfer process for direct writing of electronic and sensor materials, *Applied Physics A*, A69: 279–284.

Piqué, A., Chrisey, A. D. B., Fitz-Gerald, J. M., McGill, R. A., Auyeung, R. C. Y. *et al.*, 2000a, Direct writing of electronic and sensor materials using a laser transfer technique, *Journal of Material Research*, 15: 1872–1875.

© Woodhead Publishing Limited, 2012

Piqué, A., Fitz-Gerald, J., Chrisey, D. B., Auyeung, R. C. Y., Wu, H. D. *et al.*, 2000b, Direct writing of electronic materials using a new laser assisted transfer/annealing technique, *Proceedings of SPIE*, 3922: 105–112.

Piqué, A., Weir, D. W., Wu, P. K., Pratap, B., Arnold, C. B. *et al.* 2002, Direct-write of sensor devices by a laser forward transfer technique, *Proceedings of SPIE*, 4637: 361–368.

Piqué, A., Arnold, C. B., Pratap, B., Auyeung, R. C. Y., Kim, H. *et al.*, 2003, Laser direct-write of metal patterns for interconnects and antennas, *Proceedings of SPIE*, 4977: 602–608.

Piqué, A., Mathews, S. A., Auyeung, R. C., Ollinger, M., Kim, H. *et al.*, 2004a, Application of laser direct-write techniques for embedding electronic and micropower components, *Proceedings of SPIE*, 5662: 564–569.

Piqué, A., Arnold, C. B., Kim, H., Ollinger, M. and Sutto, T. E., 2004b, Rapid prototyping of micro-power sources by laser direct-write, *Applied Physics A*, 79: 783–786.

Piqué, A., Pratap, B., Mathews, S. A., Karns, B. J., Auyeung, R. C. *et al.*, 2005, Laser direct-write of embedded electronic components and circuits, *Proceedings of SPIE*, 5713: 223–230.

Sarangapani, S., Tilak, B. and Chen, C., 1996, Materials for electrochemical capacitors. *Journal of Electrochemical Society*, 143: 3791–3799.

Schultze, V. and Wagner, M, 1991, Laser-induced forward transfer of aluminum, *Applied Surface Science*, 52: 303–309.

Serra, P., Colina, M., Fernández-Pradas, J. M., Sevilla, L. and Morenza, J. L., 2004, Preparation of functional DNA microarrays through laser-induced forward transfer, *Applied Physics Letters*, 85: 1639–1641.

Sutto, T. E., Ollinger, M., Kim, H., Arnold, C. B. and Piqué, A., 2006, Laser transferable polymer-ionic liquid separator/electrolytes for solid-state rechargeable lithium ion microbatteries, *Electrochemical Solid-State Letters*, 9: A69–A71.

Sutto, T. E., Duncan, T. T., Wong, T. C. and McGrady, K., 2011, Ionic liquid batteries: chemistry to replace alkaline/acid energy storage devices, *Electrochem Acta*, 56: 3375–3379.

Tolbert, W. A., Lee, I.-Y. S., Doxtader, M. M., Ellis, E. W. and Dlott, D. D., 1993a, High-speed color imaging by laser ablation transfer with a dynamic release layer: fundamental mechanisms, *Journal of Imaging Science Technology*, 37: 411–421.

Tolbert, W. A., I-Yin Sandy Lee, Xiaoning Wen, Dlott, D. D., Doxtader, M. M. *et al.*, 1993b, Laser ablation transfer imaging using picosecond optical pulses: ultra-high speed, lower threshold and high resolution, *Journal of Imaging Science Technology*, 37: 485–489.

Tóth, Z., Szorenyi, T. and Tóth, A. L., 1993, Ar^+ laser-induced forward transfer (LIFT): a novel method for micrometer-size surface patterning, *Applied Surface Science*, 69: 317–320.

Trasatti, S. and Kurzweil, P., 1994, Electrochemical supercapacitors as versatile energy stores, *Platinum Metals Review*, 38: 46–56.

Vincent, C. A. and Scrosati, B., 1997, *Modern batteries*, 2nd edn, Arnold, London.

Wang, J., Auyeung, R. C. Y., Kim, H., Charipar, N. A. and Piqué, A., 2010, Three-dimensional printing of interconnects by laser direct-write of silver nanopastes, *Advanced Materials*, 22: 4462–4466.

Wartena, R. C., Curtright, A. E., Arnold, C. B., Piqué, A. and Swider-Lyons, K. E., 2004, Li-ion microbatteries generated by laser direct write, *Journal of Power Sources*, 126: 193–202.

© Woodhead Publishing Limited, 2012

Wu, P. K., Ringeisen, B. R., Callahan, J., Brooks, M., Bubb, D. M. *et al.*, 2001, The deposition, structure, pattern deposition and activity of biomaterial thin-films by matrix-assisted pulsed-laser evaporation (MAPLE) and MAPLE direct write, *Thin Solid Films*, 389–399: 607–614.

Young, D., Wu, H. D., Auyeung, R. C. Y., Modi, R., Fitz-Gerald, J. *et al.*, 2001, Dielectric properties of oxide structures by a laser-based direct-writing method, *Journal of Materials Research*, 16: 1720–1725.

Zergioti, I., Mailis, S., Vainos, N. A., Papakonstantinou, P., Kalpouzos, C. *et al.*, 1998a, Microdeposition of metal and oxide structures using ultrashort laser pulses, *Applied Physics A*, 66: 579–582.

Zergioti, I., Malilis, S., Vainos, N. A., Fotakis, C., Chen, S. *et al.*, 1998b, Microdeposition of metals by femtosecond excimer laser, *Applied Surface Science*, 127–129: 601–605.

Zergioti, I., Karaiskou, A., Papazoglou, D. G., Fotakis, C., Kapsetaki, M. *et al.* Femtosecond laser microprinting of biomaterials, *Applied Physics Letters*, 86: 163902-1–163902-3.

Zhang, C., Liu, D., Mathews, S. A., Graves, J., Schaefer, T. M. *et al.*, 2003, Laser direct-write and its application in low temperature co-fired ceramic (LTCC) technology, *Microelectronic Engineering*, 70: 41–49.

Zheng, J. P., Cygan, P. J. and Jow, T. R., 1995, Hydrous ruthenium oxide as an electrode material for electrochemical capacitors, *Journal of Electrochemical Society*, 142: 2699–2703.

© Woodhead Publishing Limited, 2012

19

Printed polymer solar cells

M. HELGESEN, M. JØRGENSEN, T. D. NIELSEN and F. C. KREBS, Technical University of Denmark, Denmark

Abstract: This chapter describes the constitution of the polymer solar cell with general focus on upscaling, large-scale industrial manufacture and demonstration of the technology. Initially, the classical device architecture and function of the polymer solar cell are described and the upscaling to large area production, with aims and limitations, is discussed. Secondly, a brief overview of different printing and coating techniques, relevant to the manufacturing of polymer solar cells, is given with examples of some of the best-described routes to 'all printed and coated' industrially manufactured polymer solar cells. Finally, small- and large-volume polymer solar cell applications are evaluated together with the potential market areas. Also recent demonstrations of the polymer solar cell technology are shown, which serves the purpose of honing our understanding of the capacity and maturity of the technology.

Key words: polymer–fullerene bulk heterojunction, flexible devices, solution processing, roll-to-roll printing/coating, high-speed manufacturing, low-cost solar cells, demonstration products.

19.1 Introduction

In this chapter, the history of polymer solar cells and an overview of the research field are given briefly, with due reference to the most recent reviews [1–5] and books [6–9] on the topic that have been extensively reviewed.

19.1.1 The polymer solar cell

The simplest form of a polymer solar cell is shown in Fig. 19.1. The illustration is simplified and focus is on the active layer, which is classically a mixture of the conjugated polymer poly-3-hexylthiophene (P3HT) and [6,6]-phenyl-C61-butyric acid methyl ester (PCBM) that comprise the active layer, responsible for light absorption, carrier generation and transport to two electrodes where at least one of the electrodes is transparent to light. When light is absorbed in the polymer material (donor), an electron is excited from the HOMO into the LUMO, which leads to a bound state (exciton) of an electron and an imaginary particle called an electron hole. Subsequently, the generated excitons need to diffuse to the polymer–fullerene interface in order to undergo photoinduced charge transfer. Generally, the exciton diffusion length is restricted to 5–20 nm in organic materials so the formation of a polymer–fullerene nanoscale interpenetrating bicontinous network

© Woodhead Publishing Limited, 2012

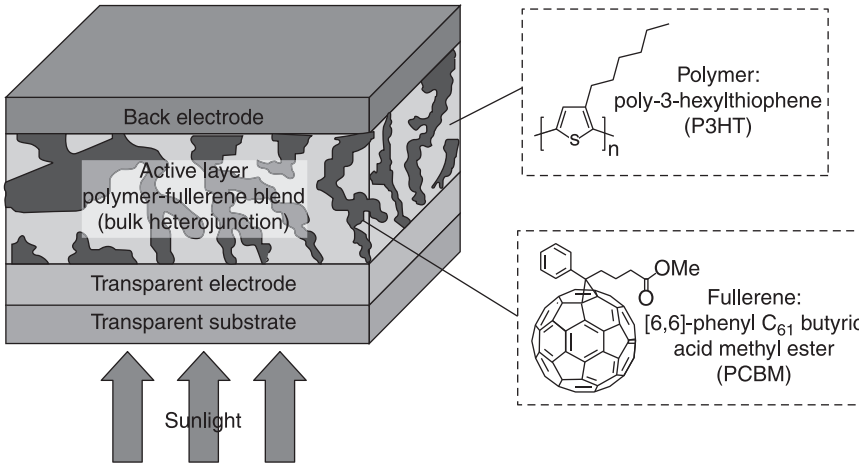

19.1 A view of a simple bulk heterojunction polymer solar cell comprising a single active layer and two electrodes.

within the active layer is essential to guarantee that every generated exciton can reach the polymer–fullerene interface. From the excited state of the polymer, an electron can be transferred into the LUMO of the fullerene acceptor if the energy levels are properly aligned (Fig. 19.2), resulting in free charge carriers that finally are transported to the electrodes, creating a photovoltaic effect.

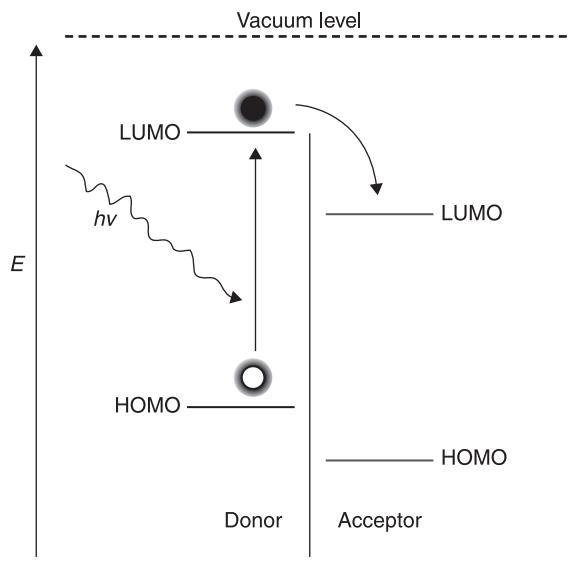

19.2 Energy-level diagram of two semiconductor materials. Upon light absorption in the donor material, an electron is excited from the HOMO to the LUMO followed by photoinduced charge transfer to the LUMO of the acceptor, resulting in free charge carriers.

© Woodhead Publishing Limited, 2012

In practical terms, the polymer solar cell also includes some extra layers to enable processing and performance. The typical geometry (or layer structure) employed in laboratory studies is mostly a result of the historical development of the technology. The research on polymer solar cells has been obsessively focused on the active layer and the disposition of the other layers has been chosen dogmatically for reasons of availability, performance and practicality. This implies that the remaining layers and procedures have not developed and, as a consequence thereof, the evolution of the laboratory cell into a commercially viable technology is somewhat slower than anticipated by many at the turn of the millennium, when the commercialization of the polymer solar cell was deemed to be imminent. As it stands today, there is still a considerable distance to cover before polymer solar cells have a chance of competing with inorganic thin-film solar cells in terms of cost, stability and performance.

The polymer solar cell, however, has a few aces up its sleeve that make it the only other viable PV technology on a huge scale. Only silicon PV exhibit limitless materials availability, whereas all other inorganic and thin-film technologies employ elements with low natural abundance or toxicity that cannot be handled in a foreseeable manner. Unlike the inorganics (i.e. Si, CdTe, CIGS), polymer solar cell devices can be solution processed under ambient conditions and do not depend on the large built-in electric field of a PN junction in order to separate the created electrons and holes when light is absorbed in the active layer. Also, in terms of material properties conjugated, polymers can easily be modified by adapting their chemical structure, through organic synthetic techniques, resulting in greater customization compared to the inorganics. Other organic thin-film solar cells based on low-cost materials that do not rely on expensive vacuum processing are the dye-sensitized solar cells (DSSCs). However, their major weakness is that they require a built-in liquid conductor (electrolyte solution), which has significant stability problems associated with temperature. Provided that the challenges of polymer solar cells can be overcome, polymer solar cells will become the prevailing PV technology in the future and also a major source of electrical energy. A balanced view of the market potential and patent landscape for polymer solar cells has been published recently [2].

19.1.2 The typical device geometry – the history of making polymer solar cells

Aside from the active layer, which is central to device function, the polymer solar cell has two electrodes and most often also some charge selective layers. The typical polymer solar cell should thus be considered as a five-layer device. In the laboratory setting, a glass substrate with a transparent electrode of indium–tin oxide is typically employed. One of the first developments was the inclusion of a semitransparent hole transporting and hole selective interlayer of PEDOT:PSS poly (3,4-ethylenedioxythiophene)-poly(styrenesulfonate), which also smoothed

© Woodhead Publishing Limited, 2012

the indium–tin oxide surface. This enabled easier processing of defect-free active layers. Later, electron-selective layers were employed between the active layer and the electrode (i.e. LiF, MgF_2).

For the first 20 years of the development of polymer solar cells most of the layers were vacuum processed, while the technology has been marketed and described as a solution-based technology that enables printing of the layers. In the standard cell described above, only PEDOT:PSS and the active layer are solution-processed, whereas ITO, LiF and the back electrode are vacuum-processed. It is clear that this has some bearing on the transfer of the technology to an all-printable setting, as multilayer solution processing only works if the previously deposited layers are not soluble in the solvents employed in the subsequently processed layers. In the case of PEDOT:PSS and typical active layer solutions, this has been fortuitous because PEDOT:PSS is traditionally processed from an aqueous solution and gives a high-energy surface that is easily wetable by low-surface-tension solutions of fullerenes and conjugated polymers in common organic solvents such as toluene, xylenes, chlorobenzene and 1,2-dichlorobenzene. The inverted solar cell geometry (also shown in Fig. 19.3) easily allows for solution processing since the holes are extracted at the back electrode, enabling use of more noble metals that can be printed, such as silver.

19.1.3 Visions for making polymer solar cells on a large scale – the need for ambient processing on flexible substrates

The standard rigid glass laboratory device falls somewhat short of enabling fulfillment of the vision of large-scale, low-cost, high-speed manufacture of polymer solar cells – especially since the capital investment in equipment based on vacuum and inert atmosphere processes is enormous compared to the common understanding of production environments based on commonly known printing and coating techniques [5]. One of the promising aspects of the polymer solar cell

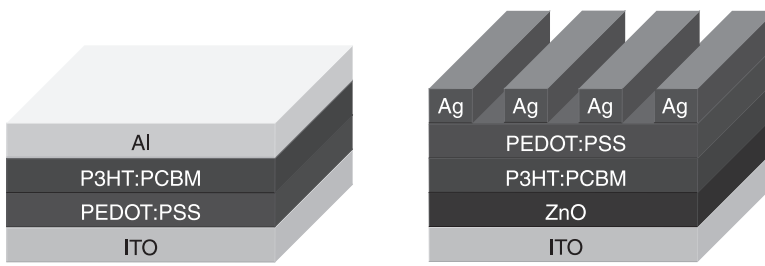

19.3 Illustration of (a) the normal geometry and (b) inverted geometry in simple forms.

© Woodhead Publishing Limited, 2012

technology is that it should enable processing under ambient conditions at low temperature on flexible plastic substrates, and this is what has driven the research of polymer solar cells for many years. The flexibility is a requirement for manufacturing at high speed and the use of simple polymer materials such as polyesters as substrates is quite possibly a requirement for achieving a low cost. The vision of low-cost, light-weight, high-performance polymer solar cells is thus likely to be reached only if all the processing can be done using simple equipment on common substrates using common coating and printing techniques. So far, however, development has not really been in this direction, and the challenges of taking the laboratory result, which typically comprises a glass substrate, evaporated electrodes and a very small area, have been grossly underestimated. In principle, a whole new knowledge platform is needed to manufacture polymer solar cells using R2R techniques under ambient conditions. Most of this knowledge is not pre-existing and the belief that the printing and coating industry can simply apply their knowledge to directly manufacturing polymer solar cells is naive. The basis for this observation is that the existing coating and printing industry is not used to the requirement that the printed or coated material needs to have an additional function after printing/coating and drying. Most often this line of business has fulfilled its goals when registry is kept and printing/coating is readable or of a particular optical appearance. To make the vision of polymer solar cells a reality much new knowledge must be built that rests on the existing state-of-the-art.

19.2 Printing and coating methods

Printing and coating techniques can be divided into a few rough groups that define their usability in the context of polymer solar cells [5]. These groups are the dimensionality of the printing, ink transfer and achievable wet layer thickness. As nearly all printing and coating in reality deals with the wet film, this is really where focus should be (the dry film is obtained in the drying process, which is a different and equally challenging matter).

19.2.1 Available printing techniques

Many techniques are available for the transfer of an ink material onto a surface and they are often termed as printing or coating techniques. The term ‘coating’ is normally employed to describe an ink transfer that is uniform (i.e. without pattern) and often implies that there is no physical contact between the surface that receives the ink and the system that supplies it. The term ‘printing’ is normally employed when dealing with a technique that supplies the ink to the surface in a two-dimensional pattern. The process is traditionally through a reversing action where in the simplest form the ink is transferred to a stamp with the desired pattern. The stamp or stencil is then brought into contact with the receiving surface whereby

© Woodhead Publishing Limited, 2012

the ink is transferred. In the modern form, the stamp has been replaced with a cylinder.

There are naturally exceptions to these general rules that are mostly historic, i.e. brush painting and ink-jet printing. All the printing techniques that have been developed had a particular purpose at that time that was rooted in either the printing or coating job at hand or in the need to coat or print a particular ink, i.e. a cheap office printer with fine resolution, and very large and even surface coating. In some cases, the development has been ink-driven and in other cases driven by the application technique. Some of the available printing and coating techniques have been summarized in Fig. 19.4, where they have been categorized according to their dimensionality and transfer type.

19.2.2 The suitability of different printing techniques

When considering printing and coating techniques in the context of polymer solar cells, it is clear that it is almost exclusively ink-driven and the success of one single coating technique has dominated the field of polymer solar cells and possibly also hindered its development. Spincoating is an excellent technique for the laboratory and combines simplicity in use with reproducibility, low ink usage (but large ink waste) and a very good control of the thickness and evenness of the coated film. In the printing and coating industry it is customary to use additives to an ink to alter

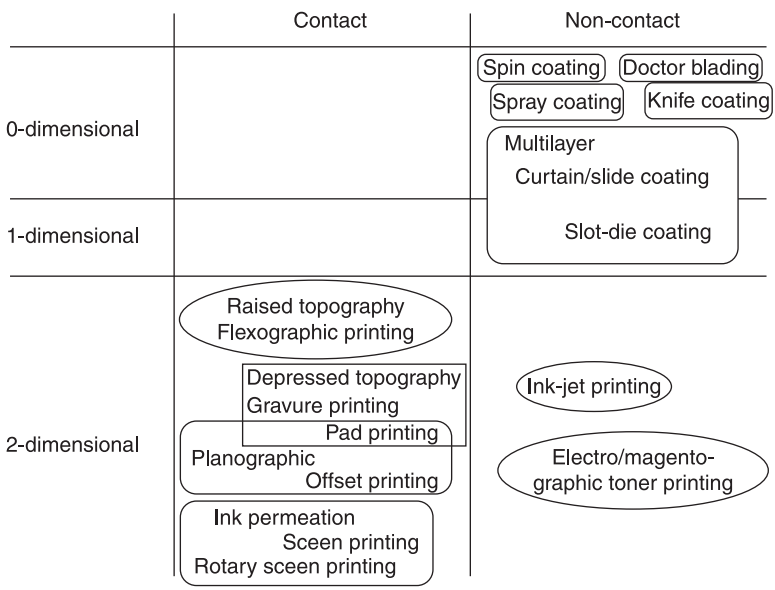

19.4 Some of the coating and printing techniques relevant to polymer solar cells categorized according to their dimensionality and mode of image formation.

© Woodhead Publishing Limited, 2012

viscosity, wetting, binding, rheology, etc. In the case of inks for polymer solar cells, this is as a general rule not possible or at least much more difficult and in the current state-of-the-art the development is ink-driven, i.e. the printing or coating technique has to match the ink properties. An additional limitation to the development is the cost of the technique. Some printing and coating methods can be adjusted to the printing needs, i.e. pattern, area, speed, at very little or no cost. The change of a screen-printing mask is, for instance, low in cost and ink-jet printing that has digital master has zero cost associated with changing the printed pattern. Gravure printing employs a very costly engraved roller and thus represents the opposite case. In terms of development, it is clear that the pursuit of an expensive technique is warranted only if it is the sole available technique. This does not mean that the expensive technique is not useful or might not be superior, it just means that if there are other available techniques they are likely to be employed instead, even with the disadvantages they might include. In the case of a typical five-layer inverted polymer solar cell, as illustrated in Fig. 19.3b, it is clear that the five different layers might require five different coating or printing techniques as each layer has different requirements. The printed back electrode, for instance, must be highly conducting and therefore it is reasonable to use a printing technique that gives rise to a thick deposit to enable high conductivity. Conversely, the active layer must be relatively thin, but must also present a large degree of evenness. While it is possible to employ the same printing or coating technique for both layers (or all layers), it is most likely that several different printing and coating techniques will be employed that match the different requirements best.

19.2.3 The different layers and the printing methods of choice

As examples, some of the best-described routes to an 'all printed and coated' polymer solar cell can be compared. The first example and first public demonstration of industrially manufactured polymer solar cells described the preparation of a five-layer inverted polymer solar cell where all layers were prepared by screen printing [10]. The solar cells were applied in a 'solar hat'. The inks for the electron transfer layer and the active layer were specifically redesigned so that they were screen printable. This required the development of a particular viscous solvent that allowed for the screen printing of thin zinc oxide and active layers. The work showed that it was possible, but also that the devices were of low overall performance limited by the manufacturing technique. The second example, termed ProcessOne [11], makes use of screen printing for processing the two electrodes. The ITO front electrode was patterned through printing an etch resist and etching of the ITO. The metallic back electrode was screen-printed silver. The three middle layers, comprising zinc oxide as the electron transport layer, P3HT-PCBM blend as the active layer and PEDOT:PSS as the hole-transport layer, were all coated into stripes using slot-die coating. It is not currently clear what printing and coating

© Woodhead Publishing Limited, 2012

techniques will win the race in the end, but it is likely that the typically industrially manufactured polymer solar cell will employ both screen printing and slot-die coating. This combination of techniques has been shown several times [12–15].

19.3 Manufacturing methods for complete polymer solar cells

In addition to the printing and coating techniques that must be mastered before one can manufacture polymer solar cells, several other fields of expertise within substrate materials, adhesives, foil handling, electrical connections, automated characterization techniques, etc. must be encompassed.

19.3.1 Substrates

The substrate is a very important part of the polymer solar cell and while many different substrates can be envisaged there are in reality only a few that have industrial relevance, due to issues of both cost and performance. The performance is meant to include aspects of optical quality and thermal stability (chemistry and shape). There are substrates that may present certain advantages such as exceptional thermal stability (i.e. Kapton) [15] or biodegradability (i.e. PLA) [16] but that are not suitable for state of the art polymer solar cell processing due to cost (Kapton) or poor temperature/solvent stability (PLA). PET is one polymer material that has a low cost and superior chemical, optical and thermal stability, and for many reasons this material is believed to be the best candidate for polymer solar cells, both for substrates and barrier foil.

19.3.2 Multilayer processing and contacting

The typical polymer solar cell comprises a multilayer structure with typically three to five or more coated and printed layers. This naturally implies that the overall process allows for printing and coating subsequent layers on top of already processed layers. With two layers this is relatively easy to achieve as one prepares the first layer from an aqueous solution and the subsequent layers from an organic solvent. The solvent orthogonality in this way solves problems of the solvents in the second layer dissolving the previously deposited layer. Incidentally, this is just the case for traditional laboratory devices that employ an already deposited (and insoluble) ITO layer whereupon PEDOT:PSS is normally spin-coated from an aqueous dispersion. The active layer is normally deposited on top of the PEDOT:PSS layer that presents a large surface energy, followed by evaporation of a metal back electrode. In many ways this is fortuitous and most laboratory workers are thus not fully aware of the extraordinarily large challenge associated with going to full solution processing on three or more layers. In order to achieve this successfully one must have the ability to switch off the solubility of previously processed layers such that the same or

© Woodhead Publishing Limited, 2012

similar solvents can be used for the entire processing chain. In the case of the solar hat [10], this was achieved using a combination of cross-linking of inorganic layers and thermocleavage of the active layer, and in the case of ProcessOne [11], this was achieved by employing cross-linking of zinc oxide nanoparticles, followed by a soluble active layer, a very thick PEDOT:PSS layer and finally a printed silver electrode. In addition to being able to print and coat multilayer structures, it is also very useful (or a requirement) that one is able to pattern some or all of the layers, such that many cells can be printed and coated and electrically interconnected.

The latter point is due to the often significant sheet resistive losses associated with making large area polymer solar cells. The solution to this problem is the well known series connection of many smaller devices. This has been illustrated in Fig. 19.5,

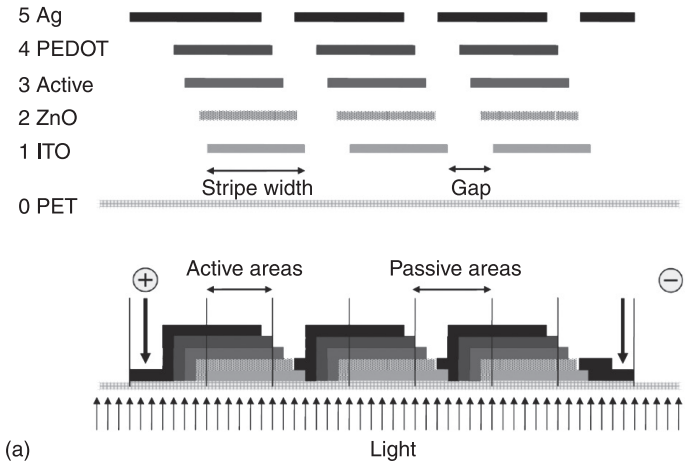

(a)

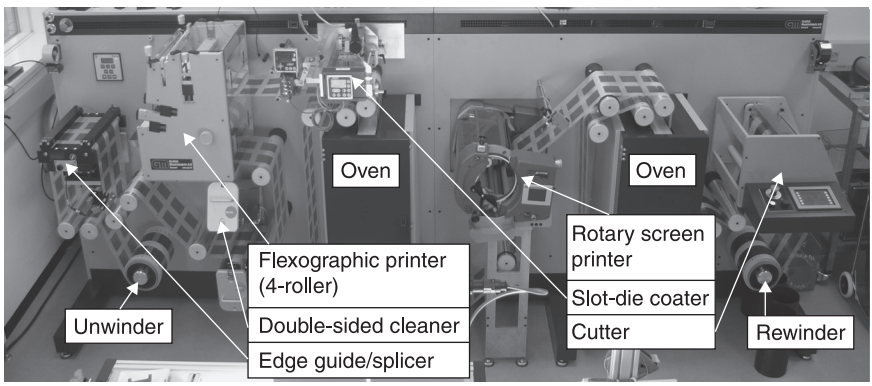

(b)

19.5 Illustration of a series connection of three individual solar cells through patterning of the printed and coated layers. (a) The printing of the final electrode completes the circuit. (b) A typical laboratory roll-to-roll coater is also shown.

© Woodhead Publishing Limited, 2012

where it is shown how the serial connection is accomplished in the final printing step. The electrical connection to the outside world is thus possible at the two electrodes and all interconnection is made through the printing process. The physical attachment of reliable electrical connections to the printed metal circuit is in itself a quite challenging technical problem, and the nature of the contacts depends highly on whether the device in the application is flexible or rigid. Electrical contacting of rigid applications can easily be achieved by careful soldering of tinned copper strips to the printed silver, whereas flexible contacts require special crimping to ensure consistent electrical contacts during flexing and bending of the solar cells (and contact area).

19.3.3 Encapsulation

Atmospheric components such as water and molecular oxygen are major causes of degradation and for this reason the freshly printed device must be protected from the direct action of the atmosphere to varying degrees depending on the type of materials employed and the device geometry. Generally, devices employing low work function metals such as aluminium and calcium are highly sensitive to water due to degradation, mainly at the metal organic interface, whereas that interface is stable towards dry oxygen. The organic layer is, however, often sensitive to molecular oxygen. The ideal encapsulation is a completely impervious (i.e. glass) encapsulation. However, the encapsulation material must be of low cost and the application of it must be compatible in speed with the manufacture of the solar cells. The low cost and fast processing requirements currently limit the choice to high-end food packaging foils that present oxygen and water vapor transmission rates of, respectively, OTR<0.01 $cm^3m^{-2}bar^{-1}day^{-1}$ (measured according to ASTM D3985-81) and WVTR<0.04 $gm^{-2}day^{-1}$ (measured according to ASTM F372-78). The typical barrier material is PET-based and has a multilayer structure. The optical appearance is to the eye indistinguishable from native PET and in terms of handling it behaves identically. This enables simple foil handling techniques to be employed as shown in Fig. 19.6, where lamination using a simple roll-to-roll laminator enables encapsulation at 20 m min^{-1}.

19.3.4 Some post-production handling and characterization methods

R2R characterization

The finished photovoltaic devices are characterized by their efficiency in converting light to electrical power by measuring the diode characteristics. Solar cell parameters such as the short circuit current (I_{sc}), open circuit voltage (V_{oc}), maximum power point and fill factor (FF) can be extracted from the diode curve to compute the power conversion efficiency (PCE). With the large volume of devices produced by R2R coating, this task becomes difficult to do by hand and is an obvious step to automate.

© Woodhead Publishing Limited, 2012

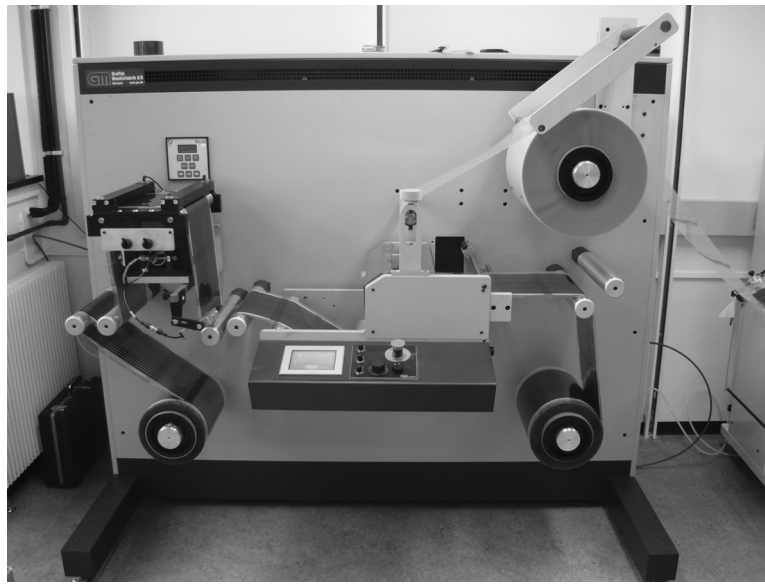

19.6 A simple roll-to-roll laminator comprising unwinder, edge guide and cutting table, laminator, laminate unwinder, longitudinal cutting knives and rewinder (left). The barrier foil with adhesive is the large roll in the upper right part of the photograph.

We have constructed a R2R characterization apparatus consisting of a computer-controlled unwinder-rewinder system with a metering wheel to advance modules one at a time under an artificial sun lamp. At this position, electrical contacts are established using a pneumatic system so that one or more IV curves can be measured via a computer-controlled source measure unit (see Fig. 19.7). Automation of the testing procedure through the use of an R2R characterization apparatus is important to match the production speed. Presently, it is possible to measure each PV module in about the same time it takes to produce it (~20 sec). Data are stored for the individual IV scan for each module and also as an overview for the whole roll of modules. These data can be used to identify failed modules due to coating errors and thus serve as a quality control. It is also an important tool for improving the coating process itself. Changes made during the coating of one roll of modules will affect the solar cell parameters that are readily identified by studying e.g. the PCE as a function of module number. R2R characterization coupled to the variation of coating parameters can thus be used as a research tool (Fig. 19.8).

Light beam-induced current (LBIC) characterization

Standard testing of a photovoltaic device by measuring the diode characteristics only gives an overall description of its function. Light beam-induced current (LBIC)

© Woodhead Publishing Limited, 2012

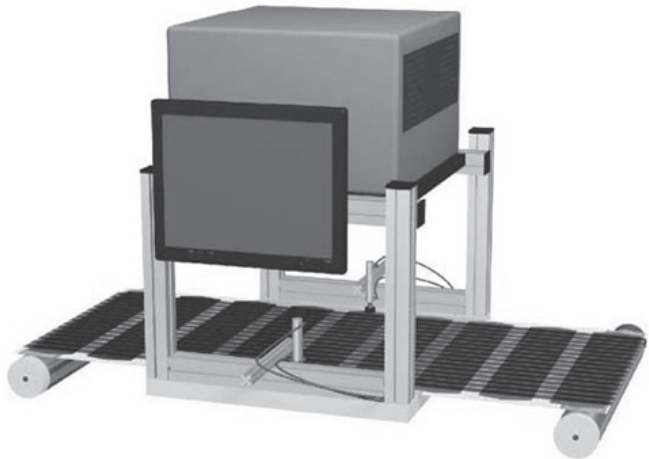

(a)

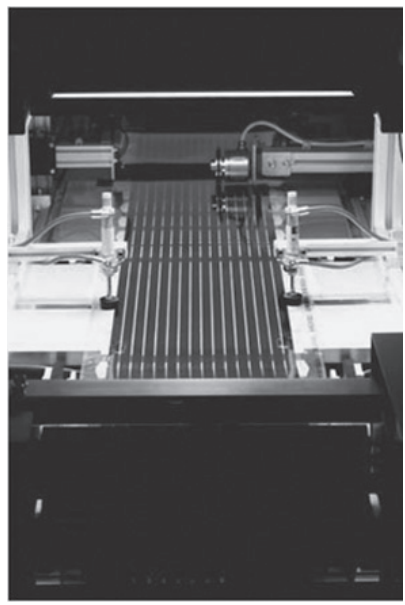

(b)

19.7 R2R characterization of R2R-coated photovoltaics shown schematically to the top. A roll of modules comprising stripes of solar cells is advanced one at a time by the unwinder-rewinder system. An artificial sun (large gray box) illuminates the devices while IV scan of the devices is obtained. Electrical contacts to electrodes are established with a pneumatic system (cylinders with tubing). A photograph of the system is shown to the bottom.

© Woodhead Publishing Limited, 2012

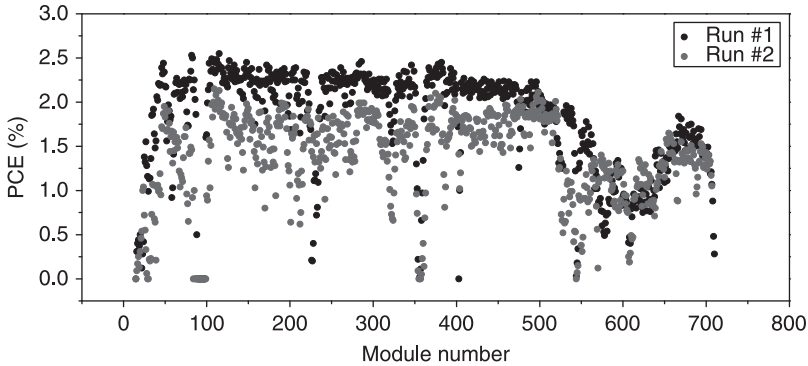

19.8 Example of a graph of efficiency (η) as a function of module number.

measurements, on the other hand, map out the current response from individual pixels in the device, and may be used as a tool to study defects and changes in different areas. The measurement can be carried by using a focused light beam (e.g. a laser) mounted on a computer-controlled XY-stage that is scanned in a raster pattern over the area of the device while the current generated is measured. A map can then be constructed from the data as pixels of varying color to represent different levels of current. The LBIC map must then be compared with the image of the device to locate features of interest.

The LBIC technique is well-established for characterizating inorganic solar cells [17] and has also been used occasionally for organic photovoltaics to study degradation, for example [18–20].

As organic solar cells evolve from small-scale laboratory devices with an area of a few square millimeters to larger-scale R2R coated devices and modules, the need to obtain a mapping of the functionality increases for which LBIC measurements seem ideally suited. Larger-scale devices can have defects arising from impurities or coating defects that can be visualized by the LBIC technique. Modules constructed from multiple serially connected solar cells can be mapped to show their individual contribution to the overall device function Fig. 19.9.

19.4 Applications and demonstrations of polymer solar cells

19.4.1 Market areas of polymer solar cells

Polymer solar cells perform exactly the same function as any other type of solar cell (the conversion of photons into an electrical current) and will as such enter a well-charted market realm with numerous types of solar cells and numerous possible applications. But the technology is still in development. The present technology's early stage of maturity, with the recent initial market introduction of

© Woodhead Publishing Limited, 2012

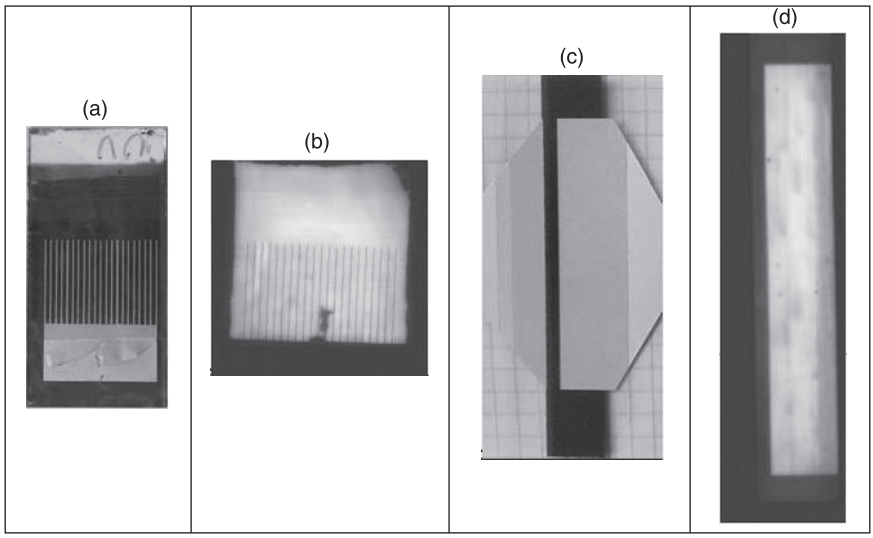

19.9 Example of LBIC maps of a functional map of a P3HT/PCBM-type solar cell with a printed silver back electrode having a grid pattern ((a) and (b)), and a R2R printed solar cell and LBIC map ((c) and (d)), showing small point defects and variations due to the coating process. In the LBIC maps ((b) and (d)), the coloring from blue to yellow represent current from low to high, respectively. The devices are photographed from the back side whereas the LBIC was recorded from the front side.

low-performing, high-cost, low-lifetime solar cells compared to other types of solar cell, poses a grand challenge. Thus, potential market areas for polymer solar cells have been a topic for much discussion over the past decade among industry, academia and technology competitors. The key observations for this discussion are centered on the performance–cost ratio of an underperforming new technology as it enters a crowded market segment. It is obvious to industry and academic insiders that the premonitions of technology development speed have been overly positive and sent a Klondike-like rush to the heads of many scientists, investors and industry stakeholders – as they all asked the question: 'what if polymer solar cells actually succeeded in providing the promised potential of very low cost solar energy?' The determining factors for market application with any solar cell technology are cost, lifetime and PCE – the balance of which here is termed the performance–cost ratio. Some may argue that polymer solar cell technology's typical features, such as light weight and flexibility, may ease market entry, but this has not yet been established as a fact. Flexibility and light weight possess great functionality in processing polymer solar cells, but in application and product integration especially flexibility seems to have limiting factors, at least at this point in technology development.

© Woodhead Publishing Limited, 2012

As polymer solar cells were not available in marketable forms until 2009, when Konarka Technologies introduced the first low-performing polymer solar panels [21], numerous application ideas have been formulated and a few of these tested. In perspective, polymer solar cells possess the potential to be applied within consumer electronics, developing world applications, leisure, military and emergency, residential building and industrial building add-on or integration and finally large-scale utility, as illustrated in Fig. 19.10.

The fulfillment of the list of application areas is determined by the continued development in PCE, cost and lifetime and as such indicates that the first market for polymer solar cells will be found to be a power source for small-scale electronic applications, i.e. battery chargers.

In comparison with existing types of solar cells, flexible solar cells (like polymer solar cells) create a number of application possibilities because they are potentially cheap, flexible, lightweight, semi-transparent, variable in color, environmentally friendly and provide portable solar energy. These technology-specific factors, in many ways, represent market opportunities as well as threats. Portable solar energy has been a dream since solar energy was discovered – and, admittedly, possesses interesting possibilities if the solar cell is cheap enough, and if the PCE matches the portable application – which is a key point. External limiting factors are the need for energy and the storage of energy, i.e. the available application and battery capacity coupled with the PCE of the solar cell.

The field of portable electronics today is power-hungry and current portable solar cells cannot power a cell phone, a music player or a laptop – it merely represents a back-up or trickle charge-scale power source and does not provide power 'on the go', as many would like it to do. In fact, solar cell being portable does not mean that it can charge the batteries in your gadget while you are on your way to work as this would take a full day or more of direct sun onto the solar cell. Accordingly, a number of disadvantages rest not only with polymer solar cells, but also with adjacent technologies necessary for product integration. The vision for

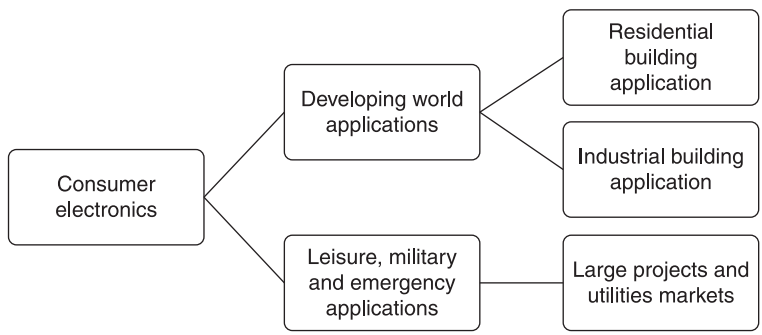

19.10 Improvements in the performance–cost ratio allows for access to new market segments.

© Woodhead Publishing Limited, 2012

polymer solar cells is power production at low cost. At the present time, the position of polymer solar cells is in between continued technology development and initial market introduction, and consequently affordable power production is far from being within reach. As the technology matures, new applications can be created and new market segments entered. A conservative timeframe estimate for the continued technology development and maturation is represented in Table 19.1. The list represents Risø DTU's interpretation of the current state of affairs within polymer solar cells indicating that, yes, polymer solar cells represent a significant opportunity, but a stepping-stone approach that allows for learning by doing and slowly evolving technology from its early commercial phase – however exciting as it may be – to the levels of standalone energy production in large volumes, is the path forward for years to come, for the simple reason that it is a complicated technology [2]. When taking a closer look at the early market segments, a few things must be emphasized. Firstly, the quality of the solar cell must be capable of meeting the implementer's need, i.e. quality, covering such elements as visual performance and general finish, together with general technical performance. Secondly, to sustain revenue, it is central to identify one or more applications that can carry forward the cost of technology development and production, which costs at this early stage are significant. External observers could claim that polymer solar cells, with their apparent superior cost and performance, should be able to outperform all other thin-film solar cells. This would be great if it were so, but polymer solar cells are currently subordinate to all other solar cells in terms of performance and cost. If polymer solar cells were competitive, another point of view could be to try to take over the market of thin-film solar cells. Again issues arise, as it proves that the thin-film solar cell market for small-area charging functions for consumer electronics is quite small [9]. Put differently, thin-film solar cells have not brought forward a portable solar energy revolution and thus, if polymer solar cells intend to do so, the cost–performance ratio should be best in the market and at the same time significant effort should be put into new and innovative application of solar cells. Thirdly, polymer solar cells may be ingenious in their complex simplicity, but it is also through scientific and technological challenge, that offers great challenges when it comes to turning profit in the pre-energy production market – if polymer solar cells cannot meet the challenges in the short-term markets, energy production will remain a dream. For polymer solar cells to compete in a crowded market, significant performance–cost ratio improvements must be made. This poses a significant economic challenge that can only be met by external capital and public funding, unless industry itself, by skilled technological development, is capable of turning below-par solar cells into revenue via uncharted market segments [2,9].

Polymer solar cell-producing energy raises the question of competition, especially with silicon solar cells. One point of view is that all the solar cells that can be produced can be installed, as demand is immense. If so, polymer solar cells should not be seen as a competitor to or substitute for silicon solar cells, but rather as an alternative for specific applications over the next 10 to 20 years.

© Woodhead Publishing Limited, 2012

Table 19.1 The polymer solar cell

	Phase 1	Phase 2	Phase 3	Phase 4
Phase implementation	2010–2013	2012–2015	2015–2018	2018–2025
Market segment categorization	Charger function for consumer electronic products	Beginning small-scale stand-alone equipment	Beginning residential building add-on panels and medium-scale stand-alone systems	Beginning large-scale implementation of OPV
Phase description	1–3% PCE	3–4% PCE	4–6%	6–9%
Continuous lighting conditions, lifetime	1–2 years' lifetime 8–12 US$/W Small-area modules T(80) 2500 hours	1–3 years' lifetime 2–4 US$/W Medium module size T(80) 5000 hours	3–5 years' lifetime 1 US$/W Large-area module T(80) 12 000 hours	5–7 years' lifetime Below 0.5 EIUS$/W Large-area modules T(80) 20 000 hours
Performance/cost ratio	2%*2500/8 = 6.25	4%*5000/2 = 100	6%*12 000/1 = 720	9%*20 000/0.5 = 3600
Expected application	Portable chargers for consumer electronics, integration in toys, low-power electronic equipment, smartcards and many electrical pieces of equipment in need of a low-power source.	Larger-area chargers for leisure and camping activities, integration in tents, sunscreens, awnings, small-scale lighting lamps for developing markets, military application and possibly early emergency and relief application.	Solar panels for retrofitting on residential buildings, solar curtains for indoor use and the possibility of OPV film for windows. Massive application in developing countries with low-power applications developed accordingly	Solar panels for large-scale commercial building integration and potential successive development of OPV solar power plant if cost/performance ratio is competitive.
OPV companies	5–10	10–15	12–18	18–30
Annual production capacity	1 GW	1.5 GW	5 GW	60 GW

Note: Phase projection development scenario was compiled from industry and academic conference presentations and discussions over the course of 2008–2010. As the performance/cost ratio of the solar cell develops, new market segments will become available. The applied time frame is an estimate of when each of the phases will begin – the overlap is intentional. Cost is indicated for large-area module for phases 3 and 4. Annual capacity is capacity and not amount of manufactured cells.

© Woodhead Publishing Limited, 2012

19.4.2 Adaptable small-volume applications

The flexibility and reasonably light weight of polymer solar cells provide much, promise and create many applications, among which examples like the polymer solar-clad blimp, solar textile and sports equipment like footballs covered with solar cells and fitted with electronics that report back on speed, height, position and maybe air pressure are among the more challenging [22,23]. However, it is flexibility in terms of processing a polymer solar cell in any shape needed that may become the primary functionality of this type of solar cell, if, the right application becomes available. The application of screen printing and flexographic printing allows for the patterning of designed shapes that again allow for unique solar cells to be prepared for any type of application [5]. If, for example, a company were in need of a solar cell sticker for a toy car or for the roof of a toy house, the printing process allows for individual design – so that design flexibility becomes a widespread factor in applying solar cells. An example of this was the Risø DTU solar cell demonstration in a hat containing a radio. The design of the solar hat made it necessary to have a round solar cell instead of the standard rectangle used in any type of solar cell product.

Figure 19.11 shows the resulting solar cell design, and as such provides the promise of potentially any shape needed. Bringing this technological ability

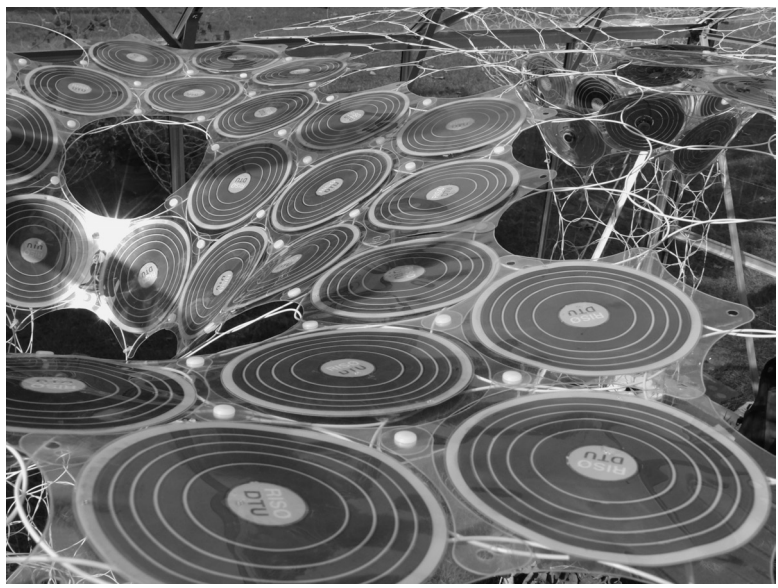

19.11 Photograph showing concentric polymer solar cell modules prepared by processing all five layers of the inverted solar cell structure using industrial screen printing. Demonstration of the same modules in St. James's Park in London, 2008.

© Woodhead Publishing Limited, 2012

forward allows for numerous product ideas to be generated. As such, polymer solar cell technology represents a previously unseen adaptability to intended applications and will, if designers learn to work with the technology, present a number of interesting application opportunities.

19.4.3 Large-volume applications – aims and limitations

The ambition of polymer solar cells is to provide affordable solar energy at a cost below 0.5€/W. This ambition is based primarily in the cost potential that lies in the application of inexpensive materials and simple manufacturing equipment with a low thermal budget, which carries low investment cost and is easily scalable.

For this ambition to have any basis to grows polymer solar cell technology must mature significantly and a vigorous testing scheme must be established for outdoor polymer solar cell panels as to understand better the issues related to degradation in order to improve lifetime significantly. Key technology developers like Konarka and Risø DTU are both engaged in outdoor testing of polymer solar cells. In April 2009, Risø DTU demonstrated a panel-scale outdoor solar testing unit for the long-term weathering effect on polymer solar cells. The applied solar tracker (AZ-225 Dual Axis, Azimuth Drive Solar Tracker) was fitted with polymer solar cell panels manufactured in collaboration with Danish silicon solar panel manufacturer Gaia Solar A/S. The three installed panels each measured 1 × 1.7 meters and were fitted with 24 solar-cell modules, each 20 × 25 cm. Power production from each panel was 11 W, of which 7 W were fed into the electrical grid, and as such these became the world's first grid-connected polymer solar panels (Fig. 19.12).

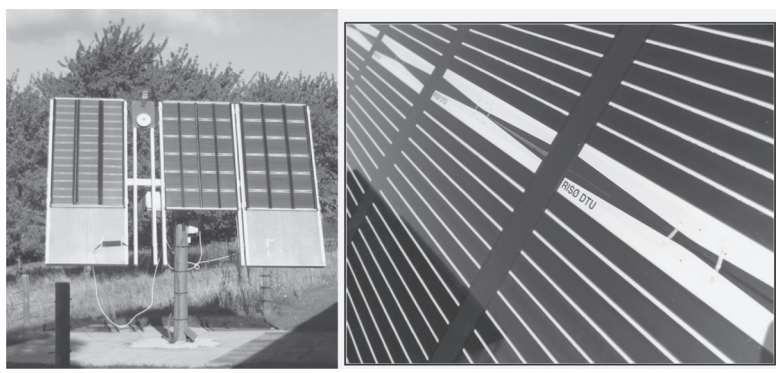

(a) (b)

19.12 (a) Photographs of a solar tracker with mounted polymer solar cell panels comprising different sizes of the individual polymer solar cell modules connected to give the same panel size (1.0 × 1.7 m^2). (b) A close-up photograph of the panel showing individual polymer solar cell modules.

© Woodhead Publishing Limited, 2012

By May 2010, third-generation polymer solar cell modules were installed and are now in daily operation. The key objective of this demonstration was to understand the long-term weathering effect on large-area polymer solar cell panels in collaboration with industry [24]. Current limiting issues with polymer solar cells with regards to energy-scale production are obviously the weak performance–cost ratio. A comparison with silicon solar cells will show that their lifetime is too short, that their PCE is too low, and that their cost is factors away from being relevant to any use resembling commercial energy production. Academia agrees that, although the lifetime of polymer solar cells is unlikely to rival that of silicon solar cells, lifetimes of 8–15 years may be within reach, that their PCE should, without too many issues, be able to reach 10–15% and that cost below the level of 0.5 €/W in large-scale production may become possible. Of these three, the determining factor will be the reduction of cost through large-scale production and novel panel manufacturing methods to take advantage of the technology features, if polymer solar cells in any way intend to contribute to the global energy production.

19.4.4 Recent demonstrations

For polymer solar cells, demonstration is a tool to create awareness of the technology outside academic circles in order to spark interest among designers, potential manufacturers and end-users, who all help to motivate the development of technology's implementation. Demonstrated polymer solar cells have proven to be a very good indicator of the maturity level of the technology. One may *say* what one can do, but if one cannot *show* what one can do, the value of what was said may be questionable. Thus a polymer solar cell that is integrated in a given product and that able to power product for its intended lifetime is a very strong indicator of the technology's capability – under the notion that anyone in a competitive technology development race is interested in attracting attention on the premises of what they are able to provide. For example, if it were possible to manufacture polymer solar cells at low cost, and with reasonable efficiency and lifetime, the product would already be on the market, but this is not so – as available polymer solar cells are short-lived, inefficient and expensive compared to other types of solar cell.

Konarka Technologies and Risø DTU are both strong proponents of demonstration. Beyond the extent to which it provides very good PR, as a significant learning process is associated with the generation of polymer solar cell application, the consecutive realization of the solar cells, product design and integration and the testing of the product in real life. In other words, demonstration projects stand as a market introduction exercise for an unproven technology.

Konarka Technologies provided a large-scale demonstration in San Francisco in 2009, where the solar-powered bus shed rooftop was introduced with the intent to install 1100 over the next few years. Local partners were 3Form, Lundberg

© Woodhead Publishing Limited, 2012

Design and Clear Channel Outdoor, who together with Konarka designed the wave-shaped polycarbonate structure [25]. There is no available information on lifetime or PCE regarding the installation, but a reasonable performance–cost ratio must be expected, as the total demonstration totals between 75 000–100 000 polymer solar panels. Another Konarka demonstration, which is now commercially available, is the shoulder solar bag. It serves as a marketing function and it seems to be the first integrated polymer solar cell product on the market – again, clearly indicating the maturity and performance level of polymer solar cells.

At Risø DTU, the demonstration of technology is used as an integrated technology development tool that allows the generation of knowledge about the full value chain from the point where a polymer solar cell product application idea is presented to the final, applicable and tested product. As the first in the world, Risø DTU demonstrated industrially manufactured polymer solar cells on the scale of thousands in collaboration with Mekoprint A/S, a Danish printed electronics manufacturer. By screen printing, a round solar cell was manufactured and integrated in a solar hat, where it charged a small AAA-battery powering a small radio. The solar hat product was first introduced and tested at the Roskilde Festival in 2008 [10] (Fig. 19.13).

19.13 A photograph of the solar hat comprising sun hat, polymer solar cells and integrated radio. Demonstrated at the Roskilde Music Festival in 2008.

© Woodhead Publishing Limited, 2012

A second demonstration was the Suntiles solar curtain in collaboration with Astrid Krogh Design (Fig. 19.14). The 'Suntiles' curtain was made from polymer solar cells modules, or tiles – thus the name 'Suntiles' – and applied the power-producing capability and lightweight character of the polymer solar panels to create a mobile-like hanging power-producing sun-shading structure. The Suntiles curtain was made from 90 tiles and was exhibited at the Danish Design Center in Copenhagen in May 2009 [26].

A third large-scale demonstration was the development of the Lighting Africa polymer solar cell-powered light-emitting diode (LED)-based lamp (Fig. 19.15), which demonstrated polymer solar cells as a power source for lighting purposes in rural communities in developing countries. The Risø solar lamp project was inspired by the World Bank initiative named Lighting Africa (www.LightingAfrica.org, with the ambition of limiting the use of kerosene and oil lamps by introduction of solar-powered lighting products) and was first established as a reading lamp for school children. The potential lies in the possibility of creating affordable LED-based lamps that meet the need of the user in the user habitat and which can replace the widespread use of kerosene lamps – including a global fuel market of US$ 38 billion. Polymer solar cells may possess the necessary performance–cost ratio for providing affordable solar lamps.

The demonstration of polymer solar-powered LED lamps continues and an improved version of the Lighting Africa lamp was ready for testing by the end of 2010 [27,28]. For the development of polymer solar cell technology, demonstration projects will play a significant role in its further market introduction as ideas are turned into demonstrations that are made into products, so that end-users learn what the technology is capable of. Polymer solor cells will mature only through step-by-step, persistent doing and learning and if there is sufficient participation in the effort to make solar energy affordable to the masses.

(a) (b) (c)

19.14 Photographs of Suntiles. (a) A small demonstration comprising solar cells and phase change materials. (b) The 3 × 4 m^2 window panel that was demonstrated as part of the international exhibition 'it's a small world' 2009–2010. (c) A window exhibition in New York (courtesy of Loop.PH).

© Woodhead Publishing Limited, 2012

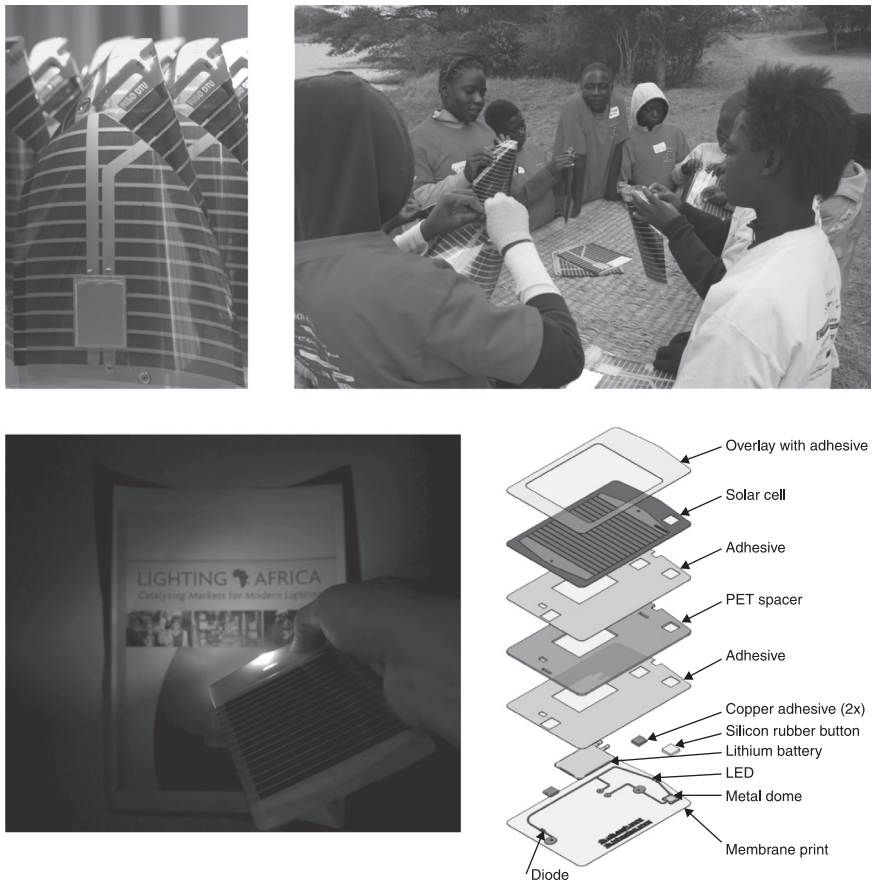

19.15 Lighting Africa lamps from field testing in Zambia (2009) (top) and a small pocket-sized torch prepared by fully automated processing (bottom).

19.5 Conclusions and future trends

To conclude, it is clear by now that polymer solar cells have a commercial potential of which the extent is largely unknown at present. They are likely to also play a role in future electrical energy production if we project the progress between 1990 and 2010 into the next decade. There are, however, still massive challenges to overcome before polymer solar cells can be envisaged to contribute significantly towards global electrical energy production, but in contrast to many of the thin-film solar cell technologies, the positive message is that there is no evidence that this is impossible. This is the case for many of the novel thin-film technologies that have great commercial potential, but if one extrapolates to a commercial

© Woodhead Publishing Limited, 2012

scale, elements such as tellurium and gallium simply do not exist in the abundance needed for the technology to be viewed as realistic. The pursuit of future versions of the polymer solar cell that reach the low-cost potential of the technology will present indium-free, vacuum-free ambient processing without the use of materials with high embedded energy, low-cost encapsulation schemes and fast manufacture.

19.6 Acknowledgements

This work was supported by the Danish Strategic Research Council (DSF 2104-05-0052 and 2104-07-0022), EUDP (j. nr. 64009-0050) and PV ERA-NET transnational POLYMOL project PolyStaR.

19.7 References

1. Helgesen M., Søndergaard R. and Krebs F. C., Advanced materials and processes for polymer solar cell devices, *Journal of Material Chemicals*, 20 (2010) 36–60.
2. Nielsen T. D., Cruickshank C., Foged S., Thorsen J. and Krebs F. C., Business, market and intellectual property analysis of polymer solar cells, *Solar Energy Materials and Solar Cells*, 94 (2010) 1553–1571.
3. Dennler G., Scharber M. C. and Brabec C. J., Polymer-fullerene bulk-heterojunction solar cells, *Advanced Materials*, 21 (2009) 1323–1338.
4. Gonzalez-Valls I. and Lira-Cantu M., Vertically-aligned nanostructures of ZnO for excitonic solar cells: a review, *Energy and Environmental Science*, 2 (2009) 19–34.
5. Krebs F. C., Fabrication and processing of polymer solar cells. A review of printing and coating techniques, *Solar Energy Materials and Solar Cells*, 93 (2009) 394–412.
6. Soga T. (ed.), *Nanostructured materials for solar energy conversion*, Elsevier, UK, 2006.
7. Krebs F. C. (ed.), *Polymer photovoltaics: a practical approach*, SPIE Press, Bellingham, 2008.
8. Brabec C. J., Scherf U. and Dyakonov V. (eds), *Organic photovoltaics: materials, device physics and manufacturing technologies*, Wiley–VCH, Weinheim, 2008.
9. Krebs F. C. (ed.), *Polymeric solar cells: materials, design, manufacture*, DEStech Publications Inc., USA, 2010.
10. Krebs F. C., Jørgensen M., Norrman K., Hagemann O. and Alstrup J., A complete process for production of flexible large area polymer solar cells entirely using screen printing—first public demonstration, *Solar Energy Materials and Solar Cells*, 93 (2009) 422–441.
11. Krebs F. C., Gevorgyan S. A. and Alstrup J., A roll-to-roll process to flexible polymer solar cells: model studies, manufacture and operational stability studies, *Journal of Material Chemistry*, 19 (2009) 5442–5451.
12. Krebs F. C., All solution roll-to-roll processed polymer solar cells free from indium-tin-oxide and vacuum coating steps, *Organic Electronics*, 10 (2009) 761–768.
13. Krebs F. C., Tromholt T. and Jørgensen M., Upscaling of polymer solar cell fabrication using full roll-to-roll processing, *Nanoscale*, 2 (2010) 878–886.
14. Krebs F. C., Polymer solar cell modules prepared using roll-to-roll methods: knife-over-edge coating, slot-die coating and screen printing, *Solar Energy Materials and Solar Cells*, 93 (2009) 465–475.

© Woodhead Publishing Limited, 2012

15. Krebs F. C. and Norrman K., Using light induced thermocleavage in a roll-to-roll process for polymer solar cells, *ACS Applied Material Interfaces*, 2 (2010) 877–887.
16. Strange M., Plackett D., Kaasgaard M. and Krebs F. C., Biodegradable polymer solar cells, *Solar Energy Materials and Solar Cells*, 92 (2008) 805–813.
17. Boyeaux J. P. and Laugier A., *Journal de Physique*, Colloque (1989) (C6, Beam Injection Assess Defects Semicond), C6-111/C6-127 (review).
18. Sirimanne P. M., Jeranko T., Bogdanoff P., Fiechter S. and Tributsch H., On the photo-degradation of dye sensitized solid-state TiO2 |dye|CuI cells, *Semiconductor Science and Technology*, 18 (2003) 708–712.
19. Cataldo S., Fabiano S., Ferrante F., Previti F., Patané S. and Pignataro B., Organoboron polymers for photovoltaic bulk heterojunctions, *Macromolecular Rapid Communication*, 31 (2010) 1281–1286.
20. Bull T. A., Pingree L. S. C., Jenekhe S. A., Ginger D. S. and Luscombe C. K., The role of mesoscopic PCBM crystallites in solvent vapor annealed copolymer solar cells, *ACS Nano*, 3 (2009) 627–636.
21. www.konarka.com (accessed on 26 August 2010).
22. Patent: US 6,224,016 B1.
23. Patent: US 6,913,713 B2.
24. Medford A. J., Lilliedal M. R., Jørgensen M., Aarø D. and Pakalski H., Grid-connected polymer solar panels: initial considerations of cost, lifetime, and practicality, *Solar Energy Materials and Solar Cells*, (2010), http://dx.doi.org/10.1016/j.solmat.2010.06.007.
25. Bus stops by Lundberg Design and 3Form generate power for San Francisco, *Interior Design*, http://www.interiordesign.net/article/ca6678576.html (accessed on 26 August 2010).
26. http://www.astridkrogh.com/html/suntiles.html (accessed on 26 August 2010).
27. Krebs F. C., Nielsen T. D., Fyenbo J., Wadstrøm M. and Pedersen M. S., Manufacture, integration and demonstration of polymer solar cells in a lamp for the 'Lighting Africa' initiative, *Energy and Environmental Science*, 3 (2010) 512–525.
28. Krebs F. C., Fyenbo J., Jørgensen M., Product integration of compact roll-to-roll processed polymer solar cell modules: methods and manufacture using flexographic printing, slot-die coating and rotary screen printing, *Journal of Material Chemistry*, 20 (2010) 8994–9001.

© Woodhead Publishing Limited, 2012

Index

AchE-modified SPCE, 394
acoustic wave resonant sensor, 235
acoustic wave sensor, 234
active phases, 31–46
  classification, 31
  conducting materials for resistors, 31–40
    palladium – silver systems, 32–3
    ruthenium and iridium system, 34–40
  conductors, 41–2
  dielectrics, 42
  materials for AlN, SiC, glass and other substrates, 45–6
  materials for nitrogen firing, 43–5
airbag initiator element, 459–60
  adapted model, 464
  fused initiator element, 464
  laser patterned thick-film initiator element, 462
  material property data, 463
  performance data, 462
  temperature distribution of the modified initiator element, 465
alkaline batteries, 537–8
  optical micrographs, 538
alumina, 50, 71, 175
  substrates, 430, 432
aluminium substrates, 434
amperometric immunosensor, 386
amperometric sensors, 356–60
  combustible sensors, 358–9
  NO differential sensors, 359–60
  oxygen sensors, 356–8
amperometry, 372–3
  typical input and output waveforms, 373
anisotropic magnetoresistance (AMR), 180, 184
anodes, 471, 476–8
  LSM/YSZ/Ni-YSZ fuel cell, 478
  thick-film of a cermet NiO-CGO, 477
  triple phase boundary (TPB), 477
antioxidants, 47
Arrhenius equation, 98, 171
ASTM D3985-81, 559
ASTM F372-78, 559
atmospheric plasma spray (APS), 24
atomic oxygen diffusion, 288
auxiliary electrode, 369
available volume fraction, 123

$BaSrTiO_3$, 139
beryllia, 50, 72
biosensor, 368
bismuth sodium titanate (BNT), 251
bismuth titanate (BT), 251
blanking, 144
blending curve, 91
BS 1904, 169
bulk micromachined silicon accelerometer, 266
bulk micromachining, 262–3

capacitive pressure microsensor, 208–9
capacitive pressure sensors, 207–8, 272–3
capacitive strain sensors, 211–12
capacitor dielectrics, 106
carbon dioxide sensors, 348–50
cathodes, 471, 478–82
  Arrhenius plot of the polarisation resistance, 482
  BSCF cathode onto SDC film, 480
  cross-section of a SOFC fuel cell, 480
  influence of oxygen partial pressure on the impedance spectra, 481
  LSM thick-film, 479
  microstructures of LSM-YSZ composite, 479
cellophane, 144
cellulose acetate, 144
ceramic capacitive pressure sensor, 271
ceramic heater, 441–4
  set-up, 441
  temperature control of water at different operation conditions, 443
  temperature distribution along the cross-section of the water-filled channel, 442
  thermal image of substrate, 443

© Woodhead Publishing Limited, 2012

ceramic MEMS, 270–4
  alumina *vs.* LTCC, 271
  low temperature co-fired, 272–4
  surface micromachined, 270–2
ceramic sensors, 174
ceramic substrates, 430, 432
charge-carrier percolation, 283
chemical systems, 339–40
chemical warfare agents, 389–92
chemo-resistive effect, 279, 282
chemo-resistive gas sensing, 280
chemo-resistive sensors, 279
cholesterol, 384–5
choline oxidase amperometric biosensor, 398
chronoamperometric screen-printed immunosensor, 386
chronoamperometry, 371–2
  typical input and output waveforms, 372
co-precipitation, 291–2
  La FeO_3 powders, 292
  WO_3 powders synthesis
    synthesis via precipitation routes, 292
CO sensing, 354
coating, 554
cobaltites, 479
colloidal composites, 112
combustible sensors, 358–9
  amperometric sensor with double cells, 359
  simultaneous oxygen and methane response, 359
Commission Directive 2008/50/EC, 318
composite active materials, 424–5
conducting particle volume fraction, 116
conduction band bottom, 285
conduction mechanisms, 112–30
  current understanding, 114–30
  filler concentration dependence of conductivity
    calculated conductivity as function of volume fraction, 124
    global tunnelling network approach, 119–27
    measured conductivity as a function of RuO_2 volume fraction, 125
    percolation interpretation, 116–19
    segregated conductor-insulator composite, 122
    tunnelling decay distance values as function of available volume fraction, 126
  future trends, 130
  non-universality of the transport critical exponent for TFR, 113
  segregated microstructure of TFR large insulating grains, 117
  temperature dependence of conductivity, 127–30
conductometry, 374
conductors, 99–105
  properties of precious and base metals used in thick-film conductor compositions, 100
  silver migration, 101–3
  thick-film metallisation for solar cells, 103–5
continuous ink-jet systems (CIJ), 15
continuum percolation approach, 117
counter electrode, 369
critical path (CP) approximation, 121
cryogenic sensors, 173–4
Curie temperature, 225
Curie–Weiss behaviour, 181
cyclic voltammetry, 370–1
  typical input and output waveforms, 371

deep reactive ion etching (DRIE), 263
densification, 81, 245
deposition medium, 46–8
dielectric, 106–8, 113
DIN 43 760, 169
direct gravure offset, 17–19
  principle of gravure printing process, 17
  printing process, 18
direct size effect, 95
direct write technologies, 425–6
Direct-write Thermal Spray (DWTS), 25, 212
directive 2009/95/EC, 251
DNA multi-walled nanotube modified SPCE, 386
drop-on-demand (DOD) ink-jet systems, 15
dual laser techniques, 535–6
dye-sensitized solar cells (DSSC), 539–41
  schematic illustration, 541
dynamic release layer, 530

Efros–Shklovskii law $\alpha = 1/2$, 129
electrical conductance, 279
electroceramics, 139
electrochemical competitive enzyme-linked immunomagnetic assay, 396
electrochemical impedance spectroscopy, 374–5
electrochemical systems, 340–1
electrodes, 476–82
  anodes, 476–8
  cathodes, 478–82
electrolytes, 471, 472–5
  dense YSZ electrolyte, 474
  influence of thickness on SOFC characteristics, 473
  SDC (Sm-doped Ceria) electrolyte film, 475
  SOFC obtained by screen-print, 473
  very dense YSZ electrolyte, 474
electromechanical coupling factor, 227
electron hole, 550
encapsulation, 559
  roll-to-roll laminator, 560
environmental monitoring, 318–23
  correlation between the results of UV analysers and ozone sensor, 321

© Woodhead Publishing Limited, 2012

dynamic measurements *vs.* conventional analysers, 320–1
integrated monitoring station, 322
single sensors and monitoring unit endowed with two sensor test chambers, 319
enzyme SPCE biosensor, 385
equilibrium electrode, 353
Escherichia coli, 387
ethanol biosensors, 384

Fermi level, 283–4, 285, 286
Fermi–Dirac distribution, 283–4
ferrites, 479
ferroelectrics, 225
ferromagnetism, 180
Ferroperm, 230
filament micro-dispersing systems, 13–14
MicroPen system, 13
films, 410–11
actuation mechanisms of bulk and film active materials, 411
fired thick-film varistors, 506–7
firing, 148, 281
profiles, 65
flat heater, 444–8
breakdown voltage of insulation layer for different testing condition, 446
change in IR of a dielectric insulation layer, 445
heater element insulated stainless steel substrate, 447
test configuration for insulation resistance and dielectric strength measurement, 445
fluctuation-induced tunnelling model, 129
Fodel, 147
Fodel pastes, 11
Fodel systems, 11
fractional capacitance, 195
fuel cells (FC), 469–71
performance (current–voltage) of a PEM-FC, 471
fugitive phases, 197
functional trimming, 96

gap printing, 146
gas sensing, 279–83
gauge factor *(GF)*, 177, 179, 203
generalised pyroelectric coefficient, 243
glass-bonded conductors, 41
glass ceramic coating, 433, 437
glass ceramics, 48–9
glass frit, 229
glass substrate heater, 440–1
demister temperature–voltage characteristics, 441
resistance of demister, 440
glasses, 48–9
global tunnelling network (GTN) approach, 119–27
glucose dehydrogenase-based screen-printed biosensors, 379, 382
sequence of reactions, 379
gold nanoparticle-modified SPCE, 394
grain size, 422–4
microstructural features that can cause degradation of actuator response, 422
granular composites, 112
Gravure printing, 556
green ceramic, 10
green tape, 10

hard PZT, 228
heater tracks, 434–8
substrate on characteristic data of PTC-resistors, 437
substrate on heating up rate of different resistor elements, 437
substrate on performance characteristic of Pt-resinate resistor elements, 438
temperature regulation for heater-element with PTC and low TCR, 436
high current region, 498–501
energy bands bending in two adjacent grains of the n-type semiconductor, 500
local ‘quasi’ Fermi level, 501
polished and chemically etched surface of a ZnO-based varistor, 499
high-temperature co-fired ceramic (HTCC) technology, 134
hot air gun, 452–4
micro-hot gas gun, 454
substrate surface temperature characteristic *vs.* air fl ow rate, 454
Howatt, G., 134
humidity sensor, 457–9
set-up, 457
temperature difference between Pt-heater elements, 460
temperature difference determined by numerical simulation at ambient temperature, 461
thermal conductivity of air in dependence in water vapour content, 458
hybrid electronics, 4
hydrogen sensors, 345–6
sintered ceramic and thin film, 345
hydrothermal synthesis, 295–8
chemical equations HY *vs.* SG route for ZnO nanopowders, 297
chemical equations presenting the HY synthetic route for lanthanum titanate nanopowders, 297
monodispersed perovskite powders, 296–7
titania thick-films, 297–8
vs. sol-gel synthesis, 297–8
ZnO, 296

© Woodhead Publishing Limited, 2012

Ink-jet printing, 5, 187
Ink-jet technologies, 14–17
InSensor, 230
instant water flow heater, 448–52
  heating up of empty tube, 453
  heating up of tube by continuous water flow, 452
  illustration, 448
  material property data, 449
  power density dependence inside the tube, 451
  thermophysical data of air, 450
  thermophysical data of water, 450
  tube-natural convection, 450
  tube-water, 450
interfacial reactions, 263–4
  layers, 421
  reaction between lead from the PZT and silicon substrate, 264
intermediate temperature solid oxide fuel cells (IT-SOFC), 472, 479
inverse size effect, 95
ion mobility spectrometer, 155
isostatic lamination, 148

kentrolite, 79
Kirkendall effect, 83

λ-sensors, 343–5
  illustration and typical response after logothetis, 344
  planar made with co-fired multi-layer technology, 344
  thin film, 345
labeless immunosensor, 398
lactate biosensors, 382–4
  biosensors for the detection of lactate using Lactate oxidase or Lactate dehydrogenase, 383
lanthanum strontium manganite (LSM), 471, 478–9
laser direct-write (LDW), 526–8
  schematic illustration, 528
laser-induced forward transfer (LIFT), 527
  overview, 528–31
    evolution, 529–31
laser-printed micro-power devices, 526–45
  challenges and opportunities, 543–4
  embedded micro-power sources, 542–3
    schematic of embedded Li-ion microbattery, 542
  future trends, 544–5
  laser-induced forward transfer, 528–31
  laser transfer of complex rheological systems, 531–2
    schematic representation of forward transfer steps, 532
  power sources, 532–41
laser-printed micro-power sources, 532–41
  dye-sensitised photovoltaics, 539–41
  laser-printed microbatteries, 537
  laser-printed ultracapacitors, 534–7
  primary alkaline batteries, 537–8
  secondary batteries made by laser printing, 539
lattice percolation approach, 117
lead lanthanum zirconate titanate (PLZT), 245
lead zirconate titanate (PZT), 211, 228, 251
light beam-induced current (LBIC), 560, 562
  functional map of a P3HT/PCBM type solar cell, 563
light-emitting diode (LED), 246–7
linear piezoelectric constitute equations, 226
lithium microbatteries, 539
  cross section made by LDW and SEM images of cathode/anode electrodes, 540
low-temperature co-fired ceramic systems (LTCC), multilayer, 134–57
  applications, 150–6
    Bluetooth device with integrated antenna, 152
    flow injection analysis LTCC module, 154
    liquid-cooled, fibre-pigtailed high-power laser diode, 156
    multilayer RF structure manufactured by Kyocera, 151
    other areas of application, 154–7
    packaging and microelectronics, 150–3
    planar, liquid-cooled electronically steerable antenna, 153
    portable ion mobility spectrometer, 156
    WLAN module, 153
  commercially available materials and their properties, 135
  comparison of different technologies, 136
  compositions, 136–41
    BT particle coated with calcium boron silicate glass with LiF, 138
    dielectric LTCCs, 137–9
    non-linear LTCCs, 139–40
    pastes for LTCC systems, 140–1
  future trends, 157
  manufacturing method
    advanced methods and future trends, 149–50
    general process, 144
    printing of paste with screen-printing method, 146
    sintering profile, 149
  manufacturing methods, 141–50
    general steps, 142–9
  product design, 141–2, 143
    dimensioning, 143
    general dimension guidelines for an LTCC product, 142
  publications introduced since 2001 based on Web of Knowledge, 136

© Woodhead Publishing Limited, 2012

low temperature co-fired ceramics (LTCC), 272–4
capacitive pressure sensor, 273
piezoresistive pressure sensor, 274

macroscopic polarisation, 225
magnetoresistance ratio (MRR), 183
magnetostriction, 416
manganese, 79
Marelli, F.I., 174
mass-action law, 287
Materials Science concepts, 63–84
chemical diffusion-related interactions, 70–9
Ag solubility and diffusivity, 75
interactions due to diffusion at resistor/terminations and dielectric/contacts, 74–6
measured concentration profiles for silver and bismuth, 76
minor constituents dissolution in vitreous matrix, 74
reactions and exchange interactions in thick-film resistors, 77–9
RuO_2 and ruthenium compound solubility in silicate glasses, 72–4
sources of possible interactions in printed-and-fired thick-film resistor, 71
substrates and silicate glasses interactions, 71–2
conducting materials interactions with the organic vehicle, 65
future trends, 83–4
Kirkendall effect, 83
reactivity interactions in other systems, 82–3
redox reactions, 65–70
firing temperature profiles for thick-films, 66
phase stability diagram for selected elements of interest, 67
sintering, grain growth and Ostwald ripening, 80–2
two spherical particles at initial stages of sintering, 80
tetrahedon used to represent cross-relations, 64
MD-Films, 5
metal organic decomposition (MOD), 15
micro single-chamber solid oxide fuel cells, 488–92
miniaturised single-chamber SOFC on alumina substrate, 490
Ni-CGO/CGO/SSC realised with moulds, 491
screen-printing of SnO_2 films on silicon micro-hotplates, 490
silicon grid obtained by dry etching DRIE, 489
silicon micro-hotplate, 491
microbatteries, 537
MicroElectroMechanical Systems (MEMS)
printed thick-film, 259–75
ceramic, 270–4
future trends, 274–5
silicon, 260–70
Microflex, 252
micromachined silicon micropump, 265
micromachining, 261–3
bulk process, 262
compatibility, 264–5
sacrificial layer surface process, 261
MicroPen, 5, 13–14, 187
mixed ionic electronic conductivity (MIEC), 481
mixed potential electrode, 353–6
modified sodium potassium niobate (KNN), 251
molten carbonate fuel cells (MCFC), 470
Mott variable-range hopping behaviour, 129
multiferroic active materials, 425
multilayer ceramic capacitors (MLCC), 100
multilayer processing/contacting, 557–9
multilayer varistors (MLV), 100, 504–5
formation process, 505
Mylar, 144

n-type sensor, 287
Nafion, 535
nanopowders, 290
negative temperature coefficient thermistors, 171–2
nickel, 476, 478
nickel oxide (NiO), 471, 476
nitrates, 389
nitrites, 389
nitrogen-fired compositions, 47
NO differential sensors, 359–60
potentiometric and amperometric sensor with diffusion hole, 360
nonlinear region, 498
NO_x sensing, 355–6
laminated-type sensor attached with catalyst, 355
potentiometric and amperometric operating principles, 360–1
NO sensor principle, 361
upstream oxygen pumping down to 1000ppm, 360
nScrypt systems, 13–14

open circuit voltage (OCV), 470
Ostwald ripening, 82
overglaze dielectrics, 106
oxide-bonded TF conductors, 41
oxygen electrode, 352–3
oxygen exchange equilibrium, 287
oxygen sensors, 356–8
amperometric sensors with diffusion hole, porous layer and response curves, 356

© Woodhead Publishing Limited, 2012

oxygen vacancy, 287

Panasonic Solar Cell Handbook, 185
paste printing process, 146
pastes, 298–301
  typical components for gas sensing devices, 299
PbO powder, 229
percolation theory, 113, 116
performance–cost ratio, 563
pesticides, 389–92
  developments in the application of screen-printed biosensors, 390–1
phase-locked loop (PLL), 238
phonon scattering, 168
phosphate, 388
phosphoric acid fuel cells (PAFC), 470
photoactivation, 322–4
photocatalysis, 322–4
photosensitive vehicles, 47
piezoelectric accelerometer, 236
piezoelectric actuators, 417–19
  cantilever beam using two piezoelectric stacks to simulate in plane shear actuation, 418
  fabrications, 419–20
piezoelectric cantilever, 272
piezoelectric constants, 226
piezoelectric materials, 417
piezoelectric Micromachined Ultrasound Transducers (pMUT), 237
piezoelectric sensors, 231–43
  examples of devices and applications, 235–43
    non-linear energy harvesting system, 242
    piezoelectric Micromachined Ultrasound Transducer, 237
    PZT-on-alumina resonant piezo-layer sensor, 241
    PZT-on-steel resonant tuning fork sensor, 239
  piezoelectric transducers modelling and configurations, 231–5
    configuration types of piezoelectric transducers, 234
    equivalent circuit lumped-element model, 232
piezoelectricity, 222–3, 412–15
  d_{33} mode activated cantilever, 415
  inimorph and bimorph actuator, 413
  parallel and series of bimorph actuator, 414
  transverse, longitudinal and shear actuation of piezoelectric materials, 412
piezoresistive pressure sensor, 274
planar thick-film sensors, 362
3Plast, 251
polar axis, 223
poling, 225
polyaromatic hydrocarbons, 393–4
polychlorinated biphenyls, 392–3
polymer active materials, 424–5
polymer solar cells, 550–73
  ambient processing on flexible substrates, 553–4
  applications and demonstrations, 562–72
    adaptable small-volume applications, 567–8
    improvements in performance-cost ratio, 564
    large-volume applications, 568–9
    lighting Africa lamps from Zambia field testing, 572
    market areas, 562–6
    recent demonstrations, 569–72
    solar cell design, 567
    solar hat composed of sun hat, polymer solar cell and integrated radio, 570
    solar tracker with mounted polymer solar cell panels, 568
    Suntiles, 571
  energy level diagram of two semiconductor materials, 551
  future trends, 572–3
  history, 552–3
    illustration of normal and inverted geometry, 553
  manufacturing methods, 557–62
    encapsulation, 559
    multilayer processing and contacting, 557–9
    post-production and characterisation methods, 559–62
    series connection illustration, 558
    substrates, 557
  printing and coating methods, 554–7
  schematics of the simplest form of polymer solar cell, 551
  timeframe estimate for continued technology development, 556
polymer systems, 437–8
polymer thick-film heater, 438–40
  characteristic, 439
  characteristic of a PTC resistor, 439
polyvinylidene fluoride (PVDF), 211
porcelain enamelled steel (PES), 433
porosity, 421
positive temperature coefficient of resistance (PTC), 435
positive temperature coefficient thermistors, 169–70
potentiometric sensors, 185–6, 338
  fluid level sensor, 186
potentiometry, 374
power–law relation, 113
pre-breakdown region, 498
pre-switching region, 498
primary pyroelectric effect, 243
printed actuators, 410–26

© Woodhead Publishing Limited, 2012

actuation mechanism, 412–17
active materials printing variability, 417
magnetostriction, 416
piezoelectricity, 412–15
shape memory alloy, 416–17
films as actuators, 410–11
future trends, 424–6
direct write technologies, 425–6
multiferroic active materials, 425
polymer and composite active materials, 424–5
piezoelectric actuator fabrications, 419–20
piezoelectric actuators, 417–19
processing–properties–microstructure interrelationship, 420–4
printed films
active phases, 31–46
classification, 31
conducting materials for resistors, 31–40
conductors, 41–2
dielectrics, 42
materials for AlN, SiC, glass and other substrates, 45–6
materials for nitrogen firing, 43–5
deposition medium – vehicle, 46–8
glasses and glass ceramics, 48–9, 50
glass compositions used in resistors, 49
glass compositions used in TG conductors, 50
materials, 30–51
Materials Science concepts, 63–84
chemical diffusion-related interactions, 70–9
conducting materials interactions with the organic vehicle, 65
future trends, 83–4
Kirkendall effect, 83
reactivity interactions in other systems, 82–3
redox reactions, 65–70
sintering, grain growth and Ostwald ripening, 80–2
microelectronics, 3–7
historical perspective, 3–7
other systems, 24–5
properties as electrical components on ceramic substrates, 90–108
conductors, 99–105
dielectrics, 106–8
thick-film resistors, 91–9
properties of typical substrates materials, 51
substrates, 49–51
technologies, 3–26
from thick-films and hybrids to printed electronics, 7–22
direct gravure offset, 17–19
direct gravure offset printing process, 18
filament micro-dispersing systems, 13–14
Fodel process illustration, 12
ink transfer unit of R2R gravure printing process, 20
Ink-jet printing, 16
Ink-jet technologies, 14–17
MicroPen system, 13
offset lithographic printing process, 22
principle of gravure printing process, 17
reel-to-reel systems, 19–24
screen-printing process, 9
screen-printing technologies, 8–13
printed gas sensors
solid electrolyte, 335–62, 336–8
amperometric sensors, 356–60
future trends, 361–2
NO_x sensing device, 360–1
potentiometric sensors, 338
thermodynamically controlled sensors, 338–51
thermodynamics and kinetics controlled sensors, 352–6
printed piezoelectric film, 275
printed resistive sensor, 167–87
future trends, 187
magnetoresistive effects and sensors, 180–4
longitudinal and transverse magnetoresistance of two layers of Ni/Co, 182
magnetic properties of NiCo-based thick-films, 181
magnetoresistance ratio variation, 183
properties of thick-film magneto-resistors based on Ni and Ni-Co alloys, 182
temperature dependence of the maximum $\Delta R/R$(at H_{sat}), 182
piezoresistive properties and related sensors, 174–9
properties of materials for piezoresistive thick-film sensors, 176
RuO_2-based TFRs strain sensitivity, 178
sensor based on ceramic diaphragm and body and insulated steel membrane on steel body, 176
thick-film ceramic pressure sensor, 175
potentiometric sensors, 185–6
fluid level sensor, 186
radiant sensors, 184–5
temperature sensors, 168–74
low-temperature, cryogenic sensors, 173–4
negative temperature coefficient thermistors, 171–2
positive temperature coefficient thermistors, 169–70
resistive temperature detectors, 168–9
ruthenate conductive phase in thick-film resistors, 170
sensor design of a thick-film flow sensor for biological microsystems, 173
thermocouples, 172–3
printed semiconducting gas sensors, 278–325
applications, 318–24

© Woodhead Publishing Limited, 2012

dynamical responses to 70 ppb of ozone for RT-UV ZnO sensor, 323
environmental monitoring, 318–22
photoactivation and photocatalysis, 322–4
sensor response based on ZnO and (Sn,W) O_3 at atmosphere variation, 324
films achieved through thick-film technology, 282
functional materials, 289–301
chemistry-controlled properties of nanopowders influencing gas sensing, 290
co-precipitation, 291–2
disadvantages of conventional solid-state synthesis route for powders, 291
hydrothermal synthesis, 295–8
processing-controlled properties of film influencing gas sensing, 290
rheology, pastes and screen-printing technology, 298–301
sol-gel synthesis, 293–5
future trends, 324
morphological, structural and electrical properties, 302–17
alternate response of a SnO_2-based thick-film sensor, 302
SnO_2-based materials, 303–7
TiO_2-based materials, 307–11
WO_3-based materials, 311–14
ZnO-based materials, 314–17
operation and modeling principles, 283–9
grain boundary barrier formation in gas environment, 284
printed thick-film
ceramic MEMS, 270–4
future trends, 274–5
MicroElectroMechanical Systems (MEMS), 259–75
silicon MEMS, 260–70
printed thick-film biosensors, 366–99
applications, 376–87
cholesterol, 384–5
ethanol biosensors, 384
food pathogens, 386–7
glucose dehydrogenase-based screen-printed biosensors, 379, 382
lactate, 382–4
miscellaneous proteins, peptides and amino acids, 385–6
nucleic acids and purines, 386
pharmaceutical and medical, 376–9
viruses, 387
environmental applications of screen-printed electrodes, 388–99
aflatoxins, 398
antibiotics, 398–9
food, 396–8
metal ion detection biosensors, 394–5
nitrates and nitrites, 389
pesticides and chemical warfare agents, 389–92
phosphate, 388
polyaromatic hydrocarbons, 393–4
polychlorinated biphenyls, 392–3
stripping voltammetry immunoassay, 395–6
whole cell photosynthetic pesticide biosensors, 392
overview, 366–76
biosensor definition, 368
electrochemical techniques, 370–5
experimental considerations, 368–70
history, 375–6
typical screen-printed electrode, 367
printed thick-film capacitive sensors, 193–217
capacitive sensing based on geometrical variations, 198–203
capacitive stain gauge with strain applied along the length, 203
normalised capacitance, sensitivity and nonlinearity, 199
normalised capacitance vs applied pressure for deformable diaphragm sensor, 200
sensing relying on changes of area, 202
sensing relying on changes of distance, 198–202
sensing relying on deformation, 202–3
three-electrode configuration for capacitive pressure sensor, 201
capacitive sensing based on permittivity variations, 203–4
three-medium model for IDT capacitor after Endres and Drost, 204
configurations and technologies, 195–8
capacitive sensors configurations, 196
devices and their applications, 205–16
capacitive absolute pressure sensor with contactless readout, 210
capacitive pressure sensor with improved linearity, 206
capacitive strain sensors configurations, 211
ceramic capacitive pressure sensor after Sippola and Ahn, 209
ceramic capacitive rain sensor, 214
Endress+Hauser ceramic capacitive pressure sensors, 207
Kavlico ceramic capacitive pressure sensor, 208
measured output signal vs time of capacitive sensor system, 216
screen-printed capacitive sensor embedded with microfluidic device, 215
thick-film capacitive differential pressure sensor cross-section, 205
thick-film capacitive humidity sensor structure, 213

© Woodhead Publishing Limited, 2012

future trends, 216–17
general concepts, 194–5
printed thick-film heater
designs, 438–54
ceramic, 441–4
glass substrates, 440–1
polymer, 438–40
stainless steel, 444–54
elements, 429–66
fabrication materials, 430–8
substrates, 430–4
tracks, 434–8
sensor and actuator applications, 455–66
printed thick-film resistors
conduction mechanisms, 112–30
current understanding, 114–30
future trends, 130
printed thick-film sensors
piezoelectric and pyroelectric sensors, 221–52
basic theory and relationships of the piezoelectric effect, 226–8
crystallography point groups and material properties, 224
ferroelectrics and hysteresis loop poling, 225
future trends, 251–2
low-curing temperature PZT films deposited by screen printing on silicon MEMS cantilever, 231
piezoelectric sensors, 231–43
piezoelectricity, pyroelectricity and ferroelectricity, 222–6
pyroelectric sensors, 243–51
PZT thick-films vs ceramic counterparts, 230
thick-films based on ferroelectric inorganic compounds, 228–31
printed varistors, 496–522
action, 497–501
current density J *vs.* the applied field F, 497
high currents, 498–501
nonlinear, switching region, 498
pre-switching or pre-breakdown, 498
ceramic ZnO-based composition, preparation and microstructure, 502–3
multilayer, 504–5
printing process in fabrication, 503–4
screen-printed and fired thick-film, 506–7
planar configuration preparation, 506
ZnO-based prepared by screen printing and tape casting, 510–21
ZnO-based thick-films and tape-casted development, 507–10
printing techniques, 554–5
different layers and method selection, 556–7
polymer solar cells categorised to dimentionality and mode of image formation, 555
suitability, 555–6
processing–properties–microstructure interrelationship, 420–4
defects and damage, 421–2
grain size, 422–4
porosity, 421
second phases, 421
ProcessOne, 556, 558
proportional exhaust oxygen sensor, 357–8
planar, 358
proton exchange membrane fuel cells (PEM-FC), 470, 472
pseudocapacitors *see* ultracapacitors
pulse trimming, 97
pyroelectric sensors, 243–51
basic theory and relationships of the pyroelectric effect, 243–5
simplified representation under short-circuit conditions, 244
examples of devices and applications, 245–51
characterisation of the pyroelectric sensor array, 249
contactless pyroelectic linear displacement sensor, 247
pyroelectric array with 8 x 8 pixels for LED spot position biaxial measurement, 248
pyroelectric elements on alumina used for thermal energy harvesting, 250
pyroelectric four-quadrant detector, 246
pyroelectricity, 223, 243

radiant sensors, 184–5
random-void model, 118, 119
redox reaction, 279
reel-to-reel systems, 19–24
flexography, 23–4
R2R flexographic printing process, 23
ink transfer unit of R2R gravure printing process, 20
offset lithography, 21–3
printing process, 22
rotogravure, 19–21
reference electrodes, 368–9
region I *see* pre-breakdown region; pre-switching region
region II *see* nonlinear region; switching region
region III *see* high current region
relaxors, 106–7
remanent polarisation, 226
resistive temperature detectors (RTD), 99, 168–9
resonant piezo-layer (ROL) sensor, 240
Restriction of Hazardous Substances (RoHSH), 251
rheology, 298–301
R2R techniques, 554, 559–60
characterisation of R2R-coated photovoltaics, 561
graph of efficiency, 562

© Woodhead Publishing Limited, 2012

ruthenium dioxide (RuO_2), 65
ruthenium oxide RTD, 173
ruthenium pyrochlores, 73

3S-rule, 279–80
sacrificial volume material (SVM), 149, 197
Salmonella, 386–7
Schottky barrier, 283, 286, 289
screen-printed biosensors
  cobalt phthalocyanine determination of hydrogen peroxide, 377–9
  analytical signal sequence of reactions in GOX based glucose biosensor, 378
screen-printed eight-electrode array, 398
screen-printed films, 508–9
  surfaces of thick-films that have been fired to remove organic additives, 509
screen-printed glucose biosensors, 376–7
  recent report summary, 380–1
screen-printed gold electrode (SPGE), 387
screen-printed piezoelectric films, 268
screen-printed varistors, 506–7
screen-printing, 281–2, 366, 510–21
  deposition, 281
  method, 146
  solid oxide fuel cells (SOFC) fabrication, 469–92
    electrodes, 476–82
    electrolytes, 472–5
    fuel cells (FC), 469–71
    future trends, 492
    micro single-chamber, 488–92
    single-chamber, 482–8
  technology, 298–301
    process yielding thick film for gas sensing devices starting engineered nanopowders, 301
    processing parameters, 300
secondary pyroelectric effect, 243
Seebeck coefficients, 172–3
selective laser sintering (SLS), 24
semi-continuum approach, 118
sequential multilayer technology, 5
serigraphy, 4
  see also silk-printing technologies
shape memory alloy, 416–17
sheet resistance, 90
silicon MEMS, 260–70
  mechanical sensors, 265–70
    circular thick-film PZT accelerometer, 269
    micromachined thick-film PZT accelerometer, 266
    micromachining for thick-film PZT accelerometer, 267
    micropump with printed thick film piezoelectric actuation, 265
  micromachining, 261–3
  process consideration, 263–5
silk-printing technologies, 8–13
  Fodel process illustration, 12
  screen printing process, 9
silver, 75, 101
silver (electrolytic) migration, 101
single-chamber solid oxide fuel cells, 482–8
  electrical performances improvement, 486
  influence of cathode material on electrical conductivity, 487
  influence of operating temperature on power density, 488
  laboratory prototype with LSM cathode, Ni-YSZ anode and gold grids, 485
  LSCF-CGO cathode deposited by screen-printing on CGO electrolyte, 487
  oscillations on the open circuit voltage (OCV) time dependence, 486
  set-up and two sides of a YSZ pellet with LSM cathode and Ni-YSZ anode, 482
  three types of geometries for single-chamber SOFC, 483
sintering, 80, 148
sintering aid, 81, 138
size effect, 95
Smart Pump, 13
soft PZT, 228
sol-gel synthesis, 293–5
  MoO_x-SnO_2 powders, 294–5
  route via inorganic salt and metaloorganic compound, 293–4
  SnO_2 powders, 294–5
    sol-gel synthesis via Sn(II)-alkoxide for NO_2 monitoring, 295
  tin dioxide (SnO_2)
    solid solutions, 295
  titanium dioxide (TiO_2), 295
  vs. hydrothermal synthesis, 297–8
  ZnO powders, 295
    gas sensors via sol-gel route, 296
solid electrolyte, 336–8
  amperometric sensors, 356–60
  future trends, 361–2
  NO_x sensing device, 360–1
  potentiometric sensors, 338
  printed gas sensors, 335–62
  thermodynamically controlled sensors, 338–51
  thermodynamics and kinetics controlled sensors, 352–6
    equilibrium electrode, 353
    mixed potential electrode, 353–6
    oxygen electrode, 352–3
solid electrolyte/mobile ions, 337–8
solid oxide fuel cells (SOFC)
  electrodes, 476–82
  electrolytes, 472–5
  fuel cells (FC), 469–71
  future trends, 492
  micro single-chamber, 488–92
  screen printing, 469–92

© Woodhead Publishing Limited, 2012

single-chamber, 482–8
spincoating, 555
stainless steel heater, 444–54
Staphylococcus, 386
stripping voltammetry, 373–4, 395–6
substrates, 49–51, 430–4, 557
ceramic material property data, 432
surface temperature in dependence on applied power, 431
temperature in homogeneity along different ceramic heater plates, 431
SunCeram II, 185
super *GF* factors, 178
supercapacitors *see* ultracapacitors
surface-micromachined ceramics, 270–2
capacitive pressure sensor, 271
surface micromachining, 261–2
surface-mount technology (SMT), 503
surface-mounted monolayer varistors (SMV), 504
surfactants, 47
switching region, 498

tape-casted varistors
progress and development, 507–10
screen-printed films, 508–9
tape casting, 508
three batches of powder, 507
tape casting, 508, 510–21
TCR drivers, 39
TCR modifiers, 39
Teflon, 144
temperature coefficient of resistance (TCR), 90, 168, 434–5
temperature humidity bias (THB) test, 102
temperature sensors, 168–74
low-temperature, cryogenic sensors, 173–4
negative temperature coefficient thermistors, 171–2
positive temperature coefficient thermistors, 169–70
resistive temperature detectors, 168–9
ruthenate conductive phase in thick-film resistors, 170
sensor design of a thick-film flow sensor for biological microsystems, 173
thermocouples, 172–3
themocrompression, 148
Thermafilm, 169
thermal spray technology, 25
thermocouples, 172–3
thermodynamic equilibrium, 342
thermodynamically controlled sensors, 338–51
electrochemical potential properties at thermodynamic equilibrium, 339–41
type I sensors, 341–6
type II sensors, 346–7
type III sensors, 347–52

thick-film actuator
heater applications, 455–66
airbag initiator element, 459–60
humidity sensor, 457–9
influence of beam width on power consumption, 456
thick-film compositions
properties as electrical components on ceramic substrates, 90–108
conductors, 99–105
dielectrics, 106–8
thick-film resistors, 91–9
thick-film printing process
multilayer low-temperature co-fired ceramic systems, 134–57
applications, 150–6
compositions, 136–41
future trends, 157
manufacturing methods, 141–50
thick-film resistors (TFRs), 91–9
laser trimming, 97
long time stability – ageing, 97–9
relative change of resistance of DuPont 1441 resistor, 98
sheet resistance, 91–3, 92
size effect, 95–6
temperature coefficient of resistance, 93–5
temperature dependence of resistance, 94
trimming, 96–7
thick-film sensor
heater applications, 455–66
airbag initiator element, 459–60
humidity, 457–9
influence of beam width on power consumption, 456
thick-film technology, 4, 282
tin dioxide (SnO_2), 44, 279
based materials, 303–7
arrhenius plot for conductance, 304
calcined powder, 305
Pd/SnO_2 film, 306
responses to CO and CH_4 for pure films loaded with Pd and Au, 306
powder synthesis, 294–5
solid solution synthesis, 295
titanium dioxide (TiO_2)
based materials, 307–11
Arrhenius plot for conductance, 310, 313
crystallite size of (Sn,Ti)-solid solution powders *vs.* Ti molar ratio, 312
HY-titania thick-film, 308
solid solution synthesis, 295
triaxial MEMS accelerometer, 269
true pyroelectric coefficient, 243
tubular heater, 448–54
tungsten trioxide (WO_3)
based materials, 311, 314
Arrhenius plot for conductance, 315

© Woodhead Publishing Limited, 2012

control of grain growth by the addition of Sn in the lattice, 316
(Sn,W)O_3 increased the ability of mixed oxide to detect oxidising gases, 316
powder synthesis, 292
tunneling, 288–9
tunnelling decay length, 129
tunnelling-percolation model, 117, 119
type I sensors, 341–6
principle, 341–3
potentiometric zirconia-based oxygen sensor, 341
type II sensors, 346–7
type IIIa sensors
structure of tubular NO_x type, 347
type IIIb sensors, 351
type IIIc sensors, 351

ultracapacitors, 534–7
micrograph of ultracapacitor and SEM detail of laser micromachined groove, 536
uniaxial lamination, 148

vaporisable solid, 47
varistors, 140, 141
vehicle *see* deposition medium
vias, 145
vitreous enamel resistance, 105

water-based printing vehicles, 47
water-drop (WD) tests, 102
whole cell photosynthetic pesticide biosensors, 392
working electrodes, 369–70

yttria-stabilised zirconia (YSZ), 471, 472, 474–5, 477, 478–9

zero shrinkage systems, 141
zinc oxide (ZnO)
based materials, 314, 317
fired thick-film, 318
powder synthesis, 295
ZnO-based ceramic varistors, 496, 497
composition, preparation and microstructure, 502–3
progress and development, 507–10
characterisation, 510
electrical properties measurement, 510
screen printing and tape casting characterisation, 510–21
electrical parameters comparison, 519
equilibrium of Bi_2O_3 in vapour and liquid phase in the film, 519
J-V characteristics measured in screen-printed varistors, 515
J-V characteristics measured in tape-casted varistors, 516
J-V curves, 520
microstructures comparison of tape casted layers, 521
nonlinear behaviour comparison, 520
nonlinear coefficient α of powders 1 and 2 fired at different peak temperature, 511
nonlinear coefficient α of three powders fired at different dwell times, 511
nonlinear coefficient α of three powders fired at different peak temperature, 511
platinum-based ink printed on sintered varistor layers, 518
quasi liquid-vapour equilibrium, 517
samples fired in a ‘closed’ space with Bi_2O_3 powder, 518
screen-printed thick-film *vs.* bulk varistor microstructure, 513
tape-casted layer, 513
tape casted *vs.* bulk varistor microstructure comparison, 515
thick-film varistors, 512
two types based microstructure comparison, 514

© Woodhead Publishing Limited, 2012